

(Resonanz)-Raman- und Redox-Sensitive Spektroskopie zur Prozessaufklärung in Funktionellen Molekülen

DISSERTATION

zur Erlangung des akademischen Grades
doctor rerum naturalium (Dr. rer. nat.)



seit 1558

vorgelegt dem Rat der Chemisch-Geowissenschaftlichen Fakultät
der Friedrich-Schiller-Universität Jena

von Diplom-Chemikerin Linda Zedler
geboren am 28. Februar 1984 in Magdeburg

Gutachter:

1. Prof. Dr. Jürgen Popp, Jena
2. Prof. Dr. Benjamin Dietzek, Jena
3. Prof. Dr. Sven Rau, Ulm

Tag der öffentlichen Verteidigung: 05.11.2014

Inhaltsverzeichnis

1. Einleitung.....	5
2. <i>In-vivo</i>-Bestimmung der räumlichen Verteilung des Sekundär-metaboliten Fucoxanthin innerhalb und außerhalb der Alge <i>Fucus vesiculosus</i>	10
3. Raman-spektroskopische Untersuchung des Selbstheilungs-Mechanismus in Metallopolymeren	17
4. Spektroelektrochemische Untersuchungen zur Prozess-aufklärung von Elektronen-Übertragungsreaktionen	26
4.1. Spektroelektrochemische Messapparatur für UV-Vis-Absorptions- und Resonanz-Raman-Spektroskopie im Transmissionsmodus.....	28
4.2. <i>In-situ</i> -UV-Vis- und Resonanz-Raman-spektroelektrochemische Untersuchung des Modellkomplexes [(H-dcbpy) ₂ Ru(NCS) ₂] ²⁻ (N719).....	33
4.3. Akkumulation von Elektronen in photoredoxaktiven schwarzen Absorbern - eine spektroelektrochemische <i>In-situ</i> -Untersuchung	37
4.4. Charakterisierung der Elektronen- und Schwingungsstruktur reaktiver Intermediate artifizieller Photokatalysatoren	42
5. Spektroskopische Charakterisierung Rutheniumfarbstoff-funktionalisierter Goldnanopartikel ..	48
6. Zusammenfassung	54
Literaturverzeichnis.....	57
Publikationen.....	63
[Grosser et al. Biofouling.].....	65
[Bode et al. Adv. Mater.]	77
[Zedler et al. Mater. Today].....	101
[Kupfer et al. PCCP]	117
[Zedler et al. JPCC].....	141
[Zedler et al. Chem. Eur. J.]	161
[Zedler et al. Chem. Comm.]	183
[Zedler et al. RSC Adv.].....	199

Autorenschaft der Publikationen	213
Veröffentlichungen	221
Danksagung	225
Selbständigkeitserklärung	227

1. Einleitung

Die naturwissenschaftliche Forschung versucht die Gesetze der Natur zu ergründen. Das geschieht nicht nur aus rein akademischem Interesse, sondern das Verständnis natürlicher Prozesse schafft die Voraussetzung dafür, in technischen Prozessen die Prinzipien der Natur nachzuahmen.^{1,2} Dadurch ist es möglich, industrielle Prozessabläufe zu optimieren, und technologische Probleme zu lösen.³⁻¹⁰ Die Natur hat in Jahrmilliarden effiziente Lösungen für ähnliche Probleme entwickelt und durch fortwährende Selektion immer weiter optimiert und verbessert.¹¹ Kein anderer Konstrukteur arbeitet und funktioniert so genial und effizient wie die Natur selbst. Doch die Komplexität und Multifunktionalität biochemischer Prozesse machen es der Forschung synthetisch und technisch unmöglich, die Natur exakt zu kopieren. Vielmehr zielt die naturwissenschaftliche Entwicklung darauf ab, sich von der Natur inspirieren zu lassen, deren Prinzipien auf physikalischer und chemischer Ebene zu verstehen und auf artifizielle, einfachere Systeme zu übertragen.^{2,12,13} Obwohl bisher nur ein Teil der natürlich ablaufenden Prozesse in hochkomplexen Molekülen im Detail aufgeklärt sind, orientieren sich viele relevante Prozess- und Konstruktionsmechanismen an dem Vorbild der Natur, z.B. in der Material-, Umwelt- und Energieforschung.

Ziel der vorliegenden Arbeit ist die spektroskopische Aufklärung komplexer natürlicher und artifizierlicher Prozesse in Abhängigkeit der Prozessvariablen, wie in Schema 1.1 dargestellt, um die Strukturänderungen während der Variation der Prozessparameter zu bestimmen. Die Untersuchung der strukturellen Änderungen als Funktion der Prozessgröße, wie z.B. Anregungswellenlänge des Lichtes, Temperatur, Ort und Dauer der Reaktion, geben Einblicke in den Mechanismus des Prozesses. Beispielsweise ermöglicht die Strukturbestimmung von metastabilen Zwischenprodukten einer Reaktion die Aufklärung des Reaktionsverlaufs (Schema 1.1). Das systematische Studium des Einflusses solcher Parameter mittels spektroskopischer Methoden ist daher von großem Interesse, sowohl für das tiefgehende Verständnis biologischer Prozesse als auch für die detaillierte Aufklärung temperatur- oder photoinduzierter Reaktionsmechanismen von der Natur inspirierter, artifizierlicher Prozesse. Insbesondere schwingungsspektroskopische Methoden sind zur Untersuchung von strukturellen Änderungen geeignet. Da die Gesamtzahl der Schwingungsbanden von der Zahl der Atome innerhalb des Moleküls abhängt und die Schwingungsfrequenzen von der Kraftkonstante der Bindung und den an der Schwingung beteiligten Massen bestimmt werden, ist das gesamte Schwingungsspektrum so molekülspezifisch wie ein Fingerabdruck. Zur Messung der Schwingungsspektren kommen die Infrarotspektroskopie und die Raman-Streuung in Betracht. Während die IR-Spektroskopie dabei auf der Absorption von infrarotem Licht beruht, handelt es sich beim Raman-Effekt um einen inelastischen Streuprozess von Licht. Die Intensität des Streulichts hängt dabei von drei Größen ab: der Polarisierbarkeit des Moleküls α sowie von der Frequenz ω_0 und der Intensität des Anregungslichts I_0 (Formel 1).

$$I_{Raman}^{Stokes} \propto |\alpha|^2 (\omega_0 - \omega_{vib})^4 I_0 \quad (\text{Formel 1})$$

Dabei hat die Raman-Spektroskopie entscheidende Vorteile im Vergleich zur IR-Spektroskopie:

- (i) Die Raman-Streuung ermöglicht die Untersuchung wässriger Lösungen, z.B. die Analyse biologischer Proben in deren natürlicher Umgebung, was aufgrund der hohen IR-Extinktion in Wasser mit der IR-Spektroskopie nur schwer möglich ist.

- (ii) Aufgrund der Anregungswellenlängen im UV-NIR-Spektralbereich lassen sich durch Kombination des Raman-Spektrometers mit einem Mikroskop Strukturen im sub- μm -Bereich auflösen, was im Falle der IR-Spektroskopie nicht möglich ist.
- (iii) Durch Resonanz-Verstärkung lässt sich die Raman-Streuung absorbierender Moleküle bei Anregung innerhalb einer molekularen Absorptionsbande gezielt verstärken, so dass μM -Konzentrationen innerhalb einer komplexen nicht absorbierenden Matrix detektiert werden können.

Deshalb wurden in der vorliegenden Arbeit Raman-spektroskopische Verfahren eingesetzt, um verschiedene natürliche und künstliche Prozesse zu untersuchen. Die im Rahmen dieser Arbeit untersuchten Fragestellungen umfassen dabei:

1. *Die orts aufgelöste In-situ-Messung der räumlichen Verteilung des sekundären Metaboliten Fucoxanthin innerhalb und außerhalb der Alge Fucus vesiculosus mit subzellulärer räumlicher Auflösung.*

Pflanzen produzieren eine Vielzahl von Substanzen, die nicht nur zur Aufrechterhaltung der primären Lebensprozesse, wie z.B. der Photosynthese dienen, sondern als Botenstoff oder zum Schutz der Pflanze aktiv an die Umgebung abgegeben werden, die Sekundärmetabolite. Im marinen Lebensraum ist die Konkurrenz um Licht und Nährstoffe groß, daher kommt den Abwehrmechanismen ortsfester Organismen wie Makroalgen eine entscheidende Bedeutung zu.¹⁴ Eine wichtige Abwehrstrategie ist die aktive Freisetzung von Abwehrsubstanzen, die direkt den Bewuchs der Alge durch Mikro- und Makroorganismen sowie das Wachstum von Fraßfeinden inhibieren.¹⁵⁻¹⁹ In der laminaren Grenzschicht um die Braunalge *Fucus vesiculosus* wurde der Sekundärmetabolit Fucoxanthin, ein Karotinoid, nachgewiesen, dessen Funktion bisher noch nicht eindeutig geklärt werden konnte. Karotinoide können aufgrund ihrer antioxidativen Wirkung zum Schutz freigesetzt werden oder als Botenstoffe zur chemischen Übermittlung von Signalen dienen.²⁰⁻²³ Bislang wurde mit Hilfe von Extraktionsverfahren die Gesamtmenge von Fucoxanthin auf der Algenoberfläche und im umgebenden Wasser ermittelt. Wichtige Hinweise auf die ökologische Funktion des Metaboliten erfordern aber die orts aufgelöste Messung von Konzentrationsgradienten *in situ*, d.h. direkt auf der Algenoberfläche und im umgebenden Wasser. Im Rahmen dieser Arbeit ist erstmalig und beispielhaft mit Hilfe der Raman-Mikro-Spektroskopie *in situ* die räumliche Verteilung des Sekundärmetaboliten Fucoxanthin um die Alge *Fucus vesiculosus* untersucht worden.

2. *Aufklärung von Selbstheilungsmechanismen in Metallopolymeren.*

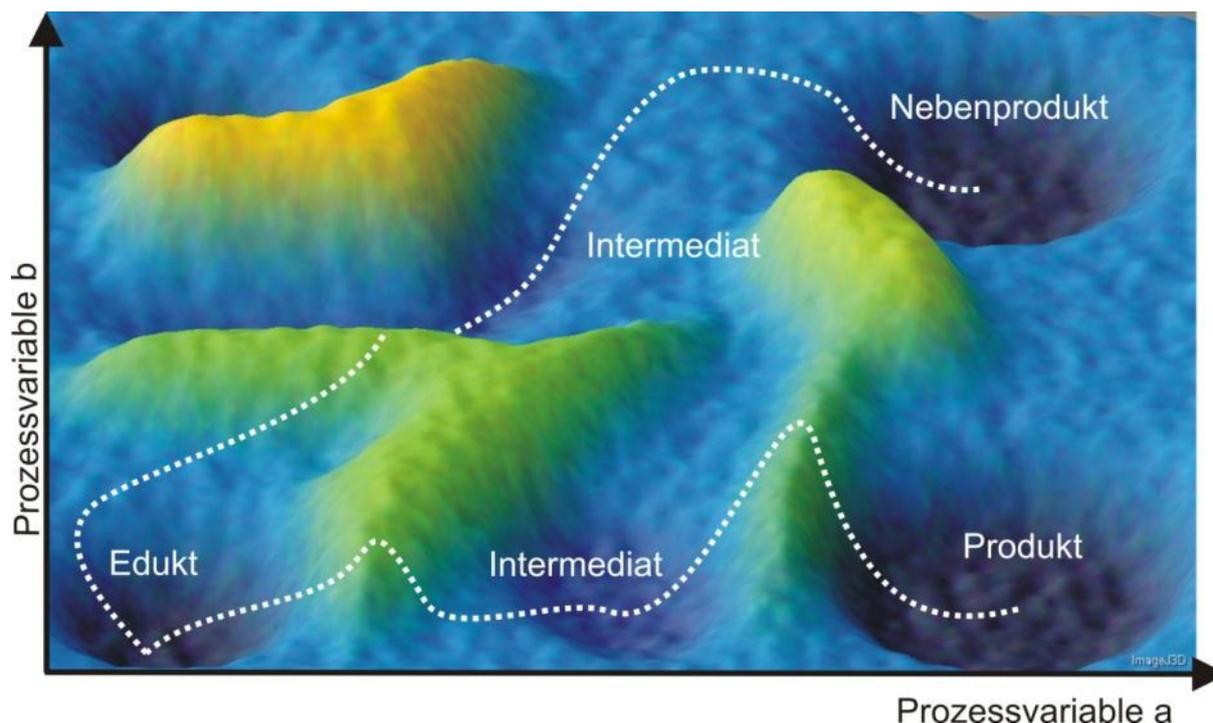
Zu den wichtigsten natürlichen Schutzmechanismen gehört die Wundheilung, eine autonome Selbstreparatur als Antwort auf Beschädigung oder Verletzung.²⁴⁻²⁶ Dabei wird das durch Verletzungen, Erkrankungen oder Umwelteinflüsse geschädigte Gewebe regeneriert, so dass die ursprünglichen mechanischen Eigenschaften und die Funktion wieder hergestellt werden. Im Detail handelt es sich um einen hochkomplexen biologischen Prozess, bei dem die benötigten Makromoleküle am Ort der Verletzung synthetisiert oder gezielt dorthin transportiert werden. Dieses Verhalten auch in künstlichen hergestellten Materialien nachzuahmen, ist Ziel der modernen Materialforschung. Das große Interesse an sogenannten selbstheilenden Materialien rührt von ihrem Potential, durch äußere Einflüsse hervorgerufene kleinere Materialbeschädigungen wie Mikro-Risse

unter Erhalt der ursprünglichen Funktionalität und der äußerlichen Erscheinung selbst zu reparieren. Dadurch kann die Lebensdauer technologisch wichtiger Werkstücke und von schwer oder vollständig unzugänglichen Bauteilen gesteigert werden. Im Vergleich zur Wundheilung stehen die künstlichen Selbstheilungssysteme in der Materialforschung noch am Anfang der Entwicklung.^{27–30} Ein Beispiel für selbstheilende Materialien sind Metallopolymere, in denen die einzelnen Polymerstränge über Metallkomplexe an Seitenketten zu einem engmaschigen Polymergerüst quervernetzt sind.^{31–34} Das Polymer ist in der Lage, beim Erhitzen auf 100°C über einen Zeitraum von einigen Stunden kleinere Beschädigungen zu regenerieren. Der dem Heilungsprozess zugrunde liegende Mechanismus hingegen ist noch ungeklärt. Zwei Prozesse kommen für die Regeneration kleiner Risse in Betracht: entweder wird die Beweglichkeit des Polymernetzwerks unter Temperatureintrag insgesamt erhöht und die Reformierung ionischer Cluster zwischen positiv geladenen Metallkomplexen und Gegenionen induziert, oder verbrückende koordinative Bindungen zwischen Metall und Ligand öffnen sich beim Erhitzen, so dass sich Polymerstränge unter dem Einfluss der erhöhten Polymerbeweglichkeit neu anordnen und quervernetzen.^{32–35} Um zu klären, welcher der beiden Mechanismen das Selbstheilungsverhalten dominiert, muss die Struktur des Polymernetzwerks, insbesondere der verbrückenden Komplex-Einheiten, während des thermisch induzierten Heilungsprozesses analysiert werden. Daher wurde im Rahmen der vorliegenden Arbeit mit Hilfe der Raman-Mikro-Spektroskopie das Polymernetzwerk auf Strukturänderungen der verbrückenden Metallkomplexe in Abhängigkeit der Temperatur untersucht.

3. Resonanz-Raman-spektroskopische Charakterisierung elektrochemisch erzeugter molekularer Spezies.

Die Forschung nach alternativen, insbesondere regenerativen, Energiequellen zur Deckung des Energiebedarfs der Menschheit ist von großer Bedeutung. Einerseits gehen die fossilen Brennstoffe in absehbarer Zeit zur Neige, andererseits würde die vollständige Freisetzung der noch ungenutzten fossilen Brennstoffe, wie z.B. Methanhydrat, Kohle, Erdöl und –gas, eine Verstärkung des künstlichen Treibhauseffekt bewirken, so dass weite Teile der Erde davon in erheblichem Maße betroffen wären: steigender Meeresspiegel, Ausbreitung der Wüsten (Desertifikation) und Zunahme von extremen Wetterlagen.^{36–38} Besonders die Nutzung der Solarenergie, z.B. mit Hilfe von farbstoffsensibilisierten Solarzellen (dye sensitized solar cells, DSSCs), kommt als Alternative zu fossilen Energieträgern in Betracht.^{7–10} Ein weiterer wichtiger Teilaspekt stellt die Umwandlung in nutzbare elektrische Energie oder die Produktion eines energiereichen chemischen Speichermediums, wie z.B. von molekularem Wasserstoff, dar. Der Gesamtprozess der photokatalytischen Wasserspaltung mit Sonnenlicht zur umweltfreundlichen Produktion des Brennstoffs Wasserstoff stellt eine erfolgversprechende Alternative zur herkömmlichen Energieerzeugung und -speicherung dar.^{3,39–42} Für eine technische Nutzung sind die Quantenausbeute und die Stabilität der Katalysatoren noch zu gering. Und auch die zugrunde liegenden Mehrelektronen-Transferprozesse sind bislang nur unzureichend aufgeklärt. Die spektroskopische Untersuchung von Elektronen-Transferprozessen zur Optimierung der Effizienz molekularer photoaktiver Systeme bildet daher den Kern dieser Arbeit. Die photoinduzierten Ladungstransferprozesse laufen im Bereich von Femto- bis Mikrosekunden ab, so dass die Prozesse nur mit zeitaufgelösten Verfahren direkt untersucht werden können. Die im Verlauf der photoinduzierten Reaktion auftretenden langlebigen Intermediate haben dabei eine Schlüsselrolle, da an diesen metastabilen Zwischenprodukten verschiedene Reaktionspfade abzweigen (Schema 1.1). Doch die Charakterisierung von intermediären Zuständen stellt aufgrund der hohen Reaktivität,

den kurzen Lebensdauern und den geringen Konzentrationen eine Herausforderung dar. Aus diesem Grund bedarf es einer Methode Intermediate photoinduzierter Prozesse zu generieren, diese strukturell zu untersuchen und deren mögliche Reaktionspfade zu verfolgen, um Strukturmodifikationen zu identifizieren, die eine Optimierung der Reaktionsmechanismen erlauben. Durch elektrochemische Verfahren ist es möglich, Radikale und andere hochreaktive Spezies unter inerten Bedingungen zu generieren. Im Rahmen der vorliegenden Arbeit wurde daher die UV-Vis-Absorptions- und Resonanz-Raman-Spektroskopie mit elektrochemischen Verfahren kombiniert, um *In-situ*-Ladungstransferprozesse in den drei im Folgenden dargestellten Modellsystemen zu analysieren.



Schema 1.1: Das Schema zeigt den möglichen Verlauf chemischer Reaktionen wie z.B. photoinduzierter Prozesse in Abhängigkeit verschiedener Prozessvariablen (a, b), wie Anregungswellenlänge, Temperatur, Ort oder Zeit.

So werden kommerziell erhältliche und strukturell vielfältige Photosensibilisatoren wie **N719** (Ditetraethylammonium cis-bis(isothiocyanato)bis(2,2'-bipyridyl-4,4'-dicarboxylato)ruthenium(II)),⁴³ in farbstoffsensibilisierten Solarzellen eingesetzt.⁴⁴⁻⁴⁸ Die Effizienz dieser artifizieller Lichtsammel-Systeme wird dabei maßgeblich durch die photoinduzierten Ladungstransferprozesse bestimmt.⁴⁹ Im Rahmen dieser Arbeit wurden zur Aufklärung der lichtinduzierten Ladungstransferprozesse Reduktionsprodukte von **N719** elektrochemisch generiert und *In-situ*-UV-Vis- sowie Raman-spektroskopisch charakterisiert.

4*H*-Imidazole bilden eine weitere Gruppe synthetisch einfach herzustellender, strukturell vielfältiger und stark absorbierender organischer Liganden, die zweifach reduziert werden können.⁵⁰⁻⁵³ Ruthenium(II)komplexe, welche neben Terpyridin-Liganden 4*H*-Imidazol-Liganden koordinieren, besitzen ein hohes Absorptionsvermögen im sichtbaren bis nahinfraroten Bereich des Spektrums, das mittels Protonierung oder gezielter Substitution des 4*H*-Imidazol-Liganden mit funktionellen Gruppen

kontrolliert werden kann.⁵⁴ Viele photokatalytische Anwendungen basieren auf Mehrelektronen-Transferprozessen, die die Generation und (Zwischen)-Speicherung von mehreren Elektronen erfordern. Daher wurde im Rahmen dieser Arbeit mit Hilfe spektroelektrochemischer Methoden der gerichtete Zweielektronenladungstransfer auf den 4*H*-Imidazol-Ligand in Abhängigkeit von Substituenten an den Aryliminoresten des 4*H*-Imidazols untersucht.

Die katalytische Aktivität von Modellkomplexen wie $[(\text{tbbpy})_2\text{Ru}(\text{tpphz})\text{Pd}(\text{Cl})_2]^{2+}$ (tbbpy = 4,4'-di-*tert.*-butyl-2,2'-bipyridin, tpphz = tetrapyrido[3,2-*a*:2'3'-*c*:3'',2''-*h*:2''',3''''-*j*]phenazine) (**RuPd**) und $[(\text{tbbpy})_2\text{Ru}(\text{tpphz})\text{Pt}(\text{Cl})_2]^{2+}$ (**RuPt**) ist bekannt.^{4,55-62} Die Komplexe bestehen aus einem photoaktiven Rutheniumzentrum, das über einen tpphz-Brückenliganden mit einem katalytisch aktiven Pt oder Pd-Zentrum verknüpft ist. Dem tpphz-Brückenligand kommt dabei die Funktion der Elektronen-Übertragung und temporären Speicherung der Ladung zu. **RuPd** weist eine um Größenordnungen höhere Katalyseeffizienz als **RuPt** auf,⁵⁹ bildet bei Photoanregung allerdings Kolloide, so dass es sich nicht um einen homogenen molekularen Katalysator handelt. Der strukturell verwandte **RuPt**-Komplex zeigt demgegenüber eine niedrigere katalytische Aktivität, bildet jedoch keine Kolloide und ist chemisch stabil. Das molekulare Verständnis von Struktur-Dynamik-Beziehungen in solchen supramolekularen Photokatalysatoren stellt einen entscheidenden Schritt auf dem Weg zur Optimierung der Katalyseeffizienz dar. Aus der molekularen und elektronischen Struktur intermediärer Zustände der Katalyse lassen sich Einflüsse einzelner Komponenten auf den katalytischen Zyklus ableiten. Daher wurden im Rahmen dieser Arbeit die Intermediate des photokatalytischen Zyklus von **RuPd** und **RuPt** elektrochemisch generiert und spektroskopisch untersucht, um einen Einblick in den Katalysemechanismus dieser Komplexe zu gewinnen.

4. Spektroskopische Untersuchung Farbstoff-funktionalisierter Nanopartikel als Modellsysteme für heterogene Photokatalysatoren.

Funktionalisierte Nanopartikel eignen sich aufgrund ihrer großen Oberfläche als heterogene Photokatalysatoren, die sowohl Licht absorbieren als auch als katalytisch aktives Substrat dienen können.⁶³⁻⁶⁹ Dabei lassen sich die optischen und photochemischen Eigenschaften durch Variation des auf der Oberfläche immobilisierten Farbstoffs und durch Größe, Form und Zusammensetzung der Nanopartikel über einen weiten Bereich verändern, z.B. um die Photostabilität und die photoinduzierten Elektronen-Transporteigenschaften innerhalb der Grenzfläche zwischen Nanopartikel und funktionalisierten Farbstoffmolekülen zu verbessern.⁷⁰ Im Rahmen dieser Arbeit wurden daher erstmals Rutheniumfarbstoffe auf Goldnanopartikeln mit verschiedenen Syntheseverfahren immobilisiert und die Anbindung und Orientierung des Farbstoffes auf der Oberfläche mit Hilfe der oberflächenverstärkten Raman-Streuung charakterisiert.

Diese Arbeit befasst sich mit der Anwendung (Resonanz)-Raman-spektroskopischer Techniken zur Aufklärung dynamischer Prozesse in Abhängigkeit von Prozessvariablen wie Ort, Reaktionsdauer oder Anregungswellenlänge. Dabei werden die mit der Variation des Parameters einhergehenden Strukturänderungen analysiert, um den Mechanismus insgesamt und die Funktion einzelner Strukturelemente zu verstehen. Die Ergebnisse werden in den folgenden Kapiteln zusammenfassend dargestellt.

2. *In-vivo*-Bestimmung der räumlichen Verteilung des Sekundärmetaboliten Fucoxanthin innerhalb und außerhalb der Alge *Fucus vesiculosus*

Teile dieses Kapitels wurden in folgendem Artikel publiziert:

[Grosser et al. Biofouling] K. Grosser, L. Zedler, M. Schmitt, B. Dietzek, J. Popp, G. Pohnert, *Biofouling* **2012**, *28*, 687–696.

Dass nonverbale Kommunikationsprozesse nicht nur ein wesentlicher Bestandteil des sozialen Zusammenlebens der Individuen der Gattung *Homo Sapiens* sind, sondern alles Leben auf den gegenseitigen Signalaustausch angewiesen ist, ist eine der wichtigsten Erkenntnisse der modernen Informationsgesellschaft. Dennoch sind weder die vielfältigen Mechanismen der Informationsübermittlung z.B. über Botenstoffe^{71–73} noch die Funktion des Gehirns,^{74–77} z.B. im Hinblick auf Informationsverarbeitung und Informationsspeicherung, bisher im Detail verstanden.^{78,79} Ein erster Schritt zum Verständnis der Vielfalt, Funktion und Bedeutung der Kommunikation für das Leben insgesamt ist die Erforschung der Signalübermittlung innerhalb von Lebensgemeinschaften niederer Organismen. So haben chemische Abwehrmechanismen und Kommunikationsprozesse eine entscheidende Bedeutung für das Ökosystem sessiler mariner Makroalgen, da diese äußeren Einflüssen, wie z.B. Beschattung durch Bewuchs oder dem Befall von Herbivoren und Räubern nicht durch Fortbewegung entkommen können.^{15,16} Die Steuerung vielfältiger Interaktionen zwischen der Alge und ihrer Umgebung erfolgt über Sekundärmetabolite, d.h. chemische Substanzen, die von der Alge selbst produziert werden, allerdings nicht primär für Wachstum und Überleben maßgeblich sind.⁸⁰ Dazu gehören vor allem ‚Infochemikalien‘ genannte Botenstoffe, die für die Kommunikation der Individuen untereinander verantwortlich sind, und Abwehrsubstanzen, welche der Bekämpfung von Fraßfeinden dienen oder den Bewuchs der Alge durch Mikro- oder Makroorganismen inhibieren.^{17,81} Sekundärmetabolite kommen direkt auf der Algenoberfläche und in der dünnen (0,1 - 0,2 mm) angrenzenden Diffusionsschicht, der laminaren Grenzschicht, vor. Dabei steuern und kontrollieren die chemischen Gradienten der verschiedenen Metabolite in dieser Grenzschicht vielfältige ökologische Interaktionen.^{82–84} Aufgrund der Komplexität der ablaufenden Prozesse und Wechselwirkungen sowie der Schwierigkeit, *In-vivo*-Untersuchungen durchzuführen, ist über die Zusammensetzung,⁸⁵ die räumliche Verteilung und die Funktion der Metabolite innerhalb der laminaren Grenzschicht bisher wenig bekannt. Das liegt einerseits an der großen Vielzahl unterschiedlicher Substanzen, die struktursensitiv detektiert und unterschieden werden müssen, andererseits an der Tatsache, dass viele Botenstoffe nur in ausgesprochen geringen, kaum nachweisbaren Konzentrationen freigesetzt werden. Zudem erfordert die Entschlüsselung der interzellulären Kommunikation neben der molekülspezifischen Identifizierung auch die nicht-invasive Analyse der dreidimensionalen räumlichen Verteilung des zu untersuchenden Botenstoffs mit subzellulärer Auflösung, was die Zahl der geeigneten Messmethoden deutlich einschränkt.

Um die ökologischen Wechselwirkungen, Abwehrmechanismen und Kommunikation der Braunalge *Fucus vesiculosus* mit ihrer unmittelbaren Umgebung zu untersuchen, ist die Identifikation und Lokalisation der Sekundärmetabolite essentiell.

Für die Identifikation unbekannter molekularer Botenstoffe werden Extraktionsverfahren mit anschließender Aufreinigung eingesetzt. Das sogenannte ‚Dipping‘ (Eintauchen) ist ein etabliertes

Verfahren zur Extraktion von Sekundärmetaboliten von der Algenoberfläche,⁸⁶ bei dem die intakte Alge kurzzeitig in organische Lösungsmittel getaucht wird, um lediglich die extrazellulären Sekundärmetabolite zu lösen. Das Verfahren hat jedoch den Nachteil, dass z.T. auch intrazelluläre Metabolite extrahiert und die Oberfläche verletzt werden kann, was zur Verfälschung der mit diesem Verfahren bestimmten Oberflächenkonzentration des Metaboliten führen kann. Zudem sind Extraktionsverfahren zur Lokalisation der Sekundärmetabolite auf der Algenoberfläche und in deren unmittelbarer Umgebung, d.h. zur Bestimmung der chemischen Gradienten, generell nicht geeignet.

Die konfokale Raman-Mikro-Spektroskopie ermöglicht neben der Strukturaufklärung und Identifikation von Sekundärmetaboliten anhand des charakteristischen Schwingungsspektrums zusätzlich die "quantitative" Gehaltsbestimmung von Sekundärmetaboliten sowohl auf der Algenoberfläche als auch in der umgebenden laminaren Grenzschicht (Abb. 2.1) mit subzellulärer räumlicher Auflösung.⁸⁷⁻⁹⁰ Dabei eignet sie sich insbesondere für die Untersuchung wässriger Lösungen, da Wasser nur einen kleinen Raman-Streuquerschnitt aufweist.⁹¹ Im Gegensatz dazu kann die IR-Spektroskopie, die ebenfalls zur Aufnahme eines molekularen Schwingungsspektrums genutzt werden kann, auf Grund der starken Absorption von IR-Licht in Wasser nur schwierig in wässrigen Medien eingesetzt werden.⁹¹ Ein empfindlicher Nachteil der Raman-Streuung ist die niedrige Sensitivität aufgrund zu geringer Quantenausbeuten (nur jedes Millionste Photon führt zur Raman-Streuung), da die Sekundärmetabolite nur in niedriger Konzentration vorliegen. Es ist aber möglich, das intrinsisch schwache Raman-Signal durch Wahl der Raman-Anregungswellenlänge in elektronischer Resonanz mit dem Analyt deutlich zu erhöhen. Durch den Resonanz-Raman-Effekt wird das Raman-Signal des Analyten um den Faktor 10^6 verstärkt, da die Polarisierbarkeit des Moleküls bei Anregung in elektronischer Resonanz steigt. Das ermöglicht den Nachweis niedriger (μM) Metabolitkonzentrationen, so dass ein Chromophor gezielt innerhalb einer umgebenden biologischen Matrix sichtbar gemacht werden kann.^{87,92} Diese Resonanz-Verstärkung erfolgt jedoch je nach Anregungswellenlänge des Lasers selektiv und betrifft nur solche Schwingungsmoden, welche charakteristisch für die Geometrieänderung des Moleküls bei dem elektronischen Übergang sind. Deshalb sind Resonanz-Raman-Spektren weniger komplex und einfacher interpretierbar als nichtresonante Raman-Spektren.

Wichtige Sekundärmetabolite in der laminaren Grenzschicht der Braunalge *Fucus vesiculosus* (Phaeophyceae, Fucales, Fucaceae, LINNÉ 1753) sind Karotinoide, deren Funktion in diesem biologischen Kontext nicht bekannt ist. Innerhalb der Chloroplasten absorbieren diese Farbstoffmoleküle das Sonnenlicht und tragen somit zur Photosynthese bei. Ihre Funktion als Sekundärmetabolite innerhalb der Diffusionschicht der Alge konnte dagegen bis heute nicht aufgeklärt werden. Es wird einerseits vermutet, dass die Karotinoide zum chemischen Schutz der Algenoberfläche freigesetzt werden, da sie potente Antioxidantien sind. Andererseits unterscheidet sich die auf der Oberfläche von *Fucus vesiculosus* angesiedelte bakterielle Gemeinschaft deutlich von der anderer Makroalgen des gleichen Habitats, was auf einen großen regulierenden Einfluss individueller Metabolite auf den bakteriellen Bewuchs schließen lässt.^{23,93} Hierfür könnte das Pigment Fucoxanthin (Abb. 2.1), ein zu den Xantophyllen zählendes Karotinoid, verantwortlich sein, das mit 70% den größten Anteil an der Gesamtkarotinoidkomposition der Alge *Fucus vesiculosus* hat.⁹⁴ Fucoxanthin zeigt in hoher Konzentration (mM) eine antimikrobielle Wirkung.^{20,21,95} Erst kürzlich konnte die Existenz des ausschließlich intrazellulär vermuteten Fucoxanthins auf der Oberfläche der Alge *Fucus vesiculosus* nachgewiesen und mithilfe von Bioassays eine eindeutige

Korrelation zwischen der Konzentration von Fucoxanthin und dem Bakterienbewuchs auf der Algenoberfläche demonstriert werden.²³

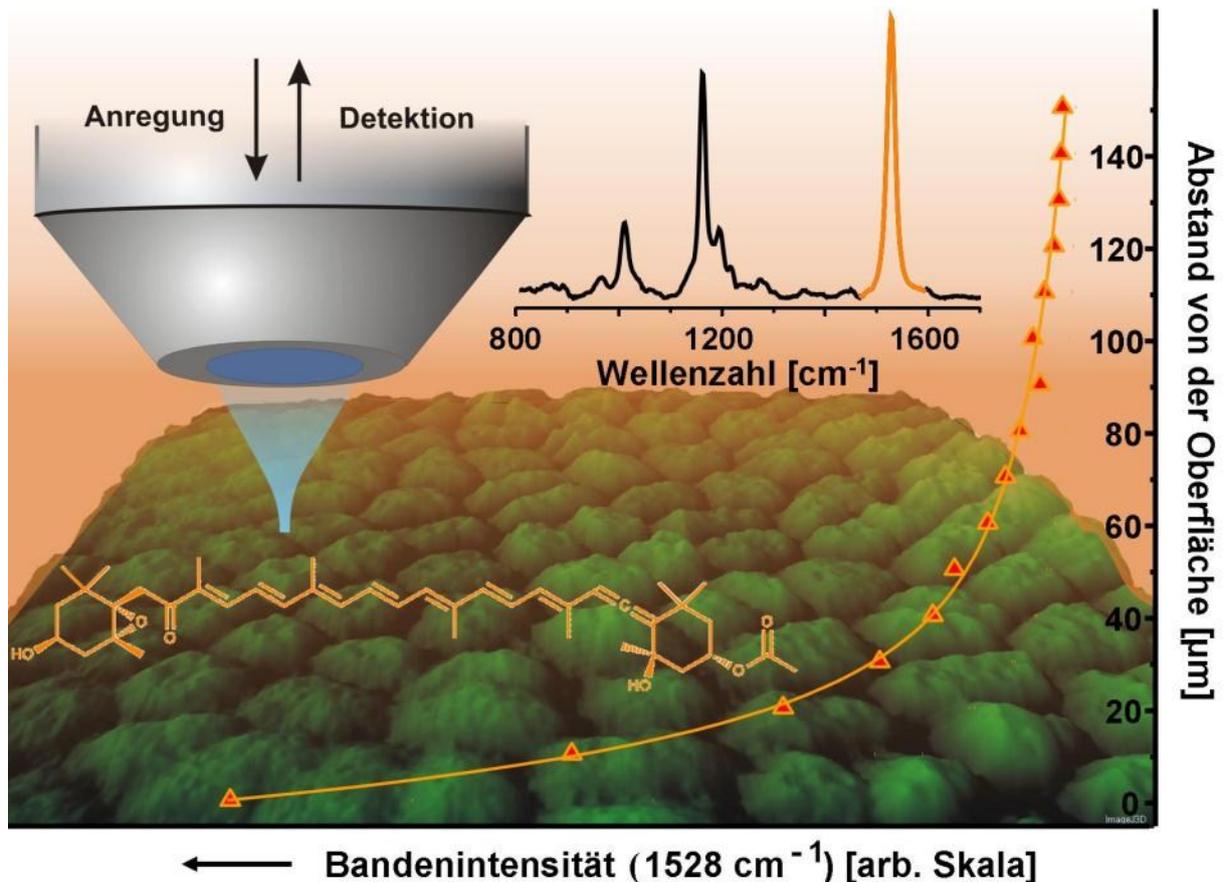


Abbildung 2.1: Schematische Darstellung des konfokalen Resonanz-Raman-Experiments für die Detektion von Metaboliten auf der Algenoberfläche und in der angrenzenden Diffusionsschicht. Zur Bestimmung der räumlichen Verteilung des Sekundärmetaboliten Fucoxanthin (Strukturformel) auf der Oberfläche und in der Umgebung der Braunalge *Fucus vesiculosus* wird die Alge in einer mit Meerwasser gefüllten Petrischale fixiert. Mithilfe eines 63x Wasserimmersionsobjektivs (C-Apochromat, Zeiss) wird der Laserstrahl ($\lambda_{\text{exc}} = 476$ nm) zur Anregung der RR-Spektren auf die Algoberfläche oder in die laminare Grenzschicht fokussiert und das inelastische Streulicht gesammelt. Zur Bestimmung der chemischen Gradienten von Fucoxanthin wurde mithilfe dieser Kombination aus Mikroskop und Raman-Spektrometer Z-Scans senkrecht zur Oberfläche, Linienscans parallel zur Oberfläche und Raman-Maps aufgenommen. Das RR-Spektrum von Fucoxanthin zeigt drei für Karotinoide charakteristische Schwingungsbanden bei 1528, 1160 und 1005 cm^{-1} . Mit zunehmender Entfernung von der Algenoberfläche nimmt die Intensität der Fucoxanthin-spezifischen Schwingungsbanden exponentiell ab, hier dargestellt für die C=C Streckschwingung bei 1528 cm^{-1} , woraus sich die räumliche Verteilung ermitteln lässt.

Das Karotinoid Fucoxanthin eignet sich besonders gut für Resonanz-Raman-Untersuchungen, da es aufgrund eines ausgedehnten delokalisierten π -Elektronensystems eine hohe Polarisierbarkeit aufweist und nur wenig der die Resonanz-Raman-Spektroskopie störenden Fluoreszenz zeigt. Bei Karotinoiden erfolgt die Anregung im sichtbaren Bereich meist in höhere elektronische Zustände wie S_2 . Nach der Regel von Kasha erfolgt die Desaktivierung eines elektronisch angeregten Moleküls in Form von Fluoreszenzemission immer vom ersten elektronisch angeregten Zustand (S_1). Eine Ausnahme bilden zwar die Karotinoide, bei denen auch der S_2 -Zustand Ausgangspunkt für

Fluoreszenz sein kann, allerdings findet diese in deutlich abgeschwächter Form statt und beeinträchtigt demzufolge weniger die Raman-Streuung.

Um das Potential der konfokalen Raman-Mikro-Spektroskopie für die nichtinvasive Analyse der räumlichen Verteilung und Funktion von Sekundärmetaboliten auf der Oberfläche und in der Umgebung mariner Makroalgen zu demonstrieren, wurden die lokalen Konzentrationsgradienten des Pigmentes Fucoxanthin in der marinen Braunalge *Fucus vesiculosus* und deren Umgebung untersucht. Aus *In-vivo*-Untersuchungen mittels orts aufgelöster Resonanz-Raman-Mikro-Spektroskopie zur Bestimmung der räumlichen Verteilung des Metaboliten sollen dabei Rückschlüsse auf die biologische Funktion des Chromophors Fucoxanthin und dessen Einfluss im chemischen Schutzmechanismus („antifouling“) der Alge gezogen werden. Die Arbeit wurde in Kooperation mit Prof. Pohnert vom Institut für Anorganische und Analytische Chemie der Friedrich-Schiller-Universität Jena durchgeführt.

Die Messung der RR-Spektren erfolgte in Resonanz mit der charakteristischen S_2 Absorption des Fucoxanthins bei einer Anregungswellenlänge von 476 nm unter Verwendung eines 63x C-Apochromat-Wasserimmersionsobjektivs (Zeiss). Zur Unterdrückung des photochemischen Bleichens der Karotinoide und zur Vermeidung von Verletzungen der Algenoberfläche wurden für die Aufnahme der RR-Spektren eine geringe Laserleistung von weniger als 1 mW an der Probe sowie eine kurze Integrationszeit von 2 s gewählt. Die räumliche Auflösung, d.h. die Ausdehnung des Laserfokus, beträgt in lateraler Richtung 250 nm, in axialer Richtung 1 μm . Das auf der Algenoberfläche gemessene RR-Spektrum wird von drei für Karotinoide charakteristischen Raman-Banden dominiert (Abb. 2.1), welche der C=C-Streckschwingung der konjugierten Doppelbindungen bei 1528 cm^{-1} , der C-C-Streckschwingung bei 1160 cm^{-1} und der Kohlenstoff-Methyl-Schwingungen (1005 cm^{-1}) zugeordnet werden können.⁹⁶ In 10- μm Schritten wurden Resonanz-Raman-Spektren in axialer Richtung gemessen. Dabei konnte in der wässrigen Umgebung der Alge mit zunehmendem Abstand von der Oberfläche eine exponentielle Abnahme der integralen Intensität aller Fucoxanthin-Raman-Banden und bei Annäherung an die Algenoberfläche eine exponentielle Zunahme der Bandenintensität detektiert werden (Abb. 2.2 A). Die Bandenintensität wurde durch Anpassen einer Gauss-Funktion bestimmt. Diese Resultate belegen, dass die Beleuchtung mit dem Laser geringer Intensität keine Penetration der Algenwand, also keine Freisetzung des Metaboliten aus dem Thallus, induziert.

Die Intensität der charakteristischen Fucoxanthinbanden nimmt mit zunehmendem Abstand von der Algenoberfläche exponentiell ab, wobei die kontinuierlich freigesetzte Fucoxanthinmenge lokal variiert, wie in Abb. 2.2. A ortsabhängig für verschiedene Thallusstücke der Alge *Fucus vesiculosus* dargestellt ist. Das charakteristische Merkmal des Konzentrationsgradienten ist die Halbwertsbreite, also der Abstand von der Oberfläche, bei dem das Fucoxanthinsignal um 50% abgenommen hat. Dabei wurden für verschiedene Positionen auf der Alge Halbwertsbreiten von 7 - 13 μm gemessen. Aufgrund der direkten Proportionalität der Raman-Streuintensität zur Konzentration des Analyten ist die Abnahme der integralen Bandenintensität mit zunehmender Entfernung von der Algenoberfläche auf einen Konzentrationsgradienten an Fucoxanthin zurückzuführen. Dieser Gradient ist weder von der Richtung der Z-Scans noch von der Probenvorbereitungszeit abhängig, so dass die erhaltenen Daten zur relativen Bestimmung der lokalen Fucoxanthin-Konzentration verwendet werden können. Aufgrund der geringen Löslichkeit von Fucoxanthin in Wasser war es nicht möglich, die zur

quantitativen Analyse notwendigen Kalibrationskurven zu erstellen, da die Resonanz-Raman-Verstärkung von der elektronischen Absorption des Chromophors abhängt und diese wiederum stark durch das verwendete Lösungsmittel beeinflusst wird. Eine semiquantitative Konzentrationsbestimmung wurde mithilfe von Dipping-Untersuchungen von Saha et al. durchgeführt.²³ Die über die Dipping-Methode erhaltene Oberflächenkonzentration von Fucoxanthin beträgt $5,7 \mu\text{g}/\text{cm}^2$. Unter der Annahme, dass der gesamte Fucoxanthingehalt innerhalb des Diffusionsvolumens bis zu einem Abstand von $150 \mu\text{m}$ von der Algenoberfläche konzentriert ist, war es möglich, eine durchschnittliche Fucoxanthinkonzentration von $580 \mu\text{mol}/\text{l}$ zu bestimmen. Zur Untersuchung der antibiotischen Aktivität von Fucoxanthin mit Hilfe von Bioassays wurden Konzentrationen von $1,5\text{-}10 \mu\text{g}/\text{cm}^2$ getestet,^{23,97,98} die bei 4 von 5 getesteten marinen Bakterienstämmen das Wachstum im gesamten Konzentrationsbereich inhibieren, während für den fünften Bakterienstamm nur die höchsten Konzentrationen wirksam sind.²³ Da mit Hilfe der Extraktions-Methode nur der Mittelwert des Fucoxanthin-Gehalts auf der gesamten oder größeren Teilen der Algenoberfläche bestimmt werden kann, wurde die Konzentration gegenüber bestimmten mikrobiellen Organismen als uneffektiv eingestuft.^{23,99} Zudem ist es nicht möglich, ortsaufgelöst die Konzentration zu messen. Die Ergebnisse der hier dargestellten RR-Messungen deuten auf eine lokal wesentlich höhere Konzentration von Fucoxanthin in der Nähe der Algenoberfläche hin (bis zu $4 \text{ mmol}/\text{l}$ in einem Abstand von ca. $10 \mu\text{m}$ von der Algenoberfläche), die für die Abwehr mikrobieller Organismen nahe der Oberfläche ausreichend sein sollte (mindestens $10 \mu\text{g}/\text{cm}^2$ Fucoxanthin).²³ Zudem lassen sich mittels ortsaufgelöster Messungen auch Unterschiede in der räumlichen Verteilung detektieren.

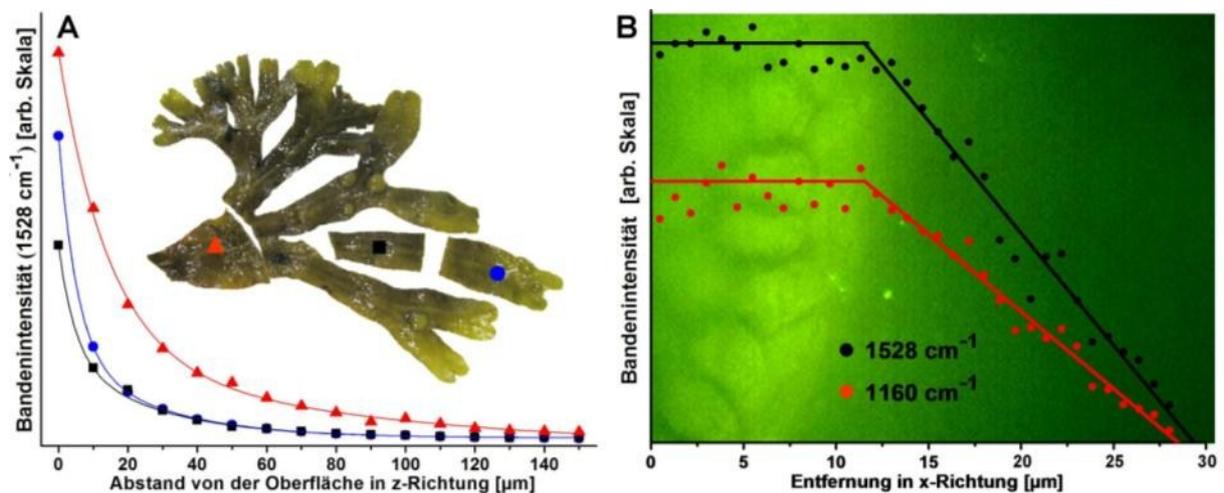


Abbildung 2.2: A: Exponentielle Abnahme der integralen Bandenintensität (1528 cm^{-1}) mit zunehmenden Abstand von der Algenoberfläche in z-Richtung für drei verschiedene Thallusabschnitte der Braunalge *Fucus vesiculosus* (Foto). B: Linienscan von der Oberfläche der Alge *Fucus vesiculosus* zum Algenrand und in die umgebende Diffusionsschicht (Mikroskopieaufnahme). Die aufgetragene Raman-Bandenintensität bei 1528 und 1160 cm^{-1} ist konstant auf der Algenoberfläche und nimmt nach Erreichen der Algengrenze linear innerhalb der ersten $15 \mu\text{m}$ ab.

Um die Homogenität der Fucoxanthinverteilung auf der Algenoberfläche zu untersuchen, wurde die Fucoxanthinkonzentration entlang einer Linie beginnend von der Thallusmitte in Richtung des Algenrandes und in die angrenzende Diffusionsschicht RR spektroskopisch untersucht (Abb. 2.2 B). Auf der Algenoberfläche variiert die integrale Intensität der Banden bei 1528 und 1160 cm^{-1} nur

leicht, während nach Erreichen des Algenrandes eine lineare Abnahme der Bandenintensitäten innerhalb der ersten 15 μm in der umliegenden laminaren Grenzschicht detektiert werden konnte (Abb. 2.2 B). Die Ergebnisse des lateralen Linienscans sind konsistent mit denen des Z-Scans, bei dem jedoch eine stärkere Abnahme der Fucoxanthinkonzentration innerhalb der ersten 15 μm festgestellt wurde (Abb. 2.2 A). Aufgrund der kürzeren gemessenen Strecke und dem geringeren Intensitätsabfall konnte der exponentielle Kurvenverlauf nicht approximiert werden.

Um die räumlichen Verteilung des Metaboliten Fucoxanthin auf der Algenoberfläche und den Einfluss anhaftender Organismen auf die Fucoxanthinkonzentration zu untersuchen, wurde ein Resonanz-Raman-Map auf einer Fläche von 50 x 50 μm^2 aufgenommen (Abb. 2.3 A). Der Abstand der Messpunkte wurde so gewählt, dass unter Berücksichtigung der Ausdehnung des Laserfokus und der Anpassung der Integrationszeit pro Messpunkt die photochemische Zerstörung des Chromophors so gering wie möglich gehalten wurde. Der in Abb. 2.3 B dargestellte Raman-Map zeigt die Intensität der C=C-Streckschwingungsbande bei 1528 cm^{-1} in Abhängigkeit der Position auf der Algenoberfläche. Dabei wurden lokale Inhomogenitäten in der Verteilung des Metaboliten im dargestellten Ausschnitt detektiert, wobei Intensitätsminima beim Vergleich mit der mikroskopischen Aufnahme eindeutig im Bereich der anhaftenden Organismen zu beobachten sind (Abb. 2.3 B).

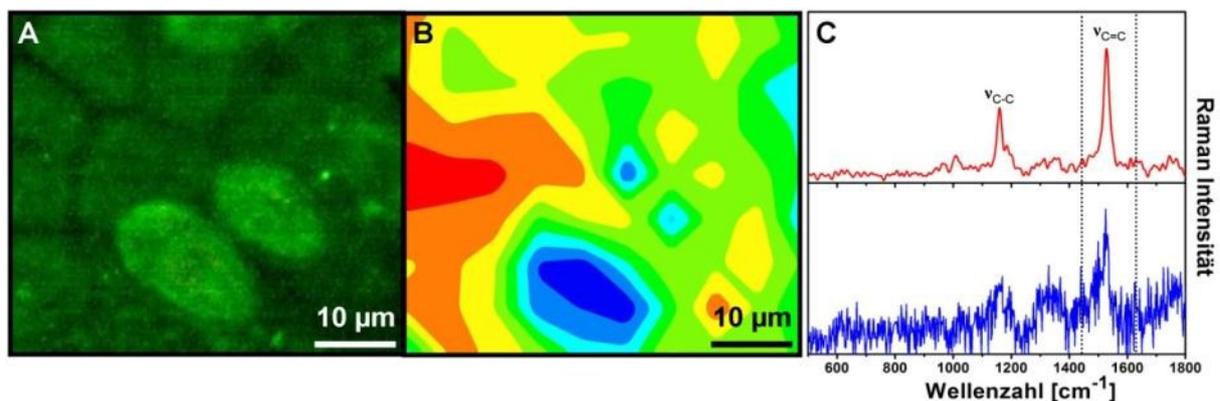


Abbildung 2.3: A: Mikroskopische Aufnahme eines 50 x 50 μm^2 großen Ausschnittes der Oberfläche von *Fucus vesiculosus* mit zwei assoziierten Diatomeen. B: Der Raman-Falschfarben-Map zeigt die Verteilung der Fucoxanthin-Konzentration basierend auf der Intensität der C=C-Streckschwingungsbande bei 1528 cm^{-1} . Rote Bereiche entsprechen einer hohen Fucoxanthin-Konzentration, während in blau gefärbten Regionen wenig Fucoxanthin angereichert ist, insbesondere im Bereich der assoziierten Diatomeen. C: RR-Spektren der Bereiche mit hoher (rot) und niedriger (blau) Metabolitkonzentration.

Bei den assoziierten Organismen handelt es sich um Diatomeen (Kieselalgen), deren Zellhülle überwiegend aus Siliziumdioxid besteht. Da Siliziumdioxid Licht sehr gut streut, ist das Signal-zu-Rausch-Verhältnis der Raman-Spektren deutlich höher als das der RR-Spektren, welche direkt auf der Algenoberfläche gemessen wurden. Zwar produzieren Diatomeen ebenfalls Karotinoide wie Fucoxanthin, allerdings wird vermutet, dass sie weniger der Metabolite an die angrenzende laminare Grenzschicht abgeben.¹⁰⁰

Die beschriebenen Ergebnisse demonstrieren das Potential der Resonanz-Raman-Mikrospektroskopie für die nichtinvasive *In-vivo*-Untersuchung von der Alge freigesetzter Metabolite mit

hoher Ortsauflösung und ohne aufwendige Probenvorbereitung. Die drei wichtigsten Ergebnisse dieser Arbeit sind im Folgenden zusammengefasst:

1) Bislang wurde angenommen, dass die Abgabe unpolarer Chromophore wie Fucoxanthin in polare Medien wie Wasser durch die Braunalge *Fucus vesiculosus* nicht aktiv und kontinuierlich erfolgt. Mit ortsaufgelösten RR-Messungen konnten Konzentrationsgradienten von Fucoxanthin detektiert werden, die auf eine kontinuierliche Freisetzung zur Aufrechterhaltung eines diffusionskontrollierten Gleichgewichts des Metabolitgehaltes innerhalb der laminaren Grenzschicht schließen lassen. Es konnte keine die Freisetzung induzierende Verletzung der Oberflächenzellen durch die Laserstrahlung festgestellt werden. Die hier dargestellten Ergebnisse beweisen damit erstmals, dass der Metabolit Fucoxanthin aktiv von der Pflanze an die Umgebung abgegeben wird.

2) Weiterhin konnte bislang mit Hilfe von Extraktionsmethoden nur der Gesamtgehalt der Sekundärmetabolite auf der Algenoberfläche und im gesamten die Alge umgebenden Flüssigkeitsvolumen bestimmt werden, nicht aber die räumliche Verteilung der Metabolite. Die dabei im Wasservolumen festgestellte mittlere Fucoxanthinkonzentration ist gegenüber einigen Bakterienstämmen zu gering, um eine antibiotische Wirkung zu entfalten. Die hochortsaufgelösten RR-Messungen hingegen weisen erstmals große Konzentrationsunterschiede in der die Alge umgebenden Lösung nach. Durch quantitative Analyse konnte erstmals die lokale Konzentration des Fucoxanthins an Hand der RR- Messungen abgeschätzt werden. Mikroorganismen werden demnach in unmittelbarer Nähe der Algenoberfläche millimolaren Konzentrationen an Fucoxanthin ausgesetzt. Die lokale Fucoxanthinkonzentration direkt auf der Algenoberfläche ist somit ausreichend, um das Wachstum von Fraßfeinden effizient zu inhibieren.

3) Mittels ortsaufgelöster RR-Messungen konnten erstmals lokale Fluktuationen in der weitgehend homogenen Fucoxanthinverteilung auf der Algenoberfläche beobachtet werden, die mit mikroskopischen Kontaminationen in Form von assoziierten Diatomeen korrelierten. Basierend auf der relativen Signalintensität konnte auf der freien Algenoberfläche eine höhere Karotinoid-Konzentration festgestellt werden als im Bereich der anhaftenden Diatomeen, was ein erster Hinweis auf eine chemische Interaktion zwischen der Alge und aufgewachsenen Diatomeen sein könnte.

3. Raman-spektroskopische Untersuchung des Selbstheilungs-Mechanismus in Metallopolymeren

Teile dieses Kapitels wurden in den folgenden Artikeln publiziert:

[Bode et al. *Adv. Mat.*] S. Bode, L. Zedler, F. H. Schacher, B. Dietzek, M. Schmitt, J. Popp, M.D. Hager, U.S. Schubert, *Adv. Mater.* **2013**, *25*, 1634-1638

[Zedler et al. *Mater. Today*] L. Zedler, M. D. Hager, U. S. Schubert, M. J. Harrington, M. Schmitt, J. Popp, B. Dietzek, *Mater. Today* **2014**, *17*, 57-69.

[Kupfer et al. *PCCP*] S. Kupfer, L. Zedler, J. Guthmuller, S. Bode, M. D. Hager, U. S. Schubert, J. Popp, S. Gräfe, B. Dietzek, *Phys. Chem. Chem. Phys.* **2014**, *16*, 12422-12432.

Die Wundheilung und die Heilung von Knochenbrüchen sind die wohl bekanntesten Selbstheilungsprozesse der Natur. Diese autonome Form der Selbstheilung, für deren Initiierung keine äußere Einflussnahme benötigt wird, beruht auf hochkomplexen zellulären Mechanismen, die nur schwer auf molekularer Ebene imitiert werden können. Dennoch ist es im Hinblick auf Ressourceneffizienz und die nachhaltige Nutzung von Werkstoffen ein wichtiges Ziel der materialwissenschaftlichen Forschung, die Selbstheilungskonzepte der Natur auf artifizielle Materialien zu übertragen.¹⁰¹⁻¹⁰⁵ Künstliche Materialien mit selbstheilenden Eigenschaften sind jedoch nicht zwingend darauf ausgelegt, ihre chemische Struktur oder Beschaffenheit nach einer Beschädigung oder Alterungsprozessen vollständig zu regenerieren. Vielmehr ist die langfristige Aufrechterhaltung der allgemeinen Funktion durch die Erhaltung funktionsrelevanter Materialeigenschaften wie z.B. Biege- und Zugfestigkeit, Elastizität oder Temperaturbeständigkeit erstrebenswert. Man unterscheidet verschiedene Materialien mit der Fähigkeit zur Regeneration danach, ob der Heilungsprozess ambient, d.h. durch externe Stimulation eingeleitet wird, oder ob das Material autonom, d.h. von selbst, Beschädigungen repariert.^{106,107} Autonom selbstheilende Materialien, welche dem biologischen Vorbild der Natur sehr ähnlich sind, haben besonders vielversprechende Anwendungen in technischen Bereichen, in denen die Materialien großen Belastungen ausgesetzt sind und/oder schwer für Reparatur und Wartung zugänglich sind, z.B. in der Luft- und Raumfahrttechnik, in Tunneln oder auch für hochbeständige Beschichtungen.^{108,109}

Die Konstruktion und Entwicklung neuartiger selbstheilender Materialien umfasst Substanzklassen wie Metalle, Keramiken, Asphalte und Polymere.^{106,107,110} Trotz unterschiedlicher intrinsischer Eigenschaften dieser Materialien können die Mechanismen der Selbstheilung mithilfe eines allgemeinen Konzeptes beschrieben werden (Abb. 3.1): Danach führt Alterung, Stress oder eine starke Beanspruchung durch Umwelteinflüsse zur Bildung von Mikrorissen (Abb. 3.1 A). Im selbstheilenden Material wird durch den Riss die Bildung einer mobilen, z.B. flüssigen, Phase induziert (B), die den Riss verfüllt und anschließend durch die Heilungsreaktion, z.B. durch Polymerisation, versiegelt (C). Nach Abschluss des Reparaturprozesses sind die mechanischen Eigenschaften (weitestgehend) regeneriert.

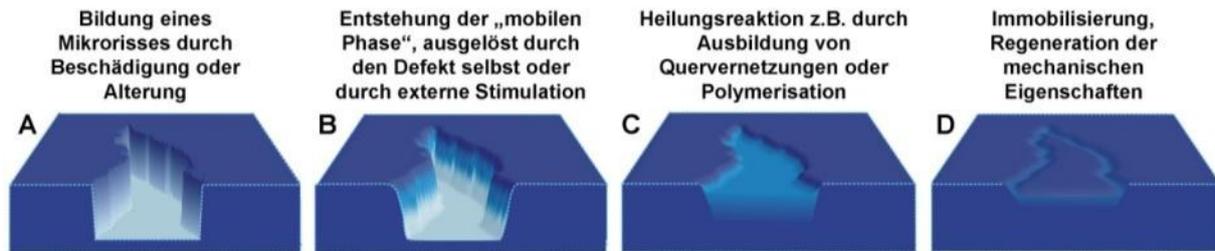


Abbildung 3.1: Durch Beschädigung oder Alterungsprozesse kommt es zur Rissbildung im Material (A). Die anschließende Entstehung der mobilen Phase wird je nach Art der Selbstheilung durch den Defekt selbst (autonome Selbstheilung) oder durch äußere Einflussnahme (ambiante Selbstheilung) z.B. Temperaturänderung ausgelöst (B). Durch gerichteten Massetransport/Materialtransport kommt es zum Auffüllen des Risses. Die dabei ablaufende Heilungsreaktion basiert entweder auf physikalischen Wechselwirkungen (z.B. Wasserstoffbrückenbindungen) und/oder auf Ausbildung chemischer Bindungen (z.B. Polymerisation) (C). Nach dem Heilungsprozess folgt das Erstarren des Materials (D). Im Idealfall führt dieser gesamte Prozess zur vollständigen Wiederherstellung der mechanischen Eigenschaften des Materials.

Intensiv wird insbesondere auf dem Gebiet der selbstheilenden Polymere und Polymerkomposite geforscht. Diese sind einerseits aufgrund ihrer geringeren Dichte im Leichtbau gegenüber klassisch etablierten Materialien wie Stahl oder Aluminium von Vorteil, andererseits durch ihre strukturelle Variabilität vielfältig funktionalisierbar. Ihr Anwendungsgebiet reicht daher von leichten Materialien für die Luft und Raumfahrt bis hin zu aktiven Materialien in Leuchtdioden auf Polymerbasis (polymer light-emitting diodes) und organischen Solarzellen.^{106,111} In Polymeren werden zwei grundlegende Mechanismen der Selbstheilung unterschieden: (i) extrinsische und (ii) intrinsische Selbstheilung. Bei der extrinsischen Heilung werden Selbstheilungsagencien nach einer Beschädigung zunächst aktiviert. Dafür werden die Träger dieser Selbstheilungsagencien (z.B. Kapseln oder Hohlfasern) in die Polymermatrix eingebracht. Bei einem auftretenden Mikroriss kommt es zur Freisetzung der Additive und anschließend zur Selbstreparatur der Beschädigung durch Polymerisation.^{112–115} Im Gegensatz dazu zeigen intrinsisch selbstheilende Materialien Heilungsvermögen ohne zusätzliche ins Polymer eingebrachte Komponenten. Beruhend auf der Ausbildung chemischer Bindungen oder physikalischer Wechselwirkungen (Adhäsion, Benetzung) zwischen den Grenzflächen eines Mikrorisses ist diese Form der Selbstheilung sicher die günstigere, allerdings nicht immer möglich und stark vom Ausmaß der Beschädigung abhängig.¹⁰⁶

Intrinsische Selbstheilungskonzepte in Polymeren und Polymerkompositen basieren auf in die Polymermatrix integrierten reversiblen Quervernetzungen, welche durch externe Trigger geöffnet werden können. Solche molekularen Wechselwirkungen beruhen entweder auf kovalenten Bindungen, welche z.B. bei Diels-Alder Reaktionen ausgebildet werden^{110,116–118} oder auf schwachen nichtkovalenten Bindungen wie z.B. Wasserstoffbrückenbindungen,¹¹⁹ ionischen Wechselwirkungen^{120,121} und π - π Wechselwirkungen^{122–125}. Ein weiteres Konzept für die Selbstheilung basiert auf reversiblen Metall-Ligand-Wechselwirkungen und konnte erst kürzlich publiziert werden.^{32–34} Inspiriert durch das biologische Vorbild der Muschelseide, deren Proteinnetz durch integrierte stabile Komplexe aus Eisenionen und L-Dopa vor Überdehnung oder Rissen geschützt wird, beruht dieses Konzept auf in Polymernetzwerke eingebaute Metall-Ligand-Strukturen, welche über koordinative Bindungen Polymerstränge miteinander quervernetzen. Die Stärke einer solchen Metall-Ligand-Bindung bestimmt sowohl das Selbstheilungsvermögen des Materials als auch die Materialeigenschaften.³⁴ Schwächer gebundene Metallkomplexe begünstigen zwar die Selbstheilung,

da leichter eine mobile Phase generiert werden kann, bedeuten aber gleichzeitig auch einen Verlust an Stabilität des Materials, da die Polymerketten durch schwache Metall-Ligand-Wechselwirkungen quervernetzt sind. Selbstheilungskonzepte auf der Basis von Metallkomplexen stellen somit immer einen Kompromiss zwischen mechanischen und Selbstheilungseigenschaften des Polymers dar. Ein spezielles System dieser Art wurde kürzlich in der Gruppe von Prof. Dr. Schubert (Institut für Organische Chemie und Makromolekulare Chemie) entwickelt. Dabei handelt es sich um ein über Terpyridin-Metallkomplexe quervernetztes Metallopolymere bestehend aus Lauryl-Methacrylat-Einheiten, welches Fähigkeiten zur Selbstheilung zeigt. Die linearen Polymerstränge sind dabei über Eisen(II)-Bisterpyridin-Komplexe oder Cadmium(II)-Bisterpyridin-Komplexe an den Seitenketten zu einem Polymergerüst quervernetzt.^{32,33} Für die Darstellung dieser Metallopolymere wurde zunächst das Terpyridin-Monomer mit Methacrylat-Monomeren copolymerisiert (Abb. 3.2 A). Die dabei angewandte RAFT (reversible addition-fragmentation chain transfer) Polymerisationstechnik ermöglicht die kontrollierte Herstellung von Polymeren mit definierter Zusammensetzung und somit regulierbaren thermischen und mechanischen Eigenschaften. Die synthetisierten Polymere weisen molare Massen von etwa 30.000 g/mol auf.^{32,33} Die Quervernetzung der Terpyridin-enthaltenden Copolymere erfolgt durch Zugabe von FeSO_4 oder CdBr_2 und führt zur Ausbildung eines Gels durch Knüpfung der koordinativen Bindung zwischen Metallion und Terpyridin-Ligand (Abb. 3.2 A).^{32,33} Durch anschließende Trocknung des Gels entsteht ein Polymerfilm mit Glasübergangstemperaturen von 30 °C, der bis zu Temperaturen von über 200 °C thermisch stabil ist.

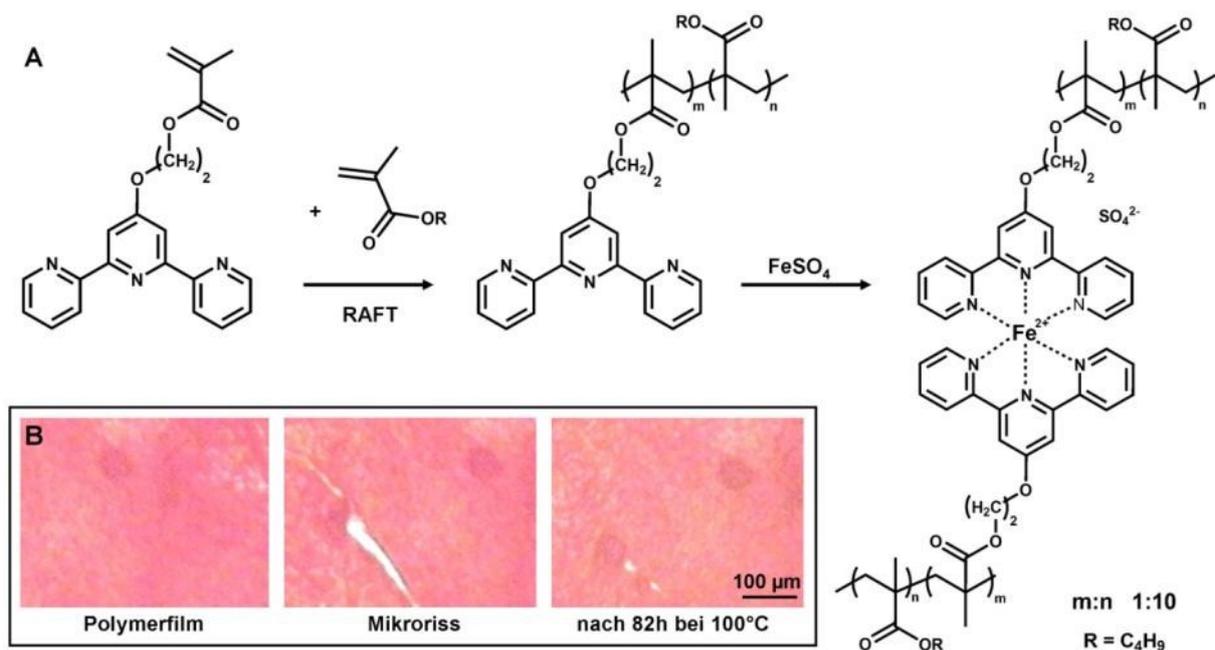
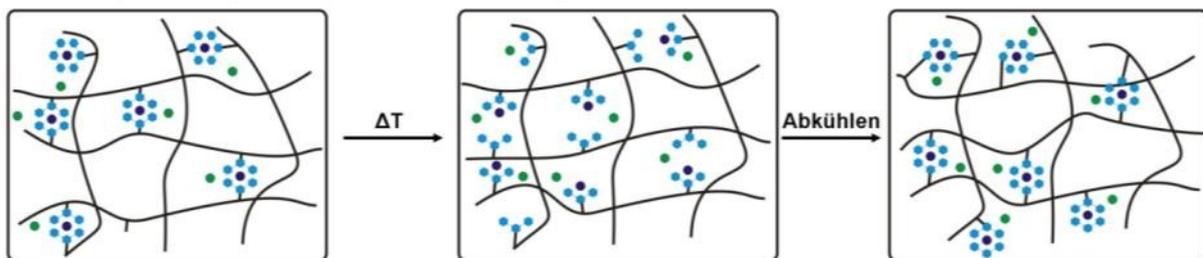


Abbildung 3.2: A) Die Herstellung des Copolymers mit einer wohldefinierten Anzahl an Terpyridin-Funktionen in den Seitenketten erfolgte mittels RAFT-Polymerisation. Die anschließende reversible Vernetzung linearer Polymerstränge beruht auf der Ausbildung von stabilen Metallkomplexen aus Terpyridin-Liganden und Fe^{2+} -Ionen. Unter identischen Bedingungen wurde das analoge Cd^{2+} -Bisterpyridin vernetzte Metallopolymere synthetisiert. B) Lichtmikroskopische Verfolgung des Selbstheilungsprozesses eines über Fe^{2+} -Bisterpyridin-Komplexe quervernetzten Polymers aus Lauryl-Methacrylateinheiten. Nach Risserzeugung erfolgte eine 82-stündige Temperierung des Polymerfilms bei 100°C. Nach dieser Heilungsphase konnte der Riss fast vollständig verfüllt werden.

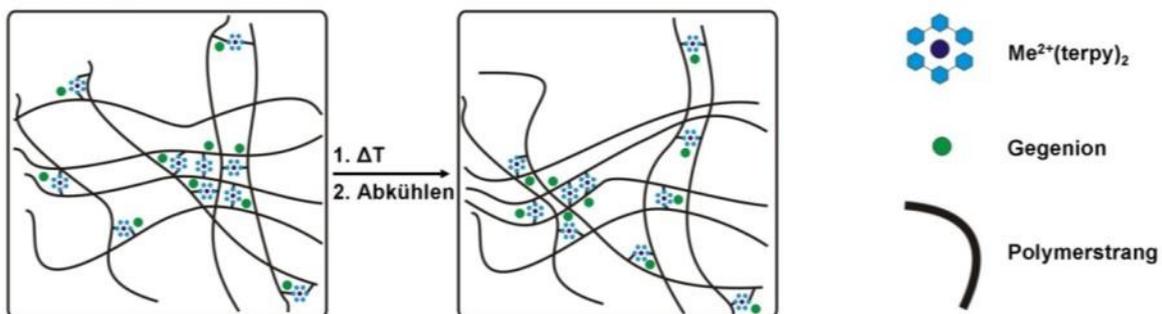
Für die Untersuchung der Selbstheilungseigenschaften wurde mechanisch mit einem Skalpell ein Riss im Film erzeugt. Ohne Energieeintrag durch Temperaturerhöhung konnte anschließend keine Selbstheilung beobachtet werden. Daher wurde der Film auf 100 °C temperiert, um eine möglichst hohe Beweglichkeit der Polymerstränge und deren Reorganisation zu ermöglichen. Die Entwicklung des Risses wurde mittels Lichtmikroskopie verfolgt (Abb. 3.2 B). Der Riss konnte im Falle des Fe²⁺-Bisterpyridin vernetzten Polymers nach 82 h bei 100 °C fast vollständig geheilt werden. Während des Temperatureintrages konnte weder das Schmelzen des Polymers noch die Bildung eines Gels aufgrund vorhandener Lösungsmittelreste beobachtet werden. Somit kann die beschriebene Regeneration des Polymerfilms ausschließlich auf die intrinsische Selbstheilungsfähigkeit des Materials zurückgeführt werden.³³ Die Prüfung der Reversibilität über drei Zyklen mittels Lichtmikroskopie ergab eine abnehmende Effizienz des Heilungsprozesses mit der Anzahl der Heilungszyklen.

Die molekularen Mechanismen dieser Selbstheilung sind noch nicht vollständig verstanden und wurden im Rahmen dieser Dissertation spektroskopisch untersucht. Auf molekularer Ebene kommen zwei Heilungsmechanismen dieser Netzwerkstruktur in Frage (Schema 3.1):

1. Dekomplexierung der Ligand-Metall-Bindung



2. Bildung ionischer Cluster



Schema 3.1: Schematische Darstellung möglicher Selbstheilungsmechanismen von Metallopolymeren. Der Aufbruch der Metall-Ligand-Bindung bei Temperaturerhöhung erhöht die Beweglichkeit der Polymerstränge und führt durch Reorganisation der Polymerstränge und Bildung neuer Vernetzungsstellen (beim Abkühlen) zur Selbstheilung (1). Die Ausbildung ionischer Cluster erfolgt durch Anhäufung mehrerer Metall-Bisterpyridin-Komplexe, welche über anziehende Kräfte mit den negativ geladenen Gegenionen zusammengehalten werden (2). Durch Temperaturerhöhung nimmt die Beweglichkeit der Polymerstränge und Gegenionen zu, die sich neu anordnen können, ohne dass das Polymernetzwerk selbst restrukturiert wird. Nach Beschädigung des Polymers führt Temperatureintrag zur (teilweisen) Auflösung und die anschließende Abkühlung zur Neubildung solcher Clusterstrukturen.

(i) Aufgrund nicht-kovalenter reversibler Bindungsmotive zwischen Metallzentrum (Fe^{2+}) und Terpyridin-Ligand besteht die Möglichkeit des Aufbruchs der Metall-Ligand-Bindung unter erhöhter Temperatur während des Heilungsprozesses (Schema 3.1). Diese (partielle) Dekomplexierung führt zur Aufhebung der Quervernetzung der linearen Polymerstränge und somit zur nötigen Flexibilität, um die Selbstheilung zu induzieren.³⁴ Im Falle eines Mikrorisses werden demnach Bindungsbrüche innerhalb der Polymerstränge nicht repariert. Durch Temperatureintrag und die damit induzierte partielle Dekomplexierung der Metall-Ligand-Bindungen ordnen sich beschädigte Polymerstränge neu an und werden durch anschließende Neuvernetzung bei Abkühlung delokalisiert.

(ii) Die zweite Möglichkeit das Selbstheilungsvermögen auf molekularer Ebene zu beschreiben, ist die über Ausbildung ionischer Cluster (Schema 3.1). Die die einzelnen Polymerstränge vernetzenden Einheiten enthalten Fe^{2+} -Ionen, die sich über anziehende Wechselwirkungen mit den ebenfalls vorliegenden negativ geladenen Sulfationen innerhalb des Polymers anordnen. Im Falle eines temperaturgesteuerten Selbstheilungsprozesses muss die Wechselwirkung innerhalb dieser Ansammlung von Metallkomplexen (partiell) aufgebrochen werden.³⁵

Im Rahmen dieser Arbeit diente die Raman-Spektroskopie zur Prozessaufklärung auf molekularer Ebene in Metall-Ligand vernetzten Polymernetzwerken unter den für den Heilungsprozess erforderlichen Bedingungen. Diese *In-situ*-Untersuchungen ermöglichen Aussagen über Änderungen der lokalen chemischen Zusammensetzung während des Selbstheilungsprozesses mit einer räumlichen Auflösung im sub- μm -Bereich. Zur Interpretation der Schwingungsspektren der komplexen Strukturen wurden von Dr. Stephan Kupfer umfangreiche QM/MM Simulationen (Kombination aus Quantenmechanik, hier Dichtefunktionaltheorie (DFT) und klassischer Mechanik, Strukturoptimierung mit Gaussian 09¹²⁶) zur Berechnungen der Raman-Spektren durchgeführt. Dazu wurden einerseits Schwingungsspektren von Strukturen, die während der Dekomplexierung des Polymernetzwerks auftreten, berechnet, andererseits die attraktiven Wechselwirkungen eines Modells für ionische Cluster untersucht. Durch Vergleich der berechneten mit den experimentellen Spektren lassen sich die an den Vernetzungsstellen ablaufenden chemischen Prozesse charakterisieren.

Die *In-situ*-Raman-Experimente wurden an zwei verschiedenen Metallopolymere durchgeführt, welche sich lediglich durch die Natur des Zentral- und Gegenions des vernetzenden Metallkomplexes unterscheiden. Das Zentralion bestimmt durch die Stärke der Metall-Ligand-Bindung maßgeblich die Stabilität des Metallopolymers sowie dessen Selbstheilungsvermögen. Die deutlich geringere Bindungsstärke des Cadmium(II)-Bisterpyridin-Komplexes im Vergleich zum Eisen(II)-Bisterpyridin-Komplex korreliert mit zu erwartenden besseren Selbstheilungseigenschaften des Cadmium-Metallopolymers, d.h. niedrigerer Aktivierungstemperatur und schnellere Heilung. Die temperaturabhängigen Messungen wurden mithilfe einer präzise temperierbaren Probenhalterung (Linkam Scientific) aufgenommen.

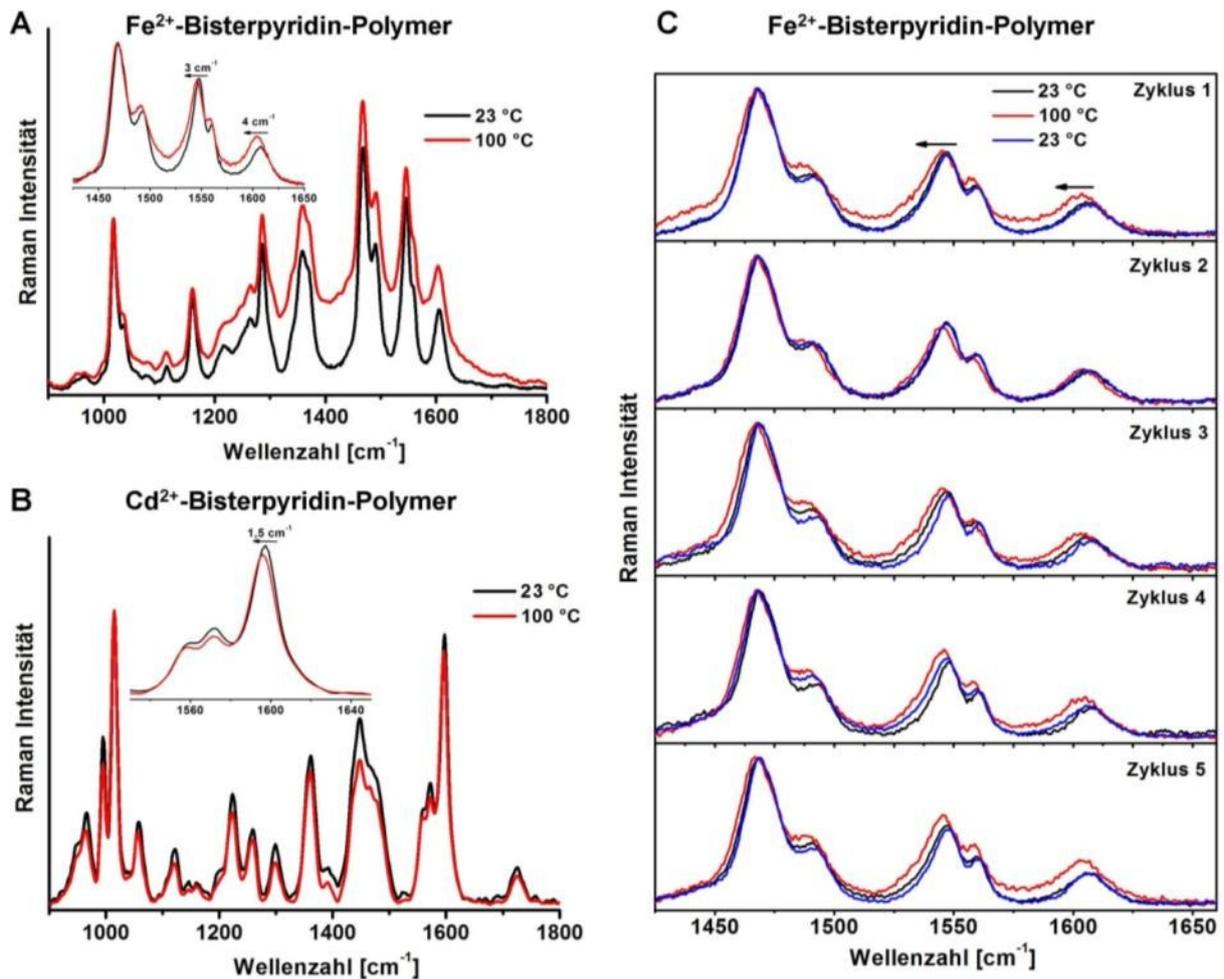


Abbildung 3.3: A) Raman-Spektren des Eisen(II)-Bisterpyridin vernetzten Metallopolymers bei 23 °C und 100°C. Die für hohe Temperaturen detektierte reversible Verschiebung der Terpyridin-Raman-Banden bei 1548 und 1608 cm^{-1} zu kleineren Wellenzahlen deutet auf den Aufbruch einiger Metall-Ligand-Bindungen innerhalb des Polymers hin. B) Aufgrund der schwächeren Metall-Ligand-Wechselwirkung innerhalb des Cadmium(II)-Bisterpyridin vernetzten Metallopolymers ist die beobachtete Verschiebung der Terpyridin-Bande bei 1600 cm^{-1} deutlich geringer ausgeprägt. C) Die Raman-Messung von fünf Heiz- und Abkühlzyklen des Eisen(II)-Bisterpyridin vernetzten Metallopolymers zeigt die Reversibilität der Bandenverschiebungen.

Abbildung 3.3 A zeigt die Raman-Spektren für das Eisen(II)-Bisterpyridin Metallopolymer gemessen bei 23 °C und 100 °C mit einer Anregungswellenlänge von 647 nm. Mit steigender Temperatur konnte eine Intensitätszunahme aller Raman-Banden sowie eine reversible Verschiebung (Abb. 3.3 C) von zwei Banden bei 1548 und 1608 cm^{-1} von jeweils 3 und 4 cm^{-1} zu kleineren Wellenzahlen detektiert werden. In guter Übereinstimmung mit den quantenmechanischen Rechnungen können diese Banden dem Terpyridin-Liganden zugeordnet werden. Das Polymergerüst aus Lauryl-Methacrylat-Einheiten trägt nicht zum theoretisch berechneten Raman-Spektrum bei, da dieses lediglich mittels Kraftfeldmethoden beschrieben ist und ihm daher keine Polarisierbarkeit zugeschrieben ist. Um die Ursache der spektralen Änderungen bei Temperaturerhöhung zu ergründen, wurden Rechnungen am freien Terpyridin-Liganden vorgenommen. Diese ergaben, dass die auf dem freien Terpyridin-Liganden lokalisierten Schwingungen eine um etwa 3 bis 14 cm^{-1} niedrigere Frequenz aufweisen als die analogen Schwingungen des komplexierten Liganden. [Kupfer et al., PCCP, Fig. 2b, Tabelle 1] Diese Ergebnisse sprechen somit für eine teilweise Dekomplexierung

der vernetzenden Metall-Ligand-Einheiten bei Temperierung des Polymers auf 100 °C. QM/MM-Simulationen am partiell dissoziierten Komplex, d.h. bei dem nur ein Terpyridin-Ligand am Fe²⁺-Ion koordiniert ist, resultieren in ähnlichen Frequenzverschiebungen (zwischen 12 und 14 cm⁻¹ zu kleineren Wellenzahlen) der Terpyridin-Banden zwischen 1450 und 1620 cm⁻¹ [Kupfer et al., PCCP, Fig. 2c, Tabelle 1). Eine zusätzliche Bestätigung der aufgestellten Hypothese, dass während der Selbstheilung die Metall-Ligand-Struktur teilweise dissoziiert, lieferten Raman-Messungen an den isolierten Strukturen, d.h. an der freien Terpyridin-Struktur, sowie dem Eisen(II)-Bisterpyridin-Komplex. Die intensivste Terpyridin-Bande erscheint im Raman-Spektrum des freien Liganden bei 1602 cm⁻¹, während für den an das Fe²⁺-Ion koordinierten Liganden eine Verschiebung dieser Bande um 6 cm⁻¹ zu höheren Wellenzahlen detektiert wird. Die Ergebnisse zeigen, dass das Selbstheilungsvermögen auf einer partiellen Dekomplexierung der vernetzenden Metall-Ligand-Strukturen basiert. Das durch Temperatureintrag induzierte reversible Aufbrechen der Metall-Ligand-Bindung erhöht die Mobilität der Polymerstränge, welche sich im Selbstheilungsprozess reorganisieren und neu vernetzen können.

Die Stabilität des Cadmium(II)-Bisterpyridin Metallpolymer wird aufgrund der schwächeren Metall-Ligand-Wechselwirkung im Vergleich zum Eisen(II)-Bisterpyridin Metallpolymer als deutlich geringer eingeschätzt, was sich ebenfalls stark auf das Ausmaß der Verschiebung der Terpyridin-Raman-Banden bei Temperatureintrag auswirken sollte. Temperaturabhängige Raman-Messungen am Cadmium(II)-Bisterpyridin Metallpolymer ($\lambda_{\text{exc}} = 785 \text{ nm}$) ergaben eine deutlich geringere Verschiebung der Terpyridin-Banden im Bereich von 1450 bis 1620 cm⁻¹ (Abb. 3.3 B). Die Terpyridin-Bande bei 1600 cm⁻¹ verschiebt sich bei Temperaturerhöhung lediglich um 1,5 cm⁻¹ zu kleineren Wellenzahlen (Abb. 3.3 B). Diese Verschiebung ist zwar reproduzierbar, aber sehr klein, d.h. sie entspricht der spektralen Breite eines Pixels der CCD, während die Spaltbreite etwa viermal größer ist, und kann somit nicht als signifikante Änderung diskutiert werden.¹ Die geringere spektrale Änderung im Vergleich zum Eisenanalogon kann mit der deutlich geringeren Stabilität des Cadmium(II)-Bisterpyridin-Komplexes erklärt werden. Die mittels QM/MM optimierte Struktur weist deutlich längere Cadmium-Stickstoff-Bindungen zwischen Cadmium und dem Terpyridin-Liganden (Cd-N: 2,33 Å (zentraler Pyridin-Ring), 2,40 Å (terminale Pyridin-Ringe des Terpyridin-Liganden)) auf als für den Eisen-Bisterpyridin-Komplex (Fe-N: 1,88 Å (zentraler Pyridin-Ring), 1,99 Å (terminale Pyridin-Ringe des Terpyridin-Liganden)) erhalten wurden. Außerdem liegt der durch die Terpyridin-Liganden aufgespannte Oktaeder im Cadmium-Komplex verzerrt vor. Verschiebungen der Terpyridin-Banden im temperaturabhängigen Raman-Spektrum sind aufgrund des geringeren Einflusses des Cadmium-Ions auf die Ligandensphäre deutlich geringer ausgeprägt. Raman-Messungen an den isolierten Verbindungen bestätigen diese Schlussfolgerung. Die intensivste Bande der Terpyridin-Struktur erscheint sowohl im Raman-Spektrum des freien Liganden als auch des Cadmium(II)-Bisterpyridin Komplexes bei 1602 cm⁻¹. Das sehr schwach koordinierende Cadmium-Ion hat demzufolge nur einen marginalen Einfluss auf die Schwingungsstruktur des komplexierten Terpyridin-Liganden. Die QM/MM-Rechnungen bestätigen die experimentell erhaltenen Daten.

¹ Die spektrale Auflösung zweier benachbarter Banden wird begrenzt durch die Abbildung des Spaltes auf dem Detektor. Zwei weniger als eine Spaltbreite voneinander auf dem Detektor entfernte Banden gleicher Intensität können nicht mehr aufgelöst werden. Im Gegensatz dazu lässt sich aber die Verschiebung einer Bande um einen Pixel relativ zu anderen, weiter entfernten Bande sicher nachweisen.

Sowohl Theorie als auch Experiment deuten auf einen Selbstheilungsmechanismus der Metallopolymere hin, der auf einer partiellen Dekomplexierung der Vernetzungsstellen beruht. D.h., die nicht-kovalenten reversiblen Bindungsmotive zwischen Metallzentrum und Terpyridin-Ligand werden bei Temperaturerhöhung aufgebrochen. Dennoch kann die Bildung ionischer Cluster innerhalb des Polymernetzwerkes nicht komplett ausgeschlossen werden.³³ Um die Eigenschaften, speziell die Dissoziationsenergien solcher ionischer Cluster zu untersuchen, wurden QM/MM-Rechnungen an Modellsystemen des Eisen(II)-Bisterpyridin und des Cadmium(II)-Bisterpyridin vernetzten Polymers durchgeführt. In einem ionischen Cluster sind mehrere Metall-Terpyridinkomplexe über Coulomb-Wechselwirkungen, vermittelt über die negativ geladenen Gegenionen, verbunden. Um diese Konformation zu modellieren, wurde die Struktur von zwei übereinanderliegenden Polymersträngen, welche um 90° gegeneinander verdreht sind, optimiert (Abb. 3.4). Am Schnittpunkt befinden sich zwei vernetzende Metallkomplexe, die über ein Gegenion verbrückt sind. Diese Struktur stellt ein kleinstmögliches Modellsystem eines ionischen Clusters dar und wurde als energetisch und somit thermodynamisch sehr stabil berechnet. Sowohl SAXS (small-angle X-ray scattering) Messungen als auch QM/MM Simulationen deuten auf die Anwesenheit stabiler ionischer Cluster hin. Dennoch ist eine Beteiligung der ionischen Cluster am Selbstheilungsmechanismus energetisch sehr unwahrscheinlich. Zur Ausbildung solcher ionischen Cluster innerhalb eines Metallopolymers bedarf es einer hohen Flexibilität der Polymerstränge. Aus den Rechnungen geht hervor, dass das Strecken der Komplexe um 30 Å, d.h. das Aufbrechen der Clusterstruktur, einem Energieaufwand von ca. 1,0 bis 2,6 eV für das Eisen(II)- und das Cadmium(II)-Metallopolymer bedarf. Ein thermischer Aufbruch der stabilen ionischen Cluster und die anschließende Bildung einer neuen Quervernetzung in Form dieser Ansammlung über Gegenionen verbrückenden Metallkomplexe ist demnach bei einem Temperatureintrag von lediglich 100°C (entspricht einer thermischen Energie von ca. 0,03 eV) sehr unwahrscheinlich.

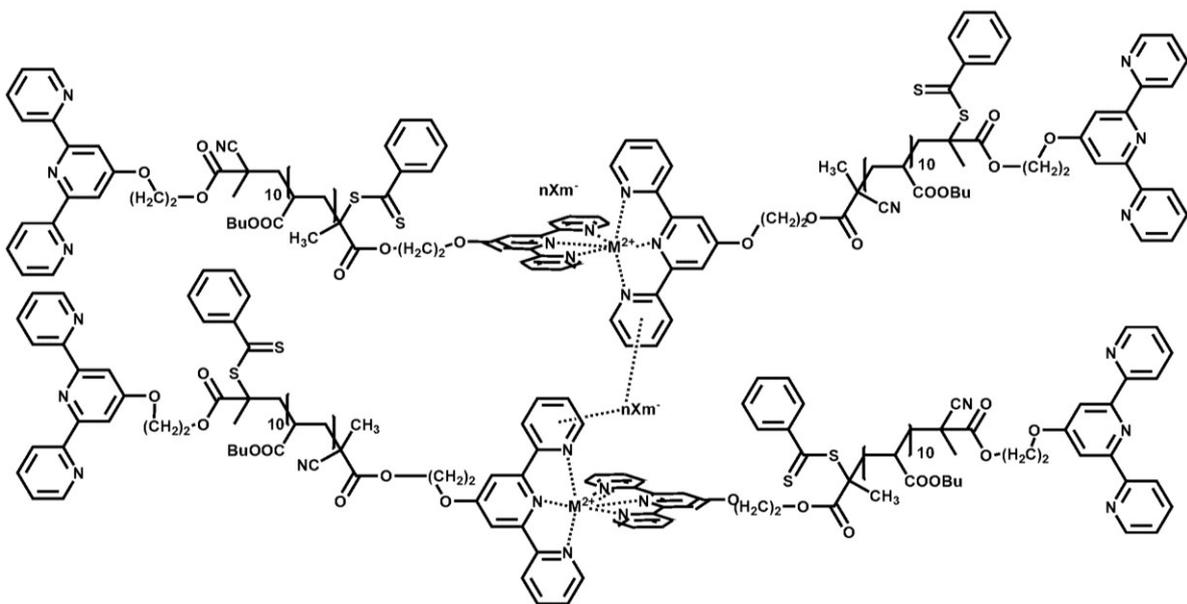


Abbildung 3.4: Polymermodell für quantenmechanische Rechnungen an ionischen Clustern ($M^{2+} = Cd^{2+}$ oder Fe^{2+}). Zwei Polymerstränge liegen um 90° verdreht übereinander, wobei sich am Schnittpunkt zwei vernetzende Metallkomplexe verbrückt über ein Gegenion befinden.

Die gewonnenen experimentellen und theoretischen Ergebnisse dokumentieren, dass die Fähigkeit der Selbstheilung der untersuchten Metallopolymere zumindest teilweise auf einer partiellen Dekomplexierung der Metall-Ligand-Bindung basiert. Die dadurch erleichterte Beweglichkeit der Polymerketten ermöglicht eine Neuordnung der Stränge und führt zur Delokalisierung der beschädigten Strukturen.

Da die Heilungsprozesse in neuartigen, zur Regeneration fähigen Materialien meist mit dem Verbrauch oder der Neubildung struktureller Einheiten gekoppelt sind, stellt die Raman-Spektroskopie als nicht-invasive und struktursensitive Methode ein vielversprechendes Werkzeug für genauere Einblicke in Selbstheilungsmechanismen auf molekularer Ebene dar. Für ein detailliertes Verständnis der in Metallopolymeren ablaufenden Selbstheilungsprozesse konnten temperaturabhängige Raman-spektroskopische Untersuchungen in Kombination mit quantenmechanischen Berechnungen einen wichtigen Beitrag leisten. Die gewonnenen Ergebnisse sind eine wichtige Voraussetzung für die Optimierung der Selbstheilungseffizienz und das maßgeschneiderte Design selbstheilender Materialien, abgestimmt auf die jeweilige Anwendung. Perspektivisch steht mit der Raman-Spektroskopie eine Methode bereit, orts aufgelöst die lokale chemische Zusammensetzung, beispielsweise innerhalb kleiner Mikrorisse, zu studieren und somit molekulare Mechanismen der Selbstheilung *in situ* zu entschlüsseln.

4. Spektroelektrochemische Untersuchungen zur Prozessaufklärung von Elektronen-Übertragungsreaktionen

Teile dieses Kapitels wurden in den folgenden Artikeln publiziert:

[Zedler et al. JPCC] L. Zedler, J. Guthmuller, I. Rabelo de Moraes, S. Kriek, M. Schmitt, J. Popp, B. Dietzek, *J. Phys. Chem. C* **2013**, *117*, 6669–6677.

[Zedler et al. Chem. Eur. J.] L. Zedler, S. Kupfer, I. Rabelo de Moraes, M. Wächtler, R. Beckert, M. Schmitt, J. Popp, S. Rau, B. Dietzek, *Chem. Eur. J.* **2014**, *20*, 3793–3799.

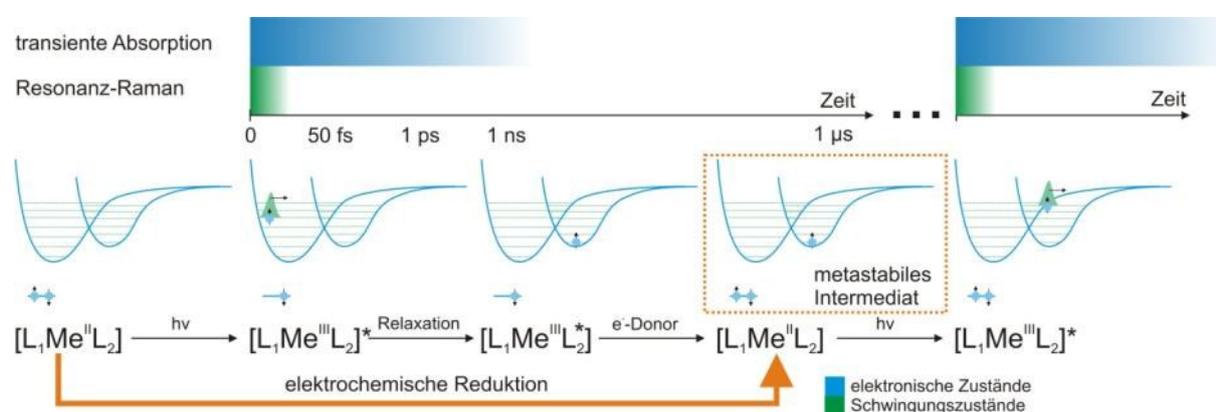
[Zedler et al. Chem. Comm.] L. Zedler, J. Guthmuller, I. Rabelo de Moraes, S. Kupfer, S. Kriek, M. Schmitt, J. Popp, S. Rau, B. Dietzek, *Chem. Commun.* **2014**, *50*, 5227-5229.

Lichtgetriebene Mehrelektronen-Transferprozesse besitzen eine enorme Bedeutung in Biologie, Chemie und Physik. Besonderes Interesse gilt der Aufklärung des Ablaufes photoinduzierter Reaktionen wie z.B. der Photosynthese.^{11,127,128} Den dabei auftretenden kurzlebigen, reaktiven Intermediaten, deren Eigenschaften, Struktur und Reaktionsverhalten oft maßgeblich die Effizienz photoinduzierter Mehrelektronen-Transferreaktionen bestimmen, kommt dabei eine Schlüsselrolle zu. Natürliche Phänomene, wie beispielsweise der menschliche Sehprozess, konnten durch spektroskopische Charakterisierung auftretender Intermediate der ultraschnellen Photoreaktionen besser verstanden und entschlüsselt werden.^{129–131} So bildet die Strukturaufklärung intermediärer Spezies chemischer Reaktionen auch die Grundlage für die synthetische Optimierung artifizierlicher lichtgetriebener molekularer Systeme, welche bislang nur unzureichend verstanden sind. Aus diesem Grund ist es neben der Aufklärung der Dynamik der photoinduzierten Prozesse erforderlich, kurzlebige und reaktive Intermediate zu generieren und strukturell und funktionell zu charakterisieren.

Zur Strukturaufklärung und Untersuchung der zeitlichen Dynamik photoinduzierter Reaktionen sind optisch-spektroskopische Verfahren besonders gut geeignet, da sich die lichtinitiierten Ladungstransferprozesse in Änderungen der Besetzung der elektronischen Zustände und der Molekülstruktur manifestieren. Das UV-Vis-Absorptionspektrum erfasst die elektronischen Übergänge der äußeren Molekülorbitale, während das gesamte Schwingungsspektrum, dessen einzelne Resonanzen jeweils von Bindungsstärke und reduzierter Masse der schwingenden funktionalen Gruppen abhängen, so charakteristisch für eine bestimmte Molekülstruktur ist wie ein Fingerabdruck. Zur Bestimmung der Struktur eignet sich besonders die Resonanz-Raman-Streuung als schwingungsspektroskopische Methode, da durch Anregung in elektronischer Resonanz (i) gezielt das Schwingungsspektrum des Chromophors gemessen wird, (ii) dessen Raman-Spektrum durch die elektronische Resonanz um einen Faktor von bis zu 10^6 verstärkt wird, wodurch sich im Vergleich zu nichtresonanter Raman-Streuung extrem niedrige Konzentrationen im μM und nM -Bereich messen lassen. (iii) Im RR-Spektrum werden die Schwingungen selektiv verstärkt, die an den elektronischen Übergang gekoppelt sind, d.h. die Moden solcher funktioneller Gruppen, welche die stärkste Geometrieänderung durch die elektronische Absorption erfahren. Zur Aufklärung der Dynamik photoinduzierter Prozesse sind zeitaufgelöste Spektroskopieverfahren wie die transiente Absorptionsspektroskopie geeignet.^{132–137}

Diese Techniken erlauben sowohl die Aufklärung von Struktur-Dynamik-Beziehungen artifizierlicher Lichtsammelkomplexe als auch die Analyse von Struktur-Eigenschafts-Beziehung lichtinduzierter Prozesse. Dennoch sind den spektroskopischen Verfahren bei der Untersuchung reaktiver

Zwischenprodukte lichtgetriebener Multielektronen-Transferprozesse gewisse Grenzen gesetzt. Zum einen können in der Regel nur Ein-Elektronen-Anregungen, aber keine Kaskade mehrerer aufeinanderfolgender Photoanregungen untersucht werden, wie in Schema 4.1 angedeutet wird. Zum anderen liefert die transiente Absorptionsspektroskopie nur begrenzte Aussagen über strukturelle Änderungen im angeregten Zustand, da selektiv die Relaxation der elektronischen Anregung verfolgt wird. Transiente Absorption erfasst die zeitliche Änderung der Absorption der elektronischen Zustände eines Moleküls nach Photoanregung, woraus sich Anzahl und Lebensdauer der angeregten Zustände sowie die Zeitkonstanten der Relaxationsprozesse ermitteln lassen. Die Methode wird primär auf Zeitskalen von Femto- bis Nanosekunden verwendet (siehe Schema 4.1). Eine Vielzahl photochemischer Reaktionen, zum Beispiel die der inter- und intramolekularen Photokatalyse, erfordern allerdings die Verfolgung von sequentiellen Multielektronen-Transferprozessen und die Charakterisierung dabei gebildeter Intermediate auf einer Zeitskala von Mikrosekunden.



Schema 4.1: Schematische Darstellung der lichtinduzierten Ladungstransferprozesse in Komplexverbindungen bestehend aus einem Metallzentrum Me und zwei Liganden L_1 und L_2 am Beispiel eines Metall-Ligand-Ladungstrfers (MLCT). Bei Lichtabsorption findet ein senkrechter (Franck-Condon) Elektronenübergang aus einem metallzentrierten Orbital in ein ligandzentriertes Molekülorbital statt. In nachfolgenden Relaxationsprozessen, z.B. Geometrieänderungen und Schwingungsrelaxation, passt sich die Kernanordnung der neuen Elektronenkonfiguration an. In photokatalytischen Systemen kann der Grundzustand durch einen Elektronendonator innerhalb von μs aufgefüllt werden. Der daraus resultierende metastabile Zustand entspricht einem elektrochemischen Reduktionsprodukt, so dass der gleiche Zustand auch elektrochemisch generiert werden kann. Von diesem Zustand ausgehend werden durch Lichtabsorption weitere Elektronen-Transferprozesse angeregt. Eine etablierte spektroskopische Methode zur zeitabhängigen Untersuchung der Entwicklung des elektronisch angeregten Zustands ist die transiente Absorption, während RR geeignet ist, um die Geometrieänderung am Franck-Condon-Punkt zu bestimmen.

Wie in Schema 4.1 dargestellt, sind die Intermediate photoinduzierter Reaktionen identisch zu Reduktionsprodukten, die elektrochemisch generiert werden können. Daher stellt die Spektroelektrochemie (SEC) einen vielversprechenden Untersuchungsansatz dar, der die elektrochemische Generation reduzierter Spezies mit der *In-situ*-spektroskopischen Charakterisierung ihrer molekularen Struktur in einer Messzelle kombiniert.^{138–141} Unter inerten Reaktionsbedingungen können durch selektive Kontrolle des Redoxzustandes auch synthetisch schwer herstellbare und reaktive Intermediate von Redoxreaktionen untersucht werden. Daher erlaubt die Spektroelektrochemie insbesondere auch die Untersuchung von Struktur und Reaktivität

elektrochemisch generierter Intermediate von Multielektronen-Transferprozessen *in situ*.^{142–144} Eine Vielzahl spektroskopischer Methoden konnte bisher mit elektrochemischen Methoden kombiniert werden. Dazu zählen insbesondere die UV-Vis/NIR Absorptions-, Raman- und ESR-Spektroskopie.^{139–141,145–149}

Aufgrund des Potentials der Spektroelektrochemie für die Strukturaufklärung von metastabilen Zwischenprodukten lichtinduzierter Ladungstransferprozesse wurde im Rahmen dieser Arbeit eine kommerziell erhältlich Messzelle für *In-situ*-UV-Vis und Resonanz-Raman (RR) spektroskopische Untersuchungen unter inerten Reaktionsbedingungen modifiziert und in einen RR-Messaufbau integriert. Die Beschreibung der Messapparatur ist in Kapitel 4.1 dargestellt. Mit diesem Aufbau wurden die photoinduzierten Prozesse in kommerziell erhältlichen, breitbandig absorbierenden Photosensibilisatoren des Typs $[(L)_2Ru(NCS)_2]$, wobei L für 2,2'-Bipyridyl-4,4'-Dicarbonsäure steht, UV-Vis- und RR-spektroelektrochemisch untersucht (Kapitel 4.2.). Kapitel 4.3 und 4.4 widmen sich der spektroelektrochemischen Untersuchung lichtinduzierter Multielektronen-Transportvorgänge in artifiziellen photoaktiven Koordinationsverbindungen basierend auf Ruthenium-Polypyridin-Farbstoffen. Kapitel 4.3 befasst sich mit der *In-situ*-Charakterisierung von breitbandig absorbierenden 4*H*-Imidazol-Chromophoren, während Kapitel 4.4 die Untersuchung des photoinduzierten Elektronen-Transfers molekularer Photokatalysatoren bestehend aus Photozentrum, Brückenligand und Katalysezentrum zum Gegenstand hat.

Vor der Darstellung der Ergebnisse der spektroelektrochemischen Untersuchungen dieser drei Systeme wird im folgenden Kapitel die spektroelektrochemische Messanordnung sowie der Ablauf eines SEC-Experiments und das prinzipielle Vorgehen bei der Interpretation der Daten mit Hilfe quantenchemischer Rechnungen vorgestellt.

4.1. Spektroelektrochemische Messapparatur für UV-Vis-Absorptions- und Resonanz-Raman-Spektroskopie im Transmissionsmodus

Im Vergleich zu reinen Elektrochemie-Zellen sind Messzellen für spektroelektrochemische Untersuchungen grundlegend anders aufgebaut, da nicht die exakte Bestimmung der Redoxpotentiale und Detektion aller Redoxstufen im Vordergrund steht, sondern die Aufnahme detaillierter Spektren der elektrochemisch generierten Spezies. Daher muss der Analyt möglichst vollständig elektrochemisch umgesetzt werden. Eine vollständige Elektrolyse allerdings kann nur mit hohem Aufwand und einer komplexen Anordnung realisiert werden, wie z.B. schnell rotierenden Netzarbeitselektroden und Trennung der Arbeitselektrode in der Analytlösung von Gegen- und Referenzelektrode über Salzbrücken.^{150,151} Meist werden Dünnschichtzellen eingesetzt, in denen einerseits durch großflächige Elektroden ein großer Teil des Analyten elektrochemisch umgesetzt wird, andererseits auch stark absorbierende Farbstoffe gemessen werden können. Weiterhin muss eine SEC-Messzelle transparent sowohl für das Anregungslicht als auch die zu detektierende Wellenlängen sein, entweder durch Verwendung von Netzelektroden oder durch transparentes Elektrodenmaterial. SEC-Zellen werden meist für Messungen im Transmissionsmodus eingesetzt, z.B. für Absorptionsmessungen in kommerziellen UV-Vis-NIR-IR-Spektrometern. Da die elektrochemisch generierten Spezies hochreaktiv sind, müssen die SEC Zellen luftdicht, lösungsmittelbeständig sowie für inertes Arbeiten geeignet sein.

Die in der Literatur am häufigsten genutzte Zelle ist die seit 2007 kommerziell erhältliche OTTLE-Zelle (OTTLE = optically transparent thin-layer electrode).^{152,153} Vorteile dieser Konfiguration sind die einfache Handhabbarkeit und die geringe Schichtdicke von weniger als 0,2 mm, so dass nur geringe Analytmengen erforderlich sind. Die Zelle ist luftdicht abgeschlossen, kann mit leichtflüchtigen Lösungsmitteln betrieben werden und erlaubt eine schnelle, vollständige Elektrolyse mit vernachlässigbarer Diffusion innerhalb der Dünnschicht. Außerdem ist eine einfache Integration der OTTLE-Zelle in alle herkömmlichen Spektrometer möglich. Für die RR-SEC Messungen in Transmission erwies sich die OTTLE-Zelle allerdings als ungeeignet, da durch das ungünstige Verhältnis von Schichtdicke der Analytlösung (200 μm) zur Dicke der durchstrahlten Kalziumfluorid-Fenster (10 mm) das Raman-Signal des Analyten vom sehr intensiven Raman-Streueuntergrund der transparenten Kalziumfluorid-Fenster überlagert wird (Abb. 4.1).

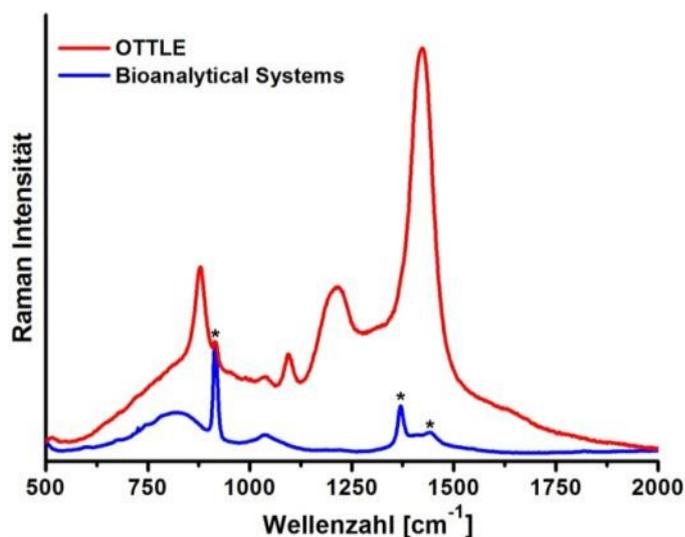


Abbildung 4.1: Raman-Spektren von Acetonitril, aufgenommen in der OTTLE-Zelle (rot) sowie in einer Dünnschichtquarzküvette mit einer Schichtdicke von 1 mm der Firma Bioanalytical Systems (blau). Während das Raman-Signal in der OTTLE-Zelle stark vom intensiven Streueuntergrund der transparenten Kalziumfluorid-Fenster überlagert wird, sind in den in der Quarzküvette gemessenen Raman-Spektrum des Acetonitrils lediglich zwei breite Quarzbanden bei 800 und 1000 cm^{-1} zu erkennen. Lösungsmittelbanden sind mit einem Stern markiert.

Aus diesem Grund wurde eine weitere Zellkonstruktion der Firma Bioanalytical Systems getestet. Diese besteht aus einer fünfseitig polierten Dünnschichtquarzküvette mit einer Schichtdicke von 1 mm und einem Fassungsvermögen von 500 μl . Quarzglas ist transparent im Bereich von 190 bis über 2000 nm, was ausreichend ist für UV-Vis und RR-Messungen. Das in der Elektrochemie häufig verwendete Lösungsmittel Acetonitril ist im Bereich zwischen 210 und 1150 nm ebenfalls transparent. Die Arbeitselektrode dieser spektroelektrochemischen Zelle ist eine Platin-Netz-Elektrode mit 80 Maschen, welche ca. 60% Transparenz aufweist und durch das große Verhältnis von Elektrodenoberfläche zu Lösungsvolumen einen großen Umsatz des Analyten an der Arbeitselektrode gewährleistet. Als Gegen- und Referenzelektrode werden eine Platin- und eine Silber/Silberchlorid Elektrode verwendet. Allerdings ist diese SEC-Zelle nicht für das Arbeiten unter inerten Bedingungen ausgelegt, da sie nicht luftdicht verschlossen werden kann. Daher wurde ein spezieller Teflonstopfen mit exakt an den Durchmesser der Elektroden angepassten Löchern und einer lösungsmittelresistenten Dichtung aus Kalrez zwischen Küvette und Stopfen angefertigt, die über 4 M2-Schrauben an einer maßangefertigten Küvettenhalterung luftdicht fixiert wird (Abb. 4.2 B). Die Konstruktion ist dabei einerseits dicht, andererseits einfach zu bedienen, so dass die Zelle in einer Glovebox unter inerten Bedingungen beladen werden kann. Die Küvettenhalterung wurde dabei so konstruiert, dass sie einerseits an Stelle der Standard Küvettenhalter in ein Cary 5000 UV-Vis-Spektrometer (Varian) eingebaut werden kann, andererseits aber auch in einen RR-Messaufbau im Transmissionsmodus integriert werden kann.

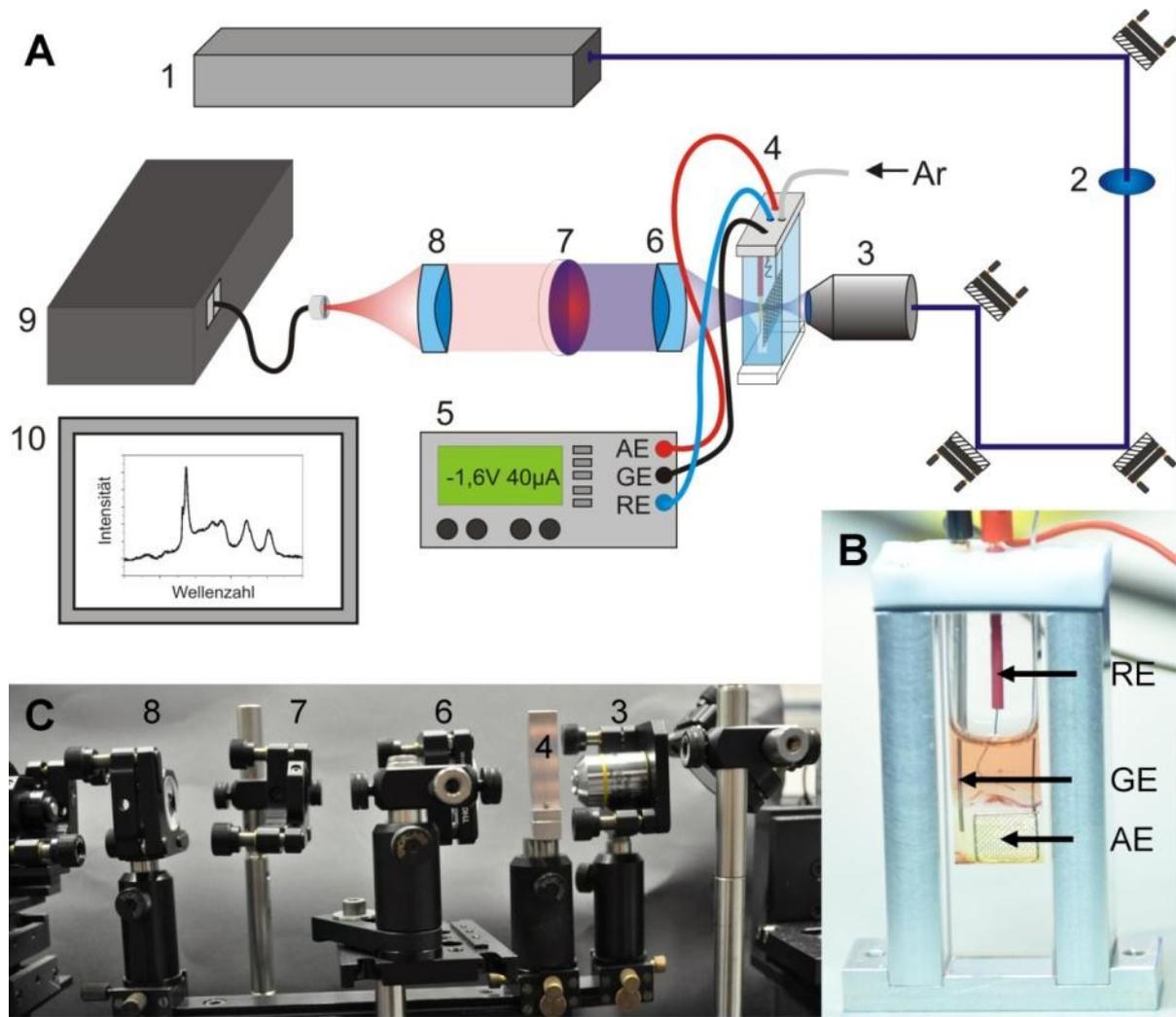


Abbildung 4.2: A) Schematische Darstellung der SEC-Messanordnung. 1: Ar-Ionen-Laser, 2: Laserlinien-Bandpassfilter, 3: Mikroskopobjektiv, 4: SEC-Messzelle, 5: Potentiostat, 6,8: UV-Vis-Achromate, 7: Langpassfilter, 9: Spektrometer, 10: Messrechner B) Foto der verwendeten SEC-Zelle in der maßgefertigten Küvettenhalterung, RE: Ag/AgCl-Referenzelektrode, GE: Pt-Gegenelektrode, AE: Platinnetz-Arbeitslektrode. C) Foto des optischen Aufbaus zur Beleuchtung der Zelle, Rekollimation des Laser- und Raman-Streulichts, (7) Filterung des Raman-Streulichts und Einkopplung in das Spektrometer.

RR-SEC Messaufbau

Im Folgenden wird der Messaufbau für RR-SEC beschrieben, der schematisch in Abbildung 4.2 A dargestellt ist. Ein Argon-Ionenlaser (1) Innova 300 (Coherent) wird als Anregungslaser verwendet. Zur Verfügung stehen im sichtbaren Bereich 528,7, 514,5, 501,7, 496,5, 488,0, 476,6, 457,9, 454,5 nm, im nahen UV 363,8 und 351,1 nm sowie im UV durch Frequenzverdopplung 257,2, 244,0, und 228,9 nm. Ein schmalbandiger Bandpassfilter (Semrock, 2) wird verwendet, um Plasmlinien zu unterdrücken. Der Laser wird über Spiegel in ein 10x Mikroskopobjektiv (3) (MPlan Olympus, NA 0,25) eingekoppelt und in der SEC-Zelle (4) in eine Masche der Arbeitslektrode fokussiert. Über den Potentiostat (5) wird das Potential an die Zelle angelegt. Eine UV-Vis entspiegelte, achromatische Linse mit 35 mm Brennweite (6, Edmund Optics) rekollimiert das Licht aus der SEC-Zelle. Ein extrem steiler Langpassfilter (7, RazorEdge, Semrock) blockiert die Laserwellenlänge, während das langwellig

Stokes-Raman-gestreute Licht den Filter passiert. Eine weitere UV-Vis entspiegelte, achromatische Linse (8) fokussiert das Raman-Streulicht auf die Endfläche einer Mehrkern-Lichtleitfaser (NA = 0,22), die das Licht zum Eintrittsspalt des hochauflösenden Gitterspektrometers (9, Acton SP2758i) weiterleitet. Das Gitterspektrometer ist mit drei Beugungsgittern von 600, 1800 und 2400 Linien pro mm ausgestattet. Das Raman-Spektrum wird mit einer mit flüssigem Stickstoff gekühlten CCD registriert (Spec-10 400B/LN, Princeton Instruments), deren Daten von einem PC ausgelesen und mit dem Programm WinSpec dargestellt werden (10). Der prinzipielle Ablauf einer spektroelektrochemischen Untersuchung wird im Folgenden dargestellt.

Ablauf und Datenanalyse eines UV-Vis- und RR-SEC-Experiments

Der Ablauf einer SEC-Untersuchung ist schematisch in Abbildung 4.3 gezeigt. Zuerst wird entweder direkt in der SEC-Zelle oder in einer konventionellen E-Chemie-Zelle mit einem Potentiostat (Autolab, Methrom) ein Zyklovoltammogramm aufgenommen, um die Redoxpotentiale des Analyten zu bestimmen (1). Dabei wird mit einer bestimmten Vorschubgeschwindigkeit (typisch $> 100 \text{ mV}\cdot\text{s}^{-1}$) die Potentialdifferenz zwischen Referenz- und Arbeitselektrode variiert und der Strom zwischen Arbeits- und Gegenelektrode als Funktion der angelegten Zellspannung gemessen. Anschließend wird der Analyt UV-Vis-spektroelektrochemisch untersucht (2). Dazu wird das UV-Vis Spektrum zuerst im stromfreien Zustand (OCP = open circuit potential) und dann bei geeigneten konstanten Potentialen aufgenommen. Am Ende der Messung wird der Analyt reoxidiert und das Spektrum im stromfreien Zustand nochmals vermessen, um die Reversibilität zu überprüfen und eine eventuelle Zersetzung des Analyten während der Messung festzustellen. Für Differenz-SEC-Messungen befindet sich während der Messung eine konventionelle mit Analytlösung gefüllte 1 mm Küvette im Referenzarm des Spektrometers.

In den UV-Vis-Spektren sind die neuen Absorptionsbanden der Reduktionsprodukte zu erkennen. Für die RR-SEC-Messungen wird eine Laser-Anregungswellenlänge in einer für das Reduktionsprodukt charakteristischen Absorptionsbande gewählt. In (2) von Abbildung 4.3 sind Anregungswellenlängen schematisch markiert, um selektiv den nichtreduzierten (blau) oder den einfach reduzierten Analyten (grün) zu untersuchen. Für RR-SEC-Messungen stehen zwei Messmodi zur Verfügung:

- (i) Die Resonanz-Raman-Spektren werden analog den UV-Vis-SEC-Messungen bei OCP und weiteren konstanten Reduktionspotentialen gemessen.
- (ii) Die Resonanz-Raman-Spektren werden synchron zu der langsamen (ca. 5 mW/s) Aufnahme eines Zyklovoltammogramm im Reduktionspotentialbereich aufgenommen. Der Vorteil dieser Methode ist, dass gleichzeitig ein Zyklovoltammogramm gemessen wird, um relative Verschiebungen der Reduktionspotentiale ausschließen zu können.

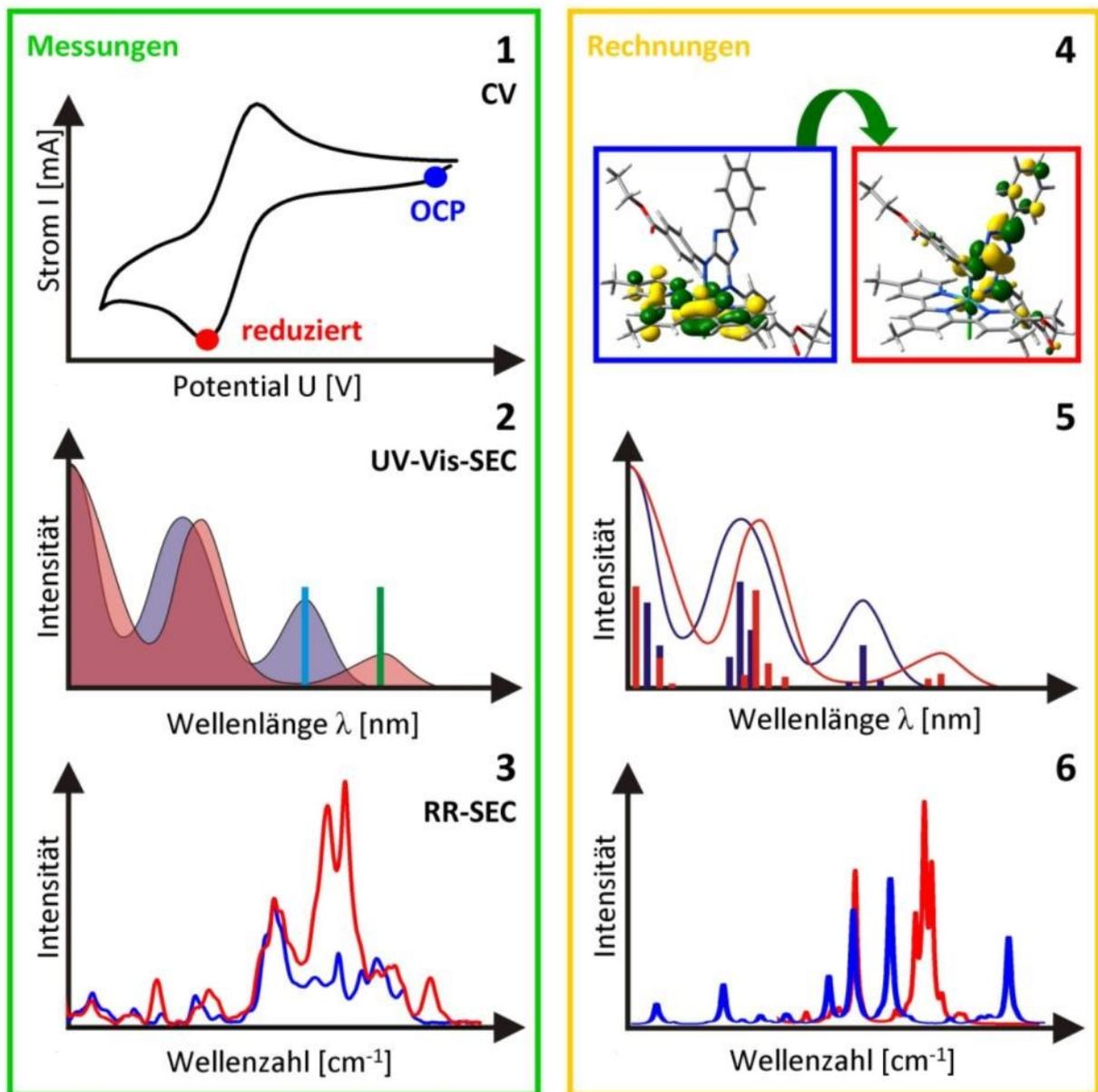


Abbildung 4.3: Prinzipieller Ablauf einer SEC-Untersuchung. Aus dem Zykelvoltammogramm werden die Reduktions- und Oxidationspotentiale des zu untersuchenden Analyten ermittelt (1), wobei für alle hier vorgestellten Messungen nur reduzierte Spezies untersucht wurden, weshalb im Folgenden nur auf die Reduktion Bezug genommen wird. UV-Vis-SEC: Das Reduktionspotential wird an die SEC-Zelle angelegt und bei konstanter Polarisierung das UV-Vis-Spektrum des reduzierten Analyten gemessen (rot), das mit dem Ausgangsspektrum (blau, OCP - open circuit potential) verglichen wird (2). Anschließend werden RR-SEC-Messung des reduzierten Analyten durchgeführt, wobei die Anregungswellenlängen für RR-SEC aus der UV-Vis-SEC-Messung entnommen werden, z.B. im Absorptionsmaximum der nichtreduzierten oder der reduzierten Spezies. Zur Interpretation der Messdaten werden quantenchemische Rechnungen durchgeführt, z.B. Berechnung der Molekülorbitale, die an den elektronischen Übergängen beteiligt sind (4), woraus die UV-Vis-Spektren abgeleitet werden können (5), sowie die Berechnung der RR-Spektren (6).

Vor jeder SEC-Messung werden die Elektroden elektrochemisch sowie die SEC-Zelle mit $\text{KMnO}_4/\text{H}_2\text{O}_2$ gründlich gereinigt, die Analytlösung erneuert und mit Argon zur Entfernung von Sauerstoff entgast.

Verwendete Lösungsmittel wurden durch Mehrfach-Destillation und der Analyt unter Vakuum getrocknet und anschließend unter Ar-Schutzgas gelagert.

Zur Interpretation der Messdaten werden umfangreiche quantenchemische Rechnungen unter Verwendung der Dichtefunktionaltheorie (TDDFT – time-dependent density functional theory) mit dem Programm Gaussian 09 durchgeführt (Abb. 4.3 (4)).¹²⁶ Dabei werden die Elektronenkonfiguration (oben), die Besetzung der Molekülorbitale, die UV-Vis- (Mitte) und die Resonanz-Raman-Spektren der neutralen und der einfach und mehrfach reduzierten Analyte berechnet (unten). Durch Vergleich der RR-Spektren der neutralen und reduzierten Spezies mit den Rechnungen von UV-Vis und RR-Spektren lässt sich der bei der Reduktion stattfindende Ladungstransfer lokalisieren. Weiterhin lässt sich bestimmen, welche molekularen Strukturen am Ladungstransfer bei Photoanregung im neutralen und reduzierten Komplex beteiligt sind. So kann aus der Verstärkung charakteristischer Schwingungsfrequenzen funktioneller Gruppen im RR-Spektrum eindeutig auf einen elektronischen Übergang entweder aus oder in das Chromophor, das diese funktionelle Gruppe trägt, geschlossen werden.

Die spektroelektrochemische Messapparatur wurde zunächst an kommerziell erhältlichen Ruthenium-Farbstoffen, welche unter anderem in Farbstoff-sensibilisierten Solarzellen Verwendung finden, getestet. Die Ergebnisse sind im folgenden Kapitel zusammenfassend dargestellt.

4.2. *In-situ*-UV-Vis- und Resonanz-Raman-spektroelektrochemische Untersuchung des Modellkomplexes $[(\text{H-dcbpy})_2\text{Ru}(\text{NCS})_2]^{2-}$ (N719)

Die kommerziell erhältlichen Ruthenium-Farbstoffe des Typs $[(\text{R-bpy})_2\text{Ru}(\text{NCS})_2]$, speziell $[(\text{H-dcbpy})_2\text{Ru}(\text{NCS})_2]^{2-}$ (dcbpy = 2,2'-Bipyridine-4,4'-Dicarboxylato) (Abb. 4.4 A) werden in den von Grätzel et al. entwickelten Farbstoff-sensibilisierten Solarzellen (dye-sensitized solar cell - DSSC)^{44,154-156} verwendet, die Effizienzen von über 10% bei der Umwandlung von Sonnenlicht in elektrische Energie erzielen.⁴³ Die Rutheniumfarbstoffe fungieren in diesen Zellen als Photosensibilisatoren und Elektronendonoren, die über Ankergruppen mit Titandioxid verbunden sind. Die durch Absorption von Sonnenlicht photoangeregten Elektronen werden dabei in das Leitungsband des Halbleiters injiziert. Wichtige Eigenschaften dieser Photosensibilisatoren sind neben einer spektral möglichst breitbandig das Emissionsspektrum der Sonne abdeckenden hohen Absorption die chemische Stabilität, die geringe Größe sowie die Redoxschaltbarkeit des Metallzentrums und eine hohe strukturelle Variabilität der Ligandensphäre. Das geringe Molekulargewicht und die damit verbundene kleine Raumausdehnung des Photosensibilisators ermöglicht eine hohe Bedeckung und damit bei kleiner Zellgröße hohe Photoströme. Die strukturelle Vielfalt der Liganden ist zur Anbindung an das Substrat von Vorteil, während die Langzeitstabilität für eine hohe Lebensdauer der Farbstoff-sensibilisierten Solarzelle erforderlich ist. Neben der Anwendung kommerziell erhältlicher Farbstoffe wie Di-tetrabutylammonium cis-bis(isothiocyanato)bis(2,2'-bipyridyl-4,4'-dicarboxylato)-Ruthenium(II) (N719) in DSSCs zielt aktuelle Forschung darauf ab, diese Strukturen hinsichtlich ihres Potentials in der heterogenen Katalyse zu untersuchen. Dafür werden katalytisch aktive Oberflächen, meist Nanopartikel, mit den Farbstoffen funktionalisiert. Im Rahmen der Katalysatorforschung werden die photophysikalischen und photochemischen Eigenschaften, insbesondere die Ladungstransferprozesse innerhalb der Farbstoffkomplexe und der funktionellen Farbstoff-Nanopartikel-Einheiten, mit spektroskopischen Methoden untersucht.^{66,68,157} Das Ziel dieser Arbeiten

ist es, strukturelle Änderungen während der Reduktion der Farbstoffkomplexe in Lösung zu studieren und konkurrierende Reaktionspfade des gerichteten Elektronen-Transfers zu identifizieren. Durch strukturelle Modifikationen der Komplexe können diese Prozesse unterbunden oder abgeschwächt werden, um die Effizienz des gerichteten Ladungstransfers zu optimieren.

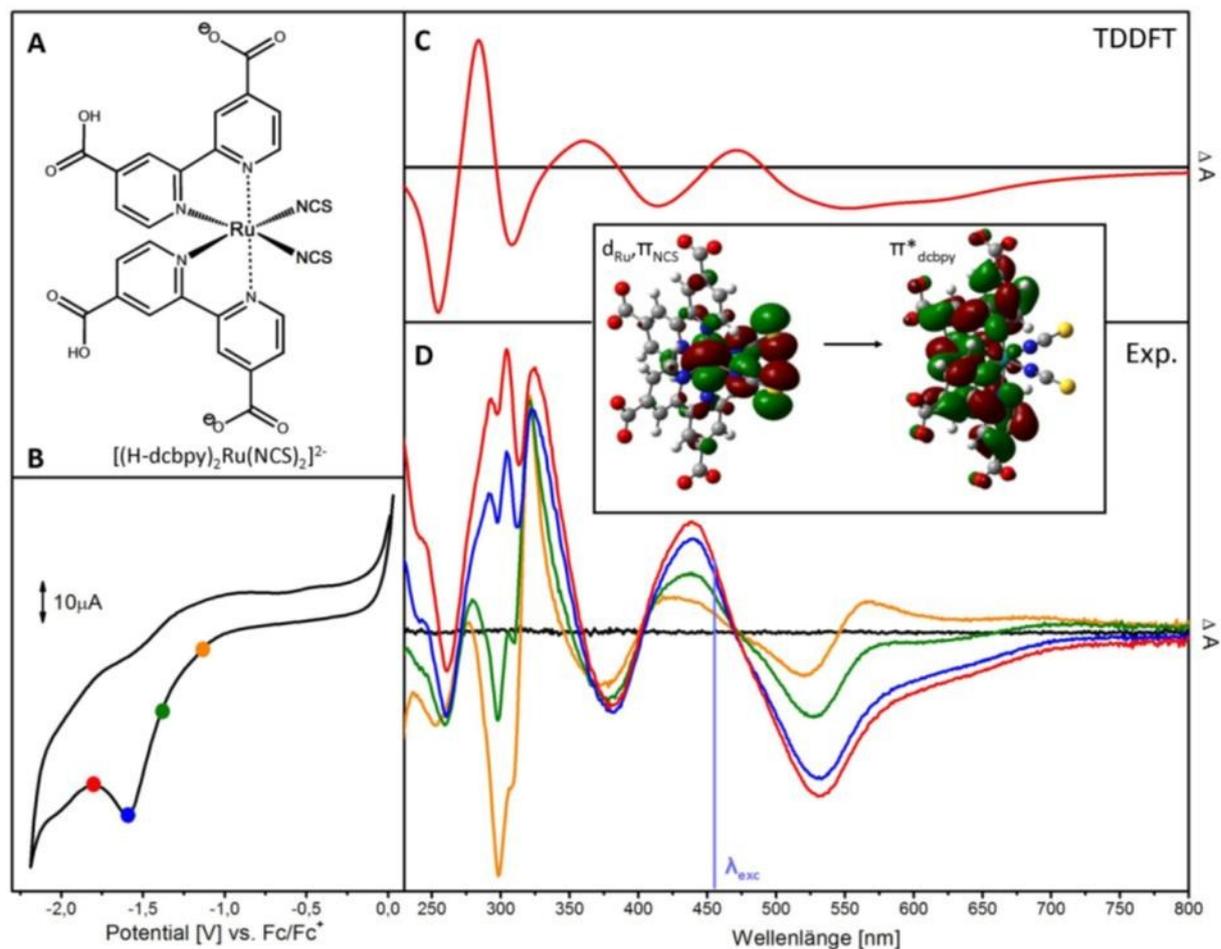


Abbildung 4.4: A) Molekulare Struktur des Modellkomplexes N719; B) Zyklovoltammogramm einer Lösung mit 0,1 mM N719 in DMF/0,2 M Bu_4NPF_6 aufgenommen unter Stickstoffatmosphäre an einer Platin-Netz-Arbeits-Elektrode gegen Fc/Fc^+ (Ferrocen) (Scangeschwindigkeit $100 \text{ mV}\cdot\text{s}^{-1}$); die markierten Punkte entsprechen den eingestellten stationären Potentialen, bei denen ein RR-Spektrum gemessen wurde; C) Das simulierte Grundzustands-UV-Vis-Differenzspektrum des deprotonierten N719 ist in guter Übereinstimmung mit dem experimentell gemessenen UV-Vis-Differenzspektrum in Abhängigkeit des Potentials (D), was darauf hindeutet, dass die Reduktion von N719 eine Deprotonierung der Carboxylgruppen induziert; Einfügung: Die neue unter Potentialkontrolle entstandene Absorptionsbande bei 440 nm entspricht einer Überlagerung mehrerer Übergänge mit einem dominanten Anteil des elektronischen Übergangs aus den d-Orbitalen des Ruthenium-Ions und den NCS- π -Orbitalen in die π^* -Orbitale des dcbpy-Liganden.

Daher wurde im Rahmen der im folgenden dargelegten Arbeiten elektrochemisch erzeugte Anionen des kommerziell erhältlichen Rutheniumkomplexes **N719** (Solaronix) als Modell für strukturell ähnliche Systeme des Typs $[(R-bpy)_2Ru(NCS)_2]$ spektroskopisch charakterisiert, um die Mechanismen photoinduzierter Elektrontransferreaktionen in diesen Farbstoffen zu untersuchen. Die Elektrochemie als auch die Photophysik von **N719** ist bereits untersucht und in der Literatur beschrieben.^{158–162} Damit dienen die hier durchgeführten Experimente zur Validierung des im

Rahmen dieser Arbeit realisierten Aufbaus. Spektroelektrochemisch wurde **N719** bisher nicht untersucht, sondern nur der strukturell ähnliche Komplex N3.^{163,164} Zur Interpretation der Messdaten wurden umfangreiche TDDFT-Rechnungen von Dr. Julien Guthmüller durchgeführt.

Da elektrochemische Messungen stark von den jeweiligen Bedingungen wie Elektrodenmaterial, -Anordnung, Elektrolyt und Lösungsmittel abhängen, wurde zunächst das voltametrische Verhalten von **N719** in der spektroelektrochemischen Zelle untersucht. Das im Zyklovoltammogramm detektierte Reduktionspotential von ca. -1,5 V entspricht der irreversiblen Reduktion des Bipyridin-Liganden.^{43,163,165,166} Das experimentelle Grundzustands-Absorptionsspektrum von **N719** in DMF weist drei Maxima bei 528, 381 und 309 nm auf und ist ähnlich dem Spektrum strukturell verwandter Rutheniumfarbstoffe.⁴³ TDDFT-Berechnungen zufolge tragen zu den Absorptionsbanden bei 528 und 381 nm insbesondere Übergänge von den d-Orbitalen des Ruthenium-Ions und den π -Orbitalen des Isothiocyanat-Liganden auf die π^* -Orbitale des Bipyridin-Liganden (Abb. 4.4, MOs) bei, während die Absorptionsbande bei 309 nm von ligandzentrierten π - π^* -Übergängen dominiert wird.

Die unter Potentialkontrolle aufgenommenen Absorptionsspektren unterscheiden sich maßgeblich von dem Grundzustandsspektrum. Um spektrale Änderungen hervorzuheben, sind in Abb. 4.4 C und D UV-Vis-Differenzspektren dargestellt. Mit Zunahme der Spannung in reduktiver Richtung kann eine deutliche Abnahme der beiden MLCT dominierten Banden detektiert werden (Abb. 4.4 D). Begleitend dazu erscheint im Spektrum des reduzierten **N719** eine neue Bande bei 440 nm. Auch für die komplett protonierte Spezies (N3) wurden ähnliche spektrale Änderungen detektiert.¹⁶³ Wolfbauer et al. nahmen an, dass die Reduktion eine Deprotonierung der Carboxylgruppen bewirkt. Um zu überprüfen, ob diese Hypothese auch die spektralen Änderungen von **N719** erklären kann, wurde das Differenzabsorptionsspektrum von protonierter und deprotonierter Form von **N719** mit Hilfe von TDDFT berechnet. Experiment und Rechnung stimmen gut überein (Abb. 4.4 C und D). Bei der elektrochemischen Reduktion von **N719** findet demnach analog zu N3 eine Deprotonierung der Carboxylsäurefunktionen statt.

Um die Struktur der reduzierten Komplexe und den photoinduzierten Ladungstransfer zu analysieren, wurde **N719** mittels RR-SEC untersucht. Die Anregungswellenlänge von 458 nm regt dabei die einfach reduzierte Form des **N719** in der Flanke der neuen Absorptionsbande an, siehe Abb. 4.4 D. Neutrale und einfach reduzierte Form des **N719** zeigen ähnliche RR Spektren mit intensiven Banden bei 1609, 1542, und 1472 cm^{-1} , die den C=C und C=N Ringschwingungen des Bipyridin-Liganden zugeordnet werden können. Diese Beobachtung suggeriert, dass die elektronische Struktur des Bipyridin-Liganden durch das zusätzliche Elektron wenig gestört wird. Dennoch konnte im RR Spektrum der reduzierten Form ein deutlich verstärkter Resonanz-Effekt der drei prominenten Raman-Banden detektiert werden, in Übereinstimmung mit dem stärker ausgeprägten Absorptionsverhalten der reduzierten Form bei einer Anregungswellenlänge von 458 nm. Außerdem konnten nach Anlegen des Reduktionspotentials Änderungen der RR-Bandenverhältnisse und -verschiebungen zu kleineren Wellenzahlen ermittelt werden. Das blaue RR-Spektrum in Abb. 4.5. A spiegelt ein Gemisch aus neutralen und einfach reduzierten **N719** wider. Eine vollständige Elektrolyse war auch nach längerem Anlegen der Spannung nicht möglich. Der unvollständige Umsatz liegt unter anderem an der nur diffusionskontrollierten Vermischung von Edukt und Produkt innerhalb des Laserfokus. Aus diesem Grund wurde das RR-Spektrum in die Anteile von Edukt und Reduktionsprodukt zerlegt. Dazu wurde das RR-Spektrum der neutralen Spezies im

Wellenzahlbereich von 1450 bis 1650 cm^{-1} (Abb. 4.5 A, schwarz) mit drei Gaussfunktionen angepasst und die berechneten Fitparameter, also Bandenposition und Halbwertsbreite, als Startwerte zur Simulation des gemessenen Spektrums der Mischung bei Reduktion (Abb. 4.5 A, blau) verwendet, wobei ebenfalls drei gaussförmige Banden angenommen wurden. Die Ergebnisse zeigen dass die Banden bei 1542 und 1609 cm^{-1} für die einfach reduzierte Form des **N719** jeweils 7 und 6 cm^{-1} zu kleineren Wellenzahlen verschoben sind.

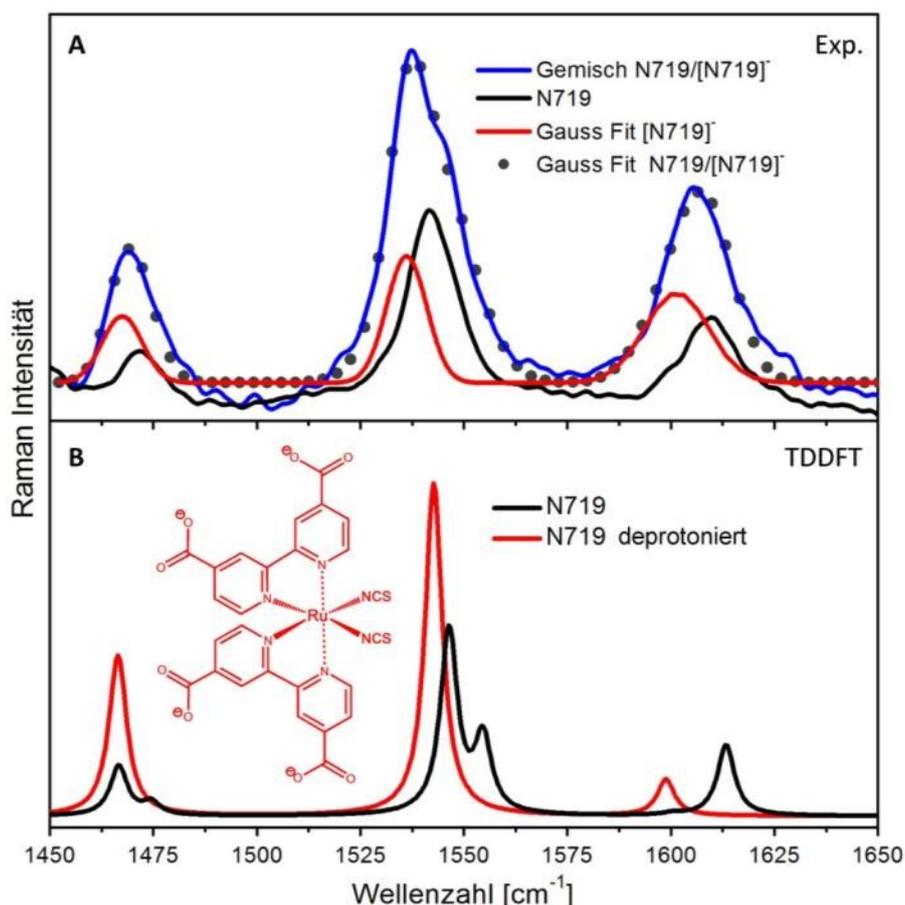


Abbildung 4.5: A) Resonanz-Raman-Spektrum der neutralen Form des N719 und einer Mischung aus N719 und $[\text{N719}]^{\bullet-}$ (blaue Kurve). Durch Fitten konnte ein simuliertes Spektrum der reduzierten Spezies aus den experimentellen Spektren extrahiert werden (rot). Experimentelle Ergebnisse zeigen eine gute Übereinstimmung mit TDDFT Rechnungen der neutralen (schwarz) und deprotonierten Form (rot) des N719 (B) und belegen die Annahme dass die Reduktion die Deprotonierung der Carboxylgruppen am Bipyridin-Liganden induziert (Struktur Einzelbild B).

Dieser Energieverlust der beiden Gerüstschwingungen des Bipyridin-Liganden ist konsistent mit der Bevölkung des zusätzlichen Elektrons eines energetisch höher liegenden π^* -Orbitals und der damit verbundenen Abnahme der Bindungsordnung dieser Liganden. Aber auch die Deprotonierung der Carboxylgruppen nach Reduktion von **N719** zeigt den gleichen Effekt, wie der Vergleich des gefitteten RR-Spektrums der einfach reduzierten Form mit TDDFT Rechnungen der vollständig deprotonierten Form des **N719** belegt (siehe rote und schwarze Spektren in Abb. 4.5 A und B). Auch die Theorie sagt eine Verschiebung zu kleineren Wellenzahlen voraus: für die Bande bei 1542 cm^{-1} um 4 cm^{-1} und für die Bande bei 1609 cm^{-1} um 14 cm^{-1} . Ebenfalls konnte der durch stärkere Absorption

begründete erhöhte Resonanz-Effekt der deprotonierten Form durch die Rechnungen bestätigt werden.

Zusammenfassend konnte gezeigt werden, dass der spektroelektrochemische Aufbau für UV-Vis und RR spektroskopische Untersuchung radikaler Spezies geeignet ist. Der in der Literatur beschriebene Mechanismus der Reduktion von **N719** konnte durch die potentialkontrollierte Detektion elektrogener Spezies untermauert werden. Es konnte gezeigt werden, dass die Reduktion mit einer Deprotonierung der Carboxylfunktionen einhergeht.

4.3. Akkumulation von Elektronen in photoredoxaktiven schwarzen Absorbern - eine spektroelektrochemische *In-situ*-Untersuchung

Die in Kapitel 4.2. untersuchten Komplexe des Typs [(R-bpy)₂Ru(NCS)₂] besitzen viele der erforderlichen Voraussetzungen für effiziente Lichtsammleinheiten, wie z.B. ein großes und spektral breitbandiges Absorptionsvermögen sowie eine hohe chemische Stabilität, kombiniert mit geringem sterischen Anspruch und niedrigem molekularem Gewicht. Dennoch besteht für diese Systeme ein enormes Optimierungspotential. So ist z.B. das Absorptionsvermögens im langwelligen sichtbaren und NIR-Bereich des Sonnenspektrums gering. Eine Möglichkeit das Absorptionsvermögen zu steigern und zu erweitern besteht darin, Ruthenium-Komplexe zu synthetisieren, die neben Polypyridin-Liganden ein organisches Chromophor komplexieren. Besonders attraktiv für Anwendungen in Multielektronen-Transferprozessen sind hoch funktionale redoxaktive Liganden, die neben hervorragenden Absorptionseigenschaften auch die Fähigkeit zur Speicherung von mehreren Elektronen aufweisen. Als zweistufige Redoxsysteme und stickstoffhaltige Chelat-Liganden mit zyklischer Amidin-Struktur sind 4*H*-Imidazole prädestiniert für die Integration als Elektronendonator- oder Elektronenakzeptoreinheiten in Ruthenium(II)-Polypyridin-Liganden. Diese Systeme finden potentielle Anwendungsmöglichkeiten in supramolekularen Architekturen, z.B. als photoaktive Komponenten in photovoltaischen Zellen, Photokatalysatoren und in Modellsystemen für die artifizielle Photosynthese.^{51,53,167}

Das chemisch stabile Anion des 2-Phenyl-*N,N'*-substituierten-5-*p*-Amino-4-*p*-Iminoimidazol Liganden hat die folgenden Eigenschaften, die es für Anwendungen in photoaktiven Komplexen prädestinieren:

1. Es ist strukturell leicht variierbar, wodurch sich sowohl elektrochemische als auch photophysikalische Eigenschaften des Moleküls gezielt anpassen lassen.
2. Durch den anionischen Charakter des Liganden wird die Ladung des Rutheniumzentralions in dessen stabilen Oxidationsstufen (+2 und +3) gut stabilisiert.
3. Das Chromophor absorbiert stark, auch im langwelligen sichtbaren Spektralbereich (λ_{\max} bis zu 580 nm, Extinktionskoeffizienten ϵ bis zu $4,5 \cdot 10^4$ L mol⁻¹ cm⁻¹ in Abhängigkeit der Substituentenstruktur).
4. Das Molekül ist zweifach reversibel reduzierbar und kann somit zwei Elektronen auf kleinem Raum speichern.¹⁶⁸ Die zweistufig reversible Reduktion nach Deprotonierung des 4*H*-Imidazols ist mit einem intensiven Farbwechsel verbunden und führt zu einem Trianion, welches mit 6 π -Elektronen aromatischen Charakter aufweist.⁵⁰

Das Zusammenspiel dieser einzigartigen Eigenschaften des 4*H*-Imidazols mit den besonderen photoelektrochemischen Eigenschaften von Ruthenium-Terpyridin-Fragmenten (Struktur in Abb. 4.6) führt zu neuartigen, kompakten und stabilen Koordinationsverbindungen.

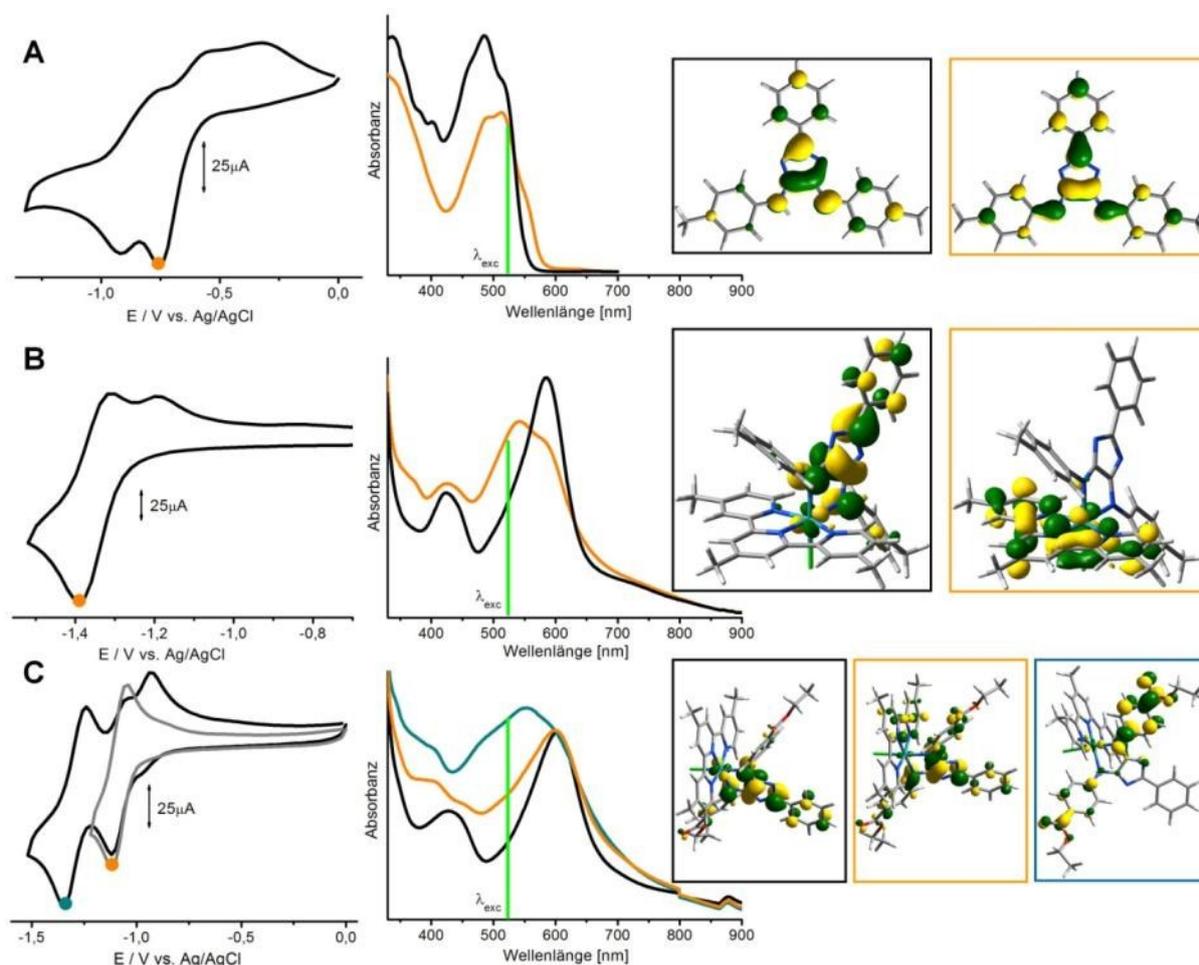


Abbildung 4.6: Zykovoltammogramme, *In-situ*-UV-Vis Spektroelektrochemie und die an der Photoanregung ($\lambda_{\text{exc}} = 514 \text{ nm}$) beteiligten Molekülorbitale der neutralen und reduzierten Spezies des freien 4*H*-Imidazol-Liganden (ImHCH₃) (A) sowie der Ruthenium-4*H*-Imidazolkomplexe RuImCH₃ (B) und RuImCOOEt (C). Einfach reduzierte Spezies sind orange farbkodiert, während die zweifach reduzierte Form von RuCOOEt cyanfarben markiert ist. Die Zykovoltammogramme wurden von 0,5 mM Lösungen in ACN/0,1 M TBABF₄ (Leitsalz) an einer Graphit-Feststoffelektrode aufgenommen ($\nu = 100 \text{ mV}\cdot\text{s}^{-1}$, Referenzelektrode: Ag/AgCl, Gegenelektrode: Platin). A) Die zweifache Reduktion des freien Liganden ist aufgrund der begleitenden Deprotonierung der exozyklischen Aminogruppe irreversibel. Die Rotverschiebung der langwelligen Absorptionbande nach Einfachreduktion ist die Folge der Besetzung energetisch höherer liegender Orbitale. Die LUMOs der neutralen und einfach reduzierten Spezies sind hauptsächlich am zentralen Fünfring des planaren Chromophors lokalisiert. B) Nach Einfachreduktion von RuImCH₃ führt die Photoanregung bei 514 nm zum MLCT von Ruthenium(II) auf dem Terpyridin-Liganden, während die Photoanregung der neutralen Spezies Ladungstransfer vom Metallzentrum auf den 4*H*-Imidazol-Liganden induziert. C) Photoanregung des sowohl einfach als auch zweifach reduzierten RuImCOOEt erfolgt ligandzentriert auf dem 4*H*-Imidazol-Liganden. Die Estergruppen an den terminalen Phenylringen stabilisieren die Aufnahme von mindestens 2 Elektronen lokal in der 4*H*-Imidazolsphäre.

Durch Kombination der zwei unterschiedlichen Ligandensphären (Terpyridin und 4*H*-Imidazol) weisen die Komplexe neben Eigenschaften der einzelnen Komponenten auch neue Eigenschaften durch Vereinen dieser Strukturen auf. Insbesondere zeigen diese Komplexverbindungen eine spektral extrem breite Absorption, die bis in den NIR Bereich reicht und somit das Spektrum des Sonnenlichts sehr gut abdeckt. Daher stellen diese Lichtsammel-Systeme ideale Einheiten für supramolekulare Architekturen zur Umwandlung von Lichtenergie in nutzbare Energieformen dar.^{52,54} Besonders für die Erforschung lichtinduzierter Multielektronen-Transferprozesse, z.B. die photokatalytische Wasserstoffgewinnung, sind Ruthenium-4*H*-Imidazol-Komplexe vielversprechende Strukturen.

Die photoinduzierte Einelektronen-Anregung der in dieser Arbeit untersuchten Ruthenium-4*H*-Imidazol-Komplexe in Abhängigkeit der Substituenten an den Aryliminoresten des 4*H*-Imidazols sowie des Protonierungsgrades wurde bereits ausführlich mittels zeitaufgelöster Spektroskopie untersucht.¹⁶⁹ Die Charakterisierung von molekularen Strukturänderungen und intermediären reduzierten Spezies während lichtinduzierter Elektronen-Transferprozesse in diesen Komplexen steht hingegen noch ganz am Anfang. Wichtige Einblicke in die Elektronen-Transferdynamik dieser Komplexe ergeben sich aus der spektroskopischen Charakterisierung der metastabilen Intermediate mittels UV-Vis und RR-SEC (Abb. 4.6 und 4.7). Wie aus Abb. 4.7 hervorgeht, führt die sequenzielle Photoanregung mit anschließender Reduktion des photo-oxidierten Ruthenium(III) Zentrums durch einen Elektronendonator zu einem Intermediat, welches identisch zum Reduktionsprodukt des Ruthenium-4*H*-Imidazol-Komplexes ist. Elektrochemisch generierte Anionen der Ruthenium-4*H*-Imidazol-Komplexe repräsentieren somit Modellverbindungen für langlebige Zweielektronen-photoaktivierte Komplexe.

Ziel dieser Arbeit ist daher einen detaillierten Einblick in Elektronen-Transferprozesse zu erhalten, indem die Struktur und Photoanregung der intermediären ein- und zweifach reduzierten Zustände der Ruthenium-4*H*-Imidazol-Komplexe spektroelektrochemisch analysiert werden. Dabei sollen insbesondere der Einfluss elektronenschiebender und -ziehender Substituenten am 4*H*-Imidazol-Chromophor auf seine Eigenschaft als Mehrelektronen-Akzeptor untersucht und mögliche Konkurrenzprozesse zur effizienten Mehrelektronen-Speicherung in einer Ligandensphäre identifiziert werden. Zur Interpretation der Messdaten wurden auch in diesem Kontext umfangreiche TDDFT-Rechnungen von Dr. Stephan Kupfer durchgeführt.

Die in Abb. 4.6 dargestellten Zyklovoltammogramme wurden in einer Standardzelle für elektrochemische Untersuchungen gemessen und zeigen das komplexe Reduktionsverhalten der untersuchten Verbindungen. Für die Bestimmung des Reduktionspotentials in der SEC-Zelle wurde vor jeder spektroskopischen Messung ein zusätzliches Zyklovoltammogramm aufgenommen und die für die SEC-Messung entsprechenden Potentialbereiche bestimmt. Der freie Ligand 2-(Phenyl)-5-*p*-Tolylamino-4-*p*-Tolylimino-4*H*-Imidazol (**ImHCH₃**) zeigt zwei irreversible Reduktionen vs. Ag/AgCl (Abb. 4.6 A). Diese Irreversibilität der eng beieinander liegenden Potentiale ist auf die Deprotonierung des Liganden während der Reduktion zurückzuführen. Da die zweifach reduzierte Form des **ImHCH₃** einem hochreaktiven Trianion entspricht, welches aufgrund der hohen Elektronendichte schon bei Anwesenheit von Spuren von Sauerstoff sofort reoxidiert,^{50,53,168} kann davon ausgegangen werden, dass in der Zelle ausschließlich die einfach reduzierte Form des **ImHCH₃** vorliegt. Für den entsprechenden Ruthenium-Komplex Chloro- η^3 -4,4',4''-Tri-tertbutyl-2,2':6',2''-Terpyridin- η^2 -Phenyl-4,5-*p*-Tolylimino-imidazolat-Ru^{II} (**RuImCH₃**) wurde ein Reduktionspotential von

-1,36 V (quasi-reversibel) mittels Zyklovoltammetrie bestimmt (Abb. 4.6 B). In oxidativer Richtung wurden zwei Potentialmaxima detektiert, was auf ein mögliches Folgeprodukt der Einfachreduktion oder eine Zweistufenreoxidation des Komplexes hindeutet. Die erste Reduktion des Chloro- η^3 -4,4',4''-Tri-tertbutyl-2,2':6',2''-Terpyridin- η^2 -Phenyl-4,5-(p-Ethylcarboxyphenyl-imino)-Imidazol-Ru^{II} (**RuImCOOEt**) ist vollständig reversibel während die zweite Reduktion ähnlich wie im Falle des **RuImCH₃** zu einem zweiten Peak in oxidativer Richtung führt. Das erste Reduktionpotential des **RuImCOOEt** ist gegenüber dem des **RuImCH₃** um +300 mV verschoben, was die erwartete bessere Stabilisierung der negativen Ladung im 4*H*-Imidazol-Liganden mit elektronenziehenden Substituenten bestätigt. Die für die 4*H*-Imidazol-Komplexe detektierten Reduktionen sind auf dem 4*H*-Imidazol-Liganden lokalisiert.⁵⁴

Während der Einfachreduktion des freien Liganden **ImHCH₃** (Abb. 4.6 A) verschiebt sich die langwellige Absorptionsbande bathochrom. Diese Rotverschiebung kann mit der Bevölkerung höher liegender Orbitale der reduzierten Spezies erklärt werden. Bemerkenswert ist, dass die berechneten LUMOs (lowest unoccupied molecular orbitals) des neutralen und einfach reduzierten **ImHCH₃** hauptsächlich am Kern des 4*H*-Imidazol-Liganden lokalisiert sind und nur geringe Beiträge der in der Ebene liegenden Toly substituenten zu verzeichnen sind. Die Lokalisierung der zusätzlichen Ladung am zentralen Fünfring des Liganden spricht für die Ausbildung eines aromatischen π -Systems. RR-SEC des freien Liganden bestärken diese Beobachtung. Sowohl für die neutralen als auch die reduzierte Spezies erfahren solche Schwingungen die größte Resonanz-Verstärkung, die am Kern des Liganden und dessen substituierten Phenylring lokalisiert sind.

Liegt der Ligand **ImHCH₃** koordiniert im Komplex **RuImCH₃** vor, ist er nicht in der Lage ein weiteres Photoelektron nach vorangegangener elektrochemischer Reduktion aufzunehmen. Eine Anregung in der neuen Absorptionsbande des reduzierten **RuImCH₃** (Abb. 4.6 B) führt zu einem MLCT vom Ruthenium(II)-Zentrum in den Terpyridin-Liganden. Während die Photoanregung des neutralen **RuImCH₃** auf den 4*H*-Imidazol-Liganden erfolgt, ist die Photoanregung des einfach reduzierten Komplexes auf dem Terpyridin-Fragment lokalisiert (MOs bei einer Anregungswellenlänge von 514nm, Abb. 4.6 B). *In-situ*-RR-spektroskopische Untersuchungen in Resonanz mit der Absorption des reduzierten **RuImCH₃** bei einer Anregungswellenlänge von 514 nm bestätigen dieses Verhalten.

Während die initiale Photoanregung des neutralen Komplexes hauptsächlich den 4*H*-Imidazol-Liganden involviert, so dass im RR Spektrum besonders dessen Schwingungen verstärkt sind (Abb. 4.7 A, blaues Spektrum), können nahezu alle zusätzlich detektierten RR-Banden des reduzierten Komplexes den Schwingungen des Terpyridin-Liganden zugeordnet werden (Abb. 4.7 B, blaues Spektrum). Da die photoangeregte einfach reduzierte Form von **RuImCH₃** formal dem zweifach reduzierten Komplex entspricht, wurden TDDFT-Rechnungen an der zweifach reduzierten Spezies des **RuImCH₃** durchgeführt. Für den Grundzustand der zweifach reduzierten Spezies sagen quantenchemische Rechnungen einen Triplett-Zustand voraus, wobei eine elektronische Ladung auf dem 4*H*-Imidazol-Liganden und die zweite auf dem Terpyridin-Liganden lokalisiert ist. Der Komplex **RuImCH₃** ist demnach nicht in der Lage, sowohl das elektrochemisch erzeugte Elektron als auch das Photoelektron innerhalb des 4*H*-Imidazol-Akzeptorliganden zu konzentrieren.

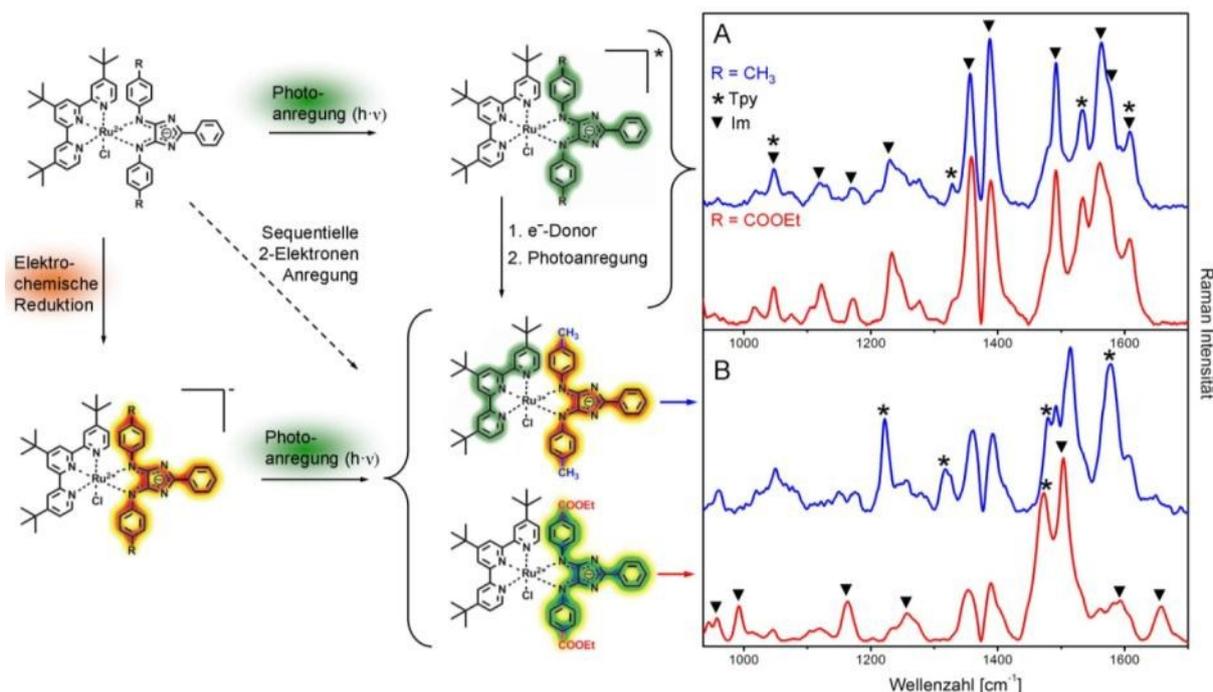


Abbildung 4.7: Die sequentielle 2-Elektronen-Anregung inklusive Reduktion des photooxidierten Ruthenium(III)-Ions kann durch elektrochemische Generierung des Anions und anschließender Photoanregung initiiert werden, wie schematisch dargestellt. SEC ermöglicht somit die Generierung und Charakterisierung intermediärer Zustände der Photokatalyse. A) Die RR-Spektren der neutralen Ruthenium-4*H*-Imidazol-Komplexe RuImCH₃ und RuImCOOEt unterscheiden sich kaum und werden dominiert von Banden des 4*H*-Imidazol-Chromophors (Dreieck). Die initiale Photoanregung führt hauptsächlich zum Ladungstransfer vom Ruthenium(II) zum 4*H*-Imidazol-Liganden (MLCT). B) Die Anregung der reduzierten Komplexe bei 514 nm führt zu unterschiedlichen RR-Spektren. Die durch Reduktion hervorgerufenen neuen RR-Banden des RuImCH₃ (blaues Spektrum) können ausschließlich dem Terpyridin-Liganden zugeordnet werden (Stern), während für RuImCOOEt (rotes Spektrum) nach Reduktion nur solche Banden resonanzverstärkt sind, die am 4*H*-Imidazol-Liganden lokalisiert sind. Die Entstehung der C=O-Bande bei 1658 cm⁻¹ deutet auf eine Planarisierung und damit Ausdehnung des Ligandenchromophors nach Reduktion hin, ausgelöst durch die Akkumulation negativer Ladung lokal auf einem Ligandfragment. Die Resonanz-Raman-Spektren wurden synchron zu der langsamen (5 mV/s) Aufnahme eines Zyklovoltammogramms im Reduktionspotentialbereich aufgenommen.

Ein anderes Verhalten wurde für den RuImCOOEt Komplex festgestellt, der elektronenziehende Estergruppen an den Aryliminosubstituenten besitzt. Sowohl Einfach- als auch Zweifachreduktion des RuImCOOEt konnten *In-situ*-UV-Vis-spektroskopisch verfolgt werden (Abb. 4.6 C). Die Reduktion geht einher mit einer starken Zunahme der Absorption mit Maxima bei 400, 550 und 700 nm. Zur Absorption tragen hauptsächlich Intra-Ligand (IL) und MLCT-Übergänge bei, die auf dem 4*H*-Imidazol-Liganden lokalisiert sind (Abb. 4.6 C, MOs). Weitere Details ergeben sich aus den RR-SEC-Daten. Obwohl die RR-Spektren der beiden neutralen Spezies fast identisch sind (Abb. 4.7 A), unterscheiden sich die bei 514 nm innerhalb der neuen Absorptionsbande angeregten RR-Spektren der reduzierten Spezies von RuImCOOEt und RuImCH₃ deutlich voneinander. Während für die neutralen Komplexe die initiale Photoanregung hauptsächlich in den 4*H*-Imidazol-Liganden erfolgt, da ein Großteil der resonanzverstärkten Schwingungen dem 4*H*-Imidazol zugeordnet werden kann, führt nur die Photoanregung der reduzierten Spezies von RuImCOOEt zur selektiven Verstärkung von 4*H*-Imidazol-

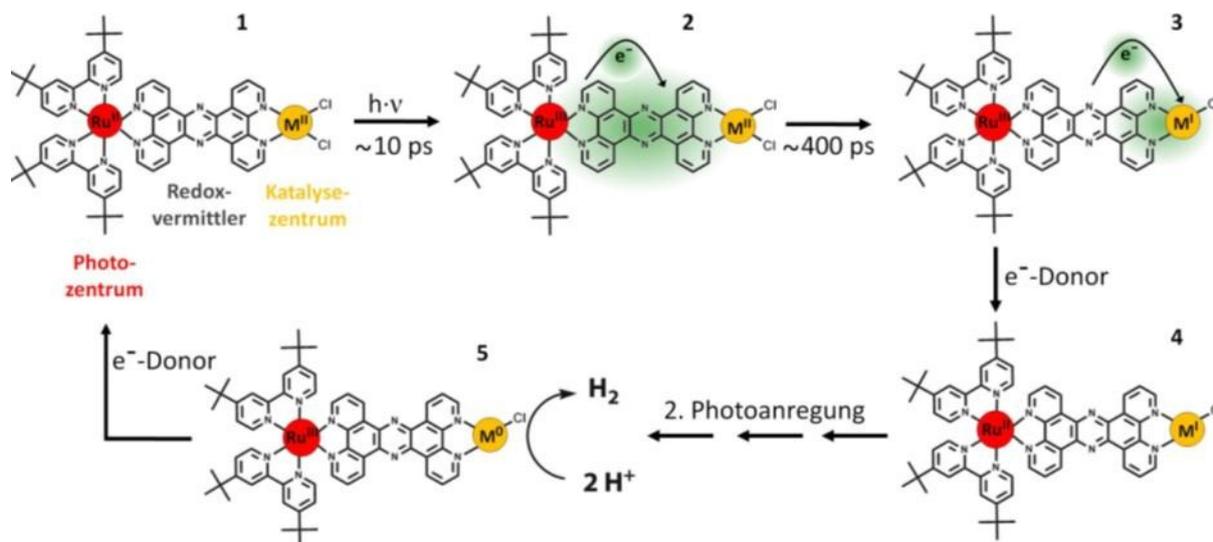
Schwingungen, während im RR-Spektrum des reduzierten **RuImCH₃** Terpyridinschwingungen verstärkt werden (Abb. 4.7, Schema SEC). Die Ergebnisse der TDDFT-Rechnungen liefern zusätzliche Beweise für die Akkumulation beider Elektronen in einer Ligandensphäre: die niedrigste Energie der zweifach reduzierten Form des **RuImCOOEt** entspricht einem Singulett-Zustand, wobei beide Elektronen ein π^* -Orbital des 4*H*-Imidazol-Liganden besetzen. Außerdem konnte für die Struktur des zweifach reduzierten **RuImCOOEt** eine starke Abnahme des Torsionswinkels, d.h. der Verdrehung der Aryliminoreste gegen die Ebene des zentralen 4*H*-Imidazolrings, von 46° für den neutralen Komplex auf 4° für die doppelt reduzierte Spezies berechnet werden. Diese Planarisierung erhöht zwar die sterische Hinderung zwischen Terpyridin- und 4*H*-Imidazol-Ligandensphäre, führt aber auch zur Ausdehnung des chromophoren Systems über den gesamten 4*H*-Imidazol-Liganden und verringert damit die Coulombabstoßung der beiden im Chromophor delokalisierten negativen Ladungen. Auch die RR-Messungen bestätigen die mit der Ladung des Liganden zunehmende Planarisierung: Auffallend im experimentellen RR-Spektrum der zweifach reduzierte Form des **RuImCOOEt** ist die Entstehung einer Bande bei 1658 cm⁻¹, welche in guter Übereinstimmung mit der Theorie der Carbonyl-Streck-Schwingung zugeordnet werden kann (Abb. 4.7 B). Das Auftreten dieser Bande signalisiert, dass die Esterfunktion in derselben Ebene angeordnet ist, wie das aromatische Chromophor des 4*H*-Imidazol-Liganden. Spektroskopisch konnte damit nachgewiesen werden, dass die zweifache Reduktion des 4*H*-Imidazol-Liganden im Komplex **RuImCOOEt** die Verdrehung der Aryliminoreste in die Ebene des zentralen 4*H*-Imidazol-Liganden bewirkt und damit zu einer Delokalisierung der negativen Ladungen innerhalb der 4*H*-Imidazol-Ligandensphäre führt. Zusammenfassend belegen die Resultate spektroelektrochemischer Untersuchung in Kombination mit TDDFT-Rechnungen damit die Fähigkeit des Komplexes **RuImCOOEt**, mindestens zwei Elektronen in einem Ligandfragment, dem 4*H*-Imidazol, aufzunehmen und für eine potentielle Zweielektronen-Reduktion zur Verfügung zu stellen.

Mittels spektroelektrochemischer Methoden konnten potentielle Intermediate lichtinduzierter Mehrelektronen-Prozesse von Ruthenium-4*H*-Imidazol-Komplexen generiert und strukturell charakterisiert werden. Durch gezielte Substitution der terminalen funktionellen Gruppen des 4*H*-Imidazol-Liganden mit elektronenziehenden Einheiten ist eine Speicherung von zwei Elektronen lokal innerhalb einer Ligandensphäre in Ruthenium-4*H*-Imidazolkomplexen möglich (Abb. 4.7, Schema SEC). Neben ihrem stetigen und herausragenden Absorptionsvermögen und ihrer hohen Stabilität eröffnet die Fähigkeit zum gerichteten sequentiellen Multielektronen-Transfer in den 4*H*-Imidazol-Liganden vielversprechende Anwendungsmöglichkeiten der hier untersuchten Systeme in supramolekularen Architekturen, z.B. als Lichtsammelinheiten in der lichtinduzierten Photokatalyse.

4.4. Charakterisierung der Elektronen- und Schwingungsstruktur reaktiver Intermediate artifizieller Photokatalysatoren

Nachdem in Kapitel 4.2. und 4.3. der Schwerpunkt auf der spektroelektrochemischen Untersuchung essentieller Fragmente für artifizielle supramolekulare Architekturen zur Umwandlung von Sonnenenergie in andere nutzbare Energieformen lag, sollen nun photokatalytisch aktive Systeme sowie deren Intermediate in katalytischen Zyklen charakterisiert werden. Molekulare Photokatalysatoren für Mehrelektronen-Transferprozesse, z.B. zur Wasserreduktion, bestehend aus einem Photozentrum, das über einen elektronenübertragenden und -speichernden Brückenliganden mit dem Katalysezentrum verbunden ist (Schema 4.2), sind Gegenstand aktueller Forschung. Der von

Rau et al. entwickelte supramolekulare Photokatalysator $[(tbbpy)_2Ru(tpphz)Pd(Cl)_2]^{2+}$ ($tbbpy = 4,4'$ -*tert.*-butyl-2,2'-bipyridin, $tpphz = \text{tetrapyrido}[3,2\text{-}a:2'3'\text{-}c:3'',2''\text{-}h:2''',3'''\text{-}j]\text{phenazin}$) (**RuPd**) ist in der Lage unter Bestrahlung mit sichtbarem Licht und in Anwesenheit eines Elektronendonors Protonen zu molekularem Wasserstoff zu reduzieren (Schema 4.2).⁵⁸ Um die einzelnen Komponenten optimal aufeinander abzustimmen und somit die Effizienz des Gesamtprozesses zu erhöhen, wurden dieses System und verwandte Strukturen umfangreich spektroskopisch untersucht. Die bisherigen Ergebnisse lassen auf den in Schema 4.2 dargestellten Katalysemechanismus schließen.^{58,170–173}



Schema 4.2: Postulierter Ablauf der photokatalytischen Erzeugung von molekularem Wasserstoff für RuPd, basierend auf den Ergebnissen der zeitaufgelösten und Resonanz-Raman-spektroskopischen Untersuchungen. Nach der initialen MLCT Anregung wird innerhalb weniger ps ein Phenanzin-zentrierter Ladungstransferzustand besetzt (1,2). Darauf folgt ein Ligand-zu-Metall-Ladungstransfer zum Katalysezentrum (3). Es wird vermutet, dass die Reduktion von der Abspaltung eines Chloridions begleitet wird.^{58,174,175} Nach Regenerierung des oxidierten Photozentrums durch einen Elektronendonator (4) folgt die zweite Photoanregung mit anschließender Reduktion von Protonen an der Oberfläche des reduzierten Metallions (5). Die Reduktion des photooxidierten Ruthenium-Ions führt schließlich zur Regenerierung des Katalysators.

Allerdings konnte kürzlich nachgewiesen werden, dass es während des sukzessiven Elektronentransfers zu einer Dekomplexierung und Kolloidbildung des katalytisch aktiven Palladium-Zentrums kommt^{59,176–178} und somit der Mechanismus statt einer vermuteten homogenen, einer heterogenen Katalyse unterliegt. Da diese Kolloidbildung die Zerstörung der molekularen Spezies und somit eine Abnahme der Stabilität und der Effizienz des katalytischen Systems zur Folge hat, wurde ein strukturell verwandter Photokatalysator $[(tbbpy)_2Ru(tpphz)Pt(Cl)_2]^{2+}$ (**RuPt**, Schema 4.3) entwickelt, welcher unter katalytischen Bedingungen nicht zur Kolloidbildung neigt und somit einen stabilen intramolekularen Katalysator darstellt.^{59,62,179} Trotz der Ähnlichkeit von **RuPd** und **RuPt** in Struktur, Absorptionsvermögen und photophysikalischen Eigenschaften zeigen sie unter identischen katalytischen Bedingungen unterschiedliche Umsatzzahlen, wobei **RuPt** mit einer integralen Umsatzzahl von 7 eine deutlich geringere katalytische Aktivität als das strukturanaloge **RuPd** (Umsatzzahl 146) zeigt (bei Bestrahlung mit Licht der Wellenlänge 470 nm über einen Bestrahlungszeitraum von 10 h). Eine zeitlich konstante Umsatzfrequenz wurde für **RuPt** beobachtet,

während **RuPd** zeitlich variierende Umsatzzahlen aufweist. Das katalytische aktive Zentrum scheint somit einen großen Einfluss auf den Katalysemechanismus zu haben.

Die durch Lichtanregung induzierten Elektronen-Transferprozesse in **RuPd** und **RuPt** laufen in weniger als 1 ns ab. Für die Optimierung des gerichteten Elektronen-Transfers ist es von Interesse, kurzlebige Zwischenprodukte der Katalyse spektroskopisch zu charakterisieren. Ziel dieser spektroelektrochemischen Untersuchungen war es, die Elektronen- und Schwingungsstruktur intermediärer Zustände des katalytischen Zyklus von **RuPt** zu untersuchen und damit zur Aufklärung des Katalysemechanismus beizutragen. Die Ergebnisse wurden mit den Daten des Modellkomplexes $[(tbbpy)_2Ru(tpphz)]^{2+}$ (**Ru**) und **RuPd** verglichen, um mechanistische Auswirkungen des Katalysezentrums auf den Katalysezyklus zu studieren. Zur Interpretation der Messdaten wurden auch in diesem Kontext umfangreiche TDDFT-Rechnungen von Dr. Julien Guthmüller durchgeführt.

Die UV-Vis Absorptionsspektren der neutralen Formen von **Ru**, **RuPd** und **RuPt** zeigen eine MLCT-Bande bei ca. 450 nm. Dieser Übergang wird durch Ladungstransfer aus den d-Orbitalen des Rutheniums auf π^* -Orbitale beider Liganden, tbbpy und tp-phz, verursacht (gezeigt für **RuPt**, Abb. 4.8 A). Spektroelektrochemische Untersuchungen ergeben eine bathochrome Verschiebung dieser MLCT-Bande für alle drei reduzierten Komplexe. TDDFT Rechnungen deuten darauf hin, dass der Ladungstransfer nach Reduktion ausschließlich in den tbbpy-Liganden (MO, Abb. 4.8 B) erfolgt. Außerdem konnte für alle reduzierten Spezies von **Ru**, **RuPd** und **RuPt** eine zusätzliche Absorptionsbande mit einem Maximum bei 600 nm detektiert und mit Hilfe der TDDFT-Rechnungen einem Intra-Liganden-Übergang ($\pi-\pi^*$), der auf dem tp-phz-Ligand lokalisiert ist, zugeordnet werden (Abb. 4.8 A und B). Bei diesem Übergang wird Ladung vom Phenazin- auf das Phenanthrolinfragment des tp-phz-Liganden transferiert (Abb. 4.8 B). Die spektroelektrochemische Beobachtung dieser Spezies deutet auf eine Lebensdauer hin, die deutlich länger ist als die mittels transientser Absorption ermittelte Zeit von Photoanregung bis zur 1. Reduktion des Katalysezentrums. Im elektrochemisch erzeugten Intermediat des **RuPt** und **RuPd** liegt das Ruthenium in der Oxidationsstufe +2 vor, während die Experimente zur ps-Dynamik nach Photoanregung zu Ruthenium(III) führen. Die Oxidationsstufe des an tp-phz $^{\bullet-}$ gebundenen Rutheniums bestimmt demnach signifikant die Geschwindigkeit und Effizienz des Ligand-zu-Metall-Ladungstransfers (LMCT), welcher letztendlich die Reduktion des Katalysezentrums bewirkt. Eine erfolgreiche Photokatalyse kann demnach nur erfolgen, wenn die Reduktion des photooxidierten Rutheniums langsamer abläuft als der LMCT zum katalytisch aktiven Metall. Eine extrem schnelle stoßinduzierte Reduktion des Ruthenium(III)-Ions mittels eines Elektronendonors kann demzufolge auch den gerichteten Elektronen-Transfer vom Brückenligand auf das Katalysezentrum behindern und somit die Effizienz der Wasserstoffproduktion beeinträchtigen.

Für die strukturelle Untersuchung katalytischer Intermediate mittels RR-Spektroskopie wurden die Anregungswellenlängen sowohl in Resonanz mit der MLCT-Bande als auch in Resonanz mit dem Intra-Liganden-Übergang gewählt (Abb. 4.8 A). Bei einer Anregungswellenlänge von 514 nm konnten aufgrund zu starker Fluoreszenz der reduzierten Komplexe **RuPd** und **Ru** lediglich RR-Spektren des **RuPt** Komplexes erhalten werden.

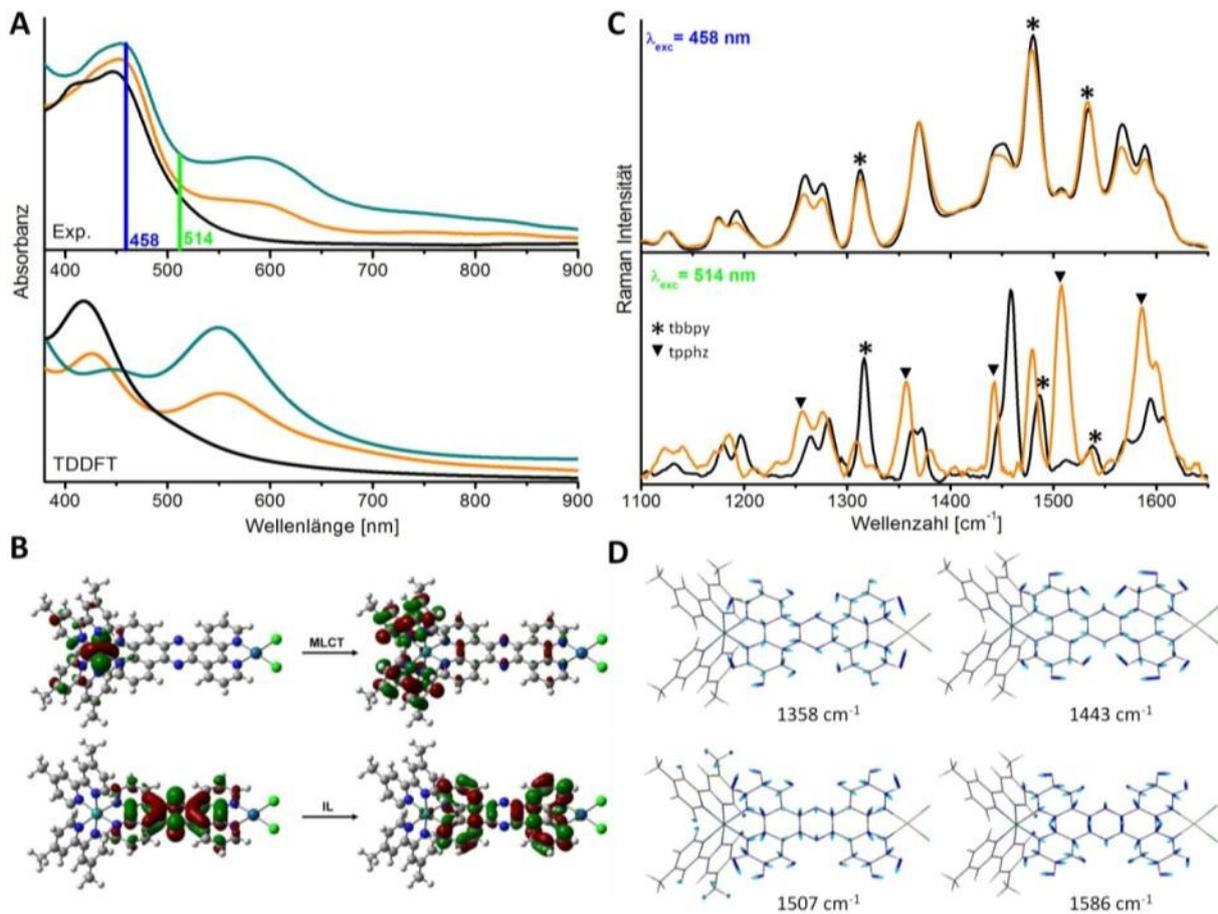
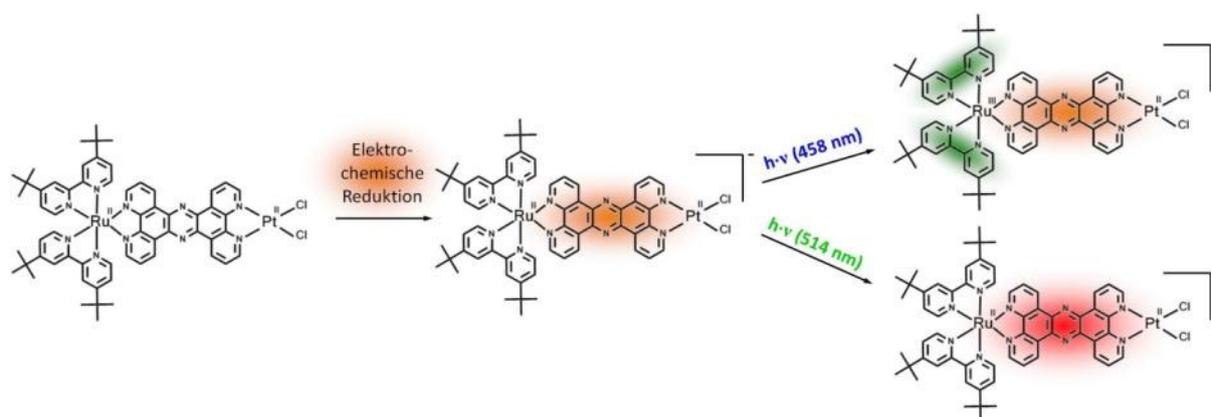


Abbildung 4.8: A) *In-situ*-UV-Vis Absorptionsspektren der einfach (orange) und zweifach (cyan) reduzierten Form des RuPt im Vergleich zum Grundzustandsspektrum. Sowohl die durch Reduktion induzierte bathochrome Verschiebung der MLCT-Bande bei 450 nm als auch die Entstehung einer neuen Bande mit einem Maximum bei etwa 600 nm ist in guter Übereinstimmung mit den TDDFT Rechnungen. Während der MLCT-Übergang des neutralen RuPt die Ladungsdichte gleichmäßig sowohl auf den tbbpy als auch auf den tpzhz-Liganden verteilt, findet in den Reduktionsprodukten ein gerichteter MLCT auf den tbbpy-Liganden statt (B, zeigt die Molekülorbitale, die an dem Übergängen der einfach reduzierten Form beteiligt sind). Die langwellige Absorption der reduzierten Spezies kann einem Intra-Liganden-Übergang, lokalisiert auf dem tpzhz-Liganden (B), zugeordnet werden. C) *In-situ*-RR-Spektren gemessen während der Reduktion von RuPt (Scan Rate: 5 mV/s) in Resonanz mit dem MLCT ($\lambda_{\text{exc}} = 458 \text{ nm}$) zeigen lediglich kleine Änderungen im Intensitätsmuster der Resonanz-Raman-Banden. Eine Abnahme der Intensitäten der tpzhz-Banden während der Reduktion von RuPt spricht für den abnehmenden Beitrag des tpzhz-Liganden an diesem Übergang. Große Unterschiede zwischen den RR-Spektren der neutralen und reduzierten Form des RuPt sind bei einer Anregung in Resonanz mit dem Intra-Liganden-Übergang zu verzeichnen. Im Spektrum der reduzierten Form kann eine Abnahme der Intensität der tbbpy-Banden und das Erscheinen neuer Banden, die ausschließlich dem tpzhz-Liganden zugeordnet werden können (C), detektiert werden.

Beim Vergleich der RR-Spektren der neutralen und reduzierten Formen von **Ru**, **RuPd** und **RuPt** bei einer Anregungswellenlänge von 458 nm sind nur kleine Änderungen in den Bandenintensitäten feststellbar (Abb. 4.8 C). Die Reduktion bewirkt demnach nur kleine Änderungen der Franck-Condon-Geometrie. Ursache dafür ist, dass das zusätzliche Elektron in der Phenanzin-Sphäre des tpzhz-Liganden lokalisiert ist, die Photoanregung bei 458 nm allerdings Ladung vom Ruthenium in den tbbpy-Ligand überträgt und demnach den tpzhz-Liganden nur wenig involviert. Kleine, durch die

Reduktion ausgelöste Änderungen in den Bandenverhältnissen können mithilfe quantenmechanischer Rechnungen erklärt werden: Nach Reduktion bleibt die Intensität der Banden, die dem tbbpy-Liganden zugeordnet werden können, weitestgehend konstant, während die Intensität der tpvhz-Moden im Vergleich zu den neutralen Spezies um etwa 20% sinkt (Abb. 4.8 C). Dieses Ergebnis bestätigt den nach Reduktion favorisierten Ladungstransfer vom Ruthenium(II)-Ion in die tbbpy-Liganden und nicht in den reduzierten tpvhz-Liganden aufgrund der Coulomb-Abstoßung.

Das bei einer Anregung von 514 nm gemessene RR-Spektrum des reduzierten **RuPt** weist große Unterschiede zu dem Spektrum des neutralen Komplexes auf (Abb. 4.8 C). Es konnte sowohl eine starke Intensitätszunahme sowie die Ausbildung neuer Schwingungsbänder detektiert werden (Abb. 4.8 C). Den TDDFT Rechnungen zufolge führt die Photoanregung des reduzierten **RuPt** bei 514 nm hauptsächlich zu einem tpvhz-zentrierten $\pi-\pi^*$ -Übergang. Entsprechend konnten die neuen RR-Banden dem tpvhz-Chromophor zugeordnet werden (Abb. 4.8 D). Weiterhin ist eine Abnahme der tbbpy-Bandenintensitäten zu verzeichnen, was auf einen geringeren Beitrag dieses Liganden zum RR-Spektrum hindeutet, wenn bei 514 nm in der Flanke des tpvhz-zentrierten $\pi-\pi^*$ -Intra-Liganden-Übergangs angeregt wird.



Schema 4.3: Schematische Darstellung der ablaufenden Prozesse der spektroelektrochemischen Untersuchung des Photokatalysators RuPt. Die erste Reduktion ist auf dem Brückenliganden tpvhz lokalisiert (orange schattiert). Eine Photoanregung in Resonanz mit dem MLCT-Übergang (grün schattiert) begünstigt aufgrund der Coulomb-Abstoßung einen Ladungstransfer auf die terminalen tbbpy-Liganden. Photoanregung in der langwelligen Absorption führt zu einem ligandenzentrierten $\pi-\pi^*$ -Übergang (rot schattiert).

Sowohl für **RuPd** als auch für **RuPt** ist bekannt, dass die initiale Photoanregung auf den Brückenliganden einen entscheidenden Einfluss auf die Photon-zu-Wasserstoff-Umwandlungseffizienz hat, da somit zusätzliche Relaxationspfade, welche den tbbpy-Liganden einbeziehen, unterdrückt werden. Aus den SEC Ergebnissen geht hervor, dass die Photoanregung des reduzierten Brückenliganden keinen Ladungstransfer zum katalytischen Zentrum begünstigt. Die initiale Photoanregung des Brückenliganden ist demnach genauso essentiell für die Katalyse wie der Oxidationszustand des Photozentrums.

Zusammenfassend lässt sich festhalten, dass im Rahmen dieser Arbeit eine spektroelektrochemische Messzelle für Experimente unter inerten Bedingungen konstruiert, erfolgreich in einen Resonanz-Raman-Aufbau integriert und getestet werden konnte. Schwer zugängliche und spektroskopisch unbekannte Intermediate photoinduzierter Prozesse konnten in nachweisbaren Konzentrationen

generiert und mittels UV-Vis- und Resonanz-Raman-Spektroskopie *in situ* strukturell identifiziert und charakterisiert werden. Als schwierig erwies sich die vollständige Elektrolyse und somit die ausschließliche Detektion der elektrochemisch aktiven Spezies. Die gewonnenen Ergebnisse dokumentieren jedoch, dass die Spektroelektrochemie eine ideale Methode zur Aufklärung photoinduzierter Mehrelektronen-Prozesse darstellt und somit das Potential besitzt, einen Beitrag zur Entschlüsselung mechanistischer Aspekte katalytischer Reaktionen, wie beispielsweise der Wasserspaltung, leisten kann.

5. Spektroskopische Charakterisierung Rutheniumfarbstoff-funktionalisierter Goldnanopartikel

Teile dieses Kapitels wurden im folgenden Artikel publiziert:

[Zedler et al. RSC] L. Zedler, F. Theil, A. Csáki, W. Fritzsche, S. Rau, M. Schmitt, J. Popp, B. Dietzek, *RSC Adv.* **2012**, *2*, 4463–4471.

Der im vorigen Kapitel dieser Arbeit vorgestellte molekulare Photokatalysator **RuPt** stellt einen vielversprechenden homogenen Katalysator für die Reduktion von Protonen zu Wasserstoff dar. Allerdings ist die katalytische Effizienz dieses Systems noch zu gering für eine industrielle Anwendung.⁵⁹ Zur Steigerung der Effizienz kommen sowohl die Optimierung der Struktur, z.B. durch Substitution der Liganden, als auch der Ladungstransferprozesse in Betracht.^{59,62,180} Eine weitere mögliche Option zur Steigerung der katalytischen Effizienz stellt die Verwendung von Nanopartikeln anstelle eines einzelnen Platin-Ions als Katalysezentrum dar. Folgende Vorteile könnten sich durch die Nutzung von Nanopartikeln ergeben:

(i) Mehrere Elektronen, die in voneinander unabhängigen Absorptionsprozessen in verschiedenen, auf der Oberfläche immobilisierten Farbstoffmolekülen generiert werden, können schnell auf das Nanopartikel übertragen werden, an dessen Oberfläche die Katalyse stattfindet, was besonders für den Zweielektronen-Prozess der Wasserstoffkatalyse oder andere Mehrelektronen-Prozesse von Vorteil wäre.

(ii) Durch die, im Vergleich zu einzelnen katalytisch aktiven Atomen in molekularen Katalysatoren wie **RuPt**, deutlich größere Oberfläche von katalytisch aktiven Nanopartikeln haben auch größere Moleküle Zugang zur katalytisch aktiven Fläche, d.h. die sterische Hinderung ist auf Nanopartikeln geringer.

(iii) Das elektrisch leitfähige Partikel ermöglicht einen schnellen Transfer von Elektronen an den Ort, an dem die Protonen reduziert werden.

Metall-Nanopartikel können wegen ihrer hohen Affinität zu Schwefel, Stickstoff und Phosphor mit einem großen Spektrum an Strukturen funktionalisiert werden.^{181–183} Aufgrund der Vielzahl von Anwendungen wurden in den letzten Jahren eine nur schwer überschaubare Zahl funktionalisierter Nanopartikelgrenzflächen synthetisch realisiert und charakterisiert.^{68–70,184–186} Zu den technisch wichtigsten Nanopartikeln aufgrund ihrer Verwendung in Farbstoff sensibilisierten Solarzellen (dye sensitized solar cells - DSSCs) zählen dabei Titandioxidnanopartikel.^{44,187,188} Die mit spektral breitbandig absorbierenden Rutheniumfarbstoffen wie **N719**, **N749** und **Z907** (Abb. 5.1) funktionalisierten Titandioxidpartikel in DSSCs ermöglichen die Umwandlung von Sonnenlicht in elektrische Energie.¹⁸⁸ Neben der Carboxylfunktion, die zur Anbindung an Titandioxidpartikel verwendet wird, verfügen diese kommerziell erhältlichen Komplexe über Isothiocyanat-Liganden als Ankergruppe für die Anbindung an Metallnanopartikel, insbesondere Goldnanopartikel.⁶⁶ Aus Gold lassen sich über verschiedene Syntheseverfahren^{181,189–192} sehr stabile und einfach handhabbare Nanopartikel von fast beliebiger Größe und Form herstellen. Durch das hohe Standard-Reduktionspotential und die geringe Reaktivität gegenüber Sauerstoff sind Nanopartikel aus Gold chemisch sehr beständig. Durch die Funktionalisierung von Goldnanopartikeln mit photoaktiven Rutheniumfarbstoffen lassen sich Modellsysteme mit neuartigen Eigenschaften herstellen, z.B. um

die Mechanismen der heterogenen Katalyse zu untersuchen.^{66,193,194} Das beinhaltet zuerst die Etablierung von (i) Syntheseverfahren zur Herstellung farbstofffunktionalisierter Nanopartikel und (ii) die detaillierte Analyse der chemischen und photophysikalischen Eigenschaften dieser Modellsysteme, um die komplexen funktionalen Grenzflächen gezielt für spezifische Anwendungen, wie z.B. die Wasserstoffkatalyse optimieren zu können. Diese Erkenntnisse lassen sich anschließend auf Kolloide höherer katalytischer Aktivität für die Wasserstoffproduktion, z.B. auf Basis von Platin oder Palladium, übertragen.⁴²

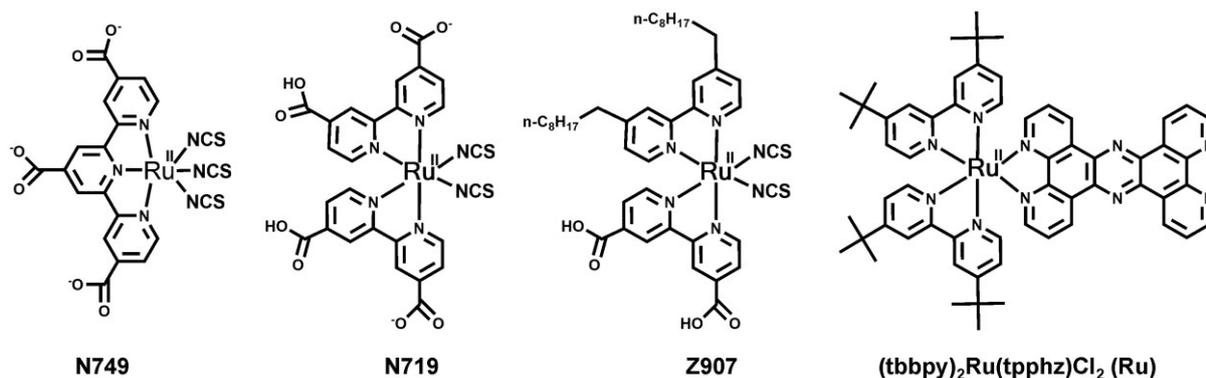


Abbildung 5.1: Molekulare Strukturen der in dieser Arbeit zur Funktionalisierung von Goldnanopartikeln eingesetzten Ruthenium-Komplexe N719, N749, Z907 und Ru.

Für die spektroskopische Charakterisierung der Struktur dieser Systeme bietet sich die oberflächenverstärkte Raman-Spektroskopie (surface-enhanced Raman scattering - SERS) an. Dieser physikalische Effekt beruht auf der Anregung von Oberflächenplasmonen der Goldnanopartikel. Als Plasmon wird dabei die im elektromagnetischen Feld des Lichtes angeregte Kollektivschwingung der Elektronen an der Oberfläche der Nanopartikel bezeichnet. Diese Anregung ist sowohl von Partikelgröße, Partikelform als auch von ihrer Umgebung abhängig und erlaubt eine optische Charakterisierung der funktionalisierten Goldnanopartikel im sichtbaren Bereich. Im Gegensatz zur Resonanz-Raman-Verstärkung, bei der der Raman-Streuquerschnitt durch die elektronische Absorption erhöht wird, wird durch den SERS-Effekt vorrangig die Lichtintensität des Lasers und des Streulichts erhöht, wenn deren Wellenlängen innerhalb der Plasmonen-Absorption des Metallnanopartikels liegen. Diese Plasmonenresonanz liegt für Edelmetallnanopartikel im sichtbaren Spektralbereich und führt zu einer substanziellen Verstärkung des Raman-Signals um einen Faktor von bis zu 10^{10} , so dass sogar Einzelmoleküle mit Hilfe der SERS-Verstärkung detektiert werden können.¹⁹⁵ Während die Resonanz-Raman-Verstärkung Franck-Condon-aktive Schwingungsmoden betrifft, hängt die SERS-Verstärkung v.a. mit der Orientierung der Schwingungskordinate zur Partikeloberfläche zusammen. Es werden solche Schwingungen besonders verstärkt, die senkrecht zur Oberfläche gerichtet sind.¹⁹⁶ Somit lässt sich durch Vergleich der spontanen Raman-Spektren eines Analyten mit SERS-Spektren funktionaler Edelmetallnanopartikel die Orientierung der Analytmoleküle relativ zur Oberfläche bestimmen. Durch Anbindung absorbierender Moleküle an die Nanopartikel lassen sich beide Verstärkungsmechanismen kombinieren, indem gleichzeitig in einer Absorptionsbande des Moleküls als auch des Oberflächenplasmons des Nanopartikels angeregt wird. Dazu müssen sich beide Absorptionsbanden spektral überlappen. Die Plasmonenresonanz kann allerdings durch Größe, Material und Form des Nanopartikels spektral sehr weit variiert werden.

Als erster Schritt auf dem Weg zu funktionalisierten Edelmetallnanopartikeln für die heterogene Photokatalyse wurden im Rahmen der vorliegenden Arbeit die photoaktiven Rutheniumkomplexe **N719**, **N749**, **Z907** und **Ru** (Abb. 5.1) in wässriger Lösung auf Goldnanopartikeln funktionalisiert. Mit Hilfe der SERS-Spektroskopie wurde anschließend die erfolgreiche Anbindung der Farbstoffe an die Oberfläche und die Orientierung der Adsorbate auf der Oberfläche untersucht. Mit **N719**, **N749**, **Z907** sowie **Ru** funktionalisierte Goldnanopartikel wurden dabei mit zwei verschiedenen Synthesemethoden hergestellt.

Für die Funktionalisierung mit **N719**, **N749**, **Z907** wurden zunächst citratstabilisierte Goldnanopartikel nach der von Turkevich 1951 publizierten Reduktion von HAuCl_4 mit Citronensäure chemisch synthetisiert.¹⁸⁹ Mit dieser Methode kann in Abhängigkeit des Verhältnisses der Konzentration der Goldsäure zum Reduktionsmittel ein breites Spektrum an citratstabilisierten Goldnanopartikeln unterschiedlicher mittlerer Partikelgröße, Größenverteilung und Form hergestellt werden. In dieser Arbeit wurden sphärische Goldnanopartikel mit einem mittleren Partikeldurchmesser von (28 ± 3) nm synthetisiert. Anschließend wurden die sphärischen Nanopartikel mit den Komplexen **N719**, **N749** und **Z907** funktionalisiert, indem der Citrat-Ligand durch Ligandenaustausch (Konjugation) gegen die Rutheniumfarbstoffe ersetzt wurde (Abb 5.2 B und D). Durch mehrmalige Zentrifugation sowie Waschen der Kolloide wurde die überschüssige Farbstofflösung entfernt. Die Bestimmung der Größenverteilung der Nanopartikel erfolgte über die Auswertung von UV-Vis-Spektren und TEM-Bildern (Transmissions-Elektronen-Mikroskopie - TEM) (Abb. 5.2 D).

Ru konnte mit der Ligandenaustauschreaktion nicht an Goldnanopartikel koordiniert werden. Das kann damit begründet werden, dass **Ru** als potentielle Ankergruppe an Goldnanopartikel eine zweizählige Phenantrolinsphäre aufweist. Da Stickstoff eine deutlich geringere Affinität zu Gold als die Schwefelfunktion der Isothiocyanat-Liganden von **N719**, **N749** und **Z907** hat, ist auch die Bindung des Phenantrolin-Liganden an die Goldnanopartikel deutlich schwächer. Tatsächlich ist die Bindung so schwach, dass **Ru** die Citrat-Liganden nicht verdrängen kann. Einen weiteren Einfluss hat die Größe der zu funktionalisierenden Nanopartikel. Aus sterischen Gründen bevorzugt ein Chelat-Ligand wie Phenantrolin mit einer Bindungstasche von ca. 270 pm^{197} deutlich kleinere Partikel zur Funktionalisierung. Daher wurde zur Synthese **Ru** stabilisierter Nanopartikel die kationische Phasentransferkatalyse eingesetzt (Abb 5.2 A).^{181,198} Dabei wird das Chloroauration $[\text{AuCl}_4]^-$ durch einen kationischen Mediator in eine Toluolphase überführt und anschließend mit NaBH_4 -Lösung reduziert. Das gebildete kolloidale Gold wird anschließend durch den anzubindenden Komplex (**Ru**) in eine wässrige Phase transferiert. **Ru** fungiert somit bei dieser Synthesemethode als Phasentransferkatalysator (Abb 5.2 A). Die erhaltenen funktionalisierten Goldnanopartikel waren deutlich kleiner ($6 \pm 1,4$) nm als die über die Methode von Turkevich synthetisierten Partikel (Abb. 5.2 B und C).

Mit beiden beschriebenen Synthesemethoden konnten funktionalisierte Goldnanopartikel hergestellt werden, welche über Monate stabil waren, ohne irreversibel zu aggregieren. Da generell Nanopartikel zur Aggregation tendieren, um die extrem hohe Oberflächenenergie zu verringern, wäre die Beobachtung von Aggregation ein Hinweis auf eine geringe Stabilität der funktionalisierten Nanopartikel.

Mit Hilfe der spektroskopischen Charakterisierung der Kolloide wird überprüft, ob die Eigenschaften der Rutheniumkomplexe nach Immobilisierung auf den Nanopartikeln erhalten bleiben. In diesem Zusammenhang wurden die Wechselwirkung zwischen Farbstoff und Nanopartikel, d.h. die neuen Eigenschaften der funktionalen Nanopartikel-Farbstoff-Grenzfläche, und die Orientierung der Farbstoffe auf der Nanopartikel-Oberfläche mit Hilfe der SERS-Spektroskopie untersucht. Die Detektion der SERS-Spektren der eingesetzten Farbstoffe ist dabei nicht nur ein Indiz für die erfolgreiche Funktionalisierung der Nanopartikel, sondern liefert zusätzlich Informationen über Orientierung, Bindungsmodalitäten und Wechselwirkungen auf der Oberfläche. Zur Identifikation von strukturellen Unterschieden der Farbstoffe in Lösung sowie zur Bestimmung der SERS-Verstärkung wurden außerdem RR-Spektren und FT-Raman-Spektren gemessen.

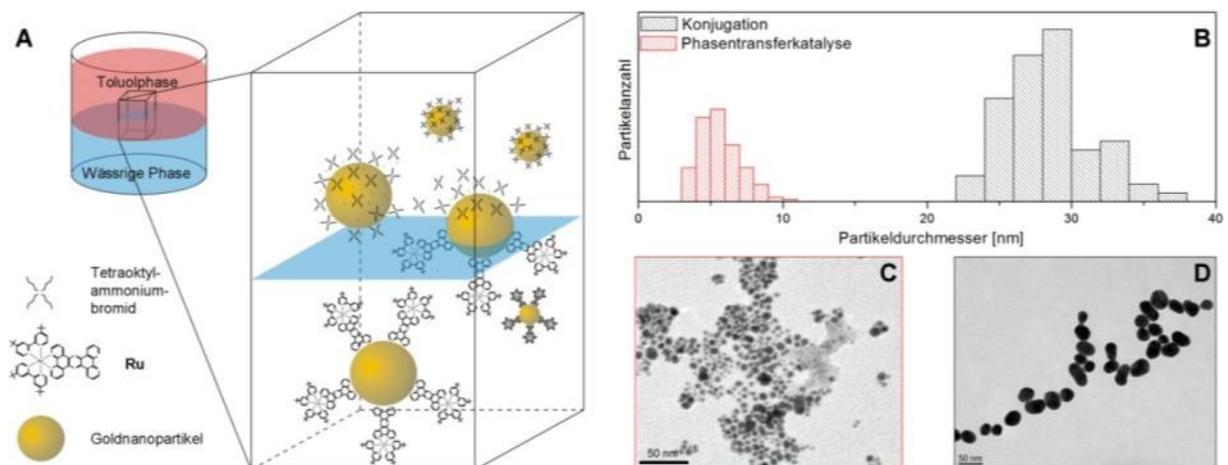


Abbildung 5.2: A) Schema der Phasentransferkatalyse zur Synthese von Goldnanopartikeln stabilisiert durch Ru. Das Chloroauration $[\text{AuCl}_4]^-$ wird durch einen kationischen Mediator (Teträoktylammoniumbromid) in die Toluolphase transferiert und anschließend mit NaBH_4 -Lösung reduziert. Die dadurch generierten Goldnanopartikel werden anschließend durch einen Phasentransferkatalysator (Ru) in die wässrige Phase überführt und funktionalisiert. B) Histogramm, d.h. Größenverteilung, der Goldnanopartikel, welche über Konjugation und Phasentransferkatalyse erhalten wurden. Die Methode der Konjugation liefert Nanopartikel mit einem mittleren Partikeldurchmesser von (28 ± 3) nm während mithilfe der Phasentransferkatalyse deutlich kleinere Partikel generiert werden ($6 \pm 1,4$) nm. Die TEM-Bilder zeigen durch Ru (C) und N749 (D) stabilisierte Goldkolloide.

Für die Komplexe **N719**, **N749** und **Z907** sind die Ergebnisse und deren Interpretation ähnlich, so dass im Folgenden nur die Ergebnisse für den Komplex **N749** vorgestellt werden. Konzentrationsabhängige RR-Spektren wurden in Resonanz mit dem MLCT-Übergang aufgenommen, SERS-Spektren in Resonanz mit dem MLCT-Übergang und der Oberflächenplasmonenabsorption der Goldnanopartikel ($\lambda_{\text{exc}} = 532$ nm). Sowohl das RR-Spektrum als auch das SERS-Spektrum von **N749** werden durch Schwingungsbanden des Terpyridin-Liganden ($1468, 1521, 1604$ cm^{-1}) dominiert (Abb. 5.3 links).¹⁹⁹ Mittels der konzentrationsabhängigen RR-Spektren wurde, basierend auf dem Signal-zu-Rausch-Verhältnis, die Nachweisgrenze für **N749** in wässriger Lösung zu 10^{-6} M abgeschätzt. Beim Vergleich des nichtresonanten Raman-Spektrums des reinen **N749** mit dem RR-Spektrum der 10^{-4} M Lösung kann die Verstärkung durch den Resonanz-Raman-Effekt mit etwa 10^4 beziffert werden (Abb. 5.3 links). Die Konzentration von **N749** in der Kolloidlösung beträgt etwa 10^{-7} M bei vollständiger

Bedeckung der Oberfläche. Dafür wurden eine monomolekulare Schicht auf der Oberfläche der ca. 30 nm großen Nanopartikel und eine Konzentration von 10^{10} Partikeln pro ml angenommen. Das SERS-Spektrum zeigt ein ähnliches Signal-zu-Rausch Verhältnis wie das RR-Spektrum der 10^{-4} M Lösung des **N749**, was einer zusätzlichen Oberflächen-Verstärkung um den Faktor 10^3 entspricht, wobei angenommen wird, dass sich beide Verstärkungsmechanismen addieren (Abb. 5.3 links).

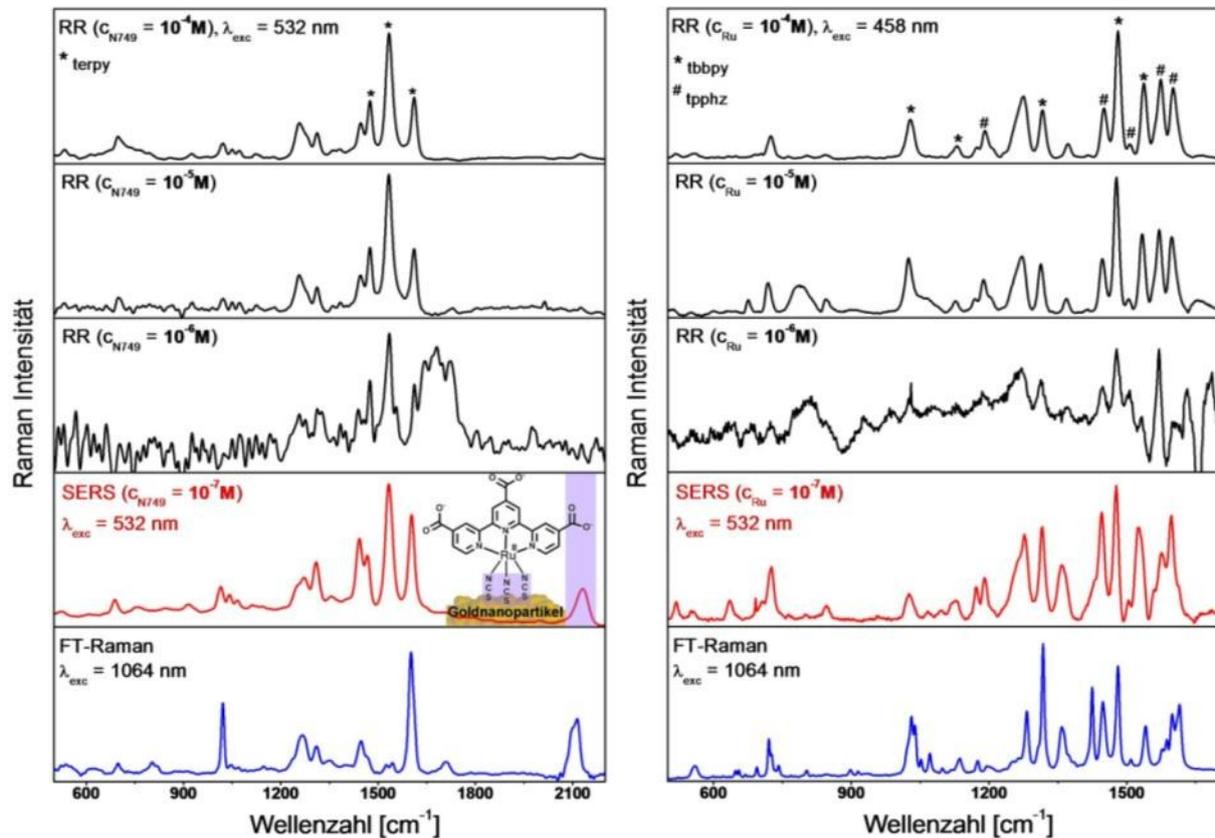


Abbildung 5.3: Bestimmung der SERS-Verstärkung, Nachweis der Anbindung der Chromophore und Orientierung auf den Kolloiden mit Hilfe von SERS für N749 (links) und Ru (rechts). Durch Vergleich der konzentrationsabhängigen RR-Spektren (schwarz) mit dem SERS- (rot) und FT-Raman-Spektrum (blau) lassen sich Resonanz- und SERS-Verstärkung sowie die Nachweisgrenze ermitteln. Die Resonanz-Verstärkung beträgt ca. 10^4 , die zusätzliche SERS-Verstärkung 10^3 , die Nachweisgrenze etwa 10^{-6} M für beide Komplexe. Links N749: Die MLCT-Anregung bei 532 nm bewirkt eine Verstärkung der Terpyridin-Banden (terpy, markiert mit einem Stern). Die nur im SERS-Spektrum selektiv verstärkte CN-Streckschwingung (violett hinterlegt) beweist die Anbindung von N749 an die Oberfläche der Nanopartikel über die Isothiocyanat-Liganden (dargestellt im kleinen Bild). Rechts Ru: Das RR-Spektrum ($\lambda_{exc} = 458 \text{ nm}$) ist von Beiträgen des MLCTs zum tpphz-Liganden (markiert mit Raute) und des MLCTs zum tbbpy-Liganden (markiert mit Stern) geprägt. Kleine Unterschiede in den Raman-Bandenverhältnissen zwischen gelöstem und auf den Goldpartikeln immobilisiertem Ru deuten auf eine leichte Änderung der elektronischen Struktur durch Anbindung an die Nanopartikeloberfläche hin. Ein Einfluss der unterschiedlichen Anregungswellenlängen für SERS und RR auf das unterschiedliche Bandenmuster ist ebenfalls nicht auszuschließen.

Die stärkste SERS-Verstärkung erfahren Schwingungen funktioneller Gruppen, die sich nahe der Oberfläche der Nanopartikel befinden und deren Schwingungsrichtung senkrecht zur Oberfläche ausgerichtet ist. Die Detektion der symmetrischen CN-Streckschwingung bei 2100 cm^{-1} ist demnach ein Beweis für die Koordination des **N749** über die Isothiocyanat-Liganden und stellt außerdem den einzigen signifikanten Unterschied zum RR-Spektrum dar, in dem diese Schwingung nicht verstärkt wird, da die Isothiocyanat-Funktion elektronisch nicht mit dem angeregten Übergang im Chromophor (Terpyridin) gekoppelt ist (Abb. 5.3 links, kleines Bild). Die Ähnlichkeit des SERS- und RR-Spektrums deutet außerdem darauf hin, dass die molekulare und elektronische Struktur des Farbstoffs durch die Immobilisierung auf der Nanopartikeloberfläche erhalten bleibt. Zusammenfassend erlaubt die direkte Anbindung an Gold einen schnellen und effizienten Ladungstransport vom Farbstoff auf die Nanopartikel, was im Hinblick auf eine katalytische Anwendung von großer Bedeutung ist.

Aufgrund des starken Fluoreszenzuntergrundes von **Ru** bei einer Anregungswellenlänge von 532 nm (Anregungswellenlänge für die Aufnahme der SERS-Spektren) wurden die konzentrationsabhängigen RR-Spektren bei 458 nm angeregt. Im RR-Spektren von **Ru** sind sowohl tpphz-Banden ($1601, 1574, 1506, 1450, 1190\text{ cm}^{-1}$) als auch tbbpy-Banden ($1538, 1481, 1317, 1131, 1028\text{ cm}^{-1}$) detektierbar (Abb. 5.3 rechts).¹⁷⁰ Die Nachweisgrenze in wässriger Lösung liegt auch für **Ru** im Bereich von 10^{-6} M . Basierend auf der gleichen Abschätzung der Konzentration von **Ru** auf Goldnanopartikeln wie für **N749** konnte beim Vergleich des SERS- und des RR-Spektrums eine zusätzliche Verstärkung um den Faktor 10^3 durch den SERS-Effekt ermittelt werden. Im SERS-Spektrum von **Ru** deutet eine selektive Verstärkung von tpphz-Banden auf eine Anbindung über die Phenantrolinsphäre von **Ru** an die Oberfläche der Goldnanopartikel hin. Speziell die Moden bei 1603 und 1453 cm^{-1} deuten auf eine starke Wechselwirkung zwischen dem zweizähligen Chelat-Liganden der tpphz-Struktur mit der Metalloberfläche hin (Abb. 5.3 rechts). Leichte Unterschiede in Bandenverhältnissen sind beim Vergleich des SERS- und RR-Spektrum von **Ru** zu verzeichnen. Aufgrund der verschiedenen Anregungswellenlängen ($\Delta\lambda \approx 70\text{ nm}$) für die Messung von SERS- und RR-Spektren können diese Unterschiede im Bandenmuster zum Teil auf unterschiedliche Resonanz-Verstärkung zurückzuführen sein. Eine Aussage über die Erhaltung der molekularen und elektronischen Eigenschaften nach Anbindung von **Ru** auf Goldnanopartikel kann aufgrund unterschiedlicher elektronischer Beiträge zum SERS- und RR-Spektrum daher nicht getroffen werden.

Durch Oberflächenmodifikation von Goldnanopartikeln können die Eigenschaften von Rutheniumfarbstoffen mit denen der Nanopartikel in einer supramolekularen Struktur kombiniert werden. In dieser Arbeit konnten erstmals die photoaktiven Verbindungen **N719**, **N749** und **Z907** und **Ru** auf Goldnanopartikeln mit definierter Größe immobilisiert sowie die Anbindung und die Eigenschaften der Nanopartikel-Farbstoff-Grenzfläche untersucht werden. Demnach binden **N719**, **N749** und **Z907** über die Schwefel-Funktion der Isothiocyanat-Liganden an die Oberfläche von Goldnanopartikeln. Da SERS- und RR-Spektren einander sehr ähnlich sind, bewirkt die Koordination keine signifikante Änderung der konjugierten elektronischen Struktur. Im Unterschied dazu deuten kleine Unterschiede im Raman-Bandenmuster des Rutheniumfarbstoffs **Ru** auf eine leichte Änderung der elektronischen Struktur nach Immobilisierung auf der Nanopartikeloberfläche hin. Allerdings sind für den eindeutigen Beweis weitere Untersuchungen notwendig, z.B. SERS- und RR-Messungen bei der gleichen Anregungswellenlänge 458 nm sowie Anbindung an Core-Shell-Nanopartikel, bei denen kein chemischer Beitrag zum SERS-Effekt zu erwarten ist.²⁰⁰

6. Zusammenfassung

Zur Aufklärung des exakten Ablaufes dynamischer Prozesse, die die Grundlage fundamentaler natürlicher wie artifizierter Vorgänge sind, ermöglicht die Raman-Spektroskopie als struktursensitive Methode die Analyse einer Vielzahl prozessrelevanter Merkmale. Neben der Aufklärung der molekularen Struktur anhand des Schwingungsspektrums, die wichtige Rückschlüsse auf die Funktion des Moleküls erlaubt, lassen sich insbesondere auch die den Prozessverlauf begleitenden strukturellen Änderungen auf molekularer Ebene, die Konzentration des Analyten und dessen räumliche Verteilung mit sub- μm Auflösung bestimmen.

Im Rahmen der vorliegenden Arbeit konnte mit Hilfe der Raman-Mikro-Spektroskopie erstmals die räumliche Verteilung des Karotinoids Fucoxanthin in der Umgebung der Braunalge *Fucus Vesiculosus* bestimmt und daraus Rückschlüsse auf dessen Funktion gezogen werden. Da dieser Sekundärmetabolit sehr homogen über die Oberfläche verteilt an das umgebende Wasser abgegeben wird, so dass die Konzentration diffusionskontrolliert exponentiell mit dem Abstand zur Oberfläche abnimmt, kann als sicher angesehen werden, dass der Metabolit aktiv freigesetzt wird. Dabei wurden lokal deutlich höhere Konzentrationen des Metaboliten gemessen, als aufgrund von Extraktionsmessungen im Vorfeld der Arbeit bekannt war. In den lokal gemessenen mM Konzentrationen wirkt Fucoxanthin antibiotisch. Daher steuert die Alge durch die Freisetzung offenbar die Zusammensetzung der auf ihr lebenden mikrobiellen Gemeinschaft. Da die Fucoxanthinkonzentration an der Oberfläche in direkter Korrelation mit den aufwachsenden Mikroorganismen lokal variiert, könnte der Stoff auch als Botenstoff zur intermikrobiellen Kommunikation beitragen.

Selbstheilende Materialien können kleine mechanische Beschädigungen wie Mikrorisse autonom reparieren und dadurch zur Verlängerung der Lebensdauer stark beanspruchter und schwer austauschbarer Bauteile beitragen. Ein vielversprechendes System stellen über Komplexverbindungen quervernetzte Polymere dar, die beim Erhitzen kleinere Beschädigungen heilen. Mechanistisch könnte dieses Verhalten entweder auf eine ionische Wechselwirkung zurückzuführen sein, so dass sich beim Erhitzen die Mobilität des Polymernetzwerks erhöht und sich neue ionische Cluster ausbilden. Alternativ könnten die Komplex-Ligand-Brücken bei Temperatureintrag partiell dekomplexieren und sich anschließend neu verknüpfen. Im Rahmen dieser Arbeit konnte bei zyklischer Änderung der Temperatur eine reversible Dekomplexierung anhand der Verschiebung charakteristischer Schwingungsbanden der Komplexe beobachtet werden, was den zweiten Heilungsmechanismus prinzipiell ermöglicht. Perspektivisch lassen sich über die orts aufgelöste Untersuchung der Heilungsprozesse mit Hilfe der Raman-Mikro-Spektroskopie wichtige Erkenntnisse über die Heilungsprozesse und die für das Selbstheilungsvermögen optimale Zusammensetzung des Polymers gewinnen.

Da die Untersuchung photoinduzierter Ladungstransferprozesse im Bereich von Femto- bis Mikrosekunden und die Aufklärung der sequentiellen Prozessfolge der Raman-Spektroskopie unter Verwendung von Dauerstrichlasern als Anregungsquellen nicht direkt zugänglich ist, können im Verlauf der photoinduzierten Reaktion auftretende Intermediate auch elektrochemisch generiert und *In-situ*-UV-Vis- sowie Raman-spektroskopisch charakterisiert werden. Im Rahmen der Arbeit wurde daher ein neuartiger experimenteller Aufbau realisiert, der in einer Dünnschicht-Küvette die

elektrochemische Generation von Reduktionsprodukten unter inerten Bedingungen und deren spektroskopische Analyse ermöglicht. Mit diesem Aufbau konnten Strukturänderungen während photochemischer Reaktionen analysiert und der reduktionsinitiierte Ladungstransfer lokalisiert werden. So wurde durch Vergleich der im Experiment gemessenen Raman-Spektren mit TDDFT-Rechnungen nachgewiesen, dass die Reduktion des Rutheniumfarbstoffs Di-tetrabutylammonium cis-bis(isothiocyanato)bis(2,2'-bipyridyl-4,4'-dicarboxylato)Ruthenium(II) (**N719**) von der Deprotonierung der Carboxylgruppen begleitet wird, wie schon zuvor in der Literatur beschrieben wurde.

Neuartige Rutheniumfarbstoffe, die das organische Chromophor 4*H*-Imidazol koordinieren, weisen eine im Vergleich zu **N719** deutlich höhere Absorption im roten und nahinfraroten Spektralbereich auf. Daher sind diese Farbstoffe vielversprechende schwarze Absorber, z.B. für Anwendungen in der Photokatalyse. Für die photokatalytische Wasserstoffproduktion müssen jedoch mindestens zwei (Photo)-Elektronen zwischengespeichert und auf das katalytische Zentrum übertragen werden. Vom 4*H*-Imidazol-Chromophor ist bekannt, dass es zweifach reduziert werden kann. In dieser Arbeit konnte erstmals mit Hilfe der Resonanz-Raman-Spektroelektrochemie (RR-SEC) gezeigt werden, dass der 4*H*-Imidazol-Ligand auch innerhalb eines Rutheniumkomplexes durch Modifikation der Substituenten an den Aryliminoresten zwei Elektronen lokal in einer Ligandensphäre speichern kann, was einen großen Fortschritt auf dem Weg zur Entwicklung kleiner funktionaler photoaktiver supramolekularer Systeme darstellt.

Die katalytische Aktivität ist für Komplexe wie $[(\text{tbbpy})_2\text{Ru}(\text{tpphz})\text{Pd}(\text{Cl})_2]^{2+}$ (tbbpy = 4,4'-di-*tert.*-butyl-2,2'-bipyridin, tpphz = tetrapyrido[3,2-*a*:2'3'-*c*:3'',2''-*h*:2''',3'''-*j*]phenazin) (**RuPd**) und $[(\text{tbbpy})_2\text{Ru}(\text{tpphz})\text{Pt}(\text{Cl})_2]^{2+}$ (**RuPt**), die aus einem photoaktiven Rutheniumzentrum bestehen, das über einen Brückenliganden mit einem katalytisch aktiven Pt oder Pd-Zentrum verknüpft ist, bereits nachgewiesen. Dem tpphz Brückenligand kommt dabei die Funktion der Elektronen-Übertragung und temporären Speicherung der Ladung zu. Die höhere Katalyseeffizienz wurde für **RuPd** nachgewiesen, allerdings häufen sich die Indizien, dass es sich nicht um einen homogenen molekularen Katalysator handelt, sondern dass **RuPd** bei Photoanregung Kolloide bildet, so dass der Katalysator zerstört wird. Der strukturell verwandte **RuPt**-Komplex zeigt eine niedrigere katalytische Aktivität, bildet jedoch keine Kolloide und ist unter katalytischen Bedingungen chemisch stabil. Daher wurden im Rahmen dieser Arbeit die Intermediate des photokatalytischen Zyklus von **RuPd** und **RuPt** elektrochemisch generiert und spektroskopisch untersucht, um einen Einblick in den Katalysemechanismus dieser Komplexe zu gewinnen. Dabei konnte sowohl spektroskopisch als auch mit Hilfe von TDDFT-Rechnungen gezeigt werden, dass die Einfachreduktion auf dem tpphz-Liganden lokalisiert ist und dass die neu auftretende Absorptionsbande im roten Spektralbereich auf einen tpphz-zentrierten Intra-Liganden-Übergang zurückzuführen ist. Diese Absorptionsbande trägt demnach nicht zur photokatalytischen Ladungstrennung bei. Weiterhin wurde festgestellt, dass durch Reduktion des Brückenliganden der photoinduzierte Metall-zu-Ligand-Ladungstransfer auf den Brückenligand vermindert wird und die Photoelektronen überwiegend auf den Terpyridin-Liganden lokalisiert sind. Daher ist die sequentielle Folge von Photoanregung und Elektronen-Übertragung auf das katalytische Zentrum, bevor die nächste Photoanregung erfolgt, von entscheidender Bedeutung, denn die Ladungstransfereffizienz von Inter-Liganden-Übergängen ist deutlich geringer. Durch Vergleich der Ergebnisse mit den Resultaten von transienten Absorptionsmessungen werden mechanistische Unterschiede deutlich. Bei transientser Absorption wird ein schneller Ladungstransfer auf das Katalysezentrum beobachtet, so dass der reduzierte Brückenligand nur einen kurzlebigen

Zwischenzustand darstellt. Im Rahmen der SEC-Messungen hingegen wurde bei Einfachreduktion nur der reduzierte tpphz-Ligand beobachtet, jedoch kein Übertrag des Elektrons auf das Katalysezentrum. Dieses Ergebnis deutet darauf hin, dass die Oxidationszahl des Photozentrums eine entscheidende Bedeutung für den Ladungstransfer auf das Katalysezentrum hat, da dieser Transfer im Falle von Ru(II) nicht beobachtet werden konnte. Somit ist auch die zeitliche Folge von Elektronen-Übertragung und Reduktion des oxidierten Photozentrums durch den Elektronendonator für den Gesamtprozess entscheidend. Alternativ könnte die Stabilisierung des reduzierten tpphz-Liganden aber auch eine Folge der in Lösung vorherrschenden hohen Ionenstärke sein. Es wird vermutet, dass die Reduktion des Pd-Katalysezentrums mit der Abspaltung eines Chlorid-Liganden verbunden ist, die durch den Ionenüberschuss möglicherweise inhibiert wird. Damit hat die Methode der Spektroelektrochemie das zusätzliche Potential, durch den Einfluss des Elektrolyten kurzlebige Intermediate gezielt für spektroskopische Langzeituntersuchungen zu stabilisieren.

Aus den in dieser Arbeit vorgestellten spektroelektrochemischen Untersuchungen eröffnen sich Einblicke in die Ladungstransferprozesse photoaktiver supramolekularer Systeme durch Beobachtung der intermediären Strukturen, insbesondere für Mehrelektronen-Transfervorgänge, die alternativen spektroskopischen Methoden nicht zugänglich sind. Es konnte gezeigt werden, wie Strukturmodifikationen das elektrochemische Verhalten beeinflussen. Außerdem konnten auf der Basis der experimentellen und theoretischen Ergebnisse Informationen über die sequentielle Abfolge von lichtinduzierten Ladungstransferprozessen gewonnen werden.

Rutheniumfarbstoffe können, immobilisiert auf Edelmetallnanopartikeln, in heterogenen Katalysatoren als Lichtsammeleinheiten verwendet werden. Das bietet weitere Möglichkeiten, gezielt die photochemischen und photophysikalischen Eigenschaften zu modifizieren. So können einerseits Größe, Form und Zusammensetzung der Nanopartikel über einen weiten Bereich variiert werden, andererseits können die Nanopartikel selbst sowohl Licht absorbieren als auch als katalytisch aktives Substrat dienen. Als Träger für Photokatalysatoren bieten sich aufgrund ihrer großen Oberfläche und chemischen Stabilität Edelmetall-Nanopartikel an, z.B. zur Untersuchung der photokatalytischen Wasserstoffgewinnung. Im Rahmen dieser Arbeit wurden daher erstmals kommerziell erhältliche Rutheniumfarbstoffe wie **N749** auf Goldnanopartikeln mit verschiedenen Syntheseverfahren immobilisiert. Weiterhin konnte mittels der Phasentransferkatalyse erstmals ein Rutheniumfarbstoff, der den tpphz-Liganden koordiniert, auf Nanopartikeln funktionalisiert werden. Solche heterogenen Systeme sind ideal geeignet, die Photostabilität und auch die photoinduzierten Elektronen-Transporteigenschaften innerhalb der Grenzfläche zwischen Nanopartikel und funktionalisierten Farbstoffmolekülen zu untersuchen und auf den Ergebnissen aufbauend zu verbessern. Die oberflächenverstärkte Raman-Streuung stellt dabei die ideale Methode zur Untersuchung dieser Systeme dar, da sie sowohl die Ausrichtung des Komplexes zur Oberfläche als auch die Bindungsstelle identifizieren kann.

Zusammenfassend konnten im Rahmen dieser Arbeit eine Vielzahl (Resonanz)-Raman-spektroskopischer Techniken erfolgreich zur Aufklärung dynamischer Prozesse und der begleitenden Strukturänderungen eingesetzt werden, die wesentlich zur Verbesserung des Verständnisses komplexer Vorgänge sowohl in biologischen als auch in artifiziellen Systemen beitragen.

Literaturverzeichnis

- (1) Kay, E. R.; Leigh, D. A.; Zerbetto, F. *Angew. Chem. Int. Ed.* **2007**, *46*, 72.
- (2) Rinaldi, A. *EMBO Rep.* **2007**, *8*, 995.
- (3) Nocera, D. G. *Chem. Soc. Rev.* **2008**, *38*, 13.
- (4) Rau, S.; Walther, D.; Vos, J. G. *Dalton Trans.* **2007**, 915.
- (5) Lewis, N. S.; Nocera, D. G. *Proc. Natl. Acad. Sci. U. S. A.* **2006**, *103*, 15729.
- (6) Kamat, P. V. *J. Phys. Chem. C* **2007**, *111*, 2834.
- (7) Armaroli, N.; Balzani, V. *Angew. Chem. Int. Ed.* **2007**, *46*, 52.
- (8) Balzani, V.; Credi, A.; Venturi, M. *ChemSusChem* **2008**, *1*, 26.
- (9) Cook, T. R.; Dogutan, D. K.; Reece, S. Y.; Surendranath, Y.; Teets, T. S.; Nocera, D. G. *Chem. Rev.* **2010**, *110*, 6474.
- (10) Turner, J. A. *Science* **1999**, *285*, 687.
- (11) Blankenship, R. E. *Molecular Mechanisms of Photosynthesis*; John Wiley & Sons, 2008.
- (12) Barber, J. *Chem. Soc. Rev.* **2008**, *38*, 185.
- (13) Diekmann, S.; Weston, J.; Anders, E.; Boland, W.; Schönecker, B.; Hettmann, T.; von Langen, J.; Erhardt, S.; Mauksch, M.; Bräuer, M.; Beckmann, C.; Rost, M.; Sperling, P.; Heinz, E. *Rev. Mol. Biotechnol.* **2002**, *90*, 73.
- (14) Wahl, M. *Marine Hard Bottom Communities: Patterns, Dynamics, Diversity, and Change*; Springer, **2009**.
- (15) Hay, M. E.; Fenical, W. *Annu. Rev. Ecol. Syst.* **1988**, *19*, 111.
- (16) Haber, M.; Carbone, M.; Mollo, E.; Gavagnin, M.; Ilan, M. *Mar. Ecol. Prog. Ser.* **2011**, *422*, 113.
- (17) Harder, T. In *Marine and Industrial Biofouling*; Flemming, P. D. H.-C.; Murthy, D. P. S.; Venkatesan, D. R.; Cooksey, P. D. K., Eds.; Springer Series on Biofilms; Berlin Heidelberg, **2009**; pp. 219–231.
- (18) Wahl, M. *Mar. Ecol. Prog. Ser.* **1989**, *58*, 175.
- (19) Wahl, M.; Hay, M. E. *Oecologia* **1995**, *102*, 329.
- (20) Viano, Y.; Bonhomme, D.; Camps, M.; Briand, J.-F.; Ortalo-Magné, A.; Blache, Y.; Piovetti, L.; Culioli, G. *J. Nat. Prod.* **2009**, *72*, 1299.
- (21) Gerasimenko, N. I.; Chaykina, E. L.; Busarova, N. G.; Anisimov, M. M. *Appl. Biochem. Microbiol.* **2010**, *46*, 426.
- (22) Lichtlé, C.; Spilar, A.; Duval, J. C. *Protoplasma* **1992**, *166*, 99.
- (23) Saha, M.; Rempt, M.; Grosser, K.; Pohnert, G.; Weinberger, F. *Biofouling* **2011**, *27*, 423.
- (24) Welling, M.; Pohnert, G.; Küpper, F. C.; Ross, C. *J. Adhes.* **2009**, *85*, 825.
- (25) Jung, V.; Pohnert, G. *Tetrahedron* **2001**, *57*, 7169.
- (26) Adolph, S.; Jung, V.; Rattke, J.; Pohnert, G. *Angew. Chem. Int. Ed Engl.* **2005**, *44*, 2806.
- (27) Trask, R. S.; Williams, H. R.; Bond, I. P. *Bioinspir. Biomim.* **2007**, *2*, P1.
- (28) Yang, Y.; Urban, M. W. *Chem. Soc. Rev.* **2013**, *42*, 7446.
- (29) Wu, D. Y.; Meure, S.; Solomon, D. *Prog. Polym. Sci.* **2008**, *33*, 479.
- (30) Amendola, V.; Meneghetti, M. *Nanoscale* **2009**, *1*, 74.
- (31) Williams, K. A.; Dreyer, D. R.; Bielawski, C. W. *MRS Bull.* **2008**, *33*, 759.
- (32) Bode, S.; Bose, R. K.; Matthes, S.; Ehrhardt, M.; Seifert, A.; Schacher, F. H.; Paulus, R. M.; Stumpf, S.; Sandmann, B.; Vitz, J.; Winter, A.; Hoepfener, S.; Garcia, S. J.; Spange, S.; Zwaag, S. van der; Hager, M. D.; Schubert, U. S. *Polym. Chem.* **2013**, *4*, 4966.
- (33) Bode, S.; Zedler, L.; Schacher, F. H.; Dietzek, B.; Schmitt, M.; Popp, J.; Hager, M. D.; Schubert, U. S. *Adv. Mater.* **2013**, *25*, 1634.
- (34) Burnworth, M.; Tang, L.; Kumpfer, J. R.; Duncan, A. J.; Beyer, F. L.; Fiore, G. L.; Rowan, S. J.; Weder, C. *Nature* **2011**, *472*, 334.
- (35) John Varley, R.; van der Zwaag, S. *Polym. Test.* **2008**, *27*, 11.

- (36) Hoffert, M. I.; Caldeira, K.; Jain, A. K.; Haites, E. F.; Harvey, L. D. D.; Potter, S. D.; Schlesinger, M. E.; Schneider, S. H.; Watts, R. G.; Wigley, T. M. L.; Wuebbles, D. J. *Nature* **1998**, *395*, 881.
- (37) Parmesan, C.; Yohe, G. *Nature* **2003**, *421*, 37.
- (38) Solomon, S. *Climate Change 2007 - The Physical Science Basis: Working Group I Contribution to the Fourth Assessment Report of the IPCC*; Cambridge University Press, **2007**.
- (39) Esswein, A. J.; Nocera, D. G. *Chem. Rev.* **2007**, *107*, 4022.
- (40) Wang, M.; Na, Y.; Gorlov, M.; Sun, L. *Dalton Trans. Camb. Engl.* **2003** **2009**, 6458.
- (41) Inagaki, A.; Akita, M. *Coord. Chem. Rev.* **2010**, *254*, 1220.
- (42) Teets, T. S.; Nocera, D. G. *Chem. Commun.* **2011**, *47*, 9268.
- (43) Nazeeruddin, M. K.; Klein, C.; Liska, P.; Grätzel, M. *Coord. Chem. Rev.* **2005**, *249*, 1460.
- (44) O'Regan, B.; Grätzel, M. *Nature* **1991**, *353*, 737.
- (45) Grätzel, M. *Acc. Chem. Res.* **2009**, *42*, 1788.
- (46) Hagfeldt, A.; Boschloo, G.; Sun, L.; Kloo, L.; Pettersson, H. *Chem Rev* **2010**, *110*, 6595.
- (47) Vos, J. G.; Kelly, J. M. *Dalton Trans.* **2006**, 4869.
- (48) Reynal, A.; Palomares, E. *Eur. J. Inorg. Chem.* **2011**, *2011*, 4509.
- (49) Campagna, S.; Puntoriero, F.; Nastasi, F.; Bergamini, G.; Balzani, V. In *Photochemistry and Photophysics of Coordination Compounds I*; Balzani, V.; Campagna, S., Eds.; Topics in Current Chemistry; Springer Berlin Heidelberg, **2007**; pp. 117–214.
- (50) Gebauer, T. Neuartige zweistufige Redoxsysteme basierend auf 4H-Imidazolen, Dissertation, Friedrich-Schiller-Universität Jena, **2005**.
- (51) Atzrodt, J.; Beckert, R.; Günther, W.; Görls, H. *Eur. J. Org. Chem.* **2000**, *2000*, 1661.
- (52) Blumhoff, J.; Beckert, R.; Rau, S.; Losse, S.; Matschke, M.; Günther, W.; Görls, H. *Eur. J. Inorg. Chem.* **2009**, *2009*, 2162.
- (53) Gebauer, T.; Beckert, R.; Weiss, D.; Knop, K.; Käpplinger, C.; Görls, H. *Chem. Commun. Camb. Engl.* **2004**, 1860.
- (54) Losse, S. Redoxaktive metallorganische Farbstoffkomplexe zur Verwendung in Photovoltaik und Photokatalyse, Dissertation, Friedrich-Schiller-Universität Jena, **2010**.
- (55) Andreiadis, E. S.; Chavarot-Kerlidou, M.; Fontecave, M.; Artero, V. *Photochem. Photobiol.* **2011**, *87*, 946.
- (56) Sakai, K.; Ozawa, H. *Coord. Chem. Rev.* **2007**, *251*, 2753.
- (57) Eckenhoff, W. T.; Eisenberg, R. *Dalton Trans.* **2012**, *41*, 13004.
- (58) Rau, S.; Schäfer, B.; Gleich, D.; Anders, E.; Rudolph, M.; Friedrich, M.; Görls, H.; Henry, W.; Vos, J. G. *Angew. Chem. Int. Ed.* **2006**, *45*, 6215.
- (59) Pfeiffer, M. G.; Schäfer, B.; Kuhnt, C.; Schmitt, M.; Popp, J.; Guthmüller, J.; Smolentsev, G.; Uhlig, J.; Nazarenko, E.; Sundström, V.; González, L.; Dietzek, B.; Rau, S. *Angew. Chem. Int. Ed. Engl.* **submitted**.
- (60) Kobayashi, M.; Masaoka, S.; Sakai, K. *Molecules* **2010**, *15*, 4908.
- (61) Ozawa, H.; Haga, M.; Sakai, K. *J. Am. Chem. Soc.* **2006**, *128*, 4926.
- (62) Ozawa, H.; Sakai, K. *Chem. Commun.* **2011**, *47*, 2227.
- (63) Schmid, D. G. *Nanoparticles: From Theory to Application*; Wiley-VCH, **2004**.
- (64) Henry, A.-I.; Bingham, J. M.; Ringe, E.; Marks, L. D.; Schatz, G. C.; Van Duyne, R. P. *J Phys Chem C* **2011**, *115*, 9291.
- (65) Chen, H. M.; Liu, R.-S. *J Phys Chem C* **2011**, *115*, 3513.
- (66) Daniel, M.-C.; Astruc, D. *Chem Rev* **2003**, *104*, 293.
- (67) Oikawa, H.; Onodera, T.; Masuhara, A.; Kasai, H.; Nakanishi, H. In *Polymer Materials*; Lee, K.-S.; Kobayashi, S., Eds.; Springer Berlin Heidelberg, **2009**; Vol. 231, pp. 147–190.
- (68) Mayer, C. R.; Dumas, E.; Sécheresse, F. *Chem Commun* **2004**, 345.
- (69) Hallett, A. J.; Christian, P.; Jones, J. E.; Pope, S. J. A. *Chem. Commun.* **2009**, 4278.
- (70) Huang, T.; Murray, R. W. *Langmuir* **2011**, *18*, 7077.
- (71) Torday, J. S. *Am. J. Physiol. - Cell Physiol.* **2013**, *305*, C682.

- (72) Brent, R. *FEBS Lett.* **2009**, *583*, 4019.
- (73) Kholodenko, B. N.; Hancock, J. F.; Kolch, W. *Nat. Rev. Mol. Cell Biol.* **2010**, *11*, 414.
- (74) Raichle, M. E.; Mintun, M. A. *Annu. Rev. Neurosci.* **2006**, *29*, 449.
- (75) Raichle, M. E.; Snyder, A. Z. *NeuroImage* **2007**, *37*, 1083.
- (76) Buzsáki, G.; Kaila, K.; Raichle, M. *Neuron* **2007**, *56*, 771.
- (77) Biswal, B. B.; et al. P. *Proc. Natl. Acad. Sci.* **2010**, *107*, 4734.
- (78) Friston, K. J. *Brain Connect.* **2011**, *1*, 13.
- (79) Deng, W.; Aimone, J. B.; Gage, F. H. *Nat. Rev. Neurosci.* **2010**, *11*, 339.
- (80) Croteau, R.; Kutchan, T. M.; Lewis, N. G. American Society of Plant Physiologists, 2000; pp. 1250–1318.
- (81) Dicke, M.; Sabelis, M. W. *Funct. Ecol.* **1988**, *2*, 131.
- (82) Hurd, C. L. *J. Phycol.* **2000**, *36*, 453.
- (83) Stevens, C. L.; Hurd, C. L. *Hydrobiologia* **1997**, *346*, 119.
- (84) Schlichting, H.; Gersten, K. *Boundary-Layer Theory*; Springer, **2000**.
- (85) Takaichi, S. *Mar. Drugs* **2011**, *9*, 1101.
- (86) Nys, R. de; Dworjanyn, S. A.; Steinberg, P. D. *Mar. Ecol. Prog. Ser.* **1998**, *162*, 79.
- (87) Petry, R.; Schmitt, M.; Popp, J. *Chem. Phys. Phys. Chem.* **2003**, *4*, 14.
- (88) Baia, L.; Gigant, K.; Posset, U.; Schottner, G.; Kiefer, W.; Popp, J. *Appl. Spectrosc.* **2002**, *56*, 536.
- (89) Krafft, C.; Dietzek, B.; Popp, J. *The Analyst* **2009**, *134*, 1046.
- (90) Schmitt, M.; Leimeister, B.; Baia, L.; Weh, B.; Zimmermann, I.; Kiefer, W.; Popp, J. *ChemPhysChem* **2003**, *4*, 296.
- (91) Parker, F. S. *Appl. Spectrosc.* **1975**, *29*, 129.
- (92) Wächtler, M.; Guthmüller, J.; González, L.; Dietzek, B. *Coord. Chem. Rev.* **2012**, *256*, 1479.
- (93) Honkanen, T.; Jormalainen, V. *Oecologia* **2005**, *144*, 196.
- (94) Haugan, J. A.; Liaaen-Jensen, S. *Biochem. Syst. Ecol.* **1994**, *22*, 31.
- (95) Blinks, L. R. *Annu. Rev. Plant Physiol.* **1954**, *5*, 93.
- (96) Rimai, L.; Kilponen, R. G.; Gill, D. *J. Am. Chem. Soc.* **1970**, *92*, 3824.
- (97) Saha, M.; Rempt, M.; Gebser, B.; Grueneberg, J.; Pohnert, G.; Weinberger, F. *Biofouling* **2012**, *28*, 593.
- (98) Dworjanyn, S. A.; Nys, R. D.; Steinberg, P. D. *Mar. Biol.* **1999**, *133*, 727.
- (99) Grosser, K. *In vivo* Analyse und Lokalisation ökologisch relevanter Sekundärmetabolite mariner Makroalgen, Dissertation, Friedrich-Schiller-Universität Jena, **2013**.
- (100) Stauber, J. L.; Jeffrey, S. W. *J. Phycol.* **1988**, *24*, 158.
- (101) Smith, B. L.; Schäffer, T. E.; Viani, M.; Thompson, J. B.; Frederick, N. A.; Kindt, J.; Belcher, A.; Stucky, G. D.; Morse, D. E.; Hansma, P. K. *Nature* **1999**, *399*, 761.
- (102) Keckes, J.; Burgert, I.; Frühmann, K.; Müller, M.; Kölln, K.; Hamilton, M.; Burghammer, M.; Roth, S. V.; Stanzl-Tschegg, S.; Fratzl, P. *Nat. Mater.* **2003**, *2*, 810.
- (103) Fantner, G. E.; Hassenkam, T.; Kindt, J. H.; Weaver, J. C.; Birkedal, H.; Pechenik, L.; Cutroni, J. A.; Cidade, G. A. G.; Stucky, G. D.; Morse, D. E.; Hansma, P. K. *Nat. Mater.* **2005**, *4*, 612.
- (104) Holten-Andersen, N.; Fantner, G. E.; Hohlbauch, S.; Waite, J. H.; Zok, F. W. *Nat. Mater.* **2007**, *6*, 669.
- (105) Rapoport, H. S.; Shadwick, R. E. *J. Exp. Biol.* **2007**, *210*, 12.
- (106) Hager, M. D.; Greil, P.; Leyens, C.; van der Zwaag, S.; Schubert, U. S. *Adv. Mater.* **2010**, *22*, 5424.
- (107) Van der Zwaag, S. *Self Healing Materials - An Alternative Approach to 20 Centuries of Materials Science*; Springer, **2007**.
- (108) Garcia, S. J.; Fischer, H. R.; White, P. A.; Mardel, J.; Gonzalez-Garcia, Y.; Mol, J. M. C.; Hughes, A. E. *Prog. Org. Coat.* **2011**, *70*, 142.
- (109) Hager, M. D.; Schubert, U. S. *Eur. Coat. J.* **2011**, *6*, 40.

- (110) Chen, X.; Dam, M. A.; Ono, K.; Mal, A.; Shen, H.; Nutt, S. R.; Sheran, K.; Wudl, F. *Science* **2002**, *295*, 1698.
- (111) Wietor, J.-L.; Sijbesma, R. P. *Angew. Chem. Int. Ed.* **2008**, *47*, 8161.
- (112) Esser-Kahn, A. P.; Odom, S. A.; Sottos, N. R.; White, S. R.; Moore, J. S. *Macromolecules* **2011**, *44*, 5539.
- (113) Blaiszik, B. J.; Kramer, S. L. B.; Olugebefola, S. C.; Moore, J. S.; Sottos, N. R.; White, S. R. *Annu. Rev. Mater. Res.* **2010**, *40*, 179.
- (114) Hamilton, A. R.; Sottos, N. R.; White, S. R. *Adv. Mater.* **2010**, *22*, 5159.
- (115) White, S. R.; Sottos, N. R.; Geubelle, P. H.; Moore, J. S.; Kessler, M. R.; Sriram, S. R.; Brown, E. N.; Viswanathan, S. *Nature* **2001**, *409*, 794.
- (116) Chen, X.; Wudl, F.; Mal, A. K.; Shen, H.; Nutt, S. R. *Macromolecules* **2003**, *36*, 1802.
- (117) Kötteritzsch, J.; Stumpf, S.; Hoepfener, S.; Vitz, J.; Hager, M. D.; Schubert, U. S. *Macromol. Chem. Phys.* **2013**, *214*, 1636.
- (118) Barthel, M. J.; Rudolph, T.; Teichler, A.; Paulus, R. M.; Vitz, J.; Hoepfener, S.; Hager, M. D.; Schacher, F. H.; Schubert, U. S. *Adv. Funct. Mater.* **2013**, n/a.
- (119) Cordier, P.; Tournilhac, F.; Soulié-Ziakovic, C.; Leibler, L. *Nature* **2008**, *451*, 977.
- (120) Kalista, S. J.; Ward, T. C. *J. R. Soc. Interface* **2007**, *4*, 405.
- (121) Kalista, S. J.; Pflug, J. R.; Varley, R. J. *Polym. Chem.* **2013**.
- (122) Burattini, S.; Colquhoun, H. M.; Fox, J. D.; Friedmann, D.; Greenland, B. W.; Harris, P. J. F.; Hayes, W.; Mackay, M. E.; Rowan, S. J. *Chem. Commun.* **2009**, 6717.
- (123) Burattini, S.; Colquhoun, H. M.; Greenland, B. W.; Hayes, W. *Faraday Discuss.* **2009**, *143*, 251.
- (124) Burattini, S.; Greenland, B. W.; Hayes, W.; Mackay, M. E.; Rowan, S. J.; Colquhoun, H. M. *Chem. Mater.* **2011**, *23*, 6.
- (125) Fox, J.; Wie, J. J.; Greenland, B. W.; Burattini, S.; Hayes, W.; Colquhoun, H. M.; Mackay, M. E.; Rowan, S. J. *J. Am. Chem. Soc.* **2012**, *134*, 5362.
- (126) Frisch, M. J.; et al. Gaussian 09, Inc., Wallingford, CT, **2009**.
- (127) Ritz, T.; Damjanović, A.; Schulten, K. *ChemPhysChem* **2002**, *3*, 243.
- (128) Miyasaka, H.; Irie, M. In *Femtosecond Technology*; Springer Series in Photonics; Springer Berlin Heidelberg, **1999**; pp. 389–400.
- (129) Kandori, H.; Shichida, Y.; Yoshizawa, T. *Biochem. Mosc. Russ. Fed. Biokhimiya Mosc. Russ. Fed.* **2001**, *66*, 1197.
- (130) Kochendoerfer, G. G.; Mathies, R. A. *Isr. J. Chem.* **1995**, *35*, 211.
- (131) Kukura, P.; McCamant, D. W.; Yoon, S.; Wandschneider, D. B.; Mathies, R. A. *Sci. Wash. DC U. S.* **2005**, *310*, 1006.
- (132) Cannizzo, A.; Milne, C. J.; Consani, C.; Gawelda, W.; Bressler, C.; van, M., F.; Chergui, M. *Coord. Chem. Rev.* **2010**, *254*, 2677.
- (133) McCusker, J. K. *Acc. Chem. Res.* **2003**, *36*, 876.
- (134) Barbara, P. F.; Meyer, T. J.; Ratner, M. A. *J. Phys. Chem.* **1996**, *100*, 13148.
- (135) Clark, R. J. H.; Dines, T. J. *Angew. Chem.* **1986**, *98*, 131.
- (136) Bell, S. E. J. *Anal. Camb. U. K.* **1996**, *121*, 107R.
- (137) Chalmers, J. M. *Handbook of Vibrational Spectroscopy*. *4*, *4*; Wiley, Chichester, **2002**.
- (138) Heineman, W. R. *J. Chem. Educ.* **1983**, *60*, 305.
- (139) Sharpe, L. R.; Heineman, W. R.; Elder, R. C. *Chem. Rev.* **1990**, *90*, 705.
- (140) Kaim, W.; Fiedler, J. *Chem. Soc. Rev.* **2009**, *38*, 3373.
- (141) Scholz, F. *Electroanalytical Methods: Guide to Experiments and Applications*; Springer, **2009**.
- (142) Best, S. P. *Coord. Chem. Rev.* **2005**, *249*, 1536.
- (143) Lee, Y. F.; Kirchhoff, J. R. *Anal. Chem.* **1993**, *65*, 3430.
- (144) Toma, H. E.; Araki, K. *Curr. Org. Chem.* **2002**, *6*, 21.
- (145) Dunsch, L. *J. Solid State Electrochem.* **2011**, *15*, 1631.
- (146) Holze, R. *J. Solid State Electrochem.* **2004**, *8*, 982.

- (147) Ashley, K. *Talanta* **1991**, *38*, 1209.
- (148) W. Plieth, G. S. W. *Pure Appl. Chem. - PURE APPL CHEM* **1998**, *70*, 1395.
- (149) Jeanmaire, D. L.; Suchanski, M. R.; Van Duyne, R. P. *J. Am. Chem. Soc.* **1975**, *97*, 1699.
- (150) Hu, Q.; Hinman, A. S. *Anal. Chem.* **2000**, *72*, 3233.
- (151) Czernuszewicz, R. S.; Macor, K. A. *J. Raman Spectrosc.* **1988**, *19*, 553.
- (152) Kaim, W.; Klein, A. *Spectroelectrochemistry*; Royal Society of Chemistry, **2008**.
- (153) Jukes, R. T. F.; Kühni, J.; Salluce, N.; Belsler, P.; Cola, L. D.; Hartl, F. *Dalton Trans.* **2009**, 3993.
- (154) Nazeeruddin, M. K.; Kay, A.; Rodicio, I.; Humphry-Baker, R.; Mueller, E.; Liska, P.; Vlachopoulos, N.; Graetzel, M. *J. Am. Chem. Soc.* **1993**, *115*, 6382.
- (155) Grätzel, M.; Kalyanasundaram, K. *Curr. Sci.* **1994**, *66*, 706.
- (156) Grätzel, M. *Nature* **2001**, *414*, 338.
- (157) Pérez León, C.; Kador, L.; Peng, B.; Thelakkat, M. *J Phys Chem B* **2005**, *109*, 5783.
- (158) Tachibana, Y.; Haque, S. A.; Mercer, I. P.; Durrant, J. R.; Klug, D. R. *J. Phys. Chem. B* **2000**, *104*, 1198.
- (159) Tachibana, Y.; Vayssieres, L.; Durrant, J. R. *Nat. Photonics* **2012**, *6*, 511.
- (160) Hannappel, T.; Burfeindt, B.; Storck, W.; Willig, F. *J Phys Chem B* **1997**, *101*, 6799.
- (161) Clifford, J. N.; Palomares, E.; Nazeeruddin, M. K.; Grätzel, M.; Durrant, J. R. *J. Phys. Chem. C* **2007**, *111*, 6561.
- (162) Asbury, J. B.; Ellingson, R. J.; Ghosh, H. N.; Ferrere, S.; Nozik, A. J.; Lian, T. *J Phys Chem B* **1999**, *103*, 3110.
- (163) Wolfbauer, G.; Bond, A. M.; Deacon, G. B.; MacFarlane, D. R.; Spiccia, L. *J. Am. Chem. Soc.* **2000**, *122*, 130.
- (164) Wolfbauer, G.; Bond, A. M.; Deacon, G. B.; MacFarlane, D. R.; Spiccia, L. *J. Electroanal. Chem.* **2000**, *490*, 7.
- (165) Cecchet, F.; Gioacchini, A. M.; Marcaccio, M.; Paolucci, F.; Roffia, S.; Alebbi, M.; Bignozzi, C. *J. Phys. Chem. B* **2002**, *106*, 3926.
- (166) Sun, Y.; Onicha, A. C.; Myahkostupov, M.; Castellano, F. N. *ACS Appl. Mater. Interfaces* **2010**, *2*, 2039.
- (167) Beckert, R.; Atzrodt, J.; Görls, H. *Heterocycles* **1999**, *51*, 763.
- (168) Blumhoff, J. Neuartige multifunktionelle Liganden basierend auf 4H-Imidazolen und deren Metallkomplexe, Dissertation, Friedrich-Schiller-Universität Jena, **2009**.
- (169) Wächtler, M.; Kupfer, S.; Guthmuller, J.; Rau, S.; González, L.; Dietzek, B. *J. Phys. Chem. C* **2012**, *116*, 25664.
- (170) Tschierlei, S.; Presselt, M.; Kuhnt, C.; Yartsev, A.; Pascher, T.; Sundström, V.; Karnahl, M.; Schwalbe, M.; Schäfer, B.; Rau, S.; Schmitt, M.; Dietzek, B.; Popp, J. *Chem. – Eur. J.* **2009**, *15*, 7678.
- (171) Tschierlei, S.; Karnahl, M.; Presselt, M.; Dietzek, B.; Guthmuller, J.; González, L.; Schmitt, M.; Rau, S.; Popp, J. *Angew. Chem. Int. Ed.* **2010**, *49*, 3981.
- (172) Karnahl, M.; Kuhnt, C.; Ma, F.; Yartsev, A.; Schmitt, M.; Dietzek, B.; Rau, S.; Popp, J. *ChemPhysChem* **2011**, *12*, 2101.
- (173) Kuhnt, C.; Karnahl, M.; Tschierlei, S.; Griebenow, K.; Schmitt, M.; Schäfer, B.; Kriek, S.; Görls, H.; Rau, S.; Dietzek, B.; Popp, J. *Phys. Chem. Chem. Phys.* **2010**, *12*, 1357.
- (174) Lehtovuori, V.; Myllyperkiö, P.; Linnanto, J.; Manzoni, C.; Polli, D.; Cerullo, G.; Haukka, M.; Korppi-Tommola, J. *J. Phys. Chem. B* **2005**, *109*, 17538.
- (175) Gabrielsson, A.; Zális, S.; Matousek, P.; Towrie, M.; Vlček, A. *Inorg. Chem.* **2004**, *43*, 7380.
- (176) Du, P.; Knowles, K.; Eisenberg, R. *J. Am. Chem. Soc.* **2008**, *130*, 12576.
- (177) Lei, P.; Hedlund, M.; Lomoth, R.; Rensmo, H.; Johansson, O.; Hammarström, L. *J. Am. Chem. Soc.* **2008**, *130*, 26.
- (178) Chakraborty, S.; Wadas, T. J.; Hester, H.; Schmehl, R.; Eisenberg, R. *Inorg. Chem.* **2005**, *44*, 6865.

- (179) Yamauchi, K.; Masaoka, S.; Sakai, K. *J. Am. Chem. Soc.* **2009**, *131*, 8404.
- (180) Rau, S.; Schwalbe, M.; Losse, S.; Görls, H.; McAlister, C.; MacDonnell, F. M.; Vos, J. G. *Eur. J. Inorg. Chem.* **2008**, *2008*, 1031.
- (181) Brust, M.; Walker, M.; Bethell, D.; Schiffrin, D. J.; Whyman, R. *J. Chem. Soc. Chem. Commun.* **1994**, 801.
- (182) Liz-Marzán, L. M.; Giersig, M.; Mulvaney, P. *Langmuir* **2011**, *12*, 4329.
- (183) Moores, A.; Goettmann, F.; Sanchez, C.; Le Floch, P. *Chem. Commun.* **2004**, 2842.
- (184) Rubim, J. C.; Temperini, M. L. A.; Corio, P.; Sala, O.; Jubert, A. H.; Chacon-Villalba, M. E.; Aymonino, P. J. *J Phys Chem* **2011**, *99*, 345.
- (185) Corio, P.; Andrade, G. F. .; Diógenes, I. C. .; Moreira, I. .; Nart, F. .; Temperini, M. L. . *J. Electroanal. Chem.* **2002**, *520*, 40.
- (186) Kotiaho, A.; Lahtinen, R.; Efimov, A.; Metsberg, H.-K.; Sariola, E.; Lehtivuori, H.; Tkachenko, N. V.; Lemmetyinen, H. *J Phys Chem C* **2011**, *114*, 162.
- (187) Peter, L. M. *J Phys Chem Lett* **2011**, *2*, 1861.
- (188) Grätzel, M. *Inorg Chem* **2005**, *44*, 6841.
- (189) Turkevich, J.; Stevenson, P. C.; Hillier, J. *Discuss Faraday Soc* **1951**, *11*.
- (190) Frens, G. *Nature* **1973**, *241*, 20.
- (191) Schmid, G.; Pfeil, R.; Boese, R.; Bandermann, F.; Meyer, S.; Calis, G. H. M.; van der Velden, J. W. A. *Chem. Ber.* **1981**, *114*, 3634.
- (192) Giersig, M.; Mulvaney, P. *Langmuir* **1993**, *9*, 3408.
- (193) Sardar, R.; Funston, A. M.; Mulvaney, P.; Murray, R. W. **2009**, 13840.
- (194) Corma, A.; Garcia, H. **2008**, 2096.
- (195) Cialla, D.; März, A.; Böhme, R.; Theil, F.; Weber, K.; Schmitt, M.; Popp, J. *Anal. Bioanal. Chem.* **2012**, *403*, 27.
- (196) Kneipp, K.; Moskovits, M.; Kneipp, H. *Surface-Enhanced Raman Scattering: Physics and Applications*; Springer, **2006**.
- (197) Karnahl, M.; Tschierlei, S.; Kuhnt, C.; Dietzek, B.; Schmitt, M.; Popp, J.; Schwalbe, M.; Kriech, S.; Görls, H.; Heinemann, F. W.; Rau, S. *Dalton Trans. Camb. Engl. 2003* **2010**, *39*, 2359.
- (198) Mayer, C. R.; Dumas, E.; Sécheresse, F. *J. Colloid Interface Sci.* **2008**, *328*, 452.
- (199) Vougioukalakis, G. C.; Stergiopoulos, T.; Kantonis, G.; Kontos, A. G.; Papadopoulos, K.; Stublla, A.; Potvin, P. G.; Falaras, P. *J. Photochem. Photobiol. Chem.* **2010**, *214*, 22.
- (200) Valley, N.; Greeneltch, N.; Van Duyne, R. P.; Schatz, G. C. **2013**, 2599.

Publikationen

Im Folgenden sind die Nachdrucke der im Rahmen der Dissertation erschienenen Publikationen aufgeführt. Auf den Deckblättern sind jeweils die Urheberrechte angegeben.

[Grosser et al. Biofouling.]

Disruption-free Imaging by Raman Spectroscopy Reveals a Chemical Sphere with Antifouling Metabolites around Macroalgae

Der Nachdruck der folgenden Publikation erfolgt mit freundlicher Genehmigung von Taylor & Francis.

Reprinted with kind permission from:

Grosser, K.; Zedler, L.; Schmitt, M.; Dietzek, B.; Popp, J.; Pohnert, G., Disruption-free Imaging by Raman Spectroscopy Reveals a Chemical Sphere with Antifouling Metabolites around Macroalgae, *Biofouling* **2012**, *28*, 687–696.

Copyright 2012 Taylor & Francis.

Disruption-free imaging by Raman spectroscopy reveals a chemical sphere with antifouling metabolites around macroalgae

Katharina Grosser^{a*}, Linda Zedler^b, Michael Schmitt^b, Benjamin Dietzek^{b,c}, Jürgen Popp^{b,c} and Georg Pohnert^{a*}

^aIAAC, Bioorganic Analytics, Friedrich Schiller University Jena, Lessingstr. 8, 07743 Jena, Germany; ^bInstitute of Physical Chemistry, Friedrich Schiller University Jena, Helmholtzweg 4, 07743 Jena, Germany; ^cInstitute of Photonic Technology Jena, Albert-Einstein-Straße 9, 07745 Jena, Germany

(Received 12 January 2012; final version received 31 May 2012)

Investigations of the surface chemistry of marine organisms are essential to understand their chemically mediated interactions with fouling organisms. In this context, the concentration of natural products in the immediate vicinity of algal surfaces, as well as their biological activity, are of particular importance. However, due to lack of appropriate methods, the distribution of compounds within the chemical sphere around marine algae is unknown. This study demonstrates the suitability of confocal resonance Raman microspectroscopy for the determination of metabolites around algal surfaces with a micrometer resolution. The spatial distribution of carotenoids in the diffusion boundary layer of the brown alga *Fucus vesiculosus* and the green alga *Ulva* sp. was determined using the disruption-free optical method. A gradient of carotenoids was determined within 0 to 150 μm from the surface of the algae, thereby demonstrating the release of the non-polar metabolites involved in antifouling processes. The differences in the carotenoid composition of the brown and green algae were reflected in the spectra. Resonance Raman microspectroscopy also allowed visualization of the lateral distribution of fucoxanthin on the algal surface and localization of concentration maxima within a $50 \times 50 \mu\text{m}^2$ area. The results from this work show clearly that established dipping techniques suitable for the extraction of the diffusion boundary layer of macroalgae only provide an average of the local strongly variable concentrations of metabolites on algal surfaces.

Keywords: diffusion boundary layer; fucoxanthin; confocal Raman microspectroscopy; *Fucus vesiculosus*; *Ulva* sp.; surface chemistry

Introduction

Surface studies reveal specific interactions between organisms and their environment. Especially for aquatic organisms, in addition to their physical surface, the immediate chemical surrounding has to be considered if ecological interactions are to be understood (Wahl 2009). For example, benthic macroalgae in seawater are surrounded by a thin laminar layer (0.1–0.2 mm) that is located between the algal surface and the surrounding water (Hurd 2000). Simple hydrodynamic considerations (Stevens and Hurd 1997; Schlichting et al. 2000) suggest that metabolites originating from the alga or from the environment have to diffuse through this layer, thereby building up chemical gradients surrounding the alga. Secondary metabolites in particular play an important role in the mediation of biotic interactions between algae and fouling organisms. Such metabolites have the potential to defend against harmful bacteria or even to mediate more subtle interactions by regulating the specific community composition on the algal surface (Persson et al. 2011; Sneed and Pohnert

2011). Therefore, knowledge regarding the distribution of metabolites around the alga is essential for an understanding of their function.

Up to the present time, investigation of the effect of active metabolites on the settlement, reproduction or development of fouling organisms were mostly based on bioassays with extracts of whole algae (Dworjanyn et al. 1999, 2006; Hellio et al. 2001). However, whole cell extracts do not reflect the real ecological relevance of antifouling metabolites, since only the concentration in the vicinity of the surface of the organism and not the concentration in the tissue is relevant for understanding biological interactions. To overcome this limitation and to obtain a better insight into chemically mediated interactions, recent research has focused on the nature, distribution and concentration of chemical compounds on algal surfaces and extraction techniques to capture the metabolites released by macroalgae have been developed. In particular, investigation of surface extracts obtained by dipping algae in organic solvents has gained much importance (De Nys et al. 1998; Nylund et al. 2005). One major disadvantage of this

*Corresponding author. Email: katharina.grosser@uni-jena.de; georg.pohnert@uni-jena.de

method is the stress caused by exposure of the alga to organic solvents and the risk of damage to cell membranes with resulting contamination of the surface extract with metabolites from inside the cells. Another weakness of this otherwise simple and successful method is the lack of spatial resolution. Only average concentrations from the alga and its surrounding water layer can be obtained using such solvent extractions. It is not possible to determine the distribution of a compound within the diffusion boundary layer (axial distribution, z-direction from the algal surface) or the localization of metabolites on the surface with microscopic lateral (x,y) resolution.

The lateral distribution of metabolites on algal surfaces was first successfully addressed by Lane et al. (2009), who used desorption electrospray ionisation (DESI) to determine the distribution and relative concentration of bromophycolides (36 ± 23 pmol mm^{-2}) on surface patches of the red alga *Callophycus serratus*. During this soft ionisation method, the alga, which is removed from water, is maintained at atmospheric pressure and treated with a focused beam of charged micro-droplets of organic solvents (methanol and acetonitrile) or aqueous mixtures of them. The desorbed molecules are then transferred to a mass spectrometer and analysed (Cooks et al. 2006; Lane et al. 2009). The spatial resolution of this method is around 200 μm in the x,y-direction (Lane et al. 2009). However, it is not possible to focus the beam in the z-direction, making the method unsuitable for investigating the diffusion boundary layer. Furthermore, a high amount of salts on surfaces of organisms removed from seawater, could lead to ion suppression of possible signals (Annesley 2003; Mazzella et al. 2009). Therefore, the DESI method does not allow measurements of diffusion processes or the possible formation of lateral gradients.

Developments in Raman spectroscopy make this method useful for biological investigations (Petry et al. 2003; Baena and Lendl 2004; Krafft et al. 2009; Wächtler et al. 2012). In particular, confocal resonance Raman microscopy allows a high spatial resolution to be achieved ($<1 \mu\text{m}$ in the x,y and in the z direction) (Baia et al. 2002; Schmitt et al. 2003). In recent years many resonance Raman studies have focused not only on the diffusion processes of metabolites in multiphase materials, but also on the investigation of biochemical processes and patterns (Mattsson et al. 1999; Schmidt et al. 2010). Compared to IR-spectroscopy, one main advantage for Raman spectroscopy is the low sensitivity to water, which is especially favourable for application to biological samples (Parker 1975; Krafft et al. 2009). This paper shows that resonance Raman microscopy can be used to determine the distribution of compounds in

the chemical sphere of marine macroalgae immersed in water. The study follows up a recent report about the presence and the biological activity of the carotenoid fucoxanthin (Figure 1) on the surface of the brown alga *Fucus vesiculosus* (Saha et al. 2011). Using the solvent dipping method developed by De Nys et al. (1998) fucoxanthin was detected on the algal surface and an average concentration was determined. Bioassays using this average concentration revealed that fucoxanthin influenced the settlement of different marine bacteria (Saha et al. 2011). Here, it is shown that resonance Raman microscopy is a suitable tool to investigate the carotenoid distribution in the chemical sphere around macroalgae and to determine the lateral distribution of the metabolite on the surface as well as its axial distribution above the algal surface with diffraction-limited resolution.

Materials and methods

Organisms

Several individuals of the brown alga *F. vesiculosus* (Phaeophyceae, Fucales, Fucaceae, LINNÉ 1753) and the green alga *Ulva* sp. (syn. *Enteromorpha*) attached to stones, were collected from the subtidal zone of the Kiel Fjord, Germany ($54^{\circ} 45' \text{N}/10^{\circ} 19' \text{E}$) in May, June, and July 2011. The algae were individually placed between wet paper towels and transported to the laboratory in a cool box. The algal individuals were held at 15°C in aerated aquaria filled with Instant Ocean (Aquarium Systems) artificial seawater adapted to the Baltic Sea conditions (PSU12) under a constant light regime of $65 \mu\text{mol m}^{-2} \text{s}^{-1}$, until immediately before the measurements. To suppress diatom growth, $0.18 \text{ mg l}^{-1} \text{ GeO}_2$ was added to the medium (Markham and Hagmeier 1982). The state of the health of the algae was monitored daily and bleached or otherwise damaged individuals were discarded. The water in the aquaria was changed daily. Measurements were performed within the first 2 weeks after collection.

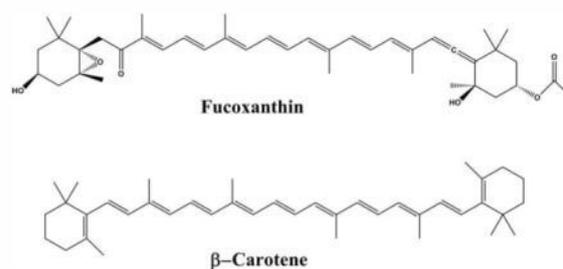


Figure 1. Structure of the carotenoids fucoxanthin and β -carotene.

Sample preparation

For resonance Raman microspectroscopy measurements, individual plants of *F. vesiculosus* were removed from the aquaria and cut into 4–5 cm pieces using a scalpel. The pieces were placed in a Petri dish (8.5 cm diameter) filled with 20 ml of Instant Ocean. For mechanically fixing the algal pieces to the Petri dish a glass frame was constructed using two glass capillaries and hot glue. Care was taken that the algal pieces were not in contact with the glue and that no additional mechanical damage was caused by the holding capillaries. The same procedure, except for the cutting, was used for preparation of samples of *Ulva* sp. Standard solutions of fucoxanthin and β -carotene (Figure 1) dissolved in hexane, methanol or methanol/water were prepared from pure carotenoids. All chemicals were purchased from Sigma-Aldrich, Deisenhofen, Germany.

Experimental set-up of the resonance Raman microspectroscopy measurements

The resonance Raman microspectroscopy measurements were performed using a LabRAM HR800 Raman spectrometer (Horiba-Jobin Yvon, Japan) equipped with a confocal aperture and a microscope (BX40, Olympus, Japan) capable of acquiring white light images. All Raman spectra were recorded using a Zeiss C-Apochromat 63x/1.2 W water immersion objective (Zeiss, Germany). A krypton ion laser (Innova 302C, Coherent, USA) was used for excitation. The incident Laser power on the sample was $P_L < 1$ mW at an excitation wavelength of 476 nm. The spectral resolution was 2 cm^{-1} and the acquisition time per spectrum was 2 s; photobleaching was negligible. The acquisition time was determined by monitoring the decrease in the Raman signal intensity of the C=C stretching (ν_1) band at 1528 cm^{-1} due to photobleaching over an acquisition time of 10 s. Samples were mounted on a x,y-motorised stage (Märzhäuser, Germany) and the z displacement was controlled manually with the z-focus of the microscope. For all measurements the confocal pinhole diameter was set to $1000\text{ }\mu\text{m}$ and the slit width to $100\text{ }\mu\text{m}$.

A Petri dish containing a piece of alga was placed under the microscope and the Raman spectra were recorded in $10\text{ }\mu\text{m}$ steps in the z-direction starting from the surface into the diffusion boundary layer or backwards on different parts of the alga. The set-up is depicted in Figure 2. The program Labspec was used to record the spectra. Measurements were taken at least 1.5 cm away from the cut to ensure that intracellular metabolites from the injured cell layers at the site of the cut did not mix with those in the diffusion boundary layer on the surface. Surface

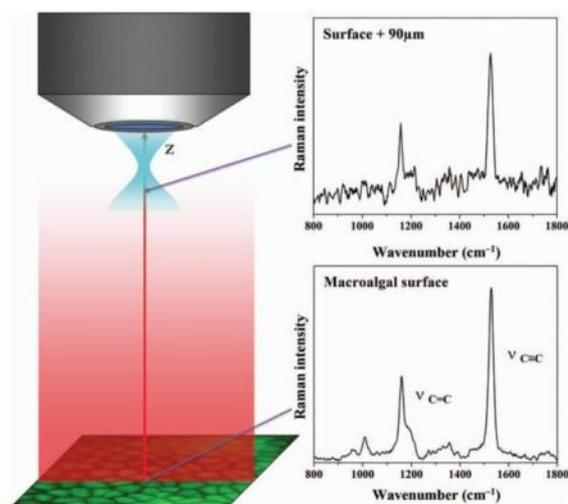


Figure 2. Left: General set-up for resonance Raman microspectroscopy measurements in the z-direction from the algal surface. Right: The Raman spectrum at $90\text{ }\mu\text{m}$ away from the surface (top) shows a lower signal to noise ratio compared to the spectrum recorded in the close vicinity of the macroalgal surface.

measurements of *F. vesiculosus* were also performed in a lateral direction from the algal centre to the uncut border at 50 measuring points over a distance of $30\text{ }\mu\text{m}$. In addition, a map of the *F. vesiculosus* surface carotenoid pattern was recorded within an area measuring $50 \times 50\text{ }\mu\text{m}^2$, 10 points per line and 10 lines per image. The measured surface area was determined using a calibrated white light image. Calibration was performed using a grid array of defined size (Thorlabs, USA). The applied Raman excitation wavelength of $\lambda = 476\text{ nm}$ and the numerical aperture of the water immersion objective $\text{NA} = 1.2$ the lateral resolution $R(x, y)$ results in approximately 250 nm , while the axial resolution $R(z)$ can be estimated to be about 900 nm . For the measurements of dissolved carotenoid standards, the LabRAM HR800 Raman spectrometer was equipped with a rotating cuvette.

Interpretation of Raman spectra

The recorded Raman spectra were corrected for background according to Lieber and Ahadevan-Jansen (2003) using the package Peaks of the Program R. A band area calculation of the background corrected spectra by gauss fit was performed for the resonantly enhanced C=C stretching (ν_1) at 1528 cm^{-1} for *F. vesiculosus* and 1526 cm^{-1} for *Ulva* sp. The resulting peak area values for the resonance Raman spectra

measured in the z-direction were plotted against the steps in the z-direction. In order to generate a detailed chemical image, the Raman band at 1528 cm^{-1} (carbon double bond stretching) was used to visualize the spatial distribution of fucoxanthin (Raman map, Figure 7).

Microscopic monitoring of algae cells after measurements

Transmitted light microscope images of the area studied were taken before and after the measurements in order to test for photodamage. Furthermore, the algal pieces were rinsed with sterile filtered seawater and stained with 0.05% Evans blue in seawater (PSU 12) for 30 min. The pieces were monitored under the microscope for the presence of lysed cells (Weinberger et al. 2005). Pieces of untreated algae served as the control.

Results

In this study, the brown alga *F. vesiculosus*, which is known to contain the carotenoid fucoxanthin (Bjornland and Aguilar-Martinez 1976) and the green alga *Ulva* sp. containing β -carotene as the dominant carotene were investigated. The algae were mechanically fixed in a Petri dish and submerged in seawater. The set-up prevented desiccation and allowed measurements to be taken from minutes up to hours after transferring the algae onto the microscope platform. Thus recording the existing gradient of exuded compounds or its formation within the water around the algal surface was possible. Due to the size of *F. vesiculosus*, the thalli had to be cut in *ca* 10 cm^2 pieces so that they could be transferred into the Petri dishes. Measurements were performed at a maximal distance from the cutting site to avoid interference from the wounded area. Cut pieces could be maintained in the Petri dish for several hours without any negative influence on the measurements.

In the Raman set-up, short measurement times of 2 s with laser power of $<1\text{ mW}$ allowed the direct detection of carotenoids on the algal surface. Using these parameters, the surface of the alga was not damaged and bleaching of the carotenoids did not occur. Furthermore, microscopic investigation of the algal cells within the region where Raman measurements were performed did not reveal any visual alterations or damage. Staining with Evans blue for visualisation of dead cells also showed no damage in the region of the Raman investigation. Prolonged measurement times up to 10 s resulted in a significant decrease of $\sim 41\%$ in the carotenoid signal, probably due to photo-bleaching processes, thus measurement

times were adjusted to 2 s. All recorded spectra showed the three characteristic peaks for a typical resonance Raman spectrum of carotenoids, with two dominant signals at 1525 cm^{-1} (ν_1 , carbon double bond stretching) and 1155 cm^{-1} (ν_2 , carbon single bond stretching) as well as a weaker signal at $\sim 1005\text{ cm}^{-1}$ (ν_3 , carbon-methyl stretching) (Rimai et al. 1970). Solutions of fucoxanthin in different solvents gave the same characteristic resonance Raman pattern as observed for the surface chemicals of *F. vesiculosus* (Figures 4, 5). Moreover, the spectra of β -carotene solutions in various solvents showed a different resonance Raman pattern compared to the *F. vesiculosus* surface (Figures 4, 5). Representative resonance Raman spectra obtained in the diffusion boundary layer of *F. vesiculosus* are shown in Figure 2. The spectra were recorded in $10\text{ }\mu\text{m}$ steps from the algal surface into the surrounding water or *vice versa*. With increasing distance from the algal surface, a decrease in the respective signals was observed (Figure 2). For the semiquantitative evaluation of the carotenoid content on the algal surface, the peak area of the C=C double bond stretching band (1528 cm^{-1}) was determined. With increasing distance from the surface, an exponential decay of the signal intensity was found for different parts of *F. vesiculosus* (Figure 3). Neither the sampling direction, from the surface into the surrounding water or *vice versa*, nor the time elapsed between sample preparation and measurements (2 min to 3 h) influenced this gradient. These data on the relative concentration gradient can be used to estimate local concentrations of fucoxanthin if combined with

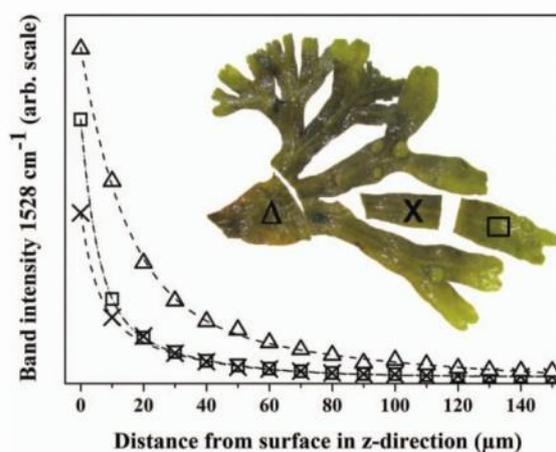


Figure 3. Decrease in band intensity (1528 cm^{-1}) with increasing distance from the surface of three different sections of *F. vesiculosus* (a-□, b-×, c-Δ). The dotted line represents the fit to a double exponential function ($y = A + B \exp(Cx) + D \exp(Ex)$).

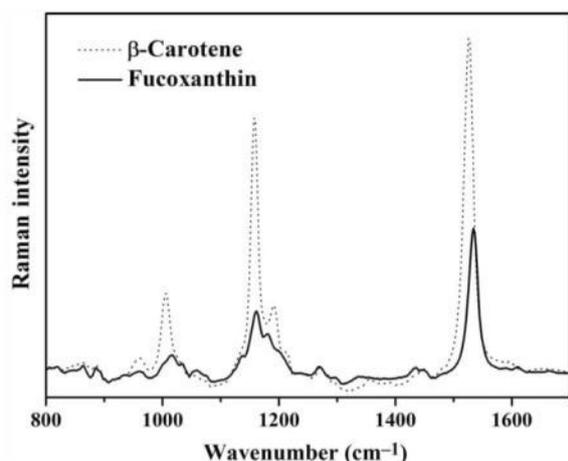


Figure 4. Raman spectrum of β -carotene (dashed line, 10^{-6} M) and fucoxanthin (solid line, 10^{-6} M) dissolved in hexane.

quantitative methods. Therefore, a fucoxanthin surface concentration of $5.7 \mu\text{g cm}^{-2}$ obtained by the dipping technique (Saha et al. 2011) was used to calculate local concentrations. It was assumed that the entire fucoxanthin content can be found within a distance of $150 \mu\text{m}$ from the surface of the alga, which leads to an average concentration in the diffusion limited layer of $580 \mu\text{M}$. Integrals of the data from Figure 3 allow concentrations encountered during the approach to the alga to be estimated (Table 1). Within $10 \mu\text{m}$ of the algal surface, fucoxanthin concentrations of *ca* 4 mM can be observed.

The semiquantitative approach was also used to investigate the surface of the green alga *Ulva* sp. using the resonance Raman signal at 1526 cm^{-1} . For this alga, a carotenoid gradient in the z-direction was also observed (Figure 5a), but a steeper decrease in the carotenoid signal within the diffusion boundary layer compared to the gradient around *F. vesiculosus* was detected (Figure 5a). Compared to *F. vesiculosus* the resonance Raman spectra of the *Ulva* sp. surface showed additional bands in the region between 1250 and 1450 cm^{-1} (Figure 5b,c marked with asterisks). Moreover, a reproducible wavenumber shift of *ca* 2 cm^{-1} for the carbon double bond stretching vibration was observed between the spectra of the two algae (Figure 5c). Measurements of β -carotene stock solutions showed a similar resonance Raman pattern, but different band positions for the three characteristic carotenoid peaks compared to the measurements of the carotenoids in the chemical sphere of *Ulva* sp. The observed patterns in the spectra of the carotenoids of *Ulva* sp. were also different from spectra of the fucoxanthin stock solution (Figures 4, 5).

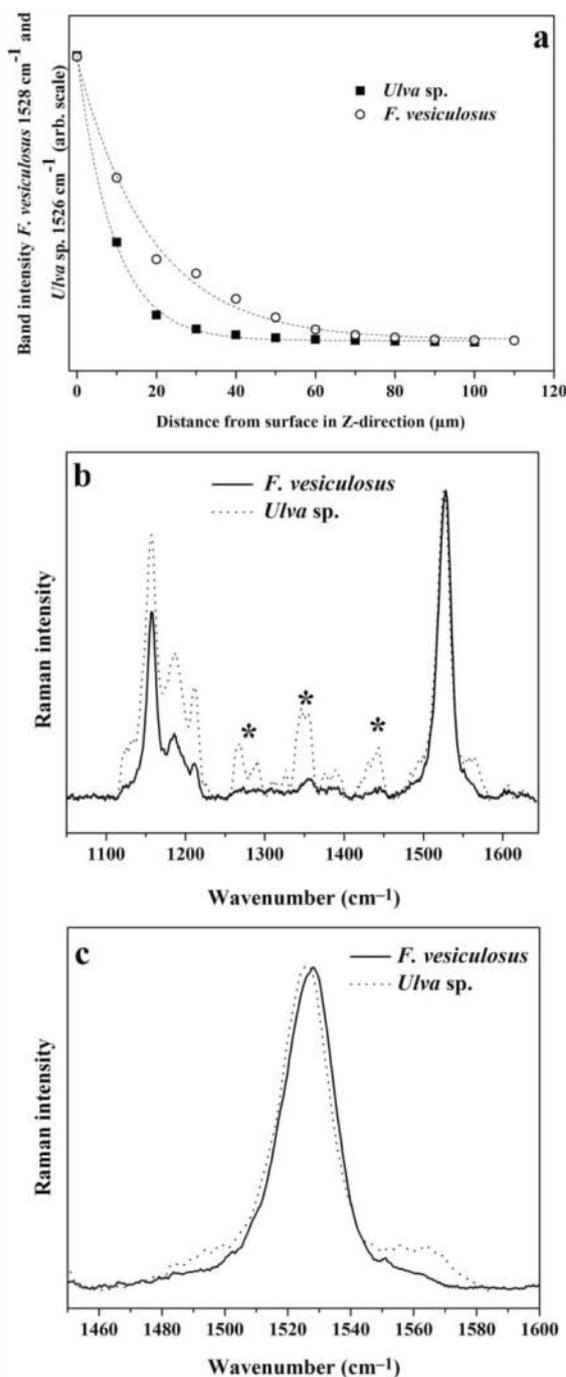


Figure 5. (a) Decrease in band intensity of the C=C stretching. The dotted line represents the fit to a double exponential function ($y = A + B \exp(Cx) + D \exp(Ex)$). (b) Resonance Raman spectra of metabolites of *F. vesiculosus* and *Ulva* sp. Additional bands in the spectra of *Ulva* sp. are marked with asterisks. (c) Difference in the resonance Raman spectra for the carotenoid C=C band stretching of *F. vesiculosus* and *Ulva* sp.

Table 1. Estimated local fucoxanthin concentrations at different distances from the surface of *F. vesiculosus*.

Distance [μm]	Concentration [mM]
0–10	4.00
10–20	1.44
20–30	0.82
30–40	0.55
40–50	0.39
50–60	0.30
60–80	0.20
80–100	0.14
100–150	0.09

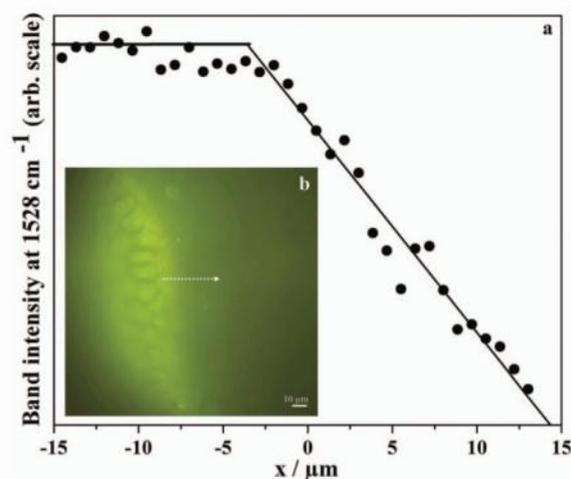


Figure 6. (a) Band intensity over the algal surface (-15 to $-2.5 \mu\text{m}$) and after passing the algal border (-2.5 to $15 \mu\text{m}$); (b) microscopic image of the line scan from the surface of *F. vesiculosus* into the surrounding water.

The lateral carotenoid distribution from the algal surface was also investigated. A line scan from the centre of the thallus to the uncut border and further into the surrounding diffusion boundary layer was performed. The band intensity varied slightly over the algal surface and exhibited a sudden decline when the algal border was reached (Figure 6). Figure 7 shows the intensity distribution of the C=C stretching band reflecting the carotenoid distribution on the surface of *F. vesiculosus* with micrometer resolution. In the false colour scheme, red parts of the map correspond to the highest and blue parts to lowest signal intensity. The concentration of fucoxanthin was lower at positions where there were associated diatoms than on the macroalgal surface, as shown by comparing the Raman image with the corresponding microscope image in Figure 7.

Discussion

The general presence of metabolites on the surface of marine macroalgae and their biological activity has been reported in several studies (De Nys et al. 1998; Dworjanyn et al. 1999; Nylund et al. 2010; Lachnit et al. 2010; Maréchal and Hellio 2011). Saha et al. (2011) reported the presence and anti-settlement activity for bacteria of the carotenoid fucoxanthin on the surface of *F. vesiculosus*. The concentration of fucoxanthin was determined using the hexane dipping approach and normalizing concentrations in the extracts to the surface area of the dipped alga. Average surface concentrations of $ca. 5.7 \mu\text{g cm}^{-2}$ were determined with a centimetre scale resolution. However, diffusion and distribution within the aqueous layer surrounding the alga could not be addressed (Saha et al. 2011).

Resonance Raman microspectroscopy allowed fucoxanthin to be detected without any previous sample preparation or extraction steps. The algal fronds were investigated *in situ* and no damage occurred. For detecting surface metabolites, it is important to ensure that only compounds outside the surface of the alga are detected, without interference from intracellular compounds. This was achieved by only taking data points recorded before the laser penetrated the tissue surface. Microscopic investigation and Evans blue staining confirmed that the measurement did not damage the cells, thereby confirming the non-disruptive nature of the method. The laser also did not cause any release of metabolites from the algal surface, since scans starting from the surface of the alga to the surrounding medium and *vice versa* gave identical results. This indicates also that no artefacts caused by, for example, selective heating of the algal surface, were detected. Not only pigments originating from the cell interior have the potential to influence the measurements, but also the length of the measurement time had to be evaluated. A prolonged exposure to the laser, ie longer than 10 s at the same spot, resulted in a significant decrease of $>40\%$ in signal intensity, probably due to photobleaching of the pigments. To avoid degradation of the carotenoids, the acquisition time per spectrum was set to 2 s, thereby ensuring minimum bleaching while maintaining sufficient signal intensity for data acquisition.

The recorded signal intensity for carotenoids was highest directly at the algal surface and decreased with increasing distance in the z-direction (Figures 2, 3, 5a). This distribution pattern was consistently observed independently of the incubation time. Since thalli were introduced under the microscope without drying or washing procedures, it was concluded that the gradient formed in the z-direction was not significantly disrupted during sample preparation. The fact that the

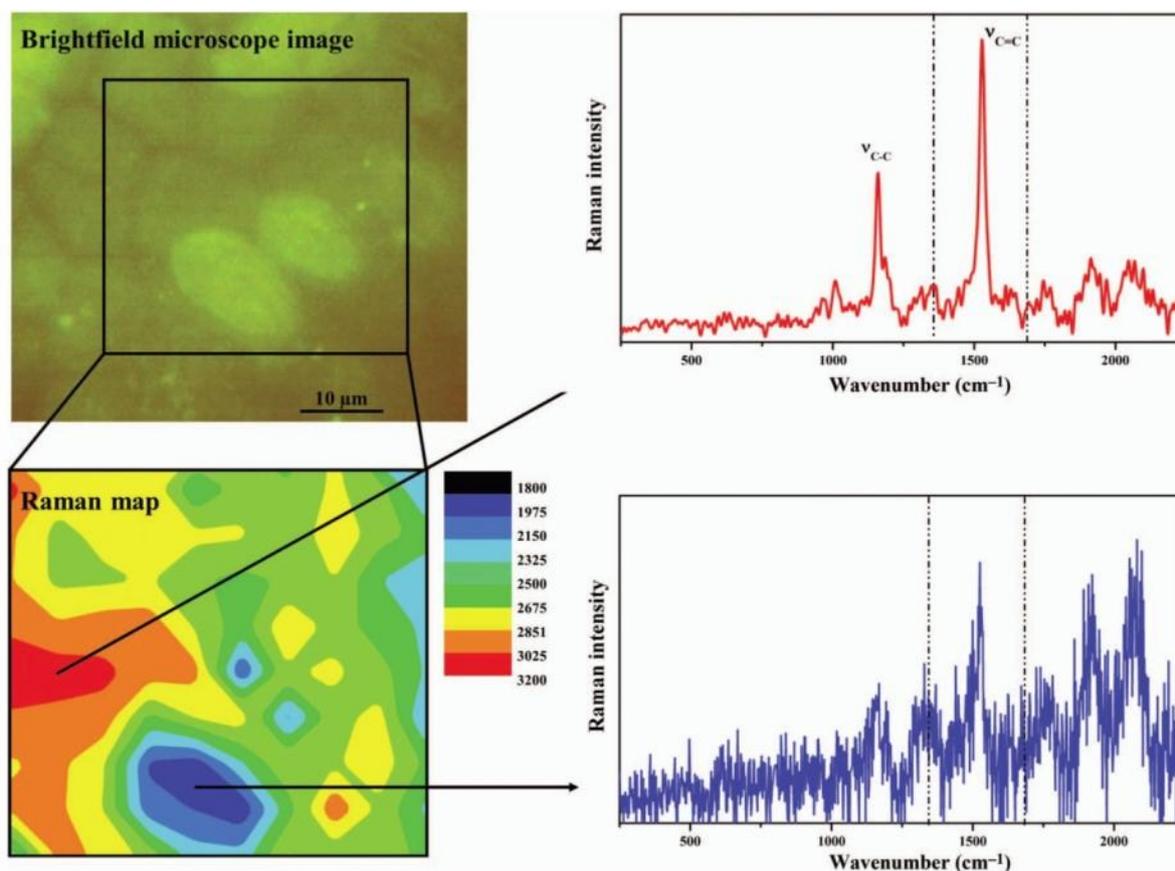


Figure 7. Map of carotenoid distribution on the surface of *F. vesiculosus* and two associated diatoms (visible as brighter green objects in the brightfield microscopy). The spectrum plotted in red was recorded in the red area of the Raman map and the blue one in the blue area. Raman map based on the C=C stretching band analysed (1528 cm^{-1}).

gradient did not change over time might be explained by fucoxanthin being continuously exuded from the surface, allowing a diffusion equilibrium to be established. Multiple repeated measurements demonstrated that the results were independent of the piece of algal tissue under investigation (Figures 3, 5a, and additional data not shown). As can be seen in Figure 3, all parts of a dissected *F. vesiculosus* thallus release fucoxanthin into the surrounding water. The data provide reliable qualitative information about gradients and the distribution of metabolites on and around surfaces. A quantitative discussion of the concentrations observed is however not possible. For quantitative resonance Raman studies calibration curves of β -carotene and fucoxanthin solutions with different molarities are required (Bakker Shut et al. 1997). However, since the observed resonance Raman enhancement depends critically on electronic absorption, which itself is influenced by the solvent environment (Wächtler et al. 2012), the calibration curves must be

recorded in the same solvent as in the experiments. Because of the low water solubility of the two carotenoids and the potentially complex matrix surrounding the algae, such calibration curves cannot be recorded. Nevertheless, it is proposed that the method can be used to determine local concentrations and the lateral distribution of the metabolites in question, if combined with a quantitative method (eg based on solvent dipping; Saha et al. 2011). This demonstrates that microorganisms that are in the micrometer size range will be exposed to millimolar concentrations of fucoxanthin in the immediate vicinity of the alga (Table 1). The concentration is considerably higher than often applied in bioassays that base the concentration of metabolites delivered on quantification of the average concentration in the laminar layer (in this example $580\ \mu\text{M}$).

A carotenoid gradient in the z-direction was also observed around the surface of *Ulva* sp. (Figure 5). Compared to the Raman spectra of *F. vesiculosus*, the

spectra for *Ulva* sp. showed additional bands in the region between 1250 and 1450 cm^{-1} (Figure 5b marked with asterisks). These additional bands indicate a different metabolite composition within the diffusion boundary layer of *Ulva* sp. compared to *F. vesiculosus*. However the nature of the metabolites causing the additional bands remains open. The more pronounced decrease in Raman intensity within the surroundings of *Ulva* sp. compared to *F. vesiculosus* could lead to the assumption that the metabolites in the layer behave differently between the two algal genera. Possible reasons, besides a different chemical nature of the exuded metabolites, include the different surface textures of the algae. The surface of *F. vesiculosus* is rather rough with microstructures consisting of cavities, which contain tufts of phaeophyceal hairs, compared to the smooth surface of *Ulva* sp. (Van den Hoek et al. 1997). Such structures could result in a more extended laminar layer; moreover polysaccharides secreted by *F. vesiculosus* could lead to a reduced diffusion compared to *Ulva* sp. (Van den Hoek et al. 1997).

In general it is possible to distinguish between different carotenoids dissolved in the same solvent on the basis of their band positions (Merlin 1985; Withnall et al. 2003). The band position of the C=C bonds is influenced by the length of the conjugated system of the carotenoid as well as by its conformation (Rimai et al. 1973). In the present study, a slight difference from *ca* 2 cm^{-1} in the band position for the C=C stretching band (shift from 1526 cm^{-1} , *Ulva* sp. to 1528 cm^{-1} , *F. vesiculosus*) was observed (Figure 5c). This difference was consistent over 10 measurements despite a spectral resolution of 2 cm^{-1} and therefore indicates a different carotenoid composition in the diffusion boundary layer of the two algae. This finding is in agreement with studies on the carotenoid composition of these particular macroalgae. The carotenoid fucoxanthin is only present in brown and red algae (Bjornland and Aguilar-Martinez 1976; Haugan and Liaaen-Jensen 1994) and in brown algae, it is the main carotenoid, followed by β -carotene. In contrast, green algae such as *Ulva* sp. do not produce fucoxanthin and their main carotenoid is β -carotene (Bianchi et al. 1997; Gantt and Cunningham 2001). Ballard et al. (1989) discussed the difference between the resonance Raman spectra of fucoxanthin and β -carotene. Two main parameters besides the band position are different between fucoxanthin and β -carotene spectra. The band intensity of the ν_2 (carbon single bond stretching) in fucoxanthin is lower than the intensity of the ν_1 band (carbon double bond stretching). The ν_1 and ν_2 bands of β -carotene showed a similar intensity, as also observed in the spectra derived from *Ulva* sp. In general the band broadening

is less for fucoxanthin than for β -carotene (Figure 4). In the present study the spectra of the *F. vesiculosus* showed a difference in the ν_1 and ν_2 band intensity as well as less band broadening compared to the non-fucoxanthin containing alga *Ulva* sp. (Figure 5b). In addition, the recorded spectra of fucoxanthin and β -carotene standards showed the same differences in the ν_1 and ν_2 band intensity, which was also recorded within the chemical sphere of the two algae (Figures 4, 5b). The spectrum of the fucoxanthin standard resembles more the spectrum recorded above the surface of *F. vesiculosus* than the one of *Ulva* sp. Such minor differences in the band position in spectra of carotenoid standards and plant tissue were also observed in the study of De Oliveira et al. (2010). The shift could be explained by molecular interaction between the carotenoid and the surrounding host tissue. Therefore differences in the spectral parameters between the measurements of brown and green algae confirm that different carotenoids are observed. The dominant presence of fucoxanthin on *F. vesiculosus* surfaces could also be confirmed by the data from hexane dipping extracts that exhibited only one dominant carotenoid peak, which showed the same chromatographic and spectroscopic properties as an authentic fucoxanthin standard (Saha et al. 2011).

Resonance Raman microspectroscopy also provides an opportunity to map carotenoid distribution in the x,y-direction on the surface of an alga. A lateral scan revealed minor fluctuations in the carotenoid concentration on a micrometer scale and a steep drop in signal intensity for the bands at 1160 cm^{-1} and 1528 cm^{-1} once the border of the alga was reached (Figure 6). More detailed surface mapping revealed that despite an overall homogeneous distribution of fucoxanthin on the surface, local fluctuations could be observed if relative concentrations within a small surface area were considered. For example, microscopic contaminations on the algal surface, such as associated diatoms could be distinguished. Also local minima and maxima could be observed. A map of the *F. vesiculosus* carotenoid revealed a difference in the relative concentration between the algal surface and associated diatoms (Figure 7). Based on signal intensity, the carotenoid content of the surface was higher than on the associated diatoms, which contain fucoxanthin as well as other carotenoids (Stauber and Jeffrey 1988). Thus, it has to be verified if the release patterns of the carotenoids differ between the heterokont microalgae and macroalgae.

Conclusions

In the present study it was shown that resonance Raman microspectroscopy is a suitable method to

investigate the diffusion boundary layer of marine macroalgae. Raman spectroscopy is however not suitable for the universal mapping of all released metabolites from algal surfaces due to its rather low sensitivity for several compound classes. Carotenoids are particularly well suited for resonance Raman measurements since these compounds give rise to strong and fluorescence-free resonance Raman enhancement. An additional advantage of resonance Raman spectroscopy compared to normal Raman spectroscopy is that the rather complex non-resonant Raman spectroscopy is significantly simplified since only vibrational modes of the resonant chromophore contribute to the spectrum. Thus, resonance Raman microspectroscopy could also be used for other Raman active substances, which may be of ecological interest.

It was possible to detect carotenoid gradients within the immediate vicinity of two different genera. The ability to localize compounds above the algal surface gives a new perspective for investigations of the ecological role of metabolites in the ecosystem. Given the size of bacteria (sub-micrometer to the micrometer range), these fouling organisms will encounter steep gradients on their approach to algal surfaces. Established extraction methods, like the hexane dipping procedure or mass spectrometric methods that only average over the entire diffusion boundary layer of several hundred micrometers, only provide a rough estimate of actual local concentrations encountered by the fouling organisms (De Nys 1998; Lane et al. 2009). Based on the distribution of carotenoids in the diffusion boundary layer, it is estimated that bacteria in the immediate vicinity of the alga will be exposed to millimolar concentrations of active metabolites and an approaching microorganism would thus encounter a steep gradient and high local concentrations of active chemicals (Table 1). This finding has implications for host selection and the preference for different parts of the host organism and bioassays would have to be designed accordingly. Evidence for general variability is provided by the present study where a difference in the carotenoid gradient above two different macroalgal genera was observed.

The release of nonpolar pigments like carotenoids into the polar aqueous environment is rather surprising. Carotenoids are known to be part of the light harvesting complex embedded in the interior part of the cell. It is not clear if general metabolic processes lead to leaking of these metabolites or if a controlled release is observed. Degradation of dead surface cells might result in the observed patterns, but since microscopic investigation showed no evidence of dead surface cells, this possibility is less likely.

In conclusion a method is described for surface mapping of metabolites with a micrometer scale lateral

resolution, which allows the gradient of a metabolite to be visualised in the z-direction from the algal surface. The analysis is performed without any addition of solvents or even removal of the diffusion boundary layer. The method is thus completely non-disruptive.

Acknowledgements

This study was supported by a PhD scholarship to KG from the IMPRS research school for Exploration of Ecological Interactions with Molecular and Chemical Techniques of the Max Planck Institute for chemical ecology in Jena. LZ acknowledges the Thüringer Ministerium für Bildung, Wissenschaft und Kultur (Grant No. B 514-09049, PhotoMic) and GP the Volkswagen Foundation for financial support.

References

- Annesley TM. 2003. Ion suppression in mass spectrometry. *Clin Chem* 49:1041–1044.
- Baena JR, Lendl B. 2004. Raman spectroscopy in chemical bioanalysis. *Curr Opin Chem Biol* 8:534–539.
- Baia L, Gigant K, Posset U, Schottner G, Kiefer W, Popp J. 2002. Confocal micro-Raman spectroscopy: theory and application to a hybrid polymer coating. *Appl Spectrosc* 56:536–540.
- Bakker Shut TC, Puppels GJ, Kraan YM, Greve J, Maas van der LLJ, Figdor CG. 1997. Intracellular carotenoid levels measured by Raman microspectroscopy: comparison of lymphocytes from lung cancer patients and healthy individuals. *Int J Cancer* 74:20–25.
- Ballard L, Glasgow L, Hoskins L, Krohe T. 1989. The resonance Raman excitation profile of fucoxanthin. *Spectrochim Acta A* 45:1235–1238.
- Bianchi TS, Kautsky L, Argyrou M. 1997. Dominant chlorophylls and carotenoids in macroalgae of the Baltic Sea (Baltic proper): their use as potential biomarkers. *Sarsia* 82:55–62.
- Bjornland T, Aguilar-Martinez M. 1976. Carotenoids in red algae I. *Phytochemistry* 15:291–296.
- Cooks RG, Ouyang Z, Takats Z, Wiseman JM. 2006. Ambient mass spectrometry. *Science* 311:1566–1570.
- De Nys R, Dworjanyn SA, Steinberg PD. 1998. A new method for determining surface concentrations of marine natural products on seaweeds. *Mar Ecol Prog Ser* 162:79–87.
- De Oliveira VE, Castro HV, Edwards HGM, de Oliveira LFC. 2010. Carotenes and carotenoids in natural biological samples: a Raman spectroscopic analysis. *J Raman Spectrosc* 41:642–650.
- Dworjanyn SA, De Nys R, Steinberg PD. 1999. Localisation and surface quantification of secondary metabolites in the red alga *Delisea pulchra*. *Mar Biol* 133:727–736.
- Dworjanyn SA, De Nys R, Steinberg PD. 2006. Chemically mediated antifouling in the red alga *Delisea pulchra*. *Mar Ecol Prog* 318:153–163.
- Gantt E, Cunningham FX. 2001. Algal pigments. eLS; [cited 2012 Jun 26]. Available from: <http://onlinelibrary.wiley.com/doi/10.1038/npg.els.0000323/references>
- Haugan JA, Liaaen-Jensen S. 1994. Algal carotenoids 54. Carotenoids of brown algae (Phaeophyceae). *Biochem Syst Ecol* 22:31–41.
- Hellio C, De La Broise D, Dufossé L, Le Gal Y, Bourgougnon N. 2001. Inhibition of marine bacteria by extracts of macroalgae: potential use for environmentally friendly antifouling paints. *Mar Environ Res* 52:231–247.

- Hurd CL. 2000. Water motion, marine macroalgal physiology, and production. *J Phycol* 36:453–472.
- Krafft C, Dietzek B, Popp J. 2009. Raman and CARS microspectroscopy of cells and tissues. *Analyst* 134:1046–1057.
- Lachnit T, Wahl M, Harder T. 2010. Isolated thallus-associated compounds from the macroalga *Fucus vesiculosus* mediate bacterial surface colonization in the field similar to that on the natural alga. *Biofouling* 26:247–255.
- Lane AL, Nyadong L, Galhena AS, Shearer TL, Stout EP, Parry RM, Kwasnik M, Wang MD, Hay ME, Fernandez FM. 2009. Desorption electrospray ionization mass spectrometry reveals surface-mediated antifungal chemical defense of a tropical seaweed. *P Natl Acad Sci USA* 106:7314–7319.
- Lieber CA, Ahadevan-Jansen AM. 2003. Automated method for subtraction of fluorescence from biological Raman spectra. *Appl Spectrosc* 57:1363–1367.
- Maréchal J-P, Hellio C. 2011. Antifouling activity against barnacle cypris larvae: do target species matter (*Amphibalanus amphitrite* versus *Semibalanus balanoides*)? *Int Biodeterior Biodegr* 65:92–101.
- Markham J, Hagmeier E. 1982. Observations on the effects of germanium dioxide on the growth of macro-algae and diatoms. *Phycologia* 21:125–130.
- Mattsson B, Ericson H, Torell L, Sundholm F. 1999. Micro-Raman investigations of PVDF-based proton-conducting membranes. *J Polym Sci Pol Chem* 37:3317–3327.
- Mazzella N, Delmas F, Delest B, Méchin B, Madigou C, Allenou J -P, Gabellec R, Caquet T. 2009. Investigation of the matrix effects on a HPLC-ESI-MS/MS method and application for monitoring triazine, phenylurea and chloroacetanilide concentrations in fresh and estuarine waters. *J Environ Monit* 11:108–115.
- Merlin JC. 1985. Resonance Raman spectroscopy of carotenoids and carotenoid-containing systems. *Pure Appl Chem* 57:785–792.
- Nylund GM, Cervin G, Hermansson M, Pavia H. 2005. Chemical inhibition of bacterial colonization by the red alga *Bonnemaisonia hamifera*. *Mar Ecol Prog Ser* 302:27–36.
- Nylund GM, Persson F, Lindegarh M, Cervin G, Hermansson M, Pavia H. 2010. The red alga *Bonnemaisonia asparagoides* regulates epiphytic bacterial abundance and community composition by chemical defence. *FEMS Microbiol Ecol* 71:84–93.
- Parker FS. 1975. Biochemical applications of infrared and Raman spectroscopy. *Appl Spectrosc* 29:129–147.
- Persson F, Svensson R, Nylund GM, Fredriksson NJ, Pavia H, Hermansson M. 2011. Ecological role of a seaweed secondary metabolite for a colonizing bacterial community. *Biofouling* 27:579–588.
- Petry R, Schmitt M, Popp J. 2003. Raman spectroscopy—a prospective tool in the life sciences. *Chem Phys Chem* 4:14–30.
- Rimai L, Kilponen R, Gill D. 1970. Excitation profiles of laser Raman spectra in the resonance region of two carotenoid pigments in solution. *J Am Chem Soc* 92:3824–3825.
- Rimai L, Heyde ME, Gill D. 1973. Vibrational spectra of some carotenoids and related linear polyenes. Raman spectroscopic study. *J Am Chem Soc* 95:4493–4501.
- Saha M, Rempt M, Grosser K, Pohnert G, Weinberger, F. 2011. Surface-associated fucoxanthin mediates settlement of bacterial epiphytes on the rockweed *Fucus vesiculosus*. *Biofouling* 27:423–433.
- Schlichting H, Gersten K, Gersten K. 2000. Boundary-layer theory. 8th ed. Berlin (Germany): Springer-Verlag. 801 pp.
- Schmidt U, Müller J, Koenen J. 2010. Confocal Raman imaging of polymeric materials. In: Dieing T, Hollricher O, Toporski J, editors. *Confocal Raman microscopy*. Berlin (Germany): Springer-Verlag. p. 237–258.
- Schmitt M, Leimeister B, Baia L, Weh B, Zimmermann I, Kiefer W, Popp J. 2003. Characterisation of diffusion-processes of pharmacological relevant molecules through PDMS-membranes by means of confocal resonance Raman spectroscopy. *Chem Phys Chem* 4:296–299.
- Sneed JM, Pohnert G. 2011. The green alga *Dicytosphaeria ocellata* and its organic extracts alter natural bacterial biofilm communities. *Biofouling* 27:347–356; [cited 2012 Jun 26]. Available from: <http://www.tandfonline.com/doi/abs/10.1080/08927014.2011.576317>
- Stauber JL, Jeffrey S. 1988. Photosynthetic pigments in fifty-one species of marine diatoms. *J Phycol* 24:158–172.
- Stevens CL, Hurd CL. 1997. Boundary-layers around bladed aquatic macrophytes. *Hydrobiologia* 346:119–128.
- Van den Hoek C, Mann D, Jahns HM. 1997. *Algae: an introduction to phycology*. Cambridge (UK): Cambridge University Press. 640 pp.
- Wächtler M, Guthmüller J, González L, Dietzek B. 2012. Analysis and characterization of coordination compounds by resonance Raman spectroscopy. *Coord Chem Rev* 256:1479–1508.
- Wahl M. 2009. *Hard bottom communities: patterns dynamics and changes*. Ecological Studies Series 206. Berlin (Germany): Springer-Verlag. p. 61–69.
- Weinberger F, Leonardi P, Miravalles A, Correa JA, Lion U, Kloareg B, Potin P. 2005. Dissection of two distinct defense-related responses to agar oligosaccharides in *Gracilaria chilensis* (Rhodophyta) and *Gracilaria conferta* (Rhodophyta). *J Phycol* 41:863–873.
- Withnall R, Chowdhry BZ, Silver J, Edwards HGM, de Oliveira LFC. 2003. Raman spectra of carotenoids in natural products. *Spectrochim Acta A* 59:2207–2212.

[Bode et al. Adv. Mater.]

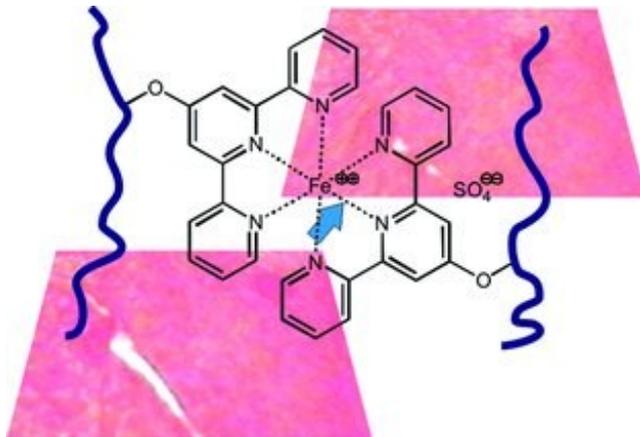
Self-Healing Polymer Coatings Based on Crosslinked Metallosupramolecular Copolymers

Der Nachdruck der folgenden Publikation erfolgt mit freundlicher Genehmigung von Wiley-VCH Verlag GmbH & Co KGaA, Weinheim.

Reprinted with kind permission from:

Bode, S.; Zedler, L.; Schacher, F. H.; Dietzek, B.; Schmitt, M.; Popp, J.; Hager, M. D.; Schubert, U. S., Self-Healing Polymer Coatings Based on Crosslinked Metallosupramolecular Copolymers, *Adv. Mater.* **2013**, 25, 1634–1638.

Copyright 2013 Wiley-VCH Verlag GmbH & Co KGaA, Weinheim.



Self-healing coating based on metallopolymers are prepared and fully characterized. Iron *bisterpyridine* complexes are incorporated into a polymer network based on methacrylates, resulting in self-healing properties of these materials. Moreover, the influence of the comonomers on the thermal properties is studied in detail.

Self-Healing Polymer Coatings Based on Crosslinked Metallosupramolecular Copolymers

Stefan Bode, Linda Zedler, Felix H. Schacher, Benjamin Dietzek, Michael Schmitt, Jürgen Popp, Martin D. Hager,* and Ulrich S. Schubert*

The most important characteristic of self-healing materials is their ability to heal inflicted mechanical damage and, thus, to recover (partially) their mechanical properties. Intrinsic self-healing is based on specific healing mechanisms, which originate from specific properties of the material itself. As a consequence, it is also possible to design systems which can heal themselves virtually endless, if reversible changes (e.g., opening and closing of a reversible bond) within the materials are utilized for the self-healing process.^[1]

In the last decade several intrinsic self-healing materials have been developed where the healing mechanism was mainly based on the reversibility of a certain structural element. For this purpose, reversible covalent bonds (e.g., based on the Diels-Alder reaction)^[2] or weaker noncovalent interactions (e.g., hydrogen bonding,^[3] ionic interactions,^[4] π - π interactions,^[5] or host-guest interactions)^[6] have been successfully utilized. In contrast, only few examples describe the self-healing based on reversible metal-ligand-interactions, although this concept can be observed in nature.^[7] As an example, the healing processes within mussel byssus threads are based on the reversible formation of metal complexes.^[7]

If metal complexes are used as structural units to promote self-healing, a compromise between the mechanical properties and the self-healing behavior must be found. Typically, the strength of the metal-ligand bond is the key factor for both.^[8]

However, weaker metal complexes would promote healing while, at the same time, the mechanical stability is reduced.

Up to now metal complexes have not been utilized often for the generation of self-healing properties, in particular not for polymer films/coatings. As an example, a recently described linear metallopolymer was capable of healing a scratch when heated up to 220 °C.^[9]

Our model system is based on the well-investigated terpyridine ligand system.^[10] Therefore, the stabilities of the metal complexes in solution are well known, which allows the tuning of the resulting properties by choosing the appropriate metal ion.^[11] Furthermore, the terpyridine ligand can be easily functionalized using straight-forward synthetic routes for the preparation of different functional monomers.^[12]

Firstly, it is necessary to design the terpyridine containing polymers. For this purpose, a terpyridine monomer was copolymerized with other monomers (i.e., alkyl methacrylates), in order to adjust the amount of the crosslinking units as well as to tune the thermal and mechanical properties of the resulting polymer networks. The reversible addition-fragmentation chain transfer (RAFT) polymerization technique was used to obtain well-defined polymers with adjustable composition.^[13] For the copolymerization three different methacrylate monomers were used: methyl methacrylate, butyl methacrylate and lauryl methacrylate. The resulting polymers have molar masses (M_n) of about 30 000 g/mol and differ in the glass-transition temperature, which indicates the different flexibility/mobility of the polymer backbones. The desired content of terpyridine of 10% could be nearly reached for all polymers (8% for MMA/P1, 9.5% for BMA/P2 and 8.3% for LMA/P3), which should enable the formation of strongly crosslinked polymer networks (Supporting Information, Table S1,S2). The obtained terpyridine contents differ only slightly, therefore the terpyridine content is not the factor which could cause differences between the polymer P1 to P3. The SEC curves confirm the existence of well-defined copolymers (Supporting Information, Figure S3).

Subsequently, the terpyridine containing copolymers were crosslinked by the addition of iron(II) sulfate (**Scheme 1**). Iron(II)-bis-terpyridine complexes have already been intensively investigated in solution and it was shown that the complex stability is higher if compared to the corresponding zinc(II) complex, but not as strong as the ruthenium(II) analogue, where the binding strength is comparable with a typical covalent bond.^[10,14]

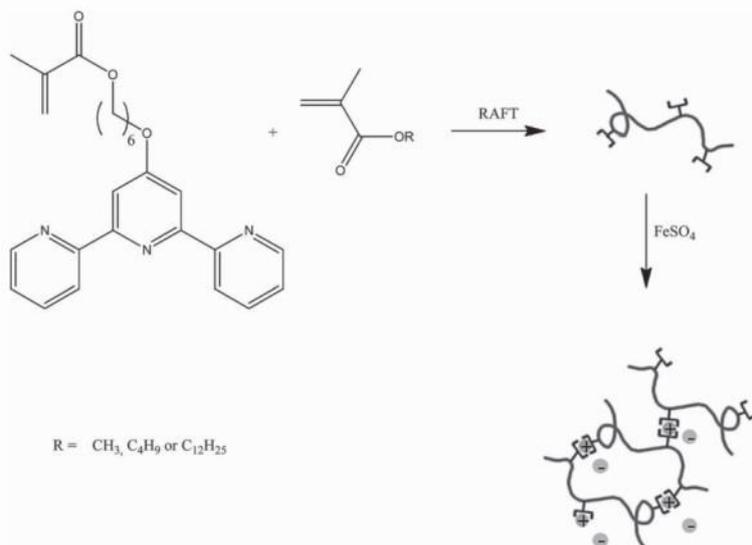
The crosslinking led to the formation of a gel via the formation of metal-ligand interactions, which is a well known phenomena described in literature.^[15] It is noteworthy that the transformation of this "organogel" to a solid material has not

S. Bode, Prof. F. H. Schacher, Dr. M. D. Hager,
Prof. U. S. Schubert
Laboratory of Organic and Macromolecular
Chemistry (IOMC)
Friedrich-Schiller-University Jena
Humboldtstr. 10, 07743 Jena, Germany
E-mail: martin.hager@uni-jena.de; ulrich.schubert@uni-jena.de



S. Bode, L. Zedler, Prof. F. H. Schacher, Prof. B. Dietzek,
Prof. M. Schmitt, Prof. J. Popp, Dr. M. D. Hager, Prof. U. S. Schubert
Jena Center for Soft Matter (JCSM)
Friedrich-Schiller-University Jena
Philosophenweg 7, 07743 Jena, Germany
L. Zedler, Prof. B. Dietzek, Prof. M. Schmitt, Prof. J. Popp
Institute of Physical Chemistry (IPC) and Abbe Center of Photonics (ACP)
Friedrich-Schiller-University Jena
Helmholtzweg 4, 07743 Jena, Germany
L. Zedler, Prof. B. Dietzek, Prof. J. Popp
Institute of Photonic Technology (IPHT) Jena
Albert-Einstein-Straße 9, 07745 Jena, Germany
Prof. U. S. Schubert
Dutch Polymer Institute (DPI)
5600 AX Eindhoven, The Netherlands

DOI: 10.1002/adma.201203865



Scheme 1. Schematic representation of the synthesis of the iron(II) crosslinked polymer network.

yet been investigated in detail. The solid polymer network was dried at room temperature resulting in the formation of a film. These films were mechanically stable and no melting could be observed in DSC (up to 250 °C) as well as under an optical microscope (up to 300 °C). Additionally, a glass-transition temperature could be observed at 30 °C in the DSC for the crosslinked polymers based on butyl (CP2) and lauryl methacrylate

(CP3) as comonomer (Supporting Information, Figure S4). The thermal stability of the polymers was investigated by TGA (Supporting Information, Figure S5). All polymers are stable up to temperatures >200 °C (i.e., healing processes can be performed at elevated temperatures).

The self-healing process was investigated after cutting a small scratch into the polymer film. Afterwards, the crosslinked polymer network was heated at 100 °C for a defined time and the scratch was monitored using optical microscopy. The heating of the material is required to induce sufficient mobility for the healing process, in particular, no healing process can be observed at room temperature. For CP2, this healing process at 100 °C of the polymer network, based on butyl methacrylate as comonomer, is depicted in Figure S6 in the Supporting Information.

The polymer with methyl methacrylate (CP1) did not show any self-healing behavior at 100 °C, whereas the copolymer network with butyl methacrylate (CP2) was able to heal small scratches (length: 180 μm; width: 10 μm) during a short period of time (only 40 minutes at 100 °C for a scratch, which is longer than 100 μm). This crosslinked copolymer also featured self-healing properties at 80 °C, but the time for the healing process increases significantly (i.e., 30 hours are required for complete healing).

Moreover, the lauryl methacrylate based copolymer (CP3) was also investigated and the healing process for a scratch is depicted in Figure 1. This material was able to heal larger and wider scratches, which we ascribe to the higher flexibility of the polymer backbone, as indicated by the lower glass-transition temperature (T_g) of the non-crosslinked sample (Table 1). Furthermore, it was possible to follow the self-healing process of CP3 by SEM measurements where it could be shown that the scratches are closed by material diffusion (Supporting Information, Figure S7). Additionally, the reversibility of the healing process was investigated via multiple healing cycles (Supporting Information, Figure S8). However, decreasing efficiency of the healing process was observed, as after three cycles the scratches only decreased in both length and width. In all self-healing studies the scratches went through the entire films with a depth of about 10 μm, as determined by a profilometer (Supporting Information, Figure S9). Furthermore, the mechanical properties of CP2 were investigated by nanoindentation and the deformation was shown to be viscous-elastic-plastic. The indentation modulus was about 2 GPa, as can be anticipated for a rather hard material (Supporting Information, Figure S10).^[16]

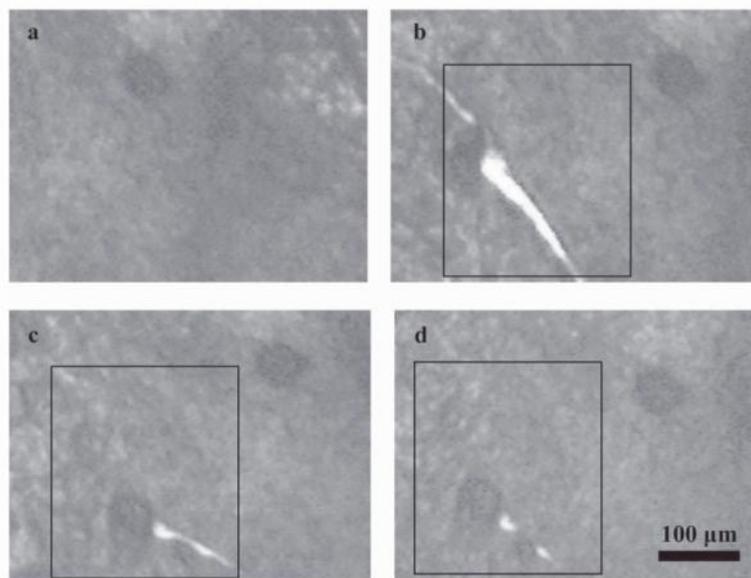


Figure 1. Self-healing of the crosslinked polymer network with lauryl methacrylate as comonomer (CP3): a) polymer film, b) scratch; c) partial healing after 16 hours at 100 °C, and d) healing after 82 hours at 100 °C.

Table 1. Summary of the self-healing behavior.

Polymer	Comonomer	Glass-transition temperature of non-crosslinked polymer [°C]	Healing temperature [°C]	Healed crack width [μm]	Healed crack length [μm]	SAXS/ <i>d</i> [°]/[nm]
CP1	methyl methacrylate	74	no self-healing	no self-healing	no self-healing	-
CP2	butyl methacrylate	-2	80	10	180	1.44/6.4
CP3	lauryl methacrylate	-65	80	35	250	1.44/6.4

In all cases, the crosslinked copolymer networks did not melt during the healing process. As no residual solvent is present, the formation of an organogel can also be excluded. Therefore, the above described healing is based on an intrinsic self-healing capability of the materials.

The healing process on the molecular level can occur principally via two mechanisms. The crosslinking leads to a connection between different polymer chains, whereby the crosslinking units represent metal complexes, which consist of an iron center and two terpyridines as ligands. Rowan and Weder and co-workers described a kind of depolymerization during the healing process of a linear metallopolymer.^[9] This process was induced through heating under UV irradiation, which resulted in temperatures above 200 °C and probably the UV-light stimulated a transition, which leads to a decomplexation. This would then lead to the cleavage of the metal-ligand bond.

In our case, the chains forming the copolymer network are connected by metal-ligand interactions. A decomplexation, like described above,^[9] would lead to a decrosslinking and hence, the copolymer chains would be sufficiently flexible to induce self-healing. However, copolymer (P3) would be in the liquid state in case a significant amount of crosslinks broke due to the low melting point ($T_m = -30$ °C), which is far below the temperature used in our experiments (up to 120 °C).^[17] Moreover, the iron-*bis*-terpyridine complex features a strong absorption band at 554 nm and, therefore, the crosslinked copolymers appear dark violet (see Supporting Information, Figure S11).^[18] This color is still present even at 100 °C and the crosslinked materials did not melt, which indicates that the reversible opening and closing of the metal-ligand interaction has no significant influence on the self-healing process.

The stability of the metal complexes is supported by temperature-dependent Raman spectroscopy measurements (Figure 2). The Raman spectra in the fingerprint region (1000–1800 cm^{-1}) show a variety of molecular vibrations associated with the terpyridine ligand.^[19] From the inset of Figure 2 it can be seen that – upon heating of the polymer – the high-wavenumber terpyridine modes at 1548 and 1608 cm^{-1} shift by 3 and 4 cm^{-1} , respectively. These reversible shifts are related to a structural rearrangement of the chemical environment in the vicinity of the iron-terpyridine complex. In particular, it should be noted that the Raman spectra do not hint towards decomplexation of the metal ions, as the general intensity pattern is preserved even after repetitive heating up to 100 °C (Supporting Information, Figure S12).

For our system, the employed healing temperatures are distinctly lower than in the case of Rowan and Weder and co-workers.^[9] We assume that the metal complexes are stable under these conditions; however, all known complex stabilities

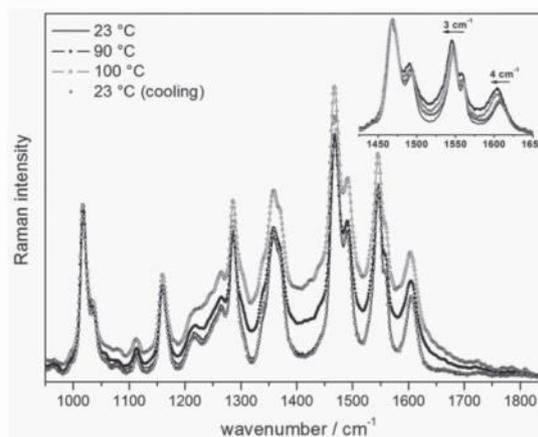


Figure 2. Raman spectra of the crosslinked polybutyl methacrylate-based polymer (CP2) at different temperatures (23 °C, 90 °C, and 100 °C, respectively). Inset: Temperature-dependent Raman spectra measured at higher resolution show notable reversible band shifts upon heating the metallopolymer.

were only investigated in solution up to now and might only be partially applicable for the solid state.

We therefore attribute the observed self-healing behavior in our case to the second possibility, the formation of ionic clusters. The crosslinking units consist of an iron center, which is doubly positively charged. This could trigger the formation of ionic clusters. Varley and van der Zwaag already proved that ionic clusters can contribute to the self-healing behavior of ionomers (e.g., Surlyn).^[20] Thereby, a certain energy is required to reach sufficient mobility/flexibility for the reformation of ionic clusters.

This assumption is also supported by small angle X-ray scattering (SAXS) measurements (Figure 3). Both crosslinked copolymers networks based on CP2 and CP3 show a signal at $2\theta = 1.44^\circ$, corresponding to a feature size of 6.4 nm. Neither the non-crosslinked analogues nor any material based on P1 did show this specific signal. Based on these observations we assume that this structural element is required for the self-healing process.

The formation of ionic clusters would strongly depend on the flexibility of the polymer backbone. This could explain the absence of self-healing properties for CP1 due to the rather low flexibility of the polymer backbone. On the other hand, CP3 based on lauryl methacrylate is the polymer network which consists of the copolymer with the lowest T_g and, thus, the highest chain flexibility and so the formation of the cluster is preferred.

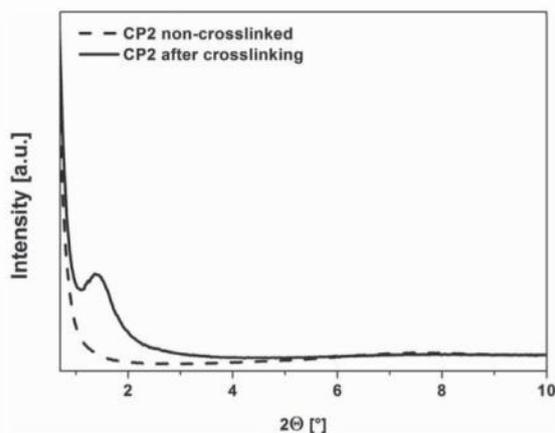


Figure 3. SAXS patterns observed for non-crosslinked P2 (dotted black line) and crosslinked (solid black line) CP2.

This results in the most pronounced self-healing behavior and the most intense reflection in SAXS.

Beside these processes, which occur on the molecular level, also macroscopic properties influence the healing process. The inflicted damage within the crosslinked metallopolymer results mainly in viscous-elastic-plastic deformation. Plastic deformation would not result in a healing.^[21]

In summary, we could demonstrate that crosslinked metallopolymer networks feature self-healing capabilities. This behavior could be directly correlated with mobility/flexibility of the copolymer backbone (Table 1). Up to now, only copolymers with a low glass-transition temperature (before the crosslinking) were able to heal large and wide scratches during short periods of time and at moderately low temperatures (100 °C).

Experimental Section

6-(2,2':6',2''-terpyridin-4'-yloxy)-hexyl Methacrylate: A solution of 6-(2,2':6',2''-terpyridin-4'-yloxy)-hexan-1-ol (689 mg, 1.97 mmol) in dichloromethane (25 mL) was cooled to 0 °C under nitrogen. Triethylamine (0.9 mL, 6.49 mmol) was added and the mixture was stirred for 30 minutes. After this methacrylic chloride (0.3 mL, 3.07 mmol) were slowly added and a gas formation was observed. The solution was stirred for two hours at 0 °C and then the solution was warmed up to room temperature. Afterwards the reaction mixture was stirred for 21 hours. After this the solvent and the triethylamine were removed in vacuo and the residue was dissolved in dichloromethane. This solution was washed with deionized water (300 mL) and the organic phase was dried over Na₂SO₄. The crude product was purified by silica gel chromatography (CHCl₃).

Yield: 650 mg, 79%; ¹H NMR (250 MHz, CDCl₃, δ): 1.48–1.94 (m, 11H, H_{β,γ,δ,ε}, -CH₃), 4.17 (t, J = 6.5 Hz, H_α, 2H), 4.23 (t, J = 6.5 Hz, H_γ, 2H), 5.54 (s, =CH₂, 1H), 6.10 (s, =CH₂, 1H), 7.33 (d, J = 4.5 Hz, H_{5,5'}, 2H), 7.84 (t, J = 7.5 Hz, H_{4,4'}, 2H), 8.00 (s, H_{3,3'}, 2H), 8.62 (d, J = 7.5 Hz, H_{3,3'}, 2H), 8.69 (d, J = 4.5 Hz, H_{6,6'}, 2H) ppm.

¹³C NMR (62.5 MHz, CDCl₃, δ): 18.3 (CH₃), 25.7 (C_δ), 25.8 (C_γ), 28.6 (C_ε), 28.9 (C_β), 63.6 (C_α), 68.0 (C_ζ), 107.4 (C_{5,5'}), 121.3 (C_{4,4'}), 123.8 (C_{3,3'}), 125.2 (C=CH₂), 136.5 (C=CH₂), 136.8 (C_{3,3'}), 149.0 (C_{6,6'}), 156.2 (C_{2,2'}), 157.0 (C_{2,6'}), 167.3 (C_{4'}), 167.5 (CO) ppm.

Anal. calcd. for C₂₅H₂₇N₃O₃: C 71.92, H 6.52, N 10.06; found: C 71.71, H 6.51, N 10.28

General Procedure for the RAFT Polymerization: In a 10 mL microwave vial, the desired amounts of the two monomers were dissolved in dry toluene. Then, the calculated volumes of the stock solutions in toluene of CPDB and AIBN were added. The ratio of [M] to [CPDB] was always 150/1 and the ratio of [CPDB] to [AIBN] 4/1.

The reaction mixture was purged with a flow of nitrogen for 30 minutes and the vial was closed. Overnight the reaction was performed in an oil bath at 70 °C.

The polymers were purified by precipitation in cold ethanol. The BMA and LMA containing polymers were also purified by BioBeads S-X3 (solvent chloroform).

General Procedure for the Crosslinking of the Polymers: The desired amount of the polymer was dissolved in acetonitrile (5 mL) in a 50 mL one neck flask. A mixture of iron(II) sulfate heptahydrate in methanol (2 mL) was added and immediately the color changed to dark violet. The solvents were evaporated slowly and the product was dried in vacuo.

Raman experiments were performed using a LabRAM HR800 Raman spectrometer (Horiba-Jobin Yvon) equipped with a confocal aperture and a microscope (BX40, Olympus). The incident laser power on the sample was P_L < 2 mW at an excitation wavelength of 647 nm of a krypton ion laser (Innova 302C, Coherent). The pinhole diameter was set to 1000 μm and the slit width to 100 μm. Raman signals were detected using a liquid-nitrogen-cooled charge coupled device (CCD).

SAXS Measurements: SAXS measurements on polymer films were performed on a Bruker AXS Nanostar (Bruker, Karlsruhe, Germany), equipped with a microfocus X-ray source (Incoatec IμS_{CU} E025, Incoatec Geesthacht, Germany), operating at λ = 0.154 nm. A pinhole setup with 750, 400, and 1000 μm (in the order from source to sample) was used and the sample-to-detector distance was 27 cm. Samples were mounted on a metal rack and fixed using tape. The scattering patterns were corrected for the beam stop and the background (Scotch tape or FEP foil) prior to evaluations. The measurement time for the samples was 4 h in all cases.

Supporting Information

Supporting Information is available from the Wiley Online Library or from the author.

Acknowledgements

The authors would like to thank Dr. Jürgen Vitz for the nanoindentation measurements and Steffi Stumpf for the SEM images. The authors thank the Deutsche Forschungsgemeinschaft (DFG, SPP 1568), the Thuringian Ministry for Education, Science and Culture (TMBWK grants #B515-10065, ChaPoNano; #B514-09051, NanoConSens; and #B515-11028, SWAXS-JSCM), the DPI (technology area HTE), and the Fond der Chemischen Industrie for financial support.

Received: September 15, 2012

Revised: November 7, 2012

Published online: January 27, 2013

- [1] M. D. Hager, P. Greil, C. Leyens, S. van der Zwaag, U. S. Schubert, *Adv. Mater.* **2010**, *5*, 5424–5430.
- [2] a) X. Chen, F. Wudl, A. K. Mal, H. Shen, S. R. Nutt, *Macromolecules* **2003**, *36*, 1802–1807; b) X. Chen, M. A. Dam, A. Ono, A. Mal, H. Shen, S. R. Nutt, K. Sheran, F. Wudl, *Science* **2002**, *295*, 1698–1702.
- [3] P. Cordier, F. Tournilhac, C. Soulié-Ziakovic, L. Leibler, *Nature* **2008**, *451*, 977–980.
- [4] S. J. Kalista, T. Ward, *J. R. Soc. Interface* **2007**, *4*, 405–411.
- [5] a) S. Burattini, H. M. Colquhoun, J. D. Fox, D. Friedmann, B. W. Greenland, P. J. F. Harris, W. Hayes, M. E. Mackay, S. J. Rowan,

- Chem. Commun.* **2009**, 6717–6719; b) S. Burattini, H. M. Colquhoun, B. W. Greenland, W. Hayes, *Faraday Discuss.* **2009**, *143*, 251–264.
- [6] a) M. Zhang, D. Xu, X. Yan, J. Chen, S. Dong, B. Zheng, F. Huang, *Angew. Chem. Int. Ed.* **2012**, *51*, 7011–7015; b) X. Yan, F. Wang, B. Zheng, F. Huang, *Chem. Soc. Rev.* **2012**, *41*, 6042–6065.
- [7] a) N. Holten-Andersen, M. J. Harrington, H. Birkedal, B. P. Lee, P. W. Messersmith, K. Y. Y. Lee, H. Waite, *Proc. Natl. Acad. Sci. USA* **2011**, *108*, 2651–2655; b) M. J. Harrington, A. Masic, N. Holten-Andersen, J. H. Waite, P. Fratzl, *Science* **2010**, *328*, 216–220.
- [8] G. R. Whittell, M. D. Hager, U. S. Schubert, I. Manners, *Nat. Mater.* **2011**, *10*, 176–188.
- [9] M. Burnworth, L. Tang, J. R. Kumpfer, A. J. Duncan, F. L. Beyer, G. L. Fiore, S. J. Rowan, C. Weder, *Nature* **2011**, *472*, 334–338.
- [10] A. Wild, A. Winter, F. Schlütter, U. S. Schubert, *Chem. Soc. Rev.* **2011**, *40*, 1459–1511.
- [11] W.-S. Tang, X.-X. Lu, K. M.-C. Wong, V. W.-W. Yam, *J. Mater. Chem.* **2005**, *15*, 2714–2720.
- [12] U. S. Schubert, C. Eschbaumer, O. Hien, P. R. Andres, *Tetrahedron Lett.* **2001**, *42*, 4705–4707.
- [13] G. Moad, E. Rizzardo, S. H. Thang, *Aust. J. Chem.* **2005**, *58*, 379–410.
- [14] R. H. Holyer, C. D. Hubbard, S. F. A. Kettle, R. G. Wilkins, *Inorg. Chem.* **1966**, *5*, 622–625.
- [15] H. Hofmeier, A. El-gharyoury, U. S. Schubert, *e-Polymers* **2003**, *53*, 1–13.
- [16] a) M. L. Oyen, R. F. Cook, *J. Mech. Behav. Biomed. Mater.* **2009**, *2*, 396–407; b) W. C. Oliver, G. M. Pharr, *J. Mater. Res.* **2004**, *19*, 3–20; c) M. L. Oyen, R. F. Cook, *J. Mater. Res.* **2003**, *18*, 139–150; d) E. F.-J. Rettler, J. M. Kranenburg, H. M. L. Lambermont-Thijs, R. Hoogenboom, U. S. Schubert, *Macromol. Chem. Phys.* **2010**, *211*, 2443–2448; e) W. C. Oliver, G. M. Pharr, *J. Mater. Res.* **1992**, *7*, 1564–1583.
- [17] G. Floudas, P. Placke, P. Stepanek, W. Brown, G. Fytas, K. L. Ngai, *Macromolecules* **1995**, *28*, 6799–6708.
- [18] M. Heller, U. S. Schubert, *Macromol. Rapid Commun.* **2001**, *22*, 1358–1363.
- [19] a) K. Heinze, K. Hempel, S. Tschierlei, M. Schmitt, J. Popp, S. Rau, *Eur. J. Inorg. Chem.* **2009**, 3119–3126; b) S. Kupfer, J. Guthmüller, M. Wächtler, S. Losse, S. Rau, B. Dietzek, J. Popp, L. González, *Phys. Chem. Chem. Phys.* **2011**, *13*, 15580–15588.
- [20] R. J. Varley, S. van der Zwaag, *Polym. Test.* **2008**, *27*, 11–19.
- [21] R. P. Wool, *Soft Matter* **2008**, *4*, 400–418.

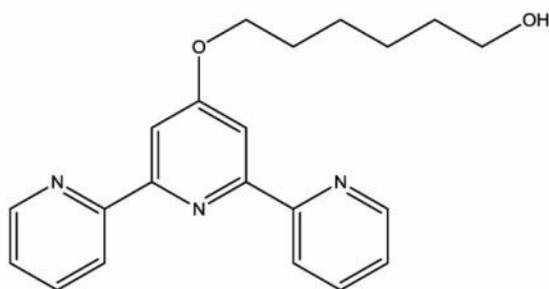
Advanced Materials

Supporting information:

Self-healing polymer coatings based on crosslinked metallosupramolecular copolymers

By *Stefan Bode, Linda Zedler, Felix H. Schacher, Benjamin Dietzek, Michael Schmitt, Jürgen Popp, Martin D. Hager** and *Ulrich S. Schubert**

6-(2,2':6',2''-Terpyridin-4'-yloxy)-hexan-1-ol (1)



A suspension of KOH (0.77 g, 13.72 mmol) in dry DMSO (18.5 mL) was prepared. This mixture was heated to 40 °C and then 1,6-hexandiol (3.33 g, 28.18 mmol) was added. After 30 minutes at 40 °C 4'-chloro-2,2':6',2''-terpyridine (0.75 g, 2.80 mmol) was added and the solution was stirred for 4 hours at 40 °C. The reaction mixture was poured into deionised water (300 mL) and the liquid phase was removed by filtration. The white solid was washed with deionised water (200 mL) and dried in *vacuo*.

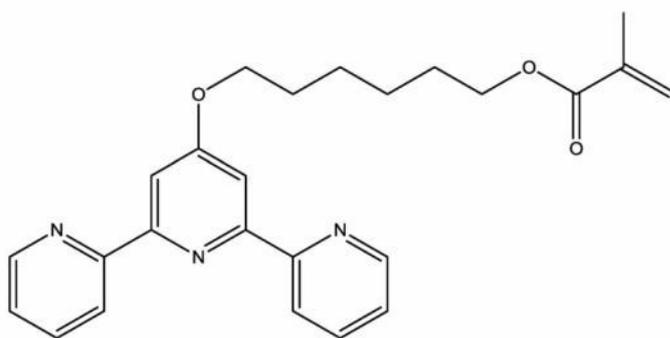
Yield: 702 mg, 72%

¹H NMR (250 MHz, CDCl₃, δ): 1.46 – 1.90 (m, 9H, H_{β,γ,δ,ε}, -OH), 3.67 (t, *J* = 6.25 Hz, H_α, 2H), 4.23 (t, *J* = 6.25 Hz, H_ζ, 2H), 7.32 (dd, *J* = 1.75 Hz, 4.75 Hz, H_{5,5''}, 2H), 7.84 (td, *J* = 1.75 Hz, 8 Hz, H_{4,4''}, 2H), 8.00 (s, H_{3,5'}, 2H), 8.61 (d, *J* = 8 Hz, H_{3,3''}, 2H), 8.68 (d, *J* = 4.75 Hz, H_{6,6''}, 2H) ppm.

¹³C NMR (62.5 MHz, CDCl₃, δ): 25.4 (C_δ), 25.8 (C_γ), 28.9 (C_ε), 32.7 (C_β), 62.8 (C_α), 68.0 (C_ζ), 107.4 (C_{5,5''}), 121.4 (C_{4,4''}), 123.8 (C_{3,3''}), 136.8 (C_{3',5'}), 149.00 (C_{6,6''}), 156.2 (C_{2,2''}), 157.0 (C_{2',6'}), 167.3 (C_{4'}) ppm.

Anal. calcd. for C₂₁H₂₃N₃O₂: C: 72.18, H 6.63, N 12.03; found: C: 72.01, H 6.74, N 12.07

6-(2,2':6',2''-Terpyridin-4'-yloxy)-hexyl methacrylate (2)



A solution of 6-(2,2':6',2''-terpyridin-4'-yloxy)-hexan-1-ol (689 mg, 1.97 mmol) in dichloromethane (25 mL) was cooled to 0 °C under nitrogen. Triethylamine (0.9 mL, 6.49 mmol) was added and the mixture was stirred for 30 minutes. After this methacrylyc chloride (0.3 mL, 3.07 mmol) were slowly added and a gas formation was observed. The solution was stirred for two hours at 0 °C and then the solution was warmed up to room temperature. Afterwards the reaction mixture was stirred for 21 hours. After this the solvent

and the triethylamine were removed in *vacuo* and the residue was dissolved in dichloromethane. This solution was washed with deionized water (300 mL) and the organic phase was dried over Na₂SO₄. The crude product was purified by silica gel chromatography (CHCl₃).

Yield: 650 mg, 79%

¹H NMR (250 MHz, CDCl₃, δ): 1.48 – 1.94 (m, 11H, H_{β,γ,δ,ε}, -CH₃), 4.17 (t, *J* = 6.5 Hz, H_α, 2H), 4.23 (t, *J* = 6.5 Hz, H_ζ, 2H), 5.54 (s, =CH₂, 1H), 6.10 (s, =CH₂, 1H), 7.33 (d, *J* = 4.5 Hz, H_{5,5''}, 2H), 7.84 (t, *J* = 7.5 Hz, H_{4,4''}, 2H), 8.00 (s, H_{3',5'}, 2H), 8.615 (d, *J* = 7.5 Hz, H_{3,3''}, 2H), 8.69 (d, *J* = 4.5 Hz, H_{6,6''}, 2H) ppm.

¹³C NMR (62.5 MHz, CDCl₃, δ): 18.3 (CH₃), 25.7 (C_δ), 25.8 (C_γ), 28.6 (C_ε), 28.9 (C_β), 63.6 (C_α), 68.0 (C_ζ), 107.4 (C_{5,5''}), 121.3 (C_{4,4''}), 123.8 (C_{3,3''}), 125.2 (C=CH₂), 136.5 (C=CH₂), 136.8 (C_{3',5'}), 149.0 (C_{6,6''}), 156.2 (C_{2,2''}), 157.0 (C_{2',6'}), 167.3 (C_{4'}), 167.5 (CO) ppm.

Anal. calcd. for C₂₅H₂₇N₃O₃: C 71.92, H 6.52, N 10.06; found: C 71.71, H 6.51, N 10.28

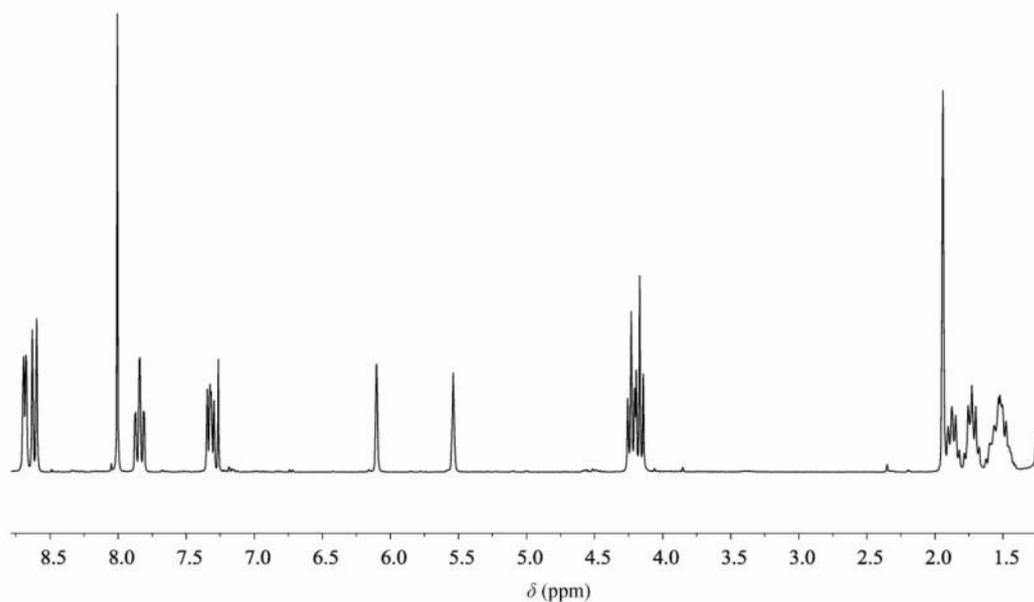


Figure S1: ¹H NMR spectra of 6-(2,2':6',2''-terpyridin-4'-yloxy)-hexyl methacrylate in CDCl₃.

General procedure for the RAFT polymerization:

In a 10 mL microwave vial the desired amounts of the two monomers were dissolved in dry toluene. Then the calculated volumes of the stock solutions in toluene of CPDB and AIBN were added. The ratio of [M] to [CPDB] was always 150/1 and the ratio of [CPDB] to [AIBN] 4/1. The amounts of all reagents are summarized in Table S1.

The reaction mixture was purged with a flow of nitrogen for 30 minutes and the vial was closed. Overnight the reaction was performed in an oil bath at 70 °C. The exact reaction times are listed in Table S1.

The polymers were purified by precipitation in cold ethanol. The BMA and LMA containing polymers were also purified by BioBeads S-X3 (solvent chloroform).

Table S1: Overview of the amounts and the reaction time for the polymerization

sample	monomers	m (monomers) [mg]	m (AIBN) [mg]	m (CPDB) [mg]	V (toluene) [μL]	reaction time [h]
P1	2	121	1.07	5.79	397	16.5
	MMA	357				
P2	2	117	0.85	4.59	285	17
	BMA	402				
P3	2	73	0.53	2.85	100	17
	LMA	447				

P1

¹H NMR (250 MHz, CDCl₃, δ): 0.85 – 1.90 (44H), 2.36 (3H), 3.60 – 4.25 (22 H), 6.89 – 7.39 (9H), 7.86 (1H), 8.01 (1H), 8.60 – 8.69 (2H) ppm.

SEC (CHCl₃, PMMA-standard): M_n = 15,500 g/mol; M_w = 27,300 g/mol; PDI = 1.76

Anal. calcd. for repeating units based on NMR: C: 62.97, H: 6.67, N: 2.52, found: C: 65.74, H: 7.89, N: 2.01, S: 0.00

DSC: T_g: 74 °C

TGA: T_d: 278 °C

P2

^1H NMR (250 MHz, CDCl_3 , δ): 0.88 – 1.95 (54H), 3.81 – 4.27 (9H), 7.34 (1H), 7.89 (1H), 8.06 (1H), 8.64 – 8.73 (2H) ppm.

SEC (CHCl_3 , PMMA-standard): $M_n = 28,900$ g/mol; $M_w = 33,300$ g/mol; PDI = 1.15

Anal. calcd. for repeating units based on NMR: C: 77.12, H: 10.33, N: 1.24, found: C: 69.48, H: 9.38, N: 2.34, S: 0.00

DSC: T_g : -2 °C

TGA: T_d : 275 °C

P3

^1H NMR (400 MHz, CDCl_3 , δ): 0.82 – 2.02 (180H); 3.94 – 4.28 (14H), 7.40 (1H), 7.88 (1H), 8.04 (1H), 8.64 – 8.72 (2H) ppm.

SEC (CHCl_3 , PMMA-standard): $M_n = 48,500$ g/mol; $M_w = 54,600$ g/mol; PDI = 1.13

Anal. calcd. for repeating units based on NMR: C: 75.10, H: 11.24, N: 1.21, found: C: 74.22, H: 11.35, N: 1.25, S: 0.00

DSC: T_g : -65 °C

TGA: T_d : 280 °C

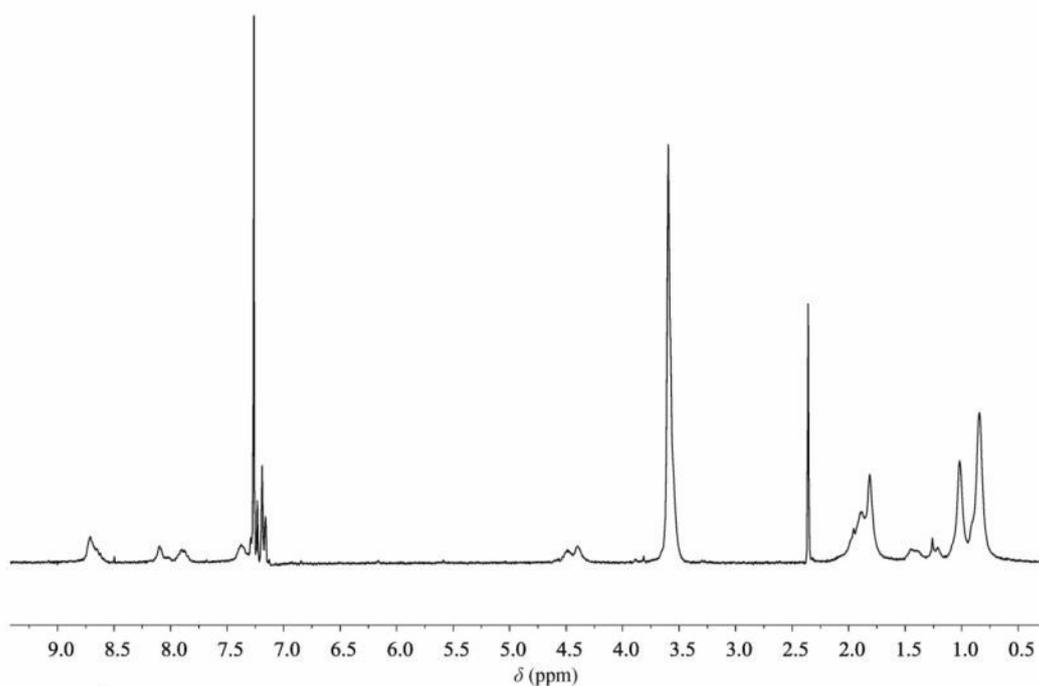


Figure S2: ^1H NMR spectrum of polymer **P1** in CDCl_3 .

Table S2: SEC-results of the copolymers synthesizes via RAFT.

Polymer	Comonomers	$M_{n, \text{SEC}}$ [g/mol]	$M_{w, \text{SEC}}$ [g/mol]	Content of terpyridine by ^1H NMR	PDI
P1	MMA	15,540	27,300	8.0%	1.76
P2	BMA	28,910	33,000	9.5%	1.15
P3	LMA	48,530	54,600	8.3%	1.13

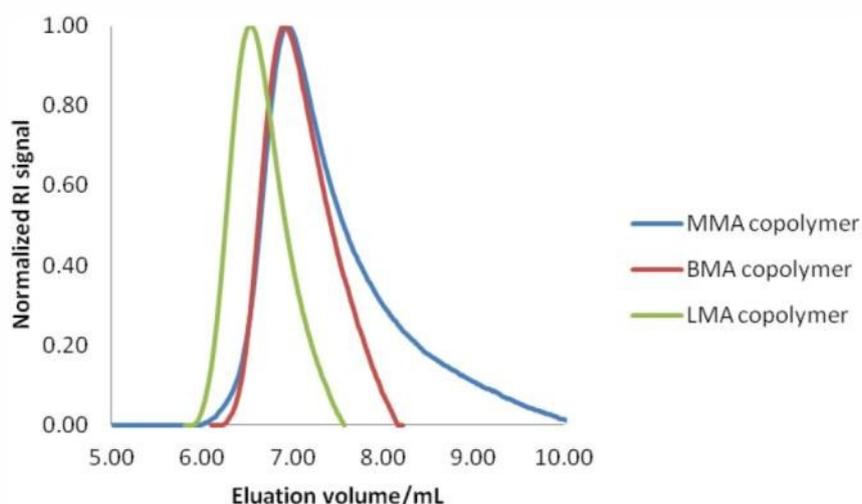


Figure S3: SEC curves of polymers **P1**, **P2** and **P3** (eluent chloroform/*iso*-propanol/triethylamine [94/2/4]).

General procedure for the crosslinking of the polymers:

In a 50 mL one neck flask the desired amount of the polymer was dissolved in acetonitrile (5 mL). A mixture of iron(II) sulfate heptahydrate in methanol (2 mL) was added and immediately the color changes to dark violet. The amounts of the polymers and the iron(II) sulfate heptahydrate are listed in Table S3. The solvents were evaporated slowly and the product was dried *in vacuo*.

Surface topography measurements:

The self-healing experiments and the surface topography were measured using an optical interferometric profiler Wyko NT9100 (Veeco, Mannheim, Germany).

Nanoindentation:

The elastic moduli of the materials were characterized via depth-sensing indentation (DSI) using a TriboIndenter TI 900 (Hysitron Inc., Minneapolis, MN) with a NanoDMA 06 transducer, equipped with a conospherical diamond indenter tip of $\sim 4.7 \mu\text{m}$ radius. The polymer was directly synthesized on a glass cavity slide. Afterwards, the polymer film was dried for 1 week at ambient temperature and humidity.

The depth-sensing indentation (DSI) was conducted at ambient conditions at 21.2 ± 0.4 °C and $32.2 \pm 0.6\%$ relative humidity (RH). For quasi-static testing, a 1 s loading, 2 s hold at maximum load, and 1 s unloading profile was applied.^[16] All measurements were performed in a single automated run in less than 3 h. The reduced modulus E_r was determined from the unloading response utilizing the analysis method proposed by Oliver and Pharr.^[16] Measurements were repeated at sixteen maximum loads, increasing in steps of 100 μN from 100 to 1600 μN . Values are averaged from at least ten measurements each. From the reduced modulus E_r , the indentation modulus E_i was calculated using the elastic modulus and Poisson's ratio of the diamond indenter, 1140 GPa and 0.07, respectively, and a Poisson's ratio of 0.4 for the polymeric material, according to

$$E_{i,sample} = \frac{1 - \nu_{sample}^2}{E_{r,sample} \frac{1 - \nu_{indenter}^2}{E_{indenter}}}$$

The hardness has the normal definition:

$$H = \frac{P_{max}}{A}$$

SEM measurements:

The self-healing experiments and the surface topography were measured using a scanning electron microscope LEO-1450 VP (Variable Pressure) from Carl Zeiss SMT. For this purpose, the crosslinked films were scratched with a hollow needle or a knife in a controlled manner, annealed at different temperatures and for individual time to obtain different healing states and sputtered with a 4 nm thick platinum layer before the measurement.

Table S3: Overview of the amounts of the crosslinking reaction

sample	polymer	m (polymer) [mg]	m ($\text{FeSO}_4 \times 7\text{H}_2\text{O}$) [mg]
CP1	P1	129	31
CP2	P2	94	8
CP3	P3	17	0.68

CP1

Anal. calcd. for repeating units based on NMR: C: 60.23, H: 7.34, N: 2.41, S: 0.92; found: C: 53.64, H: 7.04, N: 2.38, S: 2.25

DSC: T_g : no T_g observed

TGA: T_d : 238 °C

CP2

Anal. calcd. for repeating units based on NMR: C: 75.96, H: 10.18, N: 1.22, S: 0.47; found: C: 66.34, H: 8.78, N: 2.17, S: 16.13

DSC: T_g : 21 °C

TGA: T_d : 288 °C

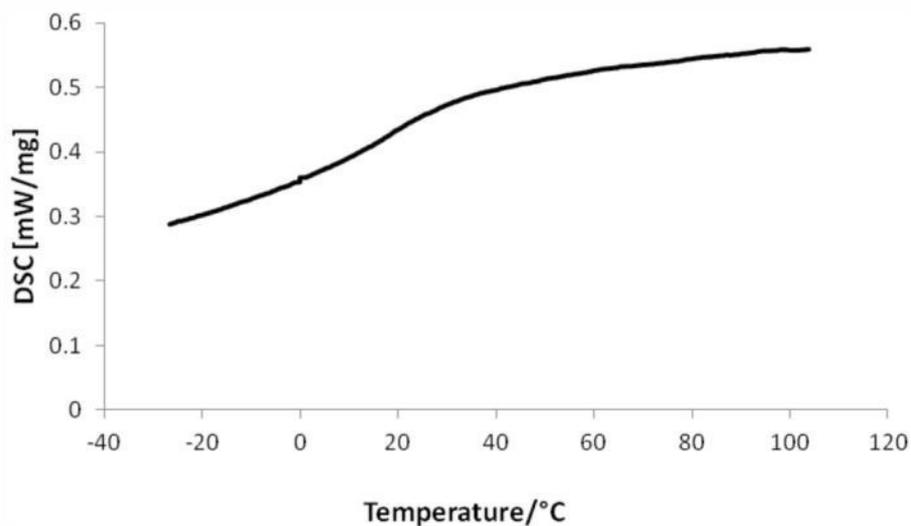
CP3

Anal. calcd. for repeating units based on NMR: C: 73.99, H: 11.07, N: 1.19, S: 0.46; found: C: 70.42, H: 10.60, N: 1.25, S: 0.85

DSC: T_g : 33 °C

TGA: T_d : 271 °C

a)



b)

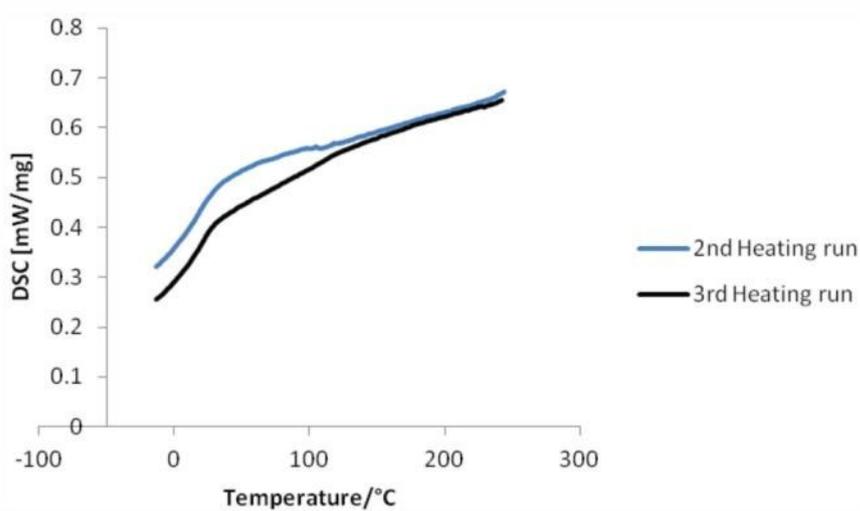


Figure S4: DSC curve of crosslinked polymer CP2: a) Zoom in the temperature range of the glass transition, b) DSC data for heating up to 250 °C for three heating runs.

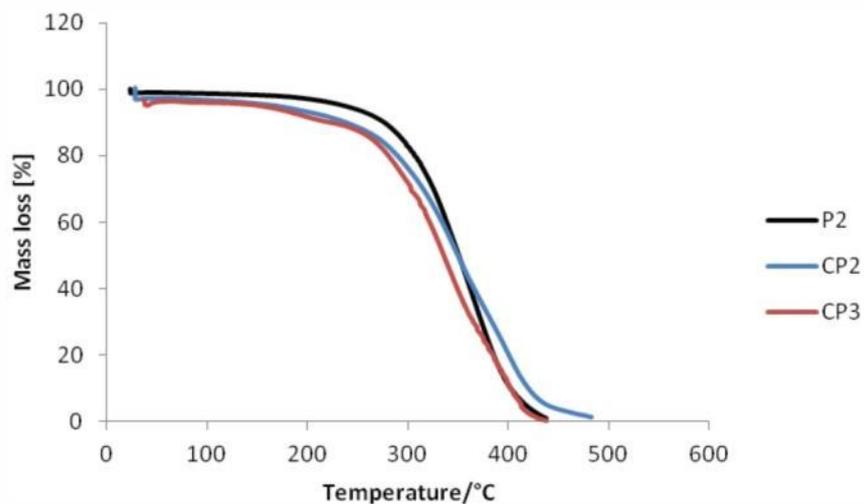


Figure S5: TGA data of the polymer **P2** and the crosslinked polymer networks **CP2** and **CP3**.

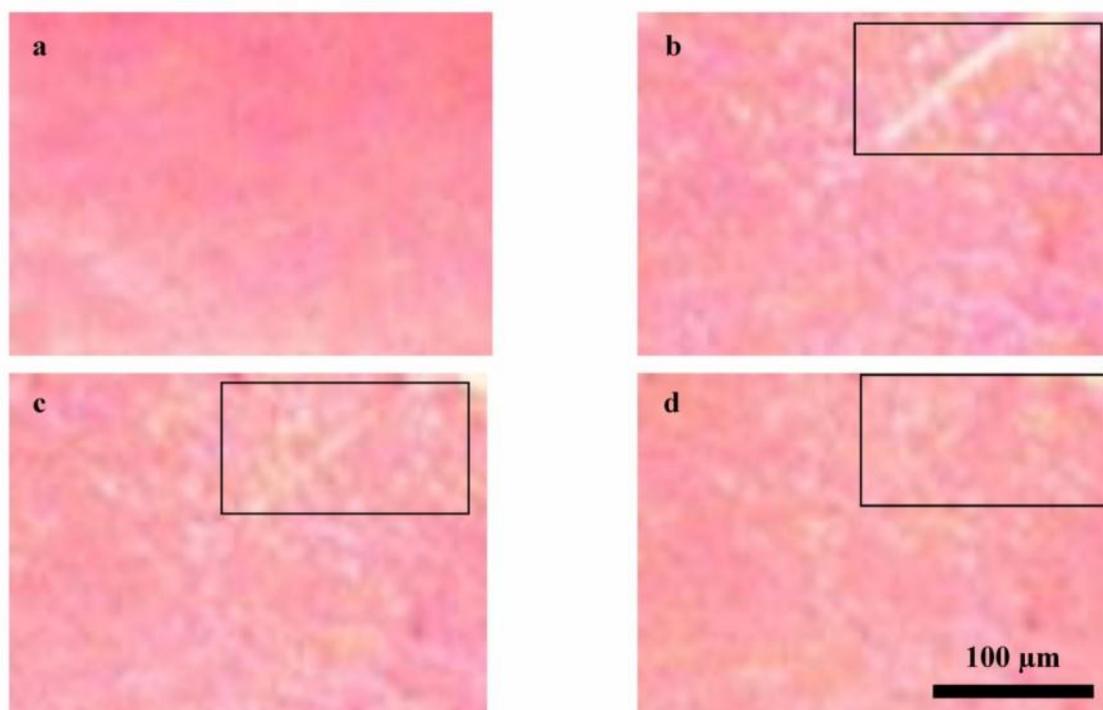


Figure S6: Self-healing of the crosslinked polymer network with butyl methacrylate as comonomer (**CP2**): a) Polymer film, b) scratch, c) partial healing after 10 min at 100 °C; d) complete healing after 40 min at 100 °C.

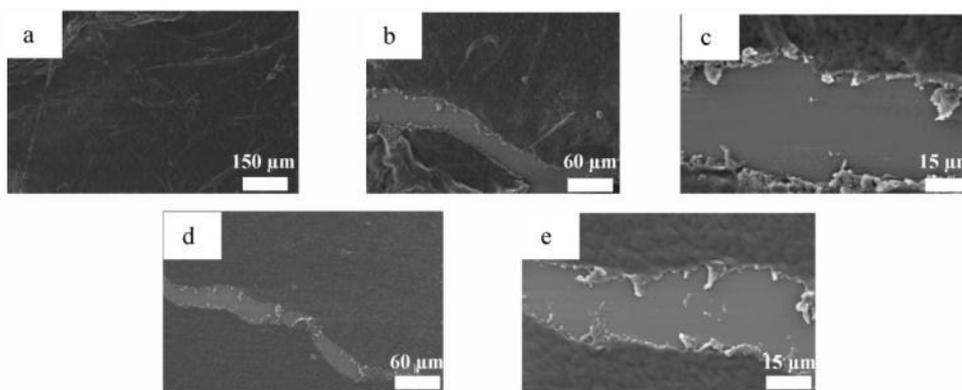
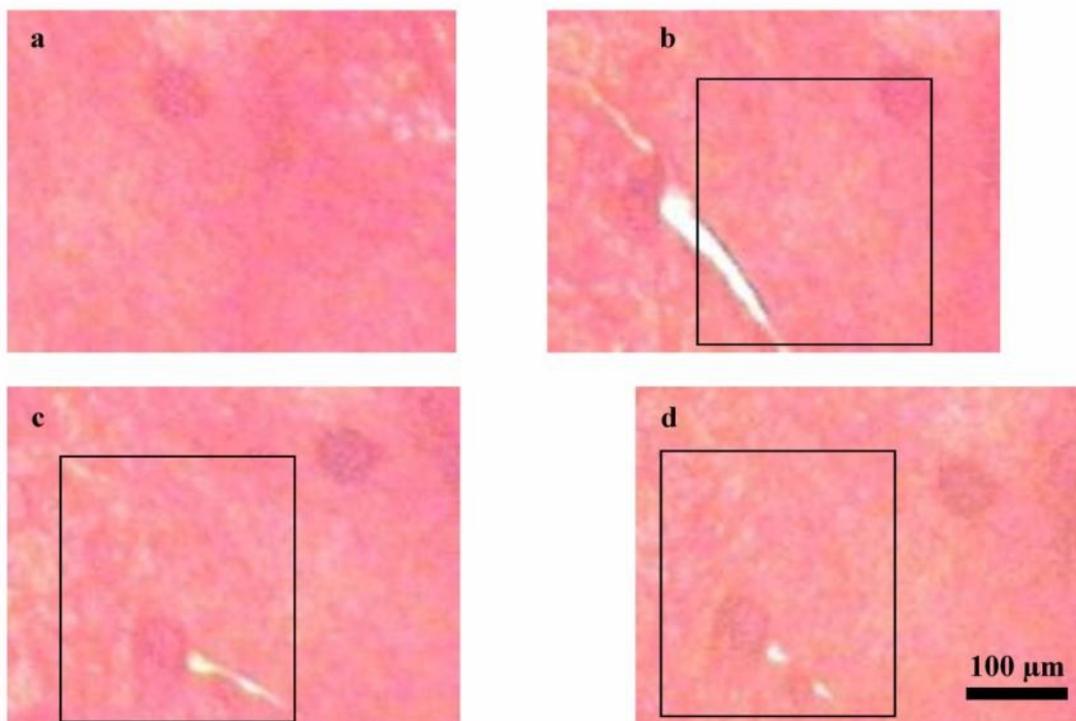


Figure S7: SEM images of the self-healing process of CP3: a) Film without scratch, b) scratch, c) zoom into the scratch, d) partially healed scratch and e) zoom in the partially healed scratch.



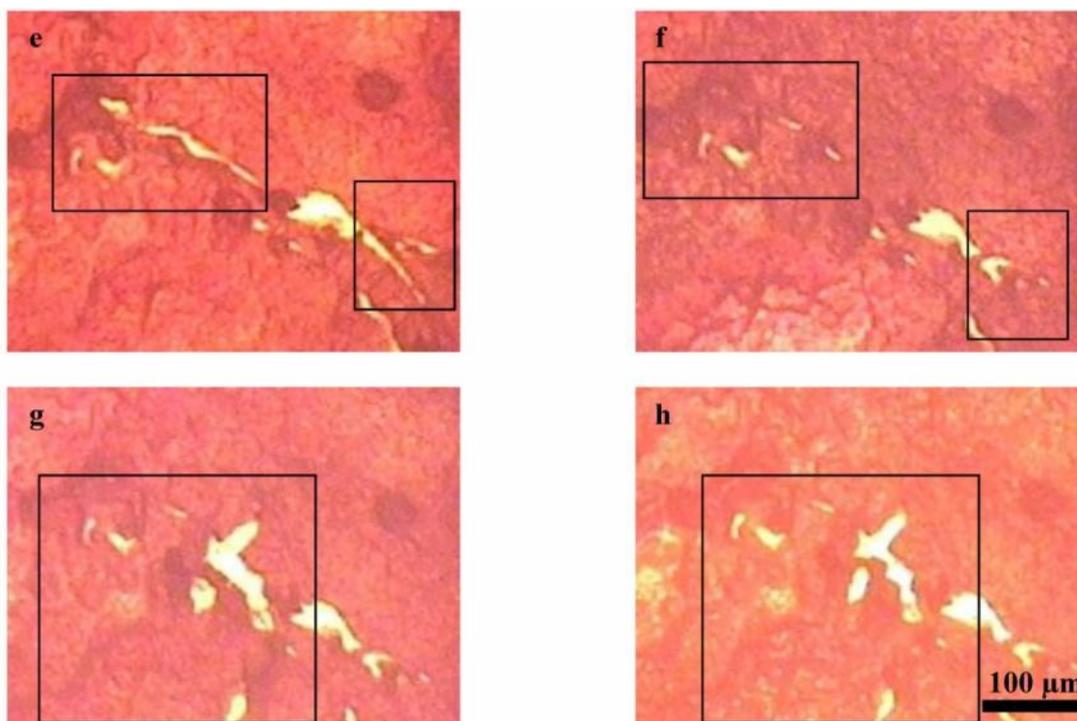


Figure S8: Multiple healing at the same position of CP3 at 100 °C: a) Film without scratch, b) first scratch, c) first partially healing after 16 h, d) first healing after 82 h, e) second scratch, f) second healing after 17 h, g) third scratch and h) third partially healing after 134 h.

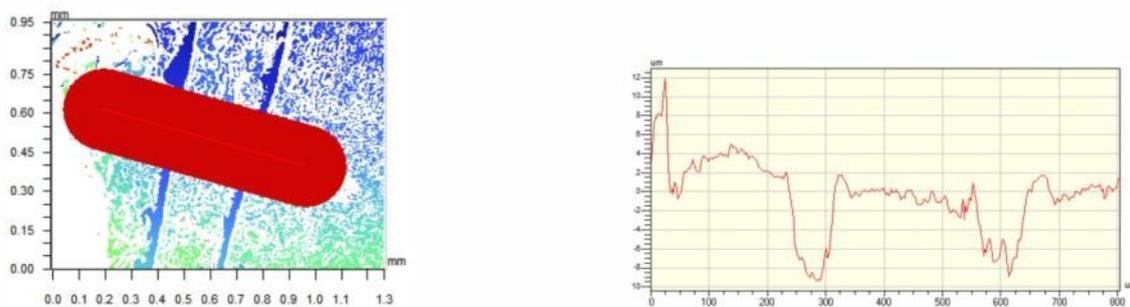


Figure S9: Profilometer measurement of a typical scratch.

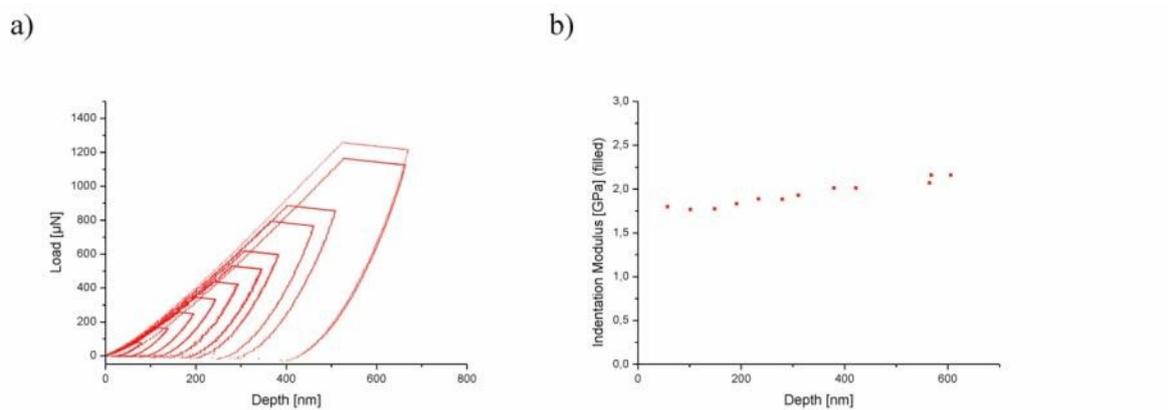


Figure S10: Mechanical properties measured by nanoindentation of CP2: a) Load-displacement data, b) indentation modulus.

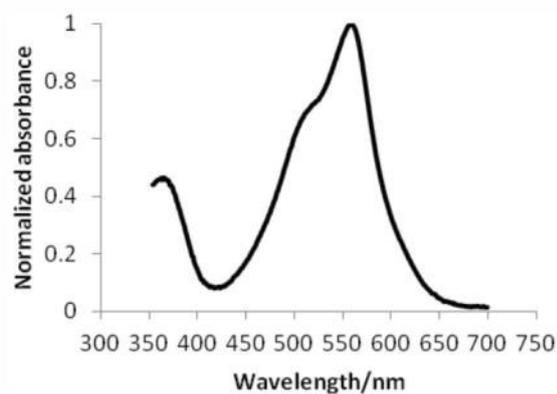


Figure S11: Violet colored crosslinked polymer network: a) Polymer film of the crosslinked polymer based on the butyl methacrylate comonomer and b) absorbance spectrum of the crosslinked polymer based on the lauryl methacrylate in CHCl_3 .

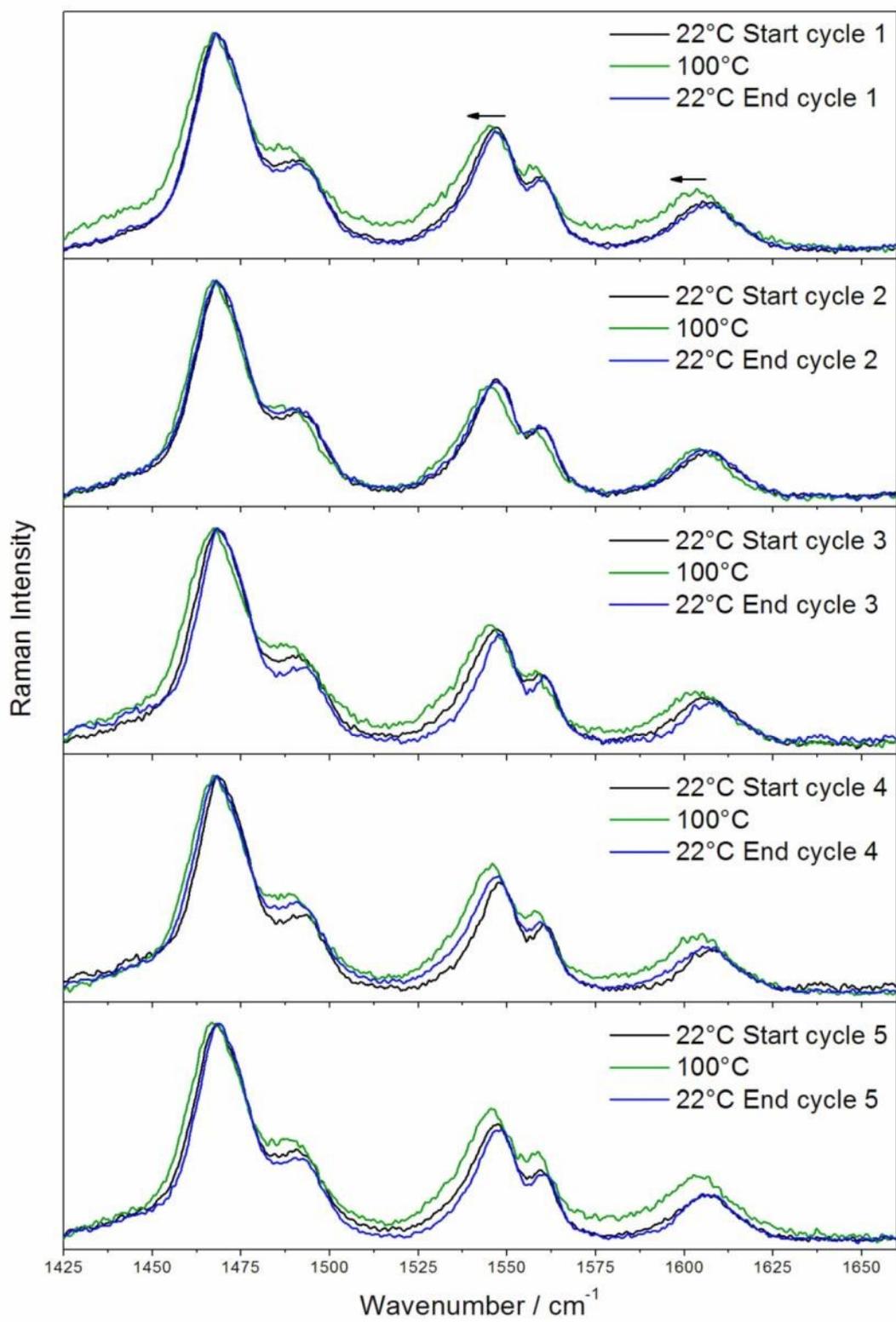


Figure S12: Raman spectra of the crosslinked polybutyl methacrylate based polymer (**CP2**) at different temperatures (23 °C and 100 °C, respectively) and after multiple healing cycles measured at high spectral resolution. The temperature dependent Raman spectra show notable reversible band shifts upon heating the metallopolymer.

[Zedler et al. Mater. Today]

**Monitoring the Chemistry of Self-Healing by Vibrational Spectroscopy –
Current State and Perspectives**

Der Nachdruck der folgenden Publikation erfolgt mit freundlicher Genehmigung von Elsevier.

Reprinted with kind permission from:

Zedler, L.; Hager, M. D.; Schubert, U. S.; Harrington, M. J.; Schmitt, M.; Popp, J.; Dietzek, B.,
Monitoring the Chemistry of Self-Healing by Vibrational Spectroscopy – Current State and
Perspectives, *Mater. Today* **2014**, *17*, 57-69.

Copyright 2014 Elsevier.



Monitoring the chemistry of self-healing by vibrational spectroscopy – current state and perspectives

Linda Zedler¹, Martin D. Hager^{2,3}, Ulrich S. Schubert^{2,3}, Matthew J. Harrington⁴, Michael Schmitt¹, Jürgen Popp^{1,3,5} and Benjamin Dietzek^{1,3,5,*}

¹Institute of Physical Chemistry and Abbe Center of Photonics, Friedrich Schiller University Jena, Helmholtzweg 4, 07743 Jena, Germany

²Institute of Organic and Macromolecular Chemistry (IOMC), Friedrich Schiller University, Humboldtstraße 10, 07743 Jena, Germany

³Jena Center for Soft Matter (JCSM), Friedrich Schiller University Jena, Philosophenweg 7, 07743, Jena, Germany

⁴Department of Biomaterials, Max-Planck-Institute for Colloids and Interfaces, Am Mühlenberg 1, 14424, Potsdam, Germany

⁵Leibniz Institute of Photonic Technology Jena e.V. (IPHT), Albert-Einstein-Straße 9, 07745 Jena, Germany

Self-healing materials are designed to heal damage caused by, for example, mechanical stress or aging such that the original functionality of the material is at least partially restored. Thus, self-healing materials hold great promise for prolonging the lifetime of machines, particularly those in remote locations, as well as in increasing the reliability and safety associated with functional materials in, for example, aeronautics applications. Recent material science applications of self-healing have led to an increased interest in the field and, consequently, the spectroscopic characterization of a wide range of self-healing materials with respect to their mechanical properties such as stress and strain resistance and elasticity was in the focus. However, the characterization of the chemical mechanisms underlying various self-healing processes locally within the damaged region of materials still presents a major challenge. This requires experimental techniques that work non-destructively *in situ* and are capable of revealing the chemical composition of a sample with sufficient spatial and temporal resolution without disturbing the healing process. Along these lines, vibrational spectroscopy and, in particular Raman spectroscopy, holds great promise, largely due to the high spatial resolution in the order of several hundreds of nanometers that can be obtained. This article aims to summarize the state of the art and prospective of Raman spectroscopy to contribute significant insights to the research on self-healing materials – in particular focusing on polymer and biopolymer materials.

Introduction

Self-healing materials are designed to heal damage inflicted upon them by, for example, mechanical stress or aging. The healing process results in the (partial) restoration of the material properties, such as mechanical properties, as well as other functions (*e.g.* conductivity, protection, esthetics). The basic concept of self-healing is not restricted to a single material class; it is applicable to polymers (and their composites), to concretes and asphalts, as well as to metals and ceramics [1–3]. The design of self-healing polymers and composites is often inspired by natural materials,

which possess the ability to manage and repair damage encountered during their lifetime [4–8]. Biological materials have been honed through eons of evolution to perform particular functions efficiently and with economical and sustainable use of building materials, thus providing a positive role model for the development of high performance synthetic polymers and composites. The self-repair capabilities of natural systems range from the active repair of photo-damaged DNA-macromolecules to the repair of daily injuries such as small cuts, the merging of broken bones and small injuries of blood vessels up to the complete restoration of lost limbs (*e.g.* Mexican salamander (*Ambystoma mexicanum*)). While wound-healing and bone-mending are the most prominent

*Corresponding author: Dietzek, B. (benjamin.dietzek@ipht-jena.de)

examples of natural self-healing, they rely on complex cellular mechanisms, which are inherently difficult to imitate at the molecular level. Alternatively, several examples of acellular biological materials exist in which autonomic healing is intrinsic to the biopolymer itself – two of which will be discussed in detail in the following section. In man-made materials, on the other hand, the aim of self-healing is not necessarily to completely restore the chemical integrity or composition of the material, but rather to restore its overall function as defined, for example, by the stiffness of the material, its flexibility or elasticity. Through autonomic repair of damage, in particular micro-cracks, such materials are designed to operate in complex machinery (e.g. airplanes), in remote locations (e.g. tunnels) or in coatings (for a schematic of material self-healing see Fig. 1) [9,10].

Of particular interest to this article are self-healing materials based on polymers and polymer composites. Such light-weight materials are utilized nowadays in a wide range of different applications, such as protective coatings, as structural materials in aircraft construction, as well as for active materials in polymer light-emitting diodes (PLEDs) or organic solar cells. Polymers are generally considered to be less stable than other engineered materials, like steel or concrete; therefore, a potential self-healing behavior is of special interest for these materials. Self-healing mechanisms in polymers can be divided into two basic categories: (1) extrinsic self-healing and (2) intrinsic self-healing. Extrinsic self-healing depends on the activation of an incorporated healing agent upon damage and is typically based on the encapsulation of chemical cross-linkers in capsules or vascular systems embedded in

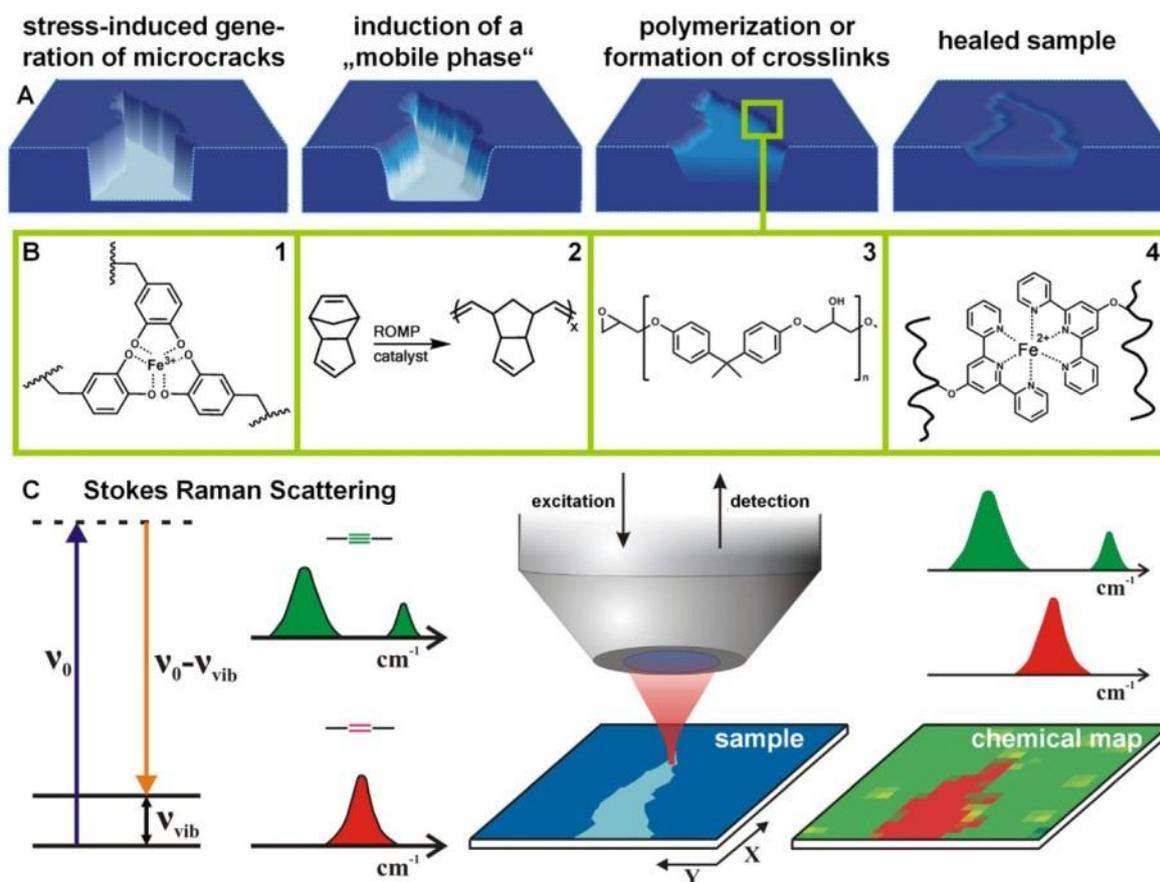


FIGURE 1

Concept of self-healing and principle of Raman microspectroscopy. (a) Upon stress induced generation of microcracks a "mobile phase" is induced, which fills the crack. Afterwards, the mobile phase solidifies by polymerization or cross-linking of polymer strands, thus restoring the mechanical properties of the material. (b) Overview of model compounds for self-healing structures based on (reversible) cross-linking processes: 1: Dopa- Fe^{3+} cross-linking by complex formation, 2: polymerization of dicyclopentadiene by ring-opening metathesis polymerization (ROMP), 3: epoxy/hardener two part adhesives, 4: Fe^{2+} -bis-terpyridine complexes in reversibly cross-linked polymer network by complex formation with terpyridine ligands. (c) Chemical and structural changes during cross-linking, for example, formation of linking functional structures, can be analyzed by Raman microspectroscopy. A Raman map reflects the spatial intensity distribution of a selected Raman band, for example, of the $\text{C}=\text{C}$ stretching band (red colored), with diffraction limited, that is, sub-micrometric spatial resolution. In the color scheme red parts of the map correspond to the highest signal intensity of the $\text{C}=\text{C}$ stretching band, while green parts refer to $\text{C}\equiv\text{C}$ stretching bands. The spatial distribution of vibrational frequencies characteristic of the mobile phase and of newly formed cross-linked structures can be visualized in contrast to the bulk material to monitor the healing process.

a polymer matrix [11–14]. In contrast, intrinsic self-healing materials exhibit self-healing properties without any external ingredients, which have to be incorporated into the polymer matrix – that is, healing is inherent to the polymer itself.

One successful approach for the production of intrinsic self-healing polymers is the utilization of reversible crosslinks, that is, molecular interactions that can be reformed following damage-induced rupture. For example, such materials have been generated based on reversible covalent bond formation, for example, based on Diels–Alder and retro-Diels–Alder reactions [2,15–17], weaker non-covalent interactions, for example, hydrogen bonding [18], ionic interactions [19,20], π – π interactions [21–24], and host–guest interactions [25–27]. Additionally, the first examples of self-healing materials based on reversible metal–ligand–interactions have been demonstrated [28–30] – a concept adopted from natural materials (*e.g.* the mussel byssus), which exploit the transient properties of metal coordination bonds to achieve self-healing behaviors in harsh ocean environments (see below) [31]. Furthermore, mussel-inspired metallopolymers employing the biological metal-binding moieties (*i.e.* catechol and imidazole) have been developed and shown to exhibit moderate self-healing behavior, although the healing efficiency has not yet been explicitly quantified in a systematic way [32–34].

Irrespective of the nature of the self-healing material, from a conceptual point-of-view it is important to not only ensure that mechanical material properties are restored, but also to address the question of which molecular processes and interactions are responsible for the healing process. Elucidating the fundamental principles underlying the healing mechanism of such materials will facilitate the directed design of future generations of novel self-healing materials whose properties could be adjusted corresponding to their applications. Self-healing of materials relying on the release of healing agents requires the generation of a mobile phase (Fig. 1a) in the material because healing agents need to flow into the damage site (*i.e.* microcracking) in order to initiate the healing processes. Considering this requirement, the spatial-temporal propagation of the chemical interactions and/or molecular species responsible for self-healing must be investigated to obtain deeper insights into the underlying principles. Addressing such questions requires non-destructive experimental techniques capable of ascertaining the chemical composition of a sample with high spatial resolution (*i.e.* to monitor the local chemical composition within (micro)cracks or in the bulk material). Vibrational spectroscopy methods such as Raman scattering or IR absorption are capable of meeting these requirements in terms of chemical specificity and sensitivity to structural modifications [35–38]. In order to investigate the integrity of composite materials both depth resolved in bulk materials and at interfaces a method is required, which enables high depth penetration and microscopic spatial resolution in order to monitor chemical processes and reactions within (micro)cracks. While IR absorption micro-spectroscopy provides high signal levels, due to absorption of IR radiation, the spatial resolution and depth penetration is significantly lower than for Raman spectroscopy. This is due to the use of mid-IR radiation in the case of the IR absorption experiments and UV/vis radiation in the case of the Raman scattering experiments. Therefore, applications of IR spectroscopy to the composition and structure of self-healing materials are rare [39–43]. This review

focuses in particular on Raman microspectroscopy, which combines Raman scattering with light microscopy, since it offers the sub-micron spatial resolution required to investigate self-healing processes within (micro)cracks.

The Raman effect is a consequence of the interaction of light with the electron cloud of molecules, in which a small fraction of the scattered light is shifted in wavelength as compared to the incoming light. This inelastic light scattering results from the fact that as the nuclei of molecules vibrate against each other, the electron cloud is deformed. Thus, Raman scattering can be interpreted as inelastic light scattering from vibrating molecules. Consequently, the wavelength shifts resulting from Raman scattering contain information about the characteristic molecular vibrations and, therefore, about the molecular structure. A Raman spectrum displays the intensity of inelastic light scattering at various wavelength shifts relative to the incident beam on the sample and can thus be seen as a characteristic “spectroscopic fingerprint” of the molecular species within the sample, allowing the identification of organic, inorganic or biological components. Furthermore, Raman spectroscopy provides important information about physical and chemical characteristics such as binding motifs, weak interactions or lone pair character since the observed Raman shifts scale with important molecular parameters like force constants or bond distances of the atoms involved in the corresponding vibration. The inter-atomic force constant determines the frequency of the vibration whereas the amount of the polarizability of the electron cloud in contrast to the atomic nuclei defines the vibrational intensities. In addition, polarization-dependent Raman spectra can deliver important information about the orientation and spatial arrangement of molecules [44]. Typical strong Raman scatterers are moieties with distributed electron clouds, such as carbon–carbon double bonds since the π -electron cloud is easily distorted in an external electric field. Bending or stretching of such bonds changes the distribution of electron density substantially, and causes a large change in the induced dipole moment. The Raman effect involves an intimate interplay between atomic positions in molecules, electron distribution and intramolecular forces. Thus, it sits at the bridgehead between structure, function and reactivity, and accordingly, Raman spectroscopy represents one of the most useful tools for obtaining information on the molecular and chemical makeup of materials, including details about the strength of the molecular bonds. Despite the many strengths of this technique, the direct assignment of Raman bands for relatively complex molecules is rather complicated. Theoretical simulations, in particular by means of density functional theory (DFT) calculations, can certainly assist to obtain a deeper understanding of the vibrational spectra of complicated molecules [45,46]. A comparison of the experimental and DFT calculated Raman spectra allows for a reliable assignment of the experimentally observed Raman bands, thus leading to a detailed understanding of the geometrical and electronic structure of the investigated molecular compounds. Due to the technical progress in the area of laser, spectrometer, optical filter- and detector development, Raman spectroscopy in combination with DFT calculations has evolved into one of the most widely used techniques in the physical and natural sciences today, providing detailed information about the structural composition of organic, inorganic and also biological molecules [36,38,47,48].

This article will review the state-of-the-art of Raman spectroscopy applied to self-healing materials by focusing on four different topical aspects. First, we discuss several cases in which Raman spectroscopy was applied to self-healing biological paradigm systems, while the remainder of the article discusses investigations of man-made polymer systems, including those based on ring-opening metathesis polymerization in the presence of a Grubbs' catalyst, as well as those based on hardening of a polymerizable epoxy resin. Finally, we discuss the potential of Raman spectroscopy to interrogate other reversible bond-formation processes, which might be implemented into self-healing materials.

Self-healing biopolymers from marine habitats – natural models for damage tolerance and repair

Extracting useful design principles from biological materials relies on understanding the material in the context of the habitat in

which it evolved and performs. Organisms inhabiting the wave-swept rocky seashore, for example, face repetitive loading by powerful wave forces and abrasive water-borne particles. Thus, it is not entirely unexpected that damage tolerant materials with self-healing properties have evolved in association with marine environments. Two such materials – the mussel byssus and the egg capsules of marine whelks – are examples of tough biopolymers that dissipate large amounts of mechanical energy during cyclic loading and that exhibit autonomic and intrinsic recovery of initial properties following damage. Recently, Raman microspectroscopy was employed to probe the molecular-level structure–function relationships leading to the self-repair behavior in both materials.

Mussels are sessile organisms that anchor themselves in turbulent wave-swept habitats with protein-based biopolymeric fibers called byssal threads (Fig. 2). The extensible fibrous core of a byssal

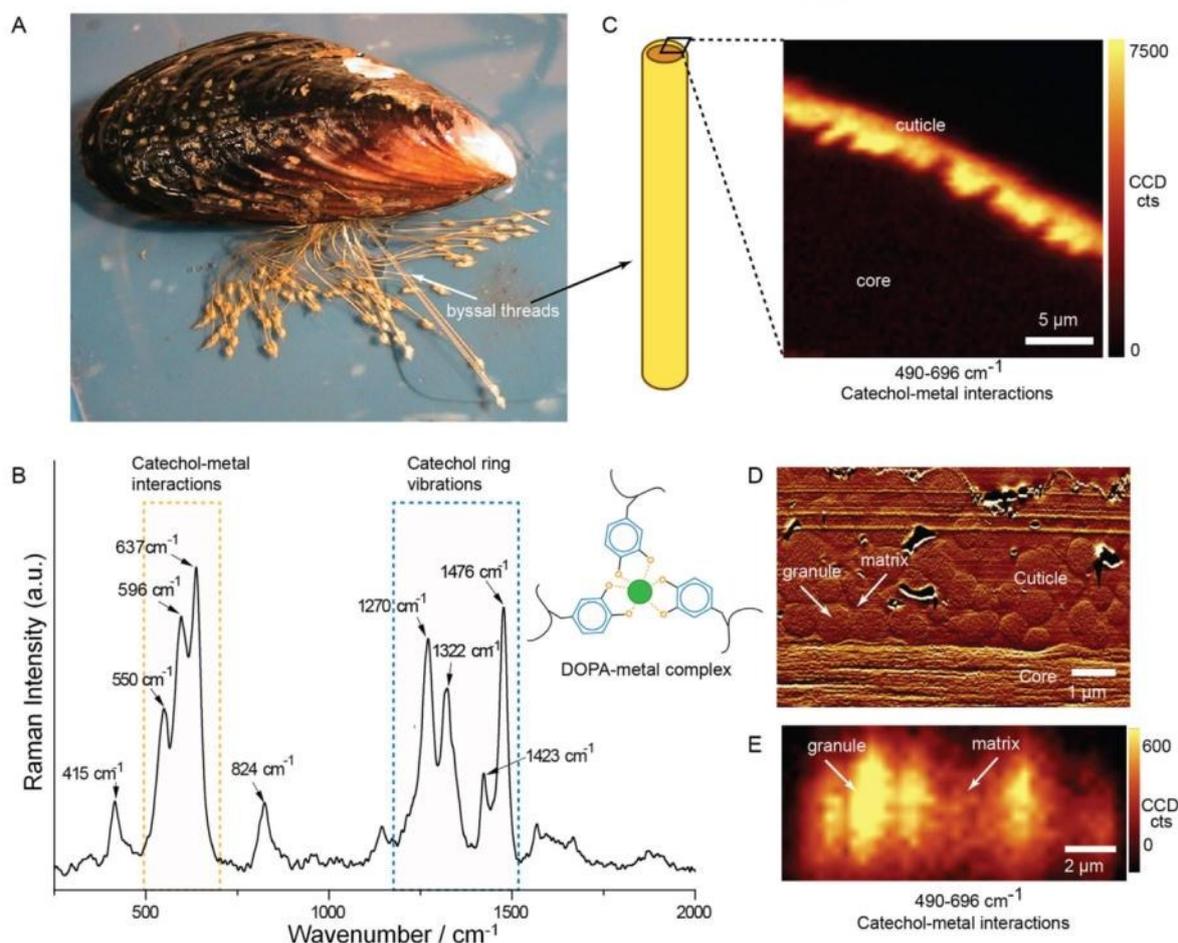


FIGURE 2

Raman evidence of metal coordination in the mussel byssus. (a) Mussels attach to hard surfaces with biopolymeric fibers called byssal threads that contain a hard, but stretchy cuticle. (b) Raman spectroscopy reveals a strong resonance signal indicative of *tris*-DOPA–metal coordination complexes, which are revealed by Raman microspectroscopy to be (c) isolated entirely within the protective cuticle and not found in the softer core of the fiber. (d) AFM image of micron-sized centers containing a high DOPA–metal complex concentration. (e) Confocal Raman microspectroscopy of thin cuticle sections reveals the chemical composition of the granular structures. Adapted from Harrington et al. with permission from AAAS [31].

thread is able to autonomically and intrinsically heal following damage from cyclic tensile deformation [49]. Additionally, the softer core is covered with a thin protective cuticle, which is remarkable in that it possesses hardness on the level of a typical epoxy, yet is extensible to up to $\approx 100\%$ strain before exhibiting large crack formation [7]. Crack propagation is hindered by the granular cuticle morphology of many species (Fig. 2d), such that microcracking occurs in the soft matrix between the hard granules, which effectively distributes damage. Microcrack formation is believed to be reversible; however, until recently the molecular mechanism underlying the peculiar cuticle mechanics remained poorly characterized at the molecular level.

The byssal cuticle consists primarily of a single DOPA-rich protein, MFP-1 and is enriched with Fe^{3+} ions [50]. DOPA (3,4-dihydroxyphenylalanine) is a post-translational modification of tyrosine consisting of a catechol as a side-chain (Fig. 2b) and known for its propensity to form very stable coordination complexes with metal ions, such as Fe^{3+} . In order to specifically investigate the role of such DOPA-metal complexes in the byssal cuticle, resonance Raman spectroscopy was employed using laser excitation at 785 nm, as DOPA-metal complexes are well-known to provide a strong and distinctive resonance signal [31]. In contrast to non-resonant Raman spectroscopy, which yields integral information about the chemical composition of the whole sample, resonance Raman spectroscopy delivers information on the molecular structure of a specific chromophore within the sample, the absorption of which is in resonance with the excitation wavelength, resulting in an up to million-fold increase in the intensity of the signal over the non-resonant signal [51]. It was demonstrated that the cuticles from several different marine mussel species exhibit nearly identical resonance Raman spectra, dominated by a triplet of bands (550 , 596 and 637 cm^{-1}) associated with catechol-metal interactions and four vibrational resonances between 1270 and 1476 cm^{-1} , assigned to catechol ring-breathing modes, which together identify the complexation of Fe^{3+} by DOPA units (Fig. 2b). This assignment of the characteristic vibrational modes is corroborated by control studies, in which DOPA-rich protein biopolymers isolated from marine mussels were admixed with various concentrations of Fe^{3+} ions [52,53]. In the absence of Fe^{3+} ions, the biopolymers did not show any pronounced features in the resonance Raman spectrum; however, upon addition of Fe^{3+} ions, the aforementioned vibrational triple-band in the range between 550 and 637 cm^{-1} , as well as the characteristic vibrations of the DOPA ring at higher wavenumbers emerge. Furthermore, Raman investigation of mussel-inspired PEG-DOPA polymers showed that the resonance Raman pattern associated with the DOPA- Fe^{3+} coordination is strongly pH-dependent – upon decreasing pH, the vibrational pattern indicative of the DOPA- Fe^{3+} coordination becomes increasingly structureless [32]. This was attributed to the presence of *mono*-complexed Fe^{3+} ions (one DOPA-unit coordinated to the metal in a bidentate fashion), *bis*-complexed and *tris*-complexed Fe^{3+} species, the equilibrium between which can be tuned by the pH value. Moreover, pH-tuning of the complex resulted in transitions in the mechanical integrity of the polymer ranging from a viscous solution (pH 5: mono-complexation) to a viscoelastic and self-healing hydrogel (pH 12: tris complexation).

After careful assignment of the resonance Raman bands in the mussel thread, the spatial distribution of the DOPA-metal complexes in the native material was then investigated by employing (resonance) Raman microspectroscopy coupled with a confocal microscope [31,54,55]. It was demonstrated that the catechol-metal complexes are isolated to the hard outer cuticle and absent in the softer core of the biopolymeric byssal threads and furthermore, that granules in the cuticles were local micron-sized hot spots of high DOPA- Fe^{3+} cross-link concentration in a less cross-linked surrounding matrix (Fig. 2c–e) [31]. This non-homogenous distribution of reversible cross-links suggests that the granular design of the cuticle allows damage to be localized to specific, low cross-link regions (*i.e.* the matrix), which may be healed when load is removed via reversible chemistry. From these findings, self-healing behavior based on reversible bonds is dependent not only on the presence of particular intermolecular interactions, but also on their spatial distribution, and thus, in order to understand the function of self-healing materials and to optimize their function, the morphochemistry and hierarchical structure of such systems needs to be considered. This is especially clear when considering the mechanical behavior of the unstructured mussel-inspired PEG-DOPA- Fe^{3+} -based polymers, which are not hard and stretchy like the mussel cuticle, but rather are soft and sticky hydrogels [32].

Whelks are marine gastropods that, like mussels, inhabit and reproduce in harsh seashore environments. The protective egg capsules they produce (Fig. 3a) are tough and compliant biopolymeric materials with the ability to dissipate $\sim 50\%$ of applied mechanical energy via mechanical yield and hysteresis [56]. Remarkably, following yield and hysteresis, which are typically associated with molecular level damage in polymeric materials, the whelk egg capsule (WEC) material instantaneously recovers its initial mechanical properties in subsequent stretching cycles (Fig. 3b) [56], a behavior reminiscent of pseudoelastic metal alloys, shape-memory polymers and certain self-healing polymers. The material design of the WEC biopolymer was investigated via traditional biochemical and materials characterization techniques, including X-ray diffraction, and it was determined that it consists of α -helical protein fibers arranged in orthogonal layers [57]. Recently, Raman-based studies have detailed the importance of reversible changes in the backbone structure of the constituent proteins in determining the self-healing behavior of the WEC.

In contrast to studying the effects of a specific chemical interaction via resonance Raman (*e.g.* DOPA-metal complexation in the mussel cuticle), traditional Raman spectroscopy was used in this case to investigate the role of protein conformational changes in the self-healing behavior of the WEC. Protein conformations, such as the α -helix and β -sheet, are organized protein backbone structures that arise from regularities or motifs in the primary amino acid sequence of a given protein. Nature makes use of regular protein conformations to stabilize three-dimensional protein topology or often as building blocks in biological materials such as hair (α -helix), spider silk (β -sheet) and collagen (triple helix). The regular conformation of an α -helix, for example, is stabilized by backbone hydrogen-bonding along the axis of the helix. While a single hydrogen-bond is weak, the effect of multiple bonds working together due to the regular structure of the α -helix makes the conformation quite stable. Proteins generally exhibit several bands in Raman spectroscopy that are strongly influenced

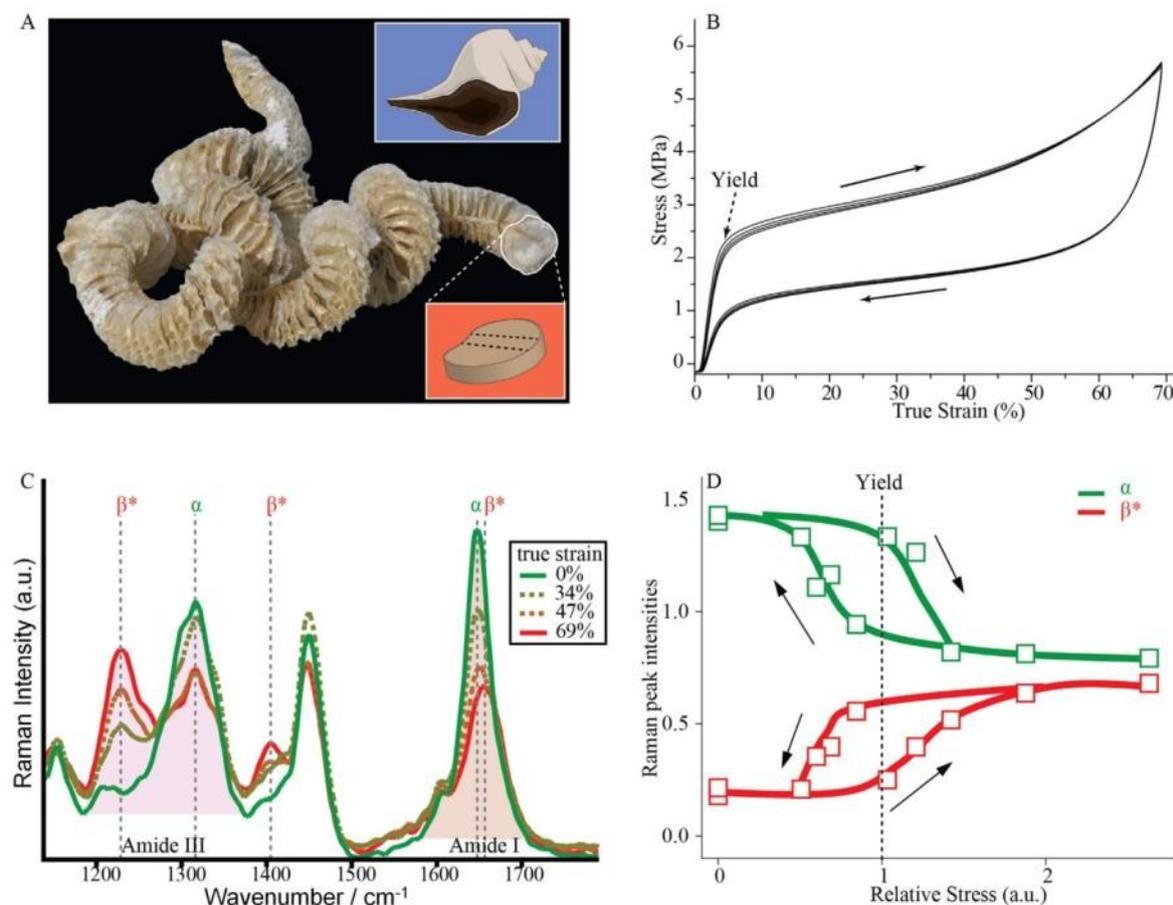


FIGURE 3

Raman spectroscopic characterization of a conformational phase transition in the whelk egg capsule (WEC). (a) Whelks are marine gastropods that lay chains of disk-like egg capsules in the marine intertidal zone. (b) When tested in tension, the WEC biopolymer exhibits pseudoelastic mechanical behavior and recovers mechanical properties immediately following yield and hysteresis – a behavior that is reproducible over many cycles. (c) *In situ* Raman microspectroscopy during mechanical stretching reveals that the α -helical proteins that make up the egg capsule undergo a reversible transition to a more extended conformation, called β^* . (d) When the intensity of the Amide III Raman peaks corresponding to the two protein conformations are plotted vs. relative stress (stress normalized so that yield occurs at a value of 1), a reversible structural phase transition between the two conformations is observed. Furthermore, slow refolding of the α -helix during unloading produces a molecular hysteresis that is correlated closely with the macroscopic mechanical hysteresis. Adapted from Harrington et al. with permission from the Royal Society [58].

by the conformation of the protein backbone, the most prominent of which are the Amide I (1620–1680 cm⁻¹) and Amide III (1200–1360 cm⁻¹) bands. Consistent with earlier X-ray diffraction measurements [57], Raman spectra obtained from the fibrous layers in the WEC gave a clear signal corresponding to α -helical structure (*i.e.* Amide I centered at 1645 cm⁻¹; Amide III centered at 1316 cm⁻¹) [58]. X-ray diffraction on fully stretched samples showed that the α -helical reflections vanished, giving rise to a new structural phase [57]. In order to better understand this transformation at the level of the protein backbone structure, *in situ* Raman spectroscopy was performed on WEC during cyclic tensile testing at various strain values [58]. Results indicate a reversible conformational transition based primarily on a progressive decrease in the intensity of the α -helical Amide III band at 1316 cm⁻¹ and a corresponding increase in the intensity of a new

Amide III band at 1224 cm⁻¹, corresponding to an extended backbone conformation (Fig. 3c). This was also corroborated by a corresponding shift in the Amide I band and the emergence of a peak at 1400 cm⁻¹, which was assigned to C_α-H stretching that is only observed in extended conformations. Interestingly, the conversion does not occur all at once, but rather the ratio of the intensities of the two peaks gradually changes during the mechanical yield plateau (*i.e.* α -helical domains convert to extended domains progressively during loading as in a classical phase transformation) (Fig. 3c and d). Additionally, there is also a molecular-level hysteresis associated with refolding of the α -helix during mechanical unloading (*i.e.* a smaller amount of α -helix for a given load during relaxation vis-à-vis loading) that corresponds nicely with the macroscopic hysteresis observed in the material. These results were found to be consistent with results from *in situ*

small- and wide-angle X-ray diffraction measurements, which examined the structural behavior of the protein building blocks at very different length scales [58]. Thus, mechanical healing of the WEC was shown to originate from a reversible conformational phase transition in the constituent biopolymeric protein building blocks, dependent on the reversible rupture of stabilizing interactions – that is, in order to unfold α -helices, the hydrogen bonding network running along the helical axis must be ruptured allowing it to extend; however, this is evidently rapidly reformed following unloading of the material. Numerical modeling of the molecular behavior based on thermodynamic and kinetic considerations were found to be in general agreement with the Raman-based interpretation of the self-healing mechanism [58,59]. The example of the WEC again reiterates that not just the presence of a reversible bond (in this case hydrogen-bonding) is necessary for tuning self-healing behavior, but also the structural organization at various levels of hierarchy is of utmost importance.

Self-healing based on encapsulated healing agents

Many of the current generation of self-healing polymer composites are based on the fracture-induced release and subsequent curing of reactive agents in (micro)cracks, as pioneered in the seminal work by White et al. [14]. Such extrinsic healing mechanisms rely on the conversion of the mobile healing agent into a cross-linked end-product, which often possess very different Raman fingerprints. Thus, Raman spectroscopy can be used to monitor the progress of the healing process locally, which can be correlated to the degree of mechanical recovery *in situ*, revealing important chemical structure–function relationships. This method has proven useful in many instances, a handful of which are summarized below. While the examples described below are not exhaustive, they provide a suitable introduction to the field, emphasizing the potential utility of vibrational spectroscopy.

The self-healing of polymer composites was first demonstrated using ring-opening metathesis polymerization (ROMP) of

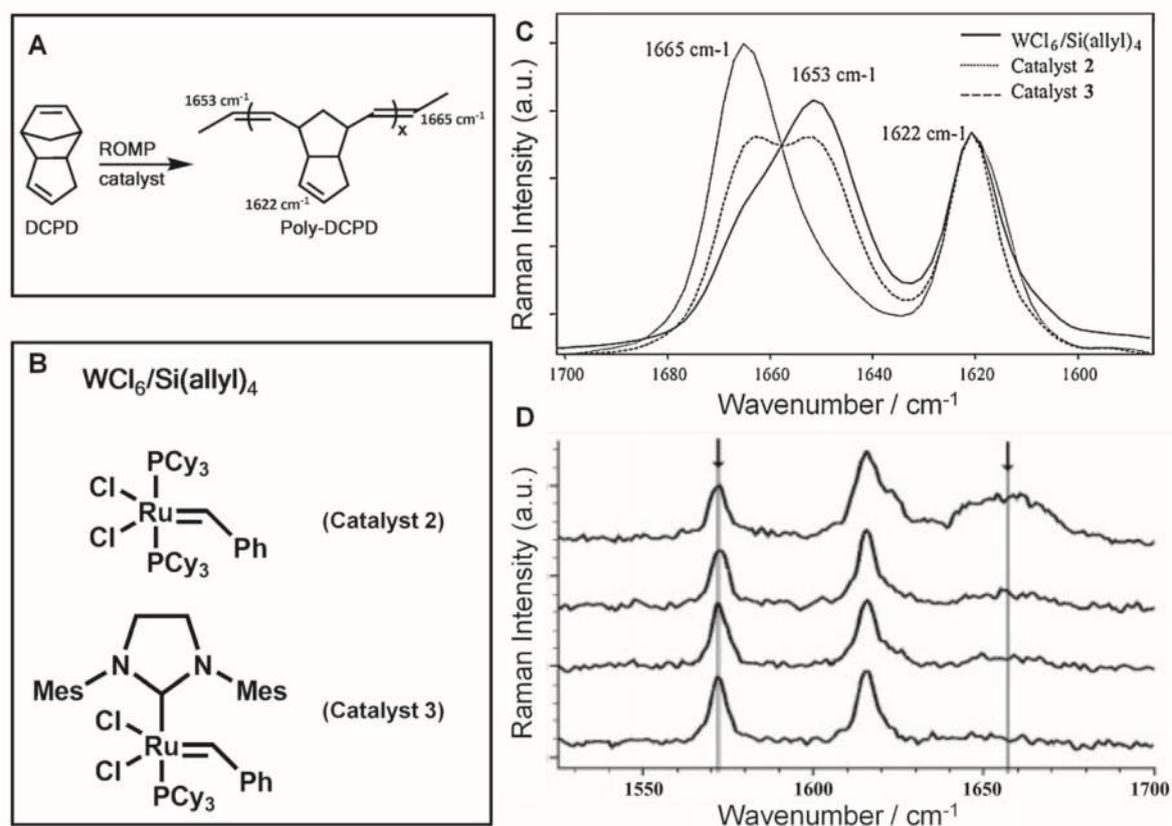


FIGURE 4

Raman spectroscopic observation of the ring-opening metathesis polymerization (ROMP). (a) ROMP of a dicyclopentadiene (DCPD). (b) Overview of Grubbs catalytic systems actuating the ROMP reaction as reported in Schaubroeck et al. [64]. (c) Raman spectra of linear poly-DCPD, illustrating the influence of the Grubbs' catalysts shown in panel B on the *trans*-*cis*-selectivity of the cross-linking reaction. The shoulder at 1665 cm^{-1} is assigned to the stretching vibration of the *trans*-conformed aliphatic double bond. Adapted from Schaubroeck et al. with permission of Elsevier [64]. (d) Raman spectra obtained during polymerization of DCPD. An increase of the Raman mode at 1660 cm^{-1} (formation of vinyl C–C bonds) and a decrease of the Raman mode at 1568 cm^{-1} (C=C stretching vibration) with respect to the initial spectrum of DCPD confirms polymerization. Adapted from Chipara et al. with permission of Wiley [62].

dicyclopentadien (DCPD) in the presence of Grubbs' catalyst, which was monitored using *inter alia* vibrational spectroscopy to show that the ring-opened product of the DCPD polymerization (*i.e.* poly(DCPD)) was formed in the presence of Grubbs' catalyst [14,60,61]. Specifically, this was revealed by the appearance of an infrared absorption band at 965 cm^{-1} indicative of the *trans* double bond of the polymerization product. Raman spectroscopy was also used in order to monitor the material curing based of ROMP in the presence of Grubbs' catalyst, in which an increase of the Raman band at 1660 cm^{-1} associated with the vinyl C–C vibration of the polymerization product and a decrease of the Raman band at 1568 cm^{-1} , which is assigned to the C=C stretching vibration of the monomer, were used as overall indicators for the progress of the self-healing reaction (Fig. 4) [62–64]. In an extension to the often used approach of embedded microcapsules (see Fig. 5a for a schematic representation) [14,65,66], Toohey et al. developed materials that possess a microvascular network for the delivery of DCPD and Grubbs catalyst to ruptured locations

within the material [67]. This approach enables multiple healing cycles of the material.

Following these initial studies, further vibrational spectroscopy investigations revealed important details concerning the mechanisms of self-healing in polymer composites based on the ROMP reaction. When following the polymerization of DCPD by non-resonant Raman spectroscopy in time-lapse experiments, clear spectroscopic changes are visible that extend far beyond the range of the vibrational bands previously discussed [63]. For example, the authors reported that the band shape of the band at around 1615 cm^{-1} changes from being rather symmetrically centered at 1612 cm^{-1} to revealing a double-peak structure (maxima at 1620 and 1612 cm^{-1}) upon completion of the polymerization reaction. Nonetheless, analysis of the time-lapse experiments focused on the prominent bands at 1568 and 1660 cm^{-1} , indicative of the reactants and the polymerization product, respectively. Within about an hour after fracturing the material, a significant rapid increase in the 1660 cm^{-1} band was observed, which is

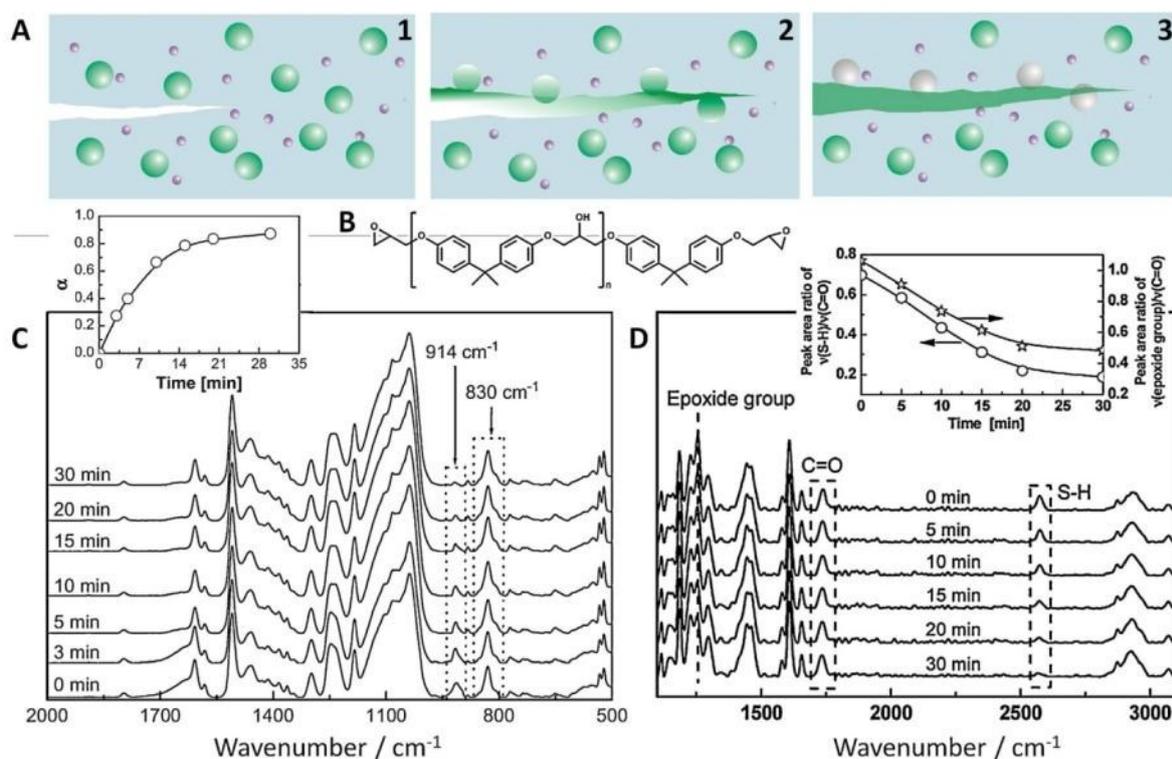


FIGURE 5

In situ time-dependent vibrational spectroscopic study of epoxy based polymerization products. (a) Principle of the autonomous self-healing process by epoxy polymerization. The matrix contains two types of microcapsules filled with epoxy prepolymer (green capsules) and a hardener, which serves as a catalyst (purple capsules) (1). When the material is damaged, the forming crack ruptures the microcapsules and the monomer is released into the crack. Upon contact with the catalyst the healing agent polymerizes (2) until the crack is mended (3). (b) Epoxy prepolymer, which reacts to an epoxy composite upon contact with a hardener. (c) FTIR spectra obtained during the curing reaction of epoxy and the hardener boron trifluoride diethyl etherate ($\text{C}_2\text{H}_5)_2\text{O}\cdot\text{BF}_3$ (95/5 by weight) at 20°C (inset: reaction degree, α , as a function of time). A decrease of a characteristic peak of the epoxide group at 914 cm^{-1} confirms consumption of the epoxide within 30 min upon fracture. Adapted from Xiao et al. with permission of Elsevier [70]. (d) Monitoring the curing reaction of epoxy and mercaptane catalyzed by benzyldimethylamine using *in situ* confocal Raman spectroscopy. Observation of the decrease of characteristic Raman features of the monomers at 1256 cm^{-1} (stretching mode of epoxide group) and 2573 cm^{-1} (S–H stretching vibration of mercaptane) is consistent with a rapid curing reaction completed within 30 min. Adapted from Yuan et al. with permission of ACS [68].

correlated with rapid changes in the polymer viscosity in the same temporal window. The 1660 cm^{-1} band possesses a minor asymmetry, which the authors associate with the inhomogeneous distribution of monomeric units within the polymer strand. Furthermore, the temporal changes of the Raman spectra were correlated with measurements of the time-of-flight of a longitudinal ultrasonic wave through the polymer sample, and it was found that – due to a change in the materials modulus – the time-of-flight of a longitudinal ultrasonic wave decreases upon increase self-healing [63]. The chemical signature upon self-healing, as revealed by the Raman spectra, is completely consistent with the macroscopic material properties of the samples as reflected in the polymer viscosity or in its density and shear moduli. While the qualitative correlations of the different experimental methodologies that shed light on complementary aspects of the self-healing process are evident, the experimental results in Barnes et al. [63] lack a quantitative correlation. For instance, the fast initial rise of the Raman-band intensity associated with the polymerization product in the first minutes of the reaction are not directly mirrored in fast changes of the bulk and shear moduli of the sample. In particular, the measured ultrasonic time-of-flight data indicate no temporal changes within the first 20 min after induction of self-healing.

Furthermore, the assignment of the vibrational bands in Barnes et al. [63] was challenged by Verpoort and coworkers [64], who associated both the vibrations at 1573 and 1617 cm^{-1} to C=C stretching vibrations of the reactant monomer. In particular, the 1573 cm^{-1} was assigned to the norbornene and the 1617 cm^{-1} mode to the cyclopentene vibration of DCPD, which are shown to decrease synchronously in time-lapse Raman experiments following the self-healing reaction. Upon ring opening of the norbornene ring in the DCPD (decrease of the band at 1573 cm^{-1}), the ring tension of the cyclopentene vibration is altered, which causes the shift of the respective C=C stretching vibration from 1617 to 1622 cm^{-1} . In order to verify the origin of the asymmetry of the 1660 cm^{-1} band, Verpoort and coworkers compared the Raman spectra of the polymerization products obtained from different Grubbs' catalysts [64], which differ in their *trans*-selectivity. While the catalyst with high *trans*-selectivity caused the slightly asymmetric band shape of the C=C stretching vibration in the polymer at 1665 cm^{-1} , the less *trans*-selective catalyst produces a polymer whose Raman spectrum reveals two almost equally intense bands at 1665 and 1653 cm^{-1} , the latter of which is assigned to the *cis*-conformed double bond. Upon application of a highly *cis*-selective catalyst, that is, $\text{WCl}_6/\text{Si}(\text{allyl})_4$, the Raman spectrum of the polymerization product reveals a dominant peak at 1653 cm^{-1} with only minor contributions from a shoulder at 1665 cm^{-1} (Fig. 4). Thus, the examples presented here further illustrate the potential of Raman spectroscopy to not only monitor temporally- and spatially-resolved changes in local chemistry, but also to monitor the stereospecificity of self-healing reactions.

In addition to ROMP reactions, other chemical approaches have been successfully integrated into microcapsule- and microvascular-based self-healing materials. For example, self-healing polymeric composites consisting of a polymerizable resin (epoxy) and a hardener as healant represent an intensively researched class of materials (see Fig. 5 for an exemplary depiction). The two-component healant is incorporated in fragile containers resembling

microcapsules, which are embedded in the epoxy matrix [14]. Upon destruction of the capsules, the monomers are released into the path of the scratch and subsequent polymerization is induced by contact with an integrated catalyst in order to hamper crack propagation and to recover the original properties of the polymer (Fig. 5a) [43]. Vibrational spectroscopic techniques are quite useful for *in situ* characterization of the epoxy based polymerization products formed at the cracked surface, since polymerization involves consumption of IR- or Raman-active functional groups on the monomers that can be quantified depending on the nature of the reacting educts.

Yuan et al. [68] monitored the self-healing of an epoxy composite, consisting of microcapsules loaded with epoxy and its hardener mercaptan by means of *in situ* confocal Raman microscopy (Fig. 5d). Time-dependent Raman spectra were collected following fracture of a polymer surface possessing 2.5 wt% epoxy loaded capsules and 2.5 wt% hardener loaded capsules. With respect to the constant carbonyl stretching vibration, the simultaneous decrease of the Raman bands assigned to the S-H stretching mode of the mercaptan and the ring stretching mode of the epoxy group permitted the curing reaction between the epoxide groups and the hydrosulfide groups catalyzed by benzyldimethylamine to be monitored. The epoxy polymer is healed in less than an hour, since approximately 50% of the epoxide groups are consumed within 30 min. Similar *in situ* Raman spectroscopic studies on materials based on a polymer containing encapsulated epoxy/mercaptan healants were published three years later by the same group [69]. Time-dependent confocal Raman measurements of the extruded healing agent indicate that 70% of epoxy healant was consumed by the reaction with hydrosulfide group in the presence of the catalyst 2,4,6-tris(dimethylaminomethyl)phenol (DMP-30) within 15 min, corresponding to a threefold faster recovery of the polymer.

Xiao et al. [70] monitored curing of an epoxy resin utilizing a different hardener by means of IR spectroscopy (Fig. 5c). Advantages of this composite, which consists of epoxy and boron trifluoride etherate ($(\text{C}_2\text{H}_5)_2\text{O}\cdot\text{BF}_3$) loaded microcapsules as compared to the epoxy-thiol-based composites are: (1) The low catalyst concentration required to initiate the curing reaction based on cationic chain polymerization, (2) the fast curing reaction at ambient temperatures and (3) high efficiency of the healing process in terms of restoring the mechanical properties of the polymer. IR spectra reveal the consumption of epoxide by direct observation of the disappearance of a characteristic peak of the epoxide group at 914 cm^{-1} , while the IR feature at 830 cm^{-1} assigned to the phenyl ring has been used as internal standard. The results indicate that the progress of the self-healing reaction correlates with the healing efficiency – consumption of 87% of the epoxide groups within 30 min coincides well with the observed 80% recovery of impact strength of the composite in the same time window.

Zhu et al. designed multilayer microcapsule-like microreactors for application within self-healing polymers [71]. Their “all-in-one” system contains a liquid healing agent (*i.e.* glycidyl methacrylate) as well as a copper catalyst and the macroinitiator for the atom transfer radical polymerization. All reactive components have to be “stored” within different compartments (*i.e.* layers) of the final multilayer microcapsule. They performed Raman

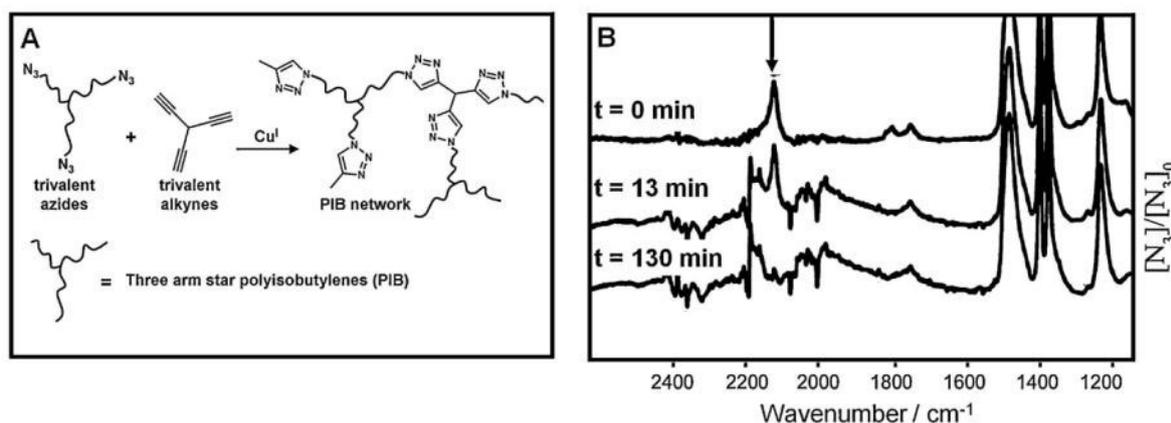


FIGURE 6

(a) "Click" reaction between trivalent polyisobutylene (PIB) azides and trivalent alkynes catalyzed by Cu(I) leads to a cross-linked polymeric network. (b) A decrease of the azide band at 2095 cm⁻¹ with time during the "click" reaction measured via ATR-IR spectroscopy at 80 °C evidences complete azide conversion within 130 min. Adapted from Schunack et al. with permission of Wiley [73].

microscopy depth profiling [72] in order to investigate the local distribution of all healing agents.

Moreover, the Cu^I catalyzed click-reaction between azide and alkyne functionalized polymers shows great potential for material self-repair [74,75]. Based on existing concepts, Binder and coworkers used this reaction to crosslink polymer chains [76,77] in order to synthesize a poly(isobutylene)-based material in which microcapsules containing either low-molar mass trivalent alkynes or azide functionalized star-like poly(isobutylenes) were embedded. Additionally, a Cu^I catalyst was dispersed into the material [73]. Upon shear-force induced rupture of the microcapsules, the reactants mix with the catalyst in the polymer material, and the click-reaction leads to the healing of the crack via reformation of a polymer network. So far only AT-IR vibrational spectroscopy has been used to follow the self-healing reaction based on the temporal evolution of the azide vibration at 2095 cm⁻¹ (Fig. 6). Although Raman spectroscopy has not yet been applied to these materials, it has a great potential in such studies considering that it can be applied both to bulk samples (in contrast to AT-IR) and *in situ* studies focusing on the distribution of $\text{C}\equiv\text{C}$ stretching vibrations even in complex biological samples as reported in a recent study on wound healing in living marine algae [78].

Prospective applications for Raman spectroscopy in monitoring reversible bond formation

Reversible temperature controlled bond formation and bond cleavage based on Diels–Alder (DA) and retro-Diels–Alder (rDA) reactions have been successfully utilized in the context of intrinsically self-healing polymers [79–81]. It was shown that the conversion of furan and maleimide to the DA product is correlated with distinct changes in the vibrational spectra, which remain clearly visible when the functional groups responsible for self-healing are diluted in a polymer matrix [82,83]. In Toncelli et al. [82] and Zeng et al. [83], the authors employed FT-IR and ATIR spectroscopy, respectively, in order to monitor the reaction and the conversion efficiency of reactants in forming the cross-linked network (Fig. 7).

Due to the generally high intensity of the C=O stretching vibration in IR-absorption spectra, Zeng and coworkers based their vibrational spectroscopic investigation on the spectral-temporal shift of the IR absorption bands at 1700 and 1730 cm⁻¹, which are assigned to the carbonyl stretching vibrations of the maleimide containing crosslinking agent and to the backbone of the poly(2,5-furandimethylene succinate) (PFS), respectively, and the imide vibration of the unreacted maleimide function at 700 cm⁻¹ [83]. During the healing DA reaction, which was initiated by briefly immersing the PFS in a solution of the crosslinking agent, the carbonyl vibrations remained unchanged indicating that the overall content of PFS backbone, as well as unreacted and reacted crosslinking agent stayed constant. However, the intensity of the imide vibration of the unreacted crosslinking unit decreased as a function of time revealing the progress of the healing reaction. Broekhuis and coworkers incorporated an even greater variety of IR active vibrations into their spectroscopic analysis of a cross-linked network of furan functionalized polyketones [82]. The authors compared different maleimide crosslinker concentrations (relative to the concentration of functional furan groups in the polymer) and could show that IR vibrational spectroscopy is capable of revealing the resultant chemical changes in the network, which were also clearly reflected in the mechanical properties of the samples. In addition to IR-based studies, Raman spectroscopic investigations on low-molar mass compounds, which serve as reactants in the DA/rDA chemistry have also been reported. To this end both non-resonant Raman scattering [84,85] and surface-enhanced Raman scattering [86] have been employed, proving the potential of Raman spectroscopy to be employed also for monitoring temperature-triggered DA/rDA based self-healing reactions *in situ*.

As mentioned earlier, metal–amino acid complexes based on DOPA and histidine residues are believed to play a central role in damage-tolerant biological materials. Although their bond strength lies somewhere between hydrogen bonds and covalent bonds, such complexes can be reversibly opened and closed

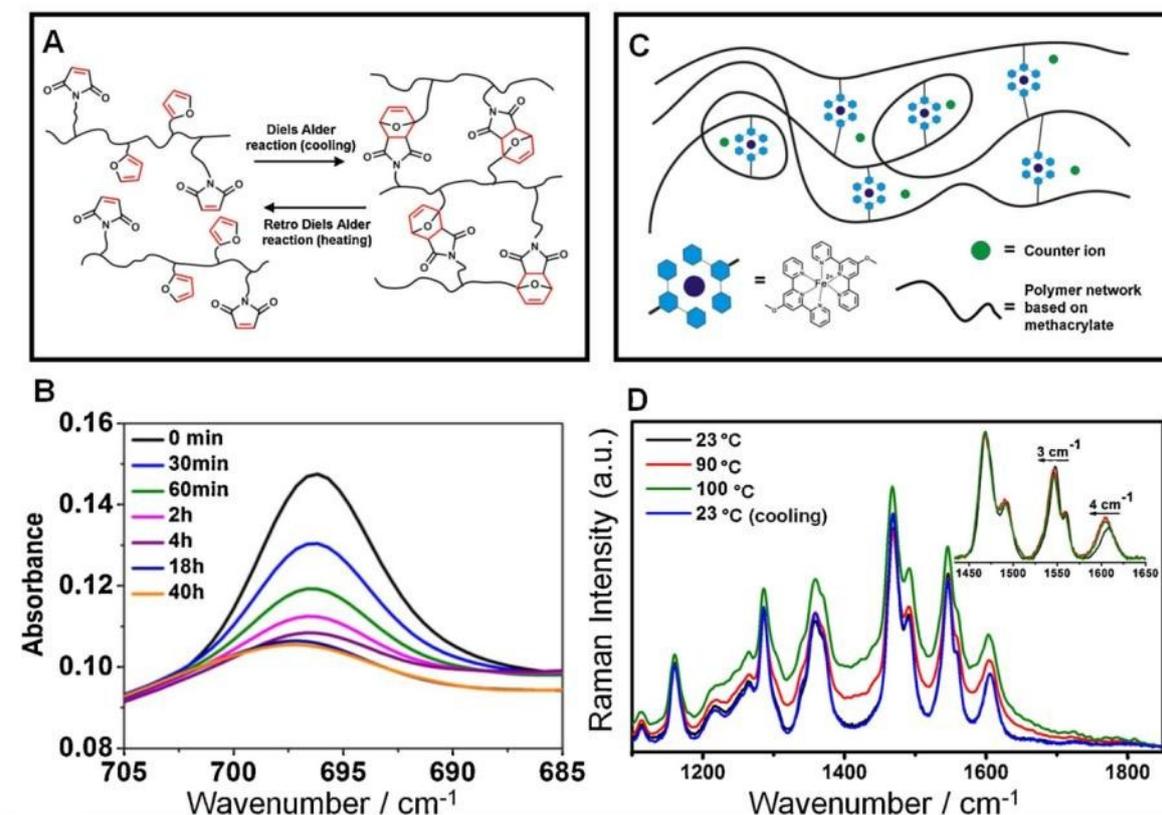


FIGURE 7

Monitoring reversible bond formation by vibrational spectroscopy. (a) Reversible Diels–Alder cycloaddition of furan and maleimide, embedded in polymer strands. (b) A progressing Diels–Alder reaction of a bio-based bis(hydroxymethyl)furan (BHF) and bismaleimide is examined by ATR-IR spectroscopy. The imide functional group is disintegrated during DA reaction. Hence, the imide peak intensity at around 700 cm^{-1} is reduced. Adapted from Zeng et al. with permission of ACS [83]. (c) Schematic drawing of a reversible cross-linked metallopolymer network based on a Fe^{2+} -terpyridine linkage. Cross-linking is based on metal–ligand interaction. (d) Terpyridine Raman modes shift to lower wavenumber upon heating the cross-linked metallopolymer indicating decomplexation of the metal–ligand structure. Adapted from Bode et al. with permission of Wiley [28].

through many cycles [87,88]. Hence, they are ideally suited to function as reversible sacrificial bonds, and this property is exploited in certain biological materials to generate self-healing behavior. For example, the large hysteresis and self-healing capabilities of the fibrous core of mussel byssal threads are – at least partially – attributed to the stabilizing effects of metal-histidine complexes [89,90]. Additionally, spider silk infiltrated with transition metal ions via atomic layer deposition (ALD) exhibits increased toughness, possibly due to the formation of coordination complexes [91]. Inspired by such findings in biomaterial paradigm systems, polymers stabilized by reversible coordination bonds based on biological ligands (e.g. DOPA and histidine) have been developed that show moderate self-healing behavior [32–34]. Additionally, in a promising new direction that expands beyond metal-binding ligands found in nature, bio-inspired metallopolymers based on synthetic ligands (e.g. between a transition metal ion and terpyridine units) have been utilized to enable self-healing. In such systems – as in the natural systems – the metal–ligand bond properties are a key factor both for the self-healing capability

of the material and the overall material properties [92]. For example, factors such as bond dissociation rates [93], bond geometry and spatial organization of bonds will also exert a strong influence on mechanical properties and must therefore be considered in the rational design of new self-healing metallopolymers. Hence, the design of man-made self-healing materials based on metal coordination cross-linking, which has been realized first for the reversible connection of linear metallopolymers via metal complexation [30], will always be a compromise between optimizing self-healing behavior and tuning the material properties – for example, in hard materials the mobility of polymer-chains is low and hence the capability for self-healing, which requires individual chains to interact with each other, might be impaired. Recently, a coating based on a functional polymer bearing terpyridine functionalities in the side chains was synthesized and tested for its self-healing capabilities [28]. The self-repair of the material was initiated by increasing temperature, which was accompanied by shifts of Raman bands of about $3\text{--}4\text{ cm}^{-1}$ to lower wavenumbers in the spectral region between 1475 and 1650 cm^{-1} . These bands

are characteristic for the terpyridine moiety [94,95], and their reversible temperature-dependent shift indicates changes in the chemical environment of the terpyridine units during self-healing. This finding was correlated with results from small-angle X-ray scattering, which reveal that only those polymer materials, which show some short-range order, can undergo self-healing. Based on this, it was speculated that both ionic clusters in the material, which originate from the interaction of the positively charged Fe^{2+} -terpyridine complexes and the sulfate counter ion, as well as the reversibility of the metal-ligand interaction could contribute to the self-healing behavior. Interestingly, organizational order was also recently shown to be vital in the metal-dependent self-healing behavior of the fibrous core of mussel byssal threads [96].

Aside from the reversible bonds based on Diels-Alder and retro-Diels-Alder reactions and terpyridine-metal complexation mentioned above, other interactions such as pincer complexes [79,97–100], π - π -stacking interactions [21,23,101] and intermolecular hydrogen bonding [102–105] have been used to ensure reversible bond formation toward intrinsic self-healing. However, these bonds are difficult to detect using Raman spectroscopy; therefore, discussion of them lies outside the confines of this review and other methods focusing on overall material properties are more appropriate for characterization.

Conclusion and outlook

In recent years, a large number of different self-healing materials, in particular polymers and polymer composites have been developed. A great deal of effort has been spent on characterizing these materials and quantifying the healing process (*i.e.* determination of healing efficiency) [106]; however, in many cases, a thorough understanding of the underlying (molecular) mechanism is still lacking. Along these lines, chemical characterization techniques including vibrational spectroscopy, are beginning to shed light on some of these open questions. As outlined in this review, Raman spectroscopy and Raman microspectroscopy, in particular, are able to decipher the molecular mechanisms of self-healing in many polymer-based materials. In particular, the features of Raman scattering, including the ability to deduce the local chemical composition of a sample non-destructively and with a spatial resolution of less than a micrometer, have revealed detailed insights into the formation and prevalence of reversible intermolecular interactions, which are essential for self-healing. Raman (micro)spectroscopy, for example, has led to an improved understanding of the design principle of self-healing biopolymers from marine environments and of the molecular mechanisms underlying self-healing epoxies, and there is good reason to believe that this technique will continue to provide further insights into self-healing materials based on other chemistries. For example, in some materials strain-induced structural changes can lead to shifts in the Raman peaks, [107] similar to the conformational changes in protein backbone structure shown to be integral to the self-healing behavior of the WEC (Fig. 3). By this manner the local strain can be investigated, which would be otherwise only possible using certain mechanophores [108]. In this context, it has been shown that single wall carbon nanotubes (SWCNT) embedded in a polymer matrix reveal strain-induced characteristic shifts of the Raman signatures [107]. The observed shift of the G'-band at 1582 cm^{-1} is linear in the applied strain and is therefore ideally suited to

examine the local strain in an epoxy resin with percolated SWCNT networks. Hence, SWCNTs embedded in (self-healing) polymer materials can be used as nanolocal Raman-spectroscopic probes for mechanochemical properties of the materials. It is expected that the general applicability of the technique will lead to deeper insights into the mechanism of self-healing polymers, in particular polymer systems based on reversible bonds/interactions. The knowledge gained can lead to a variety of novel applications, for example, in tailor-made coatings or self-healing elastomers.

Acknowledgement

The work was financially supported by the Deutsche Forschungsgemeinschaft via the Priority Program SPP 1568 "Design and Generic Principles of Self-Healing Materials".

References

- [1] S. van der Zwaag (Ed.), *Self Healing Materials – An Alternative Approach to 20 Centuries of Materials Science*, Springer, Dordrecht, 2007.
- [2] X. Chen, et al. *Science* 295 (2002) 1698.
- [3] M.D. Hager, et al. *Adv. Mater.* 22 (2010) 5424.
- [4] B.L. Smith, et al. *Nature* 399 (1999) 761.
- [5] J. Keckes, et al. *Nat. Mater.* 2 (2003) 810.
- [6] G.E. Fantner, et al. *Nat. Mater.* 4 (2005) 612.
- [7] N. Holten-Andersen, et al. *Nat. Mater.* 6 (2007) 669.
- [8] H.S. Rapoport, R.E. Shadwick, *J. Exp. Biol.* 210 (2007) 12.
- [9] S.J. Garcia, H.R. Fischer, S. van der Zwaag, *Prog. Org. Coat.* 72 (2011) 211.
- [10] M.D. Hager, U.S. Schubert, *Eur. Coat. J.* 6 (2011) 40.
- [11] A.P. Esser-Kahn, et al. *Macromolecules* 44 (2011) 5539.
- [12] B.J. Blaiszik, et al. *Annu. Rev. Mater. Res.* 40 (2010) 179.
- [13] A.R. Hamilton, N.R. Sottos, S.R. White, *Adv. Mater.* 22 (2010) 5159.
- [14] S.R. White, et al. *Nature* 409 (2001) 794.
- [15] X. Chen, et al. *Macromolecules* 36 (2003) 1802.
- [16] J. Kösteritzsch, et al. *Macromol. Chem. Phys.* 214 (2013) 1636.
- [17] M.J. Barthelemy, et al. *Adv. Funct. Mater.* 23 (2013) 4921.
- [18] P. Cordier, et al. *Nature* 451 (2008) 977.
- [19] S.J. Kalista, T.C. Ward, *J. R. Soc. Interface* 4 (2007) 405.
- [20] S.J. Kalista, J.R. Pflug, R.J. Varley, *Polym. Chem.* 4 (2013) 4910.
- [21] S. Burattini, et al. *Chem. Commun.* (2009) 6717.
- [22] S. Burattini, et al. *Faraday Discuss.* 143 (2009) 251.
- [23] S. Burattini, et al. *Chem. Mater.* 23 (2011) 6.
- [24] J. Fox, et al. *J. Am. Chem. Soc.* 134 (2012) 5362.
- [25] M. Zhang, et al. *Angew. Chem. Int. Ed.* 51 (2012) 7011.
- [26] X. Yan, et al. *Chem. Soc. Rev.* 41 (2012) 6042.
- [27] T. Kakuta, Y. Takashima, M. Nakahata, M. Otsubo, H. Yamaguchi, A. Harada, *Adv. Mater.* 25 (2013) 2849.
- [28] S. Bode, et al. *Adv. Mater.* 25 (2013) 1634.
- [29] S. Bode, et al. *Polym. Chem.* 4 (2013) 4966.
- [30] M. Burnworth, et al. *Nature* 472 (2011) 334.
- [31] M.J. Harrington, et al. *Science* 328 (2010) 216.
- [32] N. Holten-Andersen, et al. *Proc. Natl. Acad. Sci. U.S.A.* 108 (2011) 2651.
- [33] D.G. Barrett, et al. *Adv. Funct. Mater.* 23 (2013) 1111.
- [34] D.E. Fullenkamp, et al. *Macromolecules* 46 (2013) 1167.
- [35] I.R. Lewis, H.G.M. Edwards (Eds.), *Handbook of Raman Spectroscopy: From the Research Laboratory to the Process Line*, Marcel Dekker Inc., New York and Basel, 2001.
- [36] B. Schrader, D. Bougeard (Eds.), *Infrared and Raman Spectroscopy: Methods and Applications*, VCH, Weinheim, 1995.
- [37] J. Popp, A. Chiou, V.V. Tuchin, S. Heinemann (Eds.), *Handbook of Biophotonics*, Wiley-VCH, Weinheim, 2012.
- [38] J.M. Chalmers, P.R. Griffiths (Eds.), *Handbook of Vibrational Spectroscopy*, John Wiley & Sons Ltd., Chichester, 2006.
- [39] L. Guadagno, et al. *AIP Conf. Proc.* 1255 (2010) 264.
- [40] G. Scheltjens, et al. *J. Therm. Anal. Calorim.* 105 (2011) 805.
- [41] S. Neuser, V. Michaud, *Polym. Chem.* 4 (2013) 4993.
- [42] D.V. Andreeva, et al. *Adv. Mater.* 20 (2008) 2789.
- [43] T. Yin, et al. *Compos. Sci. Technol.* 67 (2007) 201.
- [44] M.-E. Rousseau, et al. *Biomacromolecules* 5 (2004) 2247.

- [45] R.G. Parr, W. Yang (Eds.), *Density-Functional Theory of Atoms and Molecules*, Oxford University Press, New York, 1989.
- [46] P. Politzer, J.M. Seminario (Eds.), *Modern Density Functional Theory: A Tool For Chemistry*, Elsevier, Amsterdam, 1995.
- [47] J. Popp, W. Kiefer, *Fundamentals of Raman spectroscopy*, in: R.A. Meyers (Ed.), *Encyclopedia of Analytical Chemistry*, Wiley, Chichester, 2000, pp. 13104–13142.
- [48] M. Schmitt, J. Popp, *J. Raman Spectrosc.* 37 (2006) 20.
- [49] E. Carrington, J.M. Gosline, *Am. Malacol. Bull.* 18 (2004) 1.
- [50] C. Sun, J.H. Waite, *J. Biol. Chem.* 280 (2005) 39332.
- [51] M. Wächtler, et al. *Coord. Chem. Rev.* 256 (2012) 1479.
- [52] S.W. Taylor, et al. *Inorg. Chem.* 35 (1996) 7572.
- [53] D.S. Hwang, et al. *J. Biol. Chem.* 285 (2010) 25850.
- [54] A. Walter, et al. *Analyst* 135 (2010) 908.
- [55] K. Grosser, et al. *Biofouling* 28 (2012) 687.
- [56] H.S. Rapoport, R.E. Shadwick, *Biomacromolecules* 3 (2002) 42.
- [57] A. Miserez, et al. *Nat. Mater.* 8 (2009) 910.
- [58] M.J. Harrington, et al. *J. R. Soc. Interface* 9 (2012) 2911.
- [59] F.D. Fischer, M.J. Harrington, P. Fratzl, *New J. Phys.* 15 (2013) 065004.
- [60] M. Kessler, N. Sottos, S. White, *Compos. A: Appl. Sci. Manuf.* 34 (2003) 743.
- [61] E.N. Brown, S.R. White, N.R. Sottos, *Compos. Sci. Technol.* 65 (2005) 2474.
- [62] M.D. Chipara, et al. *Polym. Adv. Technol.* 20 (2009) 427.
- [63] S.E. Barnes, et al. *Spectrochim. Acta A: Mol. Biomol. Spectrosc.* 61 (2005) 2946.
- [64] D. Schaubroeck, et al. *J. Mol. Catal. Chem.* 254 (2006) 180.
- [65] E.N. Brown, S.R. White, N.R. Sottos, *J. Mater. Sci.* 39 (2004) 1703.
- [66] G.O. Wilson, et al. *Adv. Funct. Mater.* 18 (2008) 44.
- [67] K.S. Toohey, et al. *Nat. Mater.* 6 (2007) 581.
- [68] Y.C. Yuan, et al. *Macromolecules* 41 (2008) 5197.
- [69] Y. Yuan, et al. *Express Polym. Lett.* 5 (2011) 47.
- [70] D.S. Xiao, et al. *Polymer* 50 (2009) 2967.
- [71] D.Y. Zhu, M.Z. Rong, M.Q. Zhang, *Polymer* 54 (2013) 4227.
- [72] C. Hu, et al. *Soft Matter* 8 (2012) 4780.
- [73] M. Gragert, M. Schunack, W.H. Binder, *Macromol. Rapid Commun.* 32 (2011) 419.
- [74] V.V. Rostovtsev, et al. *Angew. Chem. Int. Ed.* 41 (2002) 2596.
- [75] C.W. Tornøe, C. Christensen, M. Meldal, *J. Org. Chem.* 67 (2002) 3057.
- [76] W.H. Binder, R. Sachsenhofer, *Macromol. Rapid Commun.* 28 (2007) 15.
- [77] W.H. Binder, R. Sachsenhofer, *Macromol. Rapid Commun.* 29 (2008) 952.
- [78] I.A. Weissflog, et al. *Chembiochem* 14 (2013) 727.
- [79] S.D. Bergman, F. Wudl, *J. Mater. Chem.* 18 (2007) 41.
- [80] A.M. Peterson, R.E. Jensen, G.R. Palmese, *ACS Appl. Mater. Interfaces* 2 (2010) 1141.
- [81] P. Reutenauer, et al. *Chem. Eur. J.* 15 (2009) 1893.
- [82] C. Toncelli, et al. *Macromol. Chem. Phys.* 213 (2012) 157.
- [83] C. Zeng, et al. *Macromolecules* 46 (2013) 1794.
- [84] M. Karabacak, A. Çoruh, M. Kurt, *J. Mol. Struct.* 892 (2008) 125.
- [85] T. Kim, et al. *J. Raman Spectrosc.* 42 (2011) 2069.
- [86] S.W. Joo, *Bull. Korean Chem. Soc.* 29 (2008) 1761.
- [87] H. Lee, N.F. Scherer, P.B. Messersmith, *Proc. Natl. Acad. Sci. U.S.A.* 103 (2006) 12999.
- [88] L. Schmitt, et al. *Biophys. J.* 78 (2000) 3275.
- [89] E. Vaccaro, J.H. Waite, *Biomacromolecules* 2 (2001) 906.
- [90] M.J. Harrington, et al. *J. Struct. Biol.* 167 (2009) 47.
- [91] S.-M. Lee, et al. *Science* 324 (2009) 488.
- [92] G.R. Whittell, et al. *Nat. Mater.* 10 (2011) 176.
- [93] W.C. Yount, D.M. Loveless, S.L. Craig, *Angew. Chem. Int. Ed.* 44 (2005) 2746.
- [94] S. Kupfer, et al. *Phys. Chem. Chem. Phys.* 13 (2011) 15580.
- [95] M. Presselt, et al. *J. Phys. Chem. C* 112 (2008) 18651.
- [96] S. Krauss, et al. *Biomacromolecules* 14 (2013) 1520.
- [97] R. Dobrawa, F. Würthner, *J. Polym. Sci. A: Polym. Chem.* 43 (2005) 4981.
- [98] H. Hofmeier, U.S. Schubert, *Chem. Soc. Rev.* 33 (2004) 373.
- [99] P.R. Andres, U.S. Schubert, *Adv. Mater.* 16 (2004) 1043.
- [100] A. El-ghayoury, et al. *Macromolecules* 36 (2003) 3955.
- [101] R. Scott Lokoy, B.L. Iverson, *Nature* 375 (1995) 303.
- [102] J. Courtois, et al. *Adv. Funct. Mater.* 20 (2010) 1803.
- [103] F. Herbst, et al. *Macromolecules* 43 (2010) 10006.
- [104] V. Berl, et al. *Chem. Eur. J.* 8 (2002) 1227.
- [105] S. Burattini, et al. *Chem. Soc. Rev.* 39 (2010) 1973.
- [106] R.K. Bose, U. Lafont, J.M. Vega, S.J. Garcia, S. van der Zwaag, in: W.H. Binder (Ed.), *Self-Healing Polymers*, Wiley, Weinheim, 2013, pp. 335–359.
- [107] A. de la Vega, et al. *Compos. Sci. Technol.* 71 (2011) 160.
- [108] D.A. Davis, et al. *Nature* 459 (2009) 68.

[Kupfer et al. PCCP]

Self-healing Mechanism of Metallopolymers Investigated by QM/MM Simulations and Raman Spectroscopy

Der Nachdruck der folgenden Publikation erfolgt mit freundlicher Genehmigung der Royal Society of Chemistry.

Reprinted with kind permission from:

Kupfer, S.; Zedler, L.; Guthmuller, J.; Bode, S.; Hager, M. D.; Schubert, U. S.; Popp, J.; Gräfe, S. und Dietzek, B., *Phys. Chem. Chem. Phys.* **2014**, 16, 12422-12432.

Copyright 2014 Royal Society of Chemistry.

Self-healing mechanism of metallopolymers investigated by QM/MM simulations and Raman spectroscopy†

Cite this: *Phys. Chem. Chem. Phys.*, 2014, 16, 12422

Stephan Kupfer,^{‡,*ab} Linda Zedler,^{‡,ab} Julien Guthmuller,^c Stefan Bode,^{de} Martin D. Hager,^{de} Ulrich S. Schubert,^{de} Jürgen Popp,^{abf} Stefanie Gräfe^{ab} and Benjamin Dietzek^{*abf}

The thermally induced self-healing mechanisms in metallopolymers based on bisterpyridine complexes of iron(II) sulfate and cadmium(II) bromide, respectively, were studied by means of combined quantum mechanical/molecular mechanical (QM/MM) simulations and Raman spectroscopy. Two possible healing schemes, one based on a decomplexation of the cross-linking complexes and a second one relying on the dissociation of ionic clusters, have been addressed. Temperature-dependent Raman spectroscopy displayed bathochromic shifts of the Raman intensity pattern upon heating. QM/MM simulations on the polymer models assign these alterations to a partial decomplexation of the metal terpyridine complexes, *i.e.* signals originating from free terpyridine ligands increase upon heating. Thus, a healing mechanisms based on partial decomplexation of the cross-linking complexes is suggested. The possibility that the dissociation of ionic clusters, which are assumed to be present in this class of self-healing polymers, is also responsible for the self-healing process was investigated as well. However, such calculations on model clusters revealed relatively strong binding of the clusters, which renders reversible cluster breaking and reformation upon temperature cycling in the range up to 100 °C unlikely.

Received 7th February 2014,
Accepted 2nd May 2014

DOI: 10.1039/c4cp00562g

www.rsc.org/pccp

1. Introduction

Self-healing materials feature the ability to heal mechanical damage suffered by chemical or physical stress and to (partially) recover their mechanical properties autonomously or upon application of an external stimulus.^{1–8} Diverse applications for self-healing materials are conceivable ranging from coatings,^{9,10} over asphalt^{11,12} and to steel alloys.¹³ The basic concept behind such functional materials is the generation of a mobile phase, which can subsequently close the crack/scratch.⁴ One possibility to obtain self-healing is the utilization of (weak) reversible

interactions between specific molecular structures embedded, *e.g.*, in a polymer. In order to provide an ideally unlimited number of healing cycles, such interactions need to be highly reversible. A wide range of chemical and physical interactions fulfil these preliminary conditions, *e.g.*, based on Diels–Alder reactions,^{14,15} on disulfide bonds,^{16,17} or by means of supramolecular interactions like hydrogen bonds,^{18–21} ionic interactions,^{22,23} π – π interactions,^{24,25} guest–host interactions^{26,27} as well as metal–ligand interactions.^{28–30} Depending on the nature of the underlying healing mechanism the recovery of the initial (mechanical) properties can be achieved autonomously or by means of external stimuli, *e.g.*, by irradiation or thermal activation.

A promising approach is to utilize metal–ligand interactions; this principle is also known in nature, *e.g.*, in mussel byssus anchoring the mussel on a substrate, where self-healing based on reversible iron(III) dihydroxy-phenylalanine interactions is observed upon mechanical stress.^{31–33} Recently, a variety of self-healing terpyridine metallopolymers cross-linked by different metal salts such as iron(II) sulfate and cadmium(II) chloride, bromide, iodine and acetate have been synthesised, which can be schematically depicted as shown in Fig. 1a.^{29,30} These polymers are based on a lauryl methacrylate polymer backbone and exhibit pronounced healing properties upon thermal activation at moderate temperatures of approximately 100 °C.

^a Institute for Physical Chemistry, Friedrich Schiller University Jena, Helmholtzweg 4, 07743, Jena, Germany. E-mail: stephan.kupfer@uni-jena.de

^b Abbe Center of Photonics, Friedrich Schiller University Jena, Germany

^c Faculty of Applied Physics and Mathematics, Gdansk University of Technology, Narutowicza 11/12, 80233 Gdansk, Poland

^d Laboratory for Organic and Macromolecular Chemistry, Friedrich Schiller University Jena, Humboldtstr. 10, 07743, Jena, Germany

^e Jena Center of Soft Matter, Friedrich Schiller University Jena, Philosophenweg 7, 07743, Jena, Germany

^f Institute for Photonic Technology (IPHT) Jena, Albert-Einstein-Str. 9, 07745, Jena, Germany. E-mail: benjamin.dietzek@ipht-jena.de

† Electronic supplementary information (ESI) available. See DOI: 10.1039/c4cp00562g

‡ Both authors contributed equally to this article.

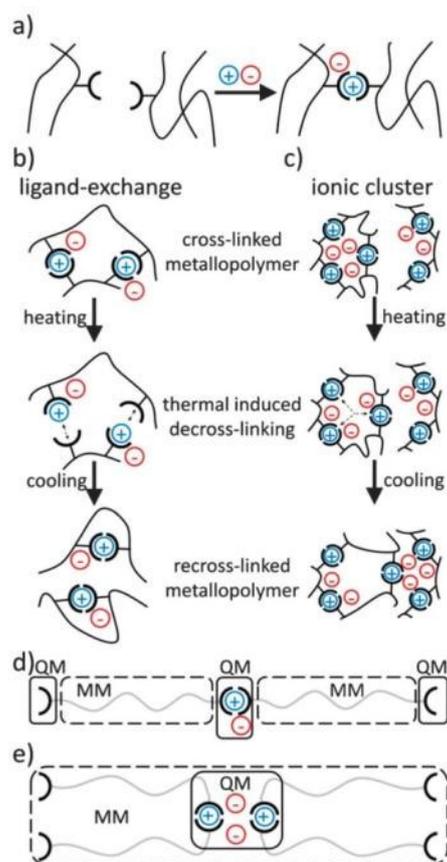


Fig. 1 Schematic representation of the reversible cross-linking process in metallopolymers. (a) Depicts the cross-linking using metal salts. (b) and (c) Illustrate the thermally induced self-healing process based on a decomplexation of the complexes (ligand-exchange; (b)) and by means of the dissociation of ionic clusters, followed by a reorganization (c). QM/MM model systems to obtain insight into the proposed healing mechanisms are shown in (d) for the ligand-exchange and in (e) for ionic clusters.

In order to improve on the self-healing properties of such materials it is of utmost importance to unravel the underlying healing mechanism at a molecular scale. One suited tool to investigate structural alterations during the thermally induced healing process is temperature dependent Raman spectroscopy.^{29,34,35} Furthermore, small angle X-ray scattering (SAXS) measurements provide an interesting opportunity to resolve nano scale structures in polymers.^{29,30,36} For example Varley and van der Zwaag proved that nano structures based on ionic clusters contribute to the healing mechanism in ionomers.^{37–40} A promising approach to investigate self-healing on a molecular level is provided by theoretical simulations aiming to describe the interactions responsible for the healing process in metallopolymers. However, the enormous size of such macromolecular systems requires the use of mixed quantum mechanical/molecular mechanical (QM/MM) simulations,^{41,42} which combine a QM description of the ligands cross-linked by metal salts and a MM description of the polymer backbone.

This work presents a joint theoretical-spectroscopic^{34,43,44} guided investigation to study the healing process of selected representative metallopolymers synthesised in the group of U. S. Schubert. Two forms of metallopolymers involving a lauryl methacrylate polymer backbone functionalized by terpyridine ligands and cross-linked by metal salts, namely iron(II) sulfate and cadmium(II) bromide, have been considered. First investigations on these metallopolymers based on SAXS measurements point to the presence of ionic clusters.^{29,30} In addition, structural changes during the healing process were monitored by temperature-dependent Raman spectroscopy for the iron(II) sulfate polymer.²⁹ Herein, the study is extended to the thermally induced self-healing in the cadmium(II) bromide analogue. Moreover, to obtain detailed insight into structural properties and to further unravel the self-healing mechanism with respect to the two concepts based on either metal–ligand interactions (see Fig. 1b) or ionic clusters (see Fig. 1c), QM/MM simulations have been performed. On the one hand, these QM/MM simulations aim at investigating the metal–ligand interactions with respect to the iron(II) sulfate and cadmium(II) bromide cross-linking. Hence, two polymer models, depicted in Fig. 1d, comprising more than 630 atoms have been constructed to mimic the metallopolymers. On the other hand, the formation of ionic clusters and a possible contribution to the self-healing mechanism is analysed by means of QM/MM simulations on a polymer models containing nearly 1300 atoms, see Fig. 1e.

The theoretical simulations provide the basis to address the origin of the alterations in the experimental Raman intensity pattern during the thermally induced healing process and, hence, to unravel the nature of the underlying self-healing mechanism.

2. Theory and computational details

Quantum chemical simulations have been performed for several metallopolymer model systems mimicking lauryl methacrylate polymers containing terpyridine ligands. The polymer models were investigated in a non-cross-linked form, *i.e.* free terpyridine ligands present, and cross-linked by iron(II) sulfate or cadmium(II) bromide. For each metallopolymer one polymer model featuring a central bisterpyridine cross-linking complex (bearing the respective counter ions), two attached methacrylate polymers and two terminal free terpyridine moieties have been created, see Fig. 2b and 3b. These polymer models have been treated using QM/MM^{41,42} as implemented in the Gaussian 09⁴⁵ program, where the central complex, the counter ions as well as the terminal terpyridine ligands have been described using density functional theory and the lauryl methacrylate at MM level of theory. The geometry, vibrational frequencies, normal coordinates and Raman intensities of the ground state were calculated with the functional B3LYP(15)^{46,47} for the QM layer and with the universal force field (UFF) for the MM layer. The B3LYP(15) functional is based on the B3LYP^{48,49} functional and combines 15% of exact exchange, 58.5% of non-local B88 exchange and the LYP correlation. The 10-electron non-relativistic effective core potential MDF-10⁵⁰ was used with its

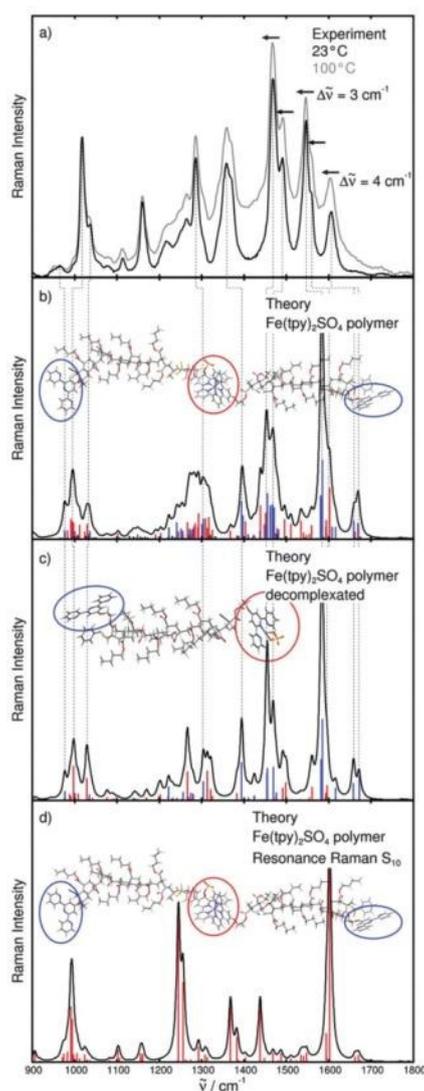


Fig. 2 Raman spectra of the iron(II) sulfate metallopolymer. (a) Depicts temperature-dependent Raman spectra at 23 and 100 °C along with the thermally induced bathochromic shifts of the intensity pattern. (b) and (c) Display calculated Raman spectra at the QM/MM level of theory using B3LYP(15) with the 6-31G(d) basis set and the universal force field for two polymer models. Vibrational modes centered at the bisterpyridine–iron(II) complex are shown in red and modes of the free terminal terpyridine moieties are shown in blue. (d) Features the simulated RR spectrum calculated at an excitation wavelength of 647 nm using the excited state gradients, transition dipole moment and excitation energy of the S_{10} state.

basis set for the iron atom, that is, 3s, 3p, 3d and 4s electrons are treated explicitly, whereas the two first inner shells are described by the core pseudopotential. For the cadmium atom the non-relativistic MWB-28 core potential was applied (treating the 4s, 4p, 4d and 5s electrons explicitly). The 6-31G(d) double- ζ basis set⁵¹ was employed for the ligands, which was shown to be adequate for

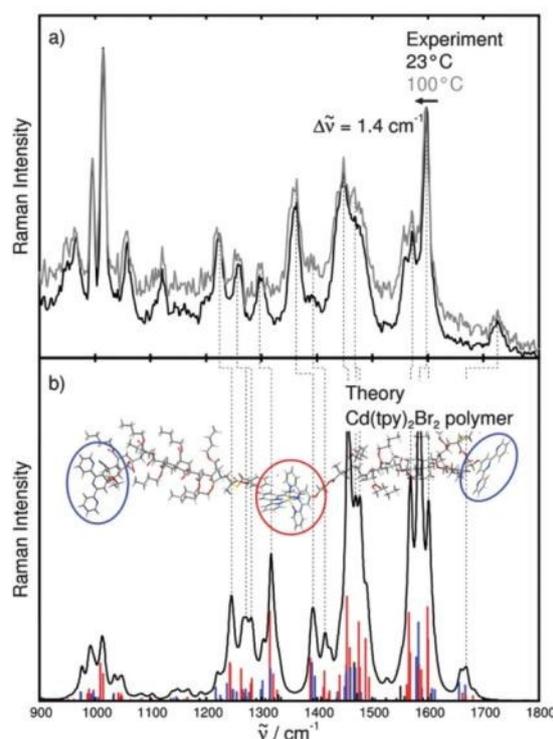


Fig. 3 Raman spectra of the cadmium(II) bromide metallopolymer. (a) Depicts temperature-dependent Raman spectra at 23 and 100 °C along with the thermally induced bathochromic shift of the intensity pattern. (b) displays calculated Raman spectrum at the QM/MM level of theory using B3LYP(15) with the 6-31G(d) basis set and the universal force field for the polymer model. Vibrational modes centered at the bisterpyridine–cadmium(II) complex are shown in red and modes of the free terminal terpyridine moieties are shown in blue.

the calculation of Raman spectra.⁵² To correct for the lack of anharmonicity and the approximate treatment of electron correlation, the harmonic frequencies were scaled by the factor 0.97.⁵³ To gain insight into the absorption properties, the 150 lowest singlet excited states have been calculated for both polymer models in gas phase as well as in acetonitrile using the polarizable continuum model.⁵⁴ Furthermore, resonance Raman spectrum of the iron(II) sulfate metallopolymer was calculated using an excitation wavelength of 647 nm, detailed information concerning the applied theory for calculating RR intensities is provided in ref. 55–57 and therein.

The model systems we used for calculating the Raman spectra of the metallopolymer are constructed based on the desired repeating unit of the experimental target structure and represent thus the smallest possible unit of the polymer, containing the necessary ingredients for a mechanistic investigation of self-healing: (i) the polymer backbone, assumed to be of minor importance for the self-healing, thus described with lower level in theory; (ii) the complexed metal, being of vital importance for the mechanism and thus described with DFT

level of theory; (iii) free ligand attached to the polymer backbone, for reasonable comparison with the complexed metal described on the same level of theory. While this model does certainly not provide the full and most accurate description of the actual experimental polymer, we believe that it mimics the complex system reasonably well.

In order to study interactions within ionic clusters, composed by the positively charged cross-linking complexes and the negatively charged counter ions, two extended polymer models have been created. These models comprise approximately 1300 atoms, in which two of the previously described models have been cross-linked by means of the respective counter ions. To get insight into the thermodynamics of such clusters, relaxed potential energy surfaces (PESs) have been calculated with respect to the distance between one complex and the bridging counter ion of the other complex (R , see Fig. S1 of the ESI†). In order to reduce the computational demand of these calculations, the MM layer was extended and contains in addition to the methacrylate polymer also the four terminal terpyridine ligands. The partial geometry optimizations along the coordinate R have been carried out using the same functional, basis set, force field, and core potential as stated above.

3. Experimental methods

Temperature-dependent Raman spectra were recorded using various experimental setups, either a LabRAM HR800 Raman spectrometer (Horiba-Jobin Yvon) or a confocal Raman microscope (model CRM 2000, WITec), both working in backscattering geometry. The LabRAM spectrometer was equipped with a confocal aperture and an upright microscope (Olympus BX40). The Raman excitation laser at 647 nm was provided by a krypton ion laser (Innova 302C, Coherent). Laser power at the sample was < 2 mW. The slit width was set to 100 μm , the pinhole either to 500 μm or to 1000 μm and the scattered light was detected by a liquid-nitrogen-cooled charge coupled device (CCD). The spectral resolution was 2 cm^{-1} for the grating 1800 mm^{-1} . Excitation at 785 nm for the WITec Raman microscope was provided by a single mode diode laser (< 10 mW laser power at the sample). The laser radiation was coupled into a Zeiss microscope and focused onto the sample through a microscope objective (Zeiss EC Epiplan Aplanat 50 \times /0.95 NA). The spectral resolution was 6 cm^{-1} for the grating 600 mm^{-1} . The sample temperature was adjusted using a Linkam stage (model LTS 350), which was fixed under the microscope objective.

4. Results

The temperature-dependent Raman spectra of the polymer cross-linked by iron(II) sulfate and cadmium(II) bromide are depicted in Fig. 2a and 3a, respectively. Both polymers feature characteristic shifts of the Raman bands in the region between 1450 and 1650 cm^{-1} towards lower wavenumbers upon heating. However, in case of the iron(II) sulfate metallopolymer the shifts

are more pronounced (approximately 3 and 4 cm^{-1}) than for the cadmium(II) bromide analogue, where a band shift of 1.4 cm^{-1} is observed. The band shifts are verified by repeatedly measuring the band position at low and high temperature and detecting the maximum of the bands. In comparison to other vibrational resonances which are not affected by heating, the shift was reproducible, always towards lower frequencies and is therefore not due to the limited accuracy of the measurements. To address the origin of the observed spectral shifts with respect to the self-healing properties of the materials, we will discuss in the following two healing mechanisms: the first one is based on a thermal decomplexation of the cross-linking terpyridine complexes, while the second one involves the cleavage of ionic clusters formed by means of the bisterpyridine-iron(II) and bisterpyridine-cadmium(II) complexes and their anionic counter ions, namely sulfate and bromide.

4.1 Decomplexation

4.1.1 Iron(II) cross-linked polymer. The ground state equilibrium geometry of the iron(II)-cross-linked polymer depicted in Fig. 2b, optimized at the QM/MM level of theory, features a linear structure, where the iron-terpyridine complex is located at the center, and the free terpyridine ligands are oriented outwards. A subsequent vibrational analysis proved that the optimized equilibrium geometry is a minimum of the electronic ground state potential energy surface. In contrast to the terpyridine ligands of the iron(II) complex, the uncoordinated ligands feature a *trans*-configuration of the pyridyl moieties due to electrostatic repulsion of the nitrogen atoms. The structure of the central bisterpyridine-iron(II) fragment is slightly distorted by virtue of the sulfate counter-ion binding to the central pyridyl ring of one terpyridine ligand. This induces a pronounced sp^3 -character of the carbon atom connecting the sulfate and in consequence a loss of planarity is observed for this terpyridine ligand. For the carbon-oxygen(sulfate)-bond a length of 1.450 Å was obtained. In case of the nitrogen-iron bonds values of 1.880 (central pyridyl-moiety), 1.988 and 2.001 Å (terminal pyridyl-moieties) were calculated for the planar terpyridine ligand. Due to the electronic and structural alterations induced by the sulfate ion, the corresponding nitrogen-iron bond lengths of the other terpyridine ligand are slightly stretched by approximately 0.025 Å.

The vibrational analysis of the iron(II) metallopolymer allowed to rationalise the temperature-dependent Raman spectra, which reflect structural changes upon heating and, hence, during the self-healing process. In Fig. 2a the Raman scattering intensity pattern is depicted exemplarily for the minimum and the maximum temperatures of 23 and 100 °C. An overall intensity increase upon heating is accompanied by a bathochromic shift of two prominent Raman features, *i.e.*, at 1547 cm^{-1} by 3 cm^{-1} and at 1607 cm^{-1} by 4 cm^{-1} towards lower frequency. The detected shift is reproducible and clearly resolvable within the accuracy of the measurement (see Fig. S2a of the ESI†). The Raman spectrum calculated by means of QM/MM (B3LYP(15)/UFF) illustrated in Fig. 2b is composed of modes of the free terpyridine ligands as well as of the iron(II)-terpyridyl complex,

while the lauryl methacrylate polymer does not contribute to the spectrum as the MM region is not assigned any polarizability.

As can be seen from Fig. 2a and b, the dominant experimentally observed Raman bands in the 1450–1700 cm^{-1} region can be assigned to modes of the free ligand and the iron(II)-terpyridyl complex. This band assignment is also in agreement with the measured spectra (Fig. S5, ESI†).⁵² The calculated spectrum, Fig. 2a and b, show more pronounced deviations in the 900–1450 region from the experiment. This can be ascribed to the neglect of Raman bands originating from the polymer backbone.

Of particular interest for the investigation of the self-healing mechanisms are the vibrational modes contributing to the Raman spectrum in the range of 1450 and 1620 cm^{-1} , where the bathochromic shifts have been observed experimentally. On the basis of the frequencies and relative intensities the experimental Raman bands localized at 1468, 1490, 1546, 1558 and 1606 cm^{-1} can be assigned to the calculated Raman bands centered at 1453, 1467, 1584, 1601 and 1669 cm^{-1} (see Fig. 2a and b). This corresponds to a mean absolute deviation (MAD) of 21 cm^{-1} , which is typical at this level of theory.⁵³ An analysis of the vibrational modes showed that modes localized at the free ligands are lower in energy than the corresponding modes of the complexed terpyridine ligand. This can be seen exemplarily by means of the calculated band structure centered around 1669 cm^{-1} , where the intensity pattern is mainly governed by five modes 1450, 1452, 1461, 1462, and 1463. The mode 1450 at 1658.7 cm^{-1} centered at a free terpyridine ligand corresponds to the complexed terpyridine mode 1452 at 1661.7 cm^{-1} . The mode at 1668.7 cm^{-1} is located at the free terpyridine ligand (mode 1461), the corresponding modes of the complexed ligand are found at 1669.8 and 1670.5 cm^{-1} (mode 1462 and 1463), respectively. The slight bathochromic shift is caused by the distortion of the equilibrium geometry of one complexed terpyridine ligand by virtue of the sulfate counter ion. Hence, the mode of the free ligand is bathochromically shifted by about 0.7 to 3 cm^{-1} with respect to the bisterpyridine-iron(II) complex. For other bands, e.g., correlated to the experimental Raman bands at 1546 and 1558 cm^{-1} , even more pronounced shifts of approximately 12.5 cm^{-1} (with respect to the free terpyridine modes 1415 and 1416 and the similar modes in the complex 1422 and 1424) and 13.9 cm^{-1} (for the free terpyridine modes 1417 and 1418 and the complexed terpyridine modes 1425 and 1428) have been calculated. More detailed information concerning the vibrational modes is given in Table 1 and Fig. S3 (ESI†).

The consistent bathochromic shift of the vibrational frequencies of the free terpyridine with respect to the bisterpyridine-iron(II) complex indicates to thermal decomplexation. In this case the cross-linking of the metallopolymer is (partially) suspended upon heating and the Raman spectrum is dominated by vibrational modes of the free terpyridine ligands. In order to study the ligand exchange mechanisms further, QM/MM simulations have been performed for a partially dissociated complex, where one terpyridine ligand is removed and the iron(II) is bound to one terpyridine and the sulfate ion; the structure as well as the simulated Raman spectrum is illustrated in Fig. 2c.

Table 1 Assignment of the calculated vibrational frequencies (cm^{-1}) and relative Raman activities ($\text{\AA}^4 \text{amu}^{-1}$) for the iron(II) sulfate cross-linked metallopolymer as well as its semi-decomplexated form

Assignment	Iron(II) sulfate metallopolymer			Iron(II) sulfate semi-decomplexed metallopolymer		
	Mode $\tilde{\nu}/\text{cm}^{-1}$	$I/\text{\AA}^4 \text{amu}^{-1}$		Mode $\tilde{\nu}/\text{cm}^{-1}$	$I/\text{\AA}^4 \text{amu}^{-1}$	
Free tpy <i>asym</i>	1415	1581.3	335	716	1581.8	305
Free tpy <i>asym</i>	1416	1581.7	309	—	—	—
Free tpy <i>sym</i>	1417	1584.9	593	717	1585.0	602
Free tpy <i>sym</i>	1418	1585.0	605	—	—	—
Complex tpy <i>asym</i>	1422	1593.5	94	720	1592.9	57
Complex tpy <i>asym</i>	1424	1594.5	200	—	—	—
Complex tpy <i>sym</i>	1425	1595.3	42	721	1595.9	113
Complex tpy <i>sym</i>	1428	1602.3	394	—	—	—
Free tpy <i>sym</i>	1450	1658.7	144	733	1658.3	127
Complex tpy <i>sym</i>	1452	1661.7	58	—	—	—
Free tpy <i>sym</i>	1461	1668.7	123	—	—	—
Complex tpy <i>sym</i>	1462	1669.7	65	739	1671.7	185
Complex tpy <i>sym</i>	1463	1670.6	113	—	—	—

Comparing the frequencies of the respective modes localized at the free terpyridine (716, 717, and 733) as well as on the complexed ligand (720, 721, and 739) yields only minor variation with respect to their analogues of the afore described polymer model (vibrational modes are visualized in Fig. S4, ESI†). However, the Raman activity of the complexed modes decreases from the bisterpyridine complex (modes 1422, 1424, 1425, 1428, 1452, 1462, and 1463) upon partial decomplexation (modes 720, 721, and 739), see Table 1, while the Raman activities of the free terpyridine ligands are almost unaffected. Hence, the enveloping Raman bands between 1450 and 1620 cm^{-1} are shifted to slightly lower frequencies compared to the bisterpyridine-iron(II) metallopolymer model (Fig. 2b).

In order to evaluate the robustness of the applied computational approach, effects of the XC functional and the basis set on the vibrational frequencies and Raman intensities have been investigated by means of the standard B3LYP functional as well as the 6-311(d) triple- ζ basis set. These simulated Raman spectra show only minor deviations from the spectra obtained by B3LYP(15) and the 6-31G(d) double- ζ basis set, while the qualitatively picture including the red-shift of the free ligand centered modes with respect to the analogous modes of the complex is preserving (see Table S4, Fig. S5 and S6 of the ESI†).

Undoubtedly, the calculated vibrational spectra differ on an absolute scale from the experimentally obtained ones. However, *relative shifts* in the calculated spectrum can be very well analyzed. Within the same method and the same basis set, changes in the spectrum induced by modest, stepwise deformation of the geometry – and here in particular the relative coordinate representing the distance between the metal center and the ligand sphere – can be extracted. With our mechanistic model systems, we can contrast the relative shifts in the spectrum for the two mechanisms of interest and compare them to the experimentally observed relative shifts. This allows us to provide a plausible explanation of the experimentally observed shifts with respect to a thermal decomplexation by

comparing the vibrational frequencies and intensities of the complexed terpyridine ligand with the analogous vibrational modes of the free ligand (formed upon heating).

The absolute frequency of vibrational modes is dependent on the applied computational method (XC functional and basis set). These effects were largely studied in the literature and were shown to be quite systematic.^{53,60} Therefore, the frequency shifts can be obtained with higher accuracy than the absolute frequencies. However, the relative shifts might depend on the theoretical method as well. In order to address this issue, we have performed a large number of additional calculations, varying both, the basis set and the functional used in the DFT. We calculated the Raman spectra of all three model systems (iron(II) sulfate metallopolymer, iron(II) sulfate semi-decomplexed metallopolymer, and cadmium(II) bromide metallopolymer) in order to address effects of the basis set as well as of the functional. It was found for all intense modes in the frequency region between 900 and 1800 cm^{-1} of the three model systems that the increase from double to triple- ζ basis set (6-311G(d)) leads to a bathochromic shift of the vibrational frequencies of approximately 10 cm^{-1} , while an increase of the exact exchange in the XC functional from 15 (B3LYP(15)) to 20% (standard B3LYP) leads to a hypochromic shift of approximately 10 cm^{-1} .

The shifts of the modes centered at the complex and the free ligand are preserved, while the frequency of the free ligand modes are found red-shifted to the respective modes localized on the complexed ligand, independent of the method or the basis set.

The theoretical investigation of the iron(II) metallopolymer indicates a self-healing mechanism based on a (partial) decomplexation of the cross-linking complexes. This is further supported by Raman spectroscopy on the terpyridine and bisterpyridine-iron(II) monomers (see Fig. S8 of the ESI[†]), where a bathochromic shift of 6 cm^{-1} was observed for the Raman features of the terpyridine monomer (1602 cm^{-1}) with respect to the complex (1608 cm^{-1}).

In order to investigate possible resonance enhancement in the Raman spectra, absorption and resonance Raman (RR) spectra were calculated for iron(II) sulfate metallopolymer by means of QM/MM simulations. In the simulation of the absorption spectrum, solely excitations of the free ligands and the complex have been taken into account by means of TDDFT. The calculated absorption spectrum is in good agreement with the experimental spectrum (in acetonitrile), see Fig. 4a. The experimental absorption band centered at 555 nm was found to stem from an intra-ligand excitation (S_4) of the iron(II)-terpyridyl-complex. The excitation energy of the S_4 state is slightly underestimated by 0.05 eV with respect to the experimental absorption maximum. For the measurement of the Raman spectra an excitation wavelength of 647 nm was used, hence, a resonance enhancement due to an excited state is unlikely. Since the Raman signals are measured in solid-state, which consists of a less polar environment, the absorption was further simulated without applying the effects of solvation, see Fig. 4b. Consequently, the bright intra-ligand state located at the bisterpyridine-iron(II) complex is lowered from 2.18 (S_4 , Fig. 4a) to 2.12 eV (S_{10} , Fig. 4b).

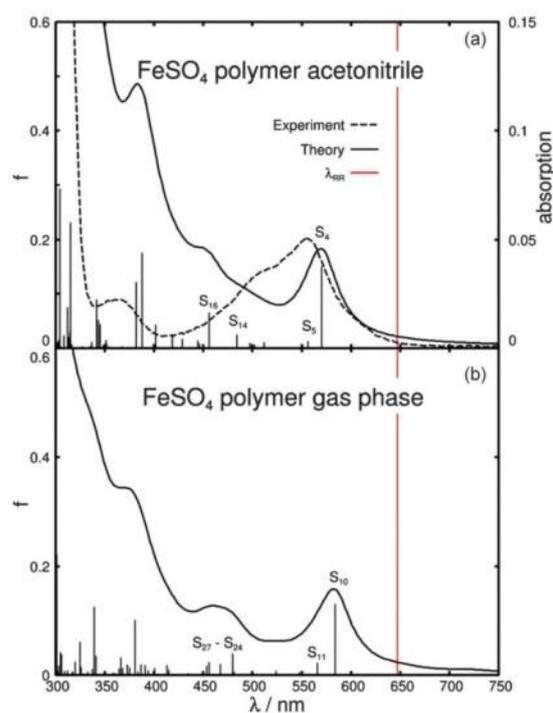


Fig. 4 Absorption spectra of the iron(II) sulfate metallopolymer. (a) Shows the experimental and simulated UV-vis spectra in acetonitrile, the simulations were performed at the QM/MM level of theory using B3LYP(15) with the 6-31G(d) basis set and the universal force field. (b) Depicts the simulated absorption in gas phase. The red line corresponds to the applied excitation wavelength of the Raman measurements.

These results indicate that effects due to resonance enhancement are of minor importance.

In order to fully exclude a resonance enhancement at the excitation wavelength of 647 nm, the resonance Raman (RR)⁵⁵ spectrum using the excited state gradients of the S_{10} (bright $\pi\pi^*$ state at 555 nm) have been calculated using the QM/MM model system with the bisterpyridine-iron(II) complex in the center and two free terminal terpyridine ligands. The simulated RR intensity pattern of Fig. 2d shows, as expected from the $\pi\pi^*$ nature of the S_{10} state, exclusively intense modes localized at the bisterpyridine-iron(II) complex. The poor agreement between the calculated RR intensities and the experimental Raman spectra of Fig. 2a and d indicates a non-resonant scattering process at 647 nm.

4.1.2 Cadmium(II) cross-linked polymer. Analogous to the metallopolymer cross-linked by iron(II) sulfate, a QM/MM model system was constructed, consisting of a DFT layer comprising the central bisterpyridine-cadmium(II) complex, the two bromide counter-ions attached to each of the complexed ligands, and the terminal free terpyridine ligands and a MM layer describing the lauryl methacrylate polymer. The equilibrium structure, confirmed by a subsequent vibrational analysis, was found to be very similar to the structure of the

iron(II) sulfate cross-linked polymer. However, for the cadmium complex a less compact structure has been obtained, *i.e.* the calculated cadmium–nitrogen bond lengths are within 2.320 and 2.334 Å for the central pyridyl-moiety and of 2.395 and 2.405 Å for the terminal pyridyl-moiety. These bonds are significantly longer than the corresponding iron–nitrogen bonds. In addition, the octahedral ligand sphere spanned by the terpyridine shows a pronounced distortion since the terpyridine-cage is undersized for coordination of cadmium(II). Hence, the bisterpyridine–cadmium(II) complexes are assumed to be less stable than the bisterpyridine–iron(II) complexes, which is reflected in the calculated frequencies of the normal modes of the metal–nitrogen bonds.^{58,59} Indeed, the cadmium–nitrogen modes are found in the range of 424 to 575 cm⁻¹, whereas the respective modes of the iron–nitrogen bonds are calculated in the range of 554 and 600 cm⁻¹.

Structural alterations occurring during the self-healing process have been investigated (analogous to the iron(II) sulfate polymer) for the metallopolymer cross-linked by cadmium(II) bromide. For the cadmium(II) bromide polymer, only a slight bathochromic shift of 1.4 cm⁻¹ was observed for the Raman band at 1597 cm⁻¹ (see Fig. 3a and Fig. S2b, ESI[†]), and the studied temperature-dependent evolution of the intensity pattern was found to be fully reversible. The evaluation of the Raman features by means of QM/MM simulations, depicted in Fig. 3b, shows a reasonable agreement with experiment, in the region between 1200 and 1800 cm⁻¹. The intensity pattern in this spectral region is dominated by terpyridine modes localized at the bisterpyridine–cadmium(II) complex while the vibrational modes of the free terminal ligands are less intense, see Table 2 and Fig. S9 (ESI[†]). Closely related to the findings of the iron(II) metallopolymer discussed in Section 4.1.1, the frequencies of the normal modes of the free terpyridine ligand are bathochromically shifted with respect to the corresponding modes of the cadmium(II) complex. This can be seen exemplarily for the

simulated band structure at 1670 cm⁻¹, where the modes of the free ligands (1441 and 1453) are calculated at 1658.1 and 1669.2 cm⁻¹ and the corresponding modes of the complex (1444 and 1454) are calculated at 1663.7 and 1670.2 cm⁻¹. Similar shifts of, *e.g.*, 4.7 and 5.8 cm⁻¹ have been obtained for the simulated Raman band at 1585 cm⁻¹, which is assigned to the experimental band at 1597 cm⁻¹ featuring a bathochromic shift of 1.4 cm⁻¹ upon heating. This band structure is correlated to several intense modes of the cadmium(II) complex (1381, 1384, 1411, 1412, 1414, 1415, 1420, and 1421) and the four intense modes of the free terpyridine ligands (1406, 1407, 1409, and 1410) found at 1584.9 and 1585.1 cm⁻¹. Hence, the bathochromic shift of 1.4 cm⁻¹ observed upon heating for the Raman band at 1597 cm⁻¹ can be explained by means of these four intense modes of the free ligand. In addition, all other vibrational modes of the free terpyridine are considerably less intense, which is consistent with the experimental observation that a shift was exclusively observed for this band. Reason for the less pronounced experimental shift, compared to the iron(II) metallopolymer, is provided by the calculated Raman activities (see Tables 1 and 2). The intensity of the free ligand is almost identical in both the iron(II) and the cadmium(II) metallopolymers, however, the intensities of the complexed terpyridine ligands are much higher for the bisterpyridine–cadmium(II). Accordingly, the measured Raman spectrum of the isolated bisterpyridine–cadmium(II) monomer exhibits a band at 1602 cm⁻¹, while the terpyridine monomer features also a band localized at 1602 cm⁻¹ (see Fig. S8, ESI[†]). This finding is consistent with the observation for the metallopolymer, where merely a shift of 1.4 cm⁻¹ was found for the Raman band at 1597 cm⁻¹. Analogous to the iron(II) metallopolymer variations of the computational method (XC functional and basis set) lead merely to small deviations of the absolute frequency, however, the relative shifts of the complexed and the free ligands are preserved, see Table S10 and Fig. S11 and S12 in the ESI[†].

To exclude a resonance enhancement at the excitation wavelength of 785 nm, the absorption spectrum of the cadmium(II) bromide metallopolymer was simulated. The calculated spectrum, depicted in Fig. S12 of the ESI[†] features two absorption bands in the visible range at approximately 650 and 480 nm. Hence, a resonance enhancement seem unlikely at the given excitation wavelength.

4.2 Dissociation of ionic clusters

As shown recently by SAXS measurements, the metallopolymers studied form nano structures, which are presumably due to the presence of ionic clusters, where several terpyridine complexes are connected by attractive interactions with anionic counter ions, *e.g.*, sulfate and bromide.^{29,30} In order to obtain insight into the intrinsic structure and energies of these ionic clusters, quantum chemical calculations have been performed. Therefore, the size of the model systems for both the iron(II) sulfate and the cadmium(II) bromide cross-linked polymer had to be (at least) doubled, while the two complexes have been placed on top of each other, twisted by 90° and bridged by a counter ion, see Fig. 5b and 6b. To investigate interactions of these bridged complexes, relaxed PES have been calculated along the

Table 2 Assignment of the calculated vibrational frequencies (cm⁻¹) and relative Raman activities (Å⁴ amu⁻¹) for the iron(II) sulfate cross-linked metallopolymer as well as its semi-decomplexed form

Cadmium(II) bromide metallopolymer			
Assignment	Mode	$\tilde{\nu}/\text{cm}^{-1}$	$I/\text{Å}^4 \text{amu}^{-1}$
Complex tpy sym	1381	1568.0	668
Complex tpy sym	1384	1569.2	366
Free tpy asym	1406	1581.3	333
Free tpy asym	1407	1581.7	318
Free tpy sym	1409	1584.9	593
Free tpy sym	1410	1585.1	586
Complex tpy asym	1411	1586.0	60
Complex tpy asym	1412	1586.3	274
Complex tpy sym	1414	1590.5	235
Complex tpy sym	1415	1591.0	99
Complex tpy asym	1420	1600.9	701
Complex tpy asym	1421	1602.1	469
Free tpy asym	1423	1608.7	96
Free tpy asym	1426	1614.3	89
Free tpy sym	1441	1658.1	143
Complex tpy sym	1444	1663.6	62
Free tpy sym	1453	1669.2	123
Complex tpy sym	1454	1670.2	41

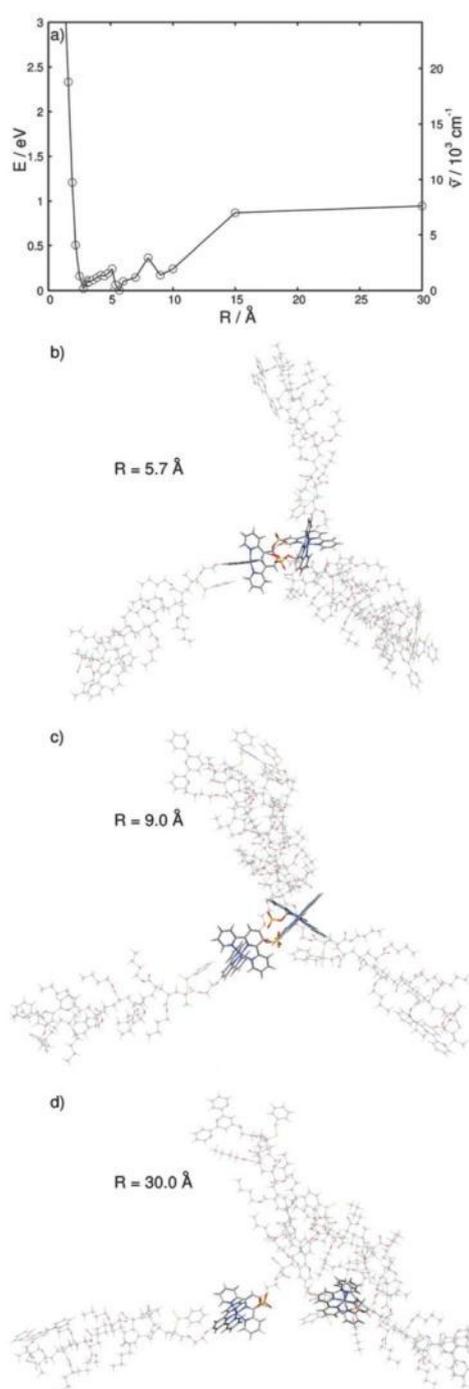


Fig. 5 Panel (a) depicts the calculated relaxed PES of the iron(II) sulfate metallopolymer at the QM/MM level of theory using B3LYP(15) with the 6-31G(d) basis set and the universal force field with respect to the distance R (between one complex and the bridging counter ion) describing the cleavage of the ionic cluster up to $R = 30$ Å. (b–d) depict the global minimum of the PES ($R = 5.7$ Å), the local minimum at $R = 9.0$ Å, and the opened cluster at $R = 30$ Å.

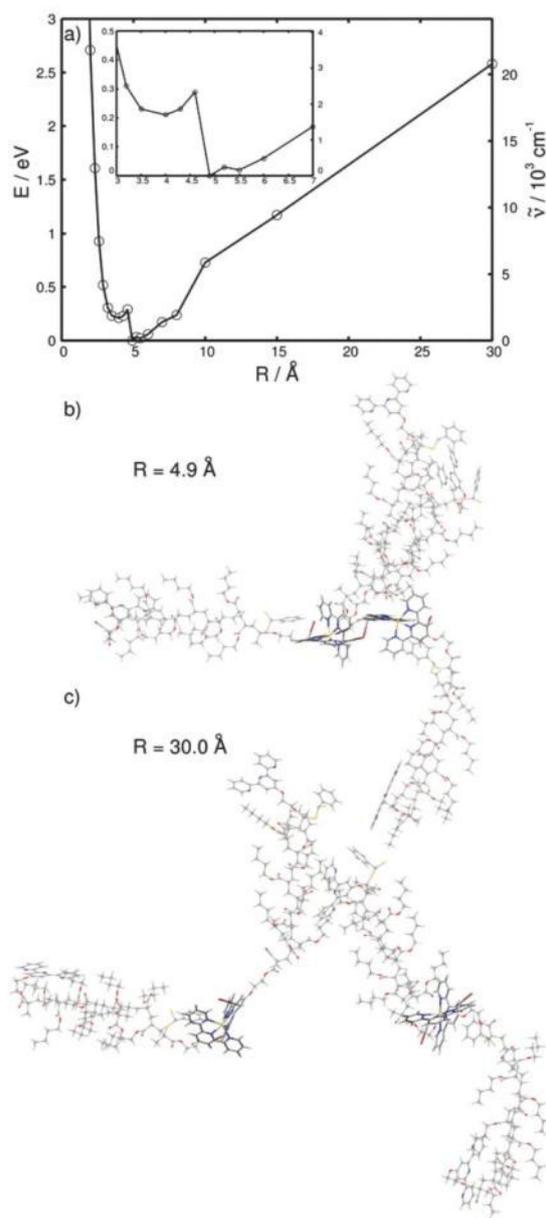


Fig. 6 Panel (a) depicts the calculated relaxed PES of the cadmium(II) bromide metallopolymer at the QM/MM level of theory using B3LYP(15) with the 6-31G(d) basis set and the universal force field with respect to the distance R (between one complex and the bridging counter ion) describing the cleavage of the ionic cluster up to $R = 30$ Å. (b) and (c) Depicts the global minimum of the PES ($R = 4.9$ Å) and the opened cluster at $R = 30$ Å.

coordinate R describing the distance between one of the complexes and the bridging counter ion. This way a prediction of a thermal dissociation along R is obtained. Considering the large size of the model, containing almost 1300 atoms, the MM region was extended to include the polymer backbone as well as the free

ligands, which are not involved in the self-healing scheme based on ionic clusters. For describing interactions between the complexes, the QM region was designed to comprise the two metal complexes and all counter ions as depicted in Fig. 1e.

4.2.1 Iron(II) cross-linked polymer. In order to study the attractive interactions between the bisterpyridine-iron(II) complexes and the sulfate counter ions in the metallopolymer, partial geometry optimizations along the coordinate R at the QM/MM level of theory have been carried out using the enhanced polymer model depicted in Fig. S1f of the ESI.† The PES along R , illustrated in Fig. 5a, was calculated starting from the fully relaxed equilibrium structure at $R = 5.7$ Å, displayed in Fig. 5b. From this structure R was stepwise decreased/increased yielding the next point of the PES. Two further minima at 3.3 (0.09 eV) and 9.0 Å (0.17 eV) have been obtained, which are separated from the global minimum at 5.7 Å by barriers of 0.24 and 0.37 eV, respectively. The presence of these three minima is related to the fact that both sulfate counter ions are localized between the bisterpyridine-iron(II) complexes, hence, increasing R for one sulfate ion leads to an enhanced interaction between the complexes and the other sulfate ion. However, after the minimum at 9.0 Å, where only one sulfate counter ion is bridging the iron(II) complexes (see Fig. 5c), the electronic ground state energy rises rapidly to 0.87 eV at $R = 15$ Å. Increasing R further to 30 Å only leads to a slight rise of the ground state energy to 0.95 eV, see structure in Fig. 5d. At this geometry the bisterpyridine complexes are isolated, while there are still interactions between the polymer backbones. Thus, a further increase of the energy is expected before the two metallopolymer are entirely separated.

SAXS measurements indicated the presence of nano structures, *e.g.*, ionic clusters. This finding is corroborated by the QM/MM simulations on the iron(II) sulfate cross-linked metallopolymer, which also point to the presence of stable ionic clusters. In fact the attractive interactions between the cationic bisterpyridine-iron(II) complexes and the sulfate counter ions lead to very stable structures, as shown here for the iron(II) sulfate ionic cluster model. A healing based on the complete dissociation of the clusters can be excluded, because the calculations indicate that in case of the iron(II) metallopolymer energies of almost one eV are necessary for a significant opening of the model clusters, which is not possible at the given temperature of 100 °C.

4.2.2 Cadmium(II) cross-linked polymer. The calculation of the relaxed PES along the coordinate R has been repeated for the cadmium(II) metallopolymer. The starting point for the PES shown in Fig. 6a was the fully relaxed equilibrium structure depicted in Fig. 6b. In this equilibrium structure, where two bromide ions are attached to each complex, the global minimum of the calculated PES is at $R = 4.9$ Å. A second minimum was found at $R = 4.0$ Å (0.21 eV), where one terpyridine complex bears three bromide ions and the other one only one. These minima are separated by barriers of 0.29 and 0.08 eV, respectively. Enlarging R from the global equilibrium structure to about 7 Å leads only to a slight increase of the electronic ground state energy, however, for distances larger than 7 Å the energy increases rapidly and reaches a value of 2.58 eV at 30 Å. Interestingly, the dissociation of the

bridged complexes takes place while the attractive interactions of the polymer are still dominant, see Fig. 6c.

In addition to the optimized clew conformation of the cadmium metallopolymer shown in Fig. 6b, a conformation bearing orthogonally oriented methacrylate moieties has been optimized (see Fig. S13b, ESI†). Hence, the dissociation energy is exclusively governed by the interactions of the bridged complexes. The PES calculated by means of the optimized metallopolymer features only one minimum at $R = 4.3$ Å, see Fig. S13a of the ESI.† Analogous to the previously described clew conformation, the region of the PES between 3.8 and 7.0 Å features no significant alterations of the ground state energy. However, further increasing R leads to a rapid energy increase. Since dissociation involves in this conformation only the bridged complexes the dissociation energy is already achieved at 15 Å (0.44 eV); and further stretching to 30 Å (0.44 eV, see structure in Fig. S13c, ESI†) does not affect the ground state energy further.

Due to strong interactions of the bisterpyridine-cadmium(II) complex bridged by bromide and of the polymer, a self-healing mechanism based on the opening and subsequent recross-linking of ionic clusters to occur at 100 °C appears highly unlikely according to the quantum chemical simulations. This is the case for both the clew conformation, where interactions of the complexes as well as of the polymer are present, as well as for the orthogonal conformation, where interactions of the complexes are predominant.

5. Conclusions

The thermally induced self-healing mechanism in lauryl methacrylate metallopolymer cross-linked by iron(II) sulfate and cadmium(II) bromide was studied by a joint theoretical-spectroscopic investigation. Experimentally, temperature-dependent Raman spectroscopy was applied to investigate structural alterations during the healing process, whereas reversible bathochromic shifts of Raman bands associated with a structural alteration upon heating have been observed for both metallopolymer. However, Raman spectroscopy alone is unable to provide detailed insight on the thermally induced structural changes of the polymer. In order to investigate these structural alterations and to unravel the underlying self-healing mechanism for this class of metallopolymer on a molecular level, theoretical methods were employed. Hence, QM/MM simulations have been carried out with respect to two scenarios: (i) a thermally activated decomplexation of the metal-terpyridine cross-linking and a subsequent new cross-linking upon cooling and (ii) a thermally induced cleavage of present ionic clusters formed by several complexes interacting with the negatively charged counter ions, *e.g.*, sulfate and bromide. The existence of ionic clusters for these metallopolymer was deduced from SAXS measurements. However, such measurements do not provide molecular information and energetics with respect to a contribution of such nanostructures to the self-healing properties.

Appropriate QM/MM model systems were constructed, containing one bisterpyridine-iron(II) or bisterpyridine-cadmium(II)

with the respective counter ion (sulfate and bromide) and two free terpyridine ligands linked by a methacrylate based polymer to the central metal complex. The focus was set on the quantum chemical description of the complex and the free ligands by means of DFT applying a functional based on B3LYP containing 15% of exact exchange, while the polymer was described by molecular mechanics. Subsequently, insight into the Raman bands could be obtained by QM/MM simulations of the vibrational frequencies and the Raman scattering intensities. The decent agreement between the theoretical and the experimental intensity pattern, in case of both metallopolymers, is encouraging since it shows that the applied QM/MM models are appropriate to study cross-linked metallopolymers. The simulations on the iron(II) sulfate as well as the cadmium(II) bromide polymers exhibit a slight bathochromic shift of the vibrational modes of the bisterpyridine-metal complex with respect to the free terpyridine ligands indicating a thermally induced decomplexation of the cross-linking complexes. Further simulations on a semi-decomplexated model, where the iron(II) ion is stabilized by merely one terpyridine moiety and the sulfate counter ion, present also bathochromic shifts of the Raman features in the range of the experimentally measured shifts (3 to 4 cm^{-1}). These relative shifts of the analogous metal complex free ligand centered vibrational modes are presumed upon variation of both the XC functional as well as of the basis set and, thus supports the assumption that the healing process is correlated to a decomplexation of the cross-linking complexes. This assumption is supported by Raman measurements on the isolated ligands and metal complexes leading to very similar shifts of the Raman bands in iron(II) terpyridine (6 cm^{-1}) and cadmium(II) bromide (0 cm^{-1}) with respect to the free terpyridine ligand.

The second mechanisms discussed for the self-healing of metallopolymers is based on reversible interactions between the complexes and the anionic counter ions. Thus, extended model systems for both metallopolymers were designed for QM/MM simulations in order to study the properties of such ionic clusters. Of particular interest was the dissociation energy of such ionic clusters since self-healing is observed at 100 °C.

The calculation of relaxed PESs with respect to the cleavage of two complexes bridged by a counter ion (as a model system for theoretical studies on a smallest possible ionic cluster) exhibit two minima, correlated to molecular structures with an imbalanced and an even distribution of the counter ions on the complexes. The global minima with an even distribution of the counter ions between the complexes were found to be energetically very stable: stretching the complexes up to 30 Å requires an energy of 0.95 and 2.58 eV for the iron(II) sulfate and the cadmium(II) bromide cross-linked polymers, respectively. Hence, a significant thermally induced dissociation of the very stable ionic clusters and a subsequent formation of a new cross-links seems highly unlikely at temperatures of about 100 °C (approximately 0.03 eV) based on the results of the quantum chemical study. Thus, the applied quantum chemical simulations and Raman spectra of the metallopolymers and the monomers point to a self-healing mechanism based on a

reversible thermal decomplexation of the bisterpyridine metal complexes.

Acknowledgements

This research was supported financially by the Deutsche Forschungsgemeinschaft within the framework of the SPP 1568 "Design and Generic Principles of Self-healing Materials". J. G. is grateful to the 7th Framework Programme of the European Union. S.B. is grateful to the Fonds der Chemischen Industrie (FCI) for a generous PhD stipend. All calculations have been performed at the Universitätsrechenzentrum of the Friedrich-Schiller University of Jena and the HP computers of the Theoretical Chemistry group of Jena.

References

- 1 X. Chen, M. A. Dam, K. Ono, A. Mal, H. Shen, S. R. Nutt, K. Sheran and F. Wudl, *Science*, 2002, **295**, 1698–1702.
- 2 R. P. Wool, *Soft Matter*, 2008, **4**, 400–418.
- 3 Y. Yang and M. W. Urban, *Chem. Soc. Rev.*, 2013, **42**, 7446–7467.
- 4 M. D. Hager, P. Greil, C. Leyens, S. van der Zwaag and U. S. Schubert, *Adv. Mater.*, 2010, **22**, 5424–5430.
- 5 N. K. Guimard, K. K. Oehlenschlaeger, J. Zhou, S. Hilf, F. G. Schmidt and C. Barner-Kowollik, *Macromol. Chem. Phys.*, 2012, **213**, 131–143.
- 6 S. Billiet, X. K. D. Hillewaere, R. F. A. Teixeira and F. E. Du Prez, *Macromol. Rapid Commun.*, 2013, **34**, 290–309.
- 7 M. Q. Zhang and M. Z. Rong, *Polym. Chem.*, 2013, **4**, 4878–4884.
- 8 F. Herbst, D. Döhler, P. Michael and W. H. Binder, *Macromol. Rapid Commun.*, 2013, **34**, 203–220.
- 9 M. Samadzadeh, S. H. Boura, M. Peikari, S. M. Kasiriha and A. Ashrafi, *Prog. Org. Coat.*, 2010, **68**, 159–164.
- 10 S. J. García, H. R. Fischer and S. van der Zwaag, *Prog. Org. Coat.*, 2011, **72**, 211–221.
- 11 Á. García, E. Schlangen, M. van de Ven and G. van Bochove, *Constr. Build. Mater.*, 2012, **30**, 59–65.
- 12 Á. García, *Fuel*, 2012, **93**, 264–272.
- 13 J. E. Gray and B. Luan, *J. Alloys Compd.*, 2002, **336**, 88–113.
- 14 X. Chen, F. Wudl, A. K. Mal, H. B. Shen and S. R. Nutt, *Macromolecules*, 2003, **36**, 1802–1807.
- 15 J. Köteritzsch, S. Stumpf, S. Hoepfener, J. Vitz, M. D. Hager and U. S. Schubert, *Macromol. Chem. Phys.*, 2013, **214**, 1636–1649.
- 16 U. Lafont, H. van Zeijl and S. van der Zwaag, *ACS Appl. Mater. Interfaces*, 2012, **4**, 6280–6288.
- 17 Y. Amamoto, H. Otsuka, A. Takahara and K. Matyjaszewski, *Adv. Mater.*, 2012, **24**, 3975–3980.
- 18 P. Cordier, F. Tournilhac, C. Soulie-Ziakovic and L. Leibler, *Nature*, 2008, **451**, 977–980.
- 19 D. Montarnal, P. Cordier, C. Soulie-Ziakovic, F. Tournilhac and L. Leibler, *J. Polym. Sci., Part A: Gen. Pap.*, 2008, **46**, 7925–7936.

- 20 L. R. Hart, J. L. Harries, B. W. Greenland, H. M. Colquhoun and W. Hayes, *Polym. Chem.*, 2013, **4**, 4860–4870.
- 21 F. Herbst, S. Seiffert and W. H. Binder, *Polym. Chem.*, 2012, **3**, 3084–3092.
- 22 S. J. Kalista and T. C. Ward, *J. R. Soc., Interface*, 2007, **4**, 405–411.
- 23 S. J. Kalista, J. R. Pflug and R. J. Varley, *Polym. Chem.*, 2013, **4**, 4910–4926.
- 24 S. Burattini, H. M. Colquhoun, D. Fox, D. Friedmann, B. W. Greenland, P. J. F. Harris, W. Hayes, M. E. Mackay and S. J. Rowan, *Chem. Commun.*, 2009, 6717–6719.
- 25 S. Burattini, H. M. Colquhoun, B. W. Greenland and W. Hayes, *Faraday Discuss.*, 2009, **143**, 251–264.
- 26 M. Zhang, D. Xu, X. Yan, J. Chen, S. Dong, B. Zheng and F. Huang, *Angew. Chem., Int. Ed.*, 2012, **51**, 7011–7015.
- 27 B. Zheng and F. Huang, *Chem. Soc. Rev.*, 2012, **41**, 6042–6065.
- 28 M. Burnworth, L. Tang, J. R. Kumpfer, A. J. Duncan, F. L. Beyer, G. L. Fiore, S. J. Rowan and C. Weder, *Nature*, 2011, **472**, 334–337.
- 29 S. Bode, L. Zedler, F. H. Schacher, B. Dietzek, M. Schmitt, J. Popp, M. D. Hager and U. S. Schubert, *Adv. Mater.*, 2013, **25**, 1634–1638.
- 30 S. Bode, R. K. Bose, S. Matthes, M. Ehrhardt, A. Seifert, F. H. Schacher, R. M. Paulus, S. Stumpf, B. Sandmann, J. Vitz, A. Winter, S. Hoepfner, S. J. Garcia, S. Spange, S. van der Zwaag, M. D. Hager and U. S. Schubert, *Polym. Chem.*, 2013, **4**, 4966–4973.
- 31 E. Carrington and J. M. Gosline, *Am. Malacol. Bull.*, 2004, 135–142.
- 32 C. Sun and J. H. Waite, *J. Biol. Chem.*, 2005, **280**, 39332–39336.
- 33 M. J. Harrington, A. Masic, N. Holten-Andersen, J. H. Waite and P. Fratzl, *Science*, 2010, **328**, 216–220.
- 34 L. Zedler, M. D. Hager, U. S. Schubert, M. J. Harrington, M. Schmitt, J. Popp and B. Dietzek, *Mater. Today*, DOI: 10.1016/j.mattod.2014.01.020.
- 35 S. Vasiliu, B. Kampe, F. Theil, B. Dietzek, D. Döhler, P. Michael, W. H. Binder and J. Popp, *Appl. Spectrosc.*, 2014, **68**, 541–548.
- 36 B. Chu and B. S. Hsiao, *Chem. Rev.*, 2001, **101**, 1727–1762.
- 37 R. J. Varley and S. van der Zwaag, *Polym. Test.*, 2008, **27**, 11–19.
- 38 R. J. Varley and S. van der Zwaag, *Polym. Int.*, 2010, **59**, 1031–1038.
- 39 R. J. Varley, S. Shen and S. van der Zwaag, *Polymer*, 2010, **51**, 679–686.
- 40 R. J. Varley and S. van der Zwaag, *Acta Mater.*, 2008, **56**, 5737–5750.
- 41 S. Dapprich, I. Komáromi, K. S. Byun, K. Morokuma and M. J. Frisch, *J. Mol. Struct.*, 1999, **462**, 1–21.
- 42 T. Vreven, K. S. Byun, I. Komáromi, S. Dapprich, J. A. Montgomery, K. Morokuma and M. J. Frisch, *J. Chem. Theory Comput.*, 2006, **2**, 815–826.
- 43 M. D. Chipara, M. Chipara, E. Shansky and J. M. Zaleski, *Polym. Adv. Technol.*, 2009, **20**, 427–431.
- 44 N. Holten-Andersen, M. J. Harrington, H. Birkedal, B. P. Lee, P. B. Messersmith, K. Y. C. Lee and J. H. Waite, *Proc. Natl. Acad. Sci. U. S. A.*, 2011, 1–5.
- 45 M. J. Frisch, G. W. Trucks, H. B. Schlegel, G. E. Scuseria, M. A. Robb, J. R. Cheeseman, G. Scalmani, V. Barone, B. Mennucci, G. A. Petersson, H. Nakatsuji, M. Caricato, X. Li, H. P. Hratchian, A. F. Izmaylov, G. Z. J. Bloino, J. L. Sonnenberg, M. Hada, M. Ehara, K. Toyota, R. Fukuda, J. Hasegawa, M. Ishida, T. Nakajima, Y. Honda, O. Kitao, H. Nakai, T. Vreven, J. J. A. Montgomery, J. E. Peralta, F. Ogliaro, M. Bearpark, J. J. Heyd, E. Brothers, K. N. Kudin, V. N. Staroverov, R. Kobayashi, J. Normand, K. Raghavachari, A. Rendell, J. C. Burant, S. S. Iyengar, J. Tomasi, M. Cossi, N. Rega, J. M. Millam, M. Klene, J. E. Knox, J. B. Cross, V. Bakken, C. Adamo, J. Jaramillo, R. Gomperts, R. E. Stratmann, A. J. A. O. Yazyev, C. P. R. Cammi, J. W. Ochterski, R. L. Martin, K. Morokuma, V. G. Zakrzewski, G. A. Voth, P. Salvador, J. J. Dannenberg, S. Dapprich, A. D. Daniels, O. Farkas, J. B. Foresman, J. V. Ortiz, J. Cioslowski and D. J. Fox, *Gaussian 09, Revision A.1*, Gaussian, Inc., Wallingford, CT, 2009.
- 46 M. Reiher, O. Salomon and B. Artur Hess, *Theor. Chem. Acc.*, 2001, **107**, 48–55.
- 47 O. Salomon, M. Reiher and B. A. Hess, *J. Chem. Phys.*, 2002, **117**, 4729–4737.
- 48 A. D. Becke, *J. Chem. Phys.*, 1993, **98**, 5648–5652.
- 49 C. Lee, W. Yang and R. G. Parr, *Phys. Rev. B: Condens. Matter Mater. Phys.*, 1988, **37**, 785–789.
- 50 M. Dolg, U. Wedig, H. Stoll and H. Preuss, *J. Chem. Phys.*, 1987, **86**, 2123–2131.
- 51 P. C. Hariharan and J. A. Pople, *Theor. Chim. Acta*, 1973, **28**, 213–222.
- 52 R. J. Davidson, E. W. Ainscough, A. M. Brodie, G. B. Jameson, M. R. Waterland, H. R. Allcock, M. D. Hindenlang, B. Moubaraki, K. S. Murray, K. C. Gordon, R. Horvath and G. N. L. Jameson, *Inorg. Chem.*, 2012, **51**, 8307–8316.
- 53 J. P. Merrick, D. Moran and L. Radom, *J. Phys. Chem.*, 2007, **111**, 11683–11700.
- 54 J. Tomasi, B. Mennucci and R. Cammi, *Chem. Rev.*, 2005, **105**, 2999–3093.
- 55 M. Wächtler, J. Guthmüller, L. González and B. Dietzek, *Coord. Chem. Rev.*, 2012, **256**, 1479–1508.
- 56 S. Kupfer, M. Wächtler, J. Guthmüller, J. Popp, B. Dietzek and L. González, *J. Phys. Chem. C*, 2012, **116**, 19968–19977.
- 57 S. Kupfer, J. Guthmüller and L. González, *J. Chem. Theory Comput.*, 2013, **9**, 543–554.
- 58 H. R. Holyer, C. D. Hubbard, S. F. A. Kettle and R. G. Wilkins, *Inorg. Chem.*, 1965, **5**, 622–625.
- 59 M. A. R. Meier, B. G. G. Lohmeijer and U. S. Schubert, *J. Mass Spectrom.*, 2003, **38**, 510–516.
- 60 M. Halls, J. Velkovski and H. Schlegel, *Theor. Chem. Acc.*, 2001, **105**, 413–421.

Supporting Information

Self-healing Mechanism of Metallopolymers investigated by QM/MM Simulations and Raman Spectroscopy

Stephan Kupfer^{1,2,§}, Linda Zedler^{1,2,§}, Julien Guthmuller³, Stefan Bode^{4,5}, Martin D. Hager^{4,5}, Ulrich S. Schubert^{4,5}, Jürgen Popp^{1,2,6}, Stefanie Gräfe^{1,2}, Benjamin Dietzek^{1,2,6*}

¹*Institute for Physical Chemistry, Friedrich Schiller University Jena, Helmholtzweg 4, 07743, Jena, Germany*

²*Abbe Center of Photonics, Friedrich Schiller University Jena*

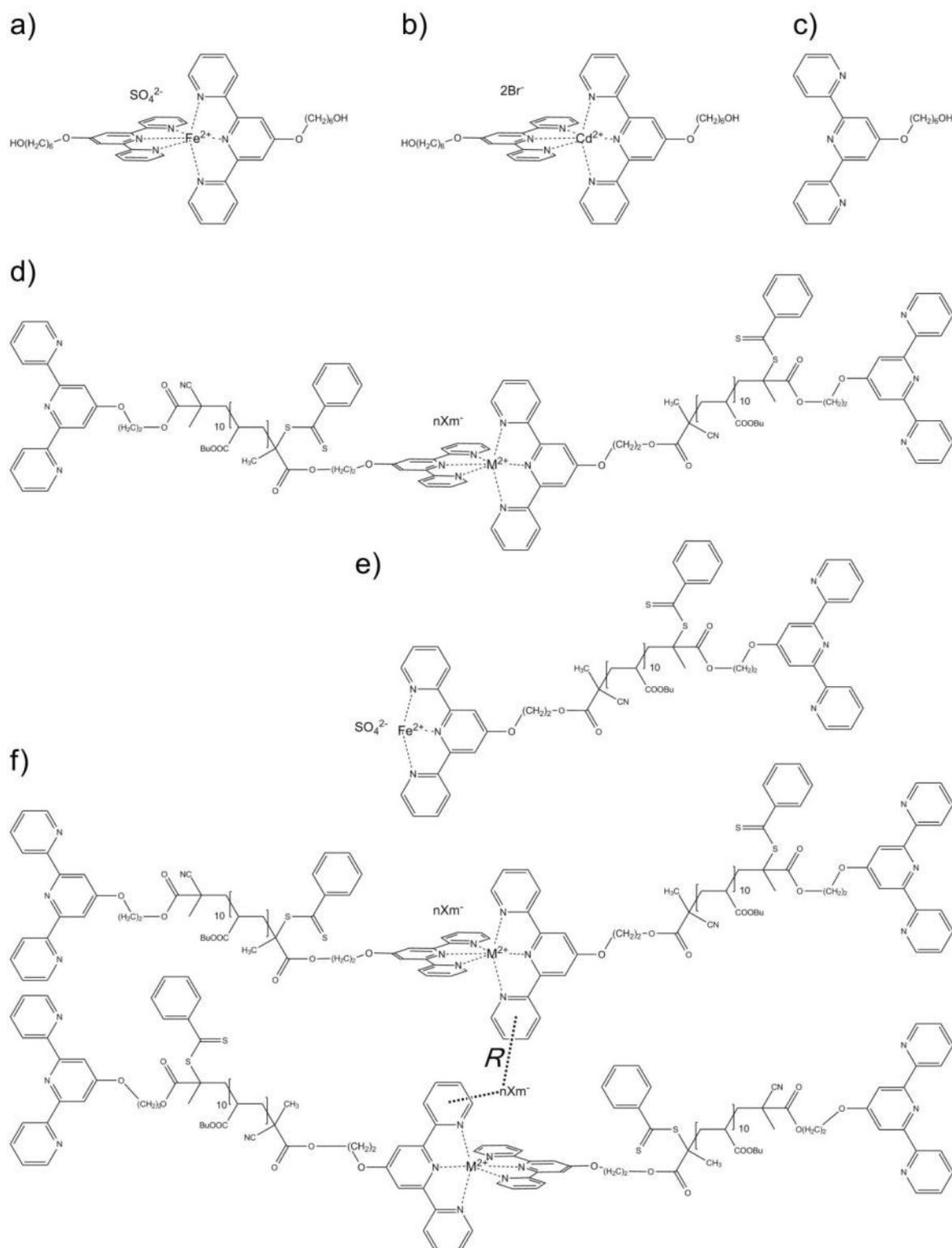
³*Faculty of Applied Physics and Mathematics, Gdansk University of Technology, Narutowicza 11/12, 80233 Gdansk, Poland*

⁴*Laboratory for Organic and Macromolecular Chemistry, Friedrich Schiller University Jena, Humboldtstr. 10, 07743, Jena, Germany*

⁵*Jena Center of Soft Matter, Friedrich Schiller University Jena, Philosophenweg 7, 07743, Jena, Germany*

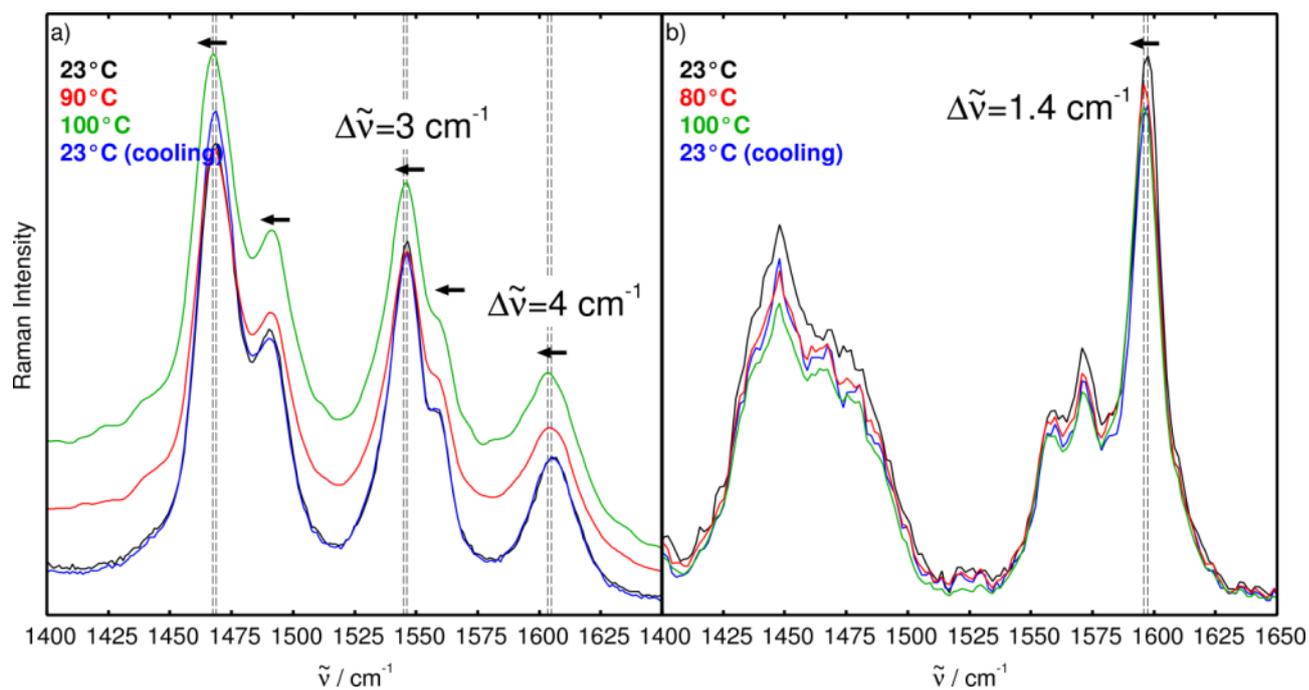
⁶*Institute for Photonic Technology (IPHT) Jena, Albert-Einstein-Str. 9, 07745, Jena, Germany*

Figure S1



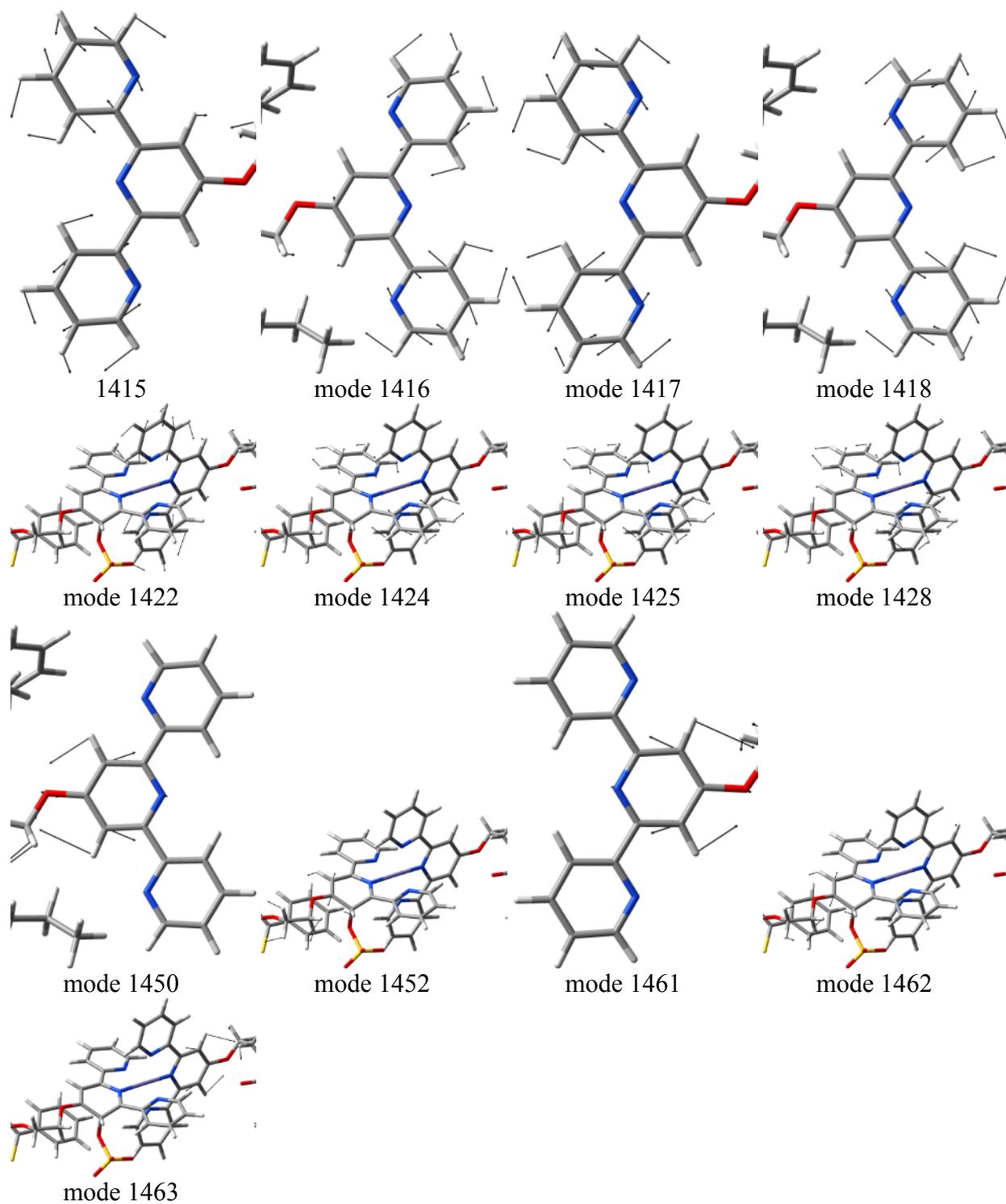
Schematic representation of the iron(II) terpyridine sulfate complex (a)), the cadmium(II) terpyridine bromide complex (b)), and the free terpyridine ligand (c)). d) depict the model systems used for the simulation of the Raman spectra of the iron(II) sulfate and the cadmium(II) bromide cross-linked metallopolymer, and e) the semi-decomplexed metallopolymer. The polymer model used in the calculation of the ionic clusters is illustrated in f); frozen coordinate *R* is indicated.

Figure S2



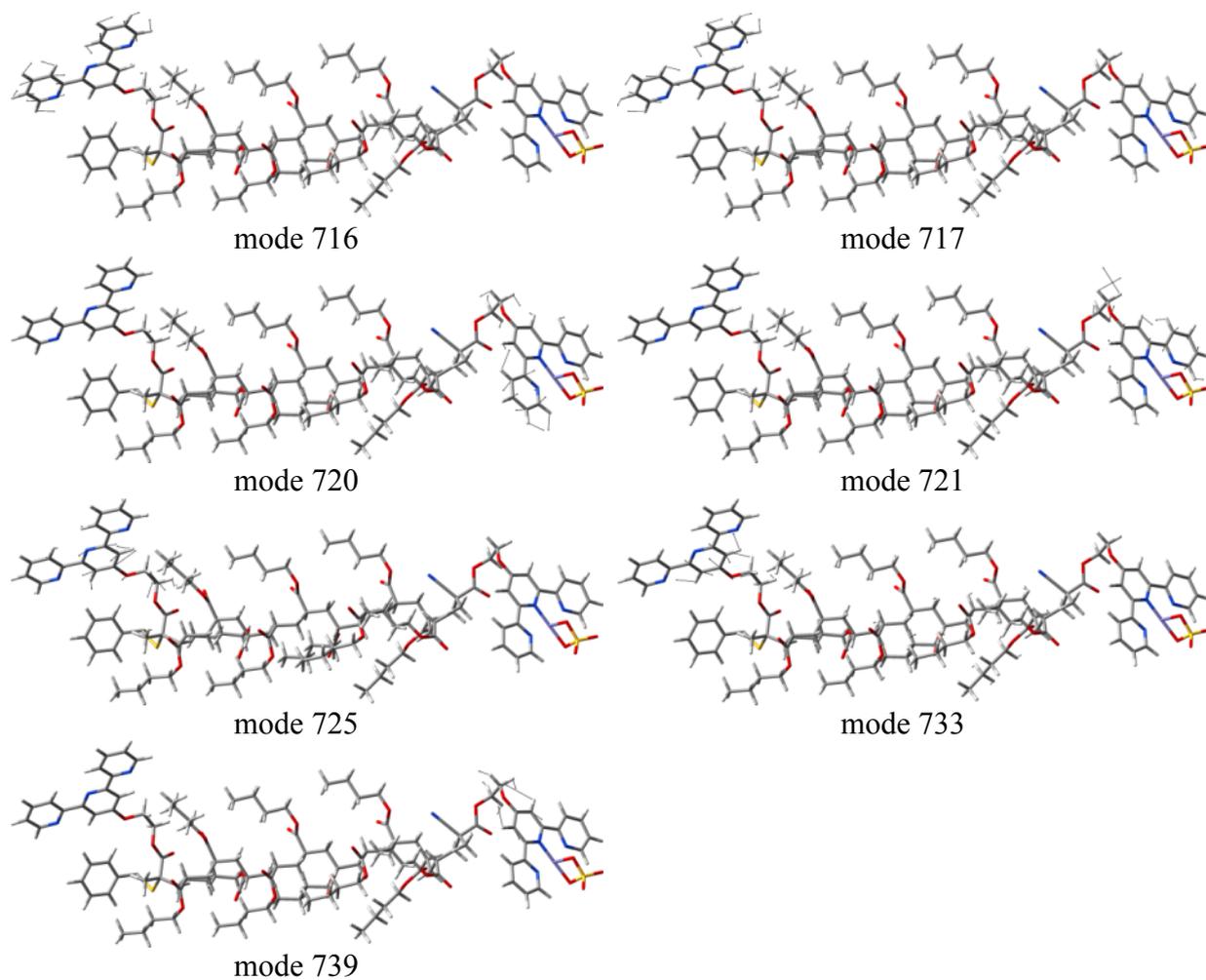
Temperature-dependent Raman spectra of the iron(II) sulfate (a) and cadmium(II) bromide (b) cross-linked metallopolymer in the spectral range between 1400 and 1650 cm^{-1} . Vertical dashed lines indicate the observed fully reversible bathochromic shifts of approximately 3 and 4 and 1.4 cm^{-1} .

Figure S3



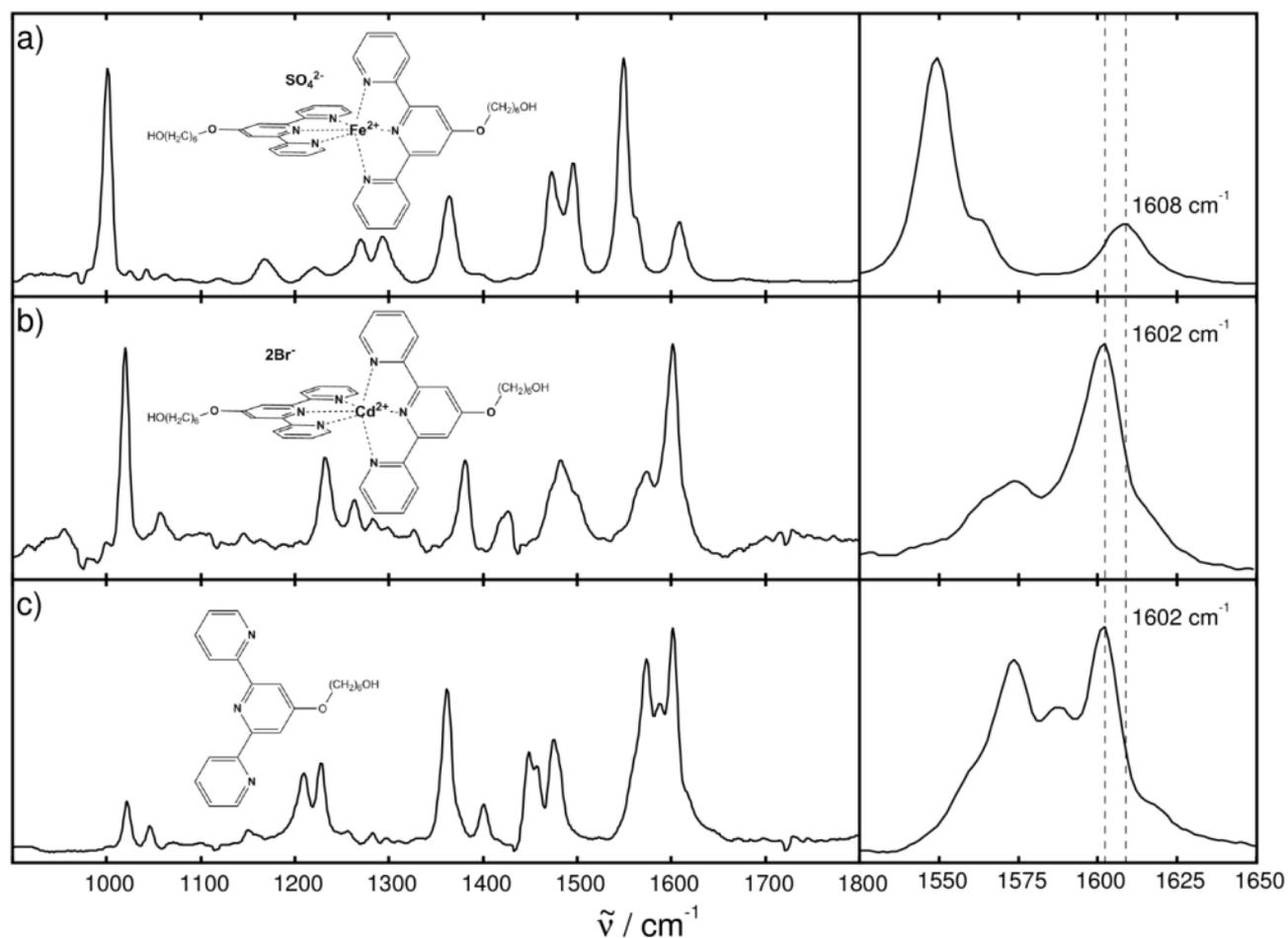
Intense vibrational modes of the iron(II) sulfate metallopolymer contributing to the experimental Raman bands at 1546, 1558, and 1606 cm^{-1} .

Figure S4



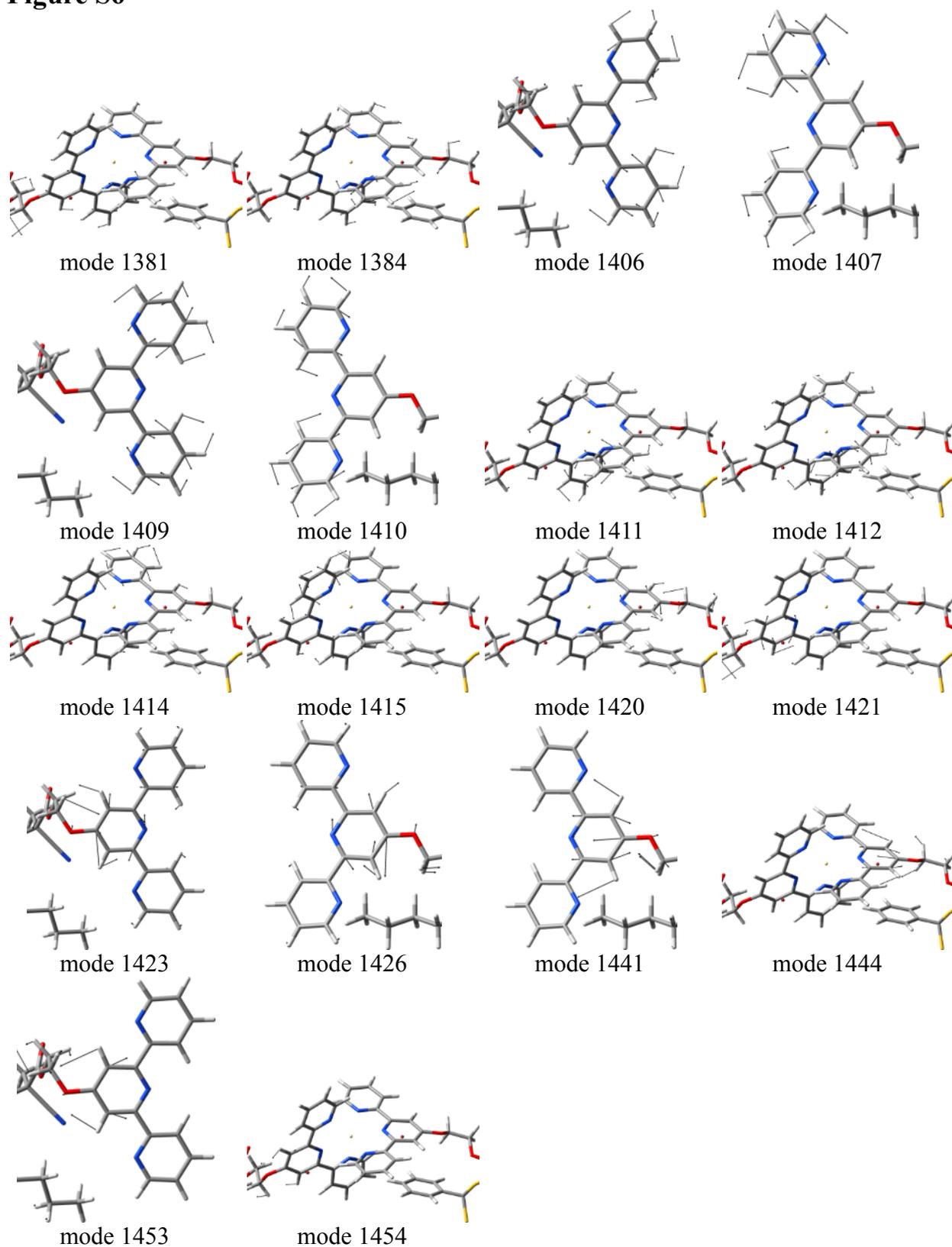
Intense vibrational modes of the semi-decomplexed iron(II) sulfate metallopolymer.

Figure S5



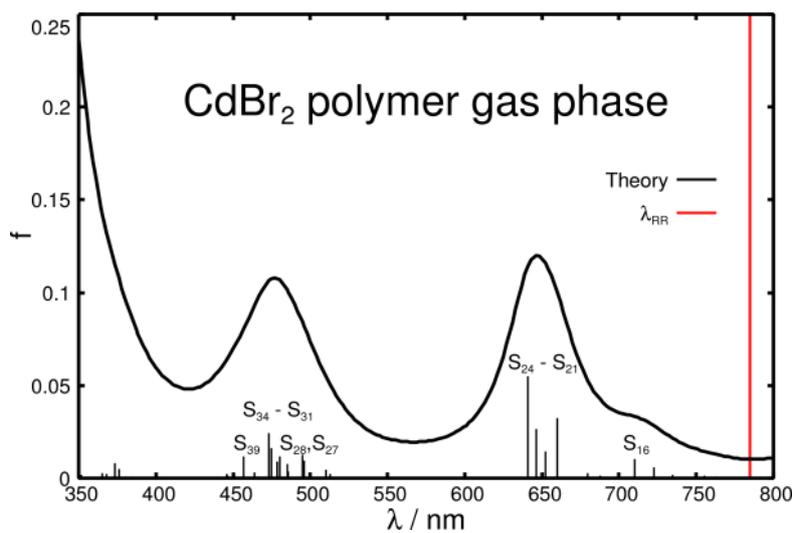
Raman spectra of the iron(II) sulfate a), cadmium(II) bromide b), and terpyridine c) monomers measured upon excitation at 568 nm. Raman frequencies for bands correlated to the observed bathochromic shifts of the metallopolymers are indicated.

Figure S6



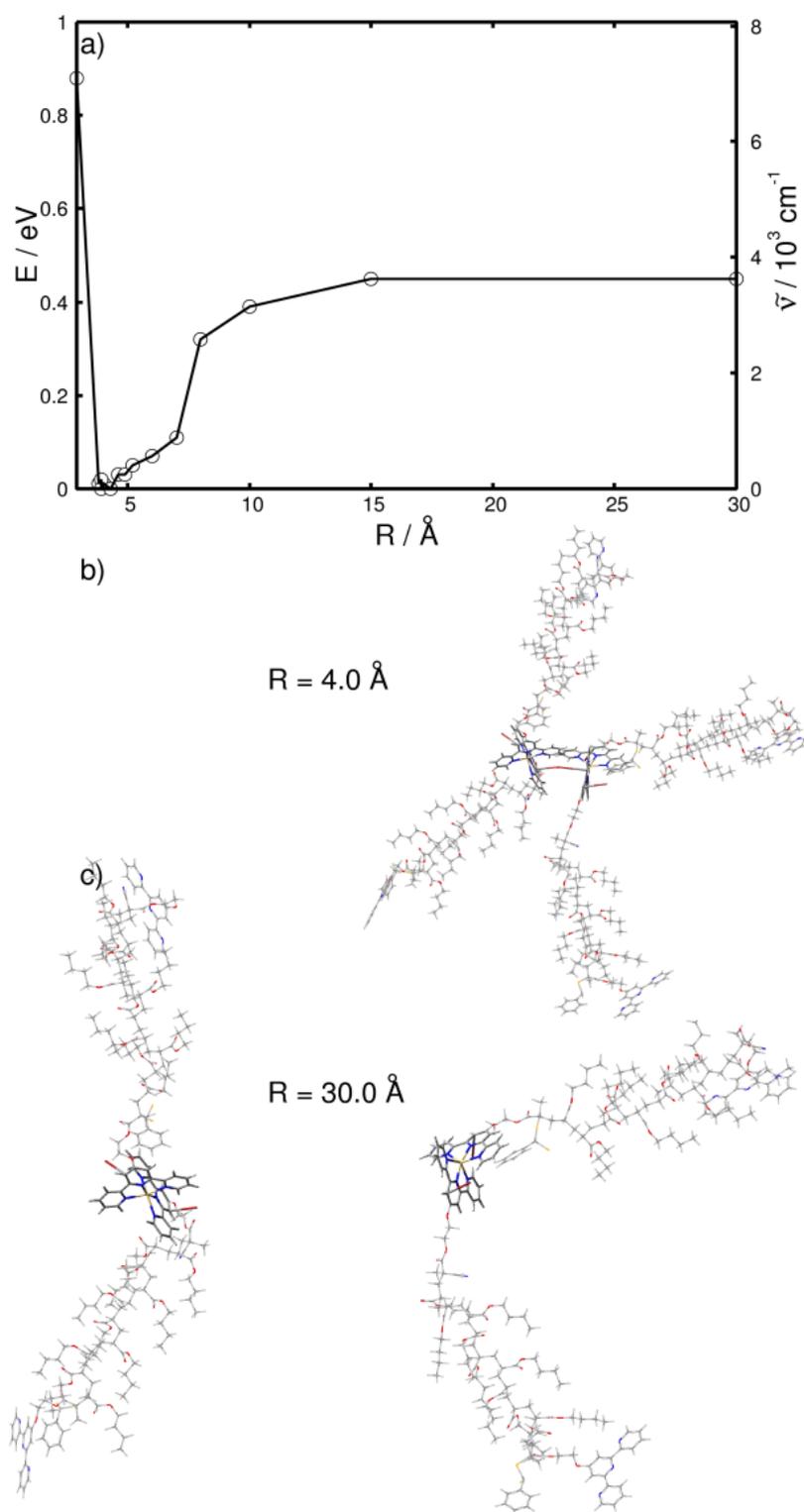
Intense vibrational modes of the cadmium(II) bromide metallopolymer contributing to the experimental Raman bands at 1597 and 1724 cm^{-1} .

Figure S7



Simulated UV-vis spectrum of the cadmium(II) bromide metallopolymer in the gas phase performed at the QM/MM level of theory using TD-B3LYP(15) with the 6-31G(d) basis set and the UFF; the red line corresponds to excitation wavelength used in the Raman measurements.

Figure S8



Calculation of the relaxed PES of the cadmium(II) bromide metallopolymer at the QM/MM level of theory using B3LYP(15) with the 6-31G(d) basis set and the universal force field with respect to the distance R describing the cleavage of the ionic cluster up to $R = 30 \text{ \AA}$. b) and c) depicts the global minimum of the PES ($R = 4.0 \text{ \AA}$) and the opened cluster at $R = 30 \text{ \AA}$ in the orthogonal oriented conformation.

[Zedler et al. JPCC]

Redox State Sensitive Spectroscopy of the Model Compound

$[(\text{H-dcbpy})_2\text{Ru}^{\text{II}}(\text{NCS})_2]^{2-}$ (dcbpy = 2,2'-Bipyridine-4,4'-dicarboxylato)

Der Nachdruck der folgenden Publikation erfolgt mit freundlicher Genehmigung der American Chemical Society.

Reprinted with kind permission from:

Zedler, L.; Guthmuller, J.; Rabelo de Moraes, I.; Kriek, S.; Schmitt, M.; Popp, J.; Dietzek, B., Redox State Sensitive Spectroscopy of the Model Compound $[(\text{H-dcbpy})_2\text{Ru}^{\text{II}}(\text{NCS})_2]^{2-}$ (dcbpy = 2,2'-Bipyridine-4,4'-dicarboxylato), *J. Phys. Chem. C* **2013**, *117*, 6669–6677.

Copyright 2013 American Chemical Society.

Redox State Sensitive Spectroscopy of the Model Compound $[(\text{H-dcbpy})_2\text{Ru}^{\text{II}}(\text{NCS})_2]^{2-}$ (dcbpy = 2,2'-Bipyridine-4,4'-dicarboxylato)

Linda Zedler,[†] Julien Guthmuller,[‡] Inês Rabelo de Moraes,[§] Sven Krieck,^{||} Michael Schmitt,[†] Jürgen Popp,^{†,§} and Benjamin Dietzek^{*,†,§}

[†]Institute of Physical Chemistry and Abbe Center of Photonics, Friedrich-Schiller University Jena, Jena, Germany

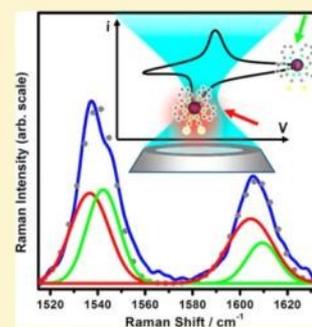
[‡]Faculty of Applied Physics and Mathematics, Gdansk University of Technology, Narutowicza 11/12, 80233 Gdansk, Poland

[§]Institute of Photonic Technology (IPHT), Research Group Ultrafast Spectroscopy, Albert-Einstein Strasse 9, 07745 Jena, Germany

^{||}Institute of Inorganic and Analytical Chemistry, Friedrich-Schiller University Jena, Jena, Germany

Supporting Information

ABSTRACT: The charge transfer reaction mechanism in a ruthenium polypyridine model complex with isothiocyanato ligands, i.e., $[(\text{H-dcbpy})_2\text{Ru}(\text{NCS})_2]^{2-} 2\text{Bu}_4\text{N}^+$ (Ru2H) (dcbpy = 2,2'-bipyridine-4,4'-dicarboxylato), has been investigated by combining UV–vis absorption, resonance Raman spectroscopy, and electrochemical methods. Understanding the photophysics of light-harvesting complexes of this class is an indispensable prerequisite to improve the efficiency and durability of photocatalysts for hydrogen production, a possible basis of future energy sources. In this study, light-induced excitation of Ru2H has been mimicked by electrochemical reduction, and the intermediate redox state has been extensively characterized by UV–vis absorption and resonance Raman spectroscopy. The reduction occurs at the dcbpy ligand, and the spectra of reduced Ru2H resemble the excited state spectra. The reduced Ru2H exhibits a new absorption band at 440 nm localized at the bipyridine framework. This assignment is consistent with the observed enhancement of the bipyridine bands with respect to nonreduced Ru2H in the resonance Raman spectra of the reduced Ru2H excited at 458 nm. The detected shifts in Raman band positions and changes in the relative band intensities between nonreduced and reduced Ru2H are rationalized on an orbital level by quantum chemical calculations. The results indicate that the reduction is accompanied by deprotonation, i.e., an intramolecular electron-transfer-induced cleavage of the O–H bond splitting off hydrogen, of the carboxylic acid groups of the dcbpy ligand.



INTRODUCTION

To sustainably meet the world's energy needs is one of the biggest challenges of this century. Important aspects of this multifaceted problem are novel concepts for energy production and storage. In this respect photocatalytic hydrogen generation is obviously one of the pathways toward a renewable energy production.¹ Consequently there is a manifold of homogeneous and heterogeneous catalysis concepts under investigation.^{2–9} However, besides difficulties in hydrogen storage, the design of efficient photocatalysts for hydrogen production remains an unsolved task.¹

Ruthenium dyes are model complexes for studying basic photoinduced activation and relaxation processes on the molecular level due to their unique optical properties, high quantum efficiency, and wide structural variability, which is coupled with high chemical stability.^{10–13} Since ruthenium polypyridine dyes are ideal candidates for a wide range of applications, e.g., primary electron donors in heterogeneous and homogeneous catalysis but also in dye-sensitized solar cells (DSSCs), they have been subject to extensive studies.^{10,14–16} In DSSCs ruthenium polypyridine complexes are used for sensitizing nanostructured TiO_2 films. Efficiencies over 10% for this kind of photoelectrochemical cells have been achieved

using the sensitizer $[(\text{H-dcbpy})_2\text{Ru}(\text{NCS})_2]^{2-} 2\text{Bu}_4\text{N}^+$ (dcbpy = 2,2'-bipyridine-4,4'-dicarboxylato) known as N719,¹⁷ which will be referred to as **Ru2H** throughout the paper. Besides the application in DSSCs, recently **Ru2H** and other sensitizers have been incorporated in functional nanoparticle–molecular interfaces to be applied as heterogeneous catalysts in solution.^{18–22} Studies in this particular field of ruthenium polypyridine based research focus on improving the photostability and the photoinduced electron transfer properties of the compounds to reduce the effect of reverse charge recombination after photoexcitation, which is essential to optimize the performance of the hypothesized devices.^{2,4,23}

Irrespective of the actual application of ruthenium polypyridine complexes and complex fragments, i.e., in DSSCs, as molecular catalysts, photoactive electron donors in supramolecular assemblies, the key to correlate structure, photoinduced processes, and finally function of the systems is a detailed spectroscopic characterization. A central spectroscopic tool to study excited states is resonance Raman (rR)

Received: January 7, 2013

Revised: March 2, 2013

Published: March 26, 2013

spectroscopy, which is suited for determining the most prominent structural differences of ground and electronically excited states.²⁴ A few rR spectroscopic studies have focused on the photoinduced structural changes of complexes of the type $[(R\text{-bpy})_2\text{Ru}(\text{NCS})_2]$.^{25,26} rR is limited to study the initial dynamics on the excited-state potential energy surface, i.e., on a time scale of a few femtoseconds.²⁴ To follow excited state dynamics on a some-hundred-picosecond to some-nanosecond time scale, different techniques (e.g., pump–probe techniques or fluorescence up-conversion) are employed.^{27–29} In doing so a detailed understanding of the scheme underlying the photophysics of **Ru2H** and structurally similar complexes has been proposed.^{30–34} After excitation the complex relaxes on a time scale of a few 100 fs^{34–36} by rapid intersystem crossing to a triplet state, which is nonemissive and has a lifetime of 10 to some 100 ns.³² Its specific photodynamics including the exceptionally fast intersystem crossing to a long-lived metastable state renders the complex a promising candidate to be used in photochemistry. Another key to photochemical activity is the long-term stability of the complex in its photoactivated form, i.e., in the state in which one of the ligands is reduced and the central metal ion oxidized.³² Despite the fact that the formation of the long-lived charge-separated state with its reduced ligand structure is generally very well understood, the photophysics of the long-lived state is much less characterized.

Thus, in this contribution spectroelectrochemistry (SEC) is employed as a straightforward spectroscopic tool to study specifically structural changes in the reduced species of **Ru2H**. rR-SEC has been reported in the context of dye-sensitized solar cells; i.e., thin dye monolayers chemically adsorbed on semiconducting surfaces as TiO_2 , to study the interaction of the redox couple at the surface with the electrolyte.^{26,37,38} However, ruthenium dyes in solution have been only sparsely analyzed until now. Even though photoactivation results neither in oxidation nor in reduction, in the generalized mechanism the catalyst is first photoactivated. This activated state is more susceptible to both reduction and oxidation. By interaction with an electron donor, the complex is reduced and can further transfer this electron to an acceptor, thus catalyzing a reaction. This scheme is specifically proposed for the photoactivated $[\text{Ru}(\text{II})(\text{bpy})_3]^{2+}$, and further similar reactions are discussed therein.¹¹ Specifically, the deprotonation, which is more appropriately described as an intramolecular electron-transfer-induced release of hydrogen by cleaving the O–H bond of the carboxylic acid groups of $[(\text{H}_2\text{-dcbpy})_2\text{Ru}(\text{NCS})_2]$ (**N3**) during reduction at platinum (Pt) electrodes,³⁹ and the influence of metal-to-ligand (Ru \rightarrow bpy) charge transfer in complexes of the type $[(R\text{-bpy})_2\text{Ru}(\text{NCS})_2]$ on the C–N stretch vibrations of the NCS ligands⁴⁰ were investigated in solution using SEC. So far the number of studies on the structural changes of $[(R\text{-bpy})_2\text{Ru}(\text{NCS})_2]$ complexes during reduction by SEC is very limited, and the results were not interpreted on an orbital level with the help of quantum chemical simulations.

This contribution applies rR-SEC on the reduction of **Ru2H** as a model compound for structurally related systems. Knowledge about the molecular structure changes of the intermediates formed upon reduction and about the mechanism of the electron-transfer reaction in solution is essential for optimizing the performance of such photoactive complexes. The spectroelectrochemical studies reported herein unravel mechanistic details of secondary electron transfer processes subsequent to the initial photoexcitation. Special attention is

paid to electrochemical potential-controlled rR studies in the fingerprint region. Such experiments reveal structural information of individual electrochemically generated species. To assign the observed spectral changes, time-dependent density functional theory (TDDFT) calculations of the rR and UV–vis absorption spectra of **Ru2H** and the hypothesized reduced form have been performed.

EXPERIMENTAL AND THEORETICAL SECTION

The complexes $[(\text{H-dcbpy})_2\text{Ru}(\text{NCS})_2]^{2+} 2\text{Bu}_4\text{N}^+$ and $[(\text{dcbpy})_2\text{Ru}(\text{NCS})_2]^{4+} 4\text{Bu}_4\text{N}^+$ ($\text{Bu}_4\text{N} =$ tetrabutylammonium, dcbpy = 2,2'-bipyridine-4,4'-dicarboxylate, NCS = isothiocyanato) (see Figure 1) were purchased from Solaronix SA (Aubonne, Switzerland) and used without further purification.

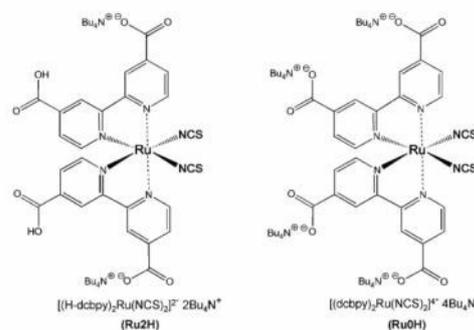


Figure 1. Molecular structures of the ruthenium complexes under investigation. The structures differ by protonation state of the carboxylic acid groups.

Spectroscopy. UV–vis absorption spectra were measured with a double beam Cary 5000 UV–vis spectrometer (Varian) in the wavelength range between 270 and 1000 nm with 1 nm spectral resolution. Optical quartz cuvettes of a path length of 1 mm were used (Hellma).

rR spectra were excited by the visible lines of an Ar ion laser (Coherent, Innova 300C) and recorded with an Acton SpectraPro 2758i spectrometer (entrance slit width 100 μm , focal length 750 mm, grating 1800/mm). The Raman spectrometer was wavenumber calibrated before measurements using the exact position of the laser line. The band of dimethylformamide (DMF) at 1406 cm^{-1} was used as a reference for normalizing intensities and wavenumbers. For recording rR spectra the laser was focused by means of a silica lens ($f = 100$ mm) into a rotating-cell cuvette to prevent heating of the samples. Raman signals were collected at 90° scattering angle and focused onto a fiber bundle by a pair of silica lenses ($f = 35$ mm and $f = 75$ mm). Optical fibers transfer the Raman scattered light to the entrance slit of the spectrometer. Spectroelectrochemical rR experiments in situ were recorded in transmission mode using a thin-layer quartz glass spectroelectrochemical cell (Bioanalytical Systems, Inc.) which was fixed between a self-made Teflon cap with a solvent-resistant seal (Kalrez) and a customized cuvette holder fitting to both the UV–vis and Raman spectrometer. The cell was equipped with a Pt-gauze working electrode, a Pt-counter electrode, and a Ag/AgCl-pseudoreference electrode and filled

up in a glovebox under inert conditions to exclude oxygen and moisture from the sample volume. The spectroelectrochemical cell was also used for performing cyclic voltammetry. Electrochemical monitoring was carried out potentiostatically (Solartron Instruments, SI 1287). The excitation laser beam was focused with a 10× microscope objective (Olympus) onto the electrode grid. To reduce the Rayleigh scattered light at the excitation wavelength a notch filter was placed between two achromatic lenses which collected and matched the scattered light to the spectrometer (see Supporting Information (SI)). The Raman signals were detected by liquid-nitrogen cooled CCD (SPEC-10, Roper Scientific).

Quantum Chemical Calculations. The structural and electronic data of the ruthenium complexes with no counterions were obtained from quantum chemistry calculations performed with the GAUSSIAN 09 program.⁴¹ The ground state properties (geometries and harmonic vibrations) were calculated by means of DFT with the exchange-correlation (XC) functional B3LYP.^{42,43} The 28-electron relativistic effective core potential MWB⁴⁴ was used with its basis set for the ruthenium atom, whereas the 6-31G(d) double- ζ basis set⁴⁵ was employed for the ligands. To correct for the lack of anharmonicity and the approximate treatment of electron correlation, the harmonic frequencies were scaled by the factor 0.97.⁴⁶ The vertical excitation energies, oscillator strengths, and analytical Cartesian energy derivatives of the excited states were obtained from TDDFT calculations with the same XC functional, pseudopotential, and basis set. It was shown in several studies that B3LYP provides a balanced description of the absorption features for related complexes.^{47–49} The absorption spectra were simulated by determining the excitation energies and oscillator strengths of the 120 lowest singlet excited states. The effects of the interaction with a solvent (DMF, $\epsilon = 37.219$, $n = 1.430$) on the geometry, frequencies, excitation energies, and excited state gradients were taken into account by the integral equation formalism of the polarizable continuum model.⁵⁰ The nonequilibrium procedure of solvation was used for the calculation of the excitation energies and of the excited state gradients. Such a procedure is well adapted for processes where only the fast reorganization of the electronic distribution of the solvent is important.

The rR intensities for fundamental transitions were calculated according to a method described in detail in the literature.²⁴ This involves the determination of the Raman polarizability tensor $(\alpha_{\alpha\beta})_{g_0 \rightarrow g_1}$. For Condon-type scattering and assuming that the electronic ground and excited state potential energy surfaces are harmonic and that they differ only by their equilibrium geometry, the Raman polarizability takes the following form⁵¹

$$(\alpha_{\alpha\beta})_{g_0 \rightarrow g_1} = \frac{1}{\hbar} \sum_e (\mu_{ge})_\alpha (\mu_{ge})_\beta \frac{\Delta_{e,l}}{\sqrt{2}} \{ \Phi_e(\omega_L) - \Phi_e(\omega_L - \omega_l) \} \quad (1)$$

where $(\mu_{ge})_\alpha$ is a component of the electronic transition dipole moment at the ground state equilibrium geometry; $\Delta_{e,l}$ is the dimensionless displacement of the e th excited state potential minimum with respect to the ground state for the l th normal coordinate; and ω_l is the vibrational frequency of the l th normal mode. The function $\Phi_e(\omega_l)$ can be approximated by

$$\Phi_e(\omega_l) = \frac{1}{\omega_{e,g} - \omega_l - i\Gamma} \quad (2)$$

where $\omega_{e,g}$ is the vertical excitation energy of the excited state e and Γ is a damping factor describing a homogeneous broadening.^{24,52} A Γ of 1500 cm^{-1} reproduced the experimental broadening, and the vertical excitation energies were corrected so that experimental and theoretical absorption maxima coincide.⁴⁸

The dimensionless displacements $\Delta_{e,l}$ were obtained from the derivatives of the excited state potential energy E^e along the normal mode Q_l evaluated at the ground state geometry according to the relation^{24,53}

$$\Delta_{e,l} = -\frac{1}{\sqrt{\hbar \omega_l^{3/2}}} \left(\frac{\partial E^e}{\partial Q_l} \right)_0 \quad (3)$$

RESULTS AND DISCUSSION

Electrochemistry. To determine spectroscopic changes during reduction, knowledge of the voltammetric behavior of **Ru2H** in the spectroelectrochemical cell is required. The reduction of ruthenium complexes, bearing bipyridine (bpy) ligands, usually occurs via several reversible one-electron ligand-centered charge-transfer processes.⁵⁴ For example the fully protonated form of **Ru2H**, $[(\text{H}_2\text{-dcbpy})_2\text{Ru}(\text{NCS})_2]$ (N3), shows two reversible responses during the ligand-based reduction in DMF,³⁹ which requires specific voltammetric conditions such as low temperature, short time domains, and glassy carbon electrodes. The reduction of N3 becomes irreversible when platinum electrodes are used for the investigation, and a much more complex cyclic voltammogram³⁹ is obtained under such conditions.

The cyclic voltammogram of **Ru2H** dissolved in DMF/tetrabutylammonium hexafluorophosphate (Bu_4NPF_6) at 298 K in the SEC cell is characterized by a broad irreversible reduction step at around $E_{p,c} = -1.5$ V assigned to the reduction of the dcbpy ligand⁵⁵ (Figure 2). The observed potential range is typical for the reduction of this class of ruthenium complexes.^{39,56} The potential is slightly more negative than for the fully protonated complex N3 since deprotonation raises the energy of the LUMO level. Therefore the reduction potential, which corresponds to the energetic HOMO–LUMO gap, is more negative.

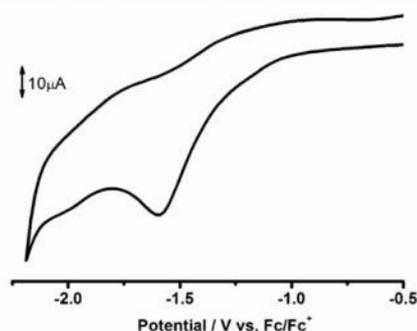


Figure 2. Cyclic voltammogram of 1.0 mM **Ru2H** in DMF/0.2 M Bu_4NPF_6 at room temperature under a nitrogen atmosphere (scan rate 100 mV/s). The working electrode is a platinum minigrad, and ferrocenium/ferrocene (Fc^+/Fc) is used as an internal standard.

Spectroelectrochemistry. Absorption. The experimental UV–vis absorption spectrum of **Ru2H** in DMF exhibits three characteristic bands at 528, 381, and 309 nm (Figure 3A). The

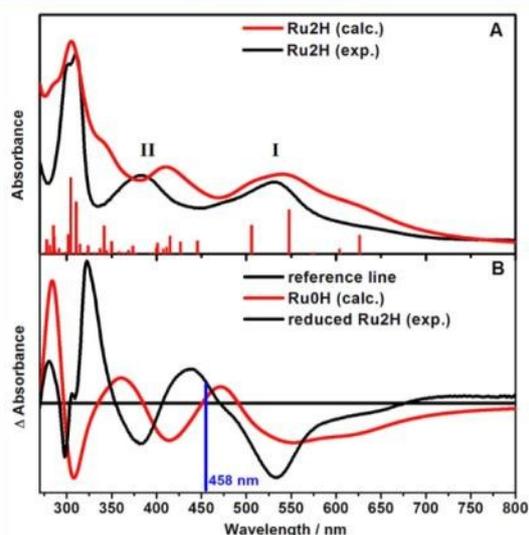


Figure 3. (A) Calculated ground state absorption spectrum with oscillator strength as histogram (red curve) and measured ground state absorption spectrum of **Ru2H** in DMF (black graph). (B) Difference UV–vis spectrum (black curve) obtained during reduction of **Ru2H** ($[(\text{H-dcbpy})_2\text{Ru}(\text{NCS})_2]^{2+}$) in deaerated DMF containing 0.2 M Bu_4NPF_6 . The spectra were measured in double beam configuration utilizing the spectroelectrochemical cell and a cuvette of the same path length containing **Ru2H** solution. The potential was applied to the spectroelectrochemical cell only; TDDFT-calculated difference UV–vis spectrum of **Ru0H** (red curve). The results indicate that **Ru0H** is formed upon reduction of **Ru2H**.

TDDFT UV–vis absorption spectrum of **Ru2H** agrees well with the measured spectrum with calculated absorption maxima at 540, 410, and 305 nm for the three first bands, respectively. According to the calculations the first (I) band is mainly assigned to a superposition of three states (S_{11} , S_5 , S_6), which present transitions from mixed ruthenium-d and NCS- π orbitals ($d_{\text{Ru}}\pi_{\text{NCS}}$) to π^* orbitals of the dcbpy ligands (π^*_{dcbpy}) (see Table 1 and Figure 4). The second (II)

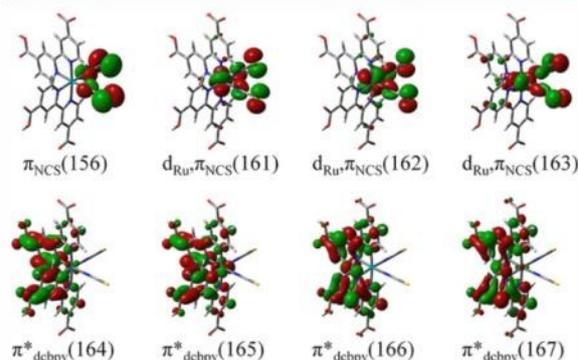


Figure 4. Molecular orbitals involved in the main configurations of the excited states of **Ru2H**.

absorption band is obtained from the superposition of several excited states (S_9 to S_{21} , Table 1) with different characters. Similarly to the first band, these states involve transitions from mixtures of $d_{\text{Ru}}\pi_{\text{NCS}}$ and pure π_{NCS} orbitals to π^*_{dcbpy} orbitals. Additionally, the higher energy states S_{19} and S_{21} show also contributions from the π_{COO} orbitals localized on the COO^- groups. These results show that the two first absorption bands do not correspond to pure MLCT transitions. Next, the third absorption band at 305 nm is dominated by intraligand π – π^* transitions of the dcbpy ligands (states S_{59} and S_{62}). The

Table 1. Calculated Vertical Excitation Energies (E^e), Oscillator Strengths (f), and Excited Configurations with Weights Larger than 10% Of the Main Excited States of **Ru2H**

state	transition	weight (%)	E^e (eV)	λ (nm)	f
S_1	$d_{\text{Ru}}\pi_{\text{NCS}}(163) \rightarrow \pi^*_{\text{dcbpy}}(164)$	89	1.98	626	0.0551
S_5	$d_{\text{Ru}}\pi_{\text{NCS}}(161) \rightarrow \pi^*_{\text{dcbpy}}(164)$	60	2.26	548	0.1299
	$d_{\text{Ru}}\pi_{\text{NCS}}(162) \rightarrow \pi^*_{\text{dcbpy}}(165)$	29			
S_6	$d_{\text{Ru}}\pi_{\text{NCS}}(161) \rightarrow \pi^*_{\text{dcbpy}}(165)$	60	2.45	506	0.0852
	$d_{\text{Ru}}\pi_{\text{NCS}}(163) \rightarrow \pi^*_{\text{dcbpy}}(165)$	22			
S_9	$d_{\text{Ru}}\pi_{\text{NCS}}(163) \rightarrow \pi^*_{\text{dcbpy}}(166)$	96	2.78	446	0.0389
S_{14}	$d_{\text{Ru}}\pi_{\text{NCS}}(163) \rightarrow \pi^*_{\text{dcbpy}}(167)$	70	2.91	427	0.0359
	$d_{\text{Ru}}\pi_{\text{NCS}}(162) \rightarrow \pi^*_{\text{dcbpy}}(166)$	12			
S_{16}	$\pi_{\text{NCS}}(156) \rightarrow \pi^*_{\text{dcbpy}}(164)$	51	2.99	415	0.0533
	$d_{\text{Ru}}\pi_{\text{NCS}}(162) \rightarrow \pi^*_{\text{dcbpy}}(166)$	26			
	$d_{\text{Ru}}\pi_{\text{NCS}}(163) \rightarrow \pi^*_{\text{dcbpy}}(167)$	18			
S_{17}	$d_{\text{Ru}}\pi_{\text{NCS}}(161) \rightarrow \pi^*_{\text{dcbpy}}(166)$	92	3.01	411	0.0208
S_{18}	$d_{\text{Ru}}\pi_{\text{NCS}}(162) \rightarrow \pi^*_{\text{dcbpy}}(167)$	92	3.04	407	0.0152
S_{19}	$\pi_{\text{NCS}}(156) \rightarrow \pi^*_{\text{dcbpy}}(165)$	73	3.09	401	0.0329
	$\pi_{\text{COO}}(154) \rightarrow \pi^*_{\text{dcbpy}}(164)$	21			
	$\pi_{\text{COO}}(154) \rightarrow \pi^*_{\text{dcbpy}}(164)$	63			
S_{21}	$\pi_{\text{NCS}}(156) \rightarrow \pi^*_{\text{dcbpy}}(165)$	24	3.10	400	0.0185
	$\pi_{\text{COO}}(155) \rightarrow \pi^*_{\text{dcbpy}}(165)$	11			
	$\pi_{\text{COO}}(155) \rightarrow \pi^*_{\text{dcbpy}}(165)$	11			
S_{59}	$\pi_{\text{dcbpy}}(149) \rightarrow \pi^*_{\text{dcbpy}}(164)$	89	3.99	311	0.1530
S_{62}	$\pi_{\text{dcbpy}}(150) \rightarrow \pi^*_{\text{dcbpy}}(165)$	89	4.07	304	0.2235

assignment of the absorption spectrum is in agreement with previously reported theoretical studies of the N3 complex.¹⁷

Since electronic spectra are highly denotative for the formation of reduced species of ruthenium polypyridine complexes, the optical absorbance of **Ru2H** was measured as a function of the electrochemical potential to determine the optimal excitation wavelength for investigating the reduced **Ru2H**. To highlight spectral changes during reduction difference UV–vis spectra have been recorded by subtracting spectra of **Ru2H** from spectra of the reduced **Ru2H**. The spectrum obtained during raising the applied potential up to -1.0 V is shown in Figure 3B. The disappearance of the first (I) and second (II) absorption bands is accompanied by the growth of a new absorption feature at around 440 nm. Furthermore, an increase of the ligand π – π^* transition below 320 nm is detected (Figure 3B). The observed spectral changes increase with increasing voltage. By comparing difference UV–vis SEC spectra of **Ru2H** during reduction in DMF with calculations of the spectra of **Ru2H** and the hypothesized reduced form of **Ru2H**, **Ru0H** (see Figure 3B and SI), the observed spectral changes agree very well with the assumption that the reduction of **Ru2H** is accompanied by deprotonation of the carboxylic acid groups of the dc bpy ligand as already suggested.³⁹ After 20 min the potential was switched to the open circuit potential (ocp) to oxidize the complex back to its neutral state. This did not result in a complete reversal of the spectral changes. Therefore, we conclude that the reduction of **Ru2H** is an irreversible process in agreement with results of cyclic voltammetry as already discussed in the previous section.

Raman. Despite the fact that the above-reported electronic absorption spectra are highly indicative of the formation of reduced ruthenium polypyridine complexes, no information about the underlying structural changes during reduction can be received, and—in particular—no information on fast excited state dynamics in the reduced complexes can be obtained. Thus, electrochemical potential controlled rR spectroscopy is well suited for the description of changes in molecular and electronic structure within a redox reaction of ruthenium polypyridine compounds.^{38,57,58} Particularly, rR spectroscopy can probe the vibrational properties of individual chromophores since this technique makes use of excitation wavelength close to a specific absorption band of the investigated ruthenium dye and allows us to investigate the sub-20-fs excited state dynamics of the electrochemically generated species.

In the case of **Ru2H**, the laser line at 458 nm, responsible for the resonant enhancement of the **Ru2H** Raman signal, is slightly off resonance and lies in between the two first absorption bands (Figure 3B). Therefore, excitation at 458 nm is resonant with $d_{Ru} \pi_{NCS} \rightarrow \pi^*_{dc bpy}$ transitions. In the rR spectrum, vibrations along those normal coordinates are selectively enhanced, which accompany the structural reorganization during excitation from $bpy \rightarrow bpy^-$. The rR spectrum of **Ru2H** dissolved in DMF shows a number of vibrational resonances in the wavenumber region between 1200 and 1700 cm^{-1} , which are typical of the bipyridine ring (Figure 5). Investigation of the calculated normal coordinates showed that the vibrations at 1260, 1609, 1542, and 1472 cm^{-1} can be assigned to C=C and C=N bpy ring-stretching vibrations.^{20,37,59,60}

In the following section the results from rR spectroscopic investigations on the electrochemically reduced **Ru2H** will be first presented and consecutively interpreted with the help of

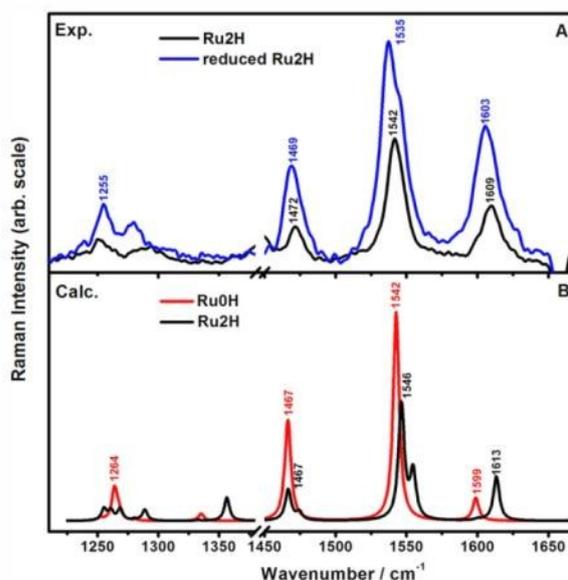


Figure 5. (A) Measured rR spectrum of **Ru2H** (10^{-4} M in DMF/0.1 M Bu_4NPF_6) (black) and reduced **Ru2H** (blue). (B) Calculated rR spectra of **Ru2H** (black) and its deprotonated form **Ru0H** (red) in DMF. The omitted region between 1375 and 1450 cm^{-1} in Panel A contains an artifact resulting from subtracting the solvent spectrum. The Raman spectrum of reduced **Ru2H** is very similar to the calculated rR spectrum of **Ru0H**. Therefore, it is postulated that **Ru2H** is reduced to **Ru0H**. The relative band intensities in rR spectra of the pure complexes and quantum chemical calculations support this interpretation.

quantum chemical calculations. The electrochemically reduced **Ru2H** possesses a similar rR spectrum with respect to **Ru2H** (see Figure 5A). This suggests that the bipyridine rings remain unaltered upon reduction. The rR spectrum of the reduced **Ru2H** shows shifts in band positions and changes in the relative band intensities in comparison to the rR spectrum of **Ru2H** (Figure 5). All Raman features are greatly enhanced when the applied potential decreases due to the increasing absorbance of the reduced **Ru2H** in contrast to **Ru2H** excited at 458 nm (Figure 5). The increase in relative Raman intensity of the reduced **Ru2H** in comparison to **Ru2H** is consistent with a higher absorption at the excitation wavelength 458 nm (see also Figure 3B) and therefore an enhanced resonance effect under reduction conditions. The Raman modes at 1542 and 1609 cm^{-1} assigned to bipyridine ligand vibrations exhibit a band broadening of 7 and 6 cm^{-1} as compared to the corresponding bands of **Ru2H**, respectively. After applying a voltage for approximately 1 min the Raman peaks at 1609 and 1542 cm^{-1} , representing the Raman band of **Ru2H**, are shifted by 6 and 7 cm^{-1} to lower wavenumbers to 1603 and 1535 cm^{-1} (see Figure 5 and Table 2). Since the band at 1542 cm^{-1} does not completely vanish even during long time measurements, we conclude that a mixture of reduced and nonreduced **Ru2H** is present in the laser focus. To prove this assumption, the spectral data were decomposed into the contribution from **Ru2H** and the reduced **Ru2H** by fitting of three Gauss peak functions per substance in the wavenumber region from 1450 to 1650 cm^{-1} (Figure 6). For the three Raman bands of reduced **Ru2H** (Figure 6A) spectral width and position were used as derived from rR spectra of **Ru2H** (Figure 6B) and not

Table 2. Comparison of the Experimentally Observed Spectral Shifts of Three Vibrations of the bpy Ligand Present in Ru2H and Its Reduced Form with Quantum Chemical Calculations of Ru2H and the Deprotonated form Ru0H Indicates That Reduction Is Accompanied by Deprotonation

species	ν_1/cm^{-1}	$\Delta\nu_1/\text{cm}^{-1}$	ν_2/cm^{-1}	$\Delta\nu_2/\text{cm}^{-1}$	ν_3/cm^{-1}	$\Delta\nu_3/\text{cm}^{-1}$
Ru2H (exp)	1472	-3	1542	-7	1609	-6
reduced Ru2H	1469		1535		1603	
Ru2H (calc.)	1467	0	1546	-4	1613	-14
Ru0H (calc.)	1467		1542		1599	

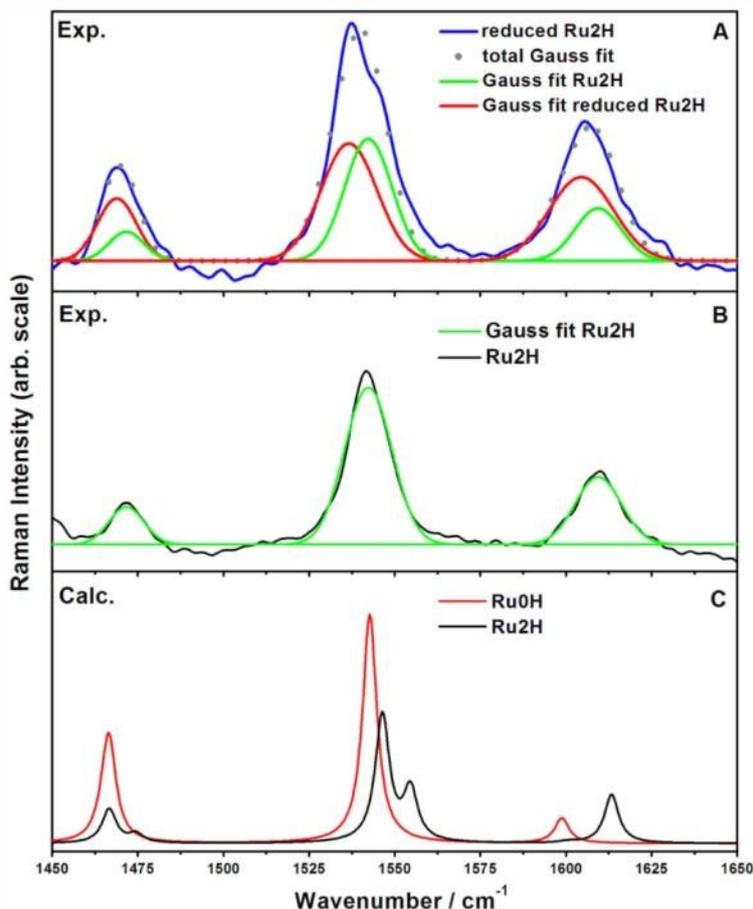


Figure 6. (A) Fitting of six Gauss peak functions of the rR spectrum **Ru2H** under reduction in the wavenumber region from 1450 to 1650 cm^{-1} . (B) Gauss fit of the rR frequencies of **Ru2H** at 1471, 1542, and 1609 cm^{-1} . (C) Calculated rR spectra of **Ru2H** (black) and its deprotonated form **Ru0H** (red) in DMF.

varied during the fit procedure. By this approach the spectral position and width of the three Raman bands of reduced **Ru2H** and band intensities of all three peaks have been obtained by optimization. The resulting fitted band position of the reduced **Ru2H** and the corresponding shift with respect to **Ru2H** are summarized in Table 2. Within the margin of error of the measurements, only the bands at 1609 and 1542 cm^{-1} are significantly shifted to lower wavenumbers, which corresponds to a reduced force constant and a lower energy of these vibrations. This decrease in energy of these two before mentioned bipyridine skeletal modes upon reduction is consistent with the population of the π^* LUMO of the bipyridine ligand which is reducing the bond order of the ligand. Furthermore, this wavenumber downshift of the Raman

bands at 1542 and 1609 cm^{-1} can be explained by deprotonation of the carboxylic acid group during reduction of **Ru2H**. This assumption will be proved by quantum chemical calculations of the rR spectrum of the hypothesized reduced form of **Ru2H**, **Ru0H** in the following section. Investigations on the fully protonated form of **Ru2H** indicate that reduction of N3 induces the loss of protons of the carboxyl groups and the formation of molecular hydrogen at the surface of platinum.³⁹

To investigate this hypothesis that deprotonation of **Ru2H** reduces the vibrational frequencies of bipyridine skeletal modes, quantum chemical calculations of **Ru2H** and its deprotonated form **Ru0H** have been performed using the DFT methods described in the theoretical section. Subsequently the results of

the calculations are compared to the experimental results. The rR calculations were performed in resonance with the excited states contributing to the two first absorption bands (Table 1) at an excitation wavelength of 458 nm. Indeed, the experimentally observed spectral shifts are in good agreement with the results of quantum chemical calculations as summarized in Table 2. The DFT methods predict a downshift of the band at 1542 cm^{-1} by 4 cm^{-1} and of the band at 1609 cm^{-1} by 14 cm^{-1} (Table 2). In addition the Raman intensity increases during reduction indicating higher resonance enhancement of the reduced **Ru2H** consistent with the observed increase of the absorption band in resonance with the excitation wavelength, 458 nm (Figure 3B). This increase of the Raman band intensity is also reproduced in the DFT calculations (Figure 6C).

CONCLUSION

Electrochemistry combined with resonance Raman spectroscopy provides a versatile tool not only to generate radical species by charge transfer reactions in situ but also to monitor their formation and to investigate their structural properties. The herein presented comparison of the experimental results of resonance Raman spectroelectrochemistry on the model compound $[(\text{H-dcbpy})_2\text{Ru}(\text{NCS})_2]^{2-}$ (**Ru2H**) with TDDFT calculations substantiates previous suggestions about the reduction mechanism of **Ru2H**.³⁹ Ligand reduction decreases the strength of binding which is reflected by shifts in the absorption spectrum as well as energy downshift of vibrational resonances assigned to skeletal bipyridine modes. This shift to lower energy is consistent with a decrease of the bond order during population of the π^* LUMO of the bipyridine ligand by the charge transfer reaction. In addition the close resemblance of UV-vis as well as resonance Raman spectra of reduced **Ru2H** with the deprotonated compound **Ru0H** both obtained experimentally and by DFT calculations shows that the reduction is accompanied by deprotonation. Furthermore, the presented DFT calculations show that the NCS orbitals contribute to the ground state of the complex. This feature might be used—when coupling the complex to a metal surface via the NCS ligands—to promote electron transfer from the metal to the photoexcited complex.^{21,22} Hence, charge accumulation on the complex might be favored, increasing the efficiency of the molecular photocatalyst. Additionally, the methodology can be used to investigate intermediates during photocatalytic processes and to analyze the reduction mechanism of heterometallic photocatalysts to deepen the understanding of light-induced charge transfer processes also in such systems.

ASSOCIATED CONTENT

Supporting Information

Time course of the band area at 1536 cm^{-1} of reduced **Ru2H**, schematic representation of the rR-SEC setup, calculated ground state absorption spectra of **Ru2H** and **Ru0H**, ESI data for **Ru0H** and **Ru2H**, calculated vertical excitation energies (E^c), oscillator strengths (f), and excited configurations of the main excited states of **Ru0H**, and complete list of coauthors for ref 41. This material is available free of charge via the Internet at <http://pubs.acs.org>.

AUTHOR INFORMATION

Corresponding Author

*E-mail: benjamin.dietzek@ipht-jena.de.

Notes

The authors declare no competing financial interest.

ACKNOWLEDGMENTS

This research was supported financially by the Thüringer Ministerium für Bildung, Wissenschaft und Kultur (grant no.: B514-09049 and grant no.: 2011 FE9096). Further financial support from the Fonds der chemischen Industrie (B.D.) is gratefully acknowledged. J.G. is grateful to the 7th Framework Programme of the European Union for his Marie Curie Career Integration Grant (VibRaman). We acknowledge the European Coordination Action COST Action CM 1202 PERSPECT-H2O.

REFERENCES

- (1) Esswein, A. J.; Nocera, D. G. Hydrogen Production by Molecular Photocatalysis. *Chem. Rev.* **2007**, *107*, 4022–4047.
- (2) Kudo, A.; Miseki, Y. Heterogeneous Photocatalyst Materials for Water Splitting. *Chem. Soc. Rev.* **2009**, *38*, 253–278.
- (3) Balzani, V.; Credi, A.; Venturi, M. Photochemical Conversion of Solar Energy. *ChemSusChem* **2008**, *1*, 26–58.
- (4) Maeda, K.; Domen, K. Photocatalytic Water Splitting: Recent Progress and Future Challenges. *J. Phys. Chem. Lett.* **2010**, *1*, 2655–2661.
- (5) Kalyanasundaram, K.; Kiwi, J.; Grätzel, M. Hydrogen Evolution from Water by Visible Light, a Homogeneous Three Component Test System for Redox Catalysis. *Helv. Chim. Acta* **1978**, *61*, 2720–2730.
- (6) Wang, M.; Na, Y.; Gorlov, M.; Sun, L. Light-Driven Hydrogen Production Catalysed by Transition Metal Complexes in Homogeneous Systems. *Dalton Trans.* **2009**, 6458–6467.
- (7) Tschierlei, S.; Karnahl, M.; Presselt, M.; Dietzek, B.; Guthmüller, J.; González, L.; Schmitt, M.; Rau, S.; Popp, J. Photochemical Fate: The First Step Determines Efficiency of H_2 Formation with a Supramolecular Photocatalyst. *Angew. Chem., Int. Ed.* **2010**, *49*, 3981–3984.
- (8) Rau, S.; Schäfer, B.; Gleich, D.; Anders, E.; Rudolph, M.; Friedrich, M.; Görls, H.; Henry, W.; Vos, J. G. A Supramolecular Photocatalyst for the Production of Hydrogen and the Selective Hydrogenation of Tolane. *Angew. Chem., Int. Ed.* **2006**, *45*, 6215–6218.
- (9) Du, P.; Schneider, J.; Li, F.; Zhao, W.; Patel, U.; Castellano, F. N.; Eisenberg, R. Bi- and Terpyridyl Platinum(II) Chloro Complexes: Molecular Catalysts for the Photogeneration of Hydrogen from Water or Simply Precursors for Colloidal Platinum? *J. Am. Chem. Soc.* **2008**, *130*, 5056–5058.
- (10) Vos, J. G.; Kelly, J. M. Ruthenium Polypyridyl Chemistry; from Basic Research to Applications and Back Again. *Dalton Trans.* **2006**, 4869–4883.
- (11) Zeitler, K. Photoredox Catalysis with Visible Light. *Angew. Chem., Int. Ed.* **2009**, *48*, 9785–9789.
- (12) Reynal, A.; Palomares, E. Ruthenium Polypyridyl Sensitizers in Dye Solar Cells Based on Mesoporous TiO_2 . *Eur. J. Inorg. Chem.* **2011**, *29*, 4509–4526.
- (13) Ward, M. D. Photoinduced Energy-Transfer in Covalently and Non-Covalently Linked Supramolecular Arrays of Metal Polypyridyl Complexes. *Int. J. Photoenergy* **1999**, *1*, 121–133.
- (14) Mishra, L.; Yadav, A. K.; Govil, G. Tailored Ruthenium Polypyridyl Complexes as Molecular Electronic Materials. *Indian J. Chem. A* **2003**, *42*, 1797–1814.
- (15) Hagfeldt, A.; Boschloo, G.; Sun, L.; Kloo, L.; Pettersson, H. Dye-Sensitized Solar Cells. *Chem. Rev.* **2010**, *110*, 6595–6663.
- (16) Grätzel, M. Dye-Sensitized Solar Cells. *J. Photochem. Photobiol. C* **2003**, *4*, 145–153.
- (17) Nazeeruddin, M. K.; Klein, C.; Liska, P.; Grätzel, M. Synthesis of Novel Ruthenium Sensitizers and Their Application in Dye-Sensitized Solar Cells. *Coord. Chem. Rev.* **2005**, *249*, 1460–1467.

- (18) Daniel, M.-C.; Astruc, D. Gold Nanoparticles: Assembly, Supramolecular Chemistry, Quantum-Size-Related Properties, and Applications toward Biology, Catalysis, and Nanotechnology. *Chem. Rev.* **2004**, *104*, 293–346.
- (19) Mayer, C. R.; Dumas, E.; Sécheresse, F. Size Controlled Formation of Silver Nanoparticles by Direct Bonding of Ruthenium Complexes Bearing a Terminal Mono- or Bi-Pyridyl Group. *Chem. Commun.* **2005**, 345–347.
- (20) Pérez León, C.; Kador, L.; Peng, B.; Thelakkat, M. Influence of the Solvent on the Surface-Enhanced Raman Spectra of Ruthenium(II) Bipyridyl Complexes. *J. Phys. Chem. B* **2005**, *109*, 5783–5789.
- (21) Zedler, L.; Theil, F.; Csáki, A.; Fritzsche, W.; Rau, S.; Schmitt, M.; Popp, J.; Dietzek, B. Ruthenium Dye Functionalized Gold Nanoparticles and their Spectral Responses. *RSC Adv.* **2012**, *2*, 4463–4471.
- (22) Theil, F.; Zedler, L.; Maerz, A.; Xie, W.; Cszaki, A.; Fritzsche, W.; Cialla, D.; Schmitt, M.; Popp, J.; Dietzek, B. Evidence for SERRS-Enhancement in the Spectra of Ruthenium-Dye Metal Nanoparticle Conjugates. *J. Phys. Chem. C* **2013**, *117* (2), 1121–1129.
- (23) McCall, K. L.; Jennings, J. R.; Wang, H.; Morandeira, A.; Peter, L. M.; Durrant, J. R.; Yellowlees, L. J.; Woollins, J. D.; Robertson, N. Novel Ruthenium Bipyridyl Dyes with S-Donor Ligands and their Application in Dye-Sensitized Solar Cells. *J. Photochem. Photobiol. A* **2009**, *202*, 196–204.
- (24) Wächtler, M.; Guthmuller, J.; González, L.; Dietzek, B. Analysis and Characterization of Coordination Compounds by Resonance Raman Spectroscopy. *Coord. Chem. Rev.* **2012**, *256*, 1479–1508.
- (25) Finnie, K. S.; Bartlett, J. R.; Woolfrey, J. L. Vibrational Spectroscopic Study of the Coordination of (2,2'-Bipyridyl-4,4'-dicarboxylic acid)Ruthenium(II) Complexes to the Surface of Nanocrystalline Titania. *Langmuir* **1998**, *14*, 2744–2749.
- (26) Greijer, H.; Lindgren, J.; Hagfeldt, A. Resonance Raman Scattering of a Dye-Sensitized Solar Cell: Mechanism of Thiocyanato Ligand Exchange. *J. Phys. Chem. B* **2001**, *105*, 6314–6320.
- (27) Lainé, P. P.; Campagna, S.; Loiseau, F. Conformationally Gated Photoinduced Processes within Photosensitizer–Acceptor Dyads Based on Ruthenium(II) and Osmium(II) Polypyridyl Complexes with an Appended Pyridinium Group. *Coord. Chem. Rev.* **2008**, *252*, 2552–2571.
- (28) Damrauer, N. H.; Cerullo, G.; Yeh, A.; Boussie, T. R.; Shank, C. V.; McCusker, J. K. Femtosecond Dynamics of Excited-State Evolution in $[\text{Ru}(\text{bpy})_3]^{2+}$. *Science* **1997**, *275*, 54–57.
- (29) Dietzek, B.; Kiefer, W.; Blumhoff, J.; Böttcher, L.; Rau, S.; Walther, D.; Uhlemann, U.; Schmitt, M.; Popp, J. Ultrafast Excited-State Excitation Dynamics in a Quasi-Two-Dimensional Light-Harvesting Antenna Based on Ruthenium(II) and Palladium(II) Chromophores. *Chem.—Eur. J.* **2006**, *12*, 5105–5115.
- (30) Hannappel, T.; Burfeindt, B.; Storck, W.; Willig, F. Measurement of Ultrafast Photoinduced Electron Transfer from Chemically Anchored Ru-Dye Molecules into Empty Electronic States in a Colloidal Anatase TiO_2 Film. *J. Phys. Chem. B* **1997**, *101*, 6799–6802.
- (31) Tachibana, Y.; Moser, J. E.; Grätzel, M.; Klug, D. R.; Durrant, J. R. Subpicosecond Interfacial Charge Separation in Dye-Sensitized Nanocrystalline Titanium Dioxide Films. *J. Phys. Chem.* **1996**, *100*, 20056–20062.
- (32) Tachibana, Y.; Haque, S. A.; Mercer, I. P.; Durrant, J. R.; Klug, D. R. Electron Injection and Recombination in Dye Sensitized Nanocrystalline Titanium Dioxide Films: A Comparison of Ruthenium Bipyridyl and Porphyrin Sensitizer Dyes. *J. Phys. Chem. B* **2000**, *104*, 1198–1205.
- (33) Clifford, J. N.; Palomares, E.; Nazeeruddin, M. K.; Grätzel, M.; Durrant, J. R. Dye Dependent Regeneration Dynamics in Dye Sensitized Nanocrystalline Solar Cells: Evidence for the Formation of a Ruthenium Bipyridyl Cation/Iodide Intermediate. *J. Phys. Chem. C* **2007**, *111*, 6561–6567.
- (34) Asbury, J. B.; Ellingson, R. J.; Ghosh, H. N.; Ferrere, S.; Nozik, A. J.; Lian, T. Femtosecond IR Study of Excited-State Relaxation and Electron-Injection Dynamics of $\text{Ru}(\text{dcbpy})_2(\text{NCS})_2$ in Solution and on Nanocrystalline TiO_2 and Al_2O_3 Thin Films. *J. Phys. Chem. B* **1999**, *103*, 3110–3119.
- (35) Kukura, P.; McCamant, D. W.; Mathies, R. A. Femtosecond Stimulated Raman Spectroscopy. *Annu. Rev. Phys. Chem.* **2007**, *58*, 461–488.
- (36) Nahhas, A. E.; Cannizzo, A.; van Mourik, F.; Blanco-Rodríguez, A. M.; Zláliš, S.; Vlček, J.; Chergui, M. Ultrafast Excited-State Dynamics of $[\text{Re}(\text{L})(\text{CO})_3(\text{bpy})]^\text{n}$ Complexes: Involvement of the Solvent. *J. Phys. Chem. A* **2010**, *114*, 6361–6369.
- (37) Hugot-Le Goff, A.; Joiret, S.; Falaras, P. Raman Resonance Effect in a Monolayer of Polypyridyl Ruthenium(II) Complex Adsorbed on Nanocrystalline TiO_2 via Phosphonated Terpyridyl Ligands. *J. Phys. Chem. B* **1999**, *103*, 9569–9575.
- (38) Bernard, M. C.; Cachet, H.; Falaras, P.; Goff, A. H.-L.; Kalbac, M.; Lukes, L.; Oanh, N. T.; Stergiopoulos, T.; Arabatzis, I. Sensitization of TiO_2 by Polypyridine Dyes Role of the Electron Donor. *Trans. Electrochem. Soc.* **2003**, *150*, E155–E164.
- (39) Wolfbauer, G.; Bond, A. M.; Deacon, G. B.; MacFarlane, D. R.; Spiccia, L. Experimental and Theoretical Investigations of the Effect of Deprotonation on Electronic Spectra and Reversible Potentials of Photovoltaic Sensitizers: Deprotonation of cis- L_2RuX_2 ($\text{L} = 2,2'$ -Bipyridine-4,4'-dicarboxylic Acid; $\text{X} = \text{CN}^-$, NCS^-) by Electrochemical Reduction at Platinum Electrodes. *J. Am. Chem. Soc.* **2000**, *122*, 130–142.
- (40) Kämper, S.; Paretzki, A.; Fiedler, J.; Zláliš, S.; Kaim, W. Solar Cell Sensitizer Models $[\text{Ru}(\text{bpy}-\text{R})_2(\text{NCS})_2]$ Probed by Spectroelectrochemistry. *Inorg. Chem.* **2012**, *51*, 2097–2104.
- (41) Frisch, M. J.; Trucks, G. W.; Schlegel, H. B.; Scuseria, G. E.; Robb, M. A.; Cheeseman, J. R.; Scalmani, G.; Barone, V.; Mennucci, B.; Petersson, G. A. et al. *Gaussian 09*, Gaussian, Inc.: Wallingford, CT, 2009.
- (42) Becke, A. D. Density - Functional Thermochemistry. III. The Role of Exact Exchange. *J. Chem. Phys.* **1993**, *98*, 5648–5652.
- (43) Lee, C.; Yang, W.; Parr, R. G. Development of the Colle-Salvetti Correlation-Energy Formula into a Functional of the Electron Density. *Phys. Rev. B* **1988**, *37*, 785–789.
- (44) Andrae, D.; Häußermann, U.; Dolg, M.; Stoll, H.; Preuß, H. Energy-Adjusted *ab initio* Pseudopotentials for the Second and Third Row Transition Elements: Molecular Test for M_2 ($\text{M} = \text{Ag}, \text{Au}$) and MH ($\text{M} = \text{Ru}, \text{Os}$). *Theor. Chim. Acta* **1991**, *78*, 247–266.
- (45) Hariharan, P. C.; Pople, J. A. The Influence of Polarization Functions on Molecular Orbital Hydrogenation Energies. *Theor. Chim. Acta* **1973**, *28*, 213–222.
- (46) Merrick, J. P.; Moran, D.; Radom, L. An Evaluation of Harmonic Vibrational Frequency Scale Factors. *J. Phys. Chem. A* **2007**, *111*, 11683–11700.
- (47) Kupfer, S.; Guthmuller, J.; Wächtler, M.; Losse, S.; Rau, S.; Dietzek, B.; Popp, J.; González, L. Protonation Effects on the Resonance Raman Properties of a Novel (terpyridine)Ru(4H-imidazole) Complex: an Experimental and Theoretical Case Study. *Phys. Chem. Chem. Phys.* **2011**, *13*, 15580–15588.
- (48) Kupfer, S.; Wächtler, M.; Guthmuller, J.; Popp, J.; Dietzek, B.; González, L. A Novel Ru(II) Polypyridine Black Dye Investigated by Resonance Raman Spectroscopy and TDDFT Calculations. *J. Phys. Chem. C* **2012**, *116*, 19968–19977.
- (49) Escudero, D.; González, L. RASPT2/RASSCF vs Range-Separated/Hybrid DFT Methods: Assessing the Excited States of a Ru(II)bipyridyl Complex. *J. Chem. Theory Comput.* **2012**, *8*, 203–213.
- (50) Tomasi, J.; Mennucci, B.; Cammi, R. Quantum Mechanical Continuum Solvation Models. *Chem. Rev.* **2005**, *105*, 2999–3094.
- (51) Peticolas, W. L.; Rush, T. *Ab initio* Calculations of the Ultraviolet Resonance Raman Spectra of Uracil. *J. Comput. Chem.* **1995**, *16*, 1261–1270.
- (52) Guthmuller, J.; González, L. Simulation of the Resonance Raman Intensities of a Ruthenium–Palladium Photocatalyst by Time Dependent Density Functional Theory. *Phys. Chem. Chem. Phys.* **2010**, *12*, 14812–14821.
- (53) Guthmuller, J.; Champagne, B. Time Dependent Density Functional Theory Investigation of the Resonance Raman Properties

of the Julolidinemalononitrile Push-Pull Chromophore in Various Solvents. *J. Chem. Phys.* **2007**, *127*, 164507–164511.

(54) Braterman, P. S.; Song, J.-I.; Peacock, R. D. Spectroelectrochemistry and Localization of Added Electrons in Ruthenium (II) Mixed-Ligand Complexes. *Spectrochim. Acta* **1992**, *48A*, 899–903.

(55) Cecchet, F.; Gioacchini, A. M.; Marcaccio, M.; Paolucci, F.; Roffia, S.; Alebbi, M.; Bignozzi, C. A. Solvent Effects on the Oxidative Electrochemical Behavior of cis-Bis(isothiocyanato)ruthenium(II)-bis-2,2'-bipyridine-4,4'-dicarboxylic Acid. *J. Phys. Chem. B* **2002**, *106*, 3926–3932.

(56) Sun, Y.; Onicha, A. C.; Myahkostupov, M.; Castellano, F. N. Viable Alternative to N719 for Dye-Sensitized Solar Cells. *ACS Appl. Mater. Interfaces* **2010**, *2*, 2039–2045.

(57) Kaim, W.; Fiedler, J. Spectroelectrochemistry: The Best of Two Worlds. *Chem. Soc. Rev.* **2009**, *38*, 3373–3382.

(58) Falaras, P.; Hugot-Le Goff, A.; Bernard, M. C.; Xagas, A. Characterization by Resonance Raman Spectroscopy of Sol-Gel TiO₂ Films Sensitized by the Ru(PPh₃)₂(dcbipy)Cl₂ Complex for Solar Cells Application. *Sol. Energy Mater. Sol. Cells* **2000**, *64*, 167–184.

(59) Stergiopoulos, T.; Karakostas, S.; Falaras, P. Comparative Studies of Substituted Ruthenium(II)–Pyrazoyl–Pyridine Complexes With Classical N3 Photosensitizer: The Influence of -NCS Dye Ligands on the Efficiency of Solid-State Nanocrystalline Solar Cells. *J. Photochem. Photobiol. A* **2004**, *163*, 331–340.

(60) Schneider, S.; Brehm, G.; Prenzel, C.-J.; Jäger, W.; Silva, M. I.; Burrows, H. D.; Formosinho, S. T. Vibrational Spectra, Normal Coordinate Analysis and Excited-State Lifetimes for a Series of Polypyridylruthenium(II) Complexes. *J. Raman Spectrosc.* **1996**, *27*, 163–175.

Supporting Information

Redox State Sensitive Spectroscopy of the Model Compound $[(\text{H-dcbpy})_2\text{Ru}^{\text{II}}(\text{NCS})_2]^{2-}$ (dcbpy = 2,2'- bipyridine-4,4'-dicarboxylato)

*Linda Zedler,[#] Julien Guthmuller,[†] Inês Rabelo de Moraes,[†] Sven Krieck,[‡] Michael Schmitt,[#]
Jürgen Popp,^{#†} Benjamin Dietzek^{#†*}*

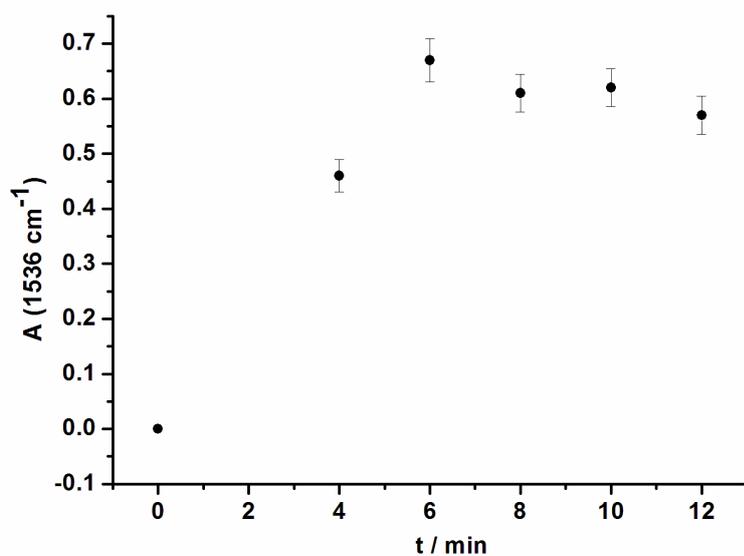
[#]Institute of Physical Chemistry and Abbe Center of Photonics, Friedrich-Schiller University
Jena, Jena, Germany

[†]Faculty of Applied Physics and Mathematics, Gdansk University of Technology, Narutowicza
11/12, 80233 Gdansk, Poland

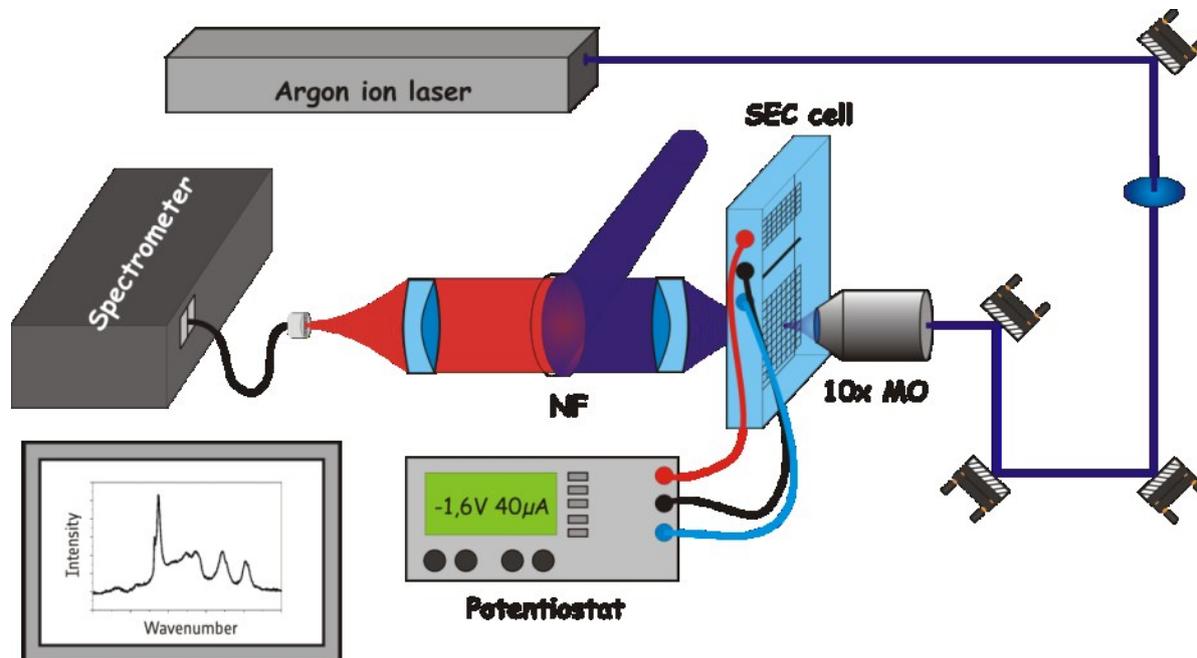
[†]Institute of Photonic Technology (IPHT), Research Group Ultrafast Spectroscopy, Albert-
Einstein Strasse 9, 07745 Jena, Germany

[‡]Institute of Inorganic and Analytical Chemistry, Friedrich-Schiller University Jena, Jena,
Germany

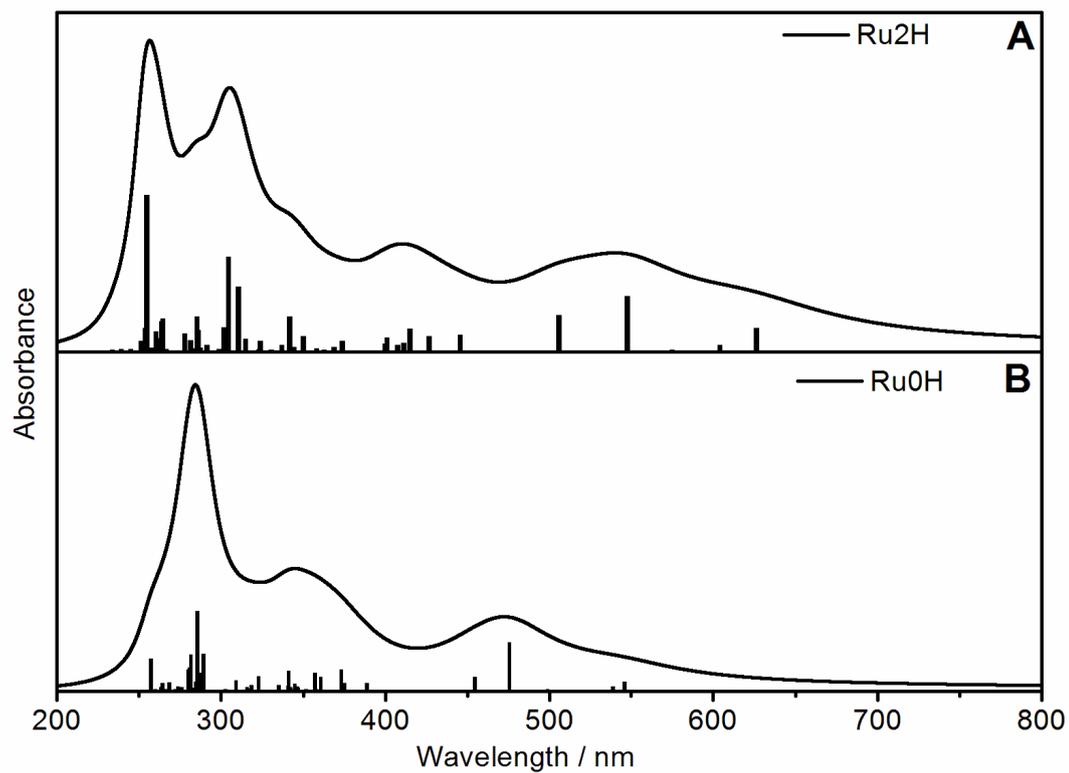
* corresponding author contact: Benjamin.Dietzek@ipht-jena.de



SI 1: Time course of the band area at 1536 cm⁻¹ of reduced **Ru2H**. The band area and thus the concentration of reduced **Ru2H** increases for app. 4 minutes until a stationary condition is reached, i.e. the electrode surfaces are completely coated and/or an equilibrium for the reduction of **Ru2H** is established.



SI 2: General rR-SEC setup: rR-SEC measurements were performed in transmission. The laser is focused onto the grid of the working electrode by a microscope objective (MO). Notchfilter (NF) is used to block the laser line.



SI 3: Calculated ground state absorption spectra of **Ru2H** (A) and **Ru0H** (B) with oscillator strength as histogram.

ESI Data:

Table S1: Molecular orbitals involved in the main configurations of the excited states of **Ru2H**.

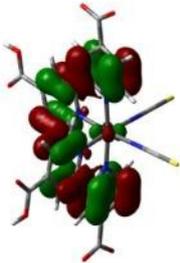
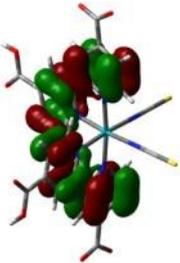
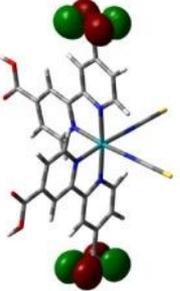
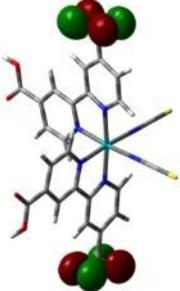
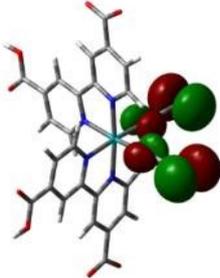
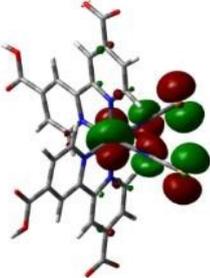
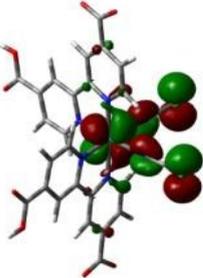
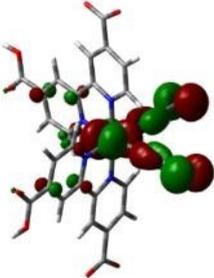
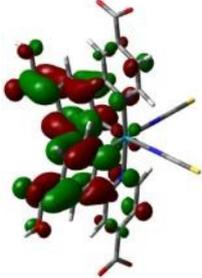
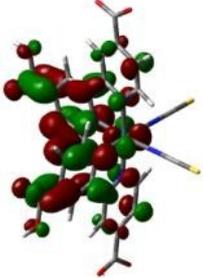
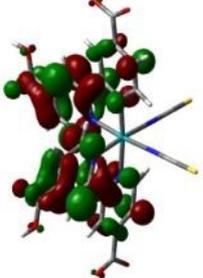
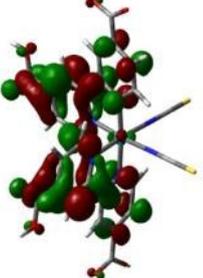
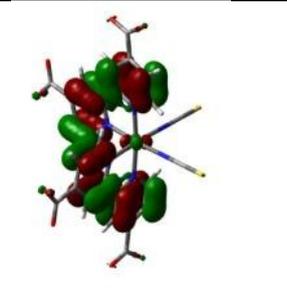
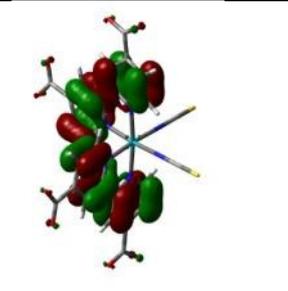
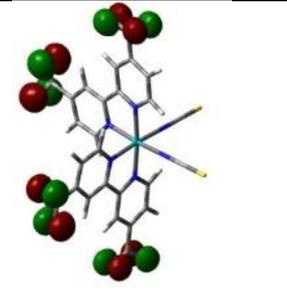
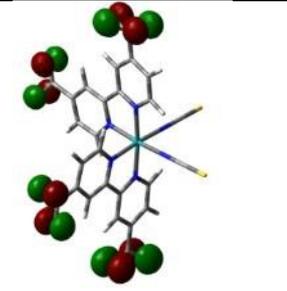
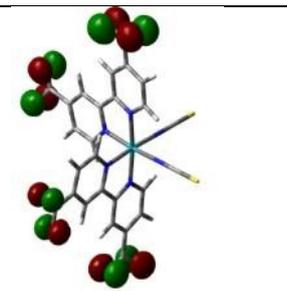
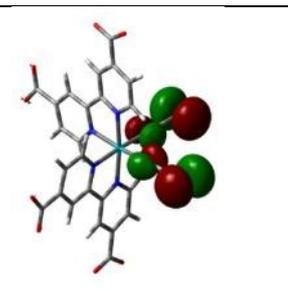
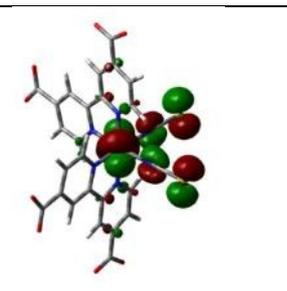
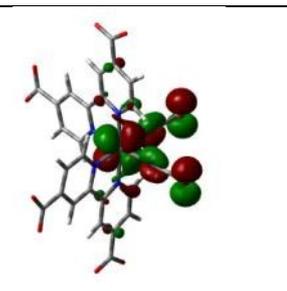
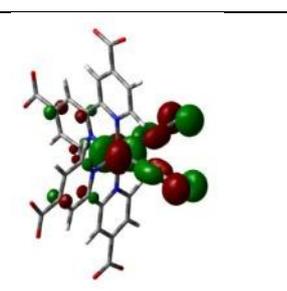
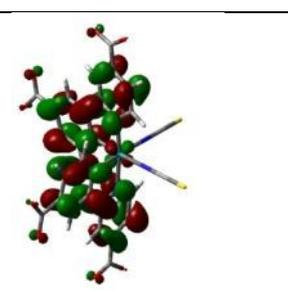
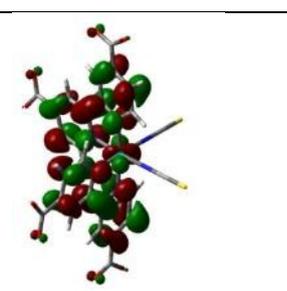
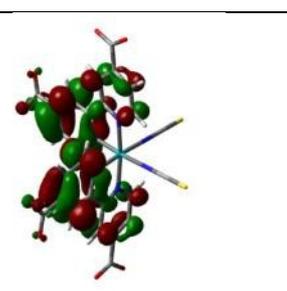
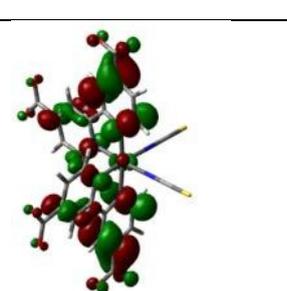
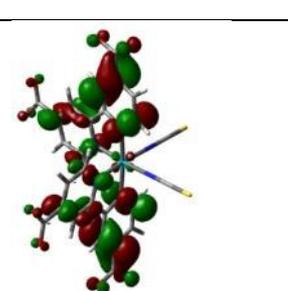
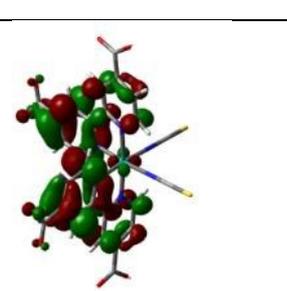
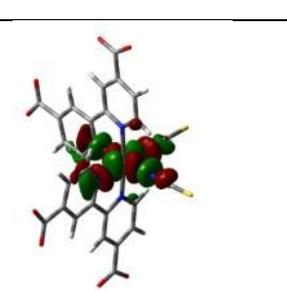
 $\pi_{\text{dcbpy}}(149)$	 $\pi_{\text{dcbpy}}(150)$	 $\pi_{\text{COO}}(154)$	 $\pi_{\text{COO}}(155)$
 $\pi_{\text{NCS}}(156)$	 $d_{\text{Ru}}, \pi_{\text{NCS}}(161)$	 $d_{\text{Ru}}, \pi_{\text{NCS}}(162)$	 $d_{\text{Ru}}, \pi_{\text{NCS}}(163)$
 $\pi^*_{\text{dcbpy}}(164)$	 $\pi^*_{\text{dcbpy}}(165)$	 $\pi^*_{\text{dcbpy}}(166)$	 $\pi^*_{\text{dcbpy}}(167)$

Table S2: Calculated vertical excitation energies (E^e), oscillator strengths (f), and excited configurations with weights larger than 10% of the main excited states of **RuOH**.

state	transition	weight (%)	E^e (eV)	λ (nm)	f
S ₁	$d_{Ru}, \pi_{NCS}(163) \rightarrow \pi^*_{dcbpy}(164)$	95	2.27	546	0.0279
S ₂	$d_{Ru}, \pi_{NCS}(163) \rightarrow \pi^*_{dcbpy}(165)$	88	2.30	539	0.0124
S ₅	$d_{Ru}, \pi_{NCS}(161) \rightarrow \pi^*_{dcbpy}(164)$	72	2.61	476	0.1433
	$d_{Ru}, \pi_{NCS}(162) \rightarrow \pi^*_{dcbpy}(165)$	23			
S ₆	$d_{Ru}, \pi_{NCS}(161) \rightarrow \pi^*_{dcbpy}(165)$	64	2.73	455	0.0409
	$d_{Ru}, \pi_{NCS}(162) \rightarrow \pi^*_{dcbpy}(164)$	20			
S ₁₁	$d_{Ru}, \pi_{NCS}(163) \rightarrow \pi^*_{dcbpy}(166)$	95	3.19	389	0.0225
S ₁₂	$d_{Ru}, \pi_{NCS}(163) \rightarrow \pi^*_{dcbpy}(167)$	83	3.31	375	0.0240
S ₁₅	$d_{Ru}, \pi_{NCS}(163) \rightarrow \pi^*_{dcbpy}(168)$	92	3.32	373	0.0628
S ₂₁	$d_{Ru}, \pi_{NCS}(163) \rightarrow \pi^*_{dcbpy}(169)$	57	3.44	361	0.0419
	$d_{Ru}, \pi_{NCS}(162) \rightarrow \pi^*_{dcbpy}(166)$	17			
	$d_{Ru}, \pi_{NCS}(162) \rightarrow \pi^*_{dcbpy}(168)$	10			
S ₂₅	$d_{Ru}, \pi_{NCS}(162) \rightarrow \pi^*_{dcbpy}(167)$	65	3.47	357	0.0531
	$d_{Ru}, \pi_{NCS}(161) \rightarrow \pi^*_{dcbpy}(166)$	27			
S ₃₁	$\pi_{NCS}(152) \rightarrow \pi^*_{dcbpy}(165)$	35	3.60	345	0.0222
	$d_{Ru}, \pi_{NCS}(162) \rightarrow \pi^*_{dcbpy}(169)$	28			
	$d_{Ru}, \pi_{NCS}(163) \rightarrow d_{Ru}, \sigma^*(173)$	22			
S ₃₄	$\pi_{COO}(150) \rightarrow \pi^*_{dcbpy}(164)$	35	3.64	341	0.0589
	$d_{Ru}, \pi_{NCS}(161) \rightarrow \pi^*_{dcbpy}(168)$	22			
	$\pi_{COO}(151) \rightarrow \pi^*_{dcbpy}(165)$	20			
S ₆₇	$\pi_{dcbpy}(144) \rightarrow \pi^*_{dcbpy}(164)$	84	4.29	289	0.1089
S ₇₀	$\pi_{dcbpy}(143) \rightarrow \pi^*_{dcbpy}(164)$	41	4.35	285	0.2346
	$d_{Ru}, \pi_{NCS}(161) \rightarrow d_{Ru}, \sigma^*(173)$	18			

S_{71}	$\pi_{\text{dcbpy}}(144) \rightarrow \pi^*_{\text{dcbpy}}(165)$	75	4.35	285	0.1372
S_{81}	$\pi_{\text{COO}}(149) \rightarrow \pi^*_{\text{dcbpy}}(166)$	37	4.41	281	0.1069
	$\pi_{\text{COO}}(150) \rightarrow \pi^*_{\text{dcbpy}}(166)$	31			

Table S3: Molecular orbitals involved in the main configurations of the excited states of **RuOH**.

			
$\pi_{\text{dcbpy}}(143)$	$\pi_{\text{dcbpy}}(144)$	$\pi_{\text{COO}}(149)$	$\pi_{\text{COO}}(150)$
			
$\pi_{\text{COO}}(151)$	$\pi_{\text{NCS}}(152)$	$d_{\text{Ru}},\pi_{\text{NCS}}(161)$	$d_{\text{Ru}},\pi_{\text{NCS}}(162)$
			
$d_{\text{Ru}},\pi_{\text{NCS}}(163)$	$\pi^*_{\text{dcbpy}}(164)$	$\pi^*_{\text{dcbpy}}(165)$	$\pi^*_{\text{dcbpy}}(166)$
			
$\pi^*_{\text{dcbpy}}(167)$	$\pi^*_{\text{dcbpy}}(168)$	$\pi^*_{\text{dcbpy}}(169)$	$d_{\text{Ru}},\sigma^*(173)$

(41) Frisch, M. J. Trucks, G. W. Schlegel, H. B. Scuseria, G. E. Robb, M. A. Cheeseman, J. R. Scalmani, G. Barone, V. Mennucci, B. Petersson, G. A. Nakatsuji, H. Caricato, M. Li, X. Hratchian, H. P. Izmaylov, A. F. J. Bloino, G. Z. Sonnenberg, J. L. Hada, M. Ehara, M. Toyota, K. Fukuda, R. Hasegawa, J. Ishida, M. Nakajima, T. Honda, Y. Kitao, O. Nakai, H. Vreven, T. Montgomery, J. J. A. Peralta, J. E. Ogliaro, F. Bearpark, M. Heyd, J. J. Brothers, E. Kudin, K. N. Staroverov, V. N. Kobayashi, R. Normand, J. Raghavachari, K. Rendell, A. Burant, J. C. Iyengar, S. S. Tomasi, J. Cossi, M. Rega, N. Millam, J. M. Klene, M. Knox, J. E. Cross, J. B. Bakken, V. Adamo, C. Jaramillo, J. Gomperts, R. Stratmann, R. E. O. Yazyev, A. J. A. R. Cammi, C. P. Ochterski, J. W. Martin, R. L. Morokuma, K. Zakrzewski, V. G. Voth, G. A. Salvador, P. Dannenberg, J. J. Dapprich, S. Daniels, A. D. Farkas, O. Foresman, J. B. Ortiz, J. V. Cioslowski, J.; Fox, D. J. *Gaussian 09*; Gaussian, Inc., Wallingford, CT, 2009.

[Zedler et al. Chem. Eur. J.]

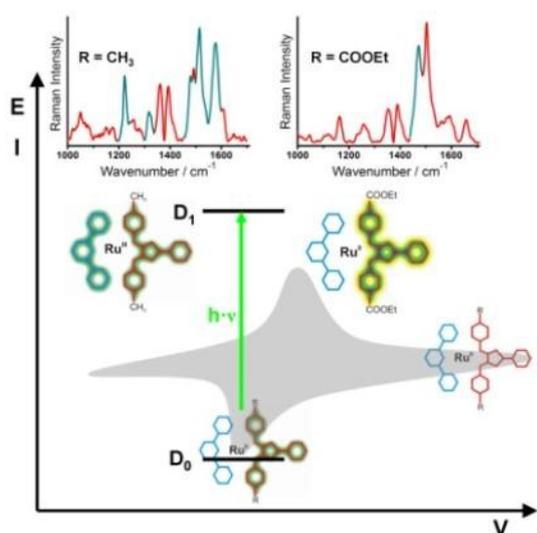
Trapped in Imidazole - How to Accumulate Multiple Photoelectrons on a Black Absorbing Ruthenium Complex

Der Nachdruck der folgenden Publikation erfolgt mit freundlicher Genehmigung von Wiley-VCH Verlag GmbH & Co KGaA, Weinheim.

Reprinted with kind permission from:

Zedler, L.; Kupfer, S.; Rabelo de Moraes, I.; Wächtler, M.; Beckert, R.; Schmitt, M.; Popp, J.; Rau, S. und Dietzek, B., *Chem. Eur. J.* **2014**, *20*, 3793–3799.

Copyright 2014 Wiley-VCH Verlag GmbH & Co KGaA, Weinheim.



The structure of short lived intermediates concentrating multiple photoelectrons strongly impacts on the efficiency of photocatalysis, e.g., for hydrogen generation, but their spectroscopic investigation is challenging. Instead electrochemically generated anions of Ru^{II}-4*H*-imidazole, which are identical to these intermediates, were studied by in situ spectro-electrochemistry and TDDFT calculations illuminating the intimate interplay of structure and charge transfer dynamics at 4*H*-imidazole.

Trapped in Imidazole: How to Accumulate Multiple Photoelectrons on a Black-Absorbing Ruthenium Complex

Linda Zedler,^[a] Stephan Kupfer,^[a] Inês Rabelo de Moraes,^[b] Maria Wächtler,^[b]
Rainer Beckert,^[c] Michael Schmitt,^[a] Jürgen Popp,^[a, b] Sven Rau,^[d] and Benjamin Dietzek^{*[a, b]}

Abstract: Ruthenium dyes incorporating a 4*H*-imidazole chromophore as a ligand exhibit a spectrally broad absorption in the UV/Vis region. Furthermore, they show the ability to store two electrons within the 4*H*-imidazole ligand. These features render them promising molecular systems, for example, as inter- or intramolecular electron relays. To optimize the structures with respect to their electron-storage capability, it is crucial to understand the impact of structural changes accompanying photoinduced charge transfer in the electronic intermediates of multistep electron-transfer processes. The photophysical properties of these (reactive) in-

termediates might impact the function of the molecular systems quite substantially. However, the spectroscopic study of short-lived intermediates in stepwise multielectron-transfer processes is experimentally challenging. To this end, this contribution reports on the electrochemical generation of anions identical to intermediate structures and their spectroscopic characterization by in situ resonance Raman and UV/Vis spectroelectrochemistry and computational methods. Thereby, an efficient two-electron pathway to the 4*H*-imidazole electron-accepting ligand is identified.

Introduction

Improving the efficiency of light-induced multielectron charge-transfer processes is a major prerequisite for the replacement of fossil fuels by sustainable solar energy to reduce the greenhouse effect and man's impact on the environment. One path towards this goal involves the design of light-driven photocatalysts capable of collecting multiple electrons from subsequent photoexcitation events, for example, for hydrogen generation.^[1–3] The optimization of these systems depends on (i) the development of efficient two-electron redox pathways and (ii) the optimization of the catalysts absorption characteristics so that they match the solar spectrum.^[4,5] These general requirements hold true both for intermolecular catalysts com-

posed of individual components^[6] and intramolecular systems, which combine antenna, primary electron donor, electron-relay structure, and a reaction center in one single molecular entity.

Ru^{II}-polypyridyl complexes, capable of multielectron storage upon light excitation present the best man-made analogues of natural light-harvesting structures for the design of light-driven energy-conversion systems.^[7,8] Although there is great demand for compact functional building blocks that are both capable of storing two or more electrons in a single acceptor ligand and exhibit electronic absorption spectra spanning the entire visible spectral range, the availability of such black-absorbing complexes is still very limited.^[5]

The small and chemically stable anion of 2-phenyl-*N,N'*-substituted-5-*p*-amino-4-*p*-iminoimidazole (4*H*-imidazole,^[9] see Figure 1 a) possesses unique properties, such as the capability to store two electrons, high absorption and, high structural variability, which can be exploited to tune the electronic structure of the system. The redox cycle of the free 4*H*-imidazole involves a reversible two-electron reduction to an aromatic trianion, spatially confining two electrons (see the Supporting Information, Figure S1).^[10,11] These properties render the 4*H*-imidazole chromophore an ideal ligand for incorporation into inter- or intramolecular electron-transfer cascades. Indeed, Ru^{II}-polypyridyl complexes incorporating the 4*H*-imidazole fragment show interesting properties, such as extremely broad absorption in the visible to NIR spectral range owing to strong metal–ligand charge-transfer (MLCT) and additional ligand-centered (LC) transitions.^[12–14] Additionally, the photoinduced electron-transfer kinetics are centered on the 4*H*-imidazole ligand and easily tuned by substitution.^[12] However, up to now, the properties of the reduced complexes have not been studied

[a] L. Zedler, Dr. S. Kupfer, Prof. Dr. M. Schmitt, Prof. Dr. J. Popp, Prof. Dr. B. Dietzek
Institute of Physical Chemistry, Friedrich Schiller University Jena
Helmholtzweg 4, 07743 Jena (Germany)
Fax: (+49) 3641-948302
E-mail: benjamin.dietzek@uni-jena.de

[b] Dr. I. R. de Moraes, Dr. M. Wächtler, Prof. Dr. J. Popp, Prof. Dr. B. Dietzek
Leibniz-Institute of Photonic Technology Jena (IPHT)
Albert-Einstein-Strasse 9, 07745 Jena (Germany)

[c] Prof. Dr. R. Beckert
Institute of Organic Chemistry and Macromolecular Chemistry
Friedrich Schiller University Jena
Humboldtstrasse 10, 07743 Jena (Germany)

[d] Prof. Dr. S. Rau
Institute of Inorganic Chemistry
University Ulm, Albert-Einstein-Allee 11, 89081 Ulm (Germany)

Supporting information for this article is available on the WWW under <http://dx.doi.org/10.1002/chem.201304937>.

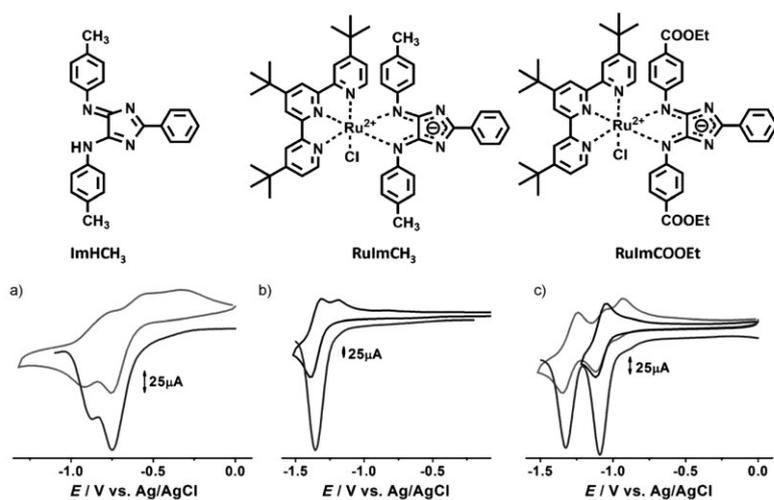
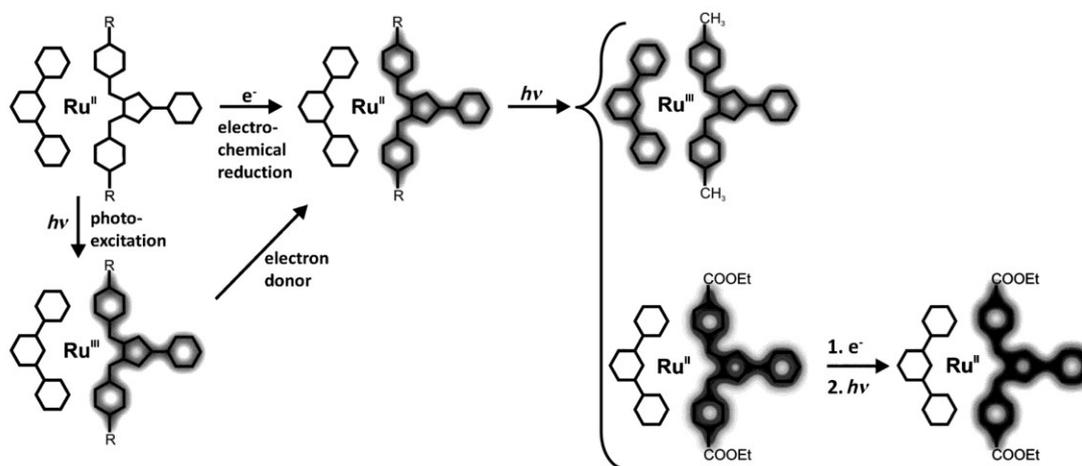


Figure 1. Molecular structures and corresponding cyclic voltammograms for the reduction of a) **ImHCH₃**, b) **RuImCH₃**, and c) **RuImCOOEt** in 0.1 M tetrabutylammonium tetrafluoroborate (TBABF₄)/ACN (acetonitrile) at a glassy carbon working electrode. The scan rate is 100 mV s⁻¹. Square-wave technique (dark grey curves) was applied for better analysis of the electrochemical data.

spectroscopically, despite their relevance to applications of the systems, for example, in accumulating charges for artificial photosynthesis.

Although time-resolved-spectroscopy-derived structure–dynamic relationships^[15] provide the molecular details of individual photoinduced charge-separation steps on the femto- to the nanosecond time scale,^[16] extended charge-transfer cycles,

for example, in inter- and intra-molecular photocatalysis, require the observation and characterization of photophysical/photochemical processes within long-lived intermediates on the microsecond time scale. As evident from Scheme 1, reduction of the photooxidized Ru^{III} ion results in a photochemically produced intermediate, that is, the aromatic anion of ruthenium-4*H*-imidazoles, which is identical to an electrochemical reduction product. Therefore, electrochemistry can be used to generate catalytically important intermediates in multielectron redox pathways.^[17] In this contribution, we utilize (resonance Raman) spectroelectrochemistry (RR-SEC)^[18] to study structural changes associated with one- or multielectron reduction and to identify photoexcited states of reduced Ru^{II}-polypyridyl 4*H*-imidazole complexes, which represent promising structures for intramolecular charge accumulation.^[2] Furthermore, we report on the effect of structural modifications with the aim to confine two electrons from reduction and photoexcitation of the ruthenium complex at the 4*H*-imidazole ligand. To this end, the study at hand combines SEC with (time-dependent) density functional theory (TDDFT).



Scheme 1. Comparison of electron-transfer processes during photoexcitation and subsequent re-reduction of the photooxidized Ru^{III} center by an electron donor with electrochemical reduction. The electrochemically reduced species is identical to the short-lived intermediate of the photochemical path, which is difficult to prepare for detailed structural investigation. The Cl⁻ ligand and the initial charge of the ligands have been omitted. The scheme represents the processes involved in electrochemical reduction and subsequent photoexcitation, as revealed by RR-SEC in combination with TDDFT calculations. Depending on the substituent bound to the arylimino residues of the 4*H*-imidazole fragment, the photoexcited reduced species either corresponds to a triplet state, in which electrons are localized on the terpyridine and 4*H*-imidazole ligand and is not suited for following efficient directional two-electron transfer (**RuImCH₃**), or a localized two-electron donor state (**RuImCOOEt**) that is well suited for subsequent catalysis. One-electron activation (light grey), two-electron activation (grey), and three-electron activation (dark grey).

Results and Discussion

We start with presenting the cyclic voltammogram (CV) for the reduction of the free ligand, **ImHCH₃** (2-(phenyl)-5-*p*-tolylimino-4-*p*-tolylimino-4*H*-imidazole), which exhibits two irreversible reduction events at potentials of -0.66 and -0.84 V (Figure 1 a, Table 1).

Table 1. Redox potentials of **ImHCH₃**, **RulmCH₃**, and **RulmCOOEt** obtained in 0.1 M TBABF₄/ACN at a glassy carbon working electrode (scan rate 100 mV s⁻¹, platinum counter electrode, Ag/AgCl reference electrode).

Compound	1st reduction [V]	2nd reduction [V]
ImHCH₃	-0.66	-0.84
RulmCH₃	-1.36	–
RulmCOOEt	-1.09	-1.29

The irreversibility of the reduction of the free ligand, **ImHCH₃**, is caused by deprotonation of the exocyclic amino groups. Square-wave techniques allow for the identification of two separate one-electron transfer steps (Figure 1 a). By deprotonation of the molecule during the first reduction step, protons are released, which preferable react with the two-electron-reduced 4*H*-imidazole to give the 1*H*-imidazole, which is immediately reoxidized in the presence of trace amounts of oxygen.^[10,11] Therefore, we most likely only detect the one-electron-reduced species of the free ligand spectroscopically. The reduction potential of **ImHCOOEt** is, according to Gebauer et al., significantly less negative than that of **ImHCH₃**.^[19] **RulmCH₃** (chloro-η³-4,4',4''-tri-*tert*-butyl-2,2':6',2''-terpyridin-η²-phenyl-4,5-*p*-tolylimino-imidazolato-Ru^{II}) and **RulmCOOEt** (chloro-η³-4,4',4''-tri-*tert*-butyl-2,2':6',2''-terpyridin-η²-phenyl-4,5-(*p*-ethylcarboxyphenyl-imino)-imidazolato-Ru^{II}) differ with respect to the substituents at the arylimino residues of the 4*H*-imidazole fragment (Figure 1). For **RulmCH₃**, a one-electron reduction at -1.36 V localized at the 4*H*-imidazole ligand is observed within the applied potential range (Figure 1 b, Table 1). Because two peaks appear in the reoxidation curve, a two-step back reaction or the formation of a follow-up product occur during reduction. In contrast to **RulmCH₃**, the first reduction of **RulmCOOEt** is fully reversible whereas the second reduction leads to the formation of an additional feature in the CV (Figure 1 c). Furthermore, the first reduction potential is shifted by nearly +300 mV in comparison to **RulmCH₃** (Table 1), thus demonstrating that the electron-withdrawing COOEt substituents facilitate the acceptance of electrons by the 4*H*-imidazole ligand.

Although cyclic voltammetry allows the identification of the presence of reduction products, no information on the location of the negative charge and accompanying structure changes is retrieved. To gain insight into the structure of the reduced compounds, the electrochemically reduced forms were investigated by UV/Vis and RR spectroscopy. For an interpretation of the spectral data, quantum chemical calculations were performed.

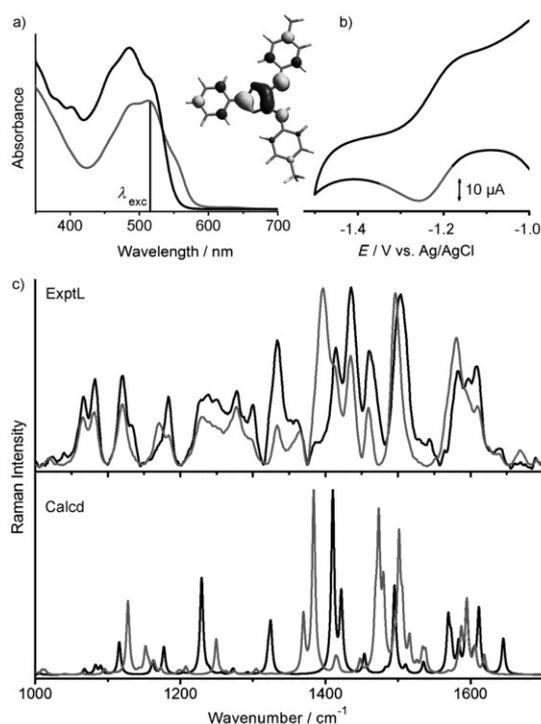


Figure 2. a) In situ UV/Vis absorption spectroelectrochemical detection of intermediate reduction states of **ImHCH₃**. The laser wavelength of 514 nm for exciting RR spectra is displayed as a vertical line in the spectra. Photoexcitation at 514 nm results in transfer of excess charge density into the LUMO, which is displayed for the neutral species. b) CV of **ImHCH₃** measured in parallel to the detection of RR spectra in the SEC cell (analyte dissolved in ACN with 0.1 M TBABF₄ electrolyte, scan rate 5 mV s⁻¹; electrode arrangement: Pt-gauze working, Pt counter, and Ag/AgCl pseudo-reference electrodes). The potential range for acquisition of the RR spectrum is indicated in grey. c) The experimental (top) and calculated (bottom) RR spectra of the neutral (black) and of the reduced (grey) 4*H*-imidazole ligand indicate that the reduction is partially accompanied by deprotonation. According to the calculations, 20% of the signal stem from protonated reduced and 80% from deprotonated reduced **ImHCH₃** (bottom grey curve).

The first reduction of the free 4*H*-imidazole ligand, **ImHCH₃**, is monitored by in situ UV/Vis spectroelectrochemistry (UV/Vis Vis-SEC, see Figure 2 a). Upon electrochemical reduction of **ImHCH₃**, the energetically lowest absorption band shifts from 550 to 575 nm owing to the population of higher-lying molecular orbitals within the 4*H*-imidazole. In order to determine the structure of the one-electron-reduced and photoactivated ligand, the electrochemically prepared one-electron-reduced ligand is investigated by RR-SEC. RR spectroscopy is the method of choice to monitor changes in the electron-density distribution upon photoexcitation: In RR spectra, normal modes are selectively enhanced and are affected by the structural reorganization during photoexcitation (that is, Franck-Condon active modes). This feature has been utilized to characterize the Franck-Condon point, the initial starting point of a photochemical reaction, for a number of different Ru^{II}-polypyridyl complexes.^[20,21]

RR studies in combination with TDDFT calculations of the neutral and one-electron-reduced free chromophore, **ImHCH₃** (Figure 2c; see the Supporting Information, Tables S1, S3, S4), reveal that the lowest unoccupied molecular orbital (LUMO) is localized on the 4*H*-imidazole core with minor contributions from the in-plane lying terminal tolyl rings bound to the exocyclic nitrogen atoms (Inset Figure 2a). Under the experimental conditions, one-electron reduction of **ImHCH₃** is, for a fraction of molecules, accompanied by proton abstraction at the exocyclic amino group to **ImCH₃**. This result is based on TDDFT calculations of the RR spectra for the protonated and deprotonated one-electron-reduced ligand (Figure 2c; see the Supporting Information, Figure S2).^[10,11] The assignment of intense RR bands to the corresponding vibrations is displayed in Figure S2. In order to interpret the experimental spectra, the fraction of reduced **ImHCH₃** molecules has been compared to linear combinations of the calculated spectra of reduced **ImHCH₃** and deprotonated reduced **ImCH₃**. From the best agreement between calculated and experimental spectra, it can be concluded that 20% of the RR signal stem from protonated reduced **ImHCH₃** and 80% from deprotonated reduced **ImCH₃** (Figure 2c, grey spectra).

When **ImHCH₃** is integrated into a complex, that is, **RuImCH₃**, photoexcitation in the UV/Vis region (>400 nm; Figure 3a) results in a MLCT transition toward 4*H*-imidazole acceptor orbitals (Figure 3d, left).^[13] Also, the first reduction of **RuImCH₃** at -1.36 V (see Table 1) is localized at the 4*H*-imidazole ligand (Figure 1b). However, in **RuImCH₃**, the reduced 4*H*-imidazole does not accept an additional excess charge density upon photoexcitation. Instead, the photoexcitation of the one-electron-reduced **RuImCH₃** at 514 nm involves acceptor orbitals localized on the terpyridine ligand (Figure 3d right). The novel band, appearing upon reduction, in the absorption spectrum of **RuImCH₃** (see Figure 3a) has been assigned to a MLCT transition from the Ru^{II} center to the terpyridine fragment by TDDFT (see the Supporting Information, Table S5). To study the details of the MLCT transition in reduced **RuImCH₃**, RR SEC was performed upon excitation within the new absorption band at 514 nm. The RR-SEC spectrum is dominated by intense Raman features at 1221, 1316, 1478, 1515, and 1578 cm⁻¹, which TDDFT calculations assign to the terpyridine ligand (Figure 3c; see the Supporting Information, Figure S5). Details on the assignment of the intense Raman bands by TDDFT are given in Figure S5. The electronic ground state of the two-electron-reduced **RuImCH₃** is, according to DFT, of triplet multiplicity (see the Supporting Information, Table S5). The triplet spin state agrees also with the calculated LUMO orbitals of the neutral and one-electron-reduced complex depicted in Figure 3d and with the RR SEC locating the photoelectron of one-electron-reduced **RuImCH₃** on the terpyridine ligand; the charge transfer following photoexcitation of nonreduced **RuImCH₃** is directed towards the 4*H*-imidazole ligand (Figure 3c; see the Supporting Information, Figure S5). Therefore, confinement of a (photo)electron at the reduced 4*H*-imidazole ligand is energetically not favored for the **RuImCH₃** complex owing to Coulomb repulsion, even though the free 4*H*-imidazole ligand can accept a second electron.

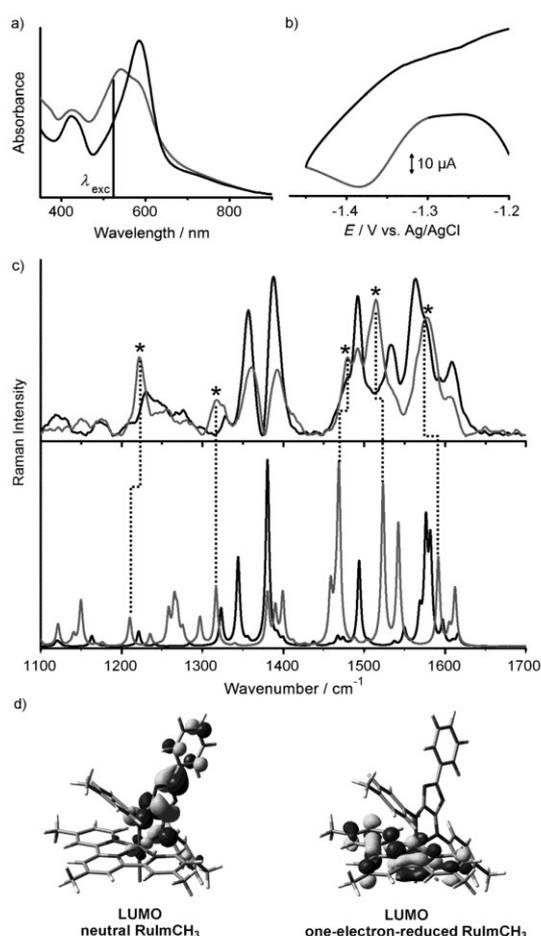


Figure 3. a) In situ UV/Vis absorption spectra of electrochemically reduced **RuImCH₃**. The laser wavelength for exciting RR spectra is displayed as a vertical line at 514 nm. b) CV acquired in a SEC cell during cyclic voltammetry of dissolved **RuImCH₃** (scan rate 5 mV s⁻¹, Pt-gauze working electrode, solvent is ACN containing 0.1 M TBABF₄). During CV acquisition, the RR spectra depicted in c were recorded in the reduction potential range indicated in grey. c) In the neutral complex **RuImCH₃**, the RR spectrum is characterized by 4*H*-imidazole bands (black spectrum), while in the reduced complex (grey spectrum), terpyridine vibrations (marked with an asterisk) are enhanced, thus indicating localization of the photoelectron on the terpyridine ligand. The results are in good agreement with TDDFT-calculated RR spectra (bottom). The labeled vibrational bands are assigned by means of quantum-chemical calculations. d) The molecular orbitals refer to the main acceptor orbitals of nonreduced **RuImCH₃** (left) and its reduction product (right) upon excitation at 514 nm. Photoexcitation results in charge transfer into the LUMO, which is displayed for the neutral and the one-electron-reduced species.

Notably, the 4*H*-imidazole ligand in **RuImCOOEt** (Figure 1c) can accept two (photo)electrons, even though the equilibrium geometries of the nonreduced complexes, **RuImCH₃** and **RuImCOOEt** (see the Supporting Information, Table S2, Figure S3), feature only minor structural differences. Both complexes exhibit a twisted 4*H*-imidazole ligand in the electronic ground state. Consequently, the central 4*H*-imidazole part and the substituted phenyl rings, which are bound to the exocyclic nitro-

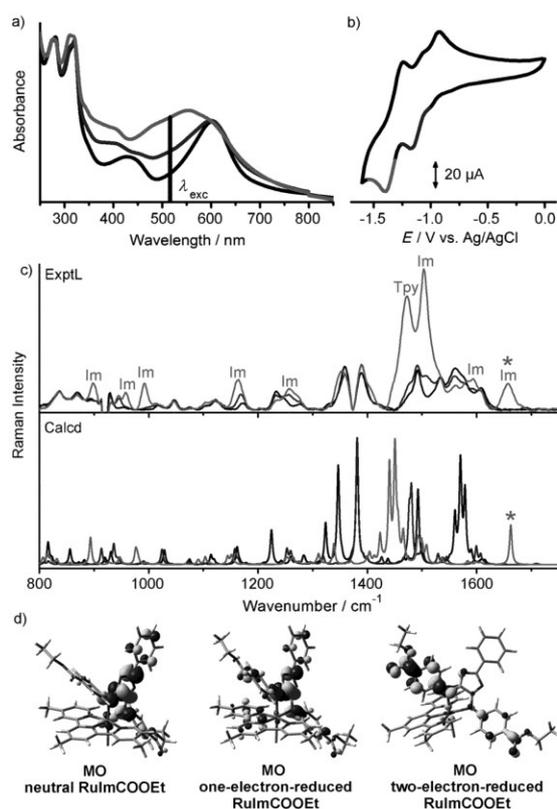


Figure 4. a) In situ UV/Vis absorption spectroelectrochemical detection of reduction states of **RuImCOOEt**. b) Corresponding CV with indicated potential region for spectroscopy, recorded in a SEC cell at a Pt-gauze working electrode, scan rate 5 mV s⁻¹, solvent 0.1 M TBABF₄/ACN. c) During one-electron (dark grey) and two-electron (grey) reduction, the RR spectrum is dominated by 4*H*-imidazole bands, indicating confinement of both electrons in the 4*H*-imidazole ligand. Observation of the CO-band (highlighted with an asterisk) in two-electron-reduced **RuImCOOEt** proves planarization of the ligand owing to energetically favored extension of the aromatic π -system by conjugation with the carbonyl double bonds. d) The molecular orbitals refer to the main acceptor orbitals of nonreduced **RuImCOOEt** and its reduction products upon excitation at 514 nm.

gen atoms, are electronically decoupled. UV/Vis absorption spectra were measured during cyclic voltammetry at the first and second reduction potentials (Figure 4a, b). The new bands in the absorption spectrum of reduced **RuImCOOEt** at around 400, 550, and 700 nm are assigned predominantly to internal ligand (IL) and MLCT excitations localized on the 4*H*-imidazole ligand in agreement with theory (see the Supporting Information, Table S6). The RR spectra of nonreduced complexes **RuImCH₃** and **RuImCOOEt** are very similar (see black graphs in Figure 3c and 4c). In contrast, the RR spectrum of the one-electron-reduced **RuImCOOEt** excited at 514 nm, that is, close to the maximum of the new absorption band as depicted in Figure 4a, differs significantly from the RR spectrum of one-electron-reduced **RuImCH₃** (compare grey graphs of Figure 3c and 4c). The Raman features in the spectrum of reduced **RuImCOOEt** at 899, 957, 992, 1163, 1257, 1503, 1592, and

1658 cm⁻¹ are assigned to 4*H*-imidazole vibrations by TDDFT calculations (Figure 4c; see the Supporting Information, Figure S5). The assignment of intense Raman bands is given in the Supporting Information, Figure S5. Hence, RR-SEC of **RuImCOOEt** confirms accumulation and spatial confinement of two electrons, one electron from reduction and one from photoexcitation, at the 4*H*-imidazole ligand only.

The ability of **RuImCOOEt** to accumulate two electronic charges is based on two structural differences in comparison to **RuImCH₃**. First, the electron-withdrawing ester substituents stabilize the two-electron-reduced singlet state as evident from the observation of prominent 4*H*-imidazole bands in the RR spectrum of two-electron-reduced **RuImCOOEt** (Figure 4c). Second, the torsion angle decreases from 46–61° for the non-reduced to 4–8° for two-electron-reduced **RuImCOOEt** according to TDDFT calculations (see the Supporting Information, Table S2 and Figure S3). Therefore, the planarization of the 4*H*-imidazole ligand increases with the total charge. Evidence for the planarization is also observed spectroscopically: the RR spectrum of two-electron-reduced **RuImCOOEt** exhibits a prominent band at 1658 cm⁻¹, the region where carbonyl-stretch vibrations of esters appear, according to TDDFT calculations (Figure 4c). This observation confirms planarization of the 4*H*-imidazole ligand such that the carbonyl bond is arranged in the same plane as the aromatic chromophore. The planarization is energetically favored despite increasing the steric hindrance, because the extension of the aromatic chromophore across the entire 4*H*-imidazole ligand partially compensates for the increasing Coulomb repulsion of the accumulated charges.

Conclusion

An efficient homogeneous photocatalyst needs to store two charges locally for subsequent catalysis. Herein, we provide for the first time a consistent picture for efficient two electron transfer in the low weight multi-electron storing and hyper-panchromatic complex **RuImCOOEt** toward the 4*H*-imidazole electron accepting ligand (Scheme 1) based on in situ spectroelectrochemical and computational studies.

Experimental Section

The ligand, **ImHCH₃**, and the ruthenium(II) complexes, **RuImCH₃** and **RuImCOOEt**, were prepared as described in the literature.^[13,22] All solutions were prepared in acetonitrile (ACN, Aldrich), which was dried using calcium hydride and distilled twice.

For cyclic voltammetry and spectroelectrochemical measurements, in the thin-layer spectroelectrochemical cell (Bioanalytical Systems), a degassed solution of the reactants (50 μM) and 0.1 M TBABF₄ in ACN is cycled in the reductive potential range (Figure 1) and monitored by using UV/Vis absorption spectroscopy.

Electrochemical data were obtained either by using a standard electrochemical cell or a thin-layer quartz-glass spectroelectrochemical cell (Bioanalytical Systems). The analytes were dissolved in ACN containing 0.1 M TBABF₄ electrolyte. The electrochemical measurements were performed by using a three-electrode arrangement: a Pt counter electrode, a Ag/AgCl pseudo-reference electrode, and either a Pt-gauze working electrode, in the case of

a spectroelectrochemical cell (Bioanalytical Systems), or a glassy carbon working electrode, in the case of a standard electrochemical cell. All solutions were thoroughly degassed with argon prior to each measurement.

UV/Vis absorption spectra were measured at room temperature with a double-beam Cary 5000 UV/Vis spectrometer (Varian) with 1 nm spectral resolution.

RR spectra were obtained through excitation by the visible lines of an Argon ion laser (Coherent, Innova 300C) and recorded with an Acton SpectraPro 2758i spectrometer (entrance slit width 100 μm , focal length 750 mm, grating 600 mm). A transmission geometry was employed for the in situ resonance Raman spectroelectrochemical experiments. The Raman signals were detected using a liquid-nitrogen-cooled CCD detector (SPEC-10, Roper Scientific). The band of acetonitrile at 1373 cm^{-1} was used as a reference for normalizing intensities and wavenumbers. The recorded resonance Raman spectra were background corrected and the solvent spectrum was subtracted.

To check for appropriate experimental conditions during the spectroelectrochemical measurements, for example, contaminant-free analyte solutions and proper sealing of the cell, RR spectra were measured at the open-circuit potential (ocp) preceding and subsequent to spectroelectrochemical data acquisition. In repeated measurements, only data sets with insignificant spectral changes at the ocp potential were selected for further analysis. Example spectra are shown in Figure S6 of the Supporting Information.

Computational methods

In order to reduce the computational cost of the simulations without affecting the accuracy for calculating the spectroscopic properties of the complexes, the three *tert*-butyl groups of terpyridine–ruthenium(II)–4*H*-imidazol were approximated in the calculations by methyl groups. The calculated structural and electronic properties of the ligands, **ImHCH₃** and **ImCH₃** (see tables S1, S3, S4), as well as for the complexes **RulmCH₃** and **RulmCOOEt** (see the Supporting Information, Tables S2, S5, S6) were obtained from quantum-chemical calculations performed with the GAUSSIAN 09 program.^[23] The calculated structural parameters are depicted in the Supporting Information, Figure S3 (bond lengths, torsion and dihedral angles). The two ruthenium complexes and the ligand were investigated for three reductive states, namely, the neutral form (singlet), the one-electron-reduced form (doublet), and the two-electron-reduced forms of singlet and triplet multiplicity. The geometries, vibrational frequencies, and normal coordinates of the electronic ground state were calculated by means of density functional theory (DFT) with the XC functional B3LYP^[24,25] for each reductive state of each compound. The 6–31G(d) double- ζ basis set^[26] was employed for all main group elements. The 28-electron relativistic core potential MWB^[27] was applied with its basis set for the ruthenium atom, that is, 4s, 4p, 4d, and 5s electrons are treated explicitly, while the first three inner shells are described by the core pseudopotential. To correct for the lack of anharmonicity and the approximate treatment of electron correlation,^[28] the harmonic frequencies were scaled by the factor 0.97. The vertical excitation energies, oscillator strengths, and analytical Cartesian energy derivatives of the excited states were obtained from time dependent DFT (TDDFT) calculations within the adiabatic approximation with the same XC functional, pseudopotential, and basis set. It is shown in Ref. [12] and [13] that B3LYP provides the most balanced description of the absorption features of such complexes.

The absorption spectra were simulated by determining the excitation energies and oscillator strengths for the 80 lowest excited

states of the respective ground-state multiplicity. The effects of the interaction with a solvent (acetonitrile, $\epsilon = 35.688$, $n = 1.344$) on the geometry, frequencies, excitation energies, and excited-state gradients were taken into account by the integral equation formalism of the polarizable continuum model.^[29] The non-equilibrium procedure of solvation was used for the calculation of the excitation energies and the excited-state gradients, a procedure that is well adapted for processes where only the fast reorganization of the electronic distribution of the solvent is important.

The resonance Raman (RR) spectra were calculated within the independent mode displaced harmonic oscillator model (IMDHOM), which assumes the electronic-ground and excited-state potentials to be harmonic oscillators with differing equilibrium positions, sharing the same set of vibrational modes. Within this approach, the RR intensity for a fundamental transition $0 \rightarrow 1$, that is, from the lowest vibrational level of the electronic ground state into the first excited vibrational level of an excited electronic state, can be calculated from the Raman polarizability tensor, as described in more detail in the Supporting Information.^[20,30–32]

The RR intensities have been calculated for the nonreduced **ImHCH₃** ligand using the S_1 state. For the one-electron-reduced protonated form, the D_1 and the D_2 states have been used, while the excitation energy of the D_2 state was bathochromically shifted by 1500 cm^{-1} as well as the D_1 (blue-shifted by 1000 cm^{-1}) and D_2 states of the deprotonated form, **ImCH₃**. The resulting RR intensity pattern was estimated by a mixing of both protonation states (80% **ImHCH₃** and 20% **ImCH₃**) of the one-electron-reduced ligand. For the two-electron-reduced singlet species, the S_2 and S_3 states have been taken into account; in case of the triplet analogue, the T_6 (blue-shifted by 1700 cm^{-1}) and the T_7 states have been utilized. Detailed information concerning the states is given in the Supporting Information, Tables S4 and S5.

For **RulmCH₃**, S_6 was used for the nonreduced form, D_{19} for the one-electron-reduced form, S_{15} for the two-electron-reduced singlet, and T_{16} for the two-electron-reduced triplet species. Table S6 in the Supporting Information summarizes the electronic properties of these states.

In order to simulate the RR spectra of **RulmCOOEt**, S_8 was used for the non-reduced form, D_{23} for the one-electron-reduced form, S_9 , S_{11} , S_{12} , S_{13} , and S_{14} for the two-electron-reduced singlet form, and T_{23} for the two-electron-reduced triplet forms. Detailed information of these states can be found in the Supporting Information, Table S7.

For further computational details, see the Supporting Information.

Acknowledgements

The authors thank Dr. Sven Kriek for his kindness to provide us a potentiostat and for preparing the solvents and electrolytes. We thank the COST Action CM1202 for support.

Keywords: electron transfer • Raman spectroscopy • ruthenium • spectroelectrochemistry • TD DFT calculations

- [1] K. Zeitler, *Angew. Chem.* **2009**, *121*, 9969–9974; *Angew. Chem. Int. Ed.* **2009**, *48*, 9785–9789.
- [2] V. Balzani, A. Juris, M. Venturi, S. Campagna, S. Serroni, *Chem. Rev.* **1996**, *96*, 759–834.
- [3] M. Elvington, J. Brown, S. M. Arachchige, K. J. Brewer, *J. Am. Chem. Soc.* **2007**, *129*, 10644–10645.
- [4] H. B. Gray, A. W. Maverick, *Science* **1981**, *214*, 1201–1205.

- [5] A. J. Esswein, D. G. Nocera, *Chem. Rev.* **2007**, *107*, 4022–4047.
- [6] N. Mourtzis, P. C. Carballada, M. Felici, R. J. M. Nolte, R. M. Williams, L. de Cola, M. C. Feiters, *Phys. Chem. Chem. Phys.* **2011**, *13*, 7903–7909.
- [7] J. Rosenthal, *Coord. Chem. Rev.* **2005**, *249*, 1316–1326.
- [8] C. Chiorboli, S. Fracasso, F. Scandola, S. Campagna, S. Serroni, R. Kon-duri, F. M. MacDonnell, *Chem. Commun.* **2003**, 1658–1659.
- [9] M. P. Sammes, A. R. Katritzky, in *Adv. Heterocycl. Chem.* (Ed.: Alan R. Ka-tritzky), Academic Press, **1984**, pp. 413–450.
- [10] T. Gebauer, R. Beckert, D. Weiss, K. Knop, C. K pplinger, H. G rls, *Chem. Commun.* **2004**, 1860–1861.
- [11] R. Beckert, J. Atzrodt, H. G rls, *Heterocycles* **1999**, *51*, 763.
- [12] M. W chtler, S. Kupfer, J. Guthmuller, S. Rau, L. Gonz lez, B. Dietzek, *J. Phys. Chem. C* **2012**, *116*, 25664–25676.
- [13] S. Kupfer, J. Guthmuller, M. W chtler, S. Losse, S. Rau, B. Dietzek, J. Popp, L. Gonz lez, *Phys. Chem. Chem. Phys.* **2011**, *13*, 15580–15588.
- [14] J. Blumhoff, R. Beckert, S. Rau, S. Losse, M. Matschke, W. G nther, H. G rls, *Eur. J. Inorg. Chem.* **2009**, 2162–2169.
- [15] P. Kukura, D. W. McCamant, R. A. Mathies, *Annu. Rev. Phys. Chem.* **2007**, *58*, 461–488.
- [16] Y. Sun, Y. Liu, C. Turro, *J. Am. Chem. Soc.* **2010**, *132*, 5594–5595.
- [17] W. Kaim, J. Fiedler, *Chem. Soc. Rev.* **2009**, *38*, 3373.
- [18] L. Zedler, J. Guthmuller, I. Rabelo de Moraes, S. Kriek, M. Schmitt, J. Popp, B. Dietzek, *J. Phys. Chem. C* **2013**, *117*, 6669–6677.
- [19] Gebauer, Tillmann, Neuartige Zweistufige Redoxsysteme Basierend auf 4H-Imidazolen, PhD Thesis, Friedrich Schiller University, Jena, **2005**.
- [20] M. W chtler, J. Guthmuller, L. Gonz lez, B. Dietzek, *Coord. Chem. Rev.* **2012**, *256*, 1479–1508.
- [21] S. Tschierlei, M. Karnahl, M. Presselt, B. Dietzek, J. Guthmuller, L. Gon-z lez, M. Schmitt, S. Rau, J. Popp, *Angew. Chem.* **2010**, *122*, 4073–4076; *Angew. Chem. Int. Ed.* **2010**, *49*, 3981–3984.
- [22] J. Atzrodt, R. Beckert, W. G nther, H. G rls, *Eur. J. Org. Chem.* **2000**, 1661–1668.
- [23] Gaussian 09, Revision A.01, M. J. Frisch, G. W. Trucks, H. B. Schlegel, G. E. Scuseria, M. A. Robb, J. R. Cheeseman, G. Scalmani, V. Barone, B. Men-nucci, G. A. Petersson, H. Nakatsuji, M. Caricato, X. Li, H. P. Hratchian, A. F. Izmaylov, J. Bloino, G. Zheng, J. L. Sonnenberg, M. Hada, M. Ehara, K. Toyota, R. Fukuda, J. Hasegawa, M. Ishida, T. Nakajima, Y. Honda, O. Kitao, H. Nakai, T. Vreven, J. A. Montgomery, Jr., J. E. Peralta, F. Ogliaro, M. Bearpark, J. J. Heyd, E. Brothers, K. N. Kudin, V. N. Staroverov, R. Ko-bayashi, J. Normand, K. Raghavachari, A. Rendell, J. C. Burant, S. S. Iyengar, J. Tomasi, M. Cossi, N. Rega, J. M. Millam, M. Klene, J. E. Knox, J. B. Cross, V. Bakken, C. Adamo, J. Jaramillo, R. Gomperts, R. E. Stratmann, O. Yazyev, A. J. Austin, R. Cammi, C. Pomelli, J. W. Ochterski, R. L. Martin, K. Morokuma, V. G. Zakrzewski, G. A. Voth, P. Salvador, J. J. Dannenberg, S. Dapprich, A. D. Daniels,  . Farkas, J. B. Foresman, J. V. Ortiz, J. Cio-slowski, D. J. Fox, Gaussian, Inc., Wallingford CT, **2009**.
- [24] A. D. Becke, *J. Chem. Phys.* **1993**, *98*, 5648–5652.
- [25] C. Lee, W. Yang, R. G. Parr, *Phys. Rev. B* **1988**, *37*, 785–789.
- [26] P. C. Hariharan, J. A. Pople, *Theor. Chim. Acta* **1973**, *28*, 213–222.
- [27] D. Andrae, U. H u ermann, M. Dolg, H. Stoll, H. Preu , *Theor. Chim. Acta* **1990**, *77*, 123–141.
- [28] J. P. Merrick, D. Moran, L. Radom, *J. Phys. Chem. A* **2007**, *111*, 11683–11700.
- [29] B. Mennucci, C. Cappelli, C. A. Guido, R. Cammi, J. Tomasi, *J Phys Chem.* **2009**, *113*, 3009–3020.
- [30] J. B. Page, D. L. Tonks, *J. Chem. Phys.* **1981**, *75*, 5694–5708.
- [31] W. L. Peticolas, T. Rush, *J. Comput. Chem.* **1995**, *16*, 1261–1270.
- [32] J. Guthmuller, L. Gonz lez, *Phys. Chem. Chem. Phys.* **2010**, *12*, 14812.

Received: December 18, 2013

Published online on February 24, 2014

Supporting Information

Trapped in Imidazole - How to Accumulate Multiple Photoelectrons on a Black Absorbing Ruthenium Complex

Linda Zedler,^[a] Stephan Kupfer,^[a] Inês Rabelo de Moraes,^[b] Maria Wächtler,^[b] Rainer Beckert,^[c] Michael Schmitt,^[a] Jürgen Popp,^[a,b] Sven Rau^[d] and Benjamin Dietzek(s)*^[a,b]

^[a] Institute of Physical Chemistry and Abbe Center of Photonics, Friedrich-Schiller-University
Jena, Helmholtzweg 4, 07743 Jena, Germany

^[b] Leibniz Institute of Photonic Technology Jena (IPHT), Albert-Einstein-Straße 9, 07745
Jena, Germany

^[c] Institute of Organic Chemistry and Macromolecular Chemistry, Friedrich-Schiller-
University Jena, Humboldtstraße 10, 07743 Jena, Germany

^[d] Institute of Inorganic Chemistry I, University Ulm, Albert-Einstein-Allee 11, 89081 Ulm,
Germany

Computational details

In order to reduce the computational cost of the simulations without affecting the accuracy for calculating the spectroscopic properties of the complexes, the three *tert*-butyl groups of terpyridine-ruthenium(II)-4*H*-imidazol were approximated in the calculations by methyl groups. The structural and electronic data for the ligand **ImHCH₃** (see Figure S2) as well as for the complexes **RuImCH₃** and **RuImCOOEt** (see Figure S4, S5, S6) were obtained from quantum chemical calculations performed with the GAUSSIAN 09 program¹. The two ruthenium complexes and the ligand were investigated for three reductive states, respectively, namely the neutral form (singlet), the single reduced form (doublet), and the double reduced forms of singlet and triplet multiplicity. The geometries, vibrational frequencies and normal coordinates of the electronic ground state were calculated by means of density functional theory (DFT) with the XC functional B3LYP^{2,3} for each reductive state of each compound, respectively. The 6-31G(d) double- ζ basis set⁴ was employed for all main group elements. The 28-electron relativistic core potential MWB⁵ was applied with its basis set for the ruthenium atom, that is, 4s, 4p, 4d and 5s electrons are treated explicitly, while the first three inner shells are described by the core pseudopotential. To correct for the lack of anharmonicity and the approximate treatment of electron correlation⁶ the harmonic frequencies were scaled by the factor 0.97. The vertical excitation energies, oscillator strengths and analytical Cartesian energy derivatives of the excited states were obtained from time dependent DFT (TDDFT) calculations within the adiabatic approximation with the same XC functional, pseudopotential and basis set. It was shown in Ref. 7 and 8 that B3LYP provides the most balanced description of the absorption features of such complexes.

The absorption spectra have been simulated by determining the excitation energies and oscillator strengths for the 80 lowest excited states of the respective ground state multiplicity. The effects of the interaction with a solvent (acetonitrile, $\epsilon=35.688$, $n=1.344$) on the geometry, frequencies, excitation energies and excited state gradients were taken into account by the integral equation formalism of the polarizable continuum model.⁹ The non-equilibrium procedure of solvation was used for the calculation of the excitation energies and of the excited state gradients, which is well adapted for processes, where only the fast reorganization of the electronic distribution of the solvent is important.

The resonance Raman (RR) spectra were calculated within the independent mode displaced harmonic oscillator model (IMDHOM), which assumes the electronic ground and excited states potentials to be harmonic oscillators with differing equilibrium positions, sharing the same set of vibrational modes. Within this approach the RR intensity for a fundamental transition $0 \rightarrow 1_l$ can be calculated from the Raman polarizability tensor¹⁰⁻¹³

$$(\alpha_{\alpha\beta})_{g0 \rightarrow g1_l} = \frac{1}{\hbar} \sum_e (\mu_{ge})_\alpha (\mu_{ge})_\beta \frac{\Delta_{e,l}}{\sqrt{2}} \{ \Phi_e(\omega_L) - \Phi_e(\omega_L - \omega_l) \} \quad (\text{S1})$$

where $(\mu_{ge})_\alpha$ is a component of the electronic transition dipole moment at the ground state equilibrium geometry, $\Delta_{e,l}$ is the dimensionless displacement of the e th excited state potential minimum with respect to the ground state for the l th normal coordinate and ω_L is the frequency of the incident light. The function $\Phi_e(\omega_L)$ is approximated by

$$\Phi_e(\omega_L) = \frac{1}{\omega_{g,e} - \omega_L - i\Gamma} \quad (\text{S2})$$

whereas $\omega_{g,e}$ is the vertical excitation energy from the electronic ground state g to the excited state e and Γ is a damping factor describing a homogeneous broadening. A value of Γ equal to 1500 cm^{-1} was assumed in the simulations to reproduce the experimental broadening. An excitation wavelength of 514 nm was employed to calculate the RR spectra, for which the

vertical excitation energies $\omega_{g,e}$ were corrected so that experimental and theoretical absorption maxima coincide.

The absorption spectrum $A(\omega_L)$ is given by

$$A(\omega_L) \propto \omega_L \sum_e (\mu_{ge})^2 \text{Im} \Phi_e(\omega_L) \quad (\text{S3})$$

The dimensionless displacement $\Delta_{e,l}$ of the excited state e is defined in the IMDHOM by the partial derivative of the excited state potential energy E^e along the normal mode Q_l evaluated at the ground state equilibrium geometry

$$\Delta_{e,l} = -\frac{1}{\sqrt{\hbar}\omega_l^{3/2}} \left(\frac{\partial E^e}{\partial Q_l} \right)_0 \quad (\text{S4}).$$

These derivatives were obtained from the analytical derivatives of the excited state electronic energy (E^e) along the Cartesian coordinates.

More details about the calculation procedure of RR intensities can be found in reference [13].¹³

The RR intensities have been calculated for the non-reduced **ImHCH₃** ligand using the S_1 state. For the single reduced protonated form the D_1 and the D_2 states have been used, while the excitation energy of the D_2 state was bathochromically shifted by 1500 cm^{-1} as well as the D_1 (blue-shifted by 1000 cm^{-1}) and D_2 states of the deprotonated form, **ImCH₃**. The resulting RR intensity pattern was estimated by a mixing of both protonation states (80% **ImHCH₃** and 20% **ImCH₃**) of the single reduced ligand. For the double reduced singlet species the S_2 and S_3 have been taken into account, in case of the triplet analogue the T_6 (blue-shifted by 1700 cm^{-1}) and the T_7 have been utilized. Detailed information concerning the states is given in Table S4 and S5.

For **RuImCH₃** S_6 was used for the non-reduced form, D_{19} for the single reduced and S_{15} for the double reduced singlet and T_{16} for the double reduced triplet species. Table S6 summarizes the electronic properties of these states.

In order to simulate the RR spectra of **RuImCOOEt** S_6 was used for the non-reduced, D_{23} for the single reduced and S_9 , S_{11} , S_{12} , S_{13} and S_{14} for the double reduced singlet and T_{23} for the double reduced triplet forms. Table S7 collects detailed information of these states.

- [1] Gaussian 09, Revision A.1, M. J. Frisch, G. W. Trucks, H. B. Schlegel, G. E. Scuseria, M. A. Robb, J. R. Cheeseman, G. Scalmani, V. Barone, B. Mennucci, G. A. Petersson, et al., Inc., Wallingford, CT, 2009.
- [2] A. D. Becke, *J. Chem. Phys.* **1993**, *98*, 5648–5652.
- [3] C. Lee, W. Yang, R. G. Parr, *Phys. Rev. B* **1988**, *37*, 785–789.
- [4] P. C. Hariharan, J. A. Pople, *Theor. Chim. Acta* **1973**, *28*, 213–222.
- [5] D. Andrae, U. Häußermann, M. Dolg, H. Stoll, H. Preuß, *Theor Chim Acta* **1990**, *77*, 123–141.
- [6] J. P. Merrick, D. Moran, L. Radom, *J. Phys. Chem. A* **2007**, *111*, 11683–11700.
- [7] S. Kupfer, J. Guthmüller, M. Wächtler, S. Losse, S. Rau, B. Dietzek, J. Popp, L. González, *Phys Chem Chem Phys* **2011**, *13*, 15580–15588.

- [8] M. Wächtler, S. Kupfer, J. Guthmuller, S. Rau, L. González, B. Dietzek, *J. Phys. Chem. C* **2012**, *116*, 25664–25676.
- [9] B. Mennucci, C. Cappelli, C. A. Guido, R. Cammi, J. Tomasi, *J Phys Chem* **2009**, *113*, 3009–3020.
- [10] J. B. Page, D. L. Tonks, *J Chem Phys* **1981**, *75*, 5694–5708.
- [11] W. L. Peticolas, T. Rush, *J. Comput. Chem.* **1995**, *16*, 1261–1270.
- [12] J. Guthmuller, L. González, *Phys Chem Chem Phys* **2010**, *12*, 14812.
- [13] M. Wächtler, J. Guthmuller, L. González, B. Dietzek, *Coord. Chem. Rev.* **2012**, *256*, 1479–1508.

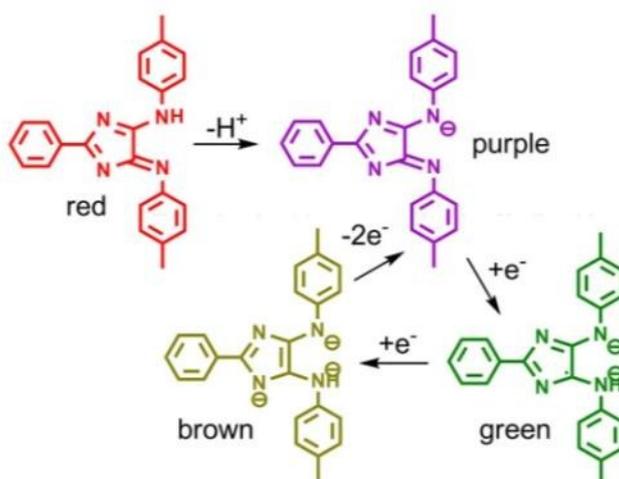


Figure S1: Reduction cycle of ImHCH₃.

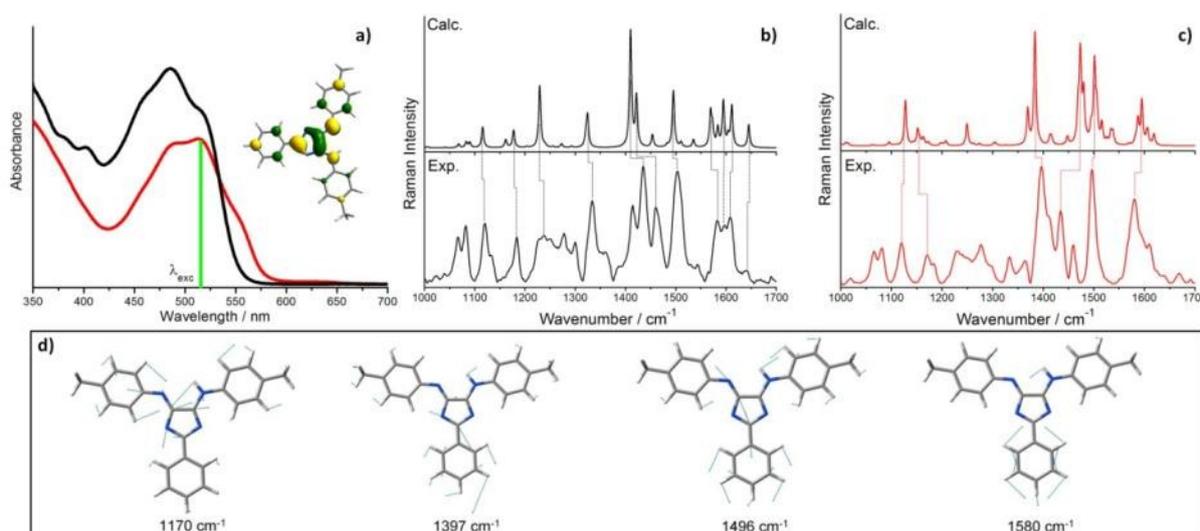


Figure S2: a) *In situ* UV-vis absorption spectro-electrochemical detection of intermediate reduction states of ImHCH₃. The laser wavelength of 514 nm for exciting RR spectra is displayed as a green line in the spectra. Photoexcitation at this wavelength, i.e. at 514 nm, results in transfer of excess charge density into the LUMO, which is displayed for the neutral species. b) Calculated (top) and experimental (bottom) RR spectra of the neutral (black) and c) of the reduced (red) 4*H*-imidazole ligand. Since single reduction of ImHCH₃ is accompanied by proton abstraction at the exocyclic amino group the calculations have been carried out for the protonated and deprotonated single reduced ligand. From the best agreement between

theory and experiment it can be estimated that under the experimental conditions 20% and 80% of the signal stem from protonated and deprotonated reduced ImHCH₃, respectively. d) Most prominent RR active vibrations of the single reduced ImHCH₃ ligand ($\lambda_{\text{exc}}=514\text{nm}$). RR features are primarily assigned to the 4*H*-imidazole modes at the core and the substituted phenyl ring. Smaller contributions from the in-plane lying terminal tolyl groups are observed.

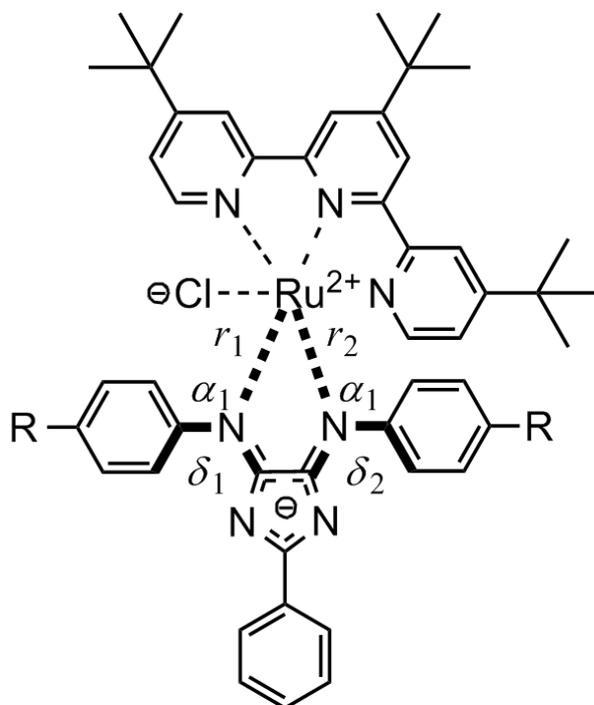


Figure S3: General structure of ruthenium complexes bearing the 4*H*-imidazole ligand of variable substituent R (R=CH₃, COOEt) characterized by the coordinative bond lengths r_1 , r_2 from ruthenium to the 4*H*-imidazole, the angles α_1 and α_2 describing the pyramidalization of the substituted phenyl rings with respect to the 4-imidazole core fragment and the two dihedral angles δ_1 and δ_2 describing torsion of the substituted phenyl rings. The values were derived from DFT calculations.

Table S1: Electronic ground state energies and geometric parameters for the free ImHCH₃ and ImCH₃ molecule.

	E / eV	$\alpha_1 / ^\circ$	$\alpha_2 / ^\circ$	$\delta_1 / ^\circ$	$\delta_2 / ^\circ$
ImHCH₃					
Non-reduced (S=0)	0.00	173	170	0	0
Single reduced (S=0.5)	-3.06	175	170	0	0
Double reduced (S=0)	-5.12	175	168	0	2
Double reduced (S=1)	-3.48	174	169	1	-1
ImCH₃					
Non-reduced (S=0)	0.00	177	177	0	0
Single reduced (S=0.5)	-2.13	178	178	-1	0
Double reduced (S=0)	-3.47	177	178	-1	0
Double reduced (S=1)	-2.15	177	178	0	0

Table S2: Electronic ground state energies and geometric parameters for the non-reduced (singlet), single (doublet) and double reduced species (singlet and triplet) of RuImCH₃ and RuImCOOEt.

	E / eV	$r_1 / \text{\AA}$	$r_2 / \text{\AA}$	$\alpha_1 / ^\circ$	$\alpha_2 / ^\circ$	$\delta_1 / ^\circ$	$\delta_2 / ^\circ$
RuImCH₃							
Non-reduced (S=0)	0.00	2.19	2.11	178	176	-48	66
Single reduced (S=0.5)	-2.64	2.21	2.13	174	177	-29	38
Double reduced (S=0)	-4.80	2.19	2.10	127	151	5	14
Double reduced (S=1)	-4.73	2.25	2.12	172	163	23	45
RuImCOOEt							
Non-reduced (S=0)	0.00	2.20	2.11	178	176	-46	61
Single reduced (S=0.5)	-2.96	2.22	2.14	172	178	-22	31
Double reduced (S=0)	-5.53	2.20	2.13	153	154	-4	-8
Double reduced (S=1)	-5.15	2.24	2.14	172	178	-19	32

Table S1 and S2 summarize the electronic ground state energies (E in eV), characteristic geometrical parameters and main structural changes upon single and double reduction for the free ligand **ImHCH₃/ImCH₃** as well as for the complexes **RuImCH₃** and **RuImCOOEt**. The most important alterations from the equilibrium geometries are described by two angles (α_1 and α_2) describing the pyramidalization of the substituted phenyl rings with respect to the 4-imidazole core fragment, the two dihedral angles (δ_1 and δ_2) describing torsion of the substituted phenyl rings, and, in case of the complexes, the ruthenium-to-4-imidazole bond lengths (r_1 and r_2).

In the case of **ImHCH₃** and **ImCH₃** only slight changes in the equilibrium structures are observed. However, the two complexes exhibit considerable characteristic structural changes upon reduction. Substitution does not significantly influence the structure of the complexes, i.e., for the non-reduced complexes almost identical equilibrium structures have been calculated. This holds also true for the single reduced and double reduced triplet forms. All these structures feature twisted substituted phenyl rings (δ) with respect to the main body of the 4*H*-imidazole and show no pyramidalization (α). However, the double reduced singlet state shows a planarization of the phenyl rings (δ) as well as a slight pyramidalization (α). These results are almost independent of the substitution pattern, however, the binding energy and therefore the population of the different spin states strongly depends on the substitution. Therefore the planarized double reduced singlet state is only populated in case of **RuImCOOEt**.

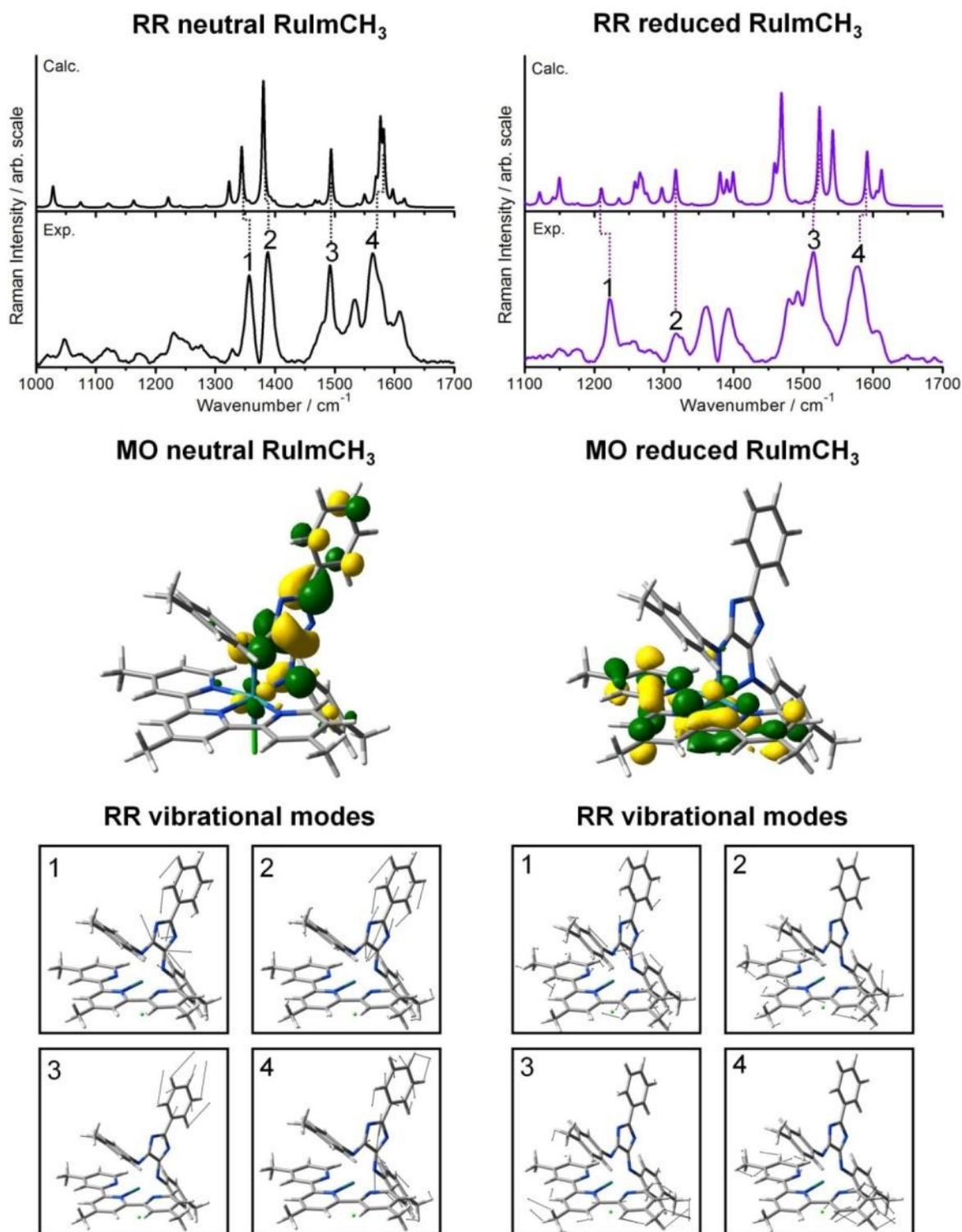


Figure S4: Comparison of the calculated and experimental RR spectra of non-reduced and single reduced RuImCH₃ excited at 514 nm (top). The labeled vibrational bands are assigned by means of quantum chemical calculations. The corresponding vibrations are displayed on the bottom. The molecular orbitals depicted in the center of the graphic refer to the main acceptor orbitals of the non-reduced RuImCH₃ and its reduction product upon excitation at 514 nm.

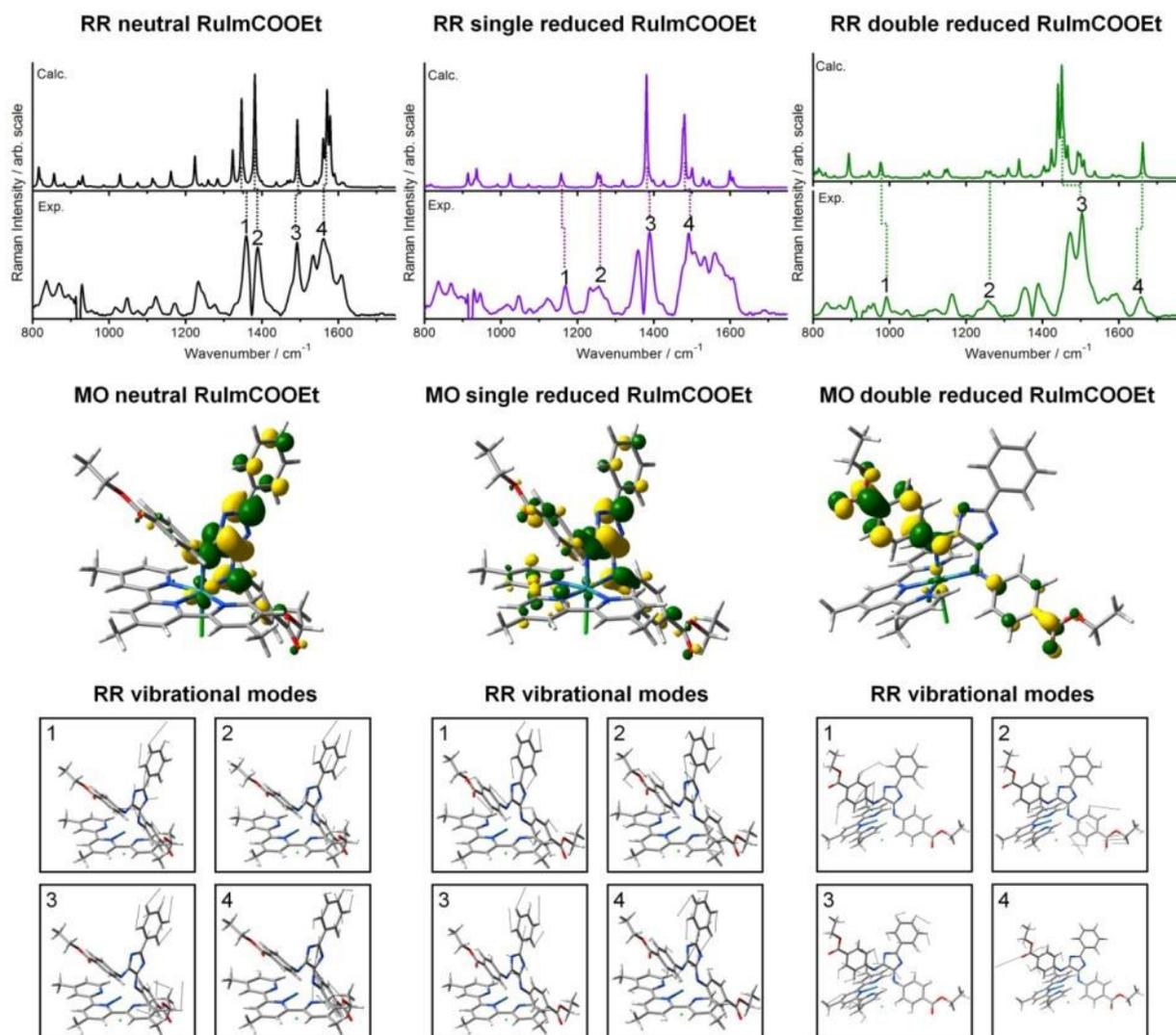


Figure S5: Comparison of the calculated and experimental RR spectra excited at 514 nm for non-reduced, single reduced and double reduced RuImCOOEt (top). The labeled vibrational bands are assigned by means of quantum chemical calculations. The corresponding vibrations are displayed on the bottom. The molecular orbitals depicted in the center of the graphic refer to the main acceptor orbitals of the non-reduced RuImCOOEt and its reduction products upon excitation at 514 nm.

Table S3: Calculated bright electronic excited states for the non-reduced (singlet), single (doublet) and double reduced (singlet and triplet) species of ImHCH₃ with the main contributing excitations, excitation energies E^e and wavelengths λ , oscillator strengths f , and the eigen values of $\langle S^2 \rangle$.

non-reduced (S=0)						
State	Main contributing excitations	Weight / %	E^e / eV	λ / nm	f	$\langle S^2 \rangle$
S ₁	$\pi_{\text{im}}(93) \rightarrow \pi_{\text{im}}^*(94)$	98	2.51	494	0.582	0.000
S ₂	$\pi_{\text{im}}(92) \rightarrow \pi_{\text{im}}^*(94)$	94	3.17	391	0.506	0.000
S ₃	$\pi_{\text{im}}(91) \rightarrow \pi_{\text{im}}^*(94)$	94	3.34	371	0.150	0.000
Single reduced (S=0.5)						
State	Main contributing excitations	Weight / %	E^e / eV	λ / nm	f	$\langle S^2 \rangle$
D ₁	$\pi_{\text{im}}(93\beta) \rightarrow \pi_{\text{im}}^*(94\beta)$	89	2.05	605	0.188	0.804
D ₂	$\pi_{\text{im}}^*(94\alpha) \rightarrow \pi_{\text{im}}^*(95\alpha)$	82	2.42	511	0.203	0.851
Double reduced (S=0)						
State	Main contributing excitations	Weight / %	E^e / eV	λ / nm	f	$\langle S^2 \rangle$
S ₂	$\pi_{\text{im}}^*(94) \rightarrow \pi_{\text{im}}^*(95)$	84	2.49	498	0.556	0.000
	$\pi_{\text{im}}(94) \rightarrow \pi_{\text{im}}^*(97)$	16				
S ₃	$\pi_{\text{im}}^*(94) \rightarrow \pi_{\text{im}}^*(97)$	83	2.56	484	0.147	0.000
	$\pi_{\text{im}}(94) \rightarrow \pi_{\text{im}}^*(95)$	15				
S ₄	$\pi_{\text{im}}^*(94) \rightarrow \pi_{\text{im}}^*(99)$	65	2.96	419	0.198	0.000
	$\pi_{\text{im}}(94) \rightarrow \pi_{\text{im}}^*(98)$	33				
S ₅	$\pi_{\text{im}}^*(94) \rightarrow \pi_{\text{im}}^*(98)$	64	2.98	416	0.516	0.000
	$\pi_{\text{im}}(94) \rightarrow \pi_{\text{im}}^*(99)$	34				
Double reduced (S=1)						
State	Main contributing excitations	Weight / %	E^e / eV	λ / nm	f	$\langle S^2 \rangle$
T ₆	$\pi_{\text{im}}(93\beta) \rightarrow \pi_{\text{im}}^*(94\beta)$	86	2.02	613	0.255	2.036
T ₇	$\pi_{\text{im}}(92\beta) \rightarrow \pi_{\text{im}}^*(94\beta)$	54	2.69	461	0.123	2.057
	$\pi_{\text{im}}(94\alpha) \rightarrow \pi_{\text{im}}^*(96\alpha)$	33				

Table S4: Calculated bright electronic excited states for the non-reduced (singlet), single (doublet) and double reduced (singlet and triplet) species of ImCH₃ with the main contributing excitations, excitation energies E^e and wavelengths λ , oscillator strengths f , and the eigen values of $\langle S^2 \rangle$.

non-reduced (S=0)						
State	Main contributing excitations	Weight / %	E^e / eV	λ / nm	f	$\langle S^2 \rangle$
S ₁	$\pi_{im}(93) \rightarrow \pi_{im}^*(94)$	99	2.44	508	0.709	0.000
S ₄	$\pi_{im}(92) \rightarrow \pi_{im}^*(94)$	98	3.47	358	0.460	0.000
S ₇	$\pi_{im}(93) \rightarrow \pi_{im}^*(95)$	77	4.00	310	0.257	0.000
	$\pi_{im}(89) \rightarrow \pi_{im}^*(94)$	13				
Single reduced (S=0.5)						
State	Main contributing excitations	Weight / %	E^e / eV	λ / nm	f	$\langle S^2 \rangle$
D ₁	$\pi_{im}(93\beta) \rightarrow \pi_{im}^*(94\beta)$	93	1.85	672	0.223	0.804
D ₂	$\pi_{im}^*(94\alpha) \rightarrow \pi_{im}^*(95\alpha)$	93	1.98	627	0.231	0.787
D ₆	$\pi_{im}(94\alpha) \rightarrow \pi_{im}^*(99\alpha)$	84	2.75	452	0.478	0.990
D ₇	$\pi_{im}^*(92\beta) \rightarrow \pi_{im}^*(94\beta)$	80	2.96	419	0.363	0.948
Double reduced (S=0)						
State	Main contributing excitations	Weight / %	E^e / eV	λ / nm	f	$\langle S^2 \rangle$
S ₂	$\pi_{im}^*(94) \rightarrow \pi_{im}^*(95)$	99	2.32	498	0.807	0.000
S ₅	$\pi_{im}^*(94) \rightarrow \pi_{im}^*(99)$	97	2.96	419	0.888	0.000
S ₆	$\pi_{im}^*(93) \rightarrow \pi_{im}^*(95)$	99	3.42	363	0.382	0.000
Double reduced (S=1)						
State	Main contributing excitations	Weight / %	E^e / eV	λ / nm	f	$\langle S^2 \rangle$
T ₅	$\pi_{im}(95\alpha) \rightarrow \pi_{im}^*(100\alpha)$	94	1.81	685	0.134	2.021
T ₆	$\pi_{im}(93\beta) \rightarrow \pi_{im}^*(94\beta)$	88	1.87	662	0.305	2.030
T ₉	$\pi_{im}(94\alpha) \rightarrow \pi_{im}^*(98\alpha)$	87	2.65	468	0.466	2.114
T ₁₀	$\pi_{im}(92\beta) \rightarrow \pi_{im}^*(94\beta)$	88	2.73	455	0.339	2.056

Table S5: Calculated bright electronic excited states for the non-reduced (singlet), single (doublet) and double reduced (singlet and triplet) species of RuImCH₃ with the main contributing excitations, excitation energies E^e and wavelengths λ , oscillator strengths f , and the eigen values of $\langle S^2 \rangle$.

non-reduced (S=0)						
State	Main contributing excitations	Weight / %	E^e / eV	λ / nm	f	$\langle S^2 \rangle$
S ₆	$d_{xy}(181) \rightarrow \pi_{im}^*(183)$	54	2.41	516	0.402	0.000
	$d_{yz}(180) \rightarrow \pi_{ipy}^*(184)$	32				
S ₉	$d_{yz}(180) \rightarrow \pi_{ipy}^*(184)$	31	2.69	461	0.060	0.000
	$d_{xy}(181) \rightarrow \pi_{ipy}^*(185)$	22				
	$d_{xy}(181) \rightarrow \pi_{im}^*(183)$	20				
	$d_{xz}(182) \rightarrow \pi_{ipy}^*(185)$	9				
S ₁₁	$\pi_{im}(179) \rightarrow \pi_{im}^*(183)$	93	2.91	425	0.215	0.000
Single reduced (S=0.5)						
State	Main contributing excitations	Weight / %	E^e / eV	λ / nm	f	$\langle S^2 \rangle$
D ₁₉	$d_{xz}(183\alpha) \rightarrow \pi_{ipy}^*(188\alpha)$	21	2.29	540	0.309	0.810
	$d_{yz}(180\beta) \rightarrow \pi_{ipy}^*(183\beta)$	17				
	$d_{xy}(181\beta) \rightarrow \pi_{im}^*(185\beta)$	15				
	$d_{yz}(180\alpha) \rightarrow \pi_{ipy}^*(184\alpha)$	14				
	$\pi_{im}^*(183\alpha) \rightarrow d_z(190\alpha)$	8				
D ₂₀	$d_{yz}(180\beta) \rightarrow \pi_{ipy}^*(184\beta)$	42	2.30	539	0.047	0.849
	$d_{yz}(180\alpha) \rightarrow \pi_{ipy}^*(185\alpha)$	35				
Double reduced (S=0)						
State	Main contributing excitations	Weight / %	E^e / eV	λ / nm	f	$\langle S^2 \rangle$
S ₉	$\pi_{im}^*(183) \rightarrow \pi_{im}^*(188)$	43	2.19	566	0.081	0.000
	$\pi_{im}^*(183) \rightarrow d_{x^2-y^2}(191)$	38				
S ₁₅	$\pi_{im}^*(183) \rightarrow \pi_{im}^*(190)$	68	2.57	482	0.291	0.000
	$\pi_{im}^*(183) \rightarrow \pi_{im}^*(188)$	15				
S ₁₇	$\pi_{im}^*(183) \rightarrow \pi_{ipy}^*(188)$	31	2.71	457	0.055	0.000
	$d_{xy}(179) \rightarrow \pi_{ipy}^*(184)$	27				
	$\pi_{im}^*(183) \rightarrow \pi_{im}^*(193)$	11				
	$d_{xy}(179) \rightarrow \pi_{ipy}^*(185)$	11				
Double reduced (S=1)						
State	Main contributing excitations	Weight / %	E^e / eV	λ / nm	f	$\langle S^2 \rangle$
T ₁₆	$\pi_{im}^*(183\alpha) \rightarrow \pi_{im}^*(187\alpha)$	26	2.07	599	0.139	2.178
	$\pi_{ipy}^*(184\alpha) \rightarrow \pi_{im}^*(190\alpha)$	18				
	$\pi_{ipy}^*(184\alpha) \rightarrow \pi_{im}^*(187\alpha)$	11				
	$d_{xy}(181\alpha) \rightarrow \pi_{ipy}^*(185\alpha)$	9				

Table S6: Calculated bright electronic excited states for the non-reduced (singlet), single (doublet) and double reduced (singlet and triplet) species of RuImCOOEt with the main contributing excitations, excitation energies E^e and wavelengths λ , oscillator strengths f , and the eigen values of $\langle S^2 \rangle$.

non-reduced (S=0)						
State	Main contributing excitations	Weight / %	E^e / eV	λ / nm	f	$\langle S^2 \rangle$
S ₆	$d_{yz}(211) \rightarrow \pi_{ipy}^*(213)$	48	2.32	534	0.310	0.000
	$d_{xy}(210) \rightarrow \pi_{ipy}^*(214)$	31				
	$d_{xy}(210) \rightarrow \pi_{im}^*(213)$	15				
S ₁₁	$\pi_{im}(209) \rightarrow \pi_{im}^*(213)$	94	2.88	431	0.278	0.000
Single reduced (S=0.5)						
State	Main contributing excitations	Weight / %	E^e / eV	λ / nm	f	$\langle S^2 \rangle$
D ₇	$\pi_{im}^*(213\alpha) \rightarrow \pi_{im}^*(216\alpha)$	60	1.78	697	0.200	0.899
	$d_{xy}(212\alpha) \rightarrow \pi_{ipy}^*(214\alpha)$	9				
	$d_{xy}(212\beta) \rightarrow \pi_{ipy}^*(214\beta)$	9				
D ₂₃	$d_{xz}(209\beta) \rightarrow \pi_{im}^*(213\beta)$	50	2.48	501	0.063	0.954
	$d_{yz}(210\alpha) \rightarrow \pi_{ipy}^*(214\alpha)$	6				
	$d_{xy}(211\alpha) \rightarrow \pi_{ipy}^*(215\alpha)$	6				
	$d_{yz}(210\beta) \rightarrow \pi_{ipy}^*(214\beta)$	6				
Double reduced (S=0)						
State	Main contributing excitations	Weight / %	E^e / eV	λ / nm	f	$\langle S^2 \rangle$
S ₉	$\pi_{im}^*(213) \rightarrow \pi_{im}^*(218)$	80	2.27	545	0.406	0.000
S ₁₁	$\pi_{im}^*(213) \rightarrow \pi_{im}^*(219)$	54	2.43	511	0.233	0.000
	$d_{yz}(209) \rightarrow \pi_{ipy}^*(214)$	22				
S ₁₂	$d_{xy}(210) \rightarrow \pi_{ipy}^*(214)$	35	2.44	509	0.086	0.000
	$\pi_{im}^*(213) \rightarrow \pi_{im}^*(219)$	26				
S ₁₃	$d_{yz}(209) \rightarrow \pi_{ipy}^*(214)$	41	2.48	500	0.187	0.000
	$d_{xy}(210) \rightarrow \pi_{ipy}^*(214)$	16				
	$\pi_{im}^*(213) \rightarrow \pi_{im}^*(219)$	15				
S ₁₄	$\pi_{im}^*(213) \rightarrow d_{x^2-y^2}(222)$	20	2.52	491	0.167	0.000
	$d_{yz}(209) \rightarrow \pi_{ipy}^*(214)$	19				
	$\pi_{im}^*(213) \rightarrow d_{x^2-y^2} + \pi_{im}^*(221)$	15				
	$\pi_{im}^*(213) \rightarrow \pi_{im}^*(219)$	8				
Double reduced (S=1)						
State	Main contributing excitations	Weight / %	E^e / eV	λ / nm	f	$\langle S^2 \rangle$
T ₂₃	$\pi_{im}^*(209\beta) \rightarrow \pi_{im}^*(213\beta)$	72	2.28	543	0.292	2.110
	$\pi_{ipy}^*(214\alpha) \rightarrow \pi_{im}^*(223\alpha)$	8				

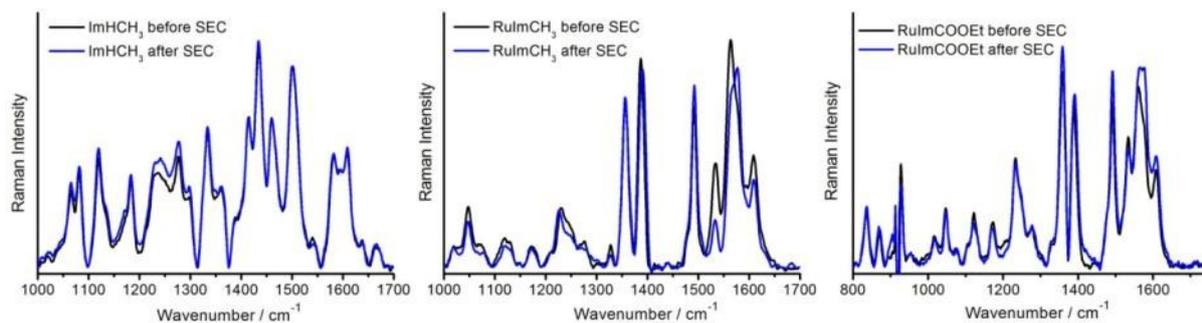


Figure S6: RR spectra of ImHCH₃ (left), RuImCH₃ (middle) and RuImCOOEt (right) before applying potential (black curve) and after recovery upon reoxidation of the reduced species at more positive potentials (blue curve). Only minor alterations in the spectra prove the general reversibility and recovery upon reoxidation of the reduced species.

[Zedler et al. Chem. Comm.]

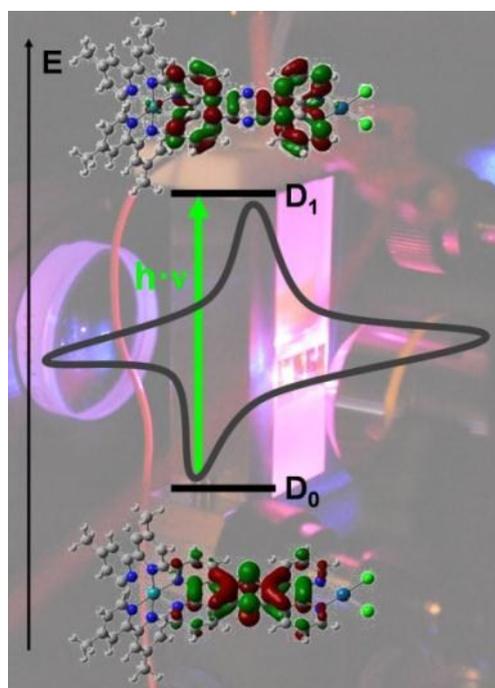
Resonance-Raman Spectro-Electrochemistry of Intermediates in Molecular Artificial Photosynthesis of Bimetallic Complexes

Der Nachdruck der folgenden Publikation erfolgt mit freundlicher Genehmigung der Royal Society of Chemistry.

Reprinted with kind permission from:

Zedler, L.; Guthmuller, J.; Rabelo de Moraes, I.; Kupfer, S.; Kriek, S.; Schmitt, M.; Popp, J.; Rau, S. und Dietzek, B., *Chem. Commun.* **2014**, 50, 5227-5229.

Copyright 2014 Royal Society of Chemistry.



Short lived and reactive intermediates during photoinduced multi-electron transfer have been studied by *in situ* UV-vis and resonance Raman spectro-electrochemistry revealing the impact of individual electronic transitions on the efficiency of a hydrogen evolving photocatalyst.

Resonance-Raman spectro-electrochemistry of intermediates in molecular artificial photosynthesis of bimetallic complexes†

Cite this: *Chem. Commun.*, 2014, 50, 5227Received 30th September 2013,
Accepted 7th January 2014

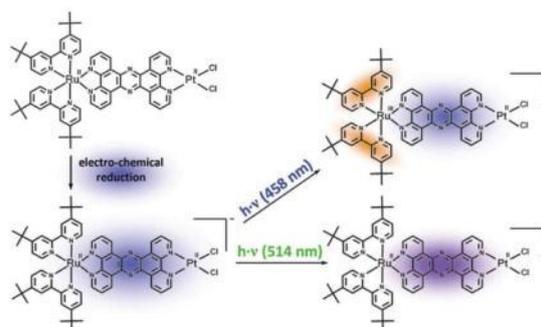
DOI: 10.1039/c3cc47487a

www.rsc.org/chemcomm

The sequential order of photoinduced charge transfer processes and accompanying structure changes were analyzed by UV-vis and resonance-Raman spectroscopy of intermediates of a Ru(II) based photocatalytic hydrogen evolving system obtained by electro-chemical reduction.

Molecular artificial photosynthesis presents one approach to cope with the increasing demand of environmentally friendly energy resources.^{1a-c} Hence, efforts towards (supra)molecular photocatalysts for water splitting (or its individual half-reactions) are pursued. However, understanding the role of individual molecular fragments in the catalytic cycles presents a mechanistic challenge.^{2a-d}

A molecular artificial photosynthetic system for photocatalytic production of hydrogen from protons is $[(\text{tbbpy})_2\text{Ru}(\text{tpphz})\text{PdCl}_2]^{2+}$ (RuPd; tbbpy = 4,4'-di-*tert*-butyl-2,2'-bipyridine, and tpphz = tetrapyrido [3,2-*a*:2',3':*c*:3'',2'',-*h*:2''',3''']phenazine). RuPd, its derivative $[(\text{tbbpy})_2\text{Ru}(\text{tpphz})\text{PtCl}_2]^{2+}$ (RuPt – Scheme 1) and model compounds such as Ru, *i.e.*, $[(\text{tbbpy})_2\text{Ru}(\text{tpphz})]^{2+}$, and $[(\text{tbbpy})_2\text{Ru}(\text{dppz})]^{2+}$ (dppz = dipyrrophenazine) have been studied spectroscopically and with respect to their catalytic performance.^{3a-g} Both RuPd and RuPt are photocatalytically active but their turnover numbers and turnover frequencies are very different. These differences might be assigned



Scheme 1 Electrochemical reduction (blue shade) and subsequent excitation of RuPt at 458 and 514 nm. Excitation of the single reduced RuPt at 458 nm leads to a MLCT involving the tbbpy ligands, whereas upon 514 nm excitation of a tpphz-center π - π^* transition occurs.

to the partial dissociation of RuPd during catalysis and the formation of colloids, which is also observed for related complexes.⁴ For RuPt no colloid formation occurs during catalysis.^{2b,5,6} Additionally, the catalytic efficiency of RuPd (*i.e.*, the number of H₂ produced per absorbed photon) increases upon increasing the excitation wavelength within the range of the visible metal-to-ligand charge transfer (MLCT) absorption.^{3b} RuPd and RuPt contain the same photo-active Ru^{II}-center and, hence, only minor differences in the absorption properties of the photocatalysts are apparent (Fig. S1, ESI†). Furthermore, the initial sub-ps photoinduced charge transfer dynamics in both RuPd and RuPt are qualitatively identical under non-catalytic conditions, *i.e.*, in pure solvents in the absence of a sacrificial electron donor.^{3c,6} While all previous studies have focused on the ultrafast photophysical and catalytic properties of RuPd and RuPt, no *in situ* spectroscopic characterization of intermediates in the catalytic cycle has been demonstrated up to now. Thus, a detailed understanding of the order of individual (slow) reaction steps during the catalytic cycle, which include first and second reduction of the catalytically active metal upon consecutive absorption of two photons and re-reduction of the photo-oxidized Ru^{III} center by a sacrificial electron donor, is lacking and discussed controversially in the literature.^{3a,c}

^a Institute of Physical Chemistry, Friedrich-Schiller-University Jena, Helmholtzweg 4, 07743 Jena, Germany. E-mail: benjamin.dietzek@uni-jena.de; Fax: +49-3641-948302; Tel: +49-3641-948360

^b Faculty of Applied Physics and Mathematics, Gdansk University of Technology, Narutowicza 11/12, 80233 Gdansk, Poland

^c Leibniz Institute of Photonic Technology Jena (IPHT), Albert-Einstein-Straße 9, 07745 Jena, Germany

^d Institute of Inorganic and Analytical Chemistry, Friedrich-Schiller University Jena, Humboldtstraße 8, 07743 Jena, Germany

^e Institute of Inorganic Chemistry I, University Ulm, Albert-Einstein-Allee 11, 89081 Ulm, Germany

† Electronic supplementary information (ESI) available: Experimental section, theoretical methods, absorption spectra, UV-vis-SEC of RuPd and Ru, molecular orbitals involved in photo-excitation of single reduced RuPt, RR-SEC of Ru, RuPd and RuPt at 458 nm, wavelength-dependent RR spectra of RuPt, TDFT-calculated and experimental RR spectra of RuPt during reduction, excited at 514 nm, RR active tpphz vibrations of reduced RuPt, and RR spectra of RuPt preceding and subsequent to SEC experiments. See DOI: 10.1039/c3cc47487a

In this study, the intermediate structure resulting from photoexcitation and subsequent reduction of the Ru^{III} center by an electron donor (Scheme 1, bottom left) was generated by electrochemical reduction (Scheme S1, ESI[†]). The structure of the intermediates was investigated in detail by UV-vis and resonance-Raman (RR) spectro-electrochemistry (SEC).^{7–10} The experimental results obtained for RuPt were analyzed by TDDFT calculations and compared to data obtained for Ru and RuPd. The electrochemically accessible single reduced species contain a reduced tpphz-bridging ligand equivalent to the short (sub-ns) lived photoexcited intermediate in the photocatalytic cycle after re-reduction of Ru^{III} to Ru^{II} (Scheme S1, ESI[†]).¹¹ The second reduction step of bimetallic complexes then reduces the Pt center. Thus, the herein presented spectro-electrochemical data provide insights into the structure and photophysical properties, *i.e.*, electronic properties of intermediates in the catalytic cycles of RuPd and RuPt, which allow for the derivation of mechanistic conclusions about the photocatalysis of the bimetallic tpphz complexes.

The UV-vis absorption spectra of non-reduced, single and double reduced RuPt (Fig. 1), Ru and RuPd (Fig. S2 and S3, ESI[†]) are dominated by a MLCT band at 450 nm. Upon MLCT transition in the non-reduced complex charge density is transferred from Ru d-orbitals to orbitals located both on the tbbpy and tpphz ligands. Electrochemical reduction results in a redshift of the MLCT absorption band at 450 nm for all species. According to TDDFT calculations the excess electron density localized at the tpphz ligand hinders an additional photo-driven charge transfer from the Ru^{II} ion to the tpphz ligand by electrostatic repulsion such that the weight of the Ru-to-tbbpy transitions within the MLCT increases (Fig. 1B and Fig. S4A, ESI[†]). Additionally, a new reduction-induced absorption band centered at 600 nm is observed. For RuPt (Fig. 1) this band extends throughout the visible range and resembles the spectral features of a

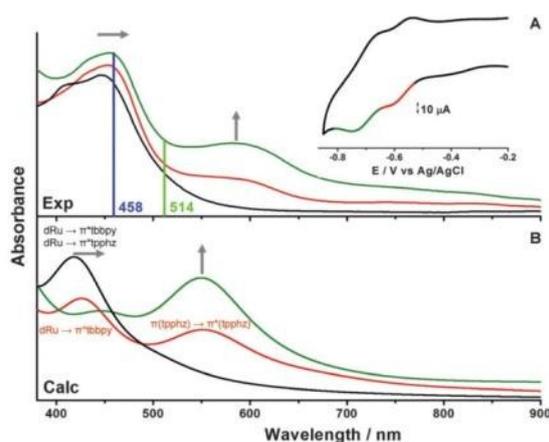


Fig. 1 (A) *In situ* UV-vis absorption spectro-electrochemical detection of intermediate reduction states. RR excitation wavelengths are displayed as vertical lines in the spectra. (B) Calculated spectra of RuPt (black: non-reduced RuPt, red: single reduced RuPt, green: double reduced RuPt (singlet character)). Inset: CV of RuPt in ACN containing the 0.1 M TBABF₄ electrolyte, recorded in the SEC cell. The voltage range for acquisition of the RR spectrum is colored (scan rate 5 mV s⁻¹, Pt-gauze working, Pt-counter, and Ag/AgCl-pseudo-reference electrodes).

short-lived (sub-ns) state observed in time-resolved spectroscopy of RuPt, Ru and RuPd.^{3a,c} TDDFT shows that this absorption band, which likely causes the *in situ* color change of RuPd and RuPt during photocatalysis, is due to an intraligand π - π^* transition on the tpphz ligand (Fig. 1B). This π - π^* transition redistributes electronic charge from the phenazine moiety of the tpphz ligand towards the phenanthroline spheres (Fig. S4C, ESI[†]). The second reduction of RuPt and RuPd leads to an increase of the spectral changes already induced by the first reduction, but no new bands or band shifts are observed. This is due to the fact that the second reduction is localized at the Pd and Pt ions, respectively,^{3a} and thus does not affect the Ru-based MLCT or the intraligand transition of the tpphz ligand.

While electronic absorption spectra indicate the formation of intermediates, they provide only little information on the accompanying structural changes upon reduction of the complex. To study the structure RR-SEC was performed (Fig. 2 and Fig. S5 and S7, ESI[†]). RR reveals Raman-active modes strongly coupled to the electronic transition. To investigate the reduced intermediates RR spectra were recorded upon excitation (i) within the MLCT transition at 458 nm (Fig. 1 and 2A), and (ii) in resonance with the ILCT transition at 514 nm (Fig. 2B). Reversibility of electrochemical reduction was confirmed by measuring RR spectra preceding and subsequent to SEC experiments (Fig. S9, ESI[†]).

(i) RR-spectra recorded in resonance with the MLCT transition of the single-reduced complexes closely resemble the spectra of the non-reduced complexes (Fig. 2A and Fig. S5, ESI[†]) indicating only minor changes in the geometry at the Franck-Condon (FC) point upon reduction of the complexes. Due to the large delocalized aromatic system of the tpphz ligand the additional electron induces only subtle changes in the nuclear arrangement, which is confirmed by TDDFT calculations. Nonetheless, reduction causes alterations of band intensity ratios of modes assigned to the tbbpy and tpphz ligands: the intensity of RR active modes associated with the peripheral tbbpy ligands, *i.e.*,

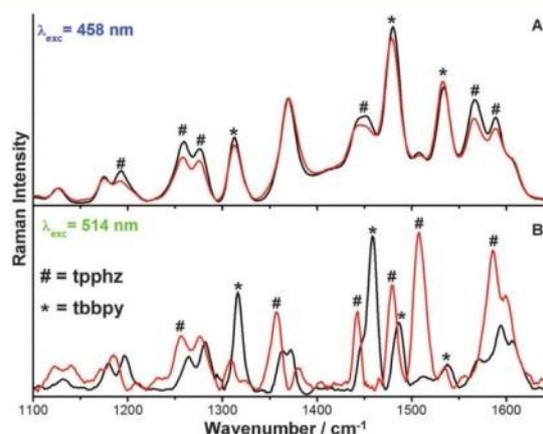


Fig. 2 Experimental RR spectra of non-reduced (black) and electro-chemically reduced (red) RuPt, excited at 458 nm (A) and 514 nm (B). Bands of the non-reduced species excited at 458 nm assigned to tbbpy modes (marked with an asterisk) remain almost unchanged in intensity whereas the modes, assigned to the tpphz ligand, are decreased by approximately 20% in intensity (A). Excitation of RuPt at 514 nm leads to new RR features, which are associated with the tpphz ligand (marked with hash).

bands at 1316, 1475 and 1532 cm^{-1} , remains constant. In contrast, the intensity of modes assigned to the tpphz bridging ligand, e.g., at 1450, 1567 and 1589 cm^{-1} , decreases by approximately 20% (displayed for RuPt in Fig. 2A) compared to the non-reduced compounds (Fig. S5, ESI[†]). Thus, in agreement with TDDFT calculations the contribution of Ru-to-tpphz MLCT transitions decreases for the reduced complexes, since the additional photoinduced electron density impedes photoactivation of the reduced tpphz ligand (Scheme 1 and Fig. S4, ESI[†]).

(ii) Upon 514 nm excitation RR-SEC spectra could only be observed for RuPt, while for Ru and RuPd the RR signals were obscured by a strong emission background. Upon reduction of RuPt a number of new RR bands, i.e., at 1257, 1358, 1443, 1507 and 1586 cm^{-1} grow in intensity relative to the solvent features (Fig. 2B). These RR features of the reduced RuPt are associated with the tpphz ligand (Fig. 2B; Fig. S7 and S8, ESI[†]; Scheme 1).^{3c} Additionally, upon reduction the tbbpy RR-bands at 1316 and 1458 cm^{-1} disappear (Fig. 2B). These findings are consistent with a significantly decreased contribution of the MLCT transition to the absorbance of the reduced sample at 514 nm (Fig. 1) as confirmed by TDDFT calculations. Hence, the dominant contribution arises from the ILCT transition which redistributes electronic charge from the phenazine moiety of the tpphz ligand towards the phenanthroline spheres (Fig. S4, ESI[†]). This is consistent with the pronounced spectral changes at 514 nm in contrast to minor modifications of the RR spectrum at 458 nm dominated by the MLCT transition.

The data show that light-absorption by the reduced complex at wavelengths longer than 500 nm does not contribute to directed charge transfer across the tpphz bridging ligand. This is due to the fact that the lowest-energy transition in the reduced complexes does not liberate charge density from Ru d-orbitals but corresponds to an excited state localized on the tpphz ligand which is also observed by transient absorption.^{3c} In relation to photocatalysis the results presented in this study provide insight into the sequential order of photoinduced charge transfer processes as discussed in the following.

In order to achieve photodriven double reduction of the catalytic center, two subsequent photo-induced MLCT transitions from Ru^{II} toward the tpphz fragment followed by charge transfer to the catalytic center are necessary. The MLCT constitutes the starting point for photocatalytic H₂ production by RuPt and RuPd. During photocatalysis the photo-oxidized Ru^{III} center is reduced by collision with a sacrificial electron donor, before a second photon is absorbed initiating electron transfer across the tpphz ligand to produce the catalytically active Pd⁰ and Pt⁰ species. The time sequence of LMCT and reduction of the Ru^{III} center by a sacrificial donor are ambiguous.^{3a,c} Time-resolved spectroscopy showed that ligand-to-metal charge transfer (LMCT) reoxidizes the reduced bridging ligand and reduces the catalytically active metal center within less than one ns after photoexcitation under non-catalytic conditions.^{3c,d,6} As the lifetime of the electro-chemically reduced tpphz-ligand in RuPt is long enough to observe this intermediate species spectro-electrochemically, it is apparent that the LMCT is significantly slowed down in the SEC experiments, i.e., if a Ru^{II} and not a Ru^{III} is coordinated to the tpphz^{•-} and a solution of high ionic strength is present (due to the TBABF₄ added in the SEC experiments,[†]).^{2b} This suggests that, as the sacrificial donor is provided in huge excess during the catalytic experiments, the collision-induced reduction mechanism of Ru^{III} might impair the electron transfer to the Pt site and hence account for the limited hydrogen generation efficiency of RuPt.

Sakai proposed a similar system for a proton attack to a Pt-orbital preceding photoinduced charge transfer towards the Pt-ion. In the absence of a proton donor in our experiments the electron transfer to the catalytically active metal might be impaired.

It was observed that RuPd shows a higher catalytic efficiency upon irradiation at 514 nm than at 458 nm.^{3b} This was tentatively assigned to additional excited-state deactivation channels, which are available upon shifting the excess charge density towards the peripheral tbbpy ligands (at 458 nm) instead of direct excitation of the bridging ligand (at 514 nm, wavelength-dependent RR spectra of RuPt are shown in Fig. S6, ESI[†]). The results presented here show that the marked wavelength-dependent photocatalytic efficiency indeed originates from the first electron transfer step, as 514 nm light-absorption by the reduced species does not provide any excess electron density to further reduce the catalytically active metal and, hence, does not promote catalytic activity.

The results discussed point to a marked sensitivity of the intramolecular charge transfer processes within the photocatalytically active bimetallic tpphz-complexes on the oxidation state of the photoactive Ru metal center. Hence, the work at hand indicates the necessity to include mechanistic considerations of the electrochemical/photochemical intermediates in order to optimize molecular artificial photosynthetic systems.

Support from COST (CM1202 Perspect-H2O) and from the 7th EU Framework Programme (J.G.) is highly acknowledged.

Notes and references

- (a) L. Sun, L. Hammarström, B. Åkermark and S. Styring, *Chem. Soc. Rev.*, 2001, **30**, 36–49; (b) Y. Tachibana, L. Vayssieres and J. R. Durrant, *Nat. Photonics*, 2012, **6**, 511–518; (c) D. Gust, T. A. Moore and A. L. Moore, *Acc. Chem. Res.*, 2009, **42**, 1890–1898.
- (a) T. S. Teets and D. G. Nocera, *Chem. Commun.*, 2011, **47**, 9268–9274; (b) H. Ozawa and K. Sakai, *Chem. Commun.*, 2011, **47**, 2227–2242; (c) A. J. Esswein and D. G. Nocera, *Chem. Rev.*, 2007, **107**, 4022–4047; (d) M. Wang, Y. Na, M. Gorlov and L. Sun, *Dalton Trans.*, 2009, 6458–6467.
- (a) S. Rau, B. Schäfer, D. Gleich, E. Anders, M. Rudolph, M. Friedrich, H. Görls, W. Henry and J. G. Vos, *Angew. Chem.*, 2006, **118**, 6361–6364; (b) S. Tschierlei, M. Karnahl, M. Presselt, B. Dietzek, J. Guthmüller, L. González, M. Schmitt, S. Rau and J. Popp, *Angew. Chem., Int. Ed.*, 2010, **49**, 3981–3984; (c) S. Tschierlei, M. Presselt, C. Kuhnt, A. Yartsev, T. Pascher, V. Sundström, M. Karnahl, M. Schwalbe, B. Schäfer, S. Rau, M. Schmitt, B. Dietzek and J. Popp, *Chem.–Eur. J.*, 2009, **15**, 7678–7688; (d) M. Karnahl, C. Kuhnt, F. Ma, A. Yartsev, M. Schmitt, B. Dietzek, S. Rau and J. Popp, *ChemPhysChem*, 2011, **12**, 2101–2109; (e) J. Guthmüller and L. González, *Phys. Chem. Chem. Phys.*, 2010, **12**, 14812–14821; (f) C. Kuhnt, M. Karnahl, S. Tschierlei, K. Griebenow, M. Schmitt, B. Schäfer, S. Kriek, H. Görls, S. Rau, B. Dietzek and J. Popp, *Phys. Chem. Chem. Phys.*, 2010, **12**, 1357; (g) M. Karnahl, S. Tschierlei, C. Kuhnt, B. Dietzek, M. Schmitt, J. Popp, M. Schwalbe, S. Kriek, H. Görls, F. W. Heinemann and S. Rau, *Dalton Trans.*, 2010, **39**, 2359–2370.
- P. Lei, M. Hedlund, R. Lomoth, H. Rensmo, O. Johansson and L. Hammarström, *J. Am. Chem. Soc.*, 2008, **130**, 26–27.
- K. Yamauchi, S. Masaoka and K. Sakai, *J. Am. Chem. Soc.*, 2009, **131**, 8404–8406.
- M. Pfeffer, B. Schäfer, C. Kuhnt, M. Schmitt, J. Popp, J. Guthmüller, G. Smolentsev, J. Uhlig, E. Nazarenko, V. Sundström, L. González, B. Dietzek and S. Rau, *Angew. Chem., Int. Ed.*, submitted.
- W. Kaim and J. Fiedler, *Chem. Soc. Rev.*, 2009, **38**, 3373.
- L. Dunsch, *J. Solid State Electrochem.*, 2011, **15**, 1631–1646.
- F. Hartl, T. L. Snoeck, D. J. Stufkens and A. B. P. Lever, *Inorg. Chem.*, 1995, **34**, 3887–3894.
- L. Zedler, J. Guthmüller, I. Rabelo de Moraes, S. Kriek, M. Schmitt, J. Popp and B. Dietzek, *J. Phys. Chem. C*, 2013, **117**, 6669–6677.
- V. Balzani, A. Juris, M. Venturi, S. Campagna and S. Serroni, *Chem. Rev.*, 1996, **96**, 759–834.

Supporting Information

Resonance-Raman spectro-electrochemistry of intermediates in molecular artificial photosynthesis of bimetallic complexes

*Linda Zedler,^a Julien Guthmuller,^b Inês Rabelo de Moraes,^c Stephan Kupfer,^a Sven Krieck,^d Michael Schmitt,^a Jürgen Popp,^{a,c} Sven Rau^e and Benjamin Dietzek^{*a,c}*

^a Institute of Physical Chemistry and Abbe Center of Photonics, Friedrich-Schiller-University
Jena, Helmholtzweg 4, 07743 Jena, Germany

^b Faculty of Applied Physics and Mathematics, Gdansk University of Technology,
Narutowicza 11/12, 80233 Gdansk, Poland

^c Leibniz Institute of Photonic Technology Jena (IPHT), Albert-Einstein-Straße 9, 07745 Jena,
Germany

^d Institute of Inorganic and Analytical Chemistry, Friedrich-Schiller University Jena,
Humboldtstraße 8, 07743 Jena, Germany

^e Institute of Inorganic Chemistry I, University Ulm, Albert-Einstein-Allee 11, 89081 Ulm,
Germany

Experimental details

The ruthenium complexes **Ru**, **RuPd** and **RuPt** were prepared according to published procedures.^{1,2} All solutions were prepared in acetonitrile (ACN, HPLC-grade, Aldrich), which was dried over calcium hydride and distilled twice. Prior to each measurement oxygen was removed by purging the solutions with argon.

Electrochemical and spectro-electrochemical data were obtained using a thin layer quartz glass spectro-electrochemical cell (Bioanalytical Systems, Inc) equipped with Pt-gauze, Pt-counter and Ag/AgCl-pseudo-reference electrodes. The thickness of the investigated layer of solution is 1 mm. The total sample volume in the cell is 500 μ l. For SEC and cyclic voltammetry (CV) solutions of **Ru**, **RuPd** and **RuPt** (100 μ M) in ACN containing 0.1 M TBABF₄ electrolyte were used. All solutions were thoroughly degassed with Argon prior to each measurement. The reduction products were analyzed by UV-vis absorption and resonance-Raman (RR) spectroscopy.

During the measurements the observed current is constant which implies continuous generation of the analyte. Even though the measurements are performed in a thin layer in the SEC-cell, the total sample volume of 500 μ l supplies educt during the course of the measurements. Therefore, we assume a quasi-constant concentration of species during the measurements, since the analyte is continuously generated.

UV-vis absorption spectra were measured at room temperature with a double beam Cary 5000 UV-vis spectrometer (Varian) with 1 nm spectral resolution.

RR spectra were excited by the visible lines of an Ar ion laser (Coherent, Innova 300C) and recorded with an Acton SpectraPro 2758i spectrometer (entrance slit width 100 μ m, focal length 750 mm, grating 600/mm). Transmission geometry was employed for the *in situ* RR spectro-electrochemical experiments. The Raman signals were detected using a liquid-nitrogen cooled CCD (SPEC-10, Roper Scientific). The spectra have been normalized with respect to an ACN band, i.e., to the solvent signal, prior to subtraction of the solvent spectrum. By normalizing to the solvent Raman signal we correct the spectra for changes in the laser intensity at the focus due to changes in the absorption of the solution as well as differences in the adjustment of the optical path for different measurements.

In the cell a diffusion controlled mixture of educt and reduction products is present. Still, by analyzing the changes in the acquired spectra we can precisely determine structural changes upon reduction by comparing the spectra at the reduction potential with the ocp (open circuit potential) spectrum, which are both normalized to the solvent. Upon complete electrolysis the spectroscopic signal intensity would simply be higher. In principle it is also possible to disentangle the contributions of educt and reduction product by decomposing the measured spectrum into an ocp-like spectrum corresponding to residual educt and the product spectrum. However, such spectral processing is not trivial since resonance-Raman spectra are affected by a broad background from luminescence of trace amounts of byproducts of the synthesis despite purification. This luminescence does also vary upon changing the voltage. For complete electrolysis a different and more complex cell arrangement needs to be used, as described in detail in Q. Hu, A. S. Hinman, *Anal. Chem.* **2000**, *72*, 3233–3235.; R. S. Czernuszewicz, K. A. Macor, *J. Raman Spectrosc.* **1988**, *19*, 553–557.^{3,4}

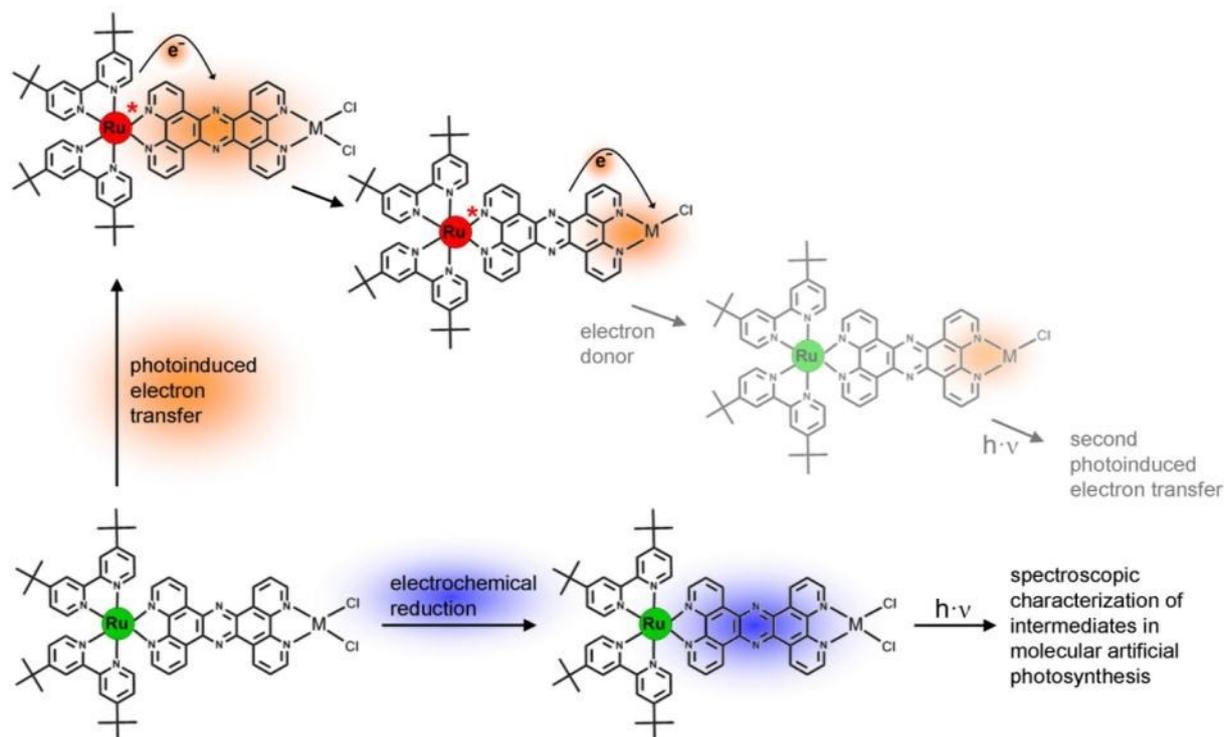
1. S. Rau, B. Schäfer, D. Gleich, E. Anders, M. Rudolph, M. Friedrich, H. Görls, W. Henry, and J. G. Vos, *Angew. Chem.*, 2006, **118**, 6361–6364.
2. M. Pfeffer, B. Schäfer, C. Kuhnt, M. Schmitt, J. Popp, J. Guthmuller, G. Smolentsev, J. Uhlig, E. Nazarenko, V. Sundström, L. González, B. Dietzek, and S. Rau, *Angew. Chem. Int. Ed.*, submitted.
3. Q. Hu, A. S. Hinman, *Anal. Chem.* **2000**, *72*, 3233–3235.
4. R. S. Czernuszewicz, K. A. Macor, *J. Raman Spectrosc.* **1988**, *19*, 553–557

Theoretical methods

Quantum chemical calculations were performed with the GAUSSIAN 09 program.³ The geometry and vibrational frequencies of the ground state was obtained by means of density functional theory (DFT) using the XC functional B3LYP. The 28-electron (60-electron) relativistic effective core potential MWB was used with its basis set for the ruthenium (platinum) atom. The 6-31G(d) double- ζ basis set was employed for the ligands. To correct for the lack of anharmonicity and the approximate treatment of electron correlation, the harmonic frequencies were scaled by the factor 0.97. The vertical excitation energies (200 states) and oscillator strengths were obtained from time dependent DFT (TDDFT) calculations within the adiabatic approximation with the same XC functional, pseudopotential and basis set. The effects of the interaction with a solvent (acetonitrile, $\epsilon=35.688$, $n=1.344$) on the geometry and excitation energies were taken into account by the integral equation formalism of the polarizable continuum model (IEFPCM). The nonequilibrium procedure of solvation was used for the calculation of the excitation energies, which is well adapted for processes where only the fast reorganization of the electronic distribution of the solvent is important. Finally, it should be mentioned that the four *tert*-butyl groups of the original catalyst were approximated in the calculations by methyl groups. This allows a reduction of the computational cost of the simulations without affecting the spectroscopic properties of the complexes.

The RR spectra of the non-reduced and reduced **RuPt** were obtained with a method described in details in the literature.^{4,5} This requires the calculation of excited state gradients for the states involved in the IL and MLCT bands. The CAM-B3LYP XC functional was employed for the computation of the gradients because this method provided the most accurate RR spectra for the related RuPd compound.⁴

3. Gaussian 09, Revision A.02, M. J. Frisch, G. W. Trucks, H. B. Schlegel, G. E. Scuseria, M. A. Robb, J. R. Cheeseman, G. Scalmani, V. Barone, B. Mennucci, G. A. Petersson, H. Nakatsuji, M. Caricato, X. Li, H. P. Hratchian, A. F. Izmaylov, J. Bloino, G. Zheng, J. L. Sonnenberg, M. Hada, M. Ehara, K. Toyota, R. Fukuda, J. Hasegawa, M. Ishida, T. Nakajima, Y. Honda, O. Kitao, H. Nakai, T. Vreven, J. A. Montgomery, Jr., J. E. Peralta, F. Ogliaro, M. Bearpark, J. J. Heyd, E. Brothers, K. N. Kudin, V. N. Staroverov, R. Kobayashi, J. Normand, K. Raghavachari, A. Rendell, J. C. Burant, S. S. Iyengar, J. Tomasi, M. Cossi, N. Rega, J. M. Millam, M. Klene, J. E. Knox, J. B. Cross, V. Bakken, C. Adamo, J. Jaramillo, R. Gomperts, R. E. Stratmann, O. Yazyev, A. J. Austin, R. Cammi, C. Pomelli, J. W. Ochterski, R. L. Martin, K. Morokuma, V. G. Zakrzewski, G. A. Voth, P. Salvador, J. J. Dannenberg, S. Dapprich, A. D. Daniels, Ö. Farkas, J. B. Foresman, J. V. Ortiz, J. Cioslowski, and D. J. Fox, *Gaussian, Inc., Wallingford CT*, 2009.
4. M. Wächtler, J. Guthmuller, L. González, and B. Dietzek, *Coord. Chem. Rev.*, 2012, **256**, 1479-1508.[3]
5. J. Guthmuller, and L. González, *Phys. Chem. Chem. Phys.*, 2010, **12**, 14812-14821.



Scheme S1 Light-induced electron transfer (red shaded) and electrochemical reduction (blue shaded) of a dinuclear hydrogen-evolving **RuM** (M=Pd) photocatalyst. Intermediates of the photochemical path under catalytic conditions are difficult to access, but can be mimicked and characterized by *in situ* spectro-electrochemical techniques.

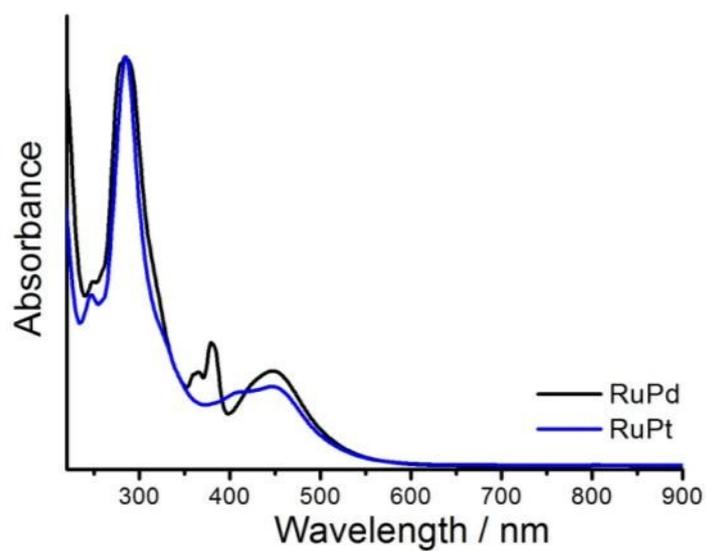


Figure S1 Comparison of the steady state absorption spectra of **RuPd** (black graph) and **RuPt** (blue graph) dissolved in ACN / 0.1 M TBABF₄.

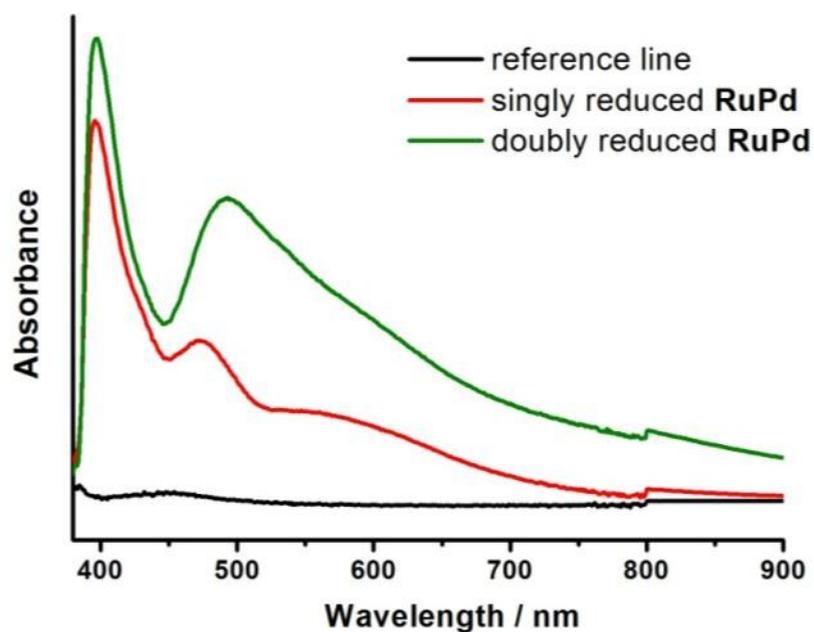


Figure S2 Difference UV-vis absorption spectra obtained during reduction of **RuPd**.

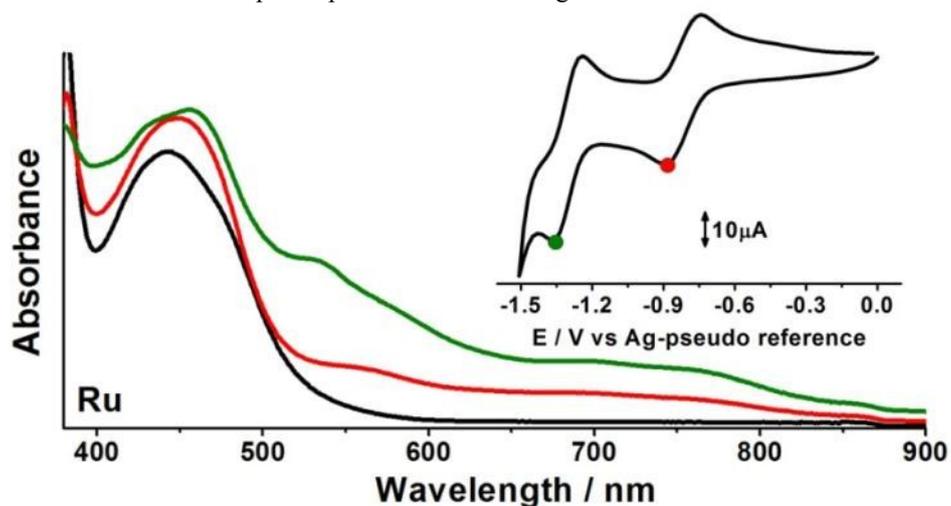


Figure S3 UV-vis absorption spectra obtained during single and double reduction of **Ru**. Inset: Corresponding CV with indicated voltage region for spectroscopy (scan rate 100 mV/s, solvent ACN containing 0.1 M TBABF₄ electrolyte, Pt-gauze working, Pt-counter, and Ag/AgCl-pseudo-reference electrodes).

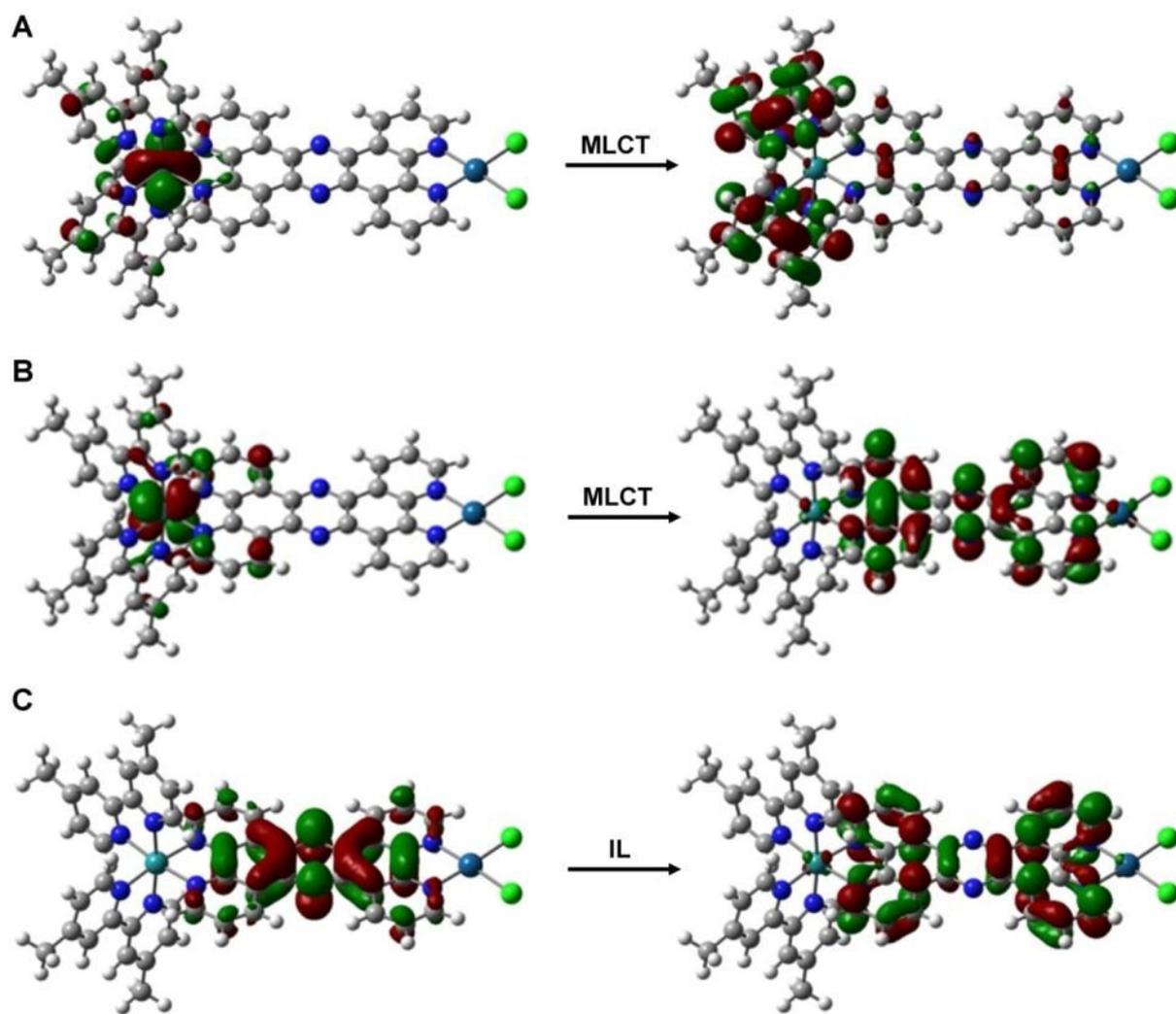


Figure S4 Calculated molecular orbitals involved in photo-excitation of single reduced **RuPt**. The MLCT at around 450 nm is dominated by charge transfer into acceptor orbitals of the tbpy ligand (A). Only minor contributions arise from the Ru-to-tpphz MLCT transition (B). The lowest energy transition at around 600 nm is assigned to an intraligand $\pi-\pi^*$ charge transfer localized on the tpphz fragment (C).

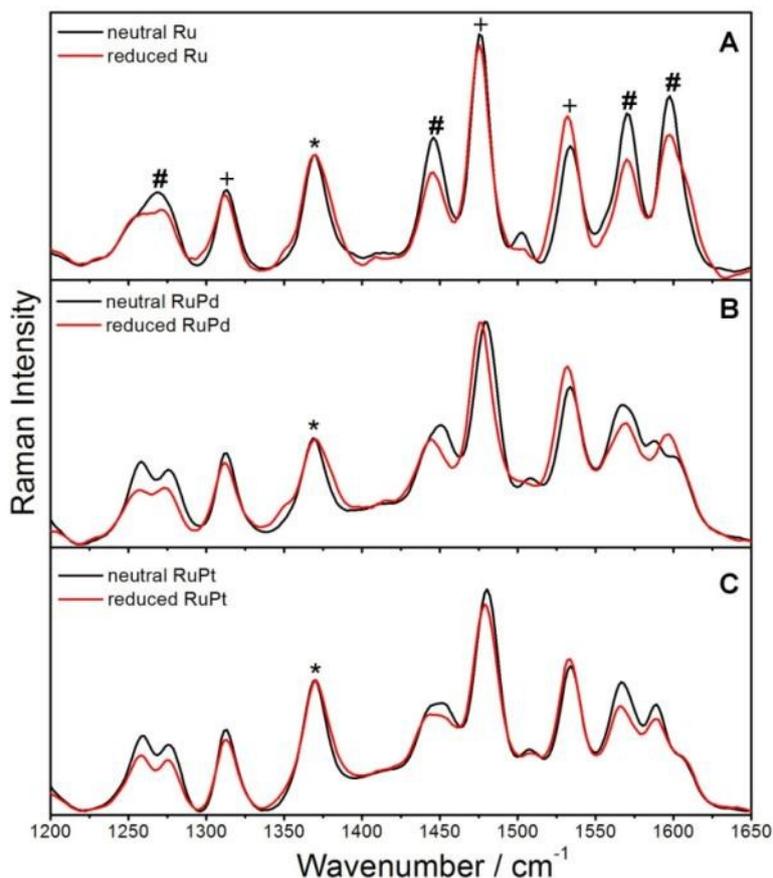


Figure S5 Resonance-Raman spectro-electrochemical response of **Ru** (A), **RuPd** (B) and **RuPt** (C) during electrochemically reduction in ACN / 0.1 M Bu₄NBF₄, excited at 458 nm. Vibrational resonances of the reduced species (red spectra) assigned to tbbpy modes (marked with a cross) either increase or remain unchanged in intensity whereas the modes, assigned to the tpphz ligand (marked with a hash key) are decreased by approximately 20% in intensity for all three complexes.

For band assignment of RR spectral features the nonresonant Raman spectrum of the tpphz ligand has been used because in case of a delocalized aromatic electronic configuration the Raman resonances of ring breathing modes of the cyclic aromatic structure have a large Raman cross section, since the polarization is strongly changing during the vibration. Upon electronic transition the photoelectron is also directed to the aromatic system, which is why vibrations of the aromatic system are enhanced. Therefore, the same vibrations are visible in resonant and nonresonant Raman spectra of this aromatic tpphz ligand. Indeed the RR spectrum of the reduced **RuPt** excited at 514 nm is in excellent agreement with the nonresonant Raman spectrum of the free tpphz ligand [M. Karnahl, S. Tschierlei, C. Kuhnt, B. Dietzek, M. Schmitt, J. Popp, M. Schwalbe, S. Krieck, H. Görls, F. W. Heinemann, et al., *Dalton Trans. Camb. Engl.* 2003 **2010**, 39, 2359–2370].

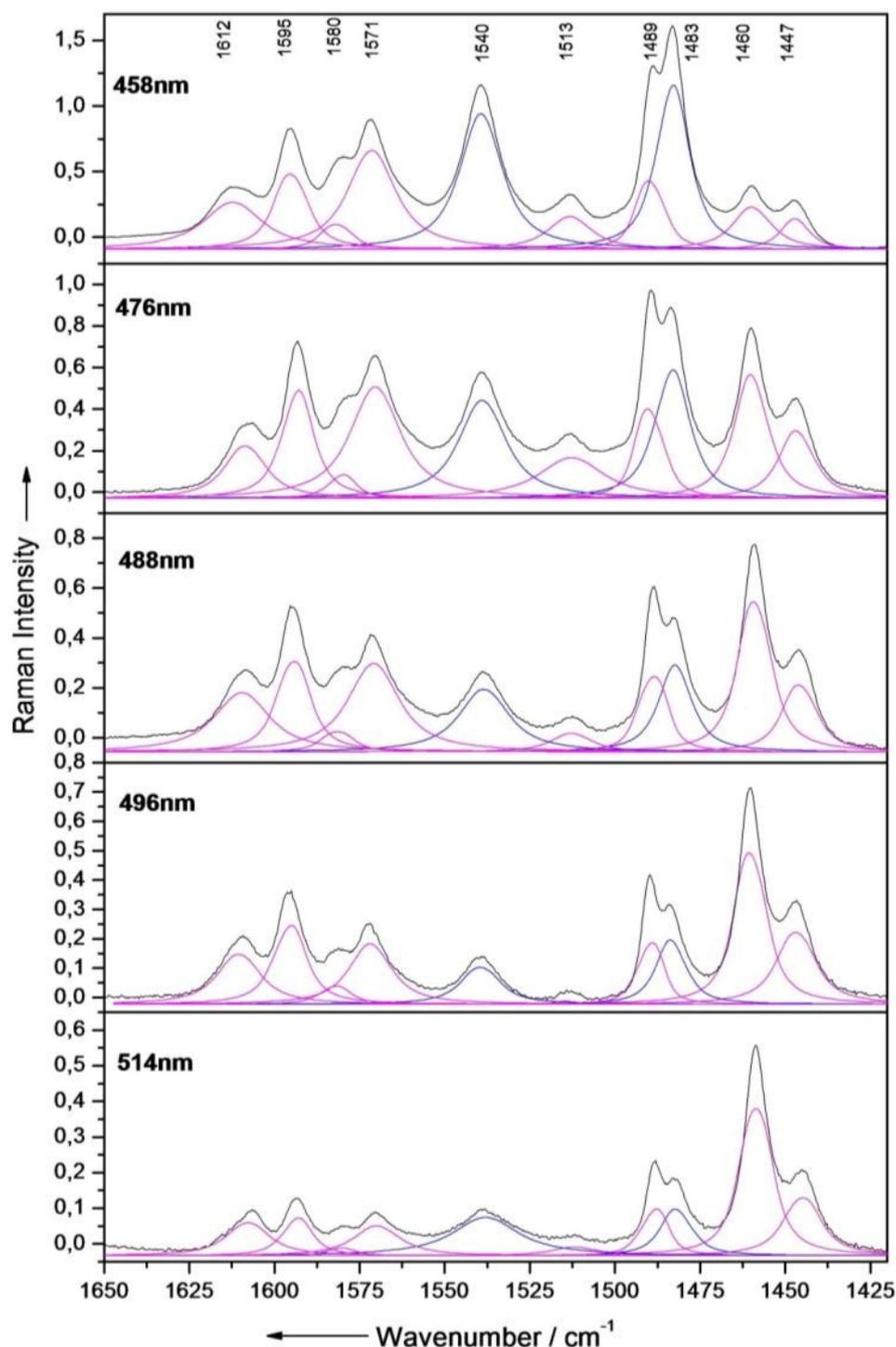


Figure S6 Wavelength dependent resonance-Raman spectra of **RuPt** dissolved in ACN. The applied Raman excitation wavelengths match the lowest energy MLCT absorption band of **RuPt**. Spectral data were decomposed by Lorentz fits into the contribution of vibrational modes of the tbbpy-ligands (blue labelled) and of the tpphz-ligand (magenta labelled bands). An increasing contribution of the tpphz ligand to the FC point with decreasing excitation energy is observed.

It should be noted that during the spectro-electrochemical RR experiments a diffusion-controlled mixture of reduced and non-reduced species is present in the laser focus volume. I.e., the experimental spectra at 514 nm excitation are the superposition of the RR spectra of

the non-reduced species and the reduced species possessing MLCT and IL transitions (Fig S7 B). This explains the only qualitative agreement of the experimental and theoretical RR spectra (Fig. S7). The calculated spectra are based on the structure of the pure reduction states of **RuPt**, but all energetically allowed transitions were taken into account, e.g., for the single reduced species electronic resonances with the tpphz IL π - π^* transition and the MLCT transition. Qualitatively, there is good agreement between experiment and calculations indicating charge transfer to the tpphz bridging ligand upon photoactivation (Fig. S8).

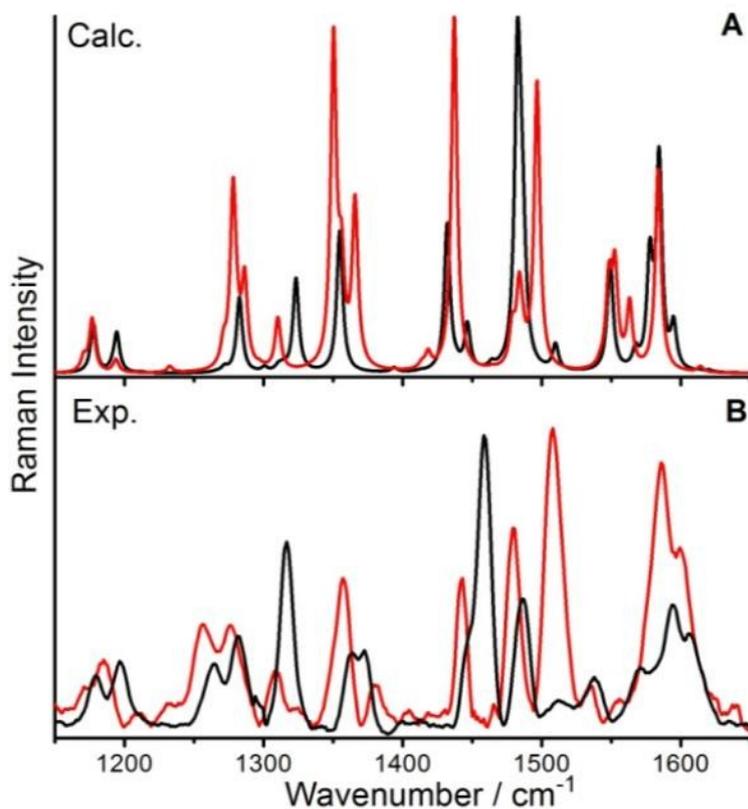


Figure S7 TDDFT-calculated (A) and experimental (B) resonance-Raman spectra of non-reduced (black) and electrochemically reduced (red) **RuPt**, excited at 514 nm. Experiment and calculations are in qualitatively good agreement, indicating charge transfer to the tpphz bridging ligand upon photoactivation.

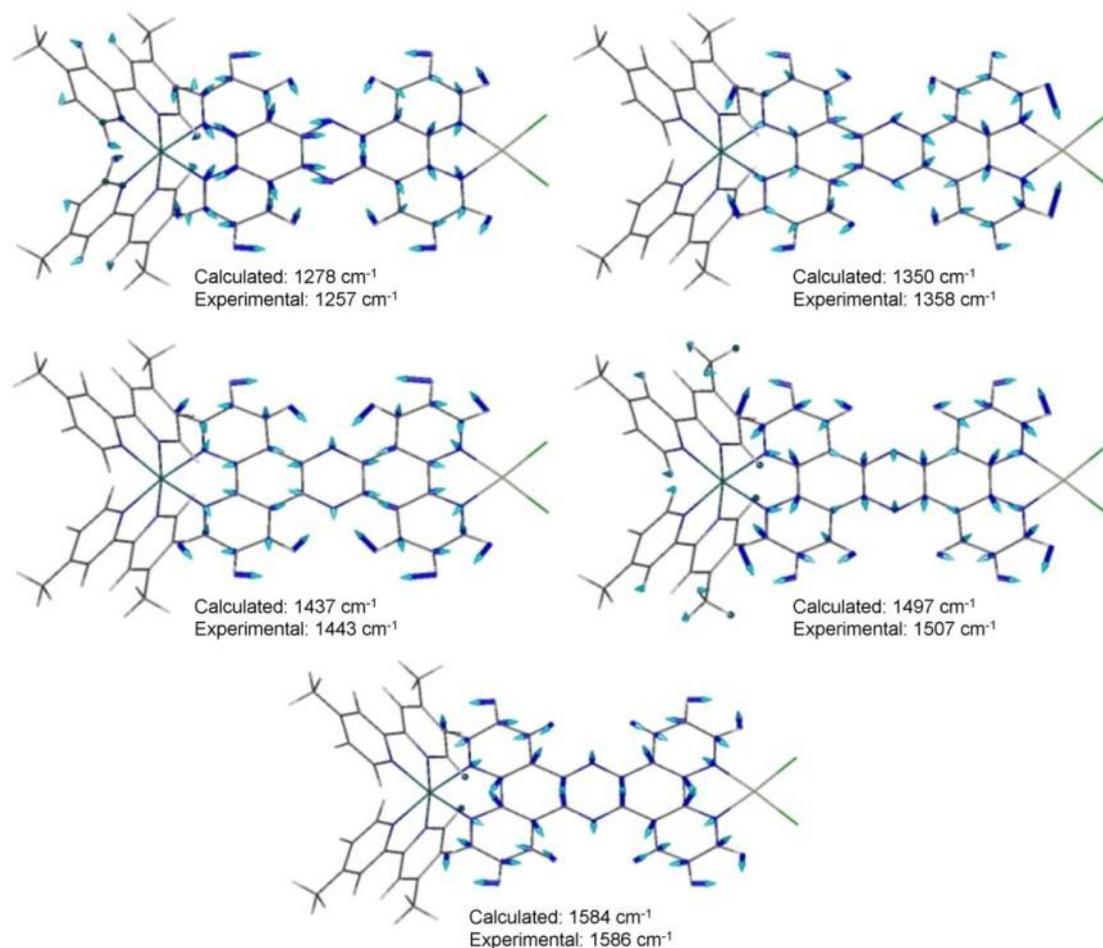


Figure S8 Most prominent resonance-Raman active vibrations of reduced **RuPt** ($\lambda_{\text{exc}} = 514\text{nm}$). Resonance-Raman features are primarily assigned to tpphz modes.

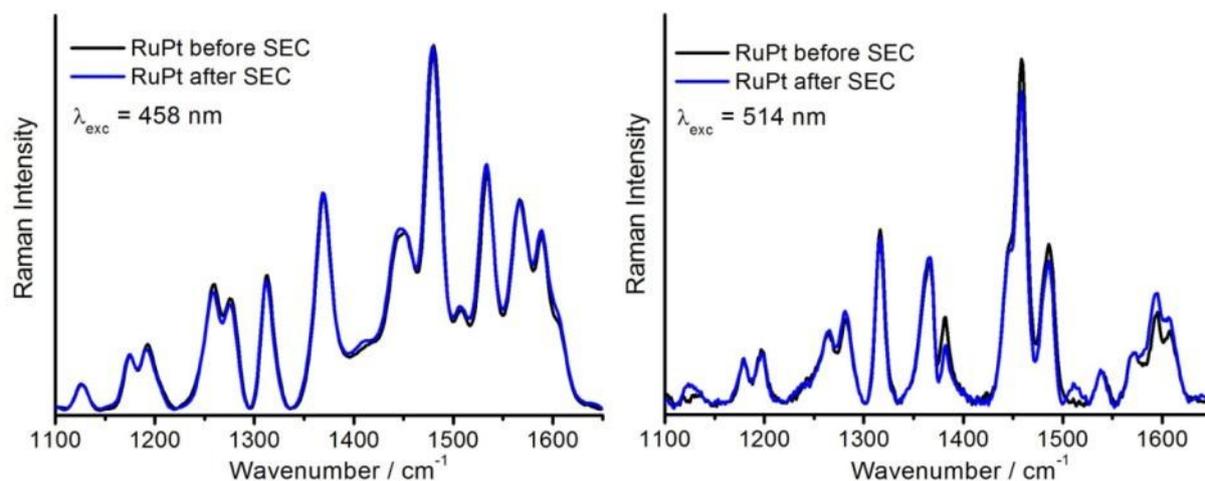


Figure S9 RR spectra of **RuPt**, excited at 458 nm (left) and at 514 nm (right) before applying potential (black curve) and after recovery upon reoxidation of the reduced species at more positive potentials (blue curve). Only minor alterations in the spectra prove the general reversibility and recovery upon reoxidation of the reduced **RuPt**.

[Zedler et al. RSC Adv.]

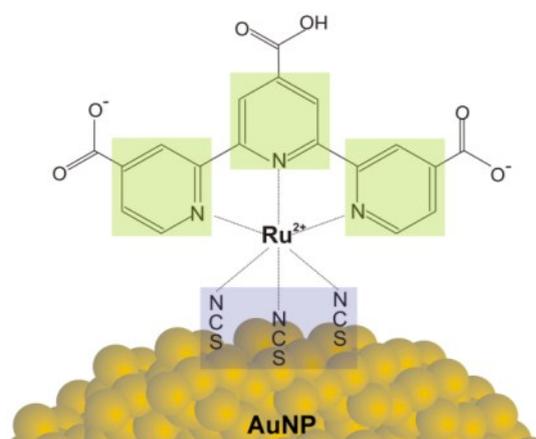
Ruthenium Dye Functionalized Gold Nanoparticles and Their Spectral Responses

Der Nachdruck der folgenden Publikation erfolgt mit freundlicher Genehmigung der Royal Society of Chemistry.

Reprinted with kind permission from:

Zedler, L.; Theil, F.; Csáki, A.; Fritzsche, W.; Rau, S.; Schmitt, M.; Popp, J.; Dietzek, B., Ruthenium Dye Functionalized Gold Nanoparticles and Their Spectral Responses, *RSC Adv.* **2012**, 2, 4463–4471.

Copyright 2012 Royal Society of Chemistry.



How binding of highly absorbing Ruthenium dyes to the surface of Au nanoparticles modifies their spectral properties for novel applications

Ruthenium dye functionalized gold nanoparticles and their spectral responses†

Linda Zedler,^a Frank Theil,^{ab} Andrea Csáki,^b Wolfgang Fritzsche,^b Sven Rau,^c Michael Schmitt,^a Jürgen Popp^{ab} and Benjamin Dietzek^{*ab}

Received 6th December 2011, Accepted 11th March 2012

DOI: 10.1039/c2ra01248k

The functionalization of metal nanoparticles provides access to materials with unique chemical and physical properties for a wide range of applications, *e.g.* in catalysis, optoelectronics and material science. However, the fundamental light induced charge transfer processes and electronic interactions at the functional nanoparticle–molecule interface, which constitute these unique properties, are not yet fully understood. In this work monodisperse spherical gold nanoparticles functionalized by the photoactive ruthenium dyes (Bu₄N)₂[Ru(dcbpyH)₂(NCS)₂], (Bu₄N)₃[Ru(tcterpy)(NCS)₃] and [Ru(dnbpy)(dcbpyH)₂(NCS)₂] (Bu₄N = tetrabutylammonium, dcbpyH = 2,2′-bipyridyl-4,4′-dicarboxylato, NCS = isothiocyanato, tcterpy = 2,2′:6′,6′′-terpyridyl-4,4′,4′′-tricarboxylato, dnbpy = 2,2′-bipyridyl-4,4′-dinonyl) known as **N719**, **N749** and **Z907**, and [Ru(tbbpy)₂(tpphz)](PF₆)₂ (tbbpy = 4,4′-butyl-2,2′-bipyridine, tpphz = tetrapyridophenazine, PF₆ = hexafluorophosphate) (**Ru**) were synthesized in aqueous solution applying a conjugation and a phase transfer reaction approach, respectively. The functionalized nanoparticles obtained were analyzed by UV-vis spectroscopy, TEM imaging and Raman spectroscopic techniques in order to investigate the molecular structures of the photoactive ruthenium dyes at the gold surface. The results indicate, that the dyes' fully conjugated electronic structure and therefore, their photophysical properties, are preserved or only slightly altered upon binding to the surface of the gold nanoparticles, which potentially allows for rapid and efficient transport of charges to the nanoparticles after photoexcitation.

Introduction

Nanostructured materials have drawn a vast amount of attention in various fields of research during the last decades, due to their unique optical, catalytic and electronic properties.^{1–3} This development includes nanomaterials composed of metals,⁴ semiconductors,⁵ polymers⁶ but also composite and alloy materials.⁴ Metal nanoparticles (NPs), and in particular silver and gold nanoparticles (AuNPs), have attracted significant interest, because they combine large structural variability and extraordinary physical properties in comparison to the respective bulk materials.⁷ These unique properties originate from their small size and large surface-to-volume ratio.^{8,9} In addition, the physical and chemical properties of NPs can be tuned by surface functionalization¹⁰ giving rise to numerous applications, *e.g.* biological “cloaking” of nanostructured materials for medical research^{11,12} or novel spectroscopic biosensing approaches at the nanoscale.¹³ Metal NPs can be functionalized by a wide range of molecules due to the high affinity of atoms such as sulfur,¹⁴

nitrogen¹⁵ and phosphorus¹⁶ to diverse metal surfaces. Thus, the design of functional nanoparticle–molecular interfaces has become a field of intense research.^{17–22} Semiconductor NPs modified with transition metal dyes have attracted interest as the main compounds of dye-sensitized solar cells.^{23–25} Classically, such solar cells are based on a ruthenium polypyridyl dye for sensitizing nanostructured TiO₂ films, converting visible light into electricity. Several transition metal complexes have been employed as photosensitizers, for example commercially available dyes such as **N719**, **N749** and **Z907** (see Fig. 1).²⁶ As a common feature these dyes carry a carboxyl-functionalized polypyridine ligand. The carboxyl groups provide efficient binding to the surface of the NPs and support injection of electrons from the photo-excited ruthenium dye into the conducting band of the TiO₂.²⁷ The dyes **N719**, **N749** and **Z907** not only exhibit carboxyl groups for binding to semiconductor surfaces, but also possess isothiocyanate ligands with free sulfur atoms that have a high affinity to metals. Although providing beneficial features for applications in photonics, electronics, material science or catalysis⁷ gold nanoparticle–molecular interfaces with photoactive molecular species—in particular ruthenium polypyridyl dyes—have only been sparsely investigated to date.^{14,28} In particular, the incorporation of photocatalytic features can increase the impact of these systems even though this represents a rather challenging approach due to the additional directional charge transfer to a catalytic center.

^aInstitute of Physical Chemistry and Abbe Center of Photonics, Jena, Germany

^bInstitute for Photonic Technology, Jena, Germany.
E-mail: Benjamin.Dietzek@ipht-jena.de

^cInstitute of Inorganic Chemistry, Ulm University, Germany

† Electronic supplementary information (ESI) available. See DOI: 10.1039/c2ra01248k

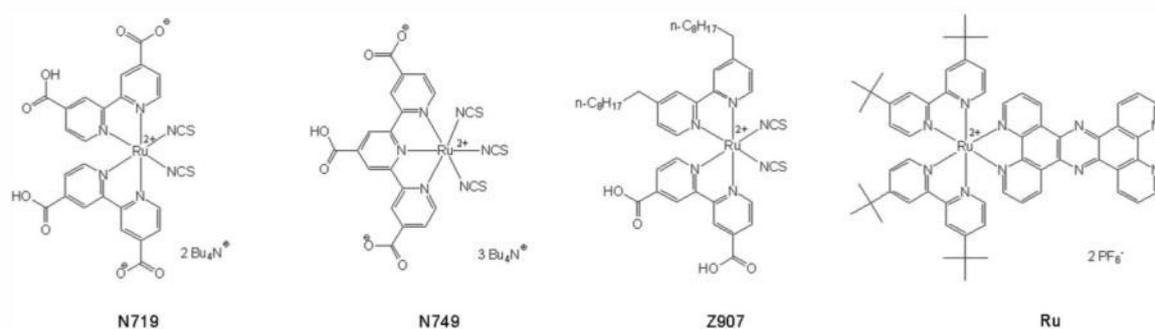


Fig. 1 Molecular structure of the ruthenium complexes N749, N719, Z907 and Ru.

Nonetheless, the successful realization of such concepts promises to open a synthetic doorway for the design of, *e.g.* supramolecular systems for efficient hydrogen generation.

This study represents a systematic investigation of the interface between gold NPs and various photoactive ruthenium dyes. N749, N719 and Z907 were attached to the surface of AuNPs to prove that adsorption occurred *via* the isothiocyanate group and to examine the orientations of the molecules with respect to the metal surface. While N719 functionalized metal NPs have already been synthesized in organic solvents, their stabilization in aqueous solution could not be realized.²⁸ However, an aqueous environment is advantageous for many potential applications, especially in catalysis and obviously for biomedical applications. To the best of our knowledge, the synthesis of N749, N719 and Z907 functionalized AuNPs in aqueous solution is reported here for the first time.

Furthermore, this study demonstrates the immobilization of Ru (see Fig. 1) on the surface of metal NPs. Ru consists of a tetrapyridophenazine (tpphz) bridging ligand and a ruthenium(II) photocenter and is known to be a light absorbing moiety in an intramolecular photocatalyst reducing protons to H₂ under irradiation.²⁹ The molecular photocatalyst, in which the uncoordinated phenantroline sphere of Ru is coordinated to a PdCl₂ group has been intensively studied with resonance Raman (RR) and ultrafast spectroscopy^{30–34} in order to understand the light induced photochemical processes underlying the catalyst's performance. A promising option to increase the efficiency of such a system might be the use of NPs as a catalytic center instead of a single palladium ion.²⁹ The use of NPs has the potential to overcome two major obstacles of the previously reported approach: in the dinuclear photocatalytic system two electrons need to be generated by photoexcitation of one chromophore and transferred to the catalytic center to produce hydrogen. This is a process of low probability and serious spatial constraints, since photoactivation and reducible hydrogen ions have to meet at the same point in space and time. These constraints are relaxed in nanoparticle systems. First, multiple electrons on the NPs can be photogenerated by different photoactive dye molecules on the NP. Second, the conductive and catalytically active NP surface provides much more area for catalysis and enables the fast distribution of electrons across the NPs. From these viewpoints, we applied a facile method to anchor Ru onto the three dimensional surface of AuNPs, which was ultimately intended to increase the catalytic efficiency.

For spectroscopic investigations of these novel AuNPs the strong surface plasmon resonance absorption band of AuNPs allows optical characterization in the visible region.³⁵ A powerful tool delivering detailed insights into structure related molecular properties is surface-enhanced Raman scattering (SERS).³⁶ We utilized SERS to investigate ruthenium complexes at the surface of the metal NPs. Detection of the molecules' SERS spectra does not only provide proof of binding, *e.g.* formation of the functional nanoparticle–molecular interface, but also information on the structure of the interface, *e.g.* the orientation of the adsorbate and its interaction with the nanoparticle's surface.

In summary we report on the synthesis of AuNPs functionalized by photoactive ruthenium dyes with ligands of different natures in an aqueous environment and their analysis by Raman enhancement techniques to investigate the molecular structures of typical photoactive ruthenium dyes in a functional nanoparticle–molecular interface.

Experimental

Synthesis of functionalized AuNPs

The ruthenium complexes (Bu₄N)₂[Ru(dcbpyH)₂(NCS)₂], (Bu₄N)₃[Ru(tcterpy)(NCS)₃] and [Ru(dnbpy)(dcbpyH)₂(NCS)₂] (Bu₄N = tetrabutylammonium, dcbpyH = 2,2'-bipyridyl-4,4'-dicarboxylato, NCS = isothiocyanato, tcterpy = 2,2':6',6''-terpyridyl-4,4''-tricarboxylato, dnbpy = 2,2'-bipyridyl-4,4'-dinonyl) known as N719, N749 and Z907 (see Fig. 1) were purchased from Solaronix SA (Aubonne, Switzerland) and used without further purification. The dyes were immobilized on monodisperse spherical AuNPs of 30 and 60 nm diameter by conjugation. The well studied, yet structurally different ruthenium dye,^{29,30} [Ru(tbbpy)₂(tpphz)](PF₆)₂ (tbbpy = 4,4'-butyl-2,2'-bipyridine, tpphz = tetrapyridophenazine, PF₆ = hexafluorophosphate) (Ru) (see Fig. 1), was bound to colloidal gold by a phase transfer reaction (PTR).

There are different reasons for the fact that two synthesis strategies had to be applied. First, N719, N749 and Z907 most likely bind to the surface of AuNPs with the sulfur atoms of the isothiocyanate ligands, which have a high affinity to gold.³⁷ Ru cannot employ this binding modality. Nevertheless, it offers the bidentate phenantroline ligand for binding to the gold surface using the lone electron pairs of the nitrogen atoms. Since nitrogen has a much smaller affinity to gold than sulfur the binding is likewise weaker than for the commercially available

dyes. Secondly, the main difference of both synthetic methods, as will be presented in the section “UV-Vis and transmission electron microscopic (TEM) imaging” is the distinct mean diameter of the NPs. Binding *via* the lone electron pairs of the nitrogen atoms of the phenantroline moieties of the tetrapyrrolophenazine (tpphz) ligand³⁸ is sterically demanding, thus, and thus favours binding to smaller particles obtained by PTR. Owing to the smaller radius of the NPs the 270 pm wide binding pocket of the tpphz ligand³³ firmly binds to the surface of an AuNP. Indeed a 6 nm AuNP is 20 times larger than the tpphz binding pocket; however, the number of nearest neighbours of a single gold atom at the surface is distinctly smaller than for a 30 nm AuNP. Thus, a single gold atom is more easily accessed by the binding pocket of the tpphz ligand. In addition, due to the NPs larger surface-to-volume ratio surface atoms exhibit higher binding energies than atoms of the bulk material. Hence, surface functionalization is also energetically beneficial for smaller particles.³⁹

Conjugation

Spherical AuNPs with mean diameters of 30 and 60 nm were synthesized by citrate reduction.⁴⁰ The colloidal solutions of the citrate stabilized AuNPs were incubated with 5 vol.% aqueous solutions of the dyes **N719**, **N749** and 5 vol.% ethanolic solution in the case of **Z907** with molarities of 10 μM . On average, 1 mL conjugate was obtained by mixing 900 μL NP suspension with 50 μL dye solution filled up with 50 μL distilled water. The conjugate was mixed on a rotating tumbler at room temperature for 2 h. Each batch was cleaned by repeated centrifugation and replacing the residual solution with 1 mL distilled water. The obtained functionalized NPs remained stable for months.

Phase transfer reaction

AuNPs stabilized by **Ru** were prepared by adopting the previously reported two-phase extraction method.^{41,42} In contrast to the literature reports the reaction time for the phase transfer of AuNPs from toluene to aqueous solution was increased to 15 h.

For the AuNP synthesis a 30 μM aqueous solution of $\text{HAuCl}_4 \cdot 3\text{H}_2\text{O}$ was added to a 50 μM solution of tetraoctylammonium bromide in toluene (4 mL). The transfer of the metal chloride to the toluene phase could be observed by a color change of the organic phase from transparent to orange within a few seconds. A 0.4 M solution of NaBH_4 (0.928 μL), freshly prepared in ice water, was then added to the two-phase mixture and stirred for 1 h at room temperature.

For the phase transfer a dye solution of a ratio $[\text{Au}^{\text{III}}]/[\text{Ru}] = 6$ was used. 5 mg (46 μmol) of the chloride salt of **Ru** dissolved in water (10 mL) were added to the stirred toluene solution. The phase transfer was completed within 15 h, which could be observed by a color change of the aqueous phase from orange to dark brown. The suspensions were purified at least three times by centrifugation. After each centrifugation the residual solvent was removed and replaced by distilled water. The obtained nanoparticles remained stable for months.

Materials and methods

TEM imaging

The size distribution and the agglomeration behaviour of the obtained AuNP suspensions were determined by TEM imaging at 80 kV (DSM 960, Zeiss, Jena, Germany).

UV-vis spectroscopy

UV-vis absorption spectra of 100 μM dye solutions and functionalized colloidal gold particles were recorded on a Jasco V670 UV-vis spectrometer using the double beam mode and a 1 mm quartz cuvette.

Raman spectroscopy

Raman, resonance Raman (RR), and SERS spectra were acquired using various experimental setups. Nonresonant FT-Raman spectra ($\lambda_{\text{exc}} = 1064 \text{ nm}$) were recorded using a “MultiRAM” (Bruker) with a fibre-coupled diode pumped solid-state laser (DENICAFC LC-3/40, KLASTECH-Karpushko Laser Technologies). The laser power was set to 100 mW. For each spectrum 100 scans were averaged. A single IR 352 objective with a working distance of 16 mm focused the laser on the sample and collected the scattered light. The signal was detected by a nitrogen-cooled Ge-Diode (Bruker D418-T). The spectral resolution was 2 cm^{-1} .

The RR and SERS spectra were excited with an Ar ion laser (Coherent) operated at 514 and 458 nm or a frequency doubled Nd-YAG-laser at 532 nm. The laser was focused into a rotating-cell cuvette for RR⁴³ or a 1 cm fluorescence cuvette for SERS measurements. Raman signals were collected at a 90° scattering angle using either a Canon 1.4 50-mm objective or a lens ($f = 100 \text{ mm}$) and focused onto the entrance slit of an Acton SpectraPro 2758i spectrometer (entrance slit width of 100 μm , focal length 750 mm, grating 600 mm^{-1}). The Raman signals were detected by a liquid-nitrogen cooled CCD (Princeton Instruments). Sample integrity was ensured by recording absorption spectra before and after the RR experiments.

Results and discussion

In this study AuNPs stabilized by ruthenium dyes in an aqueous environment were synthesized and characterized by Raman spectroscopic techniques to derive structure-related properties of the nanoparticle–molecular interfaces. The ruthenium complexes used for functionalization exhibit unique optical properties, such as a large absorption cross-section throughout the visible spectral range in the cases of **N719**, **N749** and **Z907** and favourable intramolecular charge-transfer properties in the case of **Ru**.^{29,30} The spectroscopic analysis presented in the following sections aims at investigating whether these molecular optical properties are preserved upon binding onto AuNPs or not. To this end the interaction of the dyes with the metal surface and the novel properties of this functional nanoparticle–molecular interface were examined by UV-vis absorption, TEM imaging, SERS, RR and nonresonant Raman spectroscopy.

UV-vis and TEM imaging

The size distribution of the NPs obtained by conjugation or PTR were analyzed by UV-vis spectroscopy and TEM imaging. The

maximum of the surface plasmon resonance (SPR) peak in the UV-vis absorption spectra depends on the mean particle diameter:^{7,39} the absorption maximum shifts to lower wavelengths and the spectral width narrows for decreasing particle diameter. Since this spectral feature also depends on other parameters (*e.g.* the refractive index of the solvent, particle shape and temperature), the determination of the particles' mean diameter using UV-vis spectroscopy is not very precise. In addition, functionalization alters the absorption properties of AuNPs due to *e.g.* the interaction between the ligand field and the surface electron cloud.¹³ The UV-vis spectrum in Fig. 2A displays the SPR band as expected from the literature⁷ for AuNPs of 60 nm diameter with a maximum at about 535 nm, stabilized either by citrate or by N749. A redshift of 7 nm (240 cm^{-1}) of the SPR band has been observed upon ligand exchange, indicating the interface modification of the AuNPs (Fig. 2A). In case of **Ru** anchored on AuNPs a significant redshift by 24 nm (850 cm^{-1}) was observed for the SPR band after the phase transfer (Fig. 2B). This behaviour can be explained by two effects: first, binding of **Ru** onto the surface of AuNPs causes a different surrounding environment and influences the surface electron cloud; second, the refractive index of the solvent ($n_{\text{water}} = 1.33$, $n_{\text{toluene}} = 1.496$) has been shown to induce a shift of the SPR band, according to the Mie theory⁴⁴ upon transfer of AuNPs from toluene to water.

The distinct size distribution was analyzed by TEM imaging (Fig. 3). In the case of conjugation colloidal solutions of about 30 and 60 nm mean diameter with a size distribution of 3 nm (standard deviation) were synthesized. In contrast, the PTR provided much smaller particles (average particle size is 6 ± 1.4 nm) while showing a similar uniform size distribution. The histograms of the size distributions as derived from several TEM images and two sample TEM images are shown in Fig. 3.

Raman spectroscopic characterization

SERS and RR spectroscopy have been utilized in order to study the binding modality of the ruthenium dyes onto the AuNPs, to analyze the structure and orientation of these complexes on the surface and to identify potential differences compared to the molecular structures in solution. To enable a reliable band assignment of the resonance and surface-enhanced Raman

modes of the dye molecules under investigation, nonresonant FT-Raman spectra were recorded for comparison. Furthermore, the nonresonant FT-Raman measurements have been exploited to estimate the magnitude of Raman signal enhancement in both RR and SERS measurements and to characterize the change from the ground state electronic configuration upon excitation.

Raman analysis of N719, N749 and Z907

The excitation wavelengths for RR spectroscopy measurements have been chosen to be in resonance with the metal-to-ligand charge transfer (MLCT) absorption band of the dyes in solution (see Fig. 4A). SERS spectra were recorded with an excitation wavelength lying both within the surface plasmon resonance and the MLCT absorption band.

Fig. 5 exemplarily displays the RR, SERS and nonresonant FT-Raman spectra for N749. Both RR and SERS spectra are dominated by modes which can be assigned to the terpyridine (terpy) ligand (terpy—vibrations at 1468 , 1521 , 1604 cm^{-1} and less pronounced the ring breathing mode at 1000 cm^{-1}).⁴⁵ Fig. 5A–C show RR spectra recorded for three different concentrations. Based on the S/N ratio of these RR spectra a detection limit of about 10^{-6} M can be estimated. Furthermore, Fig. 5 shows that the nonresonant FT-Raman spectrum of the pure dye (E) and the RR spectrum of the 10^{-4} M solution (A) have a comparable S/N ratio, which shows that the nonresonant Raman signal is enhanced by a factor of roughly 10^4 through resonant MLCT excitation.

The concentration of the dye on the AuNPs has been estimated to be approximately 10^{-7} M by assuming a dye monolayer on the surface of 30 nm AuNPs and a concentration of 10^{10} particles per mL (the area occupied by a dye molecule has been estimated to be about $2 \times 10^{-18}\text{ m}^2$). The SERS spectrum shown in Fig. 5D exhibits a similar S/N ratio as the RR spectrum of the 10^{-4} M dye solution; therefore we conclude that binding the dye to the surface of the AuNPs, *i.e.* the formation of a functional nanoparticle–molecular interface, leads to a further enhancement by a factor of 10^3 as compared to RR enhancement.

In order to understand the implications derived from the observed SERS spectrum we will briefly summarize which factors affect the additional SERS enhancement.^{1,2} Firstly, the

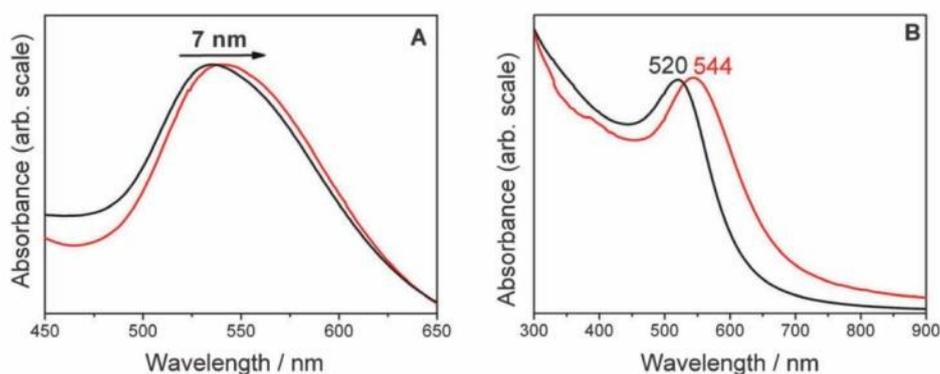


Fig. 2 A: Normalized UV-Vis absorption spectra of 60 nm gold colloid stabilized by citrate (black) and N749 (red), the SPR band of the gold colloid shifts markedly by 7 nm upon ligand exchange. B: SPR band of the organosol (black), redshift of the SPR band by 24 nm after PTR (red).

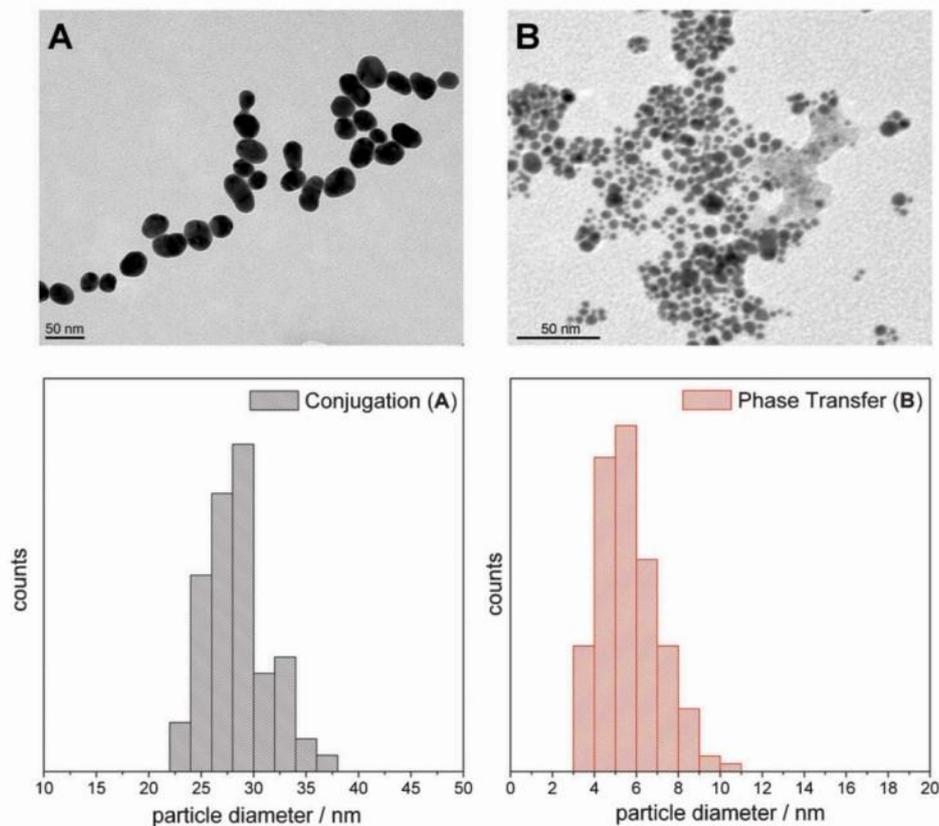


Fig. 3 In the upper panels example TEM images and in the lower panels the respective histograms of the NPs obtained by conjugation (A) and phase transfer catalysis (B) are displayed. (A) Shows NPs of 30 nm mean diameter functionalized with Z907. In (B) colloids functionalized with Ru are shown. The mean diameter for the colloid in (B) is 6 ± 1.4 nm and thus much smaller than in the case of A, 28 ± 3 nm. The histograms of the particle diameter of the ruthenium dye coated NPs as derived from multiple TEM images are shown below.

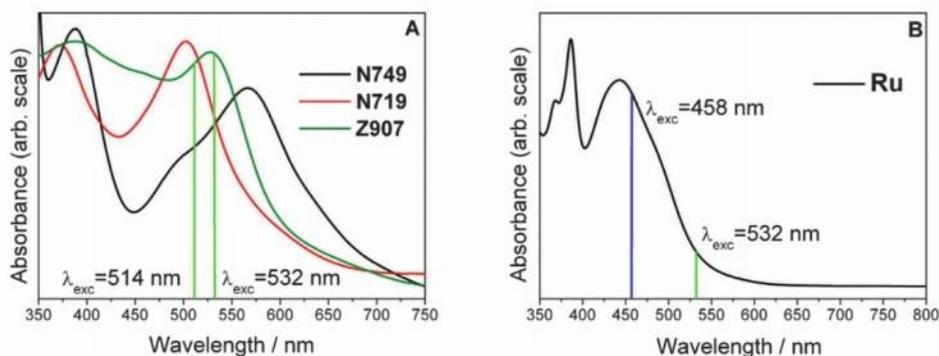


Fig. 4 UV-vis absorption spectra of 10^{-4} M solutions of N749, N719, Z907 (A) and Ru (B). The RR excitation laser lines at 532, 514, and 458 nm and the SERS excitation wavelength at 532 nm, in resonance with the dye but also with the surface plasmon resonance of AuNPs, are displayed as vertical lines.

SERS effect consists of two contributions, a pure electromagnetic enhancement responsible for most of the total enhancement and an additional chemical enhancement due to the formation of surface complexes with different electronic structure allowing for

additional resonance enhancement. The latter one is visible only if the molecule is directly bound to the surface. If the electronic structure of the surface complex is strongly altered, the Raman spectra of such surface complexes also differ significantly from

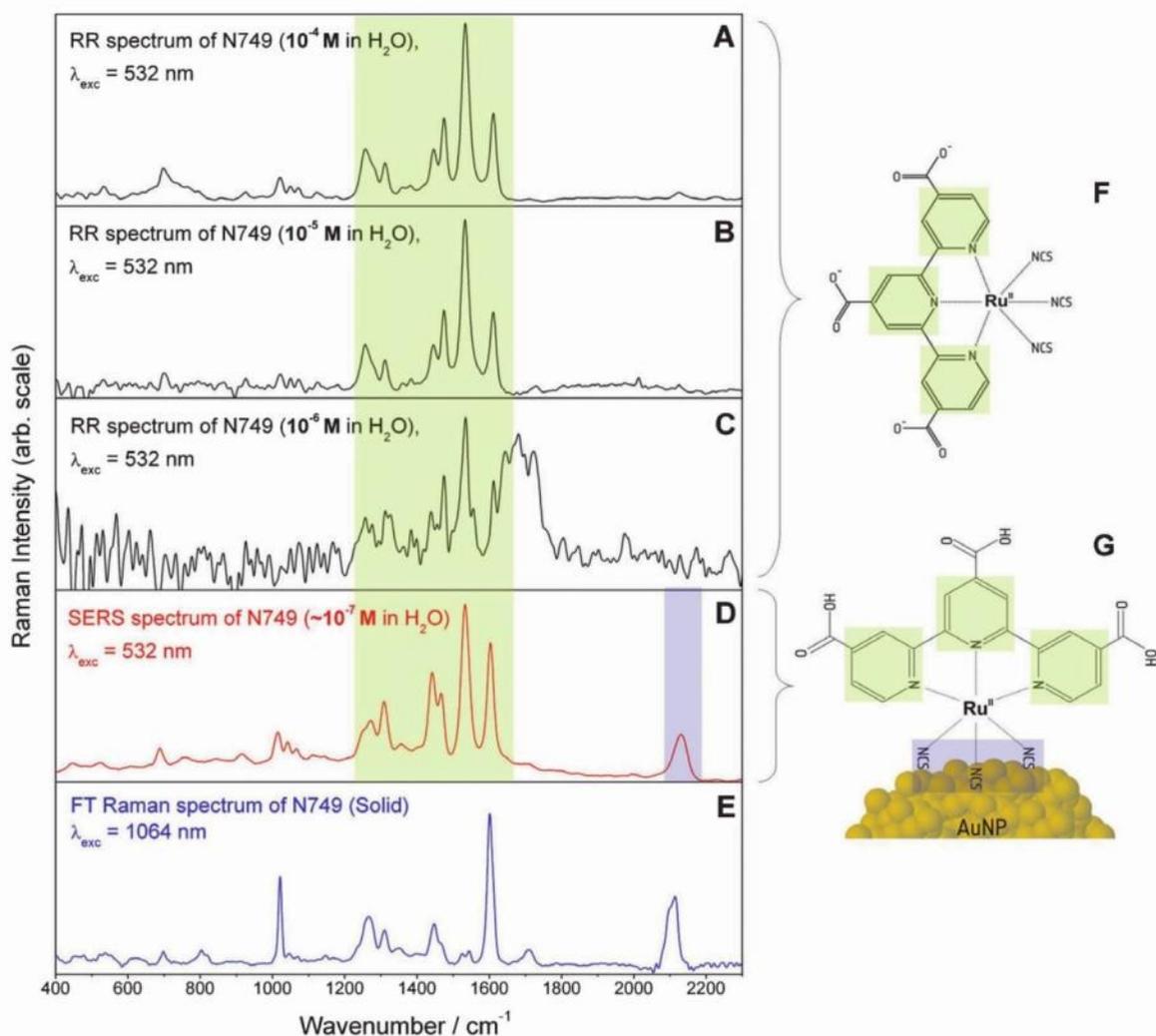


Fig. 5 Comparison of RR spectra at 10^{-4} , 10^{-5} and 10^{-6} M (A–C), SERS (D) and nonresonant FT-Raman (E) spectra of **N749**. The broad spectral feature around 1700 cm^{-1} in panel C is an artefact resulting from subtracting the solvent spectrum. The charge localization on the terpy ligand upon MLCT absorption within the fingerprint spectral region from $1000\text{--}1800\text{ cm}^{-1}$ is marked in green while the binding site *via* the isothiocyanate group at 2100 cm^{-1} is highlighted in blue. In panels F and G the structure of the ruthenium dye in solution and the hypothesized binding geometry on the NP surface are depicted. The structural elements are colour coded corresponding to the assignment of the Raman spectral features.

the RR spectra in solution. The longer ranged pure electromagnetic contribution decays more slowly but nevertheless extremely rapidly with distance from the surface. Thus vibrations of molecular bonds in close proximity to the surface are significantly more enhanced than those of structures lying further apart, since the enhancement scales inversely to the 10th power of the distance to the surface for a molecular monolayer. Furthermore the enhancement is also dependent on the orientation with respect to the surface normal. The highest enhancement is achieved for vibrations perpendicular to the surface. According to these properties of SERS enhancement a clear proof of binding to the metal is the observation of the CN-stretching vibration at about 2100 cm^{-1} due to the isothiocyanate group in the SERS spectrum (Fig. 5D), which—in

addition—is the only notable difference between the SERS and RR spectra. Further vibrational bands of this functional group *e.g.* the Au–S stretching vibration at around 450 cm^{-1} and the antisymmetric NCS stretching vibration were not observable to support our interpretation for several reasons. The strong reflections from the colloid the background are very inhibiting within the low wavenumber region, hence the Au–S stretching vibration cannot be observed. Second these vibrations are only enhanced by the electromagnetic SERS effect, since there is no evidence for a marked resonance enhancement of these bands. Otherwise they would be observable in the RR spectrum, too. Thus fortunately the symmetric CN vibration is within a silent spectral region enabling clear detection despite relatively weak enhancement. In contrast to previously published SERS

investigations of the dyes using AuNP suspensions in organic solvents,²⁸ no bands of the COO-groups are visible in the SERS spectrum (see Fig. 5D). Since surface enhancement drastically depends on the distance between a molecular fragment and the SERS active metal surface, we conclude that **N749** is anchored on the AuNPs *via* the sulfur atoms of the isothiocyanate ligands, which have a high affinity to gold.

In order to characterize the Franck-Condon region of **N749**, RR and nonresonant FT-Raman spectra were compared to identify which modes are resonantly enhanced *i.e.* are coupled to the MLCT transition. Such a comparison between Fig. 5A and E clearly shows a selective enhancement of characteristic bands of the terpy ligand at 1468, 1521 and 1604 cm^{-1} demonstrating that the electronic excitation is localized on this ligand⁴⁵ (see Fig. 5).

Of particular interest is the investigation of the dye adsorbed on the surface of AuNPs and how its structure differs from the structure of the dye in solution. By comparing the wavenumber positions and relative intensities of the terpy bands in the RR and SERS spectra (Fig. 5A and D), it is obvious that both spectra are very similar. This similarity points towards similar molecular and electronic structures of the unbound **N749** and the **N749** attached to the AuNP's surface. Thus, the fully conjugated chromophoric system within **N749** is preserved upon binding to the AuNPs, which potentially allows for rapid and efficient transport of charges to the NPs after photoexcitation.

Analogous spectroscopic results have been obtained for colloids stabilized by **Z907** and **N719**. The corresponding spectra are presented in the supplementary information.†

In the following, similar experiments on **Ru** are discussed in order to investigate, how its electronic properties are affected by immobilization on AuNPs.

Raman analysis of Ru

Fig. 6 depicts the RR, SERS and nonresonant FT-Raman spectra of **Ru**. It should be noted that in the case of **Ru** it was not possible to excite RR and SERS spectra with similar excitation wavelengths as used for **N719**, **N749** and **Z907**. Instead, SERS spectra were recorded with an excitation wavelength of 532 nm

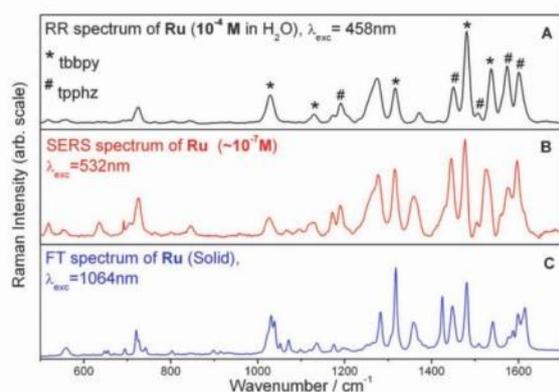


Fig. 6 Comparison of RR (A), SERS (B) (**Ru** stabilized AuNPs obtained from PTR), and FT-Raman (C) spectra for **Ru**. Raman bands which can be assigned to the tbbpy ligand are marked by a * while tpphz bands are labelled with a #, according to the literature.³¹

assuming resonant excitation conditions within the SPR band of the AuNPs. However, it was not possible to obtain RR spectra for free **Ru** in solution with 532 nm excitation due to the presence of a strong fluorescence background obscuring the RR information. Thus, RR spectra were recorded in the maximum of the MLCT band at 458 nm (see Fig. 4B) where the RR bands are spectrally well separated from the fluorescence emission. The RR spectrum is characterized by prominent bands of the tpphz ligand at 1601, 1574, 1506, 1450 and 1190 cm^{-1} and the tbbpy ligand at 1538, 1481, 1317, 1131 and 1028 cm^{-1} .³¹ This band assignment is based on a comparison between RR and nonresonant FT-Raman spectra (Fig. 6A and C) and is in agreement with previous RR spectroscopic studies and quantum-chemical calculations.³² Similar to **N749**, the detection limit of **Ru** with RR is 10^{-6} M (see Fig. S3†). The SERS spectrum recorded at 532 nm is dominated by bands of both, tbbpy and tpphz ligands, and exhibits a similar S/N ratio as the RR spectrum (Fig. 6B). The concentration of the dye on the AuNPs is estimated to be 10^{-7} M using the approximations laid out above for **N749**.

To verify the formation of a nanoparticle-molecular interface, additional SERS enhancement, *i.e.* the Raman signal enhancement due to the proximity of the metal surface and not due to the electronic resonance of the excitation wavelength, has to be estimated. Since the S/N ratio of the RR spectra (Fig. 6A) at a concentration of 10^{-4} M and the SERS spectrum (Fig. 6B) at 10^{-7} M are similar, the additional SERS enhancement is estimated to be 10^3 . The increased SERS enhancement of modes assigned to the bidentate tpphz ligand as compared to the RR spectrum is a strong indicator for an attachment of **Ru** to the gold surface *via* the tpphz ligand. In particular the tpphz bands at 1603 and 1453 cm^{-1} (Fig. S4, ESI†) exhibit a significantly larger relative intensity in the SERS spectrum than in the RR spectrum. The chelating bidentate tpphz group ensures a strong interaction with the metal surface.

As for **N719**, **N749** and **Z907** the determination of structural differences of **Ru** adsorbed on the surface of AuNPs in comparison to its structure in solution is of importance, since its photocatalytic properties, when coordinated to a catalytic active unit, are strongly dependent on the preservation of the fully conjugated electronic structure of the tpphz ligand upon binding. As pointed out above, the relative intensities of the RR and SERS bands are not identical (see Fig. 6A and B). This discrepancy might be partially explained by the different excitation wavelengths. Since the excitation wavelengths of SERS and RR spectra differ by more than 70 nm, the spectral changes in the band pattern may be due to different resonance enhancement. Such effects were observed for structurally similar complexes.^{31,33,46} Overall, we do not have sufficient evidence for assuming similar molecular and especially electronic structures of **Ru** attached to AuNPs and **Ru** in solution. In order to clarify if the conjugated electronic structure required for rapid and efficient transport of charges after photoexcitation is preserved upon immobilization on AuNPs, RR spectra need to be recorded at an excitation wavelength of 532 nm. However, as mentioned above these experiments failed due to strong fluorescence masking the RR bands of **Ru** in solution.

Conclusion

Nanostructured materials are promising candidates for a broad range of applications due to their unique optical, catalytic and

electronic properties arising from their size and the additional functionalization potential of the large surface area. By modifying the surface of AuNPs exclusive properties of a molecular monolayer can be introduced and combined with the properties and functionalities of the particles. In this contribution, the immobilization of the ruthenium based dyes (Bu₄N)₂[Ru(dcbpyH)₂(NCS)₂] (**N719**), (Bu₄N)₃[Ru(tcterpy)(NCS)₃] (**N749**), [Ru(dnbpy)(dcbpyH₂)(NCS)₂] (**Z907**) and [Ru(tbbpy)₂(tpphz)](PF₆)₂ (**Ru**) on AuNPs has been demonstrated for the first time in aqueous solution. Due to the different affinity of the various ligands to the gold surface two synthesis strategies have been applied. Phase transfer reaction and conjugation result in very uniform, homogeneous and long term stable AuNPs. In order to analyze the special optical and chemical properties arising from the functional nanoparticle–molecular interface, Raman spectroscopic methods have been employed. **N749**, **N719** and **Z907** are bound to AuNPs via the isothiocyanate ligand as concluded from the surface-enhanced Raman scattering (SERS) study. The dyes' fully conjugated electronic structure and therefore also their photochemical properties are preserved, since almost no spectral changes were detected when comparing resonance Raman (RR) of the dyes to SERS spectra of the dyes adsorbed on the surface of AuNPs.

In the case of **Ru**, a well-studied photoactive complex, the comparison between RR and SERS spectra provides evidence that the electronic structure of this ruthenium complex might be slightly changed upon anchoring to AuNPs. However, this issue needs to be further clarified. This and an analysis of a possible catalytic activity of **Ru** functionalized gold nanoparticles will be the subject of future studies.

The synthesis of ruthenium dye modified gold nanoparticles in watery environment opens the door to designing nanoparticles of unique photochemical properties. Both, the gold nanoparticles and the stabilizing agent can be independently investigated and modified at a molecular level in order to improve potential charge transfer reactions. If the applied synthesis concepts can be transferred to different transition metal colloids of known reactivity or catalytic activity, numerous new applications in the fields of catalysis, electronics, nanotechnology and material science can be addressed.

Acknowledgements

This work was supported by the Studienstiftung des deutschen Volkes, the Fonds der Chemischen Industrie and the Thüringer Ministerium für Bildung, Wissenschaft und Kultur (Grant No. B 514-09049, PhotoMIC). The authors are thankful to Franka Jahn for the TEM measurements.

References

- D. G. Schmid, *Nanoparticles: from theory to application*, Wiley-VCH, 2004.
- A.-I. Henry, J. M. Bingham, E. Ringe, L. D. Marks, G. C. Schatz and R. P. Van Duyne, Correlated Structure and Optical Property Studies of Plasmonic Nanoparticles, *J. Phys. Chem. C*, 2011, **115**(19), 9291–9305.
- H. M. Chen and R.-S. Liu, Architecture of Metallic Nanostructures: Synthesis Strategy and Specific Applications, *J. Phys. Chem. C*, 2011, **115**(9), 3513–3527.
- Y. Xia, Y. Xiong, B. Lim and S. E. Skrabalak, Shape-Controlled Synthesis of Metal Nanocrystals: Simple Chemistry Meets Complex Physics?, *Angew. Chem., Int. Ed.*, 2008, **48**(1), 60–103.
- G. Cao and C. J. Brinker, *Annual review of nano research*, World Scientific, 2008.
- S. Thomas, *Recent Advances in Polymer Nanocomposites: Synthesis and Characterization*, Brill, 2010.
- M.-C. Daniel and D. Astruc, Gold Nanoparticles: Assembly, Supramolecular Chemistry, Quantum-Size-Related Properties, and Applications toward Biology, Catalysis, and Nanotechnology, *Chem. Rev.*, 2004, **104**(1), 293–346.
- I. Pastoriza-Santos and L. M. Liz-Marzán, Colloidal silver nanoplates. State of the art and future challenges, *J. Mater. Chem.*, 2008, **18**, 1724.
- M. Grzelczak, J. Pérez-Juste, P. Mulvaney and L. M. Liz-Marzán, Shape control in gold nanoparticle synthesis, *Chem. Soc. Rev.*, 2008, **37**, 1783.
- H. Oikawa, T. Onodera, A. Masuhara, H. Kasai and H. Nakanishi, New Class Materials of Organic-Inorganic Hybridized Nanocrystals/Nanoparticles, and Their Assembled Micro- and Nano-Structure Toward Photonics, in *Polymer Materials*, vol. **231**, K.-S. Lee and S. Kobayashi, ed., Berlin, Heidelberg: Springer Berlin Heidelberg, 2009, pp. 147–190.
- C. Minelli, S. B. Lowe and M. M. Stevens, Engineering Nanocomposite Materials for Cancer Therapy, *Small*, 2010, **6**(21), 2336–2357.
- D. R. Cooper and J. L. Nadeau, Nanotechnology for in vitro neuroscience, *Nanoscale*, 2009, **1**, 183.
- A. Csaki, T. Schneider, J. Wirth, N. Jahr, A. Steinbrück, O. Stranik, F. Garwe, R. Müller and W. Fritzsche, Molecular plasmonics: light meets molecules at the nanoscale, *Philos. Trans. R. Soc. London, Ser. A*, 2011, **369**(1950), 3483–3496.
- M. Brust, M. Walker, D. Bethell, D. J. Schiffrin and R. Whyman, Synthesis of thiol-derivatised gold nanoparticles in a two-phase Liquid–Liquid system, *J. Chem. Soc., Chem. Commun.*, 1994(7), 801.
- L. M. Liz-Marzán, M. Giersig and P. Mulvaney, Synthesis of Nanosized Gold-Silica Core-Shell Particles, *Langmuir*, 1996, **12**(18), 4329–4335.
- A. Moores, F. Goettmann, C. Sanchez and P. Le Floch, Phosphinine stabilised gold nanoparticles; synthesis and immobilisation on mesoporous materials, *Chem. Commun.*, 2004, 2842.
- J. C. Rubim, Surface-Enhanced Raman Spectroscopic (SERS and FT-SERS) Investigation of the Complex Ion [Fe₂(CN)₁₀L]⁶⁻ (L = 4,4'-Bipyridine and Pyrazine) Adsorbed on Silver and Gold Electrodes, *J. Phys. Chem.*, 1995, **99**(1), 345–355.
- T. Huang and R. W. Murray, Quenching of [Ru(bpy)₃]²⁺ Fluorescence by Binding to Au Nanoparticles, *Langmuir*, 2002, **18**(18), 7077–7081.
- P. Corio, G. F. S. Andrade, I. C. N. Diógenes, I. S. Moreira, F. C. Nart and M. L. A. Temperini, Characterization of the [Ru(CN)₅(pyS)]⁴⁻ ion complex adsorbed on gold, silver and copper substrates by surface-enhanced Raman spectroscopy, *J. Electroanal. Chem.*, 2002, **520**(1–2), 40–46.
- C. R. Mayer, E. Dumas and F. Sécheresse, Size controlled formation of silver nanoparticles by direct bonding of ruthenium complexes bearing a terminal mono- or bi-pyridyl group, *Chem. Commun.*, 2005(3), 345.
- A. J. Hallett, P. Christian, J. E. Jones and S. J. A. Pope, Luminescent, water-soluble gold nanoparticles functionalised with ³MLCT emitting ruthenium complexes, *Chem. Commun.*, 2009(28), 4278.
- A. Kotiaho, Photoinduced Charge and Energy Transfer in Phthalocyanine-Functionalized Gold Nanoparticles, *J. Phys. Chem. C*, 2010, **114**(1), 162–168.
- B. O'Regan and M. Grätzel, A low-cost, high-efficiency solar cell based on dye-sensitized colloidal TiO₂ films, *Nature*, 1991, **353**(6346), 737–740.
- L. M. Peter, The Grätzel Cell: Where Next?, *J. Phys. Chem. Lett.*, 2011, **2**(15), 1861–1867.
- A. Listorti, B. O'Regan and J. R. Durrant, Electron Transfer Dynamics in Dye-Sensitized Solar Cells, *Chem. Mater.*, 2011, **23**(15), 3381–3399.
- M. Grätzel, Solar Energy Conversion by Dye-Sensitized Photovoltaic Cells, *Inorg. Chem.*, 2005, **44**(20), 6841–6851.
- G. Benkő, J. Kallioinen, J. E. I. Korppi-Tommola, A. P. Yartsev and V. Sundström, Photoinduced Ultrafast Dye-to-Semiconductor Electron Injection from Nonthermalized and Thermalized Donor States, *J. Am. Chem. Soc.*, 2002, **124**(3), 489–493.

- 28 C. Pérez León, L. Kador, B. Peng and M. Thelakkat, Influence of the Solvent on the Surface-Enhanced Raman Spectra of Ruthenium(II) Bipyridyl Complexes, *J. Phys. Chem. B*, 2005, **109**(12), 5783–5789.
- 29 S. Rau, B. Schäfer, D. Gleich, E. Anders, M. Rudolph, M. Friedrich, H. Görls, W. Henry and J. G. Vos, A Supramolecular Photocatalyst for the Production of Hydrogen and the Selective Hydrogenation of Tolane, *Angew. Chem., Int. Ed.*, 2006, **45**(37), 6215–6218.
- 30 S. Tschierlei, M. Karnahl, M. Presselt, B. Dietzek, J. Guthmüller, L. González, M. Schmitt, S. Rau and J. Popp, Photochemical Fate: The First Step Determines Efficiency of H₂ Formation with a Supramolecular Photocatalyst, *Angew. Chem., Int. Ed.*, 2010, **49**(23), 3981–3984.
- 31 S. Tschierlei, B. Dietzek, M. Karnahl, S. Rau, F. M. MacDonnell, M. Schmitt and J. Popp, Resonance Raman studies of photochemical molecular devices for multielectron storage, *J. Raman Spectrosc.*, 2008, **39**(5), 557–559.
- 32 S. Tschierlei, M. Karnahl, C. Kuhnt, F. W. Heinemann, M. Schmitt, S. Rau, J. Popp and B. Dietzek, Photophysics of an Intramolecular Hydrogen Evolving Ru-tpphz-Pd Photocatalyst, *Chem.–Eur. J.*, 2009, **15**(31), 7678–7688.
- 33 M. Karnahl, S. Tschierlei, C. Kuhnt, B. Dietzek, M. Schmitt, J. Popp, M. Schwalbe, S. Kriek, H. Görls, F. W. Heinemann and S. Rau, Synthesis and characterization of regioselective substituted tetrapyridophenazine ligands and their Ru(II) complexes, *Dalton Trans.*, 2010, **39**(9), 2359.
- 34 M. Karnahl, C. Kuhnt, F. Ma, A. Yartsev, M. Schmitt, B. Dietzek, S. Rau and J. Popp, Tuning of Photocatalytic Hydrogen Production and Photoinduced Intramolecular Electron Transfer Rates by Regioselective Bridging Ligand Substitution, *ChemPhysChem*, 2011, **12**(11), 2101–2109.
- 35 U. Kreibitz, *Optical properties of metal clusters*, Berlin, New York: Springer, 1995.
- 36 D. Ciolla, A. März, R. Böhme, F. Theil, K. Weber, M. Schmitt and J. Popp, Surface enhanced Raman spectroscopy (SERS): progress and trends, *Anal. and Bioanal. Chem.*, 2012, **403**(1), 27–54.
- 37 L. H. Dubois and R. G. Nuzzo, Synthesis, Structure, and Properties of Model Organic Surfaces, *Annu. Rev. Phys. Chem.*, 1992, **43**(1), 437–463.
- 38 Y. Peng, Z. Niu, W. Huang, S. Chen and Z. Li, Surface-Enhanced Raman Scattering Studies of 1,10-Phenanthroline Adsorption and Its Surface Complexes on a Gold Electrode, *J. Phys. Chem. B*, 2005, **109**(21), 10880–10885.
- 39 Y. Sun, S. K. Gray and S. Peng, Surface chemistry: a non-negligible parameter in determining optical properties of small colloidal metal nanoparticles, *Phys. Chem. Chem. Phys.*, 2011, **13**(25), 11814–11826.
- 40 J. Turkevich, P. C. Stevenson and J. Hillier, A study of the nucleation and growth processes in the synthesis of colloidal gold, *Discuss. Faraday Soc.*, 1951, **11**(0), 1951.
- 41 M. Brust, J. Fink, D. Bethell, D. J. Schiffrin and C. Kiely, Synthesis and reactions of functionalised gold nanoparticles, *J. Chem. Soc., Chem. Commun.*, 1995(16), 1655–1656.
- 42 C. R. Mayer, E. Dumas and F. Sécheresse, 1,10-Phenanthroline and 1,10-phenanthroline-terminated ruthenium(II) complex as efficient capping agents to stabilize gold nanoparticles: Application for reversible aqueous organic phase transfer processes, *J. Colloid Interface Sci.*, 2008, **328**(2), 452–457.
- 43 W. Kiefer and H. J. Bernstein, A Cell for Resonance Raman Excitation with Lasers in Liquids, *Appl. Spectrosc.*, 1971, **25**(4), 500–501.
- 44 S. Underwood and P. Mulvaney, Effect of the Solution Refractive Index on the Color of Gold Colloids, *Langmuir*, 1994, **10**(10), 3427–3430.
- 45 G. C. Vougioukalakis, Terpyridine- and 2,6-dipyrazinylpyridine-coordinated ruthenium(II) complexes: Synthesis, characterization and application in TiO₂-based dye-sensitized solar cells, *J. Photochem. Photobiol., A*, 2010, **214**(1), 22–32.
- 46 M. Schwalbe, M. Karnahl, S. Tschierlei, U. Uhlemann, M. Schmitt, B. Dietzek, J. Popp, R. Groake, J. G. Vos and S. Rau, The switch that wouldn't switch—unexpected luminescence from a ruthenium(II)-dppz-complex in water, *Dalton Trans.*, 2010, **39**(11), 2768–2771.

Supplementary Information

Ruthenium dye functionalized gold nanoparticles and their spectral responses

Linda Zedler,¹ Frank Theil,^{1,2} Andrea Csáki², Wolfgang Fritzsche², Sven Rau³, Michael Schmitt,¹ Jürgen Popp^{1,2}, Benjamin Dietzek^{1,2,*}

¹*Institute of Physical Chemistry and Abbe Center of Photonics, Jena, Germany*

²*Institute for Photonic Technology, Jena, Germany*

³*Institute of Inorganic Chemistry, Ulm University, Germany*

* *corresponding author contact: Benjamin.Dietzek@ipht-jena.de*

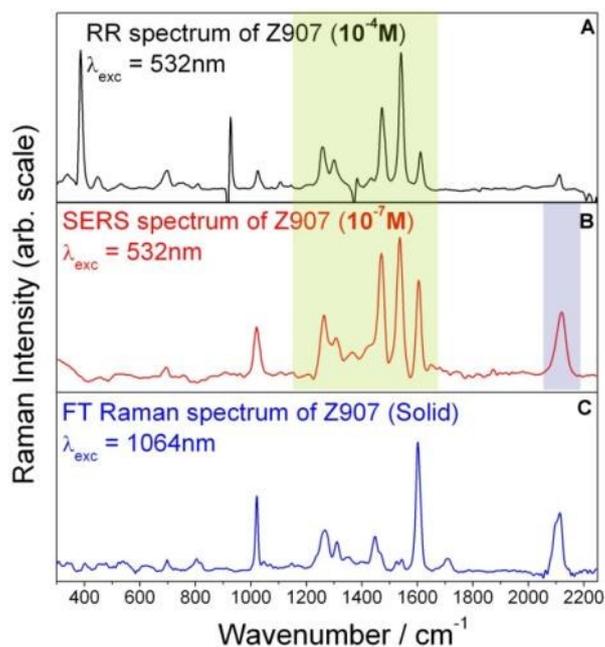


Figure S1: Comparison of RR (A), SERS (B) and Raman (C) spectra of Z907. The charge localization on the bipyridine ligand upon MLCT absorption within the fingerprint spectral region from 1000-1800 cm^{-1} is marked in green while the binding site via the isothiocyanate group at 2100 cm^{-1} is highlighted in blue.

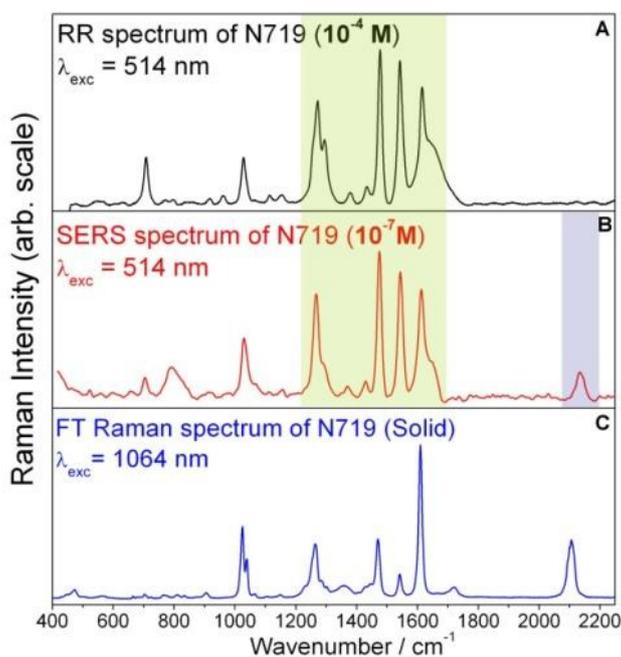


Figure S2: Comparison of RR (A, B), SERS (C) and Raman (D) spectra of N719. The charge localization on the bipyridine ligand upon MLCT absorption within the fingerprint spectral region from 1000-1800 cm^{-1} is marked in green while the binding site via the isothiocyanate group at 2100 cm^{-1} is highlighted in blue.

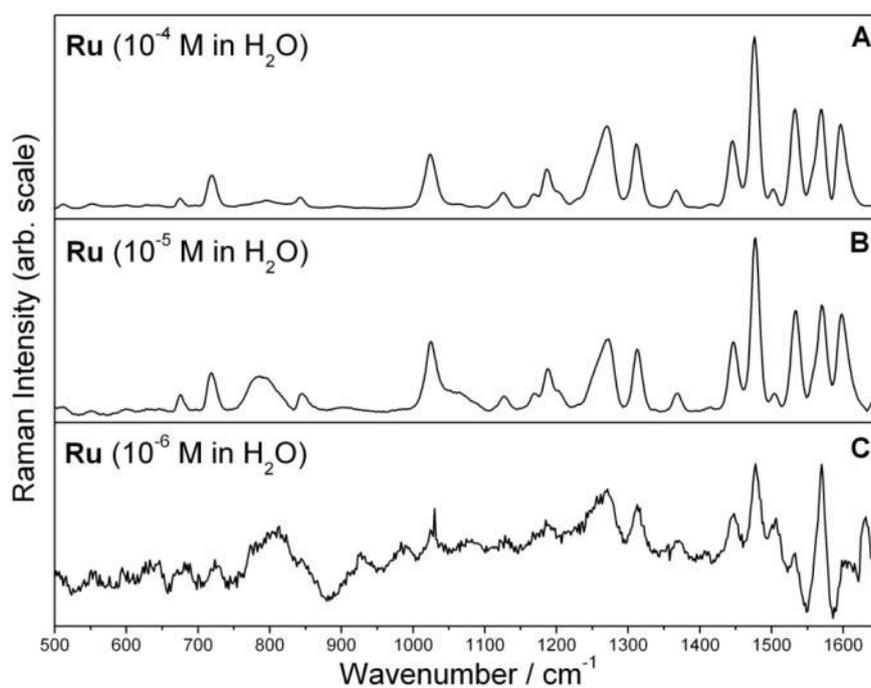


Figure S3: RR spectra of Ru for different concentrations, 10^{-4} M (A), 10^{-5} M (B), 10^{-6} M (C).

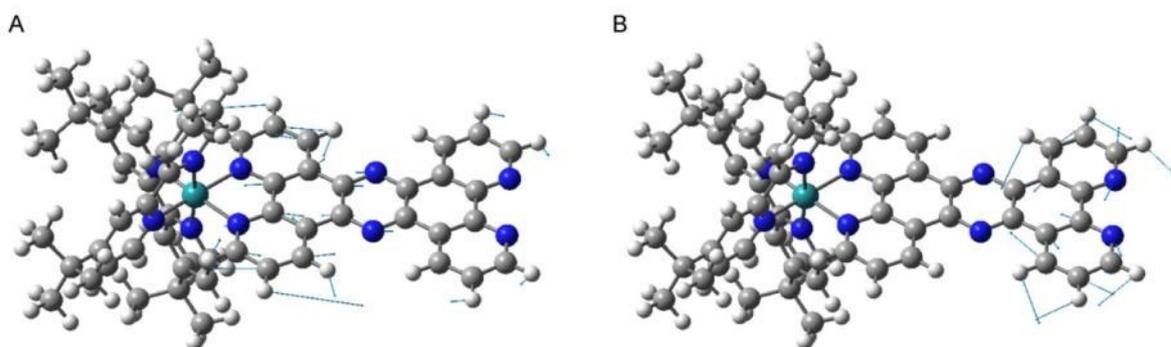


Figure S4: Normal coordinates for the Raman modes 1453 (A) and 1603 cm^{-1} (B). The displacement of the atoms is depicted by arrows.

Autorenschaft der Publikationen

[Grosser et al. Biofouling] Disruption-free Imaging by Raman Spectroscopy Reveals a Chemical Sphere with Antifouling Metabolites around Macroalgae

Grosser, K.; Zedler, L.; Schmitt, M.; Dietzek, B.; Popp, J.; Pohnert, G. *Biofouling* **2012**, *28*, 687–696.

Katharina Grosser	Probenvorbereitung, Durchführung der Resonanz-Raman-Messungen, Auswertung und Diskussion der Daten, Erstellung des Manuskripts
Linda Zedler	Durchführung der Resonanz-Raman-Messungen, Auswertung und Diskussion der Raman-Daten, Beiträge zum Manuskript, Diskussion und Korrektur des Manuskripts
Michael Schmitt	Konzept- und Ergebnisdiskussion, Diskussion und Korrektur des Manuskripts
Benjamin Dietzek	Konzept- und Ergebnisdiskussion, Diskussion und Korrektur des Manuskripts
Jürgen Popp	Konzept- und Ergebnisdiskussion, Diskussion und Korrektur des Manuskripts
Georg Pohnert	Projektleitung und Planung, Konzept- und Ergebnisdiskussion, Korrektur des Manuskripts

[Bode et al. Adv. Mater.] Self-Healing Polymer Coatings Based on Crosslinked Metallosupramolecular Copolymers

Bode, S.; Zedler, L.; Schacher, F. H.; Dietzek, B.; Schmitt, M.; Popp, J.; Hager, M. D.; Schubert, U. S. *Adv. Mater.* **2013**, *25*, 1634–1638.

Stefan Bode	Synthese und Charakterisierung der untersuchten Polymere, Experimente zur Selbstheilung, Auswertung und Diskussion der Daten, Erstellung des Manuskripts
Linda Zedler	Durchführung der Raman-Messungen, Auswertung und Diskussion der Raman-Daten, Beiträge zum Manuskript, Diskussion und Korrektur des Manuskripts
Felix H. Schacher	Konzept- und Ergebnisdiskussion, Diskussion und Korrektur des Manuskripts
Benjamin Dietzek	Projektleitung, Konzept- und Ergebnisdiskussion, Diskussion und Korrektur des Manuskripts
Michael Schmitt	Konzept- und Ergebnisdiskussion, Diskussion und Korrektur des Manuskripts
Jürgen Popp	Konzept- und Ergebnisdiskussion, Diskussion und Korrektur des Manuskripts
Martin D. Hager	Projektleitung, Konzept- und Ergebnisdiskussion, Diskussion und Korrektur des Manuskripts
Ulrich S. Schubert	Konzept- und Ergebnisdiskussion, Diskussion und Korrektur des Manuskripts

[Zedler et al. Mater. Today] Monitoring the Chemistry of Self-Healing by Vibrational Spectroscopy – Current State and Perspectives

Zedler, L.; Hager, M. D.; Schubert, U. S.; Harrington, M. J.; Schmitt, M.; Popp, J.; Dietzek, B. *Mater. Today* **2014**, *17*, 57-69.

Linda Zedler	Erstellung des Manuskripts, Diskussion und Korrektur des Manuskripts
Martin D. Hager	Beiträge zum Manuskript, Diskussion und Korrektur des Manuskripts
Ulrich S. Schubert	Diskussion und Korrektur des Manuskripts
Michael J. Harrington	Beiträge zum Manuskript, Diskussion und Korrektur des Manuskripts
Michael Schmitt	Diskussion und Korrektur des Manuskripts
Jürgen Popp	Konzept- und Ergebnisdiskussion, Diskussion und Korrektur des Manuskripts
Benjamin Dietzek	Projektleitung, Erstellung des Manuskripts, Diskussion und Korrektur des Manuskripts

[Kupfer et al. PCCP] Self-healing Mechanism of Metallopolymers Investigated by QM/MM Simulations and Raman Spectroscopy

Kupfer, S.; Zedler, L.; Guthmuller, J.; Bode, S.; Hager, M. D.; Schubert, U. S.; Popp, J.; Gräfe, S.; Dietzek, B. *Phys. Chem. Chem. Phys.* **2014**, *16*, 12422-12432.

Stephan Kupfer*	Durchführung und Auswertung der DFT-Rechnungen, Ergebnisdiskussion, Erstellung des Manuskripts, Diskussion und Korrektur des Manuskripts
Linda Zedler*	Durchführung der Raman-Messungen, Auswertung und Diskussion der Raman-Daten, Beiträge zum Manuskript, Diskussion und Korrektur des Manuskripts
Julien Guthmuller	Konzept- und Ergebnisdiskussion, Diskussion und Korrektur des Manuskripts
Stefan Bode	Synthese der Polymere, Diskussion und Korrektur des Manuskripts
Martin D. Hager	Diskussion und Korrektur des Manuskripts
Ulrich S. Schubert	Diskussion und Korrektur des Manuskripts
Jürgen Popp	Konzept- und Ergebnisdiskussion, Diskussion und Korrektur des Manuskripts
Stefanie Gräfe	Konzept- und Ergebnisdiskussion, Diskussion und Korrektur des Manuskripts
Benjamin Dietzek	Projektleitung, Konzept- und Ergebnisdiskussion, Diskussion und Korrektur des Manuskripts

*Beide Autoren haben gleichermaßen zur Publikation beigetragen.

[Zedler et al. JPCC] Redox State Sensitive Spectroscopy of the Model Compound $[(\text{H-dcbpy})_2\text{Ru}^{\text{II}}(\text{NCS})_2]^{2-}$ (dcbpy = 2,2'-Bipyridine-4,4'-dicarboxylato)

Zedler, L.; Guthmuller, J.; Rabelo de Moraes, I.; Krieck, S.; Schmitt, M.; Popp, J.; Dietzek, B. *J. Phys. Chem. C* **2013**, *117*, 6669–6677.

Linda Zedler	Durchführung spektroskopischer und elektrochemischer Messungen, Auswertung und Diskussion der Daten, Erstellung des Manuskripts, Diskussion und Korrektur des Manuskripts
Julien Guthmuller	Durchführung und Auswertung der DFT-Rechnungen, Ergebnisdiskussion, Beiträge zum Manuskript, Diskussion und Korrektur des Manuskripts
Inês Rabelo de Moraes	Durchführung elektrochemischer Messungen, Diskussion und Korrektur des Manuskripts
Sven Krieck	Bereitstellung elektrochemischer Geräte, Durchführung elektrochemischer Messungen, Diskussion und Korrektur des Manuskripts
Michael Schmitt	Konzept- und Ergebnisdiskussion, Diskussion und Korrektur des Manuskripts
Jürgen Popp	Konzept- und Ergebnisdiskussion, Diskussion und Korrektur des Manuskripts
Benjamin Dietzek	Projektleitung, Konzept- und Ergebnisdiskussion, Diskussion und Korrektur des Manuskripts

[Zedler et al. Chem. Eur. J.] Trapped in Imidazole - How to Accumulate Multiple Photoelectrons on a Black Absorbing Ruthenium Complex.

Zedler, L.; Kupfer, S.; Rabelo de Moraes, I.; Wächtler, M.; Beckert, R.; Schmitt, M.; Popp, J.; Rau, S.; Dietzek, B. *Chem. Eur. J.* **2014**, *20*, 3793–3799.

Linda Zedler	Durchführung spektroskopischer und elektrochemischer Messungen, Auswertung und Diskussion der Daten, Erstellung des Manuskripts, Diskussion und Korrektur des Manuskripts
Stephan Kupfer	Durchführung und Auswertung der DFT-Rechnungen, Ergebnisdiskussion, Beiträge zum Manuskript, Diskussion und Korrektur des Manuskripts
Inês Rabelo de Moraes	Durchführung und Auswertung elektrochemischer Messungen, Diskussion und Korrektur des Manuskripts
Maria Wächtler	Diskussion und Korrektur des Manuskripts
Rainer Beckert	Synthese der Liganden, Konzept- und Ergebnisdiskussion, Diskussion und Korrektur des Manuskripts
Michael Schmitt	Konzept- und Ergebnisdiskussion, Diskussion und Korrektur des Manuskripts
Jürgen Popp	Konzept- und Ergebnisdiskussion, Diskussion und Korrektur des Manuskripts
Sven Rau	Synthese der Komplexe, Diskussion und Korrektur des Manuskripts
Benjamin Dietzek	Projektleitung, Konzept- und Ergebnisdiskussion, Diskussion und Korrektur des Manuskripts

[Zedler et al. Chem. Comm.] Resonance-Raman Spectro-Electrochemistry of Intermediates in Molecular Artificial Photosynthesis of Bimetallic Complexes

Zedler, L.; Guthmuller, J.; Rabelo de Moraes, I.; Kupfer, S.; Kriek, S.; Schmitt, M.; Popp, J.; Rau, S.; Dietzek, B. *Chem. Commun.* **2014**, *50*, 5227-5229.

Linda Zedler	Durchführung spektroskopischer und elektrochemischer Messungen, Auswertung und Diskussion der Daten, Erstellung des Manuskripts, Diskussion und Korrektur des Manuskripts
Julien Guthmuller	Durchführung und Auswertung der DFT-Rechnungen, Ergebnisdiskussion, Beiträge zum Manuskript, Diskussion und Korrektur des Manuskripts
Inês Rabelo de Moraes	Durchführung und Auswertung elektrochemischer Messungen, Diskussion und Korrektur des Manuskripts
Stephan Kupfer	Konzept- und Ergebnisdiskussion, Diskussion und Korrektur des Manuskripts
Sven Kriek	Bereitstellung elektrochemischer Geräte, Durchführung elektrochemischer Messungen, Diskussion und Korrektur des Manuskripts
Michael Schmitt	Konzept- und Ergebnisdiskussion, Diskussion und Korrektur des Manuskripts
Jürgen Popp	Konzept- und Ergebnisdiskussion, Diskussion und Korrektur des Manuskripts
Sven Rau	Synthese der Komplexe, Diskussion und Korrektur des Manuskripts
Benjamin Dietzek	Projektleitung, Konzept- und Ergebnisdiskussion, Diskussion und Korrektur des Manuskripts

[Zedler et al. RSC Adv.] Ruthenium Dye Functionalized Gold Nanoparticles and Their Spectral Responses

Zedler, L.; Theil, F.; Csáki, A.; Fritzsche, W.; Rau, S.; Schmitt, M.; Popp, J.; Dietzek, B. *RSC Adv.* **2012**, *2*, 4463–4471.

Linda Zedler	Synthese der Nanopartikel, Durchführung spektroskopischer Messungen, Auswertung und Diskussion der Daten, Erstellung des Manuskripts, Diskussion und Korrektur des Manuskripts
Frank Theil	Synthese der Nanopartikel, Beiträge zum Manuskript, Diskussion und Korrektur des Manuskripts
Andrea Csáki	Konzept- und Ergebnisdiskussion, Diskussion und Korrektur des Manuskripts
Wolfgang Fritzsche	Konzept- und Ergebnisdiskussion, Diskussion und Korrektur des Manuskripts
Sven Rau	Synthese von Ru, Diskussion und Korrektur des Manuskripts
Michael Schmitt	Konzept- und Ergebnisdiskussion, Diskussion und Korrektur des Manuskripts
Jürgen Popp	Konzept- und Ergebnisdiskussion, Diskussion und Korrektur des Manuskripts
Benjamin Dietzek	Projektleitung, Konzept- und Ergebnisdiskussion, Diskussion und Korrektur des Manuskripts

Hiermit bestätige ich die korrekte Dokumentation der Autorenschaft der oben aufgeführten Publikationen.

Prof. Dr. Jürgen Popp

Veröffentlichungen

Veröffentlichungen in referierten Zeitschriften

- (1) Zedler, L.; Kupfer, S.; Rabelo de Moraes, I.; Wächtler, M.; Beckert, R.; Schmitt, M.; Popp, J.; Rau, S.; Dietzek, B. Trapped in Imidazole - How to Accumulate Multiple Photoelectrons on a Black Absorbing Ruthenium Complex. *Chem. Eur. J.* **2014**, *20*, 3793–3799.
- (2) Zedler, L.; Guthmuller, J.; Rabelo de Moraes, I.; Kupfer, S.; Kriek, S.; Schmitt, M.; Popp, J.; Rau, S.; Dietzek, B. Resonance-Raman Spectro-Electrochemistry of Intermediates in Molecular Artificial Photosynthesis of Bimetallic Complexes. *Chem. Commun.* **2014**, *50*, 5227-5229.
- (3) Kupfer, S.; Zedler, L.; Guthmuller, J.; Bode, S.; Hager, M. D.; Schubert, U. S.; Popp, J.; Gräfe, S.; Dietzek, B. Self-Healing Mechanism of Metallopolymers Investigated by QM/MM Simulations and Raman Spectroscopy. *Phys. Chem. Chem. Phys.* **2014**, *16*, 12422-12432.
- (4) Zedler, L.; Hager, M. D.; Schubert, U. S.; Harrington, M. J.; Schmitt, M.; Popp, J.; Dietzek, B. Monitoring the Chemistry of Self-Healing by Vibrational Spectroscopy – Current State and Perspectives. *Mater. Today* **2014**, *17*, 57-69.
- (5) Bode, S.; Zedler, L.; Schacher, F. H.; Dietzek, B.; Schmitt, M.; Popp, J.; Hager, M. D.; Schubert, U. S. Self-Healing Polymer Coatings Based on Crosslinked Metallosupramolecular Copolymers. *Adv. Mater.* **2013**, *25*, 1634–1638.
- (6) Zedler, L.; Guthmuller, J.; Rabelo de Moraes, I.; Kriek, S.; Schmitt, M.; Popp, J.; Dietzek, B. Redox State Sensitive Spectroscopy of the Model Compound [(H-dcbpy)₂Ru^{II}(NCS)₂]²⁻ (dcbpy = 2,2'-Bipyridine-4,4'-Dicarboxylato). *J. Phys. Chem. C* **2013**, *117*, 6669–6677.
- (7) Theil, F.; Zedler, L.; März, A.; Xie, W.; Csáki, A.; Fritzsche, W.; Cialla, D.; Schmitt, M.; Popp, J.; Dietzek, B. Evidence for SERRS Enhancement in the Spectra of Ruthenium Dye–Metal Nanoparticle Conjugates. *J. Phys. Chem. C* **2013**, *117*, 1121–1129.
- (8) Grosser, K.; Zedler, L.; Schmitt, M.; Dietzek, B.; Popp, J.; Pohnert, G. Disruption-Free Imaging by Raman Spectroscopy Reveals a Chemical Sphere with Antifouling Metabolites around Macroalgae. *Biofouling* **2012**, *28*, 687–696.
- (9) Zedler, L.; Theil, F.; Csáki, A.; Fritzsche, W.; Rau, S.; Schmitt, M.; Popp, J.; Dietzek, B. Ruthenium Dye Functionalized Gold Nanoparticles and Their Spectral Responses. *RSC Adv.* **2012**, *2*, 4463–4471.
- (10) Frosch, T.; Koncarevic, S.; Zedler, L.; Schmitt, M.; Schenzel, K.; Becker, K.; Popp, J. In Situ Localization and Structural Analysis of the Malaria Pigment Hemozoin. *J. Phys. Chem. B* **2007**, *111*, 11047–11056.
- (11) Kirchner, N.; Zedler, L.; Mayerhöfer, T. G.; Mohr, G. J. Functional Liquid Crystal Films Selectively Recognize Amine Vapours and Simultaneously Change Their Colour. *Chem. Commun.* **2006**, 1512.

Vorträge

1. *Evidence for SERRS enhancement in the spectra of Ru-dye metal nanoparticle conjugates*
112. Hauptversammlung der Deutschen Bunsen-Gesellschaft für Physikalische Chemie (Bunsentagung), 2013, Karlsruhe
F. Theil, L. Zedler, A. März, A. Csáki, W. Fritzsche, W. Xie, M. Schmitt, J. Popp, B. Dietzek
2. *Raman Spectroscopic Investigation of the Interaction of Algae with their Environment* Abbe School of Photonics, Friedrich-Schiller University Jena, 2012, Jena, Germany
L. Zedler, I. Weisflog, K. Grosser, G. Pohnert, M. Schmitt, B. Dietzek, J. Popp
3. *Investigation of the Chemical Sphere of Marine Macroalgae: A Novel Extraction Technique Based on Solid Sorbents*
7th European Conference on Marine Natural Products, 2011, Strömstad, Sweden
K. Grosser, L. Zedler, M. Schmitt, J. Popp, G. Pohnert
4. *Investigation of the Chemical Sphere Around Macroalgae Surfaces*
MICOM - European Student Conference on Microbial Communication, 2011, Jena,
K. Grosser, M. Saha, L. Zedler, M. Remp, F. Weinberger, M. Schmitt, B. Dietzek, J. Popp, G. Pohnert

Posterpräsentationen

1. *Spectroscopic investigations on the molecular mechanism of self-healing in polymer coatings bearing reversibly switchable metal-terpyridine complexes*
20th International Symposium on the Photophysics and Photochemistry of Coordination Compounds (ISPPCC), 2013, Michigan, USA
B. Dietzek, L. Zedler, S. Kupfer, M. Hager, U. S. Schubert, J. Popp,
2. *Redox-State Sensitive Resonance Raman Spectroscopy of Ru-polypyridine-based Complexes for Solar-Energy Conversion*
20th International Symposium on the Photophysics and Photochemistry of Coordination Compounds (ISPPCC), 2013, Michigan, USA
B. Dietzek, L. Zedler, I. Rabelo de Moraes, J. Popp, J. Guthmuller, S. Rau

3. *Self-Healing Polymer Coatings Based on Crosslinked Metallosupramolecular Copolymers*
Meeting of the GDCh-Division of Macromolecular Chemistry - Smart Polymers, 2013, Mainz
S. Bode, L. Zedler, F. H. Schacher, B. Dietzek, M. Schmitt, J. Popp, M. D. Hager, U. S. Schubert
4. *Evidence for SERRS enhancement in the spectra of Ru-dye metal nanoparticle conjugates*
Molecular Plasmonics, 2013, Jena
F. Theil, L. Zedler, A. März, A. Csáki, W. Fritzsche, W. Xie, M. Schmitt, J. Popp, B. Dietzek
5. *Spectroscopic Characterization of Ruthenium Dye Functionalized Gold Nanoparticles*
23rd International Conference on Raman Spectroscopy, 2012, Bangalore, India
L. Zedler, F. Theil, A. Csaki, W. Fritzsche, S. Rau, W. Xie, S. Schlücker, M. Schmitt, J. Popp, B. Dietzek
6. *Investigation of the Chemical Sphere around Macroalgal Surfaces by Means of Raman Spectroscopy*
23rd International Conference on Raman Spectroscopy, 2012, Bangalore, India
L. Zedler, K. Grosser, G. Pohnert, M. Schmitt, B. Dietzek, J. Popp
7. *Investigation of the chemical sphere around macroalgae using resonance Raman spectroscopy*
11th Symposium of the International Max Planck Research School (IMPRS), 2012, Dornburg
K. Grosser, L. Zedler, M. Schmitt, B. Dietzek, J. Popp, G. Pohnert
8. *Metal Nanoparticle - Ru-dye conjugates and their characterization in ultra small sample volumes*
111. Hauptversammlung der Deutschen Bunsen-Gesellschaft für Physikalische Chemie (Bunsentagung), 2012, Leipzig
F. Theil, L. Zedler, A. März, A. Csáki, W. Fritzsche, W. Xie, M. Schmitt, J. Popp, B. Dietzek
9. *Metal Nanoparticle - Ru-dye conjugates and their characterization in ultra small sample volumes*
Manfred-Eigen-Gespräche, 2012, Jena
F. Theil, L. Zedler, A. März, A. Csáki, W. Fritzsche, W. Xie, M. Schmitt, J. Popp, B. Dietzek

10. *Metal Nanoparticle - Ru-dye conjugates and their characterization in ultra small sample volumes*
International Conference on Metamaterials and Dissemination Workshop, 2012, Jena
F. Theil, L. Zedler, A. März, A. Csáki, W. Fritzsche, W. Xie, M. Schmitt, J. Popp, B. Dietzek
11. *Synthesis and Spectroscopic Characterization of Ru-Complexes Immobilized on Gold Nanoparticles*
110. Hauptversammlung der Deutschen Bunsen-Gesellschaft für Physikalische Chemie (Bunsentagung), 2011, Berlin
L. Zedler, F. Theil, B. Dietzek, A. Csaki, W. Fritzsche, M. Schmitt, J. Popp
12. *Synthesis and Spectroscopic Characterization of Photoactive Ru-Complexes Immobilized on Catalytic Active Gold Nanoparticles*
Molecular Plasmonics, 2011, Jena
L. Zedler, F. Theil, B. Dietzek, A. Csaki, W. Fritzsche, M. Schmitt, J. Popp
13. *In-Vitro and In-Vivo Raman Spectroscopic Investigations on Heme and Heme Degradation Products*
21th International Conference on Raman Spectroscopy, 2008, London, England
L. Zedler, S.H. Heinemann, D. Imhof, M. Schmitt, J. Popp

Danksagung

An erster Stelle möchte ich mich bei Prof. Dr. Jürgen Popp bedanken für die Möglichkeit meine Dissertation in seiner Arbeitsgruppe anzufertigen.

Mein besonderer Dank gilt Prof. Dr. Benjamin Dietzek für die freundliche und unkomplizierte Aufnahme in seine Arbeitsgruppe, für die Überlassung des interessanten und herausfordernden Themas, die Betreuung dieser Arbeit, ständige Gesprächsbereitschaft und die kritische Durchsicht unzähliger Paper-Manuskripte. Prof. Dr. Michael Schmitt danke ich vielmals für die Übernahme der weiteren Betreuung, die freundliche Unterstützung bei der Interpretation der Resonanz-Raman-Ergebnisse und sehr hilfreichen Diskussionen.

Dr. Stephan Kupfer und Dr. Julien Guthmüller danke ich für die Durchführung der DFT-Rechnungen und die Realisierung aller meiner Extrawünsche. Besonders bedanken möchte ich mich bei Stephan für das Korrekturlesen einiger Kapitel dieser Arbeit und diverser Paper-Manuskripte, für die vielen konstruktiven Diskussionen über Experiment und Theorie aber auch für die Nervennahrung. Prof. Dr. Stefanie Gräfe für das Korrekturlesen dieser Arbeit.

Katharina Grosser und Stefan Bode sei gedankt für die unkomplizierte und angenehme Zusammenarbeit in den kleineren Nebenprojekten.

Dr. Sven Kriek danke ich für die Einführung in die Elektrochemie und das Klären unzähliger Fragen in diesem Zusammenhang, der unkomplizierten Bereitstellung der Messgeräte, aber auch für den vielen leckeren Gräfe-Kuchen und die netten Kaffeekränzchen am IAAC. Ich danke Inês für ihre experimentelle Unterstützung in der komplizierten Welt der Elektrochemie und für ihre wochenlange unterhaltsame Gesellschaft im dunklen Laserlabor.

Auch allen anderen aktiven und ehemaligen Kollegen der AG Dietzek und AG Popp gilt mein Dank für das gute Arbeitsklima und jegliche fachliche und persönliche Unterstützung im Verlauf dieser Arbeit.

Conny, dir danke ich für die schöne, lustige und vor allem ruhige Atmosphäre in unserem Büro.

Ich danke meinem Diplomanden Frank Theil für die gute Zusammenarbeit auf dem Gebiet der Nanopartikelsynthese. Joachim Kübel danke ich für seine geduldige und tatkräftige Unterstützung im Industrieprojekt. Allen meinen Forschungspraktikanten sei an dieser Stelle auch gedankt.

Weiterhin möchte ich mich bei allen Mitarbeiterinnen und Mitarbeitern des Instituts für physikalische Chemie bedanken, auf deren Unterstützung ich stets zählen konnte. Ganz besonders möchte ich Anna Schmidt für ihre ständige Hilfsbereitschaft, ihre Ausdauer bei den Extraktionsexperimenten für das Industrieprojekt und ihre Herzlichkeit danken. Der Werkstatt am ipht und IPC sei gedankt für die schnelle, effektive und professionelle Umsetzung aller Aufträge.

Besonders herzlich danke ich meinen Eltern und meiner Familie für ihre Liebe, Geduld und ihren Beistand. Danke für euer Verständnis dass ich mich in manchen Zeiten selten hab blicken lassen und dass ihr immer an mich geglaubt habt.

Tobias, dir danke ich für alles andere, den nie nachlassenden Rückhalt und deine großartige Unterstützung in allen Lebenslagen. Ohne deine geduldige Hilfe wäre die Realisierung dieser Arbeit in dem zeitlichen Rahmen und unter diesen erfreulichen Umständen nicht möglich gewesen. Danke, dass es dich gibt.

Selbständigkeitserklärung

Ich erkläre,

dass mir die geltende Promotionsordnung der Fakultät bekannt ist;

dass ich die Dissertation selbst angefertigt und alle von mir benutzten Hilfsmittel, persönlichen Mitteilungen und Quellen in meiner Arbeit angegeben habe;

dass mich folgende Personen bei der Auswertung des Materials sowie bei der Herstellung des Manuskripts unterstützt haben: siehe Danksagung

dass die Hilfe eines Promotionsberaters nicht in Anspruch genommen wurde und dass Dritte weder unmittelbar noch mittelbar geldwerte Leistungen von mir für Arbeiten erhalten haben, die im Zusammenhang mit dem Inhalt der vorgelegten Dissertation stehen;

dass ich die Dissertation noch nicht als Prüfungsarbeit für eine staatliche oder andere wissenschaftliche Prüfung eingereicht habe;

dass ich nicht die gleiche, in wesentlichen Teilen ähnliche oder eine andere Abhandlung bei einer anderen Hochschule als Dissertation eingereicht habe.

Jena, den

Linda Zedler